

**Third Edition**



# **Steels**

**Microstructure and Properties**

**H.K.D.H. Bhadeshia  
and R.W.K. Honeycombe**



# Steels

*This page intentionally left blank*

# Steels

## Microstructure and Properties

*Third edition*

**H. K. D. H. Bhadeshia**

Professor of Physical Metallurgy  
University of Cambridge

and

Adjunct Professor of Computational Metallurgy  
Graduate Institute of Ferrous Technology, POSTECH

and

**Sir Robert Honeycombe**

Emeritus Goldsmiths' Professor of Metallurgy  
University of Cambridge



ELSEVIER

AMSTERDAM • BOSTON • HEIDELBERG • LONDON • NEW YORK • OXFORD  
PARIS • SAN DIEGO • SAN FRANCISCO • SINGAPORE • SYDNEY • TOKYO

Butterworth-Heinemann is an imprint of Elsevier



Butterworth-Heinemann is an imprint of Elsevier  
Linacre House, Jordan Hill, Oxford OX2 8DP, UK  
30 Corporate Drive, Suite 400, Burlington, MA 01803, USA

First edition 1981  
Second edition 1995  
Reprinted 1976, 2000  
Transferred to digital printing 2003  
Third edition 2006

Copyright © 2006, R. W. K. Honeycombe and H. K. D. H. Bhadeshia. Published by Elsevier Ltd.  
All rights reserved

No part of this publication may be reproduced, stored in a retrieval system or transmitted in any form or by any means electronic, mechanical, photocopying, recording or otherwise without the prior written permission of the publisher

Permissions may be sought directly from Elsevier's Science & Technology Rights Department in Oxford, UK: phone (+44) (0) 1865 843830; fax (+44) (0) 1865 853333; email: [permissions@elsevier.com](mailto:permissions@elsevier.com). Alternatively you can submit your request online by visiting the Elsevier web site at <http://elsevier.com/locate/permissions>, and selecting *Obtaining permission to use Elsevier material*

#### Notice

No responsibility is assumed by the publisher for any injury and/or damage to persons or property as a matter of products liability, negligence or otherwise, or from any use or operation of any methods, products, instructions or ideas contained in the material herein. Because of rapid advances in the medical sciences, in particular, independent verification of diagnoses and drug dosages should be made

#### British Library Cataloguing in Publication Data

A catalogue record for this book is available from the British Library

#### Library of Congress Cataloguing in Publication Data

A catalog record for this book is available from the Library of Congress

ISBN-13: 978-0-750-68084-4

ISBN-10: 0-7506-8084-9

For information on all Butterworth-Heinemann publications  
visit our website at <http://books.elsevier.com>

#### Cover Images, used with permission

Inset:  $\delta$ -TRIP steel, S. Chatterjee

Background: magnetic field due to a small particle of iron, enclosed in a carbon tube,  
T. Kasama, R. Dunin-Borkowski, K. Koziol and A. H. Windle.

Typeset by Charon Tec Ltd, Chennai, India  
[www.charontec.com](http://www.charontec.com)

Printed and bound in Great Britain

06 07 08 09 10 10 9 8 7 6 5 4 3 2 1

Working together to grow  
libraries in developing countries

[www.elsevier.com](http://www.elsevier.com) | [www.bookaid.org](http://www.bookaid.org) | [www.sabre.org](http://www.sabre.org)

ELSEVIER

BOOK AID  
International

Sabre Foundation

# CONTENTS

---

<i>Preface to the first edition</i>	ix
<i>Preface to the second edition</i>	x
<i>Preface to the third edition</i>	xi
<b>1 Iron and its interstitial solid solutions</b>	<b>1</b>
1.1 Introduction	1
1.2 The allotropes of pure iron	2
1.3 The phase transformation: $\alpha$ - and $\gamma$ -iron	4
1.4 Carbon and nitrogen in solution in $\alpha$ - and $\gamma$ -iron	8
1.5 Some practical aspects	15
Further reading	16
<b>2 The strengthening of iron and its alloys</b>	<b>17</b>
2.1 Introduction	17
2.2 Work hardening	18
2.3 Solid solution strengthening by interstitials	20
2.4 Substitutional solid solution strengthening of iron	27
2.5 Grain size	27
2.6 Dispersion strengthening	32
2.7 An overall view	33
2.8 Some practical aspects	34
2.9 Limits to strength	35
Further reading	38
<b>3 The iron–carbon equilibrium diagram and plain carbon steels</b>	<b>39</b>
3.1 The iron–carbon equilibrium diagram	39
3.2 The austenite–ferrite transformation	42
3.3 The austenite–cementite transformation	44
3.4 The kinetics of the $\gamma \rightarrow \alpha$ transformation	45
3.5 The austenite–pearlite reaction	53
3.6 Ferrite–pearlite steels	67
Further reading	69
<b>4 The effects of alloying elements on iron–carbon alloys</b>	<b>71</b>
4.1 The $\gamma$ - and $\alpha$ -phase fields	71
4.2 The distribution of alloying elements in steels	74

4.3	The effect of alloying elements on the kinetics of the $\gamma/\alpha$ transformation	77
4.4	Structural changes resulting from alloying additions	84
4.5	Transformation diagrams for alloy steels	91
	Further reading	92
<b>5</b>	<b>Formation of martensite</b>	<b>95</b>
5.1	Introduction	95
5.2	General characteristics	95
5.3	The crystal structure of martensite	100
5.4	The crystallography of martensitic transformations	103
5.5	The morphology of ferrous martensites	106
5.6	Kinetics of transformation to martensite	112
5.7	The strength of martensite	120
5.8	Shape memory effect	126
	Further reading	127
<b>6</b>	<b>The bainite reaction</b>	<b>129</b>
6.1	Introduction	129
6.2	Upper bainite (temperature range 550–400°C)	129
6.3	Lower bainite (temperature range 400–250°C)	132
6.4	The shape change	135
6.5	Carbon in bainite	135
6.6	Kinetics	139
6.7	The transition from upper to lower bainite	143
6.8	Granular bainite	144
6.9	Tempering of bainite	145
6.10	Role of alloying elements	146
6.11	Use of bainitic steels	147
6.12	Nanostructured bainite	152
	Further reading	154
<b>7</b>	<b>Acicular ferrite</b>	<b>155</b>
7.1	Introduction	155
7.2	Microstructure	155
7.3	Mechanism of transformation	157
7.4	The inclusions as heterogeneous nucleation sites	161
7.5	Nucleation of acicular ferrite	162
7.6	Summary	164
	Further reading	164
<b>8</b>	<b>The heat treatment of steels: hardenability</b>	<b>167</b>
8.1	Introduction	167
8.2	Use of <i>TTT</i> and continuous cooling diagrams	168

---

8.3	Hardenability testing	170
8.4	Effect of grain size and chemical composition on hardenability	176
8.5	Hardenability and heat treatment	177
8.6	Quenching stresses and quench cracking	179
	Further reading	181
<b>9</b>	<b>The tempering of martensite</b>	<b>183</b>
9.1	Introduction	183
9.2	Tempering of plain carbon steels	184
9.3	Mechanical properties of tempered plain carbon steels	190
9.4	Tempering of alloy steels	191
9.5	Maraging steels	207
	Further reading	207
<b>10</b>	<b>Thermomechanical treatment of steels</b>	<b>209</b>
10.1	Introduction	209
10.2	Controlled rolling of low-alloy steels	210
10.3	Dual-phase steels	220
10.4	TRIP-assisted steels	223
10.5	TWIP steels	229
10.6	Industrial steels subjected to thermomechanical treatments	231
	Further reading	233
<b>11</b>	<b>The embrittlement and fracture of steels</b>	<b>235</b>
11.1	Introduction	235
11.2	Cleavage fracture in iron and steel	235
11.3	Factors influencing the onset of cleavage fracture	237
11.4	Criterion for the ductile/brittle transition	240
11.5	Practical aspects of brittle fracture	243
11.6	Ductile or fibrous fracture	245
11.7	Intergranular embrittlement	252
	Further reading	258
<b>12</b>	<b>Stainless steel</b>	<b>259</b>
12.1	Introduction	259
12.2	The iron–chromium–nickel system	259
12.3	Chromium carbide in Cr–Ni austenitic steels	264
12.4	Precipitation of niobium and titanium carbides	267
12.5	Nitrides in austenitic steels	270
12.6	Intermetallic precipitation in austenite	270
12.7	Austenitic steels in practical applications	273



12.8	Duplex and ferritic stainless steels	274
12.9	Mechanically alloyed stainless steels	278
12.10	The transformation of metastable austenite	281
	Further reading	286
<b>13</b>	<b>Weld microstructures</b>	<b>287</b>
13.1	Introduction	287
13.2	The fusion zone	287
13.3	The HAZ	298
	Further reading	306
<b>14</b>	<b>Modelling of microstructure and properties</b>	<b>307</b>
14.1	Introduction	307
14.2	Example 1: alloy design – high-strength bainitic steel	309
14.3	Example 2: mechanical properties of mixed microstructures	315
14.4	Methods	321
14.5	Kinetics	326
14.6	Finite element method	329
14.7	Neural networks	330
14.8	Defining characteristics of models	333
	Further reading	334
	<i>Index</i>	335

# PREFACE TO THE FIRST EDITION

---

In this book, I have attempted to outline the principles which determine the microstructures of steels and through these the mechanical properties. At a time when our metallographic techniques are reaching almost to atomic resolution, it is essential to emphasize structure on the finest scale, especially because mechanical properties are sensitive to changes at this level. While this is not a book on the selection of steels for different uses, I have tried to include sufficient information to describe how broad categories of steels fulfil practical requirements. However, the main thrust of the book is to examine analytically how the  $\gamma/\alpha$  phase transformation is utilized, and to explain the many effects that non-metallic and metallic alloying elements have, both on this transformation and on other phenomena.

This book is written with the needs of metallurgists, materials scientists and engineers in mind, and should be useful not only in the later years of the first degree and diploma courses but also in postgraduate courses. An elementary knowledge of materials science, metallography, crystallography and physics is assumed.

I am indebted to several colleagues for their interest in this book, particularly Dr D. V. Edmonds, who kindly read the manuscript, Dr P. R. Howell, Dr B. Muddle and Dr H. K. D. H. Bhadeshia, who made helpful comments on various sections, and numerous other members of my research group who have provided illustrations. I wish also to thank my colleagues in different countries for their kind permission to use diagrams from their work. I am also very grateful to Mr S. D. Charter for his careful preparation of the line diagrams. Finally, my warmest thanks go to Mrs Diana Walker and Miss Rosemary Leach for their careful and dedicated typing of the manuscript.

RWKH  
Cambridge  
1980

# **PREFACE TO THE SECOND EDITION**

---

This new edition retains the basic framework of the original book; however, the opportunity has been taken to introduce several additional chapters dealing with areas which have emerged or increased in significance since the book was first published in 1981. There is now a separate chapter on acicular ferrite which has become a desirable structure in some steels. The control of microstructures during welding is undoubtedly a crucial topic which now requires a chapter, while the modelling of microstructures to achieve optimum properties has emerged as an important approach justifying the inclusion of a further new chapter. The opportunity has also been taken to include a completely revised chapter on bainite transformations.

The overall aim of the book remains to introduce students to the principles determining the microstructures of steels, and through these, the mechanical properties and behaviour in service. Steels remain the most important group of metallic alloys, possessing a very wide range of microstructures and mechanical properties, which will ensure their continued extensive use far into the foreseeable future.

RWKH  
HKDHB  
Cambridge  
1995

# PREFACE TO THE THIRD EDITION

---

Steel has the ability to adapt to changing requirements. This comes from the myriads of ways in which its structure can be influenced by processing and alloying. This is why it is the standard against which emerging materials are compared. Added to this is the commercial success, with output at record levels and a production efficiency which is uncanny. It is pleasing to see how, all over the world, iron and its alloys contribute to improving the quality of life of so many human beings. The technology is so good that most of these people rightly take it for granted.

This new edition captures developments since 1995, e.g., the extremely fine-grained alloys, steels with the ability to abnormally elongate and the properties of minute particles of iron. Questions are posed as to the theoretical limit to the finest crystals that can be manufactured on a large scale. In addition, there are major revisions in the explanations of microstructure, strengthening, kinetics and modelling.

The original aim of this book, to introduce students and technologists to the principles determining the microstructure and properties of iron and its alloys, has remained the guiding principle in the new edition.

HKDHB  
RWKH  
Cambridge  
2006

**Supporting material accompanying this book**

A full set of accompanying exercises and worked solutions for this book are available for teaching purposes.

Please visit <http://www.textbooks.elsevier.com> and follow the registration instructions to access this material, which is intended for use by lecturers and tutors.

The compilation of questions has been designed to stimulate the student to explore the subject within the context of the book.

Each question is accompanied by a complete answer, with the exception of the proposed set of topics for essays. Most of the questions and answers have been developed as a consequence of many years of teaching and have been tested on a variety of undergraduates.



---

# IRON AND ITS INTERSTITIAL SOLID SOLUTIONS

## 1.1 INTRODUCTION

Steel is frequently the ‘gold-standard’ against which emerging structural materials are compared. What is often not realized is that this is a moving standard, with notoriously regular and exciting discoveries being made in the context of iron and its alloys. This is why steel remains the most successful and cost-effective of all materials, with more than a billion tonnes being consumed annually in improving the quality of life. This book attempts to explain why steels continue to take this pre-eminent position, and examines in detail the phenomena whose exploitation enables the desired properties to be achieved.

One reason for the overwhelming dominance of steels is the endless variety of microstructures and properties that can be generated by solid-state transformation and processing. Therefore, in studying steels, it is useful to consider the behaviour of pure iron first, then the iron–carbon alloys, and finally the many complexities that arise when further solutes are added.

Pure iron is not an easy material to produce. It has nevertheless been made with a total impurity content less than 60 parts per million (ppm), of which 10 ppm is accounted for by non-metallic impurities such as carbon, oxygen, sulphur and phosphorus, with the remainder representing metallic impurities. Iron of this purity can be extremely weak when reasonably sized samples are tested: the resolved shear stress of a single crystal at room temperature can be as low as  $10 \text{ MN m}^{-2}$ , while the yield stress of a polycrystalline sample at the same temperature can be well below  $50 \text{ MN m}^{-2}$ . However, the shear strength of small single crystals has been observed to exceed  $19,000 \text{ MN m}^{-2}$  when the size of the sample is reduced to about  $2 \mu\text{m}$ . This is because the chances of finding crystal defects such as dislocations become small as the size of the crystal is reduced. The theoretical shear strength of a perfect crystal of iron is estimated to be about  $21,000 \text{ MN m}^{-2}$ , equivalent to a tensile strength of about  $11,000 \text{ MN m}^{-2}$ .

For comparison purposes the breaking strength of a very small carbon nanotube has been measured to be about  $130,000 \text{ MN m}^{-2}$ ; this number is so astonishing that it has led to exaggerated statements about their potential in structural applications. For example, the tubes are said to be a hundred times stronger than steel; in fact, there is no carbon tube which can match the strength of iron beyond a scale of 2 mm, because of the inevitable defects which arise as the tubes are grown.

The lesson from this is that systems which rely on perfection in order to achieve strength necessarily fail on scaling to engineering dimensions. Since perfection is thermodynamically impossible to achieve in large samples, steels must in practice be made stronger by other means which are insensitive to size. The mechanisms by which the strength can be increased will be discussed – suffice it to state here that it is possible to commercially buy steel with a strength of  $5500 \text{ MN m}^{-2}$ , with sufficient ductility to ensure safe application. Some of the methods by which such impressive combinations of properties are achieved without compromising safety will be discussed, before the wide range of complex structures which determine the properties is dealt with.

## 1.2 THE ALLOTROPE OF PURE IRON

At least three allotropes of iron occur naturally in bulk form, body-centred cubic (bcc,  $\alpha$ , ferrite), face-centred cubic (fcc,  $\gamma$ , austenite) and hexagonal close-packed (hcp,  $\epsilon$ ). The phase  $\beta$  in the alphabetical sequence  $\alpha, \beta, \gamma, \delta \dots$  is missing because the magnetic transition in ferrite was at one time incorrectly thought to be the  $\beta$  allotrope of iron. In fact, there are magnetic transitions in all of the allotropes of iron. The phase diagram for pure iron is illustrated in Fig. 1.1. Each point on any boundary between the phase fields represents an equilibrium state in which two phases can coexist. The *triple point* where the three boundaries intersect represents an equilibrium between all three phases which coexist. It is seen that in pure iron, the hcp form is stable only at very large pressures, consistent with its high density. The best comparison of the relative densities of the phases is made at the triple point where the allotropes are in equilibrium and where the sum of all the volume changes is zero:

$$\left. \begin{aligned} \Delta V(\text{bcc} \rightarrow \text{hcp}) &= -0.34 \\ \Delta V(\text{hcp} \rightarrow \text{ccp}) &= +0.13 \\ \Delta V(\text{ccp} \rightarrow \text{bcc}) &= +0.21 \end{aligned} \right\} \text{ cm}^3 \text{ mol}^{-1}$$

There may exist a fourth natural allotrope in the core of the earth, where the pressure reaches some three million times that at the surface and where the temperature is estimated to be about  $6000^\circ\text{C}$ . The core of the earth is predominantly iron, and consists of a solid inner core surrounded by a liquid outer core. Knowledge of the core is uncertain, but it has been suggested that the crystal structure of the solid core may be double hcp, although calculations which assume pure iron, indicate that the  $\epsilon$ -iron remains the most stable under inner-core conditions.

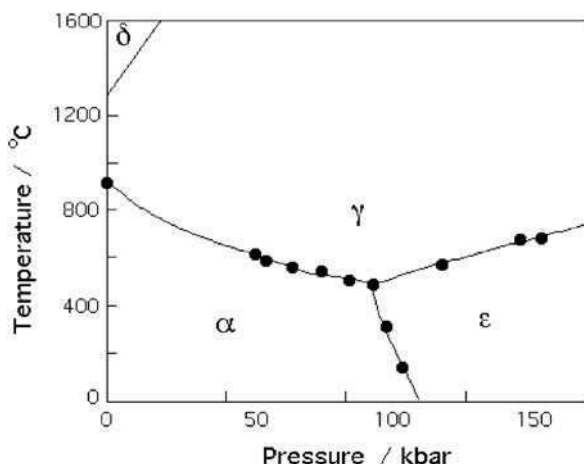


**Fig. I.1** The phase diagram for pure iron (data from Bundy, 1965). The triple point temperature and pressure are 490°C and 110 kbars, respectively.  $\alpha$ ,  $\gamma$  and  $\epsilon$  refer to ferrite, austenite and  $\epsilon$ -iron, respectively.  $\delta$  is simply the higher temperature designation of  $\alpha$ .

### I.2.1 Thin films and isolated particles

There are two further allotropes which can be created in the form of thin films. Face-centred tetragonal iron has been prepared by coherently depositing iron as a thin film on a {1 0 0} plane of a substrate such as copper with which the iron has a mismatch. The position of atoms in the first deposited layer in this case replicates that of the substrate. A few monolayers can be forced into coherency in the plane of the substrate with a corresponding distortion normal to the substrate. This gives the deposit a face-centred tetragonal structure. Growing iron on a misfitting {1 1 1} surface of a fcc substrate leads to trigonal iron.

Very thin films of iron retain their ferromagnetic character, but there are special effects due to the small dimensions. The magnetic moment per atom becomes very large: 3.1 Bohr magnetons compared with 2.2 for bulk  $\alpha$ -iron. This is due to the smaller coordination number for atoms in a thin film. The second effect is that magnetic anisotropy greatly increases for thin films because the spins tend to align normal to the surface. The Curie temperature is greatly reduced, again because of the change in coordination. For a monolayer of iron the temperature is just  $\approx 280^\circ\text{C}$ .

Many classical studies of nucleation theory have been conducted on minute (5–1000 nm) particles of iron where defects responsible for heterogeneous nucleation can be avoided. Such particles have acquired new significance in that they are exploited in the manufacture of carbon nanotubes. The particles are deposited due to the decomposition of ferrocene in chemical mixtures which also contain the ingredients necessary to grow the tubes.



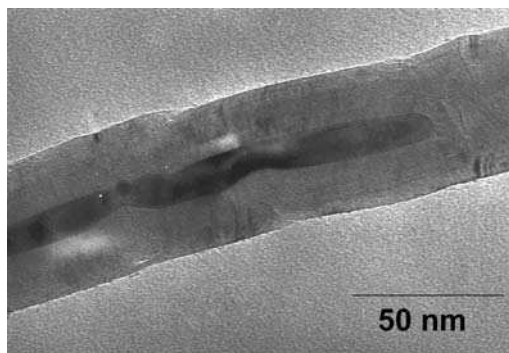


**Fig. 1.2** A multi-walled carbon nanotube containing a particle of iron (unpublished micrograph courtesy of I. Kinloch).

It is expected that the coarser particles will have the bcc crystal structure of ferrite, but it has to be appreciated that a 5 nm particle has about half its atoms at the surface. Metal surfaces are prone to reconstruction into a variety of two-dimensional structures which will complicate the interpretation of the structure of the particle as a whole. The surface also plays another role, in that it alters the total free energy of the particle leading to a depression of its melting temperature. It has been estimated that a 5 nm diameter iron particle could melt at a temperature as low as 500°C. Figure 1.2 illustrates an iron particle inside a carbon nanotube – its blobby character has been speculated to be due to melting.

Small metal particles in the size range 1–5 nm are close to a metal/insulator transition. When observed at the tips of carbon nanotubes using scanning electron microscopy, the iron particles have shown a tendency to charge, possibly indicating a loss of metallic behaviour.

### 1.3 THE PHASE TRANSFORMATION: $\alpha$ - AND $\gamma$ -IRON

The vast majority of steels rely on just two allotropes,  $\alpha$  and  $\gamma$ . Iron is a peculiar element in that at ambient pressure, bcc ferrite is stable from all temperatures up to 910°C (the  $A_3$  point), when it transforms into the fcc austenite, only to revert to ferrite at 1390°C (the  $A_4$  point). This high-temperature ferrite is traditionally labelled  $\delta$ , although it is no different in crystal structure from  $\alpha$ . The  $\delta$ -ferrite remains the stable phase until melting occurs at 1536°C.

Figure 1.3 shows the phase changes in a plot of the mean volume per atom of iron as a function of temperature. It should be noted that the  $\gamma$ - to  $\alpha$ -transformation is accompanied by an atomic volume change of approximately 1%, which can lead to the generation of internal stresses during transformation.

The detailed geometry of unit cells of  $\alpha$ - and  $\gamma$ -iron crystals is particularly relevant to, e.g., the solubility in the two phases of non-metallic elements such

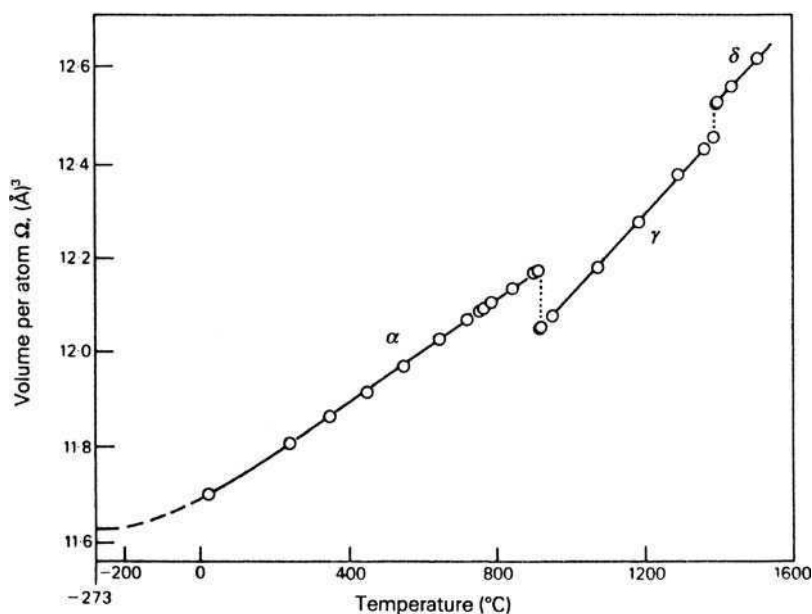


**Fig. 1.3** Temperature dependence of the mean volume per atom in iron crystals (Hume-Rothery, *The Structure of Alloys of Iron*, Pergamon Press, Oxford, UK, 1966).

as carbon and nitrogen, the diffusivity of alloying elements at elevated temperatures and the general behaviour on plastic deformation. The bcc structure of  $\alpha$ -iron is more loosely packed than that of fcc  $\gamma$ -iron (Figs 1.4a, b). The largest cavities in the bcc structure are the tetrahedral holes existing between two edge and two central atoms in the structure, which together form a tetrahedron (Fig. 1.4c). The second largest are the octahedral holes which occupy the centres of the faces and the  $\langle 001 \rangle$  edges of the body-centred cube (Fig. 1.4d). The surrounding iron atoms are at the corners of a flattened octahedron (Fig. 1.4e). It is interesting that the fcc structure, although more closely packed, has larger holes than the bcc structure. These holes are at the centres of the cube edges, and are surrounded by six atoms in the form of an octagon, so they are referred to as octahedral holes (Fig. 1.4f). There are also smaller tetrahedral interstices. The largest sizes of spheres which will enter these interstices are given in Table 1.1.

The  $\alpha \rightleftharpoons \gamma$  transformation in pure iron occurs very rapidly, so it is not generally possible to retain the high-temperature fcc form at room temperature. Rapid quenching can substantially alter the morphology of the resulting  $\alpha$ -iron, but it still retains its bcc structure. It follows that any detailed study of austenite in pure iron must be done at elevated temperatures, e.g. using X-ray or neutron diffraction. The transformation of the austenite on cooling can also be followed

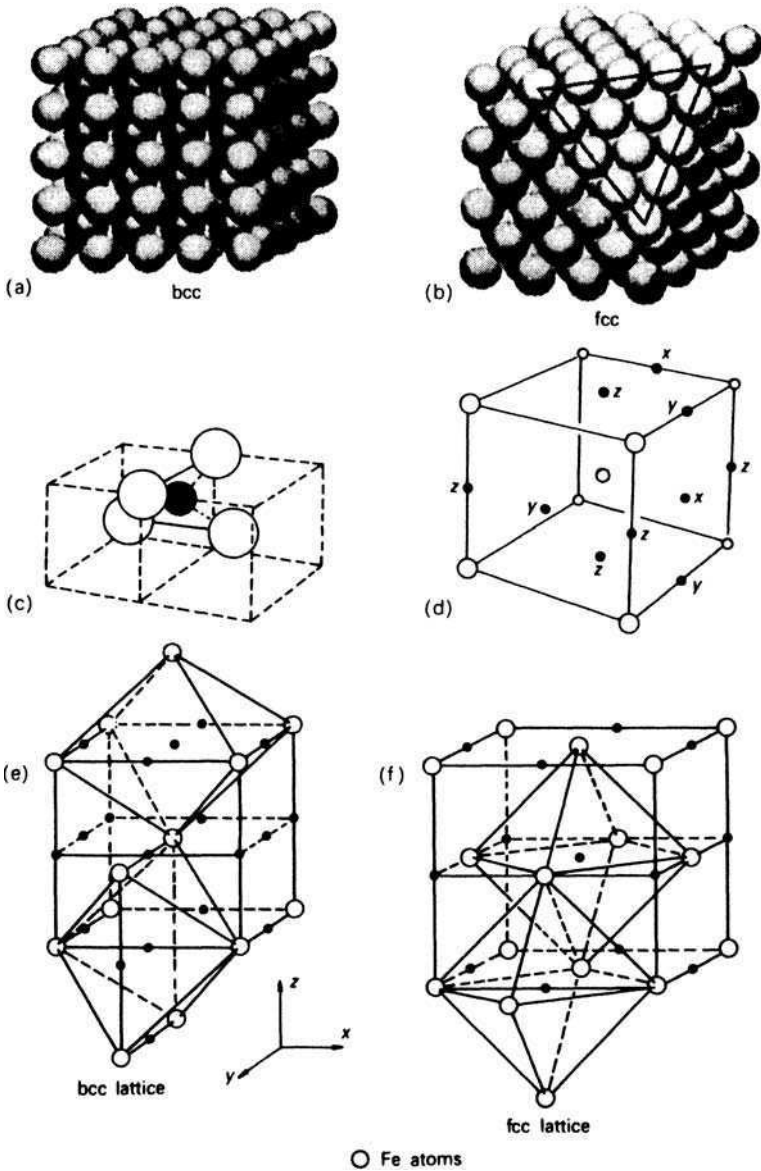


**Fig. 1.4** (a) bcc structure, (b) fcc structure (Moffat, Pearsall and Wulff, *The Structure and Properties of Materials: Vol. 1, Structure*, John Wiley, USA, 1964), (c) tetrahedral interstices in bcc structure, (d) octahedral interstices in bcc structure (Hume-Rothery, *The Structure of Alloys of Iron*, Pergamon Press, Oxford, UK, 1966), (e) and (f) octahedral interstices in bcc and fcc iron (Cohen, *Transactions of the Metallurgical Society of AIME* **224**, 638, 1962).

**Table 1.1** Size of largest spheres fitting interstices in bcc and fcc iron

		Radius	Radius in iron (Å)
bcc	Tetrahedral	$0.29r$	0.37
	Octahedral	$0.15r$	0.19
fcc	Tetrahedral	$0.23r$	0.28
	Octahedral	$0.41r$	0.51

$r$  = atomic radius of iron.

using diffraction based on the intense X-rays generated in a synchrotron, or using precision dilatometry. The latter technique relies on the volume change accompanying the transformation from austenite to ferrite.

There are circumstances where it is necessary to study pure austenite at temperatures well below ambient. Pure iron can be retained in its austenitic state to very low temperatures by coherent precipitation in copper. Copper has an fcc crystal structure and hence prevents the coherent particles of austenitic iron from transforming during cooling. This technique has been used to establish the antiferromagnetic nature of the austenite with a Néel temperature of about  $-190^{\circ}\text{C}$  (the austenite is ferromagnetic at high temperatures, with a Curie point of some  $1525^{\circ}\text{C}$ ).

### 1.3.1 Mechanisms of transformation

One of the reasons why there is a great variety of microstructures in steels is because the same allotropic transition can occur with a variety of ways in which the atoms can move to achieve the change in crystal structure. The transformation can occur either by breaking all the bonds and rearranging the atoms into an alternative pattern (*reconstructive* transformation), or by homogeneously deforming the original pattern into a new crystal structure (*displacive* or *shear* transformation) (Fig. 1.5).

In the displacive mechanism the change in crystal structure also alters the macroscopic shape of the sample when the latter is not constrained. The shape deformation during constrained transformation is accommodated by a combination of elastic and plastic strains in the surrounding matrix. The product phase grows in the form of thin plates to minimize the strains. The atoms are displaced into their new positions in a coordinated motion. Displacive transformations can, therefore, occur at temperatures where diffusion is inconceivable within the time scale of the experiment. Some solutes may be forced into the product phase, a phenomenon known as solute trapping. Both the trapping of atoms and the strains make displacive transformations less favourable from a thermodynamic point of view.

It is the diffusion of atoms that leads to the new crystal structure during a reconstructive transformation. The flow of matter is sufficient to avoid any

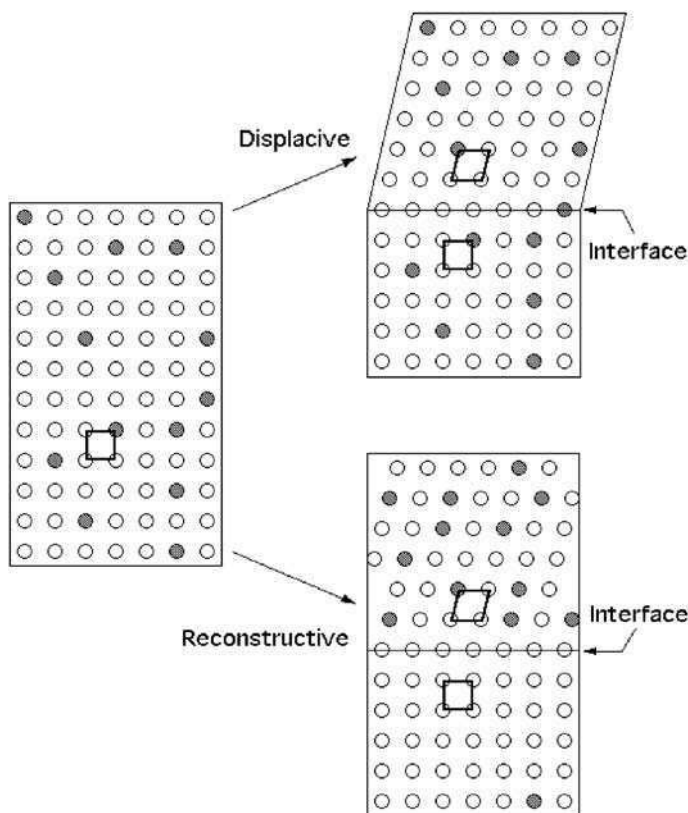


**Fig. 1.5** Schematic illustration of the mechanisms of transformation. The parent crystal contains two kinds of atoms. The figures on the right represent partially transformed samples with the parent and product unit cells outlined in bold.

shear components of the shape deformation, leaving only the effects of volume change. In alloys, the diffusion process may also lead to the redistribution of solutes between the phases in a manner consistent with a reduction in the overall free energy.

All the phase transformations in steels can be discussed in the context of these two mechanisms (Fig. 1.6). The details are presented in subsequent chapters.

## 1.4 CARBON AND NITROGEN IN SOLUTION IN $\alpha$ - AND $\gamma$ -IRON

### 1.4.1 Solubility of carbon and nitrogen in $\alpha$ - and $\gamma$ -iron

The addition of carbon to iron is sufficient to form a steel. However, steel is a generic term which covers a very large range of complex compositions. The

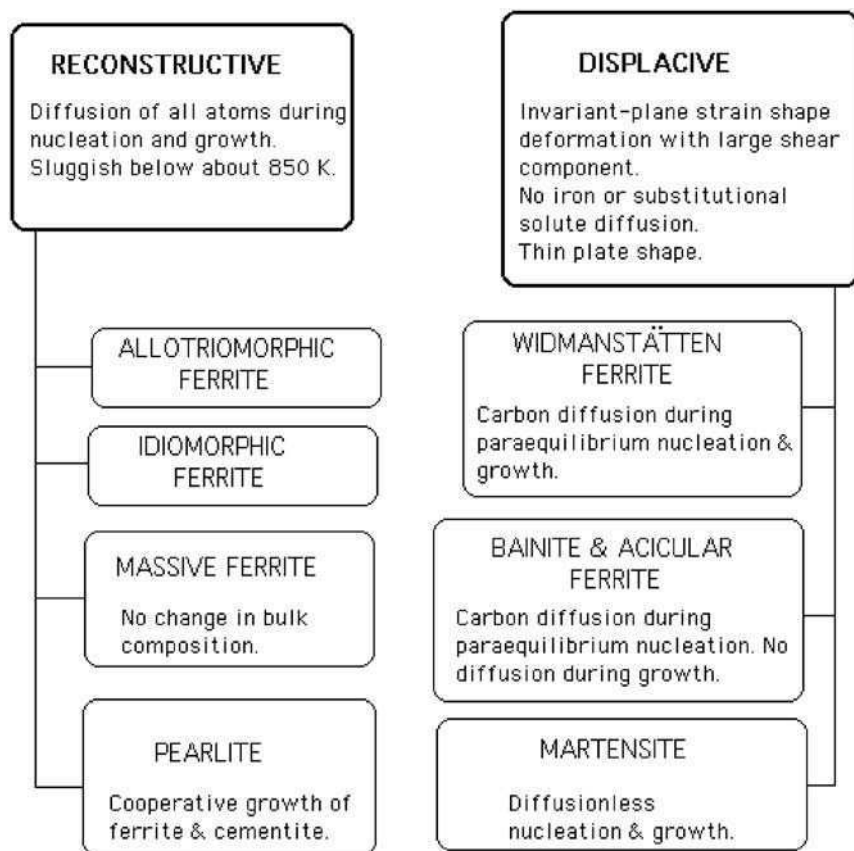


**Fig. 1.6** Summary of the variety of phases generated by the decomposition of austenite. The term 'paraequilibrium' refers to the case where carbon partitions but the substitutional atoms do not diffuse. The substitutional solute to iron atom ratio is therefore unchanged by transformation.

presence of even a small concentration of carbon, e.g. 0.1–0.2 weight per cent (wt%); approximately 0.5–1.0 atomic per cent (at%), has a great strengthening effect on ferritic iron, a fact known to smiths over 2500 years ago since iron heated in a charcoal fire can readily absorb carbon by solid-state diffusion. However, the detailed processes by which the absorption of carbon into iron converts a relatively soft metal into a very strong and often tough alloy have only recently been fully explored.

The atomic sizes of carbon and nitrogen (Table 1.2) are sufficiently small relative to that of iron to allow these elements to enter the  $\alpha$ - and  $\gamma$ -iron lattices as *interstitial* solute atoms. In contrast, the metallic alloying elements such as manganese, nickel and chromium have much larger atoms, i.e. nearer in size

**Table 1.2** Atomic sizes of non-metallic elements in iron

Element	Atomic radius, $r$ (Å)	$r/r_{\text{Fe}}$
$\alpha$ -Fe	1.28	1.00
B	0.94	0.73
C	0.77	0.60
N	0.72	0.57
O	0.60	0.47
H	0.46	0.36

to those of iron, and consequently they enter into *substitutional* solid solution. However, comparison of the atomic sizes of C and N with the sizes of the available interstices makes it clear that some lattice distortion must take place when these atoms enter the iron lattice. Indeed, it is found that C and N in  $\alpha$ -iron occupy not the larger tetrahedral holes, but the octahedral interstices which are more favourably placed for the relief of strain, which occurs by movement of two nearest-neighbour iron atoms. In the case of tetrahedral interstices, four iron atoms are of nearest-neighbour status and the displacement of these would require more strain energy. Consequently these interstices are not preferred sites for carbon and nitrogen atoms.

The solubility of both C and N in austenite should be greater than in ferrite, because of the larger interstices available. Table 1.3 shows that this is so for both elements, the solubility in  $\gamma$ -iron rising as high as 9–10 at%, in contrast to the maximum solubility of C in  $\alpha$ -iron of 0.1 at% and of N in  $\alpha$ -iron of 0.4 at%. These marked differences of the solubilities of the main interstitial solutes in  $\gamma$  and in  $\alpha$  are of profound significance in the heat treatment of steels, and are fully exploited to increase strength (see Chapter 2). It should be noted that the room

**Table 1.3** Solubilities of carbon and nitrogen in  $\gamma$ - and  $\alpha$ - iron

	Temperature (°C)	Solubility	
		wt%	at%
C in $\gamma$ -iron	1150	2.04	8.8
	723	0.80	3.6
C in $\alpha$ -iron	723	0.02	0.095
	20	<0.00005	<0.00012
N in $\gamma$ -iron	650	2.8	10.3
	590	2.35	8.75
N in $\alpha$ -iron	590	0.10	0.40
	20	<0.0001	<0.0004

temperature solubilities of both C and N in  $\alpha$ -iron are extremely low, well below the actual interstitial contents of many pure irons. It is, therefore, reasonable to expect that during simple heat treatments, excess carbon and nitrogen will be precipitated. This could happen in heat treatments involving quenching from the  $\gamma$ -state, or even after treatments entirely within the  $\alpha$ -field, where the solubility of C varies by nearly three orders of magnitude between 720°C and 20°C.

Fortunately, sensitive physical techniques allow the study of small concentrations of interstitial solute atoms in  $\alpha$ -iron. Snoek first showed that internal friction measurements on an iron wire oscillating in a torsional pendulum, over a range of temperature just above ambient temperature, revealed an energy loss peak (Snoek peak) at a particular temperature for a given frequency. It was shown that the energy loss was associated with the migration of carbon atoms from randomly chosen octahedral interstices to those holes which were enlarged on application of the stress in one direction, followed by a reverse migration when the stress changed direction and made other interstices larger. This movement of carbon atoms at a critical temperature is an additional form of damping or internal friction: below the critical temperature the diffusivity is too small for atomic migration, and above it the migration is too rapid to lead to appreciable damping. The height of the Snoek peak is proportional to the concentration of interstitial atoms, so the technique can be used not only to determine the very low solubilities of interstitial elements in iron, but also to examine the precipitation of excess carbon or nitrogen during an ageing treatment.

#### 1.4.2 Diffusion of solutes in iron

The internal friction technique can also be used to determine the diffusivities of C and N in  $\alpha$ -iron (Table 1.4). The temperature dependence of diffusivity in ferrite follows the standard exponential relationship:

$$D_C = 6.2 \times 10^{-3} \exp\left(-\frac{Q}{RT}\right) \text{ cm}^2 \text{ s}^{-1} \quad (Q = 80 \text{ kJ mol}^{-1}),$$

$$D_N = 3.0 \times 10^{-3} \exp\left(-\frac{Q}{RT}\right) \text{ cm}^2 \text{ s}^{-1} \quad (Q = 76 \text{ kJ mol}^{-1}),$$

where  $D_C$  and  $D_N$  are the diffusion coefficients of carbon and nitrogen, respectively and  $Q$  is the activation energy. The dependence of  $D_C$  and  $D_N$  on temperature is shown graphically in Fig. 1.7

Different techniques, e.g. involving radioactive tracers, have to be used for substitutional elements. A comparison of the diffusivities of the interstitial atoms with those of substitutional atoms, i.e. typical metallic solutes, on both  $\alpha$ - and  $\gamma$ -iron, shows that the substitutional atoms move several orders of magnitude more slowly (Table 1.4). This is a very important distinction which



**Table 1.4** Diffusivities of elements in  $\gamma$ - and  $\alpha$ -iron

Solvent	Solute	Activation energy, $Q$ (kJ mol <sup>-1</sup> )	Frequency factor, $D_0$ (cm <sup>2</sup> s <sup>-1</sup> )	Diffusion coefficient, $D_{910^\circ\text{C}}$ (cm <sup>2</sup> s <sup>-1</sup> )	Temperature range (°C)
$\gamma$ -iron	C	135	0.15	$1.5 \times 10^{-7}$	900–1050
	Fe	269	0.18	$2.2 \times 10^{-13}$	1060–1390
	Co	364	$3.0 \times 10^2$	$24.0 \times 10^{-12}$ (at 1050°C)	1050–1250
	Cr	405	$1.8 \times 10^4$	$58.0 \times 10^{-12}$ (at 1050°C)	1050–1250
	Cu	253	3.0	$15.0 \times 10^{-11}$	800–1200
	Ni	280	0.77	$7.7 \times 10^{-13}$	930–1050
	P	293	28.3	$3.6 \times 10^{-12}$	1280–1350
	S	202	1.35	$1.5 \times 10^{-9}$	1200–1350
	W	376	$1.0 \times 10^3$	$12.0 \times 10^{-12}$ (at 1050°C)	1050–1250
$\alpha$ -iron	C	80	$6.2 \times 10^{-3}$	$1.8 \times 10^{-6}$	
	N	76	$3.0 \times 10^{-3}$	$1.3 \times 10^{-6}$	
	Fe	240	0.5		700–750
	Co	226	0.2	$2.1 \times 10^{-11}$	700–790
	Cr	343	$3.0 \times 10^4$		
	Ni	358	9.7	$3.7 \times 10^{-11}$	700–900
	P	230	2.9	$2.0 \times 10^{-10}$	860–900
	W	293	$3.8 \times 10^2$		

Data from Askill, J., *Tracer Diffusion Data for Metals, Alloys and Simple Oxides*, IFI/Plenum Press, UK, 1970; Wohlbier, F. H., *Diffusion and Defect Data*, Materials Review Series, Vol. 12, Nos 1–4, Trans. Tech. Publication, Switzerland, 1976; Krishtal, M. A., *Diffusion Processes in Iron Alloys* (translated from Russian by Wald, A., ed. Becker, J. J.), Israel Program for Scientific Translations, Jerusalem, 1970.

is relevant to some of the more complex phenomena in alloy steels. However, for the time being, it should be noted that homogenizing treatments designed to eliminate concentration gradients of solute elements need to be much more prolonged and at higher temperatures when substitutional rather than interstitial solutes are involved.

The other major point which is illustrated in Table 1.4 is that, for a particular temperature, diffusion of both substitutional and interstitial solutes occurs much more rapidly in ferrite than in austenite. This arises because  $\gamma$ -iron is a close-packed structure whereas  $\alpha$ -iron, which is more loosely packed, responds more readily to thermal activation and allows easier passage through the structure of vacancies and associated solute atoms. In all cases, the activation energy  $Q$  is less for a particular element diffusing in  $\alpha$ -iron, than it is for the same element diffusing in  $\gamma$ -iron.

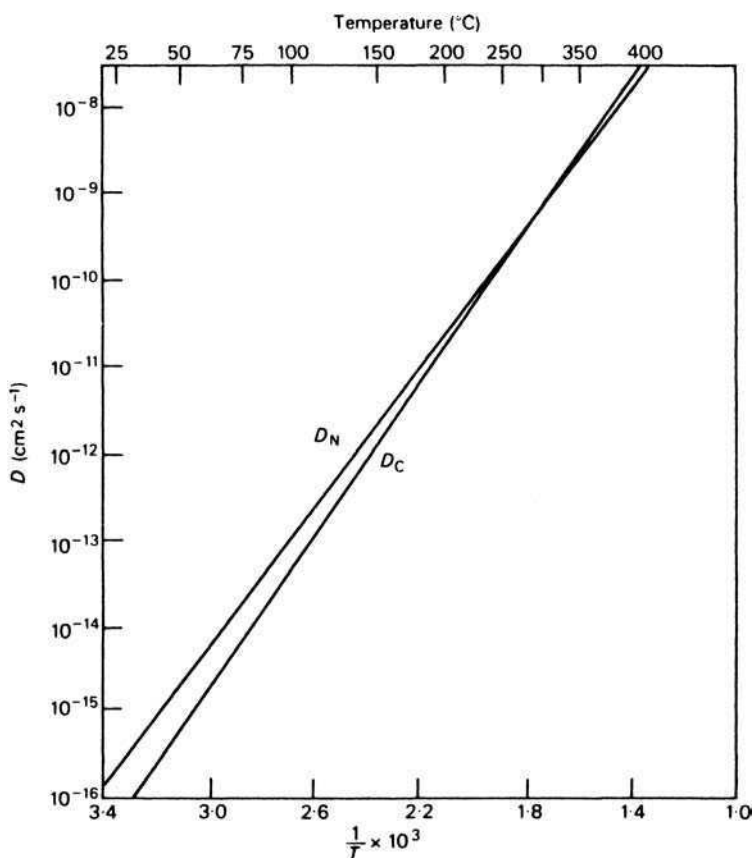


**Fig. 1.7** Temperature dependence of diffusion coefficients of nitrogen ( $D_N$ ) and carbon ( $D_C$ ) in  $\alpha$ -iron (Baird, *Iron and Steel*, Illiffe Production Publications, London, UK, 1963).  $T$  is the absolute temperature.

### 1.4.3 Precipitation of carbon and nitrogen from $\gamma$ -iron

$\alpha$ -iron containing about 0.02 wt% C is substantially supersaturated with carbon if, after being held at 700°C, it is quenched to room temperature. This supersaturated solid solution is not stable, even at room temperature, because of the ease with which carbon can diffuse in  $\alpha$ -iron. Consequently, in the range 20–300°C, carbon is precipitated as iron carbide. This process has been followed by measurement of changes in physical properties such as electrical resistivity, internal friction, and by direct observation of the structural changes in the electron microscope.

The process of ageing is a two-stage one. The first stage takes place at temperatures up to 200°C and involves the formation of a transitional iron carbide phase ( $\epsilon$ ) with a hexagonal structure which is often difficult to identify, although

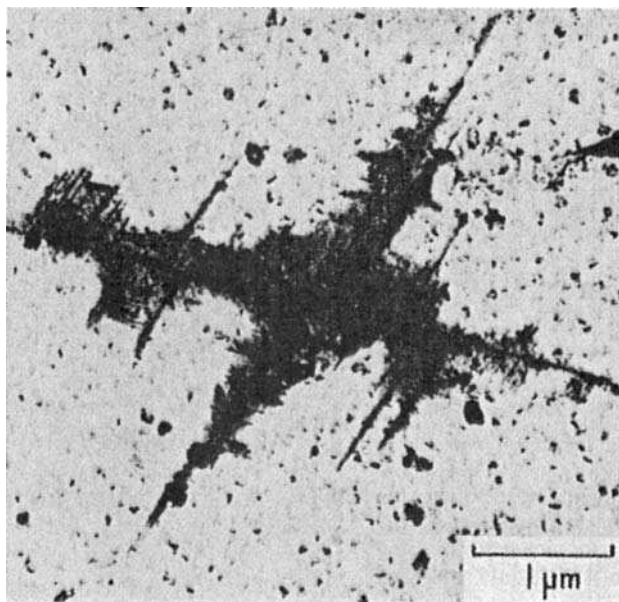


**Fig. 1.8** Cementite precipitation in quench-aged iron, 1560 min at 240°C (Langer). Replica electron micrograph.

its morphology and crystallography have been established. It forms as platelets on  $\{100\}_{\alpha}$  planes, apparently homogeneously in the  $\alpha$ -iron matrix, but at higher ageing temperatures (150–200°C) nucleation occurs preferentially on dislocations. The composition is between  $\text{Fe}_{2.4}\text{C}$  and  $\text{Fe}_3\text{C}$ . Ageing at 200°C and above leads to the second stage of ageing in which orthorhombic cementite  $\text{Fe}_3\text{C}$  is formed as platelets on  $\{110\}_{\alpha}$  planes in  $\langle 111 \rangle_{\alpha}$ -directions. Often the platelets grow on several  $\{110\}_{\alpha}$  planes from a common centre giving rise to structures which appear dendritic in character (Fig. 1.8). The transition from  $\epsilon$ -iron carbide to cementite is difficult to study, but it appears to occur by nucleation of cementite at the  $\epsilon$ -carbide/ $\alpha$  interfaces, followed by re-solution of the metastable  $\epsilon$ -carbide precipitate.

The maximum solubility of nitrogen in ferrite is 0.10 wt%, so a greater volume fraction of nitride precipitate can be obtained. The process is again two stage with a body-centred tetragonal  $\alpha''$  phase,  $\text{Fe}_{16}\text{N}_2$ , as the intermediate precipitate, forming as discs on  $\{100\}_{\alpha}$  matrix planes both homogeneously and on dislocations. Above about 200°C, this transitional nitride is replaced by the ordered fcc  $\gamma'$ ,  $\text{Fe}_4\text{N}$ , which forms as platelets with  $\{112\}_{\gamma'}/\{210\}_{\alpha}$ .

The ageing of  $\alpha$ -iron quenched from a high temperature in the  $\alpha$ -range is usually referred to as *quench ageing*, and there is substantial evidence to show that the process can cause considerable strengthening, even in relatively pure iron. Figure 1.9 plots the hardness changes in an Fe–0.02 wt% nitrogen alloy, aged at

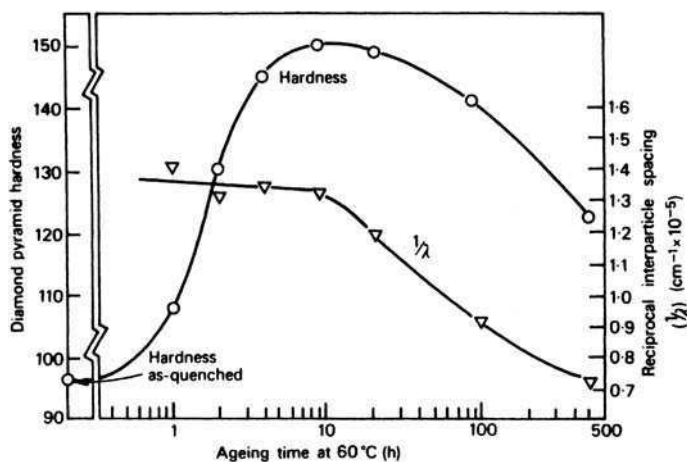


**Fig. 1.9** Quench ageing of iron with 0.02 wt% N. Variations of hardness and particle spacing ( $\lambda$ ) with ageing time at 60°C (Keh and Leslie, *Materials Science Research I*, 1963).

60°C after quenching from 500°C, which were shown by micro-examination to be due to precipitation of  $\text{Fe}_{16}\text{N}_2$ . In commercial low carbon steels, nitrogen is usually combined with aluminium, or is present in too low a concentration to make a substantial contribution to quench ageing, with the result that the major effect is due to carbon. This behaviour should be compared with that of *strain ageing* (see Section 2.3.1).

## I.5 SOME PRACTICAL ASPECTS

The very rapid diffusivity of carbon and nitrogen in iron compared with that of the metallic alloying elements is exploited in the processes of *carburizing* and *nitriding*. Carburizing can be carried out by heating a low carbon steel in contact with carbon to the austenitic range, e.g. 1000°C, where the carbon solubility,  $c_1$ , is substantial. The result is a carbon gradient in the steel, from  $c_1$  at the surface in contact with the carbon, to  $c$  at a depth  $x$ . The solution of Fick's second diffusion law for the case where the steel initially contains a carbon concentration  $c_0$  is:

$$c = c_1 - (c_1 - c_0) \operatorname{erf} \left\{ \frac{x}{2\sqrt{Dt}} \right\}, \quad (1.1)$$

which is essentially the equation of the concentration–depth curve, where  $t$  is time in seconds. The diffusion coefficient  $D$  of carbon in austenitic iron actually varies with carbon content, so the above relationship is not rigorously obeyed. Carburizing, whether carried out using carbon, or more efficiently using a carburizing gas (*gas carburizing*), provides a high carbon surface on a steel, which, after appropriate heat treatment, is strong and wear resistant.

Nitriding is normally carried out in an atmosphere of ammonia, but at a lower temperature (500–550°C) than carburizing, consequently the reaction occurs in the ferrite phase, in which nitrogen has a substantially higher solubility than carbon. Nitriding steels usually contain chromium (~0.1 wt%), aluminium (~1 wt%), vanadium or molybdenum (~0.2 wt%), which are nitride-forming elements, and which contribute to the very great hardness of the surface layer produced.

In cast steels, metallic alloying elements are usually segregated on a microscopic scale, by *coring of dendrites*. Therefore, to obtain a more uniform distribution, *homogenization* annealing must be carried out, otherwise the inhomogeneities will persist even after large amounts of mechanical working. The much lower diffusivities of the metallic alloying elements compared with carbon and nitrogen, means that the homogenization must be carried out at very high temperatures (1200–1300°C), approaching the melting point, hence the use of *soaking pits* where steel ingots are held after casting and prior to hot rolling. The higher the alloying element content of the steel, the more prolonged must be this high temperature treatment.

## FURTHER READING

- Bhadeshia, H. K. D. H., Large chunks of strong steel, *Materials Science and Technology*, **21**, 1293, 2005.
- Christian, J. W., *Theory of Transformations in Metals and Alloys*, 3rd edition, Pergamon Press, Oxford, UK, 2002.
- Cottrell, A. H., *Chemical Bonding in Transition Metal Carbides*, The Institute of Materials, London, 1995.
- Gavriljuk, V. G. and Berns, H., *High Nitrogen Steels*, Springer-Verlag Berlin and Heidelberg GmbH & Co., Germany, 1999.
- Gladman, T., *The Physical Metallurgy of Microalloyed Steels*, IOM Communications, London, 1996.
- Krauss, G., Microstructure and transformations in steels, in *Materials Science and Technology* (eds Cahn, R. W., Haasen, P. and Kramer, E. J.), Vol. 7, *Constitution and Properties of Steels* (ed. Pickering, F. B.), 1992.
- Krauss, G., *Steels: Heat Treatment and Processing Principles*, ASM International, USA, 1993.
- Krishtal, M. A., *Diffusion Processes in Iron Alloys* (translated from Russian by Wald, A.; ed. Becker, J. J.), Israel Program for Scientific Translations, Jerusalem, 1970.
- Leslie, W. C., *The Physical Metallurgy of Steels*, McGraw-Hill, USA, 1981.
- Llewellyn, D. T. and Hudd, R. C., *Steels: Metallurgy and Applications*, Butterworth-Heinemann, UK, 1998.
- Pachura, M. (ed.), *Book of Steel*, Intercept Scientific, Medical and Technical Publications, Paris, France, 1995.
- Sinha, A. K., *Ferrous Physical Metallurgy*, Butterworths, Boston, USA, 1989.

# 2

---

## THE STRENGTHENING OF IRON AND ITS ALLOYS

### 2.1 INTRODUCTION

Although pure iron can be weak, steels cover a wide range of the strength spectrum from low yield stress levels (around  $200 \text{ MN m}^{-2}$ ) to very high levels (approaching  $5500 \text{ MN m}^{-2}$ ), without compromising toughness. There are many ways of strengthening steels, which is why they are able to offer such a wide range of properties. It is also possible to combine several strengthening mechanisms, and in such circumstances it is often difficult to quantify the variety of contributions to the overall strength. On the other hand, there has been considerable progress in methods for mathematically modelling of properties, and hence of deconvoluting the overall strength into its components. The basic ways in which iron can be strengthened are discussed first, by reference to simple systems. These results should then be helpful in examining the behaviour of more complex alloys.

Like other metals, iron can be strengthened by several mechanisms, the most important of which are:

1. Work hardening.
2. Solid solution strengthening by interstitial atoms.
3. Solid solution strengthening by substitutional atoms.
4. Refinement of grain size.
5. Dispersion strengthening, including lamellar and random dispersed structures.

The most distinctive aspect of strengthening of iron is the role of the interstitial solutes carbon and nitrogen. These elements also play a vital part in interacting with dislocations, and in combining preferentially with some of the metallic alloying elements used in steels.

## 2.2 WORK HARDENING

Work hardening is an important strengthening process in steel, particularly in obtaining high strength levels in rod and wire, both in plain carbon and alloy steels. For example, the tensile strength of an 0.05 wt% C steel subjected to 95% reduction in area by wire drawing, is raised by no less than  $550 \text{ MN m}^{-2}$ , while higher carbon steels are strengthened by up to twice this amount. Indeed, without the addition of special alloying elements, plain carbon steels can be raised to strength levels above  $1500 \text{ MN m}^{-2}$  simply by the phenomenon of work hardening.

Basic work on the deformation of iron has largely concentrated on the other end of the strength spectrum, namely pure single crystals and polycrystals subjected to small controlled deformations. This approach has shown that the slip plane in  $\alpha$ -iron is not unique. Slip occurs on several planes,  $\{110\}$ ,  $\{112\}$  and  $\{123\}$ , but always in the close packed  $\langle 111 \rangle$  direction which is common to each of these planes (Fig. 2.1). The diversity of slip planes leads to rather irregular wavy slip bands in deformed crystals, as the dislocations can readily move from one type of plane to another by cross slip, provided they share a common slip direction. The Burgers vector of the slip dislocations would thus be expected to be  $\frac{a}{2}\langle 111 \rangle$ , which has been confirmed by thin-foil electron microscopy.

The yield stress of  $\alpha$ -iron single crystals is very sensitive to both temperature and strain rate, and a similar dependence has been found for less pure polycrystalline iron. Figure 2.2 shows the flow stress  $\sigma_T$  at temperature  $T$ , less than that at room temperature  $\sigma_{293}$ , plotted against  $T$ , showing that both single crystal and polycrystalline iron of different interstitial content give values falling on the one curve. Therefore, the temperature sensitivity cannot be attributed to interstitial impurities. It is explained by the effect of temperature on the stress needed to move free dislocations in the crystal, the Peierls–Nabarro stress. Direct observation of screw dislocations in iron in the electron microscope has shown that their ease of mobility decreases strongly with decreasing temperature.

If the shear stress at any point on the stress–strain curve is considered, the measured shear stress  $\tau$  for further deformation comprises two quantities:

$$\tau = \tau^* + \tau_i. \quad (2.1)$$

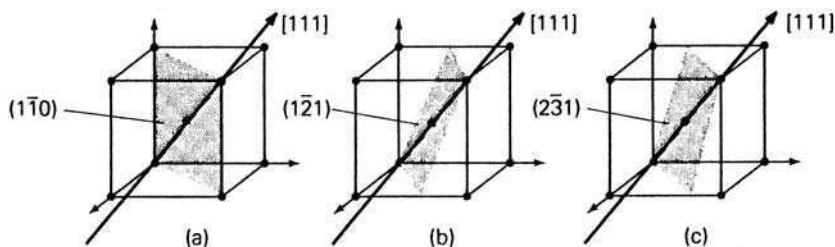
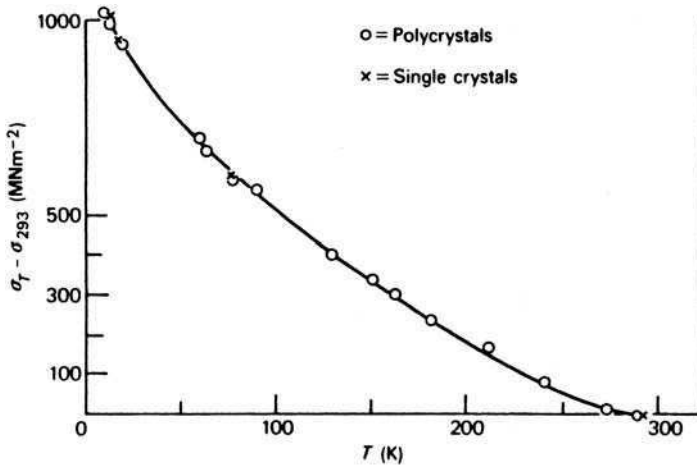


Fig. 2.1 The slip systems in the bcc structure.



**Fig. 2.2** Temperature dependence of the flow stress of single crystals and polycrystals of pure iron (Christian, *Philosophical Transactions of the Royal Society* **261**, 253, 1967).

The effective shear stress,  $\tau^*$  arises from the interaction of the dislocations with short range obstacles, e.g. isolated dislocations. This stress is strongly temperature dependent as thermal activation is helpful in moving dislocations around short range obstacles.<sup>1</sup> On the other hand,  $\tau_i$  is the internal stress arising from long range obstacles such as grain boundaries, cell walls and other complex dislocation arrays.<sup>2</sup> In these circumstances thermal fluctuations are of no assistance. The two component stresses are defined as follows:

$$\tau^* = \frac{1}{V} \left[ \Delta H_0 + kT \ln \frac{l \dot{\epsilon}}{\rho m A b \gamma} \right], \quad (2.2)$$

$$\tau_i = \alpha \mu b \rho^{1/2}, \quad (2.3)$$

where  $V$  = activation volume

$\Delta H_0$  = activation enthalpy at  $\tau = 0$

$k$  = Boltzmann's constant

$T$  = temperature

$l$  = length of dislocation line activated

$\dot{\epsilon}$  = strain rate

$m$  = mobile dislocation density

$A$  = area of glide plane covered by dislocation

<sup>1</sup> Conrad, K., *Journal of the Iron and Steel Institute* **198**, 364, 1961.

<sup>2</sup> Michalak, J. J., *Acta Metallurgica* **13**, 213, 1965.



$b$  = magnitude of Burgers vector

$\gamma$  = frequency of vibration of dislocation line length

$\alpha$  = constant

$\mu$  = shear modulus

$\rho$  = dislocation density

The initial flow stress or yield stress with its large temperature dependence arises primarily from  $\tau^*$ , while the increment in flow stress resulting from work hardening is largely independent of temperature, and is caused by the increase in  $\tau_i$  with increasing strain as the dislocation density  $\rho$  increases.

To summarize, work hardening in conventional materials is largely due to the creation of crystal defects, primarily dislocations, during plastic deformation. The hardening can reach saturation once the defect creation and annihilation rates balance.

Work hardening has an important consequence on ductility. During tensile testing, the sample will inevitably contain features which cause the stress to concentrate and hence to initiate necking. The reduced cross-sectional area at the neck increases the stress in the necked region. In the absence of work hardening to help resist local deformation, the neck becomes unstable and the sample fractures with poor overall ductility. To encourage uniform elongation, the work hardening rate must raise the yield strength at a rate greater than the increase in stress due to the reduced area at the neck.

Given the origin of work hardening, microstructures in which the dislocation density does not substantially increase during deformation should lack ductility. A pertinent example of such a microstructure, consisting of extremely fine grains, is discussed in Section 2.5.

## 2.3 SOLID SOLUTION STRENGTHENING BY INTERSTITIALS

Carbon and nitrogen have a disproportionate influence on the strength of ferritic iron and a relatively minor effect on that of austenitic iron. Solid solution strengthening occurs when the strain fields around misfitting solutes interfere with the motion of dislocations. Atoms which substitute for iron cause local expansions or contractions; these strains are isotropic and therefore can only interact with the hydrostatic components of the strain fields of dislocations. In contrast, an interstitial atom located in the irregular octahedron interstice in ferrite causes a tetragonal distortion (Fig. 2.3) which has a powerful interaction with the shear which is the dominant component of a dislocation strain field. This is why interstitial solid solution strengthening is so potent in ferrite. The corresponding interstitial site in austenite is the regular octahedron. An interstitial atom in austenite therefore behaves like a substitutional solute, with only hydrostatic strains surrounding it. This is why carbon is much less effective in strengthening austenite.

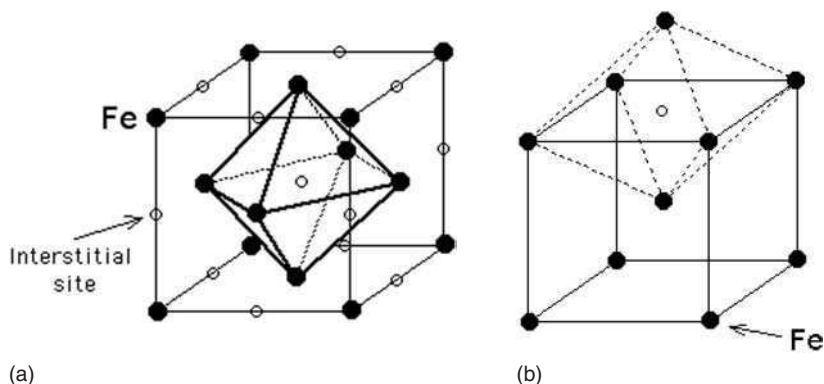


**Fig. 2.3** (a) The regular octahedron interstice in austenite. (b) Octahedral interstice in ferrite – notice that two of the axes are longer than the third (vertical axis). This leads to a tetragonal distortion when the site is occupied by carbon.

Ferritic iron has such a small solubility for carbon that there is an overwhelming tendency for the carbon to segregate to defects. This leads to another significant effect in  $\alpha$ -iron, that carbon and nitrogen can promote heterogeneous deformation by making it difficult to initiate plastic flow. This is the yield point effect, described next.

### 2.3.1 The yield point

Carbon and nitrogen, even in concentrations as low as 0.005 wt%, in iron lead to a sharp transition between elastic and plastic deformation in a tensile test performed on ferritic iron (Fig. 2.4a). Decarburization of the iron results in the elimination of this sharp transition or *yield point*, which implies that the solute atoms are in some way responsible for this striking behaviour. Frequently the load drops dramatically at the *upper yield point* (A) to another value referred to as the *lower yield point* (B). Under some experimental conditions, yield drops of about 30% of the upper yield stress can be obtained. Following the lower yield point, there is frequently a horizontal section of the stress–strain curve (BC) during which the plastic deformation propagates at a front which can move uniformly along the specimen. This front is referred to as a *Luders band* (Fig. 2.4b), and the horizontal portion, BC, of the stress–strain curve as the Luders extension. The development of Luders bands can be much less uniform and, e.g., in pressings where the stress is far from uniaxial, complex arrays of bands can be observed. These are often referred to as *stretcher strains*, but they are still basically Luders bands. When the whole specimen has yielded, general work hardening commences and the stress–strain curve begins to rise in the normal way. If, however, this deformation is interrupted, and the specimen allowed to rest either at room temperature or for a shorter time at 100–150°C,

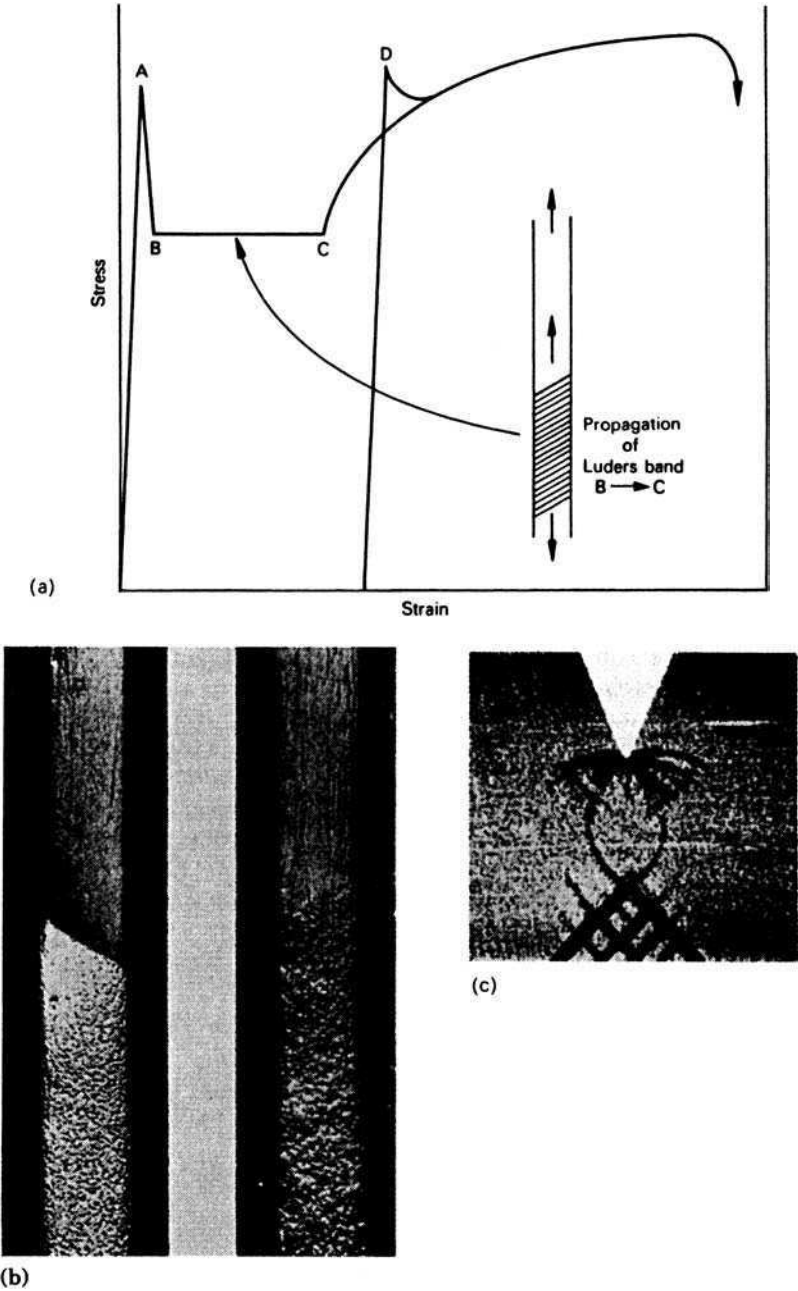


**Fig. 2.4** (a) Schematic diagram of yield phenomena as shown in a tensile test, (b) Luders bands in deformed steel specimens (Hall, *Yield Point Phenomena in Metals and Alloys*, Macmillan, London, 1970), (c) Luders bands in a notched steel specimen.

on reloading a new yield point is observed (D). This return of the yield point is referred to as *strain ageing*.

### 2.3.2 The role of interstitial elements in yield phenomena

The sharp upper and lower yield point in iron is eliminated by annealing in wet hydrogen, which reduces the carbon and nitrogen to very low levels. However, substantial strain ageing can occur at carbon levels around 0.002 wt%, and as little as 0.001–0.002 wt% N can result in severe strain ageing. Nitrogen is more effective in this respect than carbon, because its residual solubility near room temperature is substantially greater than that of carbon (Table 1.3).

Cottrell and Bilby first showed that interstitial atoms such as carbon and nitrogen would interact strongly with the strain fields of dislocations. The interstitial atoms have strain fields around them, but when such atoms move within the dislocation strain fields, there should be an overall reduction in the total strain energy. This leads to the formation of interstitial concentrations or *atmospheres* in the vicinity of dislocations, which in an extreme case can amount to lines of interstitial atoms along the cores of the dislocations (*condensed atmospheres*), e.g. in edge dislocations at the region of the strain field where there is maximum dilation (Figs 2.5a, b). The binding energy between a dislocation in iron and a carbon atom is about 0.5 eV. Consequently dislocations can be locked in position by strings of carbon atoms along the dislocations, thus substantially raising the stress which would be necessary to cause dislocation movement. A particular attraction of this theory is that only a very small concentration of interstitial atoms is needed to produce locking along the whole length of all dislocation lines in annealed iron. For a typical dislocation density of  $10^8$  lines  $\text{cm}^{-2}$  in annealed iron, a carbon concentration of  $10^{-6}$  wt% would be sufficient to provide one interstitial carbon atom per atomic plane along all the dislocation lines present, i.e. to saturate the dislocations. Consequently, this theory can explain the observation of yield phenomena at very low carbon and nitrogen concentrations.

The formation of interstitial atmospheres at dislocations requires diffusion of the solute. As both carbon and nitrogen diffuse very much more rapidly in iron

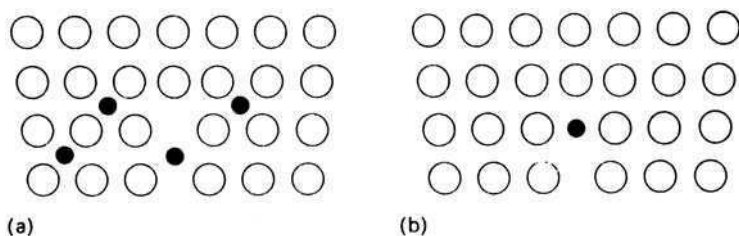


**Fig. 2.5** Interstitial atoms in the vicinity of an edge dislocation (a) random atmosphere (b) condensed.

than substitutional solutes, it is not surprising that strain ageing can take place readily in the range 20–150°C. The interstitial concentration,  $c$ , in a dislocation strain field at a point where the binding energy is  $U$  is given by:

$$c = c_0 e^{U/kT}, \quad (2.4)$$

where  $c_0$  is the average concentration. In general, this approach leads to a Maxwellian distribution of solute about the dislocation, but for carbon and nitrogen in steel, the elastic interaction energy  $U$  between solute and dislocation is so large that  $U \geq kT$ . Consequently the atmosphere condenses to form rows of interstitial atoms along the cores of the dislocations.

The critical temperature  $T_{\text{crit}}$  below which there is condensation of the atmosphere, occurs when  $c = 1$  and  $U = U_{\text{max}}$ :

$$T_{\text{crit}} = \frac{U_{\text{max}}}{k \ln \frac{1}{c_0}}. \quad (2.5)$$

Therefore, if  $c_0 = 10^{-4}$  and  $U_{\text{max}} \simeq 10^{-19} \text{ J}$ ,  $T_{\text{crit}} = 700 \text{ K}$ . Thus the yield point would be expected at temperatures below 700 K, but it should disappear at higher temperatures when dislocations can escape from their atmospheres as a result of thermal activation. This corresponds approximately with results of experiments showing the temperature dependence of the stress–strain curve of mild steel (Fig. 2.6). As expected, the zone of yielding is well defined at the lower testing temperatures, becoming less regular as the temperature is raised, until it is replaced by fine serrations along the whole stress–strain curve. This phenomenon is referred to as *dynamic strain ageing*, in which the serrations represent the replacement of the primary yield point by numerous localized yield points within the specimen. These arise because the temperature is high enough to allow interstitial atoms to diffuse during deformation, and to form atmospheres around dislocations generated throughout the stress–strain curve. Steels tested under these conditions also show low ductilities, due partly to the high dislocation density and partly to the nucleation of carbide particles on the dislocations where the carbon concentration is high. The phenomenon is often referred to as *blue brittleness*, blue being the interference colour of the steel surface when oxidized in this temperature range.

The break away of dislocations from their carbon atmospheres as a cause of the sharp yield point became a controversial aspect of the theory because it was found that the provision of free dislocations, e.g., by scratching the surface of a specimen, did not eliminate the sharp yield point. An alternative theory was developed which assumed that, once condensed carbon atmospheres are formed in iron, the dislocations remain locked, and the yield phenomena arise from the generation and movement of newly formed dislocations (Gilman and Johnston). The velocity of movement  $v$  of these fresh dislocations is related to

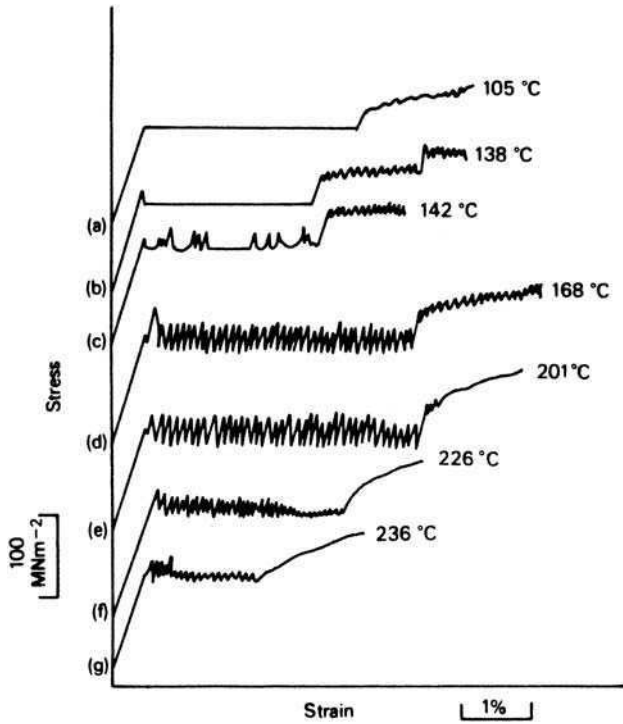


**Fig. 2.6** Typical stress–strain curves for mild steel at elevated temperatures (Hall, *Yield Point Phenomena in Metals and Alloys*, Macmillan, 1970).

the applied stress as follows:

$$v = \left( \frac{\sigma}{\sigma_T} \right)^m, \quad (2.6)$$

where  $\sigma_T$  is a reference stress,  $\sigma$  is the yield stress and  $m$  is an index characteristic of the material, varying between 1 and 60. The strain rate  $\dot{\epsilon}$  can be defined in terms of the movement of dislocations, as

$$\dot{\epsilon} = n v b, \quad (2.7)$$

where  $n$  is the number of mobile dislocations per unit area,  $v$  is their average velocity and  $b$  is Burgers vector.

Using Equation (2.7) the strain rates at the upper yield point ( $\dot{\epsilon}_U$ ) and the lower yield point ( $\dot{\epsilon}_L$ ) can be defined as follows:

$$\dot{\epsilon}_U = \rho_U v_U b,$$

where  $\rho_U$  is the mobile dislocation density at the upper yield point and

$$\dot{\epsilon}_L = \rho_L v_L b,$$

where  $\rho_L$  is the mobile dislocation density at the lower yield point, so

$$\frac{v_U}{v_L} = \frac{\rho_L}{\rho_U},$$

and using Equation (2.6)

$$\frac{\sigma_U}{\sigma_L} = \left( \frac{\rho_L}{\rho_U} \right)^{\frac{1}{m}}. \quad (2.8)$$

Thus the ratio  $\sigma_U/\sigma_L$  will be large, i.e. there will be a large yield drop, where  $m$  is small, and when  $\rho_L$  is much larger than  $\rho_U$ . Consequently, if at the upper yield stress the density of mobile dislocations is low, e.g. as a result of solute atom locking, a large drop in yield stress will occur if a large number of new dislocations is generated. Observations indicate that the dislocation density just after the lower yield stress is much higher than that observed at the upper yield point.

To summarize, the occurrence of a sharp yield point depends on the occurrence of a sudden increase in the number of mobile dislocations. However, the precise mechanism by which this takes place will depend on the effectiveness of the locking of the pre-existing dislocations. If the pinning is weak, then the yield point can arise as a result of unpinning. However, if the dislocations are strongly locked, either by interstitial atmospheres or precipitates, the yield point will result from the rapid generation of new dislocations.

Under conditions of dynamic strain ageing, where atmospheres of carbon atoms form continuously on newly generated dislocations, it would be expected that a higher density of dislocations would be needed to complete the deformation, if it is assumed that most dislocations which attract carbon atmospheres are permanently locked in position. Electron microscopic observations have shown that in steels deformed at 200°C, the dislocation densities are an order of magnitude greater than those in specimens similarly deformed at room temperature. This also accounts for the fact that increased work hardening rates are obtained in the blue-brittle condition as compared to tests at room temperature.

### 2.3.3 Strengthening at high interstitial concentrations

Austenite can take into solid solution up to 10 at% carbon which can be retained in solid solution by rapid quenching. However, in these circumstances the phase transformation takes place, not to ferrite but to a body-centred tetragonal structure referred to as *martensite* (see Chapter 5). This phase forms as a result of a diffusionless shear transformation leading to characteristic laths or plates, which normally appear acicular in polished and etched sections. If the quench is sufficiently rapid, the martensite is essentially a supersaturated solid solution of carbon in a tetragonal iron matrix, and as the carbon concentration can be greatly in excess of the equilibrium concentration in ferrite, the strength is raised very substantially. High carbon martensites are normally very hard but brittle, the yield strength reaching as much as 1500 MN m<sup>-2</sup>; much of this increase can be directly

attributed to increased interstitial solid solution hardening, but there is also a contribution from the high dislocation density which is characteristic of martensitic transformations in iron–carbon alloys. Martensite will be dealt with in more detail in Chapter 5, which shows that by subjecting it to a further heat treatment at intermediate temperatures (*tempering*), a proportion of the strength is retained, with a substantial gain in the toughness and ductility of the steel.

## 2.4 SUBSTITUTIONAL SOLID SOLUTION STRENGTHENING OF IRON

Many metallic elements form solid solutions in  $\gamma$ - and  $\alpha$ -iron. These are invariably substitutional solid solutions, but for a constant atomic concentration of alloying elements there are large variations in strength. Using single crystal data for several metals, Fig. 2.7 shows that an element such as vanadium has a weak strengthening effect on  $\alpha$ -iron at low concentrations (<2 at%), while silicon and molybdenum are much more effective strengtheners. Other data indicate that phosphorus, manganese, nickel and copper are also effective strengtheners. However, it should be noted that the relative strengthening may alter with the temperature of testing, and with the concentrations of interstitial solutes present in the steels.

The strengthening achieved by substitutional solute atoms is, in general, greater the larger the difference in atomic size of the solute from that of iron, applying the Hume-Rothery size effect. However, from the work of Fleischer and Takeuchi it is apparent that differences in the elastic behaviour of solute and solvent atoms are also important in determining the overall strengthening achieved. In practical terms, the contribution to strength from solid solution effects is superimposed on hardening from other sources, e.g. grain size and dispersions. Also it is a strengthening increment, like that due to grain size, which need not adversely affect ductility. In industrial steels, solid solution strengthening is a far from negligible factor in the overall strength, where it is achieved by a number of familiar alloying elements, e.g. manganese, silicon, nickel, molybdenum, several of which are frequently present in a particular steel and are additive in their effect. These alloying elements are usually added for other reasons, e.g. Si to achieve deoxidation, Mn to combine with sulphur or Mo to promote hardenability. Therefore, the solid solution hardening contribution can be viewed as a useful bonus.

## 2.5 GRAIN SIZE

### 2.5.1 Hall–Petch effect

The refinement of the grain size of ferrite provides one of the most important strengthening routes in the heat treatment of steels. The first scientific analysis of the relationship between grain size and strength, carried out on ARMCO



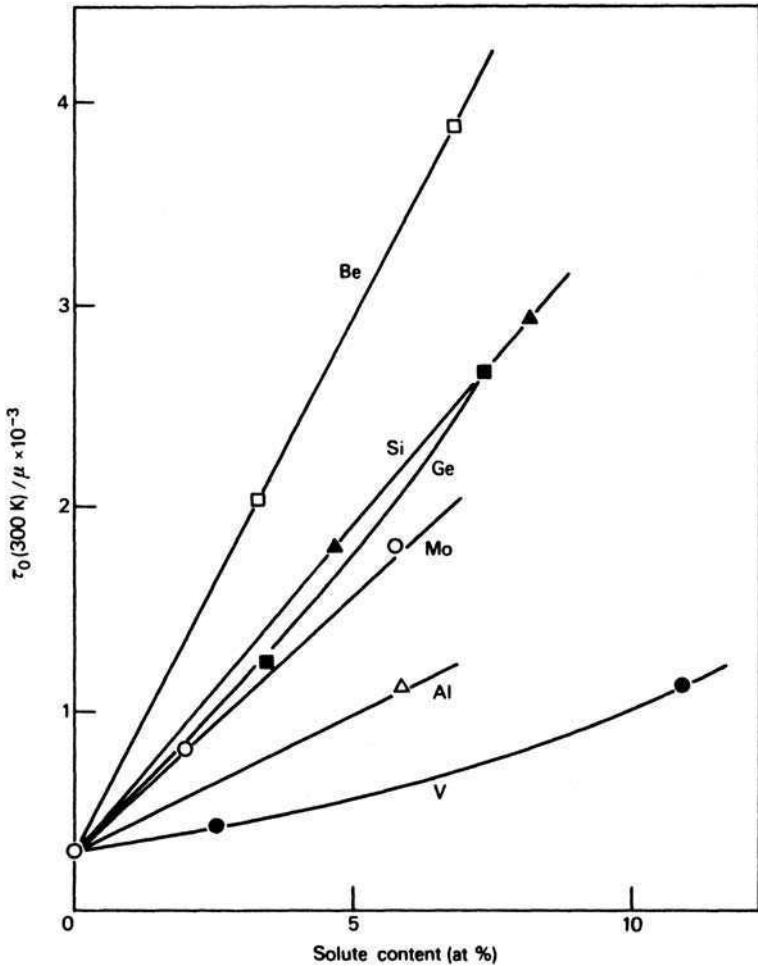


**Fig. 2.7** Solid solution strengthening of  $\alpha$ -iron crystals by substitutional solutes. Ratio of the critical resolved shear stress  $\tau_0$  to shear modulus  $\mu$  as a function of atomic concentration (Takeuchi, *Journal of the Physical Society of Japan* **27**, 929, 1969).

iron by Hall and Petch, led to the Hall–Petch relationship between the yield stress  $\sigma_y$  and the grain diameter  $d$ ,

$$\sigma_y = \sigma_0 + k_y d^{-1/2}, \tag{2.9}$$

where  $\sigma_0$  and  $k_y$  are constants. This type of relationship holds for a wide variety of irons and steels as well as for many non-ferrous metals and alloys. A typical set of results for mild steel is given in Fig. 2.7, where the linear relationship between  $\sigma_y$  and  $d^{-1/2}$  is clearly shown for the three test temperatures.

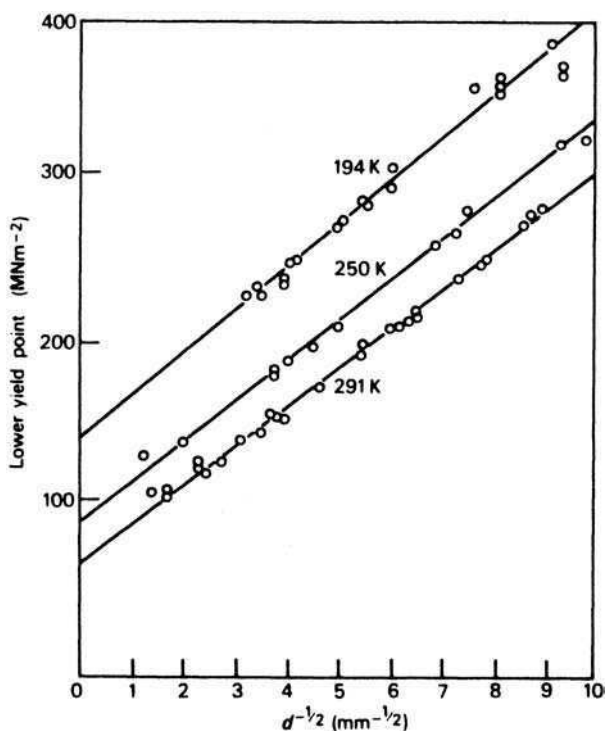


**Fig. 2.8** Dependence of the lower yield stress of mild steel on grain size (Petch, in *Fracture* (eds Averbach et al.), John Wiley, USA, 1959).

The constant  $\sigma_0$  is called the *friction stress*. It is the intercept on the stress axis, representing the stress required to move free dislocations along the slip planes in the bcc crystals, and can be regarded as the yield stress of a single crystal ( $d^{-1/2} = 0$ ). This stress is particularly sensitive to temperature (Fig. 2.7) and composition. The  $k_y$  term represents the slope of the  $\sigma_y - d^{-1/2}$  plot which has been found not to be sensitive to temperature (Fig. 2.8), composition and strain rate.

In line with the Cottrell–Bilby theory of the yield point involving the break away of dislocations from interstitial carbon atmospheres,  $k_y$  has been referred to as the unpinning parameter. However, the insensitivity of  $k_y$  to temperature suggests that unpinning rarely occurs, and emphasizes the theory that new dislocations are generated at the yield point. This is consistent with the theories explaining the yield point in terms of the movement of new dislocations, the velocities of which are stress dependent (Section 2.3.2).

The grain size effect on the yield stress can therefore be explained by assuming that a dislocation source operates within a crystal causing dislocations to move and eventually to pile-up at the grain boundary. The pile-up causes a stress to be generated in the adjacent grain, which, when it reaches a critical

value, operates a new source in that grain. In this way, the yielding process is propagated from grain to grain. This can be observed macroscopically by the passage of a Luders band. The grain size determines the distance dislocations have to move to form grain boundary pile-ups, and thus the number of dislocations involved. With large grain sizes, the pile-ups will contain larger numbers of dislocations which will in turn cause higher stress concentrations in neighbouring grains. The shear stress  $\tau_1$  at the head of a dislocation pile-up is equal to  $n\tau$ , where  $n$  is the number of dislocations involved and  $\tau$  is the shear stress on the slip plane. This means that the coarser the grain size, the easier it will be to propagate the yielding process.

In practical terms, the finer the grain size, the higher the resulting yield stress and, as a result, in modern steel working much attention is paid to the final ferrite grain size. While a coarse grain size of  $d^{-1/2} = 2$ , i.e.  $d = 0.25$  mm, gives a yield stress in mild steels of around  $100 \text{ MN m}^{-2}$ , grain refinement to  $d^{-1/2} = 20$ , i.e.  $d = 0.0025$  mm, raises the yield stress to over  $500 \text{ MN m}^{-2}$ , so that achieving grain sizes in the range  $2\text{--}10 \mu\text{m}$  is extremely worthwhile. Over the last 40 years, developments in rolling practice and the addition of small concentrations of particular alloying elements to mild steels, have resulted in dramatic improvements in the mechanical properties of this widely used engineering material (Chapter 9).

### 2.5.2 Nanostructured steels

Modern technologies allow steels to be made routinely and in large quantities with grain sizes of about  $1 \mu\text{m}$ . Limited processes, generally involving severe thermomechanical processing, have been developed to achieve nanostructured ferrite grains in steel, with a size in the range  $20\text{--}100 \text{ nm}$ . Experiments have revealed that the Hall–Petch equation holds down to some  $20 \text{ nm}$ , confirming that enormous strengths can be achieved by refining the grain size. The equation begins to fail at grain sizes less than about  $20 \text{ nm}$ , possibly because other mechanisms of deformation, such as grain boundary sliding, begin to play a prominent role. The volume fraction  $V_B$  of material occupied by the boundaries is given by:

$$V_B \simeq 2a/\bar{L},$$

where  $\bar{L}$  is the mean linear intercept defining the grain size and  $a$  is the thickness of the boundary layer. Clearly, the fraction of atoms located at the grain surfaces becomes very large in the nanostructured materials, facilitating diffusional processes such as grain sliding (Fig. 2.9).

Although the nanostructured steels are strengthened as expected from the Hall–Petch equation, they tend to exhibit unstable plasticity after yielding. The plastic instability occurs in both tension and in compression testing, with shear bands causing failure in the latter case. It is as if the capacity of the material to work harden following yielding diminishes. The consequence is an unacceptable

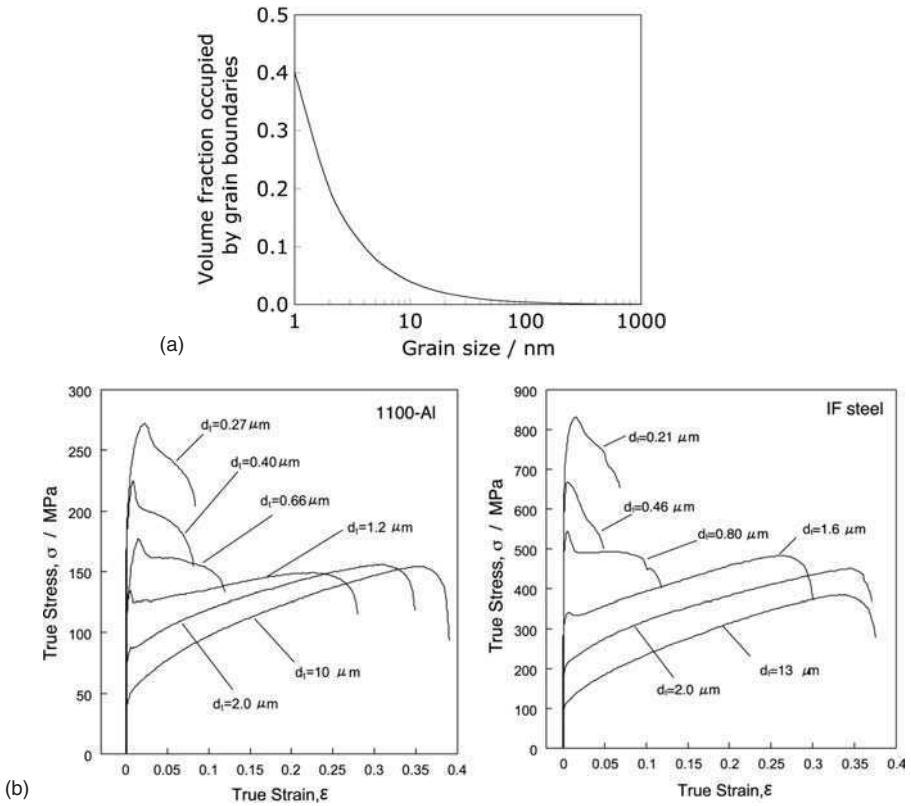


**Fig. 2.9** (a) The volume fraction of grain boundary within a given volume, as a function of the grain size. (b) Loss of ductility as the strength is increased by dramatically reducing the grain size in aluminium and iron alloys (Tsuji, Ito, Saito and Minamino, *Scripta Materialia* **47**, 893, 2002, reproduced with permission from Elsevier).

reduction in ductility as the grain size is reduced in the nanometre range. At very fine grain sizes, the conventional mechanisms of dislocation multiplication fail because of the proximity of the closely spaced boundaries. It then becomes impossible to accumulate dislocations during deformation. Grain boundaries are also good sinks for defects. This would explain the observed inability of nanostructured materials to work harden. One way of overcoming this difficulty is described in Chapter 6.

The difficulty that nanocrystalline grains have in deforming by a dislocation mechanism is highlighted in recent experiments<sup>3</sup> where nanocrystals of ferrite

<sup>3</sup> Ivanisenk, Y., MacLaren, I., Vailiev, R. Z., and Fecht, H.-J., *Advanced Engineering Materials* **7**, 1011, 2005.

were forced to deform in shear. The crystals underwent a shear transformation into austenite.

## 2.6 DISPERSION STRENGTHENING

In all steels there is normally more than one phase present, and indeed it is often the case that several phases can be recognized in the microstructure. The matrix, which is usually ferrite (bcc structure) or austenite (fcc structure) strengthened by grain size refinement and by solid solution additions, is further strengthened, often to a considerable degree, by controlling the dispersions of the other phases in the microstructure. The commonest other phases are carbides formed as a result of the low solubility of carbon in  $\alpha$ -iron. In plain carbon steels this carbide is normally  $\text{Fe}_3\text{C}$  (cementite) which can occur in a wide range of structures from coarse lamellar form (pearlite), to fine rod or spheroidal precipitates (tempered steels). In alloy steels, the same range of structures is encountered, except that in many cases iron carbide is replaced by other carbides which are thermodynamically more stable. Other dispersed phases which are encountered include nitrides, intermetallic compounds and, in cast irons, graphite.

Most dispersions lead to strengthening, but often they can have adverse effects on ductility and toughness. In fine dispersions, ideally small spheres randomly dispersed in a matrix, there are well-defined relationships between the yield stress, or initial flow stress, and the parameters of the dispersion. The simplest is that due to Orowan relating the yield stress of the dispersed alloy  $\tau_0$  to the interparticle spacing  $\Lambda$ :

$$\tau_0 = \tau_s + \frac{T}{b\Lambda/2}, \quad (2.10)$$

where  $\tau_s$  is the yield strength of the matrix,  $T$  is the line tension of a dislocation and  $b$  is the Burgers vector. This result emerges from an analysis of the movement of dislocations around spherical particles, showing that the yield stress varies inversely as the spacing between the particles. If the dispersion is coarsened by further heat treatment, the strength of the alloy falls. A more precise form of the Orowan equation, due to Ashby, takes into account the radius  $r$  of the particles:

$$\tau_0 = \tau_s + \frac{G}{4r}\phi \ln \left( \frac{\Lambda - 2r}{2b} \right) \left( \frac{1}{(\Lambda - 2r)/2} \right), \quad (2.11)$$

where  $\phi$  is a constant and  $G$  is the shear modulus.

These relationships can be applied to simple dispersions sometimes found in steels, particularly after tempering, when, in plain carbon steels, the structure consists of spheroidal cementite particles in a ferritic matrix. However, they can provide approximations in less ideal cases, which are the rule in steels, where the dispersions vary over the range from fine rods and plates to irregular polyhedra.

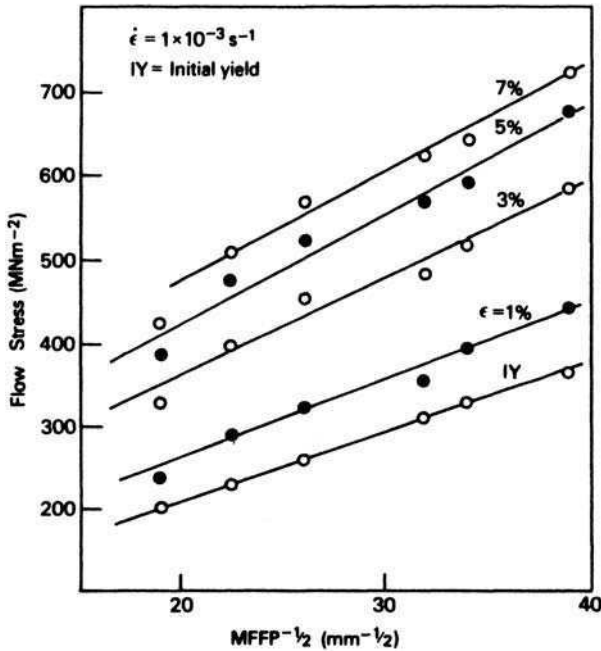


**Fig. 2.10** Dependence of the flow stress at several strains on the MFFP in a pearlitic steel (Takahashi and Nagumo, *Transactions of the Japan Institute of Metals* 11, 113, 1970).

Perhaps the most familiar structure in steels is that of the eutectoid pearlite, usually approximated as a lamellar mixture of ferrite and cementite. This can be considered as an extreme form of dispersion of one phase in another, and undoubtedly provides a useful contribution to strengthening. The lamellar spacing can be varied over wide limits, and again the strength is sensitive to such changes (see Chapter 3). When the coarseness of the pearlite is represented by a mean uninterrupted free ferrite path (MFFP) in the pearlitic ferrite, it has been shown that the flow stress is related to  $\text{MFFP}^{-1/2}$ , i.e. there is a relationship of the Hall-Petch type (Fig. 2.10).

## 2.7 AN OVERALL VIEW

Strength in steels arises from several phenomena, which usually contribute collectively to the observed mechanical properties. The heat treatment of steels is aimed at adjusting these contributions so that the required balance of mechanical properties is achieved. Fortunately the  $\gamma/\alpha$  change allows a great variation in microstructure to be produced, so that a wide range of mechanical properties can be obtained even in plain carbon steels. The additional use of metallic alloying elements, primarily as a result of their influence on the transformation,

provides an even greater control over microstructure, with consequent benefits in the mechanical properties.

We have not discussed in this chapter the strengthening and deformation behaviour of mixed microstructures, such as the dual-phase steels which consist of ferrite and harder martensite. This can radically alter the stress *versus* strain behaviour with the deformation being heterogeneous on a microscopic scale with complex constraint and compatibility issues governing plasticity. Some of these aspects of mixed microstructures are described in Chapter 14 as one of the two case studies.

## 2.8 SOME PRACTICAL ASPECTS

The presence of a sharp yield point in a steel can be detrimental to its behaviour, e.g., when used for pressings, where complex patterns of Luders bands can produce rough surfaces and lead to poor workability. The severity of the yield point is directly related to the amount of carbon and nitrogen in solution in the ferrite, so that steps taken to reduce these concentrations are helpful. Unfortunately, yield points can be obtained with very low concentrations of carbon and nitrogen, and it is impracticable in industrial conditions to obtain steels below these limits. However, any heat treatment which reduces interstitial solid solution is beneficial, e.g. slow cooling from annealing treatments. The yield point can be more reliably eliminated prior to working by a small amount of cold rolling (0.5–2%), referred to as *temper rolling*. As both nitrogen and carbon diffuse appreciably in ferrite at ambient temperatures, it is desirable to fabricate steels soon after rolling and annealing.

While carbon and nitrogen can both cause strain ageing and consequently a yield point, the higher solubility of nitrogen in ferrite means that it provides the greater problem in steels used for deep drawing and pressing. Steps are taken during steelmaking to keep the nitrogen level down, but to minimize its effects, the easiest solution is to add small concentrations of strong nitride formers such as aluminium, titanium or vanadium, which reduce the nitrogen in solution to very low levels.

The occurrence of strain ageing can, by increasing both the yield stress and ultimate tensile stress, benefit mild steels which are used for constructional purposes. Furthermore, the fatigue properties are improved, both at room temperature and in the range up to 350°C. The existence of a well-defined fatigue limit in steels, i.e. a fatigue stress limit below which failure does not occur, has been linked to the occurrence of strain ageing during the test, but even very pure iron shows the same behaviour. It should be emphasized that even in a relatively simple low carbon steel, the strength arises not only from these effects of carbon and nitrogen, but also from the solid solution hardening of elements such as silicon and manganese, and potentially from the refinement of the ferrite grain size by various means.

## 2.9 LIMITS TO STRENGTH

Strength is not always a useful entity. It may not in fact be safe to load an engineering structure to the full capability of the material. To illustrate this and some other limits of scale, a comparison is presented here of the potential strength of steel and that of carbon nanotubes which are the subject of much contemporary discussion.

### 2.9.1 Theoretical strength

The strength of crystals increases sharply as they are made smaller. This is because the chances of avoiding defects become greater as the volume of the sample decreases. In the case of metals, imperfections in the form of dislocations are able to facilitate shear at much lower stresses than would be the case if whole planes of atoms had to collectively slide across each other. Since defects are very difficult or impossible to avoid, the strength in the absence of defects is said to be that of an *ideal* crystal.

In an ideal crystal, the tensile strength  $\sigma_t \simeq 0.1E$  where  $E$  is the Young's modulus. The corresponding ideal shear strength is  $\sigma_s \simeq b\mu/2\pi a$ , where  $\mu$  is the shear modulus,  $b$  is a repeat period along the displacement direction and  $a$  is the spacing of the slip planes. For ferritic iron,  $\mu = 80.65$  GPa and  $E \simeq 208.2$  GPa. It follows that the ideal values of tensile and shear strength should be about 21 and 11 GPa, respectively. In fact, tensile strengths approaching the theoretical values were achieved by Brenner as long ago as 1956 (Fig. 2.11a) during the testing of whiskers of iron with diameters less than  $2\ \mu\text{m}$ . It is interesting that these stress levels fall out of the regime where Hooke's law applies (Fig. 2.11b).

The strength decreased sharply as the dimensions of the whiskers were increased (Fig. 2.11a), because the chances of finding defects increase as the sample gets bigger. It was therefore recognized many decades ago that it is not wise to rely on perfection as a method of designing strong materials,

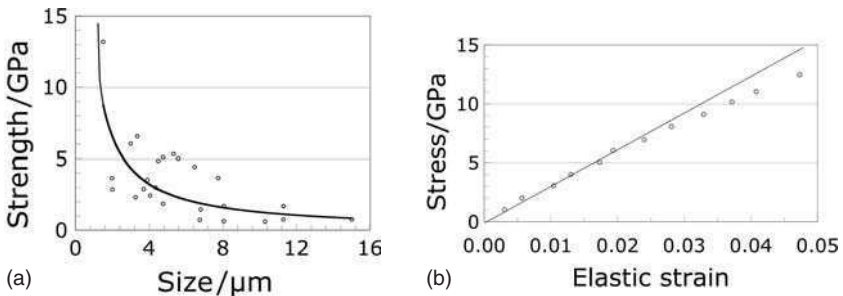


**Fig. 2.11** (a) The tensile strength of whiskers of iron. (b) Non-linear elasticity at large stresses (after Brenner, S., *Acta Metallurgica* **4**, 62, 1956; *Journal of Applied Physics* **27**, 1484, 1956).



although it remains the case that incredible strength can be achieved by reducing dimensions, in the case of iron, to a micrometre scale.

It is in this context that we now proceed to examine the notion that large-scale engineering structures can be designed using very long carbon nanotubes.<sup>4</sup> The particular structure proposed is a space elevator to replace rocket launches, and would require ropes which are some 120,000 km in length.

### 2.9.2 Gigatubes

Carbon nanotubes can be imagined to be constructed from sheets of graphene consisting of  $sp^2$  carbon arranged in a two-dimensional hexagonal lattice (Fig. 2.12). The sheets, when rolled up and with the butting edges appropriately bonded, are the nanotubes, which may or may not be capped by fullerene hemispheres. The actual form can be complex, e.g. with occasional pentagonal rings of carbon atoms instead of hexagonal to accommodate changes in shape.

The breaking strength of such a tube has been estimated to be an extraordinary 130 GPa; this number is astonishing and has led to many exaggerated comparisons against steel. However, this is the strength of an invisibly small nanotube. Larger tubes will contain defects which lead to a gross deterioration of strength, rather like the behaviour of whiskers of iron. Some of these defects will be there at equilibrium and hence are unavoidable. For example, it is known that metals contain an *equilibrium* concentration of vacancies. The enthalpy change associated with the formation of a vacancy opposes its existence, whereas the change in configurational entropy due to the formation of a vacancy favours its

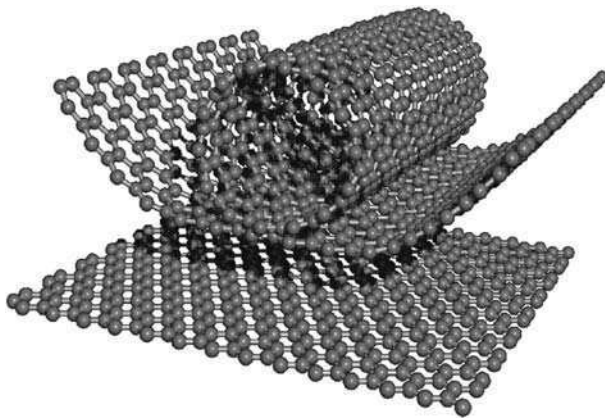


**Fig. 2.12** Schematic diagram showing how a sheet of graphene might be rolled to form a tube (courtesy of M. Endo).

<sup>4</sup> Edwards, B. C., *Acta Astronautica* **47**, 735, 2000.

formation. The total change in free energy on forming  $n$  vacancies in a crystal is given by:<sup>5</sup>

$$\Delta G = n\Delta g - kT[(N + n) \ln(N + n) - N \ln N - n \ln n],$$

where  $k$  is the Boltzmann constant,  $T$  is the absolute temperature,  $N$  is the number of atoms,  $\Delta g = \Delta h - T\Delta s$ ,  $\Delta h$  is the enthalpy of formation of one vacancy and  $\Delta s$  is the entropy of formation of a vacancy excluding any contribution from configurational entropy, which is the second term in the equation. The equilibrium mole fraction of vacancies ( $x$ ) is obtained by writing  $\partial \Delta G / \partial n = 0$  giving:

$$x = n/N \simeq \exp\{-\Delta g/kT\}.$$

On this basis, and taking the energy of a vacancy in a nanotube as 7 eV, and setting  $T$  to be the manufacturing temperature of the tubes (2000–4000 K), it is possible to show that a carbon nanotube strand appropriate for a space elevator, weighing 5000 kg, would roughly  $10^{10}$ – $10^{20}$  defects. It is not therefore possible to scale the properties of a nanotube by some 18 orders of magnitude and assume that the strength will be retained.

This emphasizes again that systems which rely on perfection in order to achieve strength necessarily fail on scaling to engineering dimensions. Indeed, there is no carbon tube which can match the strength of iron beyond a scale of 2 mm.

### 2.9.3 Fracture

Suppose that gigatubes of carbon could be made capable of supporting a stress of 130 GPa. Would this allow for safe engineering design? One aspect of safe design is that fast fracture should be avoided; most metals absorb energy in the form of plastic deformation before ultimate fracture. Energy absorption in an accident is a key aspect of automobile safety. Carbon nanotubes are not in this sense defect tolerant; their deformation prior to fracture is elastic. The stored energy density in a tube stressed to 130 GPa, given an elastic modulus along its length of  $E = 1.2$  TPa is in excess of that associated with dynamite (Table 2.1). Dynamite is explosive because of its high energy density and because this energy is released rapidly, the detonation front propagating at some  $6000 \text{ m s}^{-1}$ . The speed of an elastic wave in the carbon is given by  $\sqrt{E/\rho}$  where  $\rho$  is the density. In the event of fracture, the rate at which the stored energy would be released is much greater than that of dynamite (Table 2.1), meaning that fracture is unlikely to occur in a safe manner.

It follows that structures in tension, which reversibly store energy far in excess of their ability to do work during fracture must be regarded as unsafe.

<sup>5</sup> Christian, J. W., *Theory of Transformations in Metals and Alloys*, 3rd edition, Pergamon Press, Oxford, 2003.

**Table 2.1** Comparison of a fully loaded carbon nanotube and dynamite

	$\text{J g}^{-1}$	$\text{m s}^{-1}$
Dynamite	4650	6000
Carbon nanotube	5420	21,500

Strength can only be exploited in a safe manner if the material is capable of absorbing sufficient energy during fracture.

**FURTHER READING**

AIME, *Iron and its Dilute Solutions*, Interscience, New York, 1963.

Baird, J. D., *Strain Ageing of Steel – A Critical Review*, Reprinted from *Iron and Steel*, **36**, 186, 1963.

Baker, T. N. (ed.), *Yield, Flow and Fracture*, Professor N. J. Petch Retirement Meeting, Applied Science Publishers, UK, 1982.

Bhadeshia, H. K. D. H., Bulk nanocrystalline steels, *Ironmaking and Steelmaking* **32**, 405, 2005.

Bhadeshia, H. K. D. H. and Muruganath, M., *Components of the Creep Strength of Welds*, Mathematical Modelling of Weld Phenomena 6, Maney Publishers, London, 243, 2002.

Charles, J. A. and Smith, G. C. (eds), *Advances in Physical Metallurgy*, Sir Alan Cottrell 70th Birthday Meeting, The Institute of Materials, London, UK, 1990.

Christian, J. W., Some surprising features of the deformation of bcc metals, *Metallurgical Transactions* **14A**, 1237, 1983.

Cottrell, A. H., *Dislocations and Plastic Flow in Crystals*, Oxford University Press, Oxford, 1953.

Gleiter, H., Nanocrystalline materials, *Progress in Materials Science* **33**, 223, 1989.

Hall, E. O., *Yield Point Phenomena in Metals and Alloys*, Macmillan, London, 1970.

Hansen, N., Hall–Petch relation and boundary strengthening, *Scripta Materialia* **51**, 801, 2004.

Honeycombe, R. W. K., *The Plastic Deformation of Metals*, 2nd edition, Edward Arnold, London, 1984.

Howe, A. A., Ultrafine grained steels: industrial prospects, *Materials Science and Technology* **16**, 1264, 2000.

Langer, E. W., *The Quench Ageing Process in Iron*, Copenhagen, 1967.

Leslie, W. C., *Metallurgical Transactions* **3**, 5, 1972.

Pickering, F. B., *Physical Metallurgy and the Design of Steels*, Applied Science Publishers, London, 1978.

Speich, G. R. and Clark, J. B. (eds), *Precipitation from Iron–base Alloys*, Gordon and Breach, New York, 1965.

Takeuchi, S., *Journal of the Physical Society of Japan* **27**, 929, 1969.

Valiev, Z., Islamgaliev, R. K. and Alexandrov, I. V., Bulk nanostructured materials from severe plastic deformation, *Progress in Materials Science* **45**, 103, 2000.

Yokota, T., Garica–Mateo, C. and Bhadeshia, H. K. D. H., Formation of nanostructured steel by phase transformation, *Scripta Materialia* **51**, 767, 2004.

# 3

## THE IRON-CARBON EQUILIBRIUM DIAGRAM AND PLAIN CARBON STEELS

### 3.1 THE IRON-CARBON EQUILIBRIUM DIAGRAM

A study of the constitution and structure of all steels and irons must first start with the iron-carbon equilibrium diagram. Many of the basic features of this system (Fig. 3.1) influence the behaviour of even the most complex alloy steels. For example, the phases found in the simple binary Fe-C system persist in complex steels, but it is necessary to examine the effects alloying elements have on the formation and properties of these phases. The iron-carbon diagram provides a valuable foundation on which to build knowledge of both plain carbon and alloy steels in their immense variety.

It should first be pointed out that the normal equilibrium diagram really represents the metastable equilibrium between iron and iron carbide (cementite). Cementite is metastable, and the true equilibrium should be between iron and graphite. Although graphite occurs extensively in cast irons (2–4 wt% C), it is usually difficult to obtain this equilibrium phase in steels (0.03–1.5 wt% C). Therefore, the metastable equilibrium between iron and iron carbide should be considered, because it is relevant to the behaviour of most steels in practice.

The much larger phase field of  $\gamma$ -iron (austenite) compared with that of  $\alpha$ -iron (ferrite) reflects the much greater solubility of carbon in  $\gamma$ -iron, with a maximum value of just over 2 wt% at 1147°C (E, Fig. 3.1). This high solubility of carbon in  $\gamma$ -iron is of extreme importance in heat treatment, when solution treatment in the  $\gamma$ -region followed by rapid quenching to room temperature allows a supersaturated solid solution of carbon in iron to be formed. The  $\alpha$ -iron phase field is severely restricted, with a maximum carbon solubility of 0.02 wt% at 723°C (P), so over the carbon range encountered in steels from 0.05 to 1.5 wt%,  $\alpha$ -iron is normally associated with iron carbide in one form or another. Similarly, the  $\delta$ -phase field is very restricted between 1390 and 1534°C and disappears completely when the carbon content reaches 0.5 wt% (B).

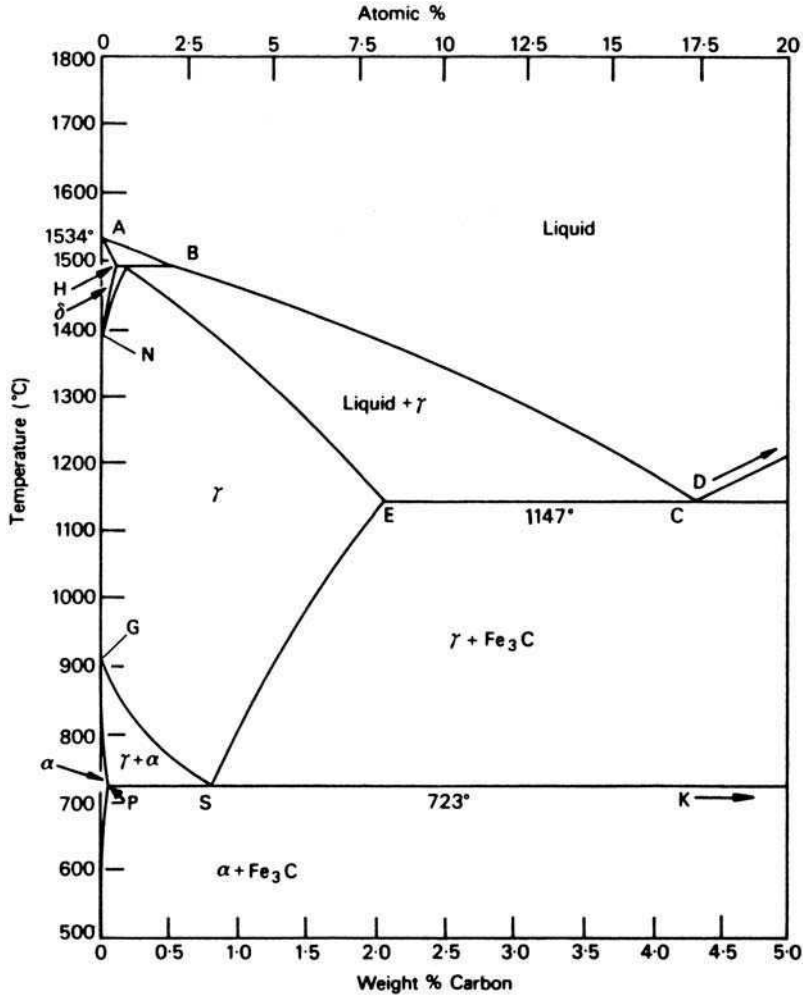


**Fig. 3.1** The iron–carbon diagram (after Hansen, *Constitution of Binary Alloys*, 2nd edition, McGraw-Hill, New York, USA, 1958).

There are several temperatures or critical points in Fig. 3.1 which are important, both from the basic and from the practical point of view. Firstly, there is the  $A_1$  temperature at which the eutectoid reaction occurs (P–S–K), which is 723°C in the binary diagram. Secondly, there is the  $A_3$  temperature when  $\alpha$ -iron transforms to  $\gamma$ -iron. For pure iron this occurs at 910°C, but the transformation temperature is progressively lowered along the line GS by the addition of carbon. The third point is  $A_4$  at which  $\gamma$ -iron transforms to  $\delta$ -iron, 1390°C in pure iron, but this is raised as carbon is added. The  $A_2$  point is the Curie point

when ferritic iron changes from the ferro- to the paramagnetic condition. This temperature is  $769^{\circ}\text{C}$  for pure iron, but no change in crystal structure is involved. The  $A_1$ ,  $A_3$  and  $A_4$  points are easily detected by thermal analysis or dilatometry during cooling or heating cycles, and some hysteresis is observed. Consequently, three values for each point can be obtained,  $A_c$  for heating (chauffage),  $A_r$  for cooling (refroidissement) and  $A_e$  (equilibrium), but it should be emphasized that the  $A_c$  and  $A_r$  values will be sensitive to the rates of heating and cooling, as well as to the presence of alloying elements.

The great difference in carbon solubility between  $\gamma$ - and  $\alpha$ -iron leads normally to the rejection of carbon as iron carbide at the boundaries of the  $\gamma$ -phase field. The transformation of  $\gamma \rightarrow \alpha$ -iron occurs via a eutectoid reaction which plays a dominant role in heat treatment. The eutectoid temperature is  $723^{\circ}\text{C}$  while the eutectoid composition is about 0.8 wt% C(S) (Fig. 3.1). On cooling alloys containing less than 0.8 wt% C slowly, hypo-eutectoid ferrite is formed from austenite in the range  $910$ – $723^{\circ}\text{C}$  with enrichment of the residual austenite in carbon, until at  $723^{\circ}\text{C}$  the remaining austenite, now containing 0.8 wt% carbon transforms to pearlite, a lamellar mixture of ferrite and iron carbide (cementite) (Fig. 3.2a). In austenite with 0.8–2.06 wt% carbon, on cooling slowly in the temperature interval from  $1147$  to  $723^{\circ}\text{C}$ , cementite first forms progressively depleting the austenite in carbon, until at  $723^{\circ}\text{C}$ , the austenite contains 0.8 wt% carbon and transforms to pearlite.

Steels with less than about 0.8 wt% carbon are thus hypo-eutectoid alloys with ferrite and pearlite as the prime constituents (Fig. 3.2b), the relative volume fractions being determined by the lever rule which states that as the carbon content is increased, the volume percentage of pearlite increases, until it is 100% at the eutectoid composition.

The three phases, ferrite, cementite and pearlite are thus the principal constituents of the microstructure of plain carbon steels, provided they have

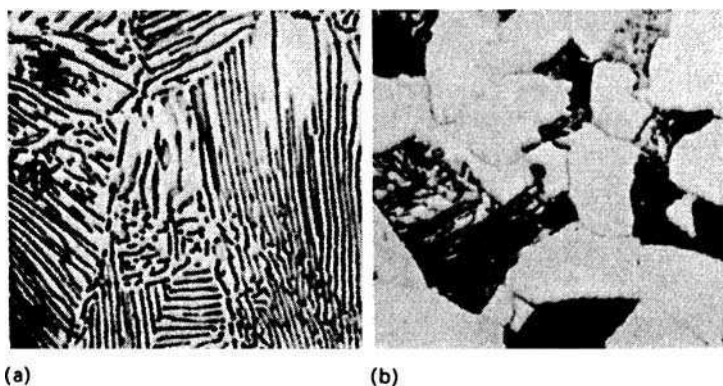


**Fig. 3.2** (a) 0.8 wt% C steel-pearlite (Ricks). Optical micrograph  $\times 1000$  (b) 0.4 wt% C steel-ferrite and pearlite (courtesy of Ricks). Optical micrograph  $\times 1100$ .

been subjected to relatively slow cooling rates to avoid the formation of metastable phases. Consequently, it is important to examine the nucleation and growth of these phases, and to determine the factors which control their morphology.

### 3.2 THE AUSTENITE-FERRITE TRANSFORMATION

Under equilibrium conditions, pro-eutectoid ferrite will form in iron-carbon alloys containing up to 0.8 wt% carbon. The reaction occurs at 910°C in pure iron, but takes place between 910°C and 723°C in iron-carbon alloys. However, by quenching from the austenitic state to temperatures below the eutectoid temperature, ferrite can be formed down to temperatures as low as 600°C. There are pronounced morphological changes as the transformation temperature is lowered, which it should be emphasized apply in general to hypo- and hyper-eutectoid phases, although in each case there will be variations due to the precise crystallography of the phases involved. For example, the same principles apply to the formation of cementite from austenite, but it is not difficult to distinguish ferrite from cementite morphologically.

As a result of a survey of the behaviour of plain carbon steels, Dubé proposed a classification of morphologies of ferrite which occur as the  $\gamma/\alpha$  transformation temperature is lowered. Dubé recognized four well-defined morphologies based on optical microscopy, later extended by Aaronson:

1. *Grain boundary allotriomorphs*: An allotriomorph has a shape which does not reflect its internal crystalline symmetry. This is because it tends to nucleate at the austenite grain surfaces, forming layers which follow the grain boundary contours (Fig. 3.3a). The allotriomorph is in contact with at least two of the austenite grains and will have a random orientation with one of them, but an orientation which is more coherent with the other. It may, therefore, be crystallographically faceted on one side but with a curved boundary on the other side.
2. *Widmanstätten ferrite plates or laths*: These plates grow along well-defined planes of the austenite and do not grow across the austenite grain boundaries. Primary Widmanstätten ferrite grows directly from the austenite grain surfaces, whereas secondary Widmanstätten ferrite develops from allotriomorphs of ferrite already present in the microstructure (Fig. 3.3b).
3. *Intragranular idiomorphs*: These are equi-axed crystals which nucleate inside the austenite grains (Fig. 3.3c), usually on non-metallic inclusions present in the steel. An idiomorph forms without contact with the austenite grain surfaces and has a shape which some shows crystallographic facets.
4. *Intragranular plates*: These plates are similar to those growing from the grain boundaries, but they nucleate entirely within the austenite grains (Fig. 3.3d).

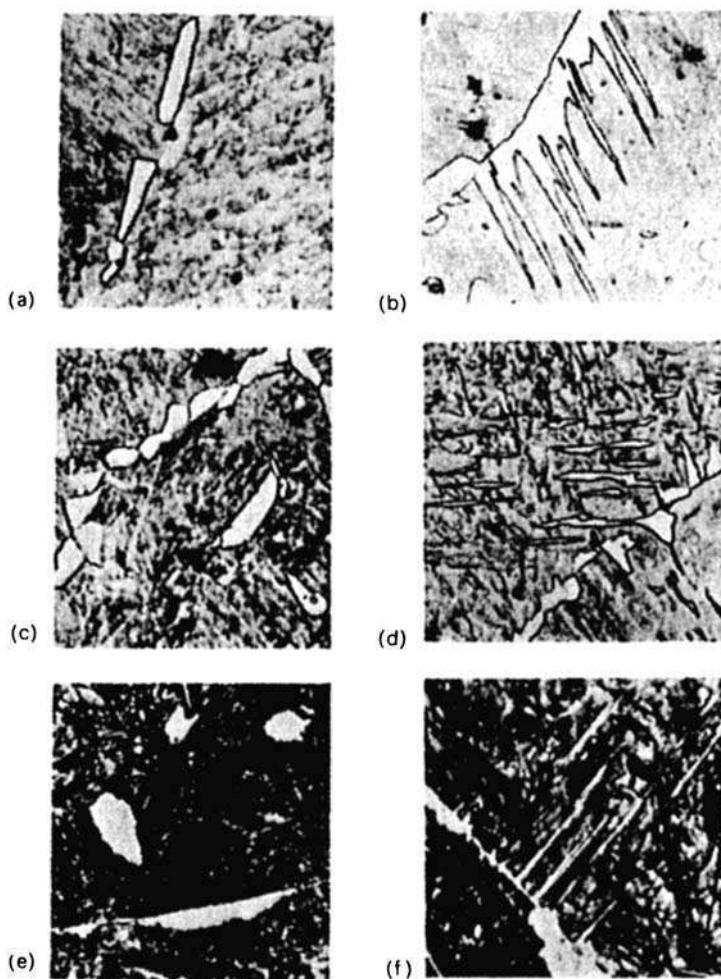


**Fig. 3.3** Growth of pro-eutectoid ferrite and hyper-eutectoid cementite: (a) 0.34 wt% C steel, 12 min at 790°C. Grain boundary allotriomorphs of ferrite. (b) 0.34 wt% C steel, 15 min at 725°C. Widmanstätten ferrite growing from grain boundary ferrite. (c) 0.34 wt% C steel, 12 min at 790°C. Grain boundary allotriomorphs and intragranular idiomorphs of ferrite. (d) 0.34 wt% C steel, 15 min at 725°C. Intragranular Widmanstätten ferrite plates. (e) 1.2 wt% C steel, 10 min at 730°C. Grain boundary allotriomorphs and intragranular idiomorphs of cementite. (f) 1.2 wt% C steel, 10 min at 730°C. Widmanstätten cementite: optical micrographs, (a)–(d)  $\times 500$ , (e) and (f)  $\times 350$  (courtesy of R. A. Ricks).

Grain boundary allotriomorphs are the first morphology to appear over the whole range of composition and temperature. However, at the highest temperatures (above 800°C), they predominate by growing along the boundaries, and also into the grains to give a well-defined grain structure, generally referred to



as equi-axed ferrite. The allotriomorphs nucleate having a reproducible orientation relationship such as the approximate Kurdjumov–Sachs orientation with one austenite grain ( $\gamma_1$ ):

$$\begin{aligned}\{111\}_{\gamma_1} &\parallel \{110\}_{\alpha}, \\ \langle \bar{1}10 \rangle_{\gamma_1} &\parallel \langle \bar{1}11 \rangle_{\alpha}.\end{aligned}$$

But they also grow into the adjacent austenite grain ( $\gamma_2$ ) with which they should normally have a random orientation relationship. The disordered boundary responsible for this growth should migrate more readily at high temperatures, although there is evidence that such boundaries readily develop growth facets, indicating that there is anisotropy of growth rate.

At lower transformation temperatures, the mobility of curved or random  $\gamma/\alpha$  boundaries decreases, while the coherent interfaces become more dominant. For example, laths (narrow plates) of ferrite grow from protuberances on the grain boundary ferrite on the side of the coherent boundary, so the laths are moving into austenite with which they have the Kurdjumov–Sachs relationship. The laths can also grow from clean austenite grain boundaries, the net result being a structure which is normally referred to as primary Widmanstätten ferrite. This structure is encouraged by large austenite grain sizes which prevent the impingement of grain boundary ferrite by growth across grains, thus allowing Widmanstätten ferrite room to grow. If the carbon content is too high ( $>0.4$  wt%), the pearlitic regions are sufficiently large to prevent ferrite laths growing. However, if the carbon content is below 0.2 wt%, impingement of allotriomorphs across  $\gamma$ -grains again minimizes the growth of Widmanstätten ferrite. But the most important factor is the temperature of growth of the ferrite, which is determined by the overall rate of cooling of the steel, or the temperature of isothermal transformation. An important structural feature found in Widmanstätten ferrite is that the formation of laths is accompanied by surface relief effects in the form of invariant-plane strains with a large shear component.

In common with many other phases presenting a planar coherent or semi-coherent interface to a matrix, Widmanstätten ferrite plates have been suggested to grow by the lateral movement of small steps on the interface (Fig. 3.4). Some evidence has been obtained to support the view that shear displacements can be involved at low transformation temperatures. The dislocation density of the ferrite increases with decreasing transformation temperature, and surface relief is observed after transformation.

### 3.3 THE AUSTENITE–CEMENTITE TRANSFORMATION

The Dubé classification applies equally well to the various morphologies of cementite formed at progressively lower transformation temperatures. The initial development of grain boundary allotriomorphs is very similar to that of ferrite, and the growth of side plates or Widmanstätten cementite follows the

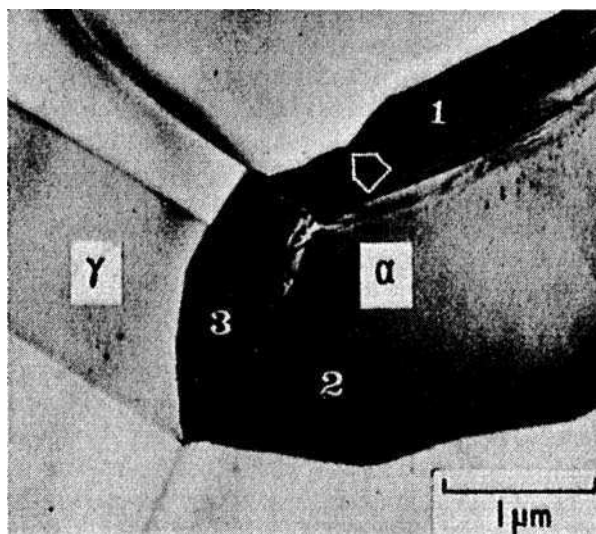


**Fig. 3.4** Allotriomorphic ferrite forming in austenite with planar and stepped interfaces in a low carbon alloy steel (Edmonds and Honeycombe). Photoemission electron micrograph.

same pattern (Figs 3.3e, f). The cementite plates are more rigorously crystallographic in form, despite the fact that the orientation relationship with austenite (found by Pitsch) is a more complex one, i.e.:

$$(100)_c // (\bar{5}\bar{5}4)_\gamma,$$

$$(010)_c // (110)_\gamma,$$

$$(001)_c // (\bar{2}25)_\gamma.$$

As in the case of ferrite, most of the side plates originate from grain boundary allotriomorphs, but in the cementite reaction more side plates tend to nucleate at twin boundaries in austenite.

### 3.4 THE KINETICS OF THE $\gamma \rightarrow \alpha$ TRANSFORMATION

The transformation of austenite in steels can be studied during continuous cooling using various physical measurements, e.g. dilatometry, thermal analysis, electrical resistivity, etc., however, the results obtained are very sensitive to the cooling rate used. Davenport and Bain first introduced the isothermal transformation approach, and showed that by studying the reaction isothermally at a series of temperatures, a characteristic time–temperature–transformation or *TTT* curve can be obtained for each particular steel. In their simplest form, these transformation curves have a well-defined ‘C’ shape (Fig. 3.5), where the nose of the curve represents the temperature at which the reaction proceeds most

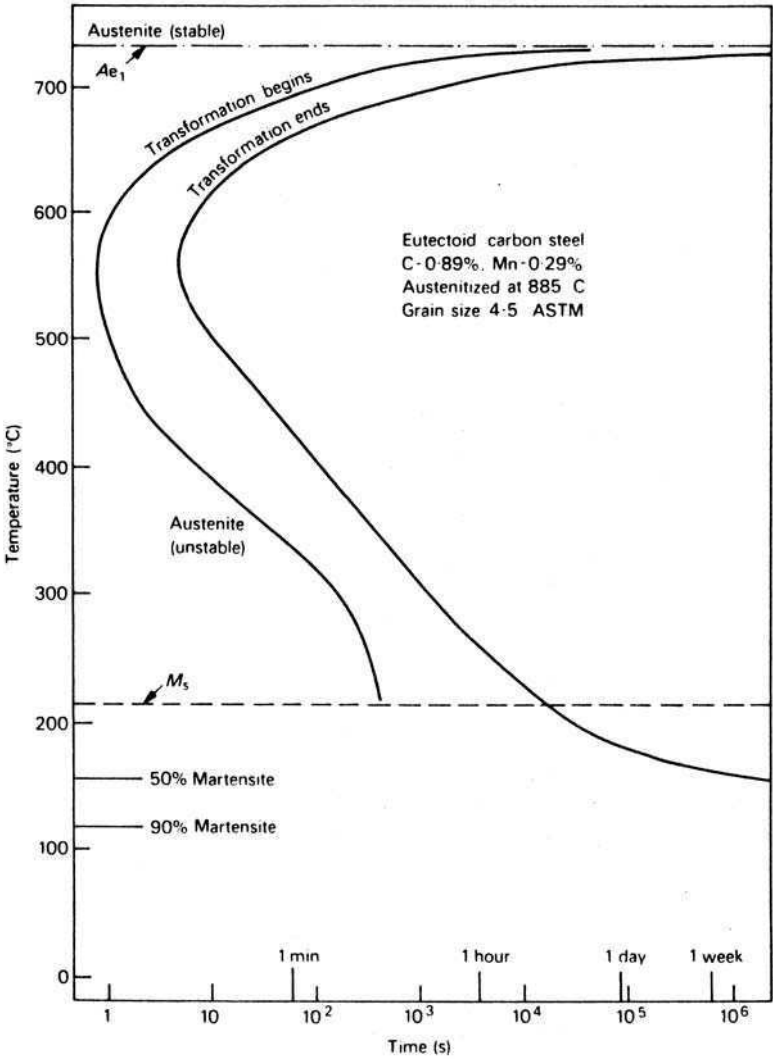


**Fig. 3.5** TTT diagram for a 0.89% carbon steel (US Steel Co., *Atlas of Isothermal Diagrams*).

rapidly, slowing down both at higher and at lower temperatures. This can be explained in general terms as follows. For a eutectoid steel transformed close to the eutectoid temperature, the degree of undercooling,  $\Delta T$ , is low so the driving force for the transformation is small. However, as  $\Delta T$  increases the driving force also increases, and the reaction occurs more quickly, until the maximum rate at the nose of the curve. Below this temperature, the driving force for the reaction continues to increase, but the reaction is now impeded by the slow diffusivity of the rate-controlling element, which in plain carbon steels may be carbon or iron.

One of the simplest examples of a  $TTT$  curve is that for a 0.8 wt% eutectoid carbon steel. In Fig. 3.5 the beginning and end of transformation over a wide temperature range is plotted to produce two curves making up the diagram. When the carbon content of the steel is lowered, the ferrite reaction will also take place and this is represented by another curve which is frequently imposed on the same diagram, and which normally precedes the pearlite reaction. Similarly, the cementite reaction can be recorded in hyper-eutectoid steels. The  $TTT$  curve strictly applies to the nucleation and growth of one phase in austenite, but at the lower transformation temperatures other constituents can appear, e.g. bainite, martensite. These have quite different characteristics to ferrite and pearlite, so they will be dealt with separately (Chapters 5 and 6).

### 3.4.1 Growth kinetics of ferrite

Both the lengthening and thickening of grain boundary allotriomorphs has been studied. The latter process is considered first, represented as the one-dimensional thickening of allotriomorphs into the austenite grains, controlled by the diffusion of carbon in the austenite ahead of the interface.

Ferrite has a lower solubility ( $c^{\alpha\gamma}$ ) for carbon than austenite ( $c^{\gamma\alpha}$ ), so carbon is partitioned into the latter. As the ferrite grows, so does the extent of its diffusion field in the austenite. This retards growth because the solute then has to diffuse over ever larger distances. As will be proven the thickness of the ferrite increases with the square root of time, i.e. the growth rate slows down as time increases. Following Zener, it is assumed in the derivation that the concentration gradient in the matrix is constant, and that the far-field concentration  $\bar{c}$  never changes (i.e. the matrix is semi-infinite normal to the advancing interface). This is to simplify the mathematics without losing any of the insight into the problem.

For isothermal transformation in a plain carbon steel, the concentrations at the interface are given by a tie-line of the phase diagram as shown in Fig. 3.6. The diffusion flux of solute from the interface must equal the rate at which solute is incorporated in the precipitate so that:

$$\underbrace{(c^{\gamma\alpha} - c^{\alpha\gamma}) \frac{\partial z^*}{\partial t}}_{\text{Rate solute partitioned}} = \underbrace{-D_C^\gamma \frac{\partial c}{\partial z}}_{\text{Diffusion flux from interface}} \simeq D_C^\gamma \frac{\bar{c} - c^{\gamma\alpha}}{\Delta z}, \quad (3.1)$$

where  $z$  is a coordinate normal to the interface with a value  $z^*$  at the position of the interface. Note that the concentration gradient is evaluated at the position of the interface ( $z = z^*$ ).

A second equation can be derived by considering the overall conservation of mass:

$$(c^{\alpha\gamma} - \bar{c})z^* = \frac{1}{2}(\bar{c} - c^{\gamma\alpha})\Delta z.$$

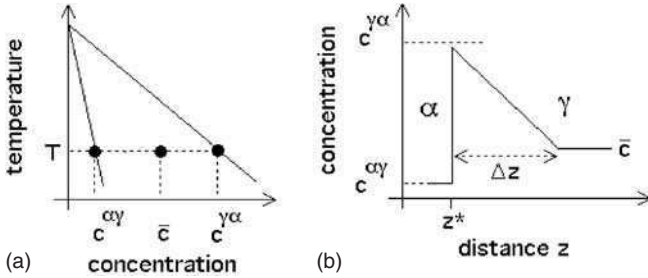


**Fig. 3.6** Phase diagram and its relationship to the concentration profile at the ferrite/austenite interface during diffusion-controlled growth.

On combining these expressions to eliminate  $\Delta z$  we get:

$$\frac{\partial z^*}{\partial t} = \frac{D_C^\gamma (\bar{c} - c^{\gamma\alpha})^2}{2z^* (c^{\alpha\gamma} - c^{\gamma\alpha})(c^{\alpha\gamma} - \bar{c})}.$$

It follows that:

$$z^* = \frac{(\bar{c} - c^{\gamma\alpha})}{[2(c^{\alpha\gamma} - c^{\gamma\alpha})(c^{\alpha\gamma} - \bar{c})]^{1/2}} \times \sqrt{D_C^\gamma t}. \quad (3.2)$$

Consider now a ternary steel, say Fe–Mn–C. It would be necessary to satisfy two equations of the form of Equation (3.1), simultaneously, for each of the solutes:

$$\left. \begin{aligned} (c_C^{\gamma\alpha} - c_C^{\alpha\gamma})v &= -D_C^\gamma \nabla c_C \\ (c_{Mn}^{\gamma\alpha} - c_{Mn}^{\alpha\gamma})v &= -D_{Mn}^\gamma \nabla c_{Mn} \end{aligned} \right\}. \quad (3.3)$$

Because  $D_C^\gamma \gg D_{Mn}^\gamma$ , these equations cannot in general be simultaneously satisfied for the tie-line passing through the alloy composition  $\bar{c}_C, \bar{c}_{Mn}$ . It is, however, possible to choose other tie lines which satisfy equation (3.3). If the tie-line is such that  $c_C^{\gamma\alpha} = \bar{c}_C$  (e.g. line  $cd$  for alloy A of Fig. 3.7a), then  $\nabla c_C$  will become very small, the driving force for carbon diffusion in effect being reduced, so that the flux of carbon atoms is forced to slow down to a rate consistent with the diffusion of manganese. Ferrite forming by this mechanism is said to grow by a ‘Partitioning, Local Equilibrium’ (or PLE) mechanism, in recognition of the fact that  $c_{Mn}^{\alpha\gamma}$  can differ significantly from  $\bar{c}_{Mn}$ , giving considerable partitioning and long-range diffusion of manganese into the austenite.

An alternative choice of tie-line could allow  $c_{Mn}^{\alpha\gamma} \rightarrow \bar{c}_{Mn}$  (e.g. line  $cd$  for alloy B of Fig. 3.7b), so that  $\nabla c_{Mn}$  is drastically increased since only very small amounts of Mn are partitioned into the austenite. The flux of manganese atoms at the interface correspondingly increases and manganese diffusion can then keep pace with that of carbon, satisfying the mass conservation conditions of Equation (3.3). The growth of ferrite in this manner is said to occur by a ‘Negligible Partitioning, Local Equilibrium’ (or NPLE) mechanism, in recognition of

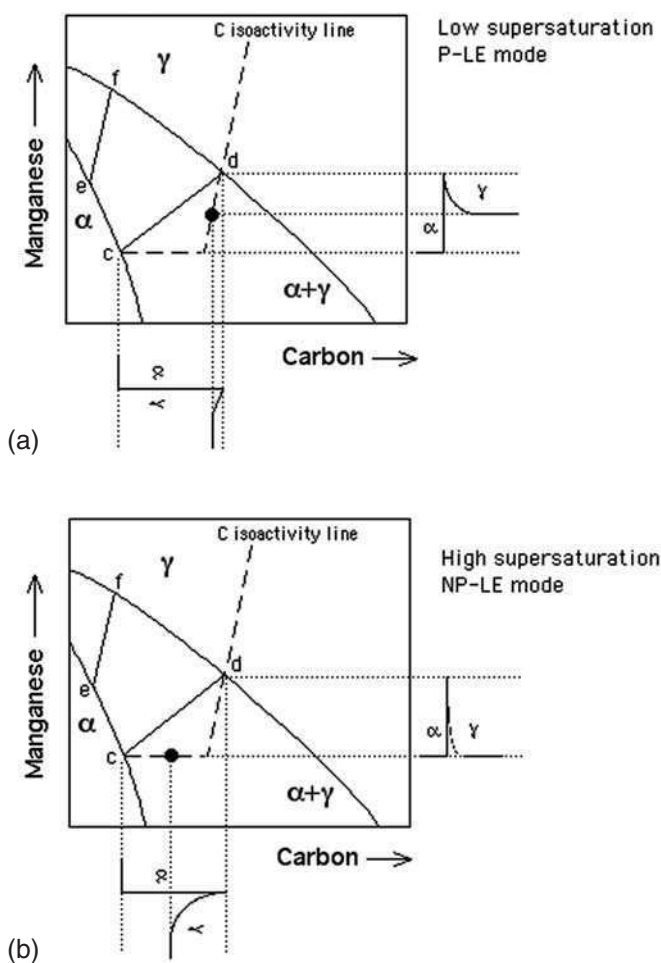


**Fig. 3.7** Schematic isothermal sections of the Fe-Mn-C system, illustrating ferrite growth occurring with local equilibrium at the  $\alpha/\gamma$  interface. (a) Growth at low supersaturations (PLE) with bulk redistribution of manganese, (b) growth at high supersaturations (NP-LE) with negligible partitioning of manganese during transformation. The bulk alloy compositions are designated by the symbol  $\bullet$  in each case.

the fact that the manganese content of the ferrite approximately equals  $\bar{c}_{\text{Mn}}$ , so that little if any manganese partitions into austenite.

What circumstances determine whether growth follows the PLE or NP-LE mode? Figure 3.8 shows the Fe-Mn-C phase diagram, now divided into domains where either PLE or NP-LE is possible but not both. The domains are obtained by drawing right-handed triangles on each tie-line in the  $\alpha + \gamma$  phase field and joining up all the vertices. For example, if an attempt is made

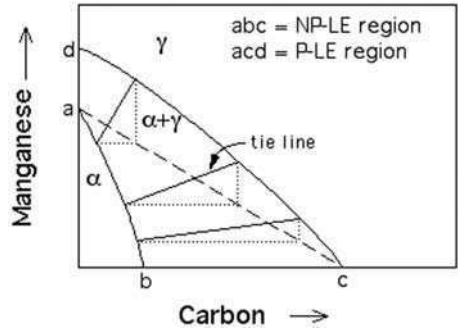


**Fig. 3.8** Regions of the two-phase field where either PLE or NPLE modes of transformation are possible.

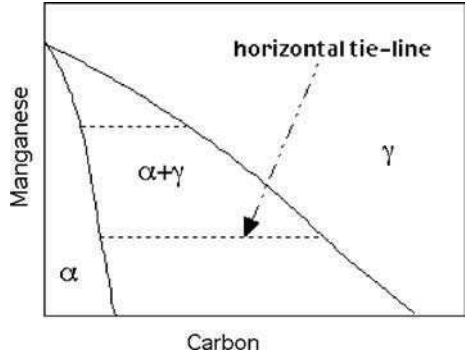


**Fig. 3.9** A para-equilibrium phase diagram.

to define NPLE conditions in the PLE domain, then the tie-line determining interface compositions will incorrectly show that both austenite and ferrite contain less carbon than  $\bar{c}_C$ , a circumstance which is physically impossible.

Para-equilibrium is a constrained equilibrium. It occurs at temperatures where the diffusion of substitutional solutes is not possible within the time scale of the experiment. Nevertheless, interstitials may remain highly mobile. Thus, in a steel, manganese does not partition between the ferrite and austenite, but subject to that constraint, the carbon redistributes until it has the same chemical potential in both phases.

Therefore, the tie lines in the phase diagram (Fig. 3.9) are all virtually parallel to the carbon axis, since Mn does not partition between ferrite and austenite.

In an isothermal section of the ternary phase diagram, the para-equilibrium phase boundaries must lie within the equilibrium phase boundaries as illustrated in Fig. 3.10.

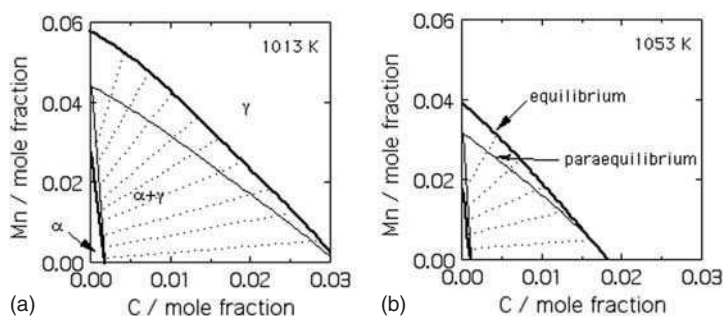


**Fig. 3.10** The para-equilibrium phase field lies within the equilibrium field. The tie lines illustrated are for equilibrium.

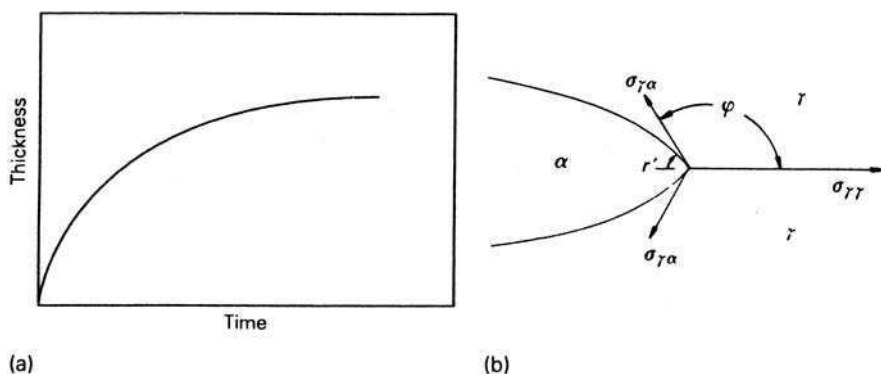


**Fig. 3.11** (a) Plot of the parabolic thickening process described by Equation (3.1). (b) Interfacial energies at the advancing edge of a ferrite allotriomorph (after Hillert, *Jernkontorets Annaler* 141, 757, 1957).

Since the thickness of an allotriomorph increases parabolically with time (Fig. 3.11a), the growth rate decreases as the ferrite thickens. This is because increasing quantities of carbon are rejected into the austenite as the ferrite thickens, making the diffusion of carbon away from the transformation front more difficult.

Zener, and later Hillert, investigated theoretically the edgewise growth of an allotriomorph with curved ends (Fig. 3.11b) assuming that the rate is controlled by the diffusion of carbon in the austenite. The plate shape ensures that the carbon rejected by the growing ferrite is distributed to the sides of the plates. The carbon concentration profile ahead of the plate tip therefore remains constant as the plate lengthens. Consequently, unlike the thickening process, the allotriomorphic ferrite lengthens at a constant rate  $G_L$ :

$$G_L = D_C^\gamma \frac{(c^{\gamma\alpha} - \bar{c})}{4r'(\bar{c} - c^{\alpha\gamma}) \sin \Phi}, \quad (3.4)$$



where

$r'$  = radius of curvature of the allotriomorph adjacent to the grain junction (Fig. 3.11)

$\Phi$  = equilibrium growth angle determined by the relative energies of the interphase and grain boundaries (Fig. 3.11).

The  $\sin \Phi$  term is present because each side of the allotriomorph makes an angle  $\Phi - \pi/2$  with the  $\gamma/\gamma$  grain boundary (Fig. 3.11).

### 3.4.2 Growth kinetics of Widmanstätten ferrite

To apply Equation (3.4) to the growth of ferrite plates (Widmanstätten ferrite) it is simply necessary to replace the term  $r' \sin \Phi$  by  $r$ , the radius of curvature of the edge of the plate. More precise expressions for the growth rate  $G_L$  can be obtained by allowing for the variation of  $D_C^\gamma$  with carbon concentration and temperature. In fact, for Widmanstätten ferrite, the lengthening rate goes through a maximum as the radius of curvature of the plate increases (Fig. 3.12). This is because a smaller tip radius allows the excess carbon to diffuse away more rapidly, but a finer radius also leads to an increased surface to volume ratio, so that a greater proportion of energy has to be expended in creating the surface. Zener argued that the plate would assume a radius consistent with the maximum growth rate, and this is generally observed to be the case in practice.

Thickening studies on Widmanstätten ferrite plates using thermionic emission microscopy have shown that the process is irregular (Fig. 3.13). These irregularities have been interpreted to imply that the thickening occurs by the repeated migration of steps. Jones and Trivedi found that the velocity  $v$  of such steps is given by:

$$v = \frac{D_C^\gamma (c^{\gamma\alpha} - \bar{c})}{\delta \beta (c^{\gamma\alpha} - c^{\alpha\gamma})}, \quad (3.5)$$

where  $\delta$  is the step height, and  $\beta$  is a function of the velocity parameter  $p = v\delta/2D_C^\gamma$ . Notice that this equation cannot be applied unless the step height is determined experimentally. An alternative interpretation of the irregular growth is that the observations simply reflect the formation of new plates adjacent to the original.

It is worth emphasizing that the growth of Widmanstätten ferrite is accompanied by a shape deformation which is an invariant-plane strain, frequently involving the back-to-back growth of self-accommodating pairs of plates. This gives an overall morphology which has the appearance of wedge shaped plates emanating from the austenite grain surfaces. Therefore, Widmanstätten ferrite in alloy steels always grows by a para-equilibrium mechanism, without any partitioning of substitutional solutes.

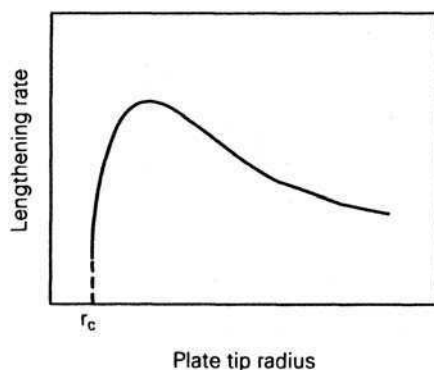


**Fig. 3.12** Variation in the plate lengthening rate as a function of its tip radius.  $r_c$  is the critical radius at which the lengthening rate becomes zero.

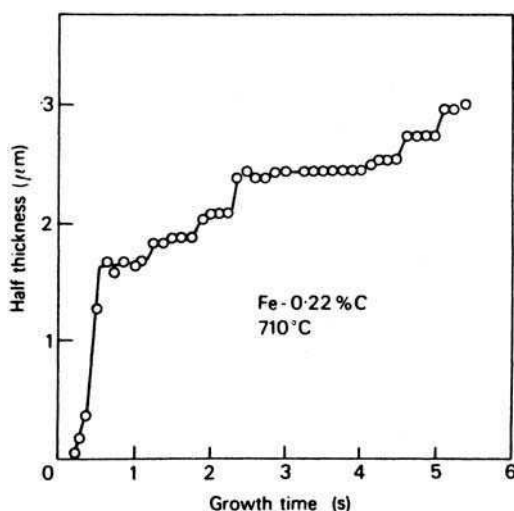


**Fig. 3.13** Thickening of ferrite plates in an Fe–0.22C wt% alloy at 710°C (Aaronson *et al.*, in *Phase Transformations*, ASM, USA, 1970).

### 3.5 THE AUSTENITE–PEARLITE REACTION

Pearlite is probably the most familiar microstructural feature in the whole science of metallography (Figs 3.14a, b). It was discovered by Sorby over 120 years ago, who correctly assumed it to be a lamellar mixture of iron and iron carbide. Pearlite is a very common constituent of a wide variety of steels, where it provides a substantial contribution to strength, so it is not surprising that this phase has received intensive study. Lamellar eutectoid structures of this type are widespread in metallurgy, and frequently pearlite is used as a generic

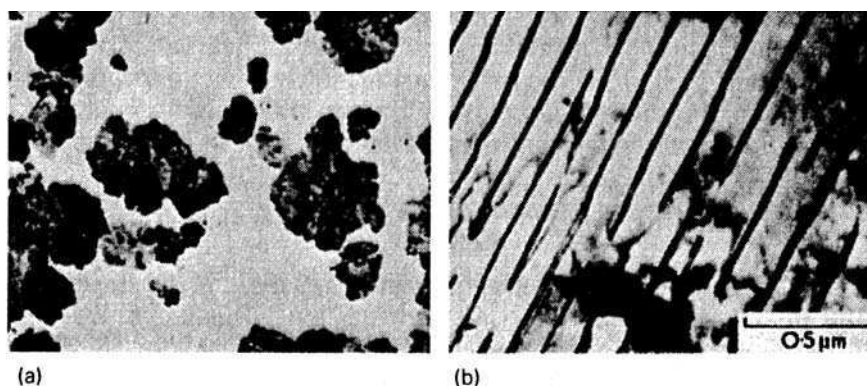


**Fig. 3.14** Isothermal transformation of a 0.8C steel, 10 s at 650°C. (a) Optical micrograph,  $\times 80$ , (b) thin-foil electron micrograph of part of a pearlite nodule  $\times 34,000$  (courtesy of Ohmori).

term to describe them. These structures have much in common with the cellular precipitation reactions. Both types of reaction occur by nucleation and growth (Fig. 3.14a), and rely on diffusion. Pearlite nuclei occur on austenite grain boundaries, but it is clear that they can also be associated with both pro-eutectoid ferrite and cementite. In commercial steels, pearlite nodules can nucleate on inclusions.

### 3.5.1 The morphology of pearlite

The idealized view of pearlite is a hemispherical nodule nucleated at an austenite grain boundary, and growing gradually into one austenite grain (Fig. 3.15). Apart from examining possible sites for nucleation, the following information is needed:

- (a) how the lamellae increase in number,
- (b) the crystallographic relationships between the phases,
- (c) the nature of the pearlite/austenite interface,
- (d) the rate-controlling process.

Not all these questions can yet be fully answered, but the essentials are established. Following the classical work of Mehl and colleagues, Hillert and co-workers were able to show that pearlite could be nucleated either by ferrite, or by cementite, depending on whether the steel was hypo- or hyper-eutectoid in composition. They came to this conclusion after observing lattice continuity between the ferrite in pearlite and pro-eutectoid ferrite, as well as between cementite in pearlite and hyper-eutectoid cementite.

Mehl and co-workers took the view that pearlite nodules formed by sideways nucleation and edge-ways growth (Fig. 3.15). In this way, the rapid increase

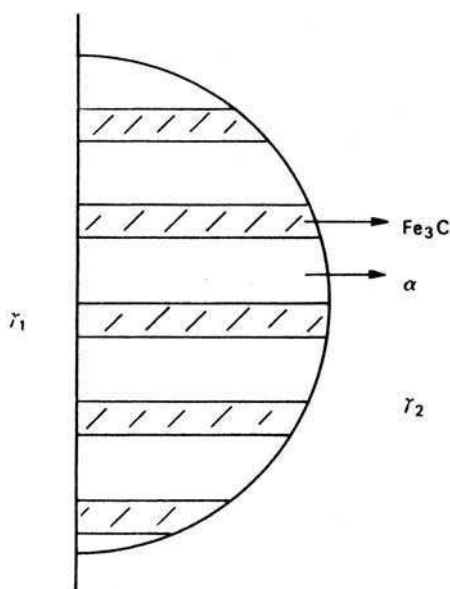


**Fig. 3.15** Idealized pearlite nodule at austenite grain boundary.

in the number of lamellae in a nodule which occurred during growth could be explained, but Modin indicated that this could equally well result from the branching of lamellae during growth. Thin-foil electron microscopy work by Dippenaar and Honeycombe on 13% Mn 0.8% carbon steel allowed the examination of very small nodules at an early stage of growth in an austenitic matrix rendered stable by addition of manganese. This steel is hyper-eutectoid, so grain boundary cementite forms prior to nucleation of pearlite which frequently takes place on the cementite. This work showed conclusively the continuity of grain boundary and pearlitic cementite (Fig. 3.16), and also indicated that both the cementite and ferrite possessed unique orientations within a particular nodule. Figure 3.16 also shows the beginning of branching of the  $\text{Fe}_3\text{C}$  lamella. However, in other nodules, sideways nucleation of laths of cementite and ferrite was observed. Nucleation of pearlite also took place on clean austenite boundaries. Hillert has shown that nucleation also occurs on ferrite, so all three types of site are effective, and the predominant sites will be determined primarily by the composition.

C. S. Smith first pointed out that the moving pearlite interface in contact with austenite was an incoherent high-energy interface growing into a grain with which the pearlitic ferrite and cementite had no orientation relationship. Therefore, the nodules which nucleated on pre-existing grain boundary cementite and ferrite would choose the higher energy interfaces across which the boundary phase had no orientation relationship with the adjacent austenite.

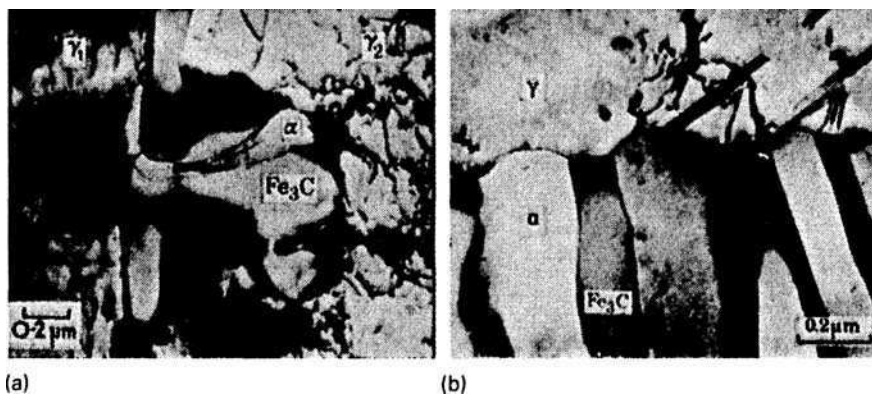


**Fig. 3.16** Fe-13Mn-0.8C partly transformed at 600°C. Austenite is retained in conjunction with ferrite and cementite: (a) nucleation of a pearlite nodule on grain boundary cementite, (b) interface of nodule with austenite. Thin-foil electron micrographs (courtesy of Dippenaar).

Hillert and co-workers were able to show by suitable heat treatments that pearlite did nucleate in this way, while on the low-energy interfaces Widmanstätten growth of ferrite (or cementite) was usually observed. Electron microscopy observations have confirmed that the pearlite interface with austenite is an incoherent one. Figure 3.16b shows a typical interface on a 13Mn-0.8C wt% steel, where the untransformed austenite has been retained at room temperature.

The spacing of the lamellae in pearlite is a sensitive parameter which, in a particular steel, is larger the higher the transformation temperature. The spacing was first measured systematically for a number of steels by Mehl and co-workers, who demonstrated that the spacing decreased as the degree of undercooling,  $\Delta T$ , below the eutectoid temperature increased. Zener provided the first theoretical analysis of these observations by considering a volume of pearlite (Fig. 3.17) of depth  $\delta$  and interlamellar spacing  $S_0$  growing unidirectionally in the  $x$ -direction. If growth is allowed to occur by  $dx$  then the volume of austenite transformed per lamellar spacing is  $S_0 \delta dx \rho$ , where  $\rho$  is the density. The free energy  $G$ , available to form this volume of pearlite is:

$$G = \Delta H \left( \frac{T_e - T}{T_e} \right) S_0 \delta dx \rho, \quad (3.6)$$

where

$T_e$  = eutectoid temperature  
 $T$  = transformation temperature  
 $\Delta H$  = latent heat of transformation.

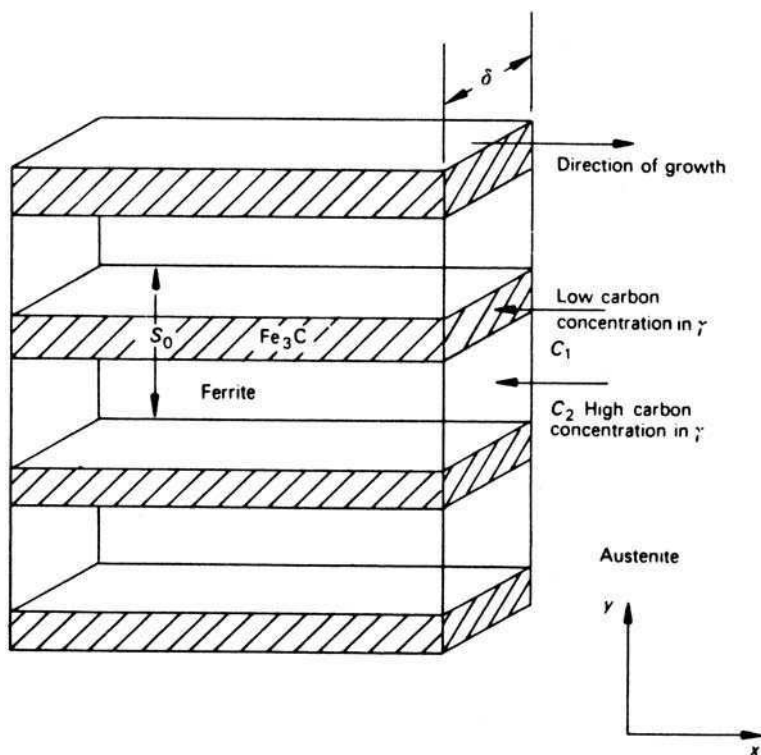


**Fig. 3.17** A pearlite growth model.

The formation of this new volume of pearlite causes an increase in interfacial energy by virtue of the new ferrite and cementite interfaces formed. Therefore:

$$\text{increase in interfacial area} = 2\delta \, dx,$$

and

$$\text{increase in interface energy} = 2\sigma\delta \, dx, \quad (3.7)$$

where  $\sigma$  is interfacial energy per unit area.

Growth of the lamellae can only occur if the increases in surface energy is less than the decrease in energy resulting from the transformation. Therefore, the condition for growth can be found from Equations (3.4) and (3.5):

$$\Delta H \left( \frac{T_e - T}{T_e} \right) \rho S_0 = 2\sigma. \quad (3.8)$$

This is a very simple treatment which neglects any strain energy term. Also the free energy change is found from the enthalpy change per unit mass, and it

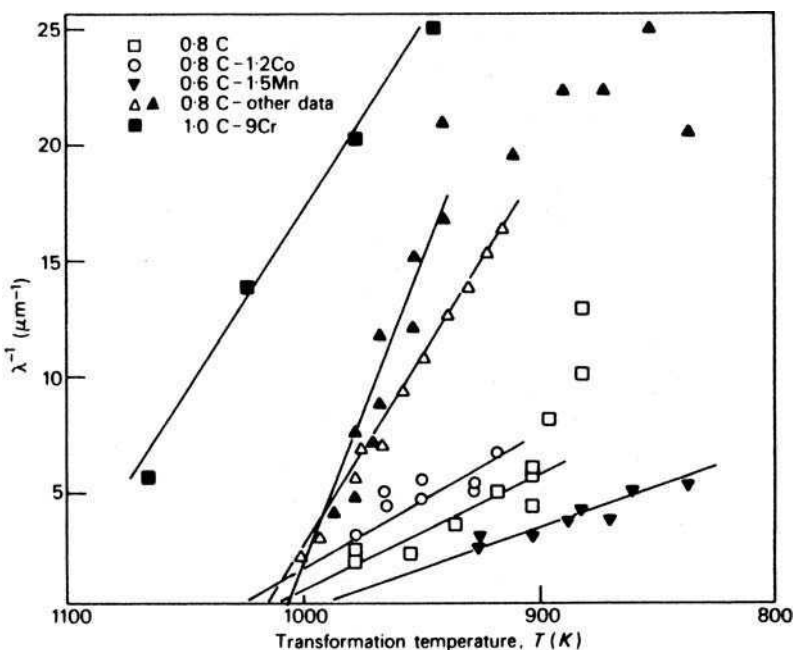


**Fig. 3.18** Reciprocal of the interlamellar spacing of pearlite from several alloys as a function of temperature. Concentrations in wt%.

assumes that the specific heats of austenite and pearlite are identical. Nevertheless, the equation predicts three important aspects of the transformation:

1. The pearlite spacing  $S_0$  decreases with transformation temperature.
2. The fineness of the spacing is limited by the free energy available from the transformation.
3. A linear relation should exist between the reciprocal of the spacing and the degree of undercooling.

The dependence of spacing on temperature for several plain carbon and alloy steels is shown in Fig. 3.18 where it is seen that the Zener analysis holds at lower degrees of supercooling, but as  $\Delta T$  increases the results are more scattered. The earlier spacing measurements can be criticized, partly because of the difficulty of making effective measurements on nodules with complex lamellar morphology. In recent years this problem has been eliminated by causing pearlite to grow unidirectionally by imposing a large temperature gradient along a steel rod. This technique leads to regular spacings, and closer correlation of the spacing with the velocity of growth.

The interlamellar spacing has in the previous discussion been assumed to be constant for a given alloy and transformation temperature. This is valid for a plain carbon steel where the average composition of the pearlite is identical

to that of the austenite from which it grows. However, when substitutional solutes are present they may partition between the phases so that the austenite may become enriched or depleted as the transformation proceeds, leading to a decrease in the driving force for transformation. This in turn leads to an increase in the interlamellar spacing as the pearlite grows, a phenomenon known as *divergent pearlite*.

In plain carbon steels it is only possible for cementite, ferrite and austenite to coexist in equilibrium at the eutectoid temperature. Therefore, fully pearlitic steels in which all of the austenite is consumed. In substitutionally alloyed steels it is possible to find a range of temperatures over which the three phases can coexist in equilibrium. Transformation in this temperature range cannot ever reach completion, in which case the microstructure is seen to be pearlite colonies in austenite, as is common in isothermally transformed Hatfield manganese steels.

The true morphology of pearlite is sometimes not evident in two-dimensional sections. In three-dimensions, each colony consists of an interpenetrating bi-crystal of cementite and ferrite, which when sectioned gives the lamellar appearance.

### 3.5.2 The crystallography of pearlite

In a typical pearlite nodule there are two interpenetrating single crystals of ferrite and of cementite, neither of which is orientation related to the austenite grain in which they are growing. However, there is always a well-defined crystallographic orientation between the cementite and ferrite lamellae within a pearlite nodule. At least two different relationships have been identified, the most important being:

#### *Pitsch/Petch relationship*

$$\begin{aligned}(001)_c // (\bar{5}2\bar{1})_\alpha, \\ (010)_c \text{ } 2-3^\circ \text{ from } [11\bar{3}]_\alpha, \\ (100)_c \text{ } 2-3^\circ \text{ from } [131]_\alpha.\end{aligned}$$

#### *Bagaryatski relationship*

$$\begin{aligned}(100)_c // (0\bar{1}1)_\alpha, \\ (010)_c // (1\bar{1}\bar{1})_\alpha, \\ (001)_c // (211)_\alpha.\end{aligned}$$

The two relationships are found side by side in the same steel, and the frequency of each varies rather unpredictably. Thin-foil electron microscopy has



shown that the pearlite nodules nucleating on clean austenite boundaries exhibit the Pitsch/Petch relationship. The pearlitic ferrite is related to the austenite grain  $\gamma_1$  (Fig. 3.15) into which it is not growing. The relationship is always close to the Kurdjumov–Sachs relationship. Also the pearlitic cementite is related to austenite grain  $\gamma_1$ , by a relationship found by Pitsch for Widmanstätten cementite in austenite. Both the pearlitic cementite and ferrite are unrelated to austenite grain,  $\gamma_2$ .

In contrast, the Bagaryatski relationship is found to hold for pearlite nodules nucleated on hyper-eutectoid cementite, usually formed at the austenite grain boundaries. In this case, the pearlitic cementite is related to austenite grain  $\gamma_1$  by the Pitsch relationship for Widmanstätten cementite, while the pearlitic ferrite is not related to grain  $\gamma_1$ . Clearly the grain boundary cementite shields the newly formed ferrite from any contact with  $\gamma_1$ . It also follows that the grain boundary cementite and the pearlitic cementite are continuous, i.e. of the same orientation. Again, neither the pearlitic ferrite or cementite are related to austenite grain  $\gamma_2$ .

It is, therefore, predicted that Pitsch/Petch-type colonies predominate as the true eutectoid composition is approached, whereas Bagaryatski-type colonies should prevail at higher carbon levels. It is also likely that the Bagaryatski relationship will become more dominant in hypo-eutectoid steels as the carbon level is reduced, but this has not yet been conclusively proved.

### 3.5.3 The kinetics of pearlite formation

The formation of pearlite is a good example of a nucleation and growth process. The pearlite nucleates at preferred sites in the austenite and the nuclei then grow until they impinge on each other. The process is both time and temperature dependent, as it is controlled by the diffusivity of the relevant atoms. Johnson and Mehl first applied a detailed analysis of nucleation and growth to the pearlite reaction, which assumed that the fraction of austenite transformed ( $X$ ) could be expressed in terms of a rate of nucleation  $\dot{N}$  defined as the number of nuclei per unit volume of untransformed austenite formed per second, and a rate of growth of these nuclei  $G$ , expressed as radial growth in  $\text{cm s}^{-1}$ . They made certain simplifying assumptions of which the most significant were:

1. Nucleation was regarded as a random event.
2. The rate of nucleation  $\dot{N}$  was assumed to be constant with time.
3. The rate of growth  $G$  was assumed to be constant with time.
4. The nuclei were regarded as spherical and in due course impinged on neighbouring spheres.

An expression was obtained for the fraction of austenite transformed  $X$ , in time  $t$ :

$$X = 1 - e^{-(\pi/3)\dot{N}G^3t^4}. \quad (3.9)$$

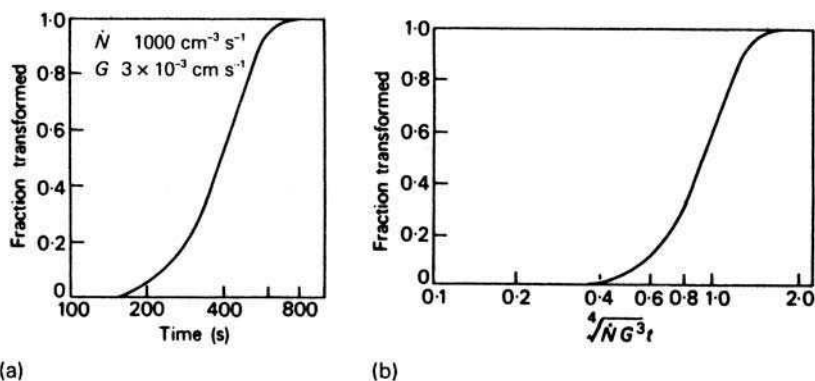


**Fig. 3.19** Kinetics of pearlite reaction: (a) calculated curve for specific  $\dot{N}$  and  $G$ , (b) master reaction curve for general nucleation (Mehl and Hagel, *Progress in Metal Physics* **6**, 74, 1956).

This relationship gives a sigmoidal type of curve, when  $X$  is plotted against  $t$  for chosen values of  $\dot{N}$  and  $G$ . A typical curve is shown in Fig. 3.19a for particular values of  $\dot{N}$  and  $G$ . If  $X$  is plotted against  $\sqrt[4]{(\dot{N}G^3)t}$ , a sigmoidal master curve is obtained which expresses the basic kinetic behaviour expected of a nucleation and growth process in a given alloy (Fig. 3.19b).

In practice, however, the pearlitic reaction does not conform to the simple nucleation and growth model referred to above. Amongst the difficulties, the following are predominant:

1.  $\dot{N}$  is not constant with time.
2.  $G$  can vary from nodule to nodule and with time.
3. The nuclei are not randomly distributed.
4. The nodules are not true spheres.

This led Cahn and Hagel to a new theoretical approach which fully recognized the inhomogeneous nature of nucleation in the pearlite reaction. It was pointed out that not all grain boundary nucleation sites were equivalent, that grain corners would be more effective than edges, and that edges would be better than grain surfaces. Cahn assumed that, normally, a high rate of nucleation would occur at these special sites, and that consequently site saturation would occur at an early stage of the reaction. In these circumstances, the reaction would then be controlled by the radial growth velocity which, in the simple theory, is assumed again to be constant.

The expression for the fraction of austenite transformed assuming site saturation of grain corner sites is:

$$X = 1 - e^{-(4/3)\pi\eta G^3 t^3}, \quad (3.10)$$

where  $\eta$  is the number of grain corners per unit volume. In practice, site saturation sets in before 20% transformation, so the actual nucleation rate

is unimportant, and does not come into the Equation (3.9). The time for completion of the reaction,  $t_f$ , is simply defined as:

$$t_f = 0.5d/G, \quad (3.11)$$

where  $d$  is austenite grain diameter and  $d/G$  is the time taken for one nodule to absorb one grain, so the presence of only several nodules per grain will meet the above criterion for  $t_f$ . Only at small degrees of undercooling below  $Ae_1$  will the rate of nucleation  $\dot{N}$  be sufficiently low to avoid site saturation at austenite grain boundaries. In these circumstances,  $\dot{N}$  would then enter into the expression for the overall reaction rate. The nucleation rate, where measured, does seem to vary with time according to the relation:

$$\dot{N} = kt^n, \quad (3.12)$$

where  $k$  and  $n$  are constants. However, for most experimental conditions, the rate of growth  $G$  is the dominant quantity.

The rate of growth of pearlite nuclei can be measured by reacting a series of samples for increasing times at a particular temperature. As a result of measurements on polished and etched sections, the radius of the largest pearlite area, assumed to be a projection of the first nodule to nucleate, can be plotted against time. Normally a straight line is obtained, the slope of which is  $G$  (Fig. 3.20). It has been found that  $G$  is structure insensitive, i.e. structural changes such as grain size, presence or absence of carbide particles have little effect. However,  $G$  is markedly dependent on temperature, specifically the degree of cooling  $\Delta T$  below  $T_e$ , and increases with increasing degree of undercooling until the nose of the  $TTT$  curve is reached,  $G$  is also strongly influenced by the concentration of alloying elements present.

The role of substitutional elements in pearlite formation is obviously complex. Pearlite is a diffusional transformation so its growth requires the diffusion of all elements including iron. Substitutional solutes therefore always partition between the phases, no matter what the reaction temperature. Pearlite has never been shown to grow by the para-equilibrium transformation of austenite.

### 3.5.4 The rate-controlling process

Early work on plain carbon steels assumed that the rate-controlling process in the growth of pearlite was the diffusion of carbon in austenite, and Mehl proposed the following relationship for  $G$ :

$$G = \frac{K D_c^\gamma}{S_0}, \quad (3.13)$$

where  $D_c^\gamma$  is the diffusion coefficient of carbon in austenite,  $S_0$  is the interlamellar spacing and  $K$  is a constant. The growth rate increases as the transformation

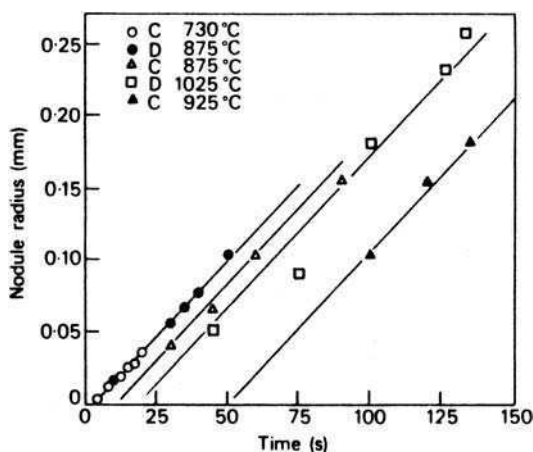


**Fig. 3.20** Growth of pearlite in two 0.8C 0.6Mn wt% steels, C and D (Mehl and Hagel, *Progress in Metal Physics* 6, 74, 1956).

temperature is lowered, because the driving force of the reaction is increased. However, the reaction is still diffusion-controlled so the diffusion distance must be reduced to compensate for the decrease in diffusivity with decreasing temperature. Consequently, as the temperature is lowered the pearlite interlamellar spacing is reduced.

The early theoretical treatments of Brandt and Zener, therefore, attempted to calculate the growth rate of pearlite in terms of a simple model in which the diffusion of carbon in austenite was assumed to be the rate-controlling process. Figure 3.17 represents the model used in which a planar front of pearlite is advancing into an austenite grain. It was assumed that the carbon concentration in the austenite would be low ( $c_1$ ) at the mid-points of cementite lamellae, and high at the mid-points ( $c_2$ ) of ferrite lamellae. The values  $c_1$  and  $c_2$  were obtained from the iron–carbon equilibrium diagram using and extrapolation of the austenite–ferrite and austenite–cementite phase boundaries first proposed by Hultgren (Fig. 3.21). Brandt, by solving the applicable diffusion equation, obtained a relationship of the same form as Equation (3.13), but he was also able to evaluate  $K$  in terms of the carbon concentration differences  $c_1$  and  $c_2$ , which are assumed to develop at the austenite–pearlite interface. Zener likewise derived an expression for  $G$  of a similar type involving two concentration terms:

$$G = \left( \frac{\Delta c}{c_p - c_\gamma} \right) \left( \frac{D_c^\gamma}{S_0} \right), \quad (3.14)$$

where  $c_p$  and  $c_\gamma$  are the number of solute atoms per unit volume in the two phases, and  $\Delta c$  is the difference in concentration in the austenite at the advancing boundary, given by  $c_2 - c_1$ . This is the solute gradient which leads to diffusion.

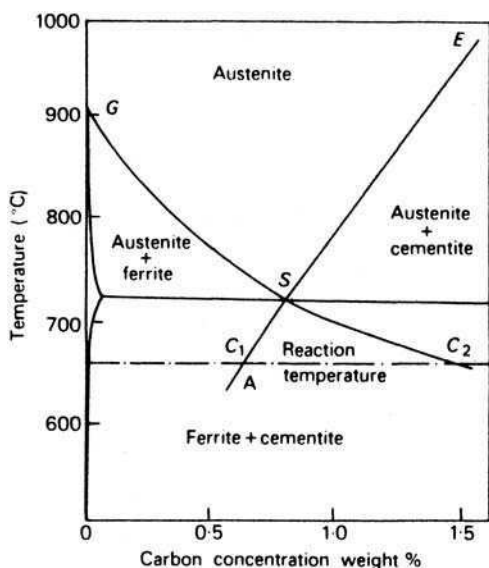


**Fig. 3.21** Hultgren extrapolation of phase boundaries in Fe-C diagram (Mehl and Hagel, *Progress in Metal Physics* 6, 74, 1956).

However, these early theories have now been supplanted by others due to Hillert, Cahn and Hagel, Kirkaldy and Lundquist which have been developed to a stage where the simple iron-carbide system has been treated in a sophisticated way, and the role of alloying elements also explained. While diffusion of carbon in austenite has again been assumed to be the rate-controlling process, some treatments have assumed that boundary diffusion is rate controlling. Hillert using this latter approach, and assuming that the austenite has periodic compositional differences along the interface, depending on whether a ferrite or carbide lamella is in the vicinity, arrived at the following relationship:

$$G = \left( \frac{12AD_b\delta S_0^2(c_2 - c_1)}{S_\alpha S_\beta(c_\beta - c_\alpha)} \right) \left( \frac{1}{S_0^2} \right) \left( 1 - \frac{S_c}{S_0} \right), \quad (3.15)$$

where

$D_b$  = interphase boundary diffusion coefficient

$\delta$  = thickness of interphase boundary

$A$  = constant

$c_1$  and  $c_2$  = concentrations previously referred to, from the Hultgren extrapolation

$c_\beta$  = concentration of carbon in cementite

$c_\alpha$  = concentration of carbon in ferrite

$S_0$  = interlamellar spacing of the pearlite

$S_c$  = spacing at zero growth rate and

$S_\alpha$  and  $S_\beta$  = widths of the ferrite and cementite lamellae.

The equation is similar in form to equations involving volume diffusion, except that it involves an  $S_0^2$  term rather than  $S_0$ . Also the present model must involve some volume diffusion in the austenite ahead of the interface to allow the differences in austenite composition at the interface to develop.

### 3.5.5 The strength of pearlite

The strength of pearlite would be expected to increase as the interlamellar spacing is decreased. Early work by Gensamer and colleagues showed that the yield stress of a eutectoid plain carbon steel, i.e. fully pearlitic, varied inversely as the logarithm of the mean free ferrite path in the pearlite. Later, Hugo and Woodhead used 3 wt% nickel steels to obtain a uniform pearlitic structure throughout the test pieces. They confirmed that the interlamellar spacing was inversely proportional to the degree of undercooling. It was shown that both the yield strength and the ultimate tensile stress (UTS) could be linearly related to the reciprocal of the square root of the interlamellar spacing or of the degree of undercooling. Figure 3.22 gives results for a 3Ni–0.67C wt% eutectoid steel where this linear relationship is illustrated. Steels of lower carbon contents,

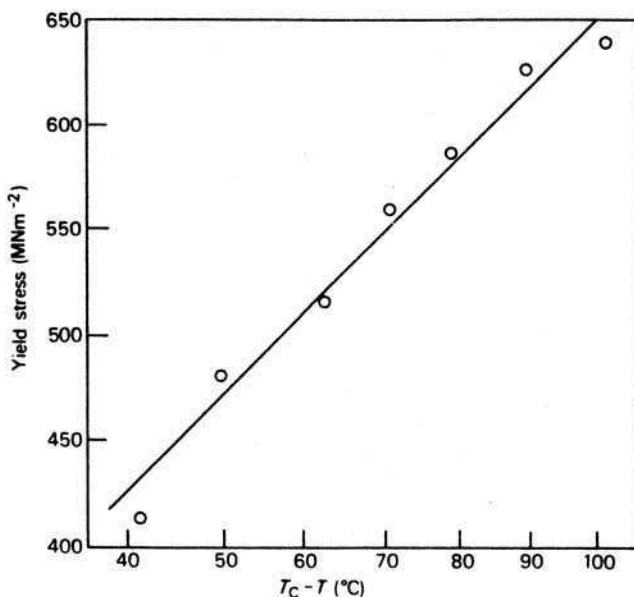


**Fig. 3.22** Effect of degree of undercooling on the strength of a pearlitic nickel steel 0.67C, 0.49Mn, 2.92Ni wt% (Hugo and Woodhead, *Journal of the Iron and Steel Institute* **186**, 174, 1957).

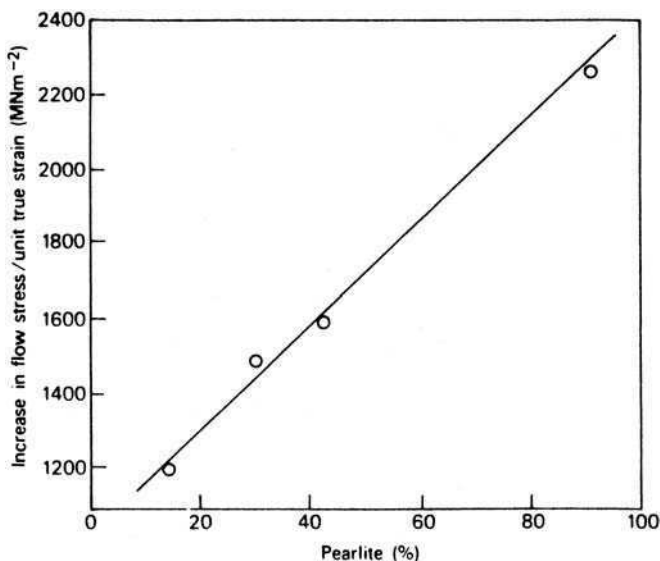


**Fig. 3.23** Effect of pearlite content on work hardening (Burns and Pickering, *Journal of the Iron and Steel Institute* **202**, 899, 1964).

i.e. down to 0.3 wt%, gave similar results, when allowance was made for the presence of proeutectoid ferrite.

The situation is rather different for lower carbon steels, i.e. below 0.3 wt%, where pearlite occupies a substantially smaller volume of the microstructure. In these steels the yield stress is not markedly affected as the proportion of pearlite is increased, provided other factors, e.g. ferrite grain size, are kept constant. However, the tensile strength is quite sensitive to the pearlite content which is explained by the fact that there is a linear relationship between work hardening and the pearlite content (Fig. 3.23), which arises because pearlite work hardens much more rapidly than ferrite.

Pearlite has, however, an adverse effect on ductility and toughness of plain carbon steels. For example, the impact transition temperature (see Chapter 11) is raised substantially as the carbon content is increased (Fig. 3.24), and quantitative studies have shown that 1 wt% by volume of pearlite raises the transition temperature by about 2°C. The presence of pearlite in the microstructure provides sites of easy nucleation of cracks, particularly at the ferrite–cementite interfaces. However, as a crack can only propagate in ferrite a short distance before encountering another cementite lamella, energy is absorbed during propagation. The result is that there is a wide transition temperature range (Fig. 3.24). In contrast, the low energy absorbed overall in impact tests on pearlitic structures arises from the fact that many crack nuclei can occur at the pearlitic interfaces which, together with the high work hardening rate, restricts plastic deformation in the vicinity of the crack.

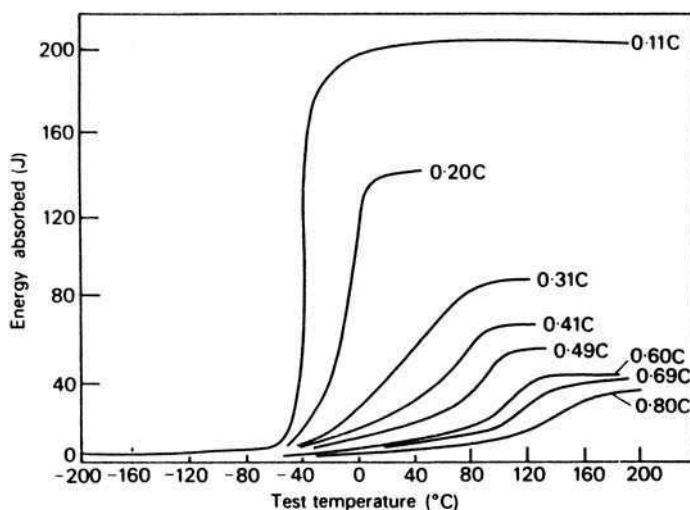


**Fig. 3.24** Effect of pearlite on toughness measured by Charpy impact transition temperature (Burns and Pickering, *Journal of the Iron and Steel Institute*. **202**, 899, 1964).

### 3.6 FERRITE-PEARLITE STEELS

A very high proportion of the steels used in industry has a ferrite-pearlite structure. These include a wide range of plain carbon steels where alloying additions are primarily made for steel-making purposes, although they do have a strengthening role as well. For example, manganese is added to combine with sulphur, but it is also a strengthener, while manganese and silicon are deoxidizers and aluminium is used as a deoxidizer and as a grain refiner, and therefore a strengthener. Many low and medium alloy steels, e.g. those with nickel, give ferrite-pearlite structures, but here only essentially plain carbon steels will be dealt with.

Most plain carbon steels are not subject to heat treatment in the sense of quenching followed by tempering, but they are cooled at different rates to obtain a range of structures. Two important treatments are *normalizing* and *annealing* which have special, but not very precise, meanings when applied to steels.

**Normalizing:** In the process of normalizing the steel is reheated about 100°C above the  $A_{c3}$  temperature to form austenite, followed by air cooling through the phase transformation. This has as its object the refinement of the austenite and ferrite grain sizes, and the achievement of a relatively fine pearlite. It is often used after hot rolling, where a high finishing temperature can lead to a coarse microstructure.

The rate of cooling during normalizing is dependent on the dimensions of the steel, but some control can be exerted by using forced air cooling.



**Annealing:** An annealed steel usually means one which has been austenitized at a fairly high temperature, followed by slow cooling, e.g. in a furnace. This results in transformation high in the pearlite range, giving a coarse pearlite which provides good machinability.

There are other types of annealing which are commonly practiced, e.g. *isothermal annealing*, in which the steel is cooled to a high subcritical transformation temperature, where it is allowed to transform isothermally to ferrite and coarse pearlite. *Spheroidize annealing* is applied to higher carbon pearlitic steels to improve their machinability. The steel is held at a temperature just below  $A_{e1}$  for sufficient time for the cementite lamellae of the pearlite to spheroidize. This happens because it leads to a reduction in surface energy of the cementite–ferrite interfaces.

The plain carbon ferrite–pearlite steels are essentially steels which depend for their properties on the presence of carbon and manganese. The carbon content can be varied from 0.05–1.0 wt% while the manganese content is from 0.25 wt% up to about 1.7 wt%. Figure 3.25 shows the effect on the tensile strength of varying the concentration of these two elements. It has also been possible by regression analysis to determine the relative contributions to the strength of the three important mechanisms: solid solution hardening; grain size and dispersion strengthening from lamellar pearlite. The results plotted are from steels in the normalized condition which ensures that the austenite grain sizes are roughly comparable. Variation of the carbon at constant manganese level causes a substantial increase in strength, which is almost entirely due to an increasing proportion of pearlite in the structure. The situation is rather more complex when manganese is varied at constant carbon content, as all three strengthening mechanisms are influenced. Manganese causes the eutectoid composition to occur at lower carbon contents, and so increases the proportion of pearlite in the microstructure. Manganese is also an effective solid solution strengthener, and has a grain refining influence.

It is clear that carbon provides a very cheap way of strengthening normalized steels, but the extent to which this approach can be used depends on whether the steel is to be welded or not. Welding of higher carbon steels leads to the easier formation of cracks within the weld zone, so it is usually necessary to limit the carbon content to not greater than 0.2 wt%. In these circumstances, additional strength can then be obtained by solid solution hardening by raising the manganese content to between 1 and 1.5 wt%.

Alternatively, refinement of the grain size can be achieved by minor alloying additions such as aluminium, vanadium, titanium and niobium, in concentrations not normally exceeding 0.1 wt% (Chapter 9). Aluminium forms a stable dispersion of AlN particles, some of which remain in the austenite grain boundaries at high temperatures, and by pinning these boundaries prevent excessive grain growth. On transformation to ferrite and pearlite, grain sizes around 12 ASTM (5–6  $\mu\text{m}$  diameter) can be achieved with as little as 0.03 wt% AlN in the steel. Vanadium, titanium and niobium form very stable carbides, which also

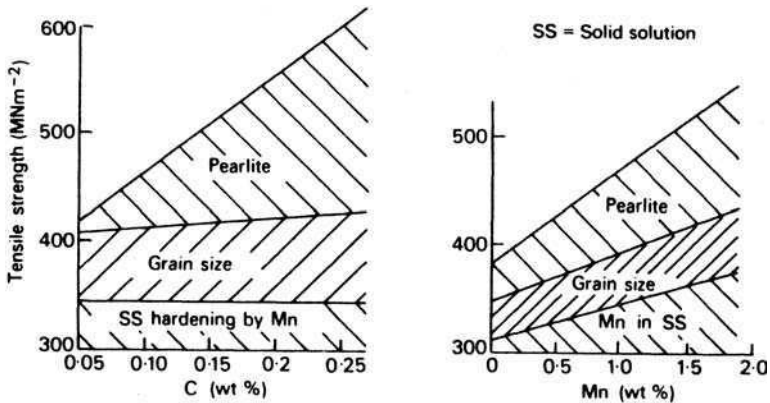


**Fig. 3.25** Factors contributing to the strength of C-Mn steels (Irvine et al., *Journal of the Iron and Steel Institute*. **200**, 821, 1962).

lock austenite grain boundaries, and thus allow much finer ferrite grain sizes to be achieved when the austenite transforms (Chapter 10).

Much plain carbon steel is used in the hot-finished condition, i.e. straight from hot rolling without subsequent cold rolling or heat treatment. This represents the cheapest form of steel which is usually used in low carbon and medium carbon grades, because of the loss of ductility and weldability at high carbon contents. The most important group of hot-finished plain carbon steels contains less than 0.25 wt% carbon and is used in structural shapes such as plates, I-beams, angles, etc., in buildings, bridges, ships, pressures vessels and storage tanks. Hot-rolled low carbon steel sheet is an important product and used extensively for fabrication where surface finish is not of prime importance. Cold rolling is used for finishing where better finish is required, and the additional strength from cold working is needed. However, for high quality sheet to be used in intricate pressing operations it is necessary to anneal the cold-worked steel to cause the ferrite to recrystallize. This is done below the  $A_{e1}$  temperature (subcritical annealing).

Carbon steels are also used extensively for closed die or drop forgings, usually in the range 0.2–0.5% carbon, and covering a very wide range of applications, e.g. shafts and gears. The other important field of application of plain carbon steels is as castings. Low carbon cast steels containing up to 0.25% C are widely used for miscellaneous jobbing casting as reasonable strength and ductility levels are readily obtained. Yield strengths of  $240 \text{ MN m}^{-2}$  and elongations of 30% are fairly typical for this type of steel.

## FURTHER READING

Bhadeshia, H. K. D. H., Diffusional formation of ferrite in iron and its alloys, *Progress in Materials Science* **29**, 321, 1985.

- Bhadeshia, H. K. D. H., Alternatives to the ferrite–pearlite microstructures, *Materials Science Forum* **284–286**, 29, 1998.
- Cahn, R. W., Haasen, P. and Kramer, E. J. (eds), *Materials Science and Technology*, Vol. 7, *Constitution and Properties of Steels* (ed. Pickering, F. B.).
- Christian, J. W., *The Theory of Phase Transformations in Metals and Alloys*, 3rd edition, Pergamon Press, Oxford, 2004.
- Dippenaar, R. J. and Honeycombe, R. W. K., *Proceedings of the Royal Society of London Series A* **333**, 455–671, 1973.
- Hackney, S. A. and Shiflet, G. J., Pearlite growth mechanism, *Acta Materialia* **35**, 1019, 1987.
- Hornbogen, E., in *Physical Metallurgy* (ed. Cahn, R. W.), 2nd edition, North Holland, Amsterdam, The Netherlands, 1970.
- Howell, P. R., The pearlite reaction in steels: mechanism and crystallography, *Materials Characterisation* **40**, 227, 1998.
- Hutchinson, C. R., Hackenberg, R. E. and Shiflet, G. J., The growth of partitioned pearlite in Fe–C–Mn steels, *Acta Materialia* **52**, 3565, 2004.
- International Conference on Phase Transformations in Ferrous Alloys* (eds Marder, A. R. and Goldstein, J. I.), American Society of Metals, Cleveland, 1984.
- Leslie, W. C., *The Physical Metallurgy of Steels*, McGraw-Hill, Tokyo, Japan, 1982.
- Phase Transformations*, American Society for Metals, Ohio, USA, 1970.
- Sinha, A. K., *Ferrous Physical Metallurgy*, Butterworths, Boston, USA, 1989.
- Van der Ven, A. and Delaey, L., Models for precipitate growth during transformation in Fe–C and Fe–C–M alloys, *Progress in Materials Science* **40**, 181, 1996.
- Zhenghong G., Furuhashi, T. and Maki, T., Intragranular pearlite on MnS and VC inclusions, *Scripta Materialia* **45**, 525, 2001.

# 4

---

## THE EFFECTS OF ALLOYING ELEMENTS ON IRON-CARBON ALLOYS

### 4.1 THE $\gamma$ - AND $\alpha$ -PHASE FIELDS

It would be impossible to include a detailed survey of the effects of alloying elements on the iron–carbon equilibrium diagram in this book. In the simplest version this would require analysis of a large number of ternary alloy diagrams over a wide temperature range. However, Wever pointed out that iron binary equilibrium systems fall into four main categories (Fig. 4.1): open and closed  $\gamma$ -field systems, and expanded and contracted  $\gamma$ -field systems. This approach indicates that alloying elements can influence the equilibrium diagram in two ways:

- (a) By expanding the  $\gamma$ -field, and encouraging the formation of austenite over wider compositional limits. These elements are called  $\gamma$ -stabilizers.
- (b) By contracting the  $\gamma$ -field, and encouraging the formation of ferrite over wider compositional limits. These elements are called  $\alpha$ -stabilizers.

The form of the diagram depends to some degree on the electronic structure of the alloying elements which is reflected in their relative positions in the periodic classification.

*Class 1: Open  $\gamma$ -field* To this group belongs the important steel alloying elements nickel and manganese, as well as cobalt and the inert metals ruthenium, rhodium, palladium, osmium, iridium and platinum. Both nickel and manganese, if added in sufficiently high concentration, completely eliminate the bcc  $\alpha$ -iron phase and replace it, down to room temperature, with the  $\gamma$ -phase. So nickel

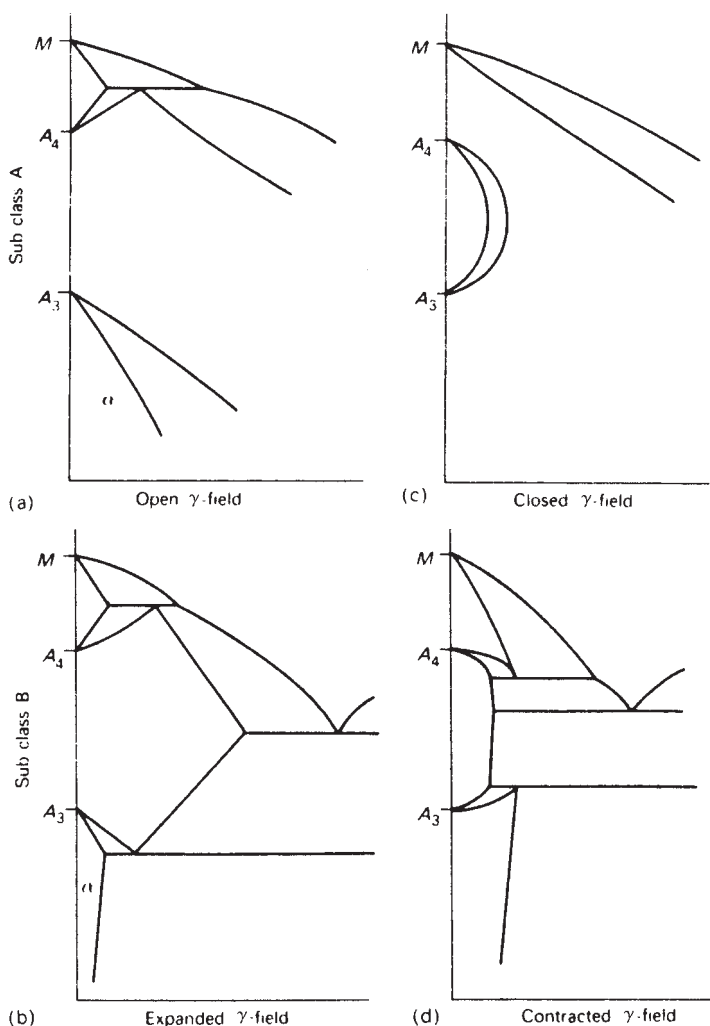


**Fig. 4.1** Classification of iron alloy phase diagrams: (a) open  $\gamma$ -field; (b) expanded  $\gamma$ -field; (c) closed  $\gamma$ -field; (d) contracted  $\gamma$ -field (Wever, *Archiv für Eisenhüttenwesen* **2**, 193, 1928–1929).

and manganese depress the phase transformation from  $\gamma$  to  $\alpha$  to lower temperatures (Fig. 4.1a), i.e. both  $A_{e1}$  and  $A_{e3}$  are lowered. It is also easier to obtain metastable austenite by quenching from the  $\gamma$ -region to room temperature, consequently nickel and manganese are useful elements in the formulation of austenitic steels (Chapter 11).

*Class 2: Expanded  $\gamma$ -field* Carbon and nitrogen are the most important elements in this group. The  $\gamma$ -phase field is expanded, but its range of existence is cut

short by compound formation (Fig. 4.1b). Copper, zinc and gold have a similar influence. The expansion of the  $\gamma$ -field by carbon, and nitrogen, underlies the whole of the heat treatment of steels, by allowing formation of a homogeneous solid solution (austenite) containing up to 2.0 wt% of carbon or 2.8 wt% of nitrogen.

*Class 3: Closed  $\gamma$ -field* Many elements restrict the formation of  $\gamma$ -iron, causing the  $\gamma$ -area of the diagram to contract to a small area referred to as the gamma loop (Fig. 4.1c). This means that the relevant elements are encouraging the formation of bcc iron (ferrite), and one result is that the  $\delta$ - and  $\alpha$ -phase fields become continuous. Alloys in which this has taken place are, therefore, not amenable to the normal heat treatments involving cooling through the  $\gamma/\alpha$ -phase transformation. Silicon, aluminium, beryllium and phosphorus fall into this category, together with the strong carbide-forming elements, titanium, vanadium, molybdenum and chromium. It is sometimes useful to avoid austenite altogether. A coarse ferrite grain structure is useful in steels which have to be magnetically soft for applications in electrical transformers. The  $\delta$ -ferrite grains form at temperatures close to melting and hence are coarse. By adding 4 wt% Si, austenite is avoided enabling the grains to be retained at room temperature.

*Class 4: Contracted  $\gamma$ -field* Boron is the most significant element of this group, together with the carbide-forming elements tantalum, niobium and zirconium. The  $\gamma$ -loop is strongly contracted, but is accompanied by compound formation (Fig. 4.1d).

The overall behaviour is best described in thermodynamic terms along the lines developed by Zener and by Andrews. If  $c_\alpha$  and  $c_\gamma$  are the fractional concentrations of an alloying element in the  $\alpha$ - and  $\gamma$ -phases, the following relation holds:

$$\frac{c_\alpha}{c_\gamma} = \beta e^{\Delta H/RT}, \quad \text{i.e. } \log_e \frac{c_\alpha}{c_\gamma} = \frac{\Delta H}{RT} + \log_e \beta,$$

where  $\Delta H$  is the enthalpy change which is the heat absorbed per unit of solute dissolving in  $\gamma$ -phase minus the heat absorbed per unit of solute dissolving in  $\alpha$ -phase, i.e.  $\Delta H = H_\gamma - H_\alpha$ .  $\beta$  is a constant.

$$\begin{array}{ll} \text{for ferrite formers,} & H_\alpha < H_\gamma \quad \therefore \Delta H \text{ is positive} \\ \text{for austenite formers,} & H_\alpha > H_\gamma \quad \therefore \Delta H \text{ is negative.} \end{array}$$

In the simple treatment two fundamentally different types of equilibrium diagrams are obtained where the phase boundaries are represented by similar thermodynamic equations, but, depending on whether  $\Delta H$  is positive or negative, are mirror images of each other (Fig. 4.2). In the  $\Delta H$  negative case the  $\gamma$ -field is unlimited, while in the  $\Delta H$  positive case, the  $\gamma$ -loop is introduced.  $\Delta H$  will vary widely from element to element. In Fig. 4.3 histograms illustrate the relative strengths of alloying elements in terms of  $\Delta H$ . The ferrite formers are listed in (a) and the austenitic formers in (b).

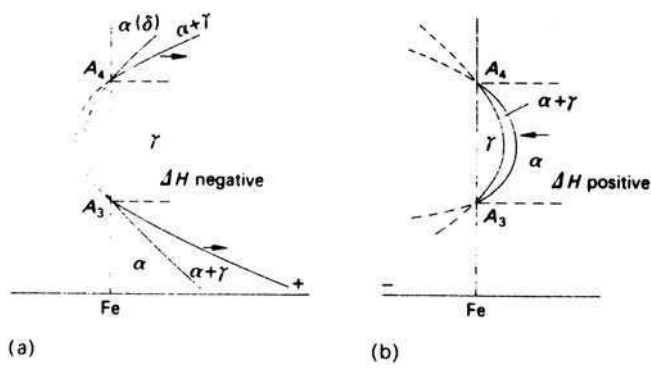


**Fig. 4.2** Two basic phase diagrams: (a)  $\Delta H$  negative,  $H_\alpha > H_\gamma$ ,  $\gamma$  favoured; (b)  $\Delta H$  positive,  $H_\alpha < H_\gamma$ ,  $\alpha$  favoured (after Zener, In: Andrews, *Journal of the Iron and Steel Institute* **184**, 414, 1956).

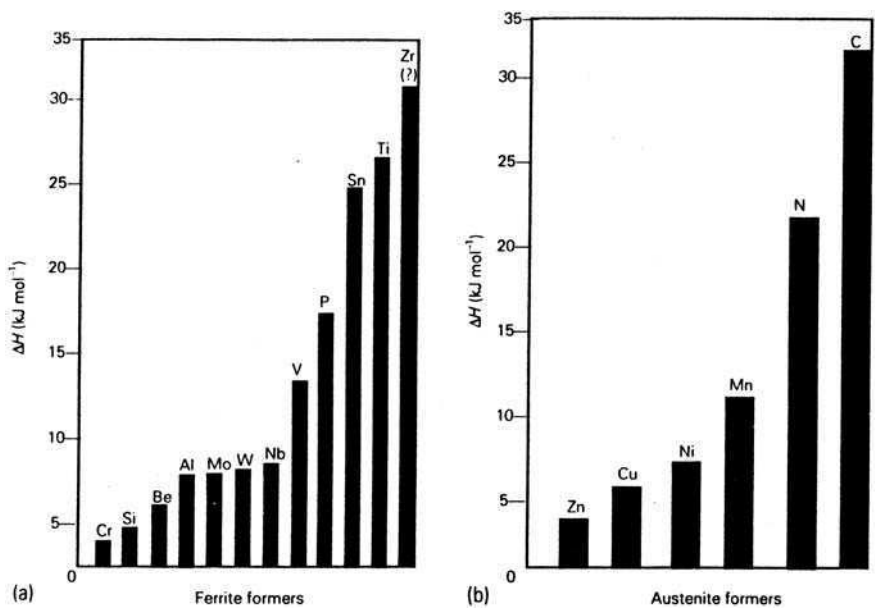


**Fig. 4.3** Relative strength of alloying elements as: (a) ferrite formers; (b) austenite formers (Andrews, *Journal of the Iron and Steel Institute* **184**, 414, 1956).

### 4.2 THE DISTRIBUTION OF ALLOYING ELEMENTS IN STEELS

Although only binary systems have been considered so far, when carbon is included to make ternary systems the same general principles usually apply. For a fixed carbon content, as the alloying element is added the  $\gamma$ -field is either expanded or contracted depending on the particular solute. With an element

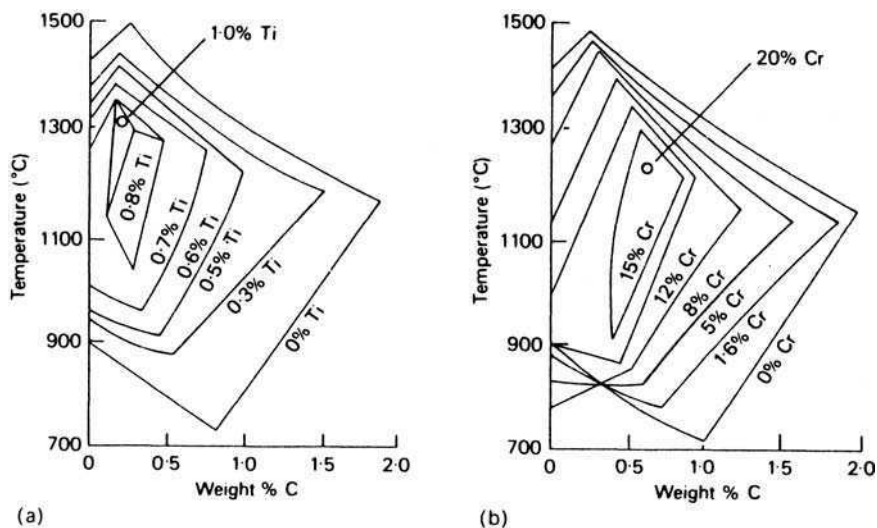


**Fig. 4.4** Effect of alloying elements on the  $\gamma$ -phase field: (a) titanium; (b) chromium (after Tofaute and Büttinghaus, *Archiv für Eisenhüttenwesen* **12**, 33, 1938).

such as silicon the  $\gamma$ -field is restricted and there is a corresponding enlargement of the  $\alpha$ -field. If vanadium is added, the  $\gamma$ -field is contracted and there will be vanadium carbide in equilibrium with ferrite over much of the ferrite field. Nickel does not form a carbide and expands the  $\gamma$ -field. Normally elements with opposing tendencies will cancel each other out at the appropriate combinations, but in some cases anomalies occur. For example, chromium added to nickel in a steel in concentrations around 18 wt% helps to stabilize the  $\gamma$ -phase, as shown by 18Cr–8Ni wt% austenitic steels (Chapter 12).

One convenient way of illustrating quantitatively the effect of an alloying element on the  $\gamma$ -phase field of the Fe–C system is to project on to the Fe–C plane of the ternary system the  $\gamma$ -phase field boundaries for increasing concentration of a particular alloying element. This is illustrated in Fig. 4.4 for titanium and chromium, from which it can be seen that just over 1 wt% Ti will eliminate the  $\gamma$ -loop, while 20 wt% Cr is required to reach this point. Other ternary systems can be followed in the same way, e.g. in Fe–V–C, vanadium has an effect intermediate between that of titanium and of chromium.

For more precise and extensive information, it is necessary to consider series of isothermal sections in true ternary systems Fe–C–X, but even in some of the more familiar systems the full information is not available, partly because the acquisition of accurate data can be a difficult and very time-consuming process. Recently the introduction of computer-based methods has permitted the synthesis of extensive thermochemical and phase equilibria data, and its presentation in the form, e.g., of isothermal sections over a wide range of temperatures



(Chapter 14). A journal<sup>1</sup> now publishes the work of laboratories concerned with such work, for example, the detailed data on the Fe-Mn-C and Fe-Cr-C systems.<sup>2</sup>

If only steels in which the austenite transforms to ferrite and carbide on slow cooling are considered, the alloying elements can be divided into three categories:

- (a) elements which enter only the ferrite phase;
- (b) elements which form stable carbides and also enter the ferrite phase;
- (c) elements which enter only the carbide phase.

In the first category there are elements such as nickel, copper, phosphorus and silicon which, in transformable steels, are normally found in solid solution in the ferrite phase, their solubility in cementite or in alloy carbides being quite low.

The majority of alloying elements used in steels fall into the second category, in so far as they are carbide formers and as such, at low concentrations, go into solid solution in cementite, but will also form solid solutions in ferrite. At higher concentrations most will form alloy carbides, which are thermodynamically more stable than cementite. Typical examples are manganese, chromium, molybdenum, vanadium, titanium, tungsten and niobium. The stability of the alloy carbides and nitrides frequently found in steels relative to that of cementite is shown in Fig. 4.5, where the enthalpies of formation,  $\Delta H$ , are plotted. Manganese carbide is not found in steels, but instead manganese enters readily into solid solution in  $\text{Fe}_3\text{C}$ . The carbide-forming elements are usually present greatly in excess of the amounts needed in the carbide phase, which are determined primarily by the carbon content of the steel. The remainder enter into solid solution in the ferrite with the non-carbide-forming elements nickel and silicon. Some of these elements, notably titanium, tungsten and molybdenum, produce substantial solid solution hardening of ferrite.

In the third category there are a few elements which enter predominantly the carbide phase. Nitrogen is the most important element and it forms carbonitrides with iron and many alloying elements. However, in the presence of certain very strong nitride-forming elements, e.g. titanium and aluminium, separate alloy nitride phases can occur.

While ternary phase diagrams, Fe-C-X, can be particularly helpful in understanding the phases which can exist in simple steels, isothermal sections for a number of temperatures are needed before an adequate picture of the equilibrium phases can be built up. For more complex steels the task is formidable and equilibrium diagrams can only give a rough guide to the structures likely

---

<sup>1</sup> *Calphad, Computer Coupling of Phase Diagrams and Thermochemistry*, Pergamon Press, Oxford.

<sup>2</sup> Hillert, M. and Walderström, M., *Calphad* **1**, 97, 1977 (Fe-Mn-C); Lundberg, R., Waldenström, M. and Uhrenius, B., *Calphad* **1**, 159, 1977 (Fe-Cr-C).

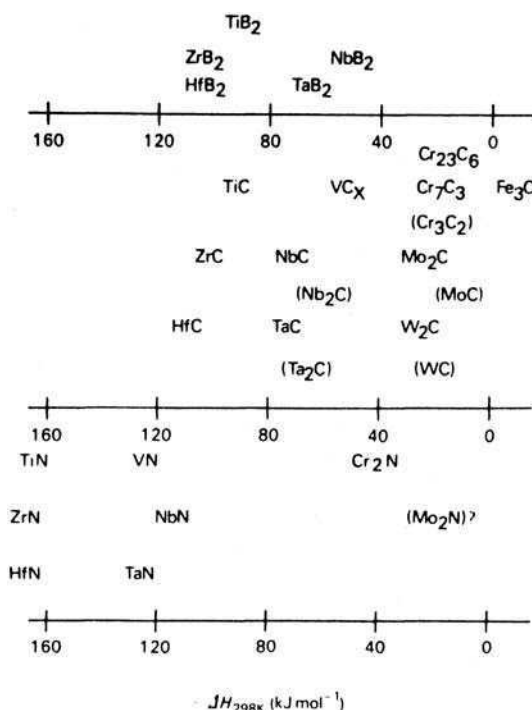


**Fig. 4.5** Enthalpies of formation of carbides, nitrides and borides (after Schick, *Thermodynamics of Certain Refractory Compounds*, Academic Press, New York, 1966).

to be encountered. It is, however, possible to construct pseudobinary diagrams for groups of steels, which give an overall view of the equilibrium phases likely to be encountered at a particular temperature. For example, Cr–V steels are widely used in the heat-treated condition, and both chromium and vanadium are carbide formers. If a particular carbon level, e.g. 0.2 wt% and a temperature at which equilibrium can be readily reached, e.g. 700°C, is chosen, it is possible to examine a wide range of different compositions to identify the carbide phases in equilibrium with ferrite at that temperature. The phase fields can then be plotted on a diagram as a function of chromium and vanadium, as shown in Fig. 4.6. It should be noted that cementite is only stable up to about 1.5 wt% chromium or 0.6 wt% vanadium and, for much of the diagram, several alloy carbides replace cementite.

### 4.3 THE EFFECT OF ALLOYING ELEMENTS ON THE KINETICS OF THE $\gamma/\alpha$ TRANSFORMATION

Since alloying elements have different tendencies to exist in the ferrite and carbide phases, it might be expected that the rate at which the decomposition of

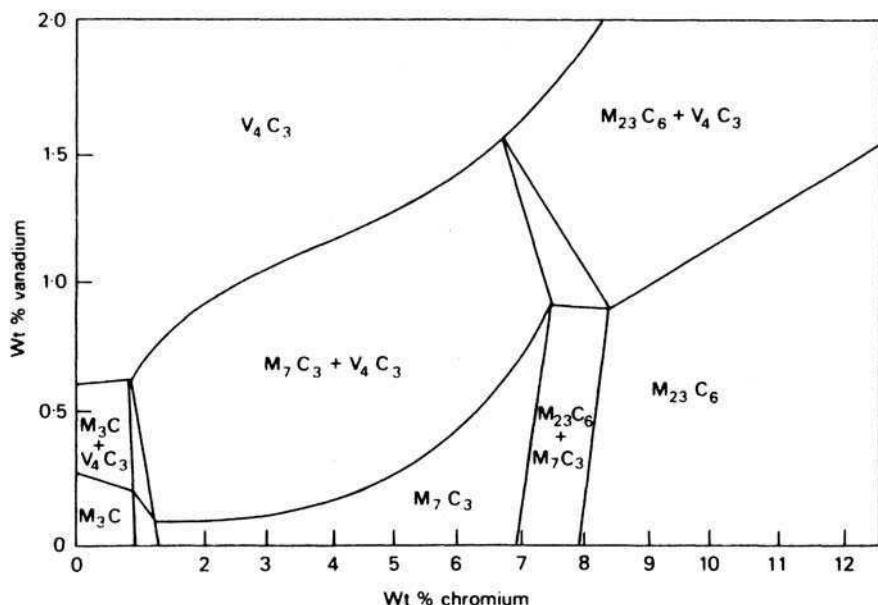


**Fig. 4.6** Carbide constitution in 0.2%C steels at 700°C as a function of vanadium and chromium content (Shaw and Quarrell, *Journal of the Iron and Steel Institute* **185**, 10, 1957).

austenite occurs would be sensitive to the concentration of alloying elements in steel. Both the growth of ferrite or pearlite are affected, so these reactions will be considered separately. Most familiar alloying elements displace the time-temperature-transformation (TTT) curve for a plain carbon steel to the right, i.e. towards longer transformation times. However, a small group of elements move the curve to shorter transformation times.

#### 4.3.1 The effect of alloying elements on the ferrite reaction

Two basically different modes of growth of pre-eutectoid ferrite in austenite have been observed in Fe-C-X alloys. The actual mode observed is dependent on the composition of the alloy but the two modes may occur at different temperatures in the same alloy (Chapter 3). The modes are:

- growth with partition of the alloying element X between  $\alpha$  and  $\gamma$  under local equilibrium conditions;
- growth with no partition of X between  $\alpha$  and  $\gamma$  under local equilibrium conditions.

In the first mode, the ferrite grows at a slow rate determined by the diffusivity of the alloying element X in the  $\gamma$ -phase. This behaviour is sensitive to alloy

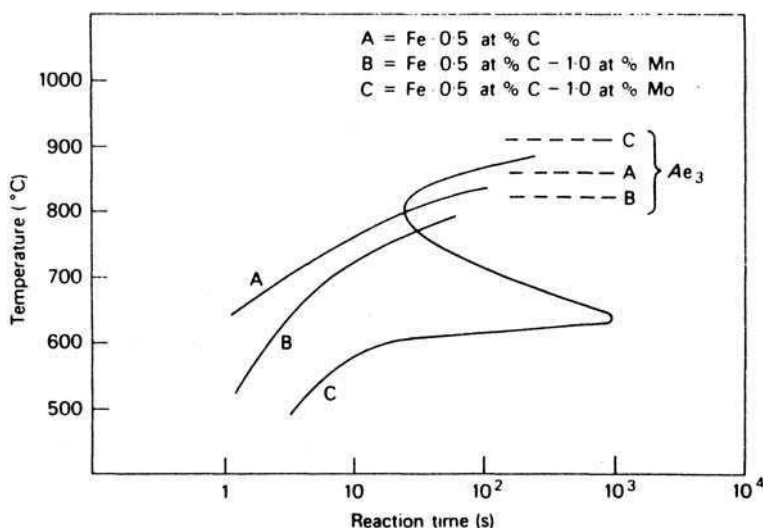


**Fig. 4.7** Effect of manganese and molybdenum on the kinetics of the ferrite reaction (Kinsman and Aaronson, in *Transformation and Hardenability in Steels*, Climax Molybdenum Co., Michigan, USA, 1967).

composition which is shown by the fact that an Fe - 1.3 at%, C - 3.2 at%, Mn alloy exhibits Mn partition at 742°C, whereas an Fe - 1.0 at%, C - 1.5 at%, Mn alloy shows partition of manganese at 725°C. Alloys in which X is Ni or Pt also show partition at higher transformation temperatures.

The mode where no partition occurs gives rise to a narrow zone of enrichment or depletion, depending on whether X is a  $\gamma$ - or  $\alpha$ -stabilizer, which moves ahead of the  $\alpha/\gamma$  interface. Aaronson and Domian have shown the lack of substitutional solute partitioning for alloys in which X = Si, Mo, Co, Al, Cr and Cu for all temperatures investigated. Ni, Mn and Pt on the other hand showed a greater tendency to partition to the  $\gamma$ -phase. In the no-partition regime the observed growth rates are relatively high, being determined by the diffusivity of carbon which diffuses several orders of magnitude faster than the metallic alloying elements. However, it has been shown that in Fe-C-X alloys, ferrite still grows much more slowly than in Fe-C alloys, even when no partition of X is observed. Some of this retardation is because the substitutional solute affects the thermodynamic stability of  $\gamma$  relative to  $\alpha$ . This is illustrated in Fig. 4.7 from the work of Kinsman and Aaronson for X = Mn and Mo. To explain the results for the molybdenum containing alloy they proposed that the  $\alpha/\gamma$  boundary collects atoms during the transformation and, as a result, experiences an *impurity drag*.

A third approach to the ferrite reaction was introduced by Hultgren, who proposed a state of *para-equilibrium* at the  $\gamma/\alpha$  boundary. In this, the transformation occurs at such a rate that the substitutional solutes are unable to

partition. Thus, the substitutional solute/iron atom ratio remains fixed everywhere. Subject to this constraint, the carbon, which is a fast diffusing species in iron, partitions to an extent which allows it to achieve local (para)equilibrium at the interface. This is a metastable mode of transformation, which allows the growth of ferrite to be controlled by the diffusion of carbon, without any partitioning of alloying element X. The latter primarily influences transformation by affecting the thermodynamic stabilities of austenite and ferrite.

### 4.3.2 The effect of alloying elements on the pearlite reaction

The pearlite reaction is a typical nucleation and growth reaction and, under the appropriate experimental conditions, rates of nucleation  $N$  and rates of growth  $G$  can be determined (see Chapter 3). The work of Mehl and coworkers showed that many alloying elements reduce both  $N$  and  $G$ . For example, in molybdenum steels of eutectoid composition both  $N$  and  $G$  were decreased, and nickel steels behaved in a similar manner. The growth rate  $G$  as a function of atomic concentration of alloying elements in several groups of steels is shown in Fig. 4.8. The change in slope for Mo steels was correlated with the substitution of cementite by a molybdenum-rich carbide. Certain elements, notably cobalt, increased both  $N$  and  $G$  for the pearlite reaction. The rates of growth of pearlite nodules at 660°C in cobalt steels are compared with that of a Co-free steel in Fig. 4.9.

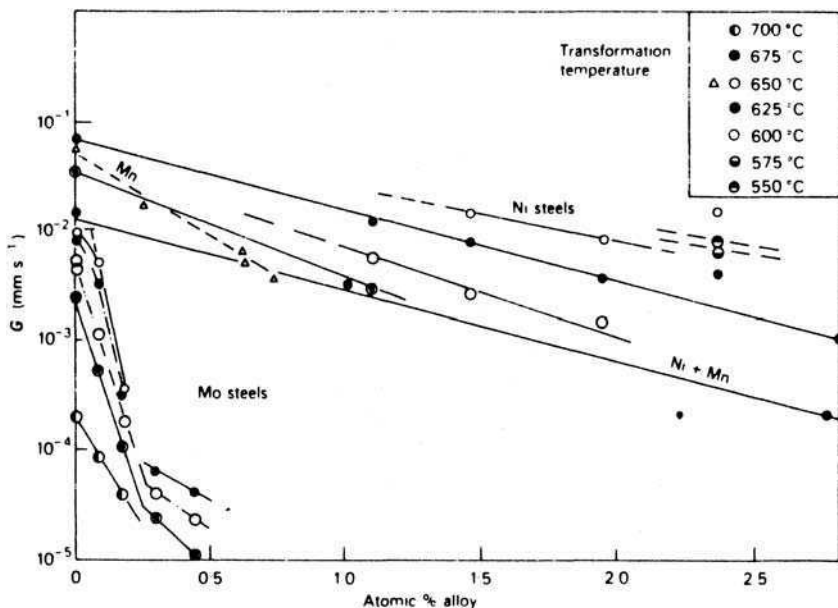


**Fig. 4.8** Effect of alloying elements on the rate of growth of pearlite in the range 550–700°C (Mehl and Hagel, *Progress in Metal Physics* **6**, 74, 1956).

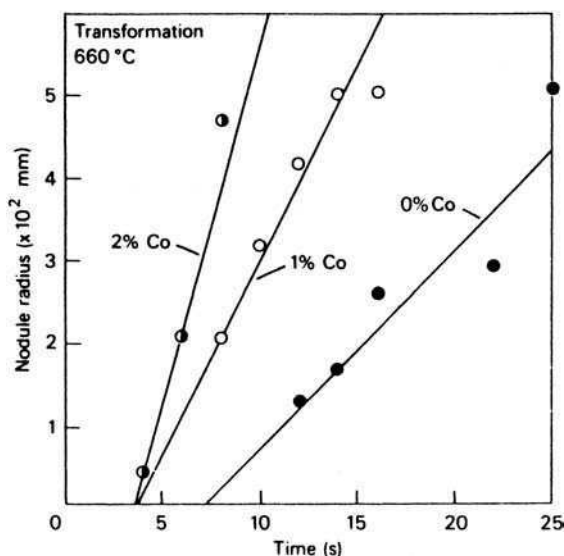


**Fig. 4.9** Effect of cobalt on pearlite growth rate (Mehl and Hagel, *Progress in Metal Physics* **6**, 74, 1956).

Recent work on chromium steels has shown that the addition of 1 wt% Cr to an eutectoid steel results in substantially lower growth rates of pearlite. It follows that in general the C-curve for a pearlitic steel will be moved to longer times as the concentration of alloying element is increased.

On examining the interface between pearlite and austenite during transformation, it appears that the basic nature of the pearlite reaction requires partition of carbon between the cementite and the ferrite (Chapter 3). However, in the presence of metallic alloying elements, it is not obvious, *ab initio*, whether partition of these elements will take place, taking partition to mean partition at the pearlite/austenite interface so that element X partitions between cementite and ferrite as they are formed. At a later stage of the reaction, and after its completion, alloying elements can partition within the pearlite over a wide temperature range.

It is now generally agreed that partition of X between cementite and ferrite at the interface with austenite does occur in many systems, even at relatively low transformation temperatures. While partition can be predicted on theoretical grounds, it can now be investigated experimentally<sup>3</sup> using electron probe microanalysis, where a probe size of  $<0.1 \mu\text{m}$  allows the *in situ* analysis of pearlitic ferrite and cementite in partly transformed alloys. Atom-probe techniques

<sup>3</sup> Ridley N., *Solid-Solid Phase Transformations*, TMS-AIME, Pennsylvania, p. 807, 1981.

allow even higher resolution.<sup>4</sup> In this way the systems Fe–Mn–C and Fe–Cr–C have been examined, and partition has been found at temperatures as low as 550°C.

An approach to the pearlite reaction, similar to that described earlier for the ferrite reaction, is to distinguish two modes of growth, a partition local equilibrium and a non-partition local equilibrium situation,<sup>5</sup> which are both temperature and composition dependent. Elements which favour the formation of austenite, and so depress the eutectoid temperature, and also have low solubilities in cementite, e.g. Ni, will encourage the non-partitioning reaction. Those elements which are strong ferrite formers and consequently raise the eutectoid temperature, as well as being soluble in cementite, are likely to exhibit the partitioning type of reaction at the higher transformation temperature, e.g. Cr, Mo, Si. The growth of pearlite in the non-partitioning case is probably controlled by volume diffusion of carbon in austenite, but this diffusivity is reduced by the presence of other alloying elements, in part accounting for the observed effect of elements such as Ni on the pearlite growth rate. Where partitioning of X takes place, the diffusivity of the alloying element in austenite must be a limiting factor.

Whatever the alloying element distribution is at the growing interface, subsequent redistribution between the ferrite and the cementite takes place, i.e. those elements with substantial solubility in cementite (carbide formers) will diffuse into that phase and the non-carbide formers will not. In this way the composition of cementite can vary over wide limits, e.g. manganese is very soluble in Fe<sub>3</sub>C; up to 20% of the iron atoms can be replaced by chromium, while vanadium will replace 10% and molybdenum only 4%. The change in composition of cementite, while not affecting the crystal structure, will influence, e.g., the pearlite interlamellar spacing, the detailed morphology and the tendency to spheroidize.

Once the alloying element concentration reaches a critical level, the cementite will be replaced by another carbide phase. For example, in a chromium, tungsten or molybdenum steel, the complex cubic M<sub>23</sub>C<sub>6</sub> carbide can form, where M can include iron, chromium, molybdenum or tungsten (Figs 4.10 and 4.11). This change in the carbide phase does not necessarily alter the basic pearlitic morphology and consequently alloy pearlites are obtained in which an alloy carbide is associated with ferrite (Fig. 4.11). These pearlites occur only in medium and highly alloyed steels, usually at the highest transformation temperatures. At lower transformation temperatures in the same steel, cementitic pearlite may still form because of the inadequate diffusion of the alloying element.

---

<sup>4</sup> Williams, P. R., Miller, M. K. and Smith, G. D. W., *Solid–Solid Phase Transformations*, TMS-AIME, Pennsylvania, p. 813, 1981.

<sup>5</sup> Coates, D. E., *Metallurgical Transactions* **4**, 2313, 1973.

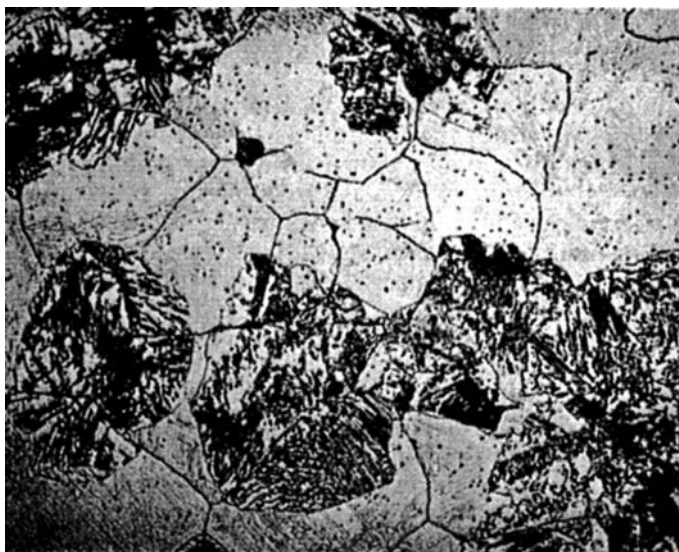


**Fig. 4.10** Fe-12Cr-0.2C transformed 30 min at 775°C. Pearlite-type reaction involving  $M_{23}C_6$  (courtesy of Campbell). Optical micrograph  $\times 300$ .

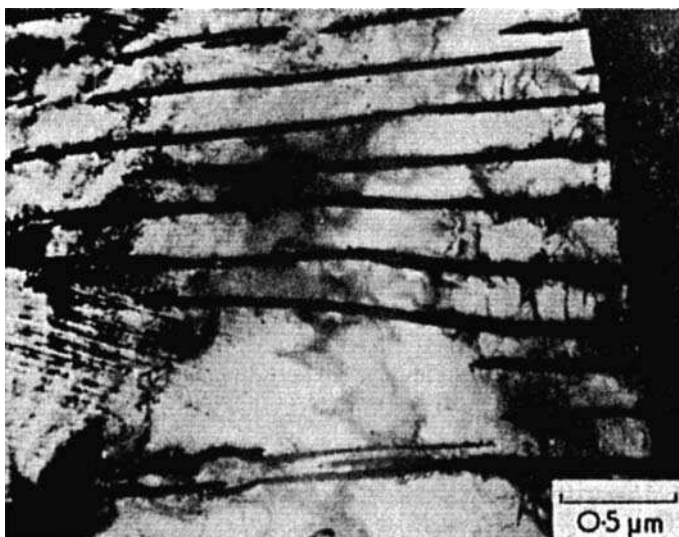


**Fig. 4.11** Fe-12Cr-0.2C transformed 15 min at 750°C. Alloy pearlite.  $M_{23}C_6$ /ferrite (courtesy of Campbell). Thin-foil electron micrograph.



#### 4.4 STRUCTURAL CHANGES RESULTING FROM ALLOYING ADDITIONS

The addition to iron-carbon alloys of elements such as nickel, silicon, manganese, which do not form carbides in competition with cementite, does not basically alter the microstructures formed after transformation. However, in the case of strong carbide-forming elements such as molybdenum, chromium and tungsten, cementite will be replaced by the appropriate alloy carbides, often at relatively low alloying element concentrations. Still stronger carbide-forming elements such as niobium, titanium and vanadium are capable of forming alloy carbides preferentially at alloying concentrations less than 0.1 wt%. It would, therefore, be expected that the microstructures of steels containing these elements would be radically altered.

The tendency for forming carbides and nitrides can be expressed in terms of bonding. Cottrell has been able to explain many of the observed trends in the stability, crystal structure and stoichiometry of the carbides of transition metals in terms of chemical bonds (see Further Reading). He points out that Ti, Zr and Hf, which in the periodic table are elements near the beginning of the long periods, form very stable MC carbides but the affinity for carbon diminishes further along the rows of the periodic table (Fig. 4.12). A part of the reason for this is that more electrons have to be accommodated for elements further along the rows, so antibonding states are progressively filled thereby reducing the bond order.<sup>6</sup> This does not completely explain the trend because the maximum bond order occurs with Cr, Mo and W and we know that carbides of these elements are less stable.

With MC carbides (where 'M' stands for metal atoms), the metal has to sacrifice four electrons to form the bonds with carbon. Titanium has exactly the right number so that its *d*-orbitals are left empty on forming TiC. This is not the case with VC, since vanadium has an additional *d*-electron which forms a V-V bond. The electrons in the two kinds of bonds, V-C and V-V mutually repel, leading to a reduction in the stability of VC when compared with TiC. This problem becomes larger along the row of the periodic table until MC carbide formation becomes impossible or unlikely.

Although Cottrell has not considered the carbides in the lanthanide or actinide series of elements, it is possible that the same principles should apply there. Both NdC and UC exist. Remarkably, neodymium nitride has already been incorporated into a ferritic creep-resistant steel by Igarashi and Sawaragi with

---

<sup>6</sup> When two hydrogen atoms, each with a single electron, are brought together, they no longer have separate atomic orbitals. Instead they have a pair of communal orbitals (bonding and antibonding) each of which can hold two electrons. It follows that for H<sub>2</sub> both the electrons are in the bonding orbitals giving a bond order of 2 and a strong molecule. For He<sub>2</sub>, on the other hand, the four electrons fill up both the bonding and the antibonding orbitals so the bond order is zero, the molecule is not formed.

--	--	--	--	--	--	--	--	--	--	--	--	--	--	--	--	--	--	--	--	--	--	--	--	--	--	--	--	--	--	--	--	--	--	--	--	--	--	--	--	--	--	--	--	--	--	--	--	--	--	--	--	--	--	--	--	--	--	--	--	--	--	--	--	--	--	--	--	--	--	--	--	--	--	--	--	--	--	--	--	--	--	--	--	--	--	--	--	--	--	--	--	--	--	--	--	--	--	--	--	--	--	--	--	--	--	--	--	--	--	--	--	--	--	--	--	--	--	--	--	--	--	--	--	--	--	--	--	--	--	--	--	--	--	--	--	--	--	--	--	--	--	--	--	--	--	--	--	--	--	--	--	--	--	--	--	--	--	--	--	--	--	--	--	--	--	--	--	--	--	--	--	--	--	--	--	--	--	--	--	--	--	--	--	--	--	--	--	--	--	--	--	--	--	--	--	--	--	--	--	--	--	--	--	--	--	--	--	--	--	--	--	--	--	--	--	--	--	--	--	--	--	--	--	--	--	--	--	--	--	--	--	--	--	--	--	--	--	--	--	--	--	--	--	--	--	--	--	--	--	--	--	--	--	--	--	--	--	--	--	--	--	--	--	--	--	--	--	--	--	--	--	--	--	--	--	--	--	--	--	--	--	--	--	--	--	--	--	--	--	--	--	--	--	--	--	--	--	--	--	--	--	--	--	--	--	--	--	--	--	--	--	--	--	--	--	--	--	--	--	--	--	--	--	--	--	--	--	--	--	--	--	--	--	--	--	--	--	--	--	--	--	--	--	--	--	--	--	--	--	--	--	--	--	--	--	--	--	--	--	--	--	--	--	--	--	--	--	--	--	--	--	--	--	--	--	--	--	--	--	--	--	--	--	--	--	--	--	--	--	--	--	--	--	--	--	--	--	--	--	--	--	--	--	--	--	--	--	--	--	--	--	--	--	--	--	--	--	--	--	--	--	--	--	--	--	--	--	--	--	--	--	--	--	--	--	--	--	--	--	--	--	--	--	--	--	--	--	--	--	--	--	--	--	--	--	--	--	--	--	--	--	--	--	--	--	--	--	--	--	--	--	--	--	--	--	--	--	--	--	--	--	--	--	--	--	--	--	--	--	--	--	--	--	--	--	--	--	--	--	--	--	--	--	--	--	--	--	--	--	--	--	--	--	--	--	--	--	--	--	--	--	--	--	--	--	--	--	--	--	--	--	--	--	--	--	--	--	--	--	--	--	--	--	--	--	--	--	--	--	--	--	--	--	--	--	--	--	--	--	--	--	--	--	--	--	--	--	--	--	--	--	--	--	--	--	--	--	--	--	--	--	--	--	--	--	--	--	--	--	--	--	--	--	--	--	--	--	--	--	--	--	--	--	--	--	--	--	--	--	--	--	--	--	--	--	--	--	--	--	--	--	--	--	--	--	--	--	--	--	--	--	--	--	--	--	--	--	--	--	--	--	--	--	--	--	--	--	--	--	--	--	--	--	--	--	--	--	--	--	--	--	--	--	--	--	--	--	--	--	--	--	--	--	--	--	--	--	--	--	--	--	--	--	--	--	--	--	--	--	--	--	--	--	--	--	--	--	--	--	--	--	--	--	--	--	--	--	--	--	--	--	--	--	--	--	--	--	--	--	--	--	--	--	--	--	--	--	--	--	--	--	--	--	--	--	--	--	--	--	--	--	--	--	--	--	--	--	--	--	--	--	--	--	--	--	--	--	--	--	--	--	--	--	--	--	--	--	--	--	--	--	--	--	--	--	--	--	--	--	--	--	--	--	--	--	--	--	--	--	--	--	--	--	--	--	--	--	--	--	--	--	--	--	--	--	--	--	--	--	--	--	--	--	--	--	--	--	--	--	--	--	--	--	--	--	--	--	--	--	--	--	--	--	--	--	--	--	--	--	--	--	--	--	--	--	--	--	--	--	--	--	--	--	--	--	--	--	--	--	--	--	--	--	--	--	--	--	--	--	--	--	--	--	--	--	--	--	--	--	--	--	--	--	--	--	--	--	--	--	--	--	--	--	--	--	--	--	--	--	--	--	--	--	--	--	--	--	--	--	--	--	--	--	--	--	--	--	--	--	--	--	--	--	--	--	--	--	--	--	--	--	--	--	--	--	--	--	--	--	--	--	--	--	--	--	--	--	--	--	--	--	--	--	--	--	--	--	--	--	--	--	--	--	--	--	--	--	--	--	--	--	--	--	--	--	--	--	--	--	--	--	--	--	--	--	--	--	--	--	--	--	--	--	--	--	--	--	--	--	--	--	--	--	--	--	--	--	--	--	--	--	--	--	--	--	--	--	--	--	--	--	--	--	--	--	--	--	--	--	--	--	--	--	--	--	--	--	--	--	--	--	--	--	--	--	--	--	--	--	--	--	--	--	--	--	--	--	--	--	--	--	--	--	--	--	--	--	--	--	--	--	--	--	--	--	--	--	--	--	--	--	--	--	--	--	--	--	--	--	--	--	--	--	--	--	--	--	--	--	--	--	--	--	--	--	--	--	--	--	--	--	--	--	--	--	--	--	--	--	--	--	--	--	--	--	--	--	--	--	--	--	--	--	--	--	--	--	--	--	--	--	--	--	--	--	--	--	--	--	--	--	--	--	--	--	--	--	--	--	--	--	--	--	--	--	--	--	--	--	--	--	--	--	--	--	--	--	--	--	--	--	--	--	--	--	--	--	--	--	--	--	--	--	--	--	--	--	--	--	--	--	--	--	--	--	--	--	--	--	--	--	--	--	--	--	--	--	--	--	--	--	--	--	--	--	--	--	--	--	--	--	--	--	--	--	--	--	--	--	--	--	--	--	--	--	--	--	--	--	--	--	--	--	--	--	--	--	--	--	--	--	--	--	--	--	--	--	--	--	--	--	--	--	--	--	--	--	--	--	--	--	--	--	--	--	--	--	--	--	--	--	--	--	--	--	--	--	--	--	--	--	--	--	--	--	--	--	--	--	--	--	--	--	--	--	--	--	--	--	--	--	--	--	--	--	--	--	--	--	--	--	--	--	--	--	--	--	--	--	--	--	--	--	--	--	--	--	--	--	--	--	--	--	--	--	--	--	--	--	--	--	--	--	--	--	--	--	--	--	--	--	--	--	--	--	--	--	--	--	--	--	--	--	--	--	--	--	--	--	--	--	--	--	--	--	--	--	--	--	--	--	--	--	--	--	--	--	--	--	--	--	--	--	--	--	--	--	--	--	--	--	--	--	--	--	--	--	--	--	--	--	--	--	--	--	--	--	--	--	--	--	--	--	--	--	--	--	--	--	--	--	--	--	--	--	--	--	--	--	--	--	--	--	--	--	--	--	--	--	--	--	--	--	--	--	--	--	--	--	--	--	--	--	--	--	--	--	--	--	--	--	--	--	--	--	--	--	--	--	--	--	--	--	--	--	--	--	--	--	--	--	--	--	--	--	--	--	--	--	--	--	--	--	--	--	--	--	--	--	--	--	--	--	--	--	--	--	--	--	--	--	--	--	--	--	--	--	--	--	--	--	--	--	--	--	--	--	--	--	--	--	--	--	--	--	--	--	--	--	--	--	--	--	--	--	--	--	--	--	--	--	--	--	--	--	--	--	--	--	--	--	--	--	--	--	--	--	--	--	--	--	--	--	--	--	--	--	--	--	--	--	--	--	--	--	--	--	--	--	--	--	--	--	--	--	--	--	--	--	--	--	--	--	--	--	--	--	--	--	--	--	--	--	--	--	--	--	--	--	--	--	--	--	--	--	--	--	--	--	--	--	--	--	--	--	--	--	--	--	--	--	--	--	--	--	--	--	--	--	--	--	--	--	--	--	--	--

**Fig. 4.12** The periodic table showing the positions of strong carbide-forming elements.

rather good results. The concentration of neodymium used was only 0.04 wt% but gave an increase in the creep rupture life by a factor of about two during tests at 650°C. They also tried hafnium but did not recommend it due to a tendency to form coarse particles.

It has been shown how the difference in solubility of carbon in austenite and ferrite leads to the familiar ferrite/cementite aggregates in plain carbon steels. This means that, because the solubility in austenite is much greater than in ferrite, it is possible to redistribute the cementite by holding the steel in the austenite region to take it into solution, and then allowing transformation to take place to ferrite and cementite. Examining the possible alloy carbides, and nitrides, in the same way, shows that all the familiar ones are much less soluble in austenite than is cementite. In Fig. 4.13 the solubility products in austenite of vanadium, titanium and niobium carbides and nitrides are plotted as a function of  $1/T$ . Chromium and molybdenum carbides are not included, but they are substantially more soluble in austenite than the other carbides. Detailed consideration of such data, together with practical knowledge of alloy steel behaviour, indicates that, for niobium and titanium, concentrations of greater than about 0.25 wt% will form excess alloy carbides which cannot be dissolved in austenite at the highest solution temperatures. With vanadium the limit is higher at 1–2 wt%, and with molybdenum up to about 5 wt%. Chromium has a much higher limit before complete solution of chromium carbide in austenite becomes difficult. This argument assumes that sufficient carbon is present in the steel to combine with the alloying element. If not, the excess metallic element will go into solid solution both in the austenite and the ferrite.

#### 4.4.1 Ferrite/alloy carbide aggregates

Steels containing strong carbide-forming elements transform from austenite to ferrite in a similar way to, e.g., steels containing nickel or silicon.

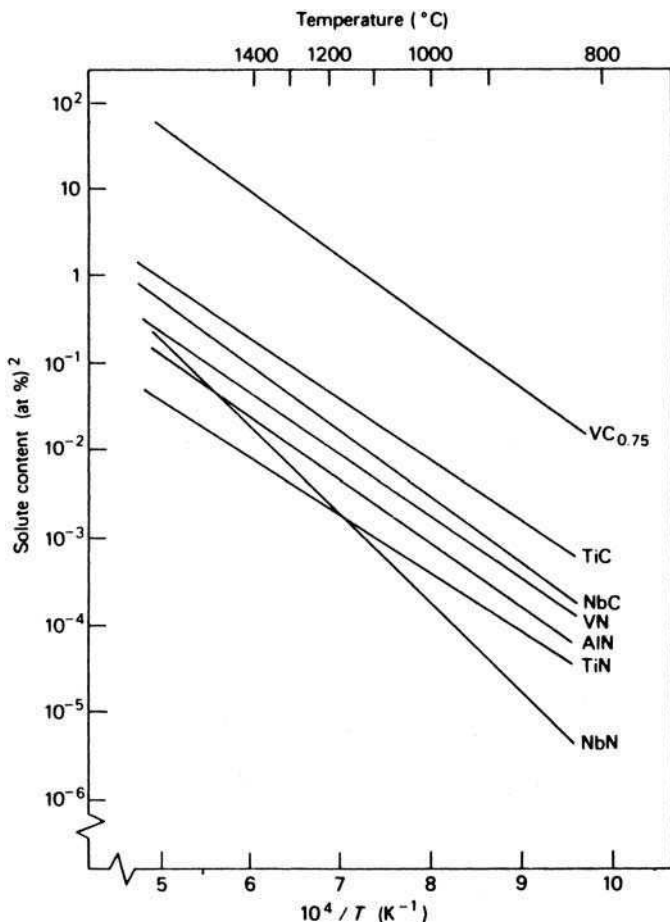


**Fig. 4.13** Solubility products of carbides and nitrides in austenite as a function of temperature (Aronsson, in *Steel Strengthening Mechanisms*, Climax Molybdenum Co., Michigan, USA, 1969).

However, the carbide-forming elements restrict very substantially the  $\gamma$ -loop (Fig. 4.4), so that the eutectoid composition is depressed to much lower carbon levels and to higher transformation temperatures. One result is that pearlite can completely disappear from the transformed microstructures, which now exhibit very different ferrite/carbide aggregates, usually on a very much finer scale than pearlite. Apart from the alloy carbide-pearlites, particularly found in high chromium steels, there are three morphologies of alloy carbides which are intimately associated with ferrite in the transformation temperature range in which plain carbon steels form ferrite/pearlite structures.

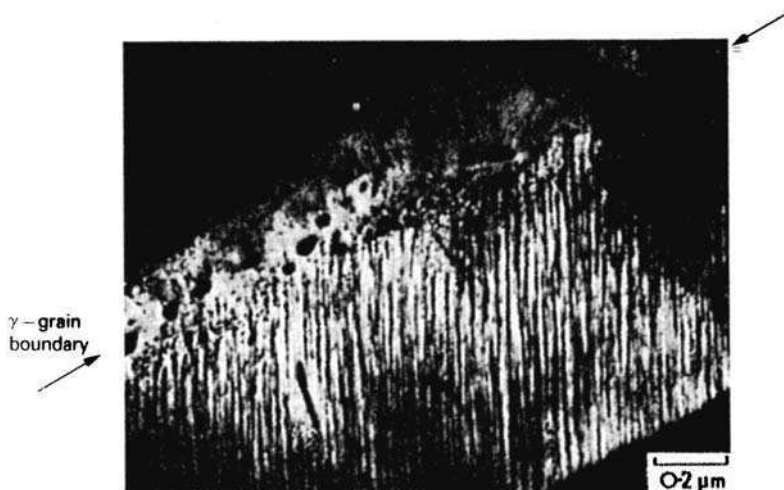


**Fig. 4.14** Fe-4Mo-0.2C transformed 20 min at 650°C. Fibrous  $\text{Mo}_2\text{C}$  growth from  $\gamma$  boundary (courtesy of Berry). Thin-foil electron micrograph.

**Continuous growth of fibres/laths** The alloy carbides form as fine fibres or laths which grow normal to the  $\gamma$ - $\alpha$  interface which then moves forward forming fibrous aggregates of carbide and ferrite (Fig. 4.14).

**Repeated nucleation of carbides (interphase precipitation)** In this growth mode the carbide particles, usually in the form of small plates or rods, nucleate at the  $\gamma$ - $\alpha$  interface which then moves to a new position where the nucleation cycle again occurs. This process can be repeated many hundreds of time within a particular austenite grain leading to a ferrite matrix with very fine banded dispersions as, e.g., in the 0.75 wt% vanadium steel shown in Fig. 4.15. Chromium steels give coarser dispersions (Fig. 4.17).

**Nucleation in supersaturated ferrite** In microalloyed steels, where strong carbide-forming elements are present in concentrations less than 0.1 wt%, it is often possible to obtain the ferrite in a supersaturated condition with little or no carbide precipitation taking place during the  $\gamma/\alpha$  transformation. Instead, while the steel is held at the transformation temperature, carbide precipitates form within the newly formed ferrite grains, usually on dislocations (Fig. 4.16).

While it is possible by careful choice of alloy and experimental conditions to obtain each of the above microstructures separately, in practice they are often all present in transformed alloy steels, provided the steel contains a strong carbide-forming element. Consequently the microstructures of transformable alloy steels can be very complex, the full extent of these complexities only being revealed when high-resolution electron microscopy is used to study them.



**Fig. 4.15** Fe-0.75V-0.15C transformed 5 min at 725°C. Interphase precipitation of VC in ferrite (courtesy of Batte). Thin-foil electron micrograph.

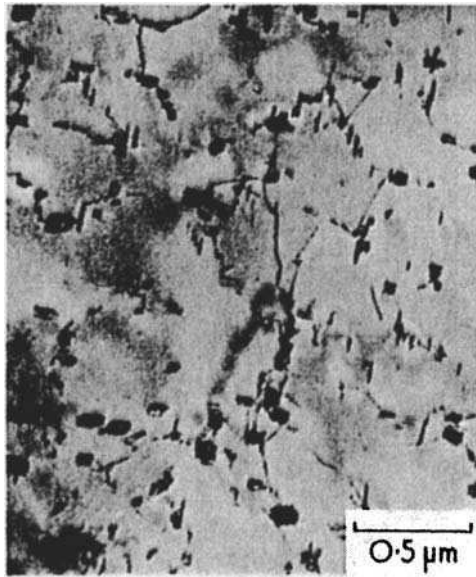


**Fig. 4.16** Fe-0.25V-0.05C transformed and held at 2½ h at 740°C. VC precipitation on dislocations (courtesy of Ballinger). Thin-foil electron micrograph.

In general, the fibrous morphology represents a closer approach to an equilibrium structure so it is more predominant in steels which have transformed slowly. In contrast, the interphase precipitation and dislocation nucleated structures occur more readily in rapidly transforming steels, where there is a high driving force, e.g., in microalloyed steels (Chapter 10).

#### 4.4.2 Alloy carbide fibres and laths

The clearest analogy with pearlite is found when the alloy carbide in lath morphology forms nodules in association with ferrite. These pearlitic nodules are often encountered at temperatures just below  $A_{e1}$  in steels which transform relatively slowly. For example, these structures are obtained in chromium steels with between 4 and 12 wt% chromium (Fig. 4.11), and the morphology is analogous to that of cementitic pearlite. It is, however, different in detail because of the different crystal structures of the possible carbides, e.g.  $Cr_7C_3$  is hexagonal and  $Cr_{23}C_6$  is complex cubic. The structures observed are relatively coarse, but finer than pearlite formed under equivalent conditions, because of the need for the partition of the alloying element, e.g. chromium between the carbide and the ferrite. To achieve this, the interlamellar spacing must be substantially finer than in the equivalent iron–carbon case.

At lower temperatures the lath morphology is largely replaced by much finer fibrous aggregates, e.g. in high Cr steels coarse laths of  $Cr_{23}C_6$  can be replaced by fine fibres of the same carbide usually 500 Å in diameter. Their length, which is determined by the size of the ferrite colony, can be up to 10 μm with little or no branching. Similar morphologies occur, but are much less dominant, in steels containing W, Ti, V and Nb.

Carbide fibres are frequently associated with planar interfaces, as well as with pearlitic-type interfaces. Nevertheless, these are boundaries which can apparently propagate rapidly without the need for step migration. A computer analysis of similar boundaries in austenitic steels has shown that they possess comparatively high densities of coincident lattice sites.<sup>7</sup>

#### 4.4.3 Interphase precipitation

Interphase precipitation has been shown to nucleate periodically at the  $\gamma/\alpha$  interface during the transformation. The precipitate particles form in bands which are closely parallel to the interface, and which follow the general direction of the interface even when it changes direction sharply. A further characteristic is the frequent development of only one of the possible Widmanstätten variants, e.g. VC platelets in a particular region are all only of one variant of the habit, i.e. that in which the plates are most nearly parallel to the interface. The bands are often associated with planar low-energy interfaces, and the interband spacing is determined by the height of steps which move along the interface (Fig. 4.17).

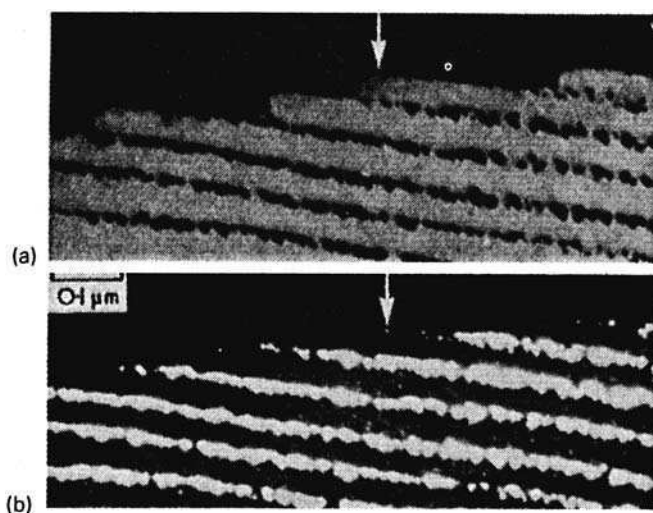


**Fig. 4.17** Fe-12Cr-0.2C wt% transformed 30 min at 650°C. Precipitation of  $M_{23}C_6$  at stepped  $\gamma/\alpha$  interface: (a) bright field; (b) precipitate spot dark field (courtesy of Campbell). Thin-foil electron micrograph.

The nucleation of the carbide particles occurs normally on the low energy planar interfaces, rather than on the rapidly moving high-energy steps.<sup>7</sup>

The need for step movement on the  $\gamma/\alpha$  interface is in contrast to the growth of fibrous carbides behind an interface on which no steps are observed. Indeed if, in these circumstances, a step does move along the interface, the fibrous growth is stopped and replaced by interphase precipitation. The step height and, therefore, the band spacing of the precipitation, is dependent on the temperature of transformation and on the composition. As the temperature of transformation is lowered the band spacing is reduced, e.g. in a 1 wt% V 0.2 wt% carbon steel, the spacing varies from 25 nm at 825°C to 7.5 nm at 725°C (Fig. 4.18), and at lower temperatures has been observed to be less than 5 nm. The extremely fine scale of this phenomenon in vanadium steels, which also occurs in Ti and Nb steels, is due to the rapid rate at which the  $\gamma/\alpha$  transformation takes place. At the higher transformation temperatures, the slower rate of reaction leads to coarser structures. Similarly, if the reaction is slowed down by addition of further alloying elements, e.g. Ni and Mn, the precipitate dispersion coarsens. The scale of the dispersion also varies from steel to steel, being coarsest in chromium, tungsten and molybdenum steels where the reaction is relatively slow, and much finer in steels in which vanadium, niobium and titanium are the dominant alloying elements and the transformation is rapid.

<sup>7</sup> Ainsley, M. H., Cocks, G. J. and Miller, D. R., *Metal Science* **13**, 20, 1979.

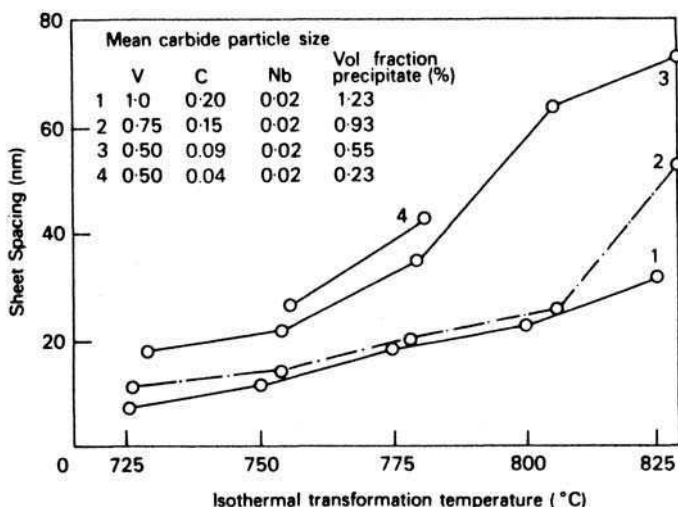


**Fig. 4.18** Interphase precipitation of VC in vanadium steels. Precipitate sheet spacing as a function of transformation temperature (courtesy of Ballinger).

#### 4.4.4 Nucleation in supersaturated ferrite

It has been shown that ferrite can occur in different morphologies depending on the transformation temperature. At the highest transformation temperatures, equi-axed boundary allotriomorphs form at the austenite grain boundaries, and carbon diffuses to the austenite. In alloy steels, e.g. low V steels, there is evidence that the alloying element can also partition. As a result no alloy carbide forms in this ferrite, which is thus truly pro-eutectoid. At lower temperatures the ferrite formed is still equi-axed, but the alloy carbide forms at the same time either as interphase precipitate or as fibres. This is probably the closest approach to true eutectoid behaviour in an alloy steel containing a strong carbide-forming element.

At still lower transformation temperatures the ferrite adopts a Widmanstätten habit and forms as laths, as in pure iron–carbon alloys. However, this ferrite can be supersaturated when first formed. If held only for a short time at the transformation temperature, precipitation of the alloy carbide occurs within the ferrite on dislocations. Such behaviour would be expected in alloy steels with acicular ferrite provided a strong carbide former such as V, Ti or Nb is present although, in theory, similar structures should be possible in plain carbon steels.

### 4.5 TRANSFORMATION DIAGRAMS FOR ALLOY STEELS

The transformation of austenite below the eutectoid temperature can best be presented in an isothermal transformation diagram (Chapter 3), in which the



beginning and end of transformation is plotted as a function of temperature and time. Such curves are known as time–temperature–transformation, or *TTT*, curves and form one of the important sources of quantitative information for the heat treatment of steels. In the simple case of an eutectoid plain carbon steel, the curve is roughly ‘C’-shaped with the pearlite reaction occurring down to the nose of the curve and a little beyond. At lower-temperatures bainite and martensite form (see Chapters 5 and 6). The diagrams become more complex for hypo- and hyper-eutectoid alloys as the ferrite or cementite reactions have also to be represented by additional lines.

Alloying elements, on the whole, retard both the pro-eutectoid reactions and the pearlite reaction, so that *TTT* curves for alloy steels are moved increasingly to longer times as the alloy content is increased. Additionally, those elements which expand the  $\gamma$ -field depress the eutectoid temperature, with the result that they also depress the position of the *TTT* curves relative to the temperature axes. This behaviour is shown by steels containing manganese or nickel. For example, in a 13Mn–0.8C wt% steel, pearlite can form at temperatures as low as 400 C. In contrast, elements which favour the ferrite phase raise the eutectoid temperature and the *TTT* curves move correspondingly to higher temperatures. The slowing down of the ferrite and pearlite reactions by alloying elements enables these reactions to be more readily avoided during heat treatment, so that the much stronger low-temperature phases such as bainite and martensite can be obtained in the microstructure. The hard martensitic structure is only obtained in plain carbon steels by water quenching from the austenitic condition whereas, by the addition of alloying elements, a lower critical cooling rate is needed to achieve this condition. Consequently, alloy steels allow hardening to occur during oil quenching, or even on air cooling, if the *TTT* curve has been sufficiently displaced to longer times.

## FURTHER READING

- Andrews, K. W., *Metal Treatment* **19**, 425; 489, 1952; *Iron and Steel*, March 1961.
- Bain, E. C. and Paxton, H. W., *Alloying Elements in Steel*, American Society for Metals, Ohio, USA, 1966.
- Bullens, D. K., *Steel and Its Heat Treatment*, Vols 1 and 2, John Wiley, USA, 1956.
- Cerjak, H., Hofer, P. and Schaffernak, B., *ISIJ International* **39**, 874, 1999.
- Cottrell, A. H., *Chemical Bonding in Transition Metal Carbides*, The Institute of Materials, London, 1995.
- De Ardo, A. J. (ed.), *Proceedings of the Conference on Processing, Microstructure and Properties of HSLA Steels*, TMS-AIME, Pittsburgh, 1987.
- Goldschmidt, H. J., *Interstitial Alloys*, Butterworths, UK, 1967.
- Gray, J. M., Ko, T., Zhang Shouhwa, Wu Barong and Xie Xishan (eds), *HSLA Steels: Metallurgy and Applications*, ASM International, Ohio, USA, 1986.
- Hillert, M., *ISIJ International* **30**, 559, 1990.
- Honeycombe, R. W. K., Ferrite, *Hatfield Memorial Lecture*, 1979, *Metal Science* **14**, 1980.

- Igarashi, M. and Swaragi, Y. *Proceedings of the International Conference on Power Engineering – 1997*, Japan Society of Mechanical Engineers, Tokyo, Japan, p. 107, 1997.
- Krauss, G., *Steels: Heat Treatment and Processing Principles*, ASM International, Ohio, USA, 1990.
- Leslie, W. C., *The Physical Metallurgy of Steels*, McGraw-Hill, Tokyo, Japan, 1981.
- Marden, A. R. and Goldstein (eds) *Phase Transformations in Ferrous Alloys*, TMS-AIME, Warrendale, 1984.
- Pickering, F. B., *Physical Metallurgy and the Design of Steels*, Applied Science Publishers, London, UK, 1978.
- Pierson, H. O., *Handbook of Refractory Carbides and Nitrides*, Noyes Publications, USA, 1996.

*This page intentionally left blank*

# 5

## FORMATION OF MARTENSITE

### 5.1 INTRODUCTION

The quenching to room temperature of austenite in a steel can lead to the formation of martensite, a very hard phase in which the carbon, formerly in solid solution in the austenite, remains in solution in the new phase. Unlike ferrite or pearlite, martensite forms by a deformation of the austenite lattice without any diffusion of atoms. The deformation causes a change in the shape of the transformed region, consisting of a large shear and a volume expansion. Martensite is, therefore, often referred to as a diffusionless, shear transformation, which is highly crystallographic in character because it is generated by a specific deformation of the austenite. When the formation of martensite is constrained by its surroundings, it forms as thin plates or laths in order to minimize the strain energy due to the deformation.

### 5.2 GENERAL CHARACTERISTICS

The martensite reaction in steels normally occurs athermally, i.e. the fraction transformed depends on the undercooling below a *martensite-start temperature*,  $M_s$ . The extent of transformation does not seem to depend on time, as expressed in the Koistinen and Marburger equation<sup>1</sup> which describes the progress of transformation below  $M_s$ :

$$1 - V_{\alpha'} = \exp\{\beta(M_s - T_q)\} \quad \text{where } \beta \simeq -0.011 \quad (5.1)$$

$V_{\alpha'}$  is the fraction of martensite and  $T_q$  the temperature below  $M_s$ , to which the sample is cooled. This athermal character is a consequence of very rapid nucleation and growth, so rapid that the time taken can be neglected. Instead, the

---

<sup>1</sup> Koistinen, D. P. and Marburger, R. E., *Acta Metallurgica* **7**, 59, 1959.

**Table 5.1** The temperature  $M_s$  at which martensite first forms on cooling, and the approximate Vickers hardness of the resulting martensite for a number of materials

Composition	$M_s$ /K	Hardness HV
ZrO <sub>2</sub>	1200	1000
Fe–31Ni–0.23C wt%	83	300
Fe–34Ni–0.22C wt%	<4	250
Fe–3Mn–2Si–0.4C wt%	493	600
Cu–15Al	253	200
Ar–40N <sub>2</sub>	30	

fraction transformed depends only on the number of nucleation sites triggered, with the less potent sites contributing at higher undercoolings.

From Equation (5.1) it is evident that some austenite remains untransformed when  $T_q$  is set to room temperature. This is referred to as *retained austenite*. It is also clear that there is no *martensite-finish temperature*,  $M_f$  but for convenience, the latter is frequently defined at the point where 95% of the martensitic transformation is completed.

Martensite is not restricted to steels although its technological importance in steels is unsurpassed. Table 5.1 lists a variety of materials which exhibit martensitic transformation, together with  $M_s$  temperatures and hardness values.

To obtain martensite, it is usually necessary for the steel to be cooled from the austenite phase field at a rate which is sufficiently fast to avoid all other solid-state transformations such as ferrite and pearlite. This cooling rate can be very high for plain carbon steels but quite slow for a heavily alloyed steel containing large concentrations of austenite stabilizing solutes.

Martensite can form at very low temperatures, where diffusion, even of interstitial atoms, is not conceivable over the time period of the experiment. Table 5.1 gives typical values of the martensite-start temperature for a variety of materials. Martensite plates can grow at speeds which are a significant fraction of the speed of sound in the steel, some  $1100\text{ m s}^{-1}$ . Such a high rate of growth is inconsistent with diffusion during transformation. Transformations which involve diffusion are much slower – the fastest recorded solidification rate is about  $80\text{ m s}^{-1}$  in pure nickel. The chemical composition of martensite can be measured and shown to be identical to that of the parent austenite. These observations demonstrate convincingly that martensitic transformations are diffusionless.

**5.2.1 The habit plane**

The habit refers to the interface plane between austenite and martensite as measured on a macroscopic scale (Fig. 5.1). For unconstrained transformations this

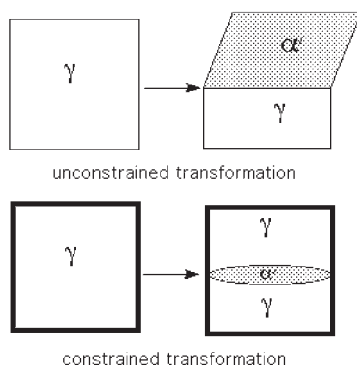


**Fig. 5.1** An illustration of the habit plane between austenite ( $\gamma$ ) and martensite ( $\alpha'$ ).

**Table 5.2** Habit plane indices for martensite. With the exception of  $\epsilon$ -martensite, the quoted indices are approximate because the habit planes are in general irrational (the square root of 2 is not a rational number)

Composition/wt%	Approximate habit plane indices
Low-alloy steels, Fe-28Ni	$\{1\ 1\ 1\}_{\gamma}$
Plate martensite in Fe-1.8C	$\{2\ 9\ 5\}_{\gamma}$
Fe-30Ni-0.3C	$\{3\ 15\ 10\}_{\gamma}$
Fe-8Cr-1C	$\{2\ 5\ 2\}_{\gamma}$
$\epsilon$ -martensite in 18/8 stainless steel	$\{1\ 1\ 1\}_{\gamma}$

interface plane is flat, but the need to minimize strains introduces some curvature when the transformation is constrained by its surroundings. Nevertheless, the macroscopic habit plane is identical for both cases, as illustrated in Fig. 5.1.

Steels of vastly different chemical composition can have martensite with the same habit plane (Table 5.2), and indeed, other identical crystallographic characteristics.

### 5.2.2 Orientation relationships

The formation of martensite involves the coordinated movement of atoms. It follows that the austenite and martensite lattices will be intimately related. All martensitic transformations therefore lead to a reproducible orientation relationship between the parent and product lattices. It is frequently the case that a pair of corresponding close-packed<sup>2</sup> planes in the ferrite and austenite are

<sup>2</sup> The body-centred cubic lattice does not have a close-packed plane but  $\{0\ 1\ 1\}_{\alpha}$  is the most densely packed plane.

parallel or nearly parallel, and it is usually the case that corresponding directions within these planes are roughly parallel:

$$\begin{aligned} \{111\}_\gamma &\parallel \{011\}_\alpha, \\ \langle 10\bar{1} \rangle_\gamma &\parallel \langle 11\bar{1} \rangle_\alpha, \end{aligned} \quad \text{Kurdjumov-Sachs}$$

$$\begin{aligned} \{111\}_\gamma &\parallel \{011\}_\alpha, \\ \langle 10\bar{1} \rangle_\gamma &\text{ about } 5.3^\circ \text{ from } \langle 11\bar{1} \rangle_\alpha \text{ towards } \langle \bar{1}1\bar{1} \rangle_\alpha, \end{aligned} \quad \text{Nishiyama-Wasserman}$$

$$\begin{aligned} \{111\}_\gamma &\text{ about } 0.2^\circ \text{ from } \{011\}_\alpha, \\ \langle 10\bar{1} \rangle_\gamma &\text{ about } 2.7^\circ \text{ from } \langle 11\bar{1} \rangle_\alpha \text{ towards } \langle \bar{1}1\bar{1} \rangle_\alpha. \end{aligned} \quad \text{Greninger-Troiano}$$

Note that these have been stated approximately: the true relations are irrational, meaning that the indices of the parallel planes and directions cannot be expressed using rational numbers.

### 5.2.3 Structure of the interface

Any process that contributes to the formation of martensite cannot rely on assistance from thermal activation. There must, therefore, exist a high level of continuity across the interface between martensite and austenite. The interface must be coherent or semicoherent; in the latter case, the dislocations in the interface must be able to glide as the martensite grows. It turns out that a stress-free coherent interface cannot be found between austenite and martensite, the best that can be achieved is semicoherency, with one direction within the interface remaining fully coherent. This direction is known as an *invariant-line* since it is unrotated and undistorted.

### 5.2.4 The shape deformation

The passage of a slip dislocation through a crystal causes the formation of a step where the glide plane intersects the free surface (Figs 5.2a, b). The passage of many such dislocations on parallel slip planes causes macroscopic shear (Figs 5.2c, d). Slip causes a change in shape but not a change in the crystal structure, because the Burgers vectors of the dislocations are also lattice vectors.

During martensitic transformation, the pattern in which the atoms in the parent crystal are arranged is *deformed* into that appropriate for martensite, there must be a corresponding change in the macroscopic shape of the crystal undergoing transformation. The dislocations responsible for the deformation

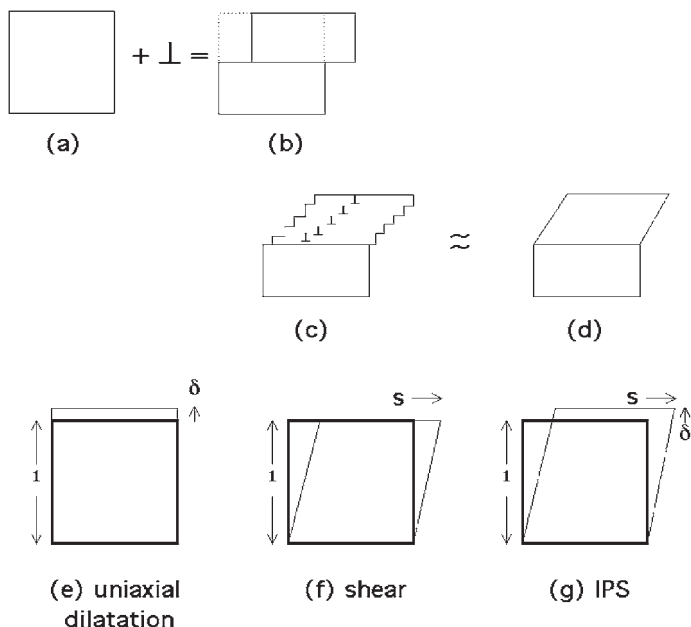


**Fig. 5.2** (a) and (b) Step caused by the passage of a slip dislocation. (c) and (d) Many slip dislocations, causing a macroscopic shear. (e) An invariant-plane strain with a uniaxial dilatation. (f) An invariant-plane strain which is a simple shear. (g) An invariant-plane strain which is the combined effect of a uniaxial dilatation and a simple shear.

are in the  $\alpha'/\gamma$  interface, with Burgers vectors such that in addition to deformation they also cause the change in crystal structure. The deformation is such that an initially flat surface becomes uniformly tilted about the line formed by the intersection of the interface plane with the free surface. Any scratch traversing the transformed region is similarly deflected though the scratch remains connected at the  $\alpha'/\gamma$  interface. These observations, and others, confirm that the measured shape deformation belongs to a class of deformations known as invariant plane strains (Figs. 5.2e–g), with martensite being the most general case in this class with a combined shear and dilatational strain ( $\delta \simeq 0.03$ ) normal to the habit plane.

Evidence that the transformation involves large shears can easily be obtained by polishing a surface, or better two surfaces at right angles, prior to transformation. After martensite plates form, the surface reveals relief including large shear displacements (Fig. 5.3) and any scratches present prior to transformation are themselves displaced (Fig. 5.4). The characteristic surface relief can also be analysed by using two-beam interferometry or atomic force microscopy, and quantitative data obtained from the displacement of the fringe patterns or surface contours, respectively. Experiments like these reveal that the shear strain



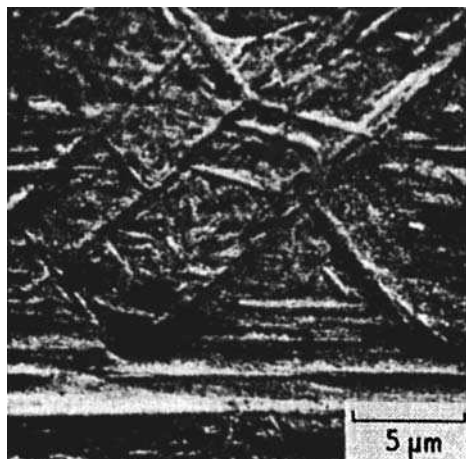


**Fig. 5.3** Martensite in a Fe-0.4C-4Ni wt% steel shown in relief on a pre-polished surface,  $\times 3400$ .

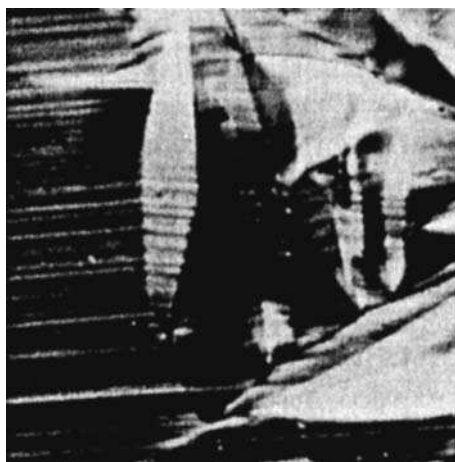


**Fig. 5.4** Fe-30.5Ni-0.3C wt% illustrating the displacement of surface scratches by the martensitic shear. Nomarski interference contrast,  $\times 650$ .

is of the order of  $s \simeq 0.22$  and the dilatational strain normal to the habit plane is typically  $\delta \simeq 0.03$ .

### 5.3 THE CRYSTAL STRUCTURE OF MARTENSITE

Martensite in steels is a supersaturated solid solution of carbon in ferritic iron. For alloys which have a low martensite-start temperature or a high carbon concentration, the carbon atoms tend to order in such a way that the crystal structure

changes from body-centred cubic (bcc) to body-centred tetragonal (bct). The tetragonality of the ordered martensite, measured by the ratio between the axes,  $c/a$ , increases with carbon content:

$$\frac{c}{a} = 1 + 0.045 \text{ wt\% C} \quad (5.2)$$

implying that at zero carbon content the structure would be bcc, free of distortion. The effect of carbon on the lattice parameter of austenite, and on the  $c$  and  $a$  parameters of martensite is shown in Fig. 5.5.

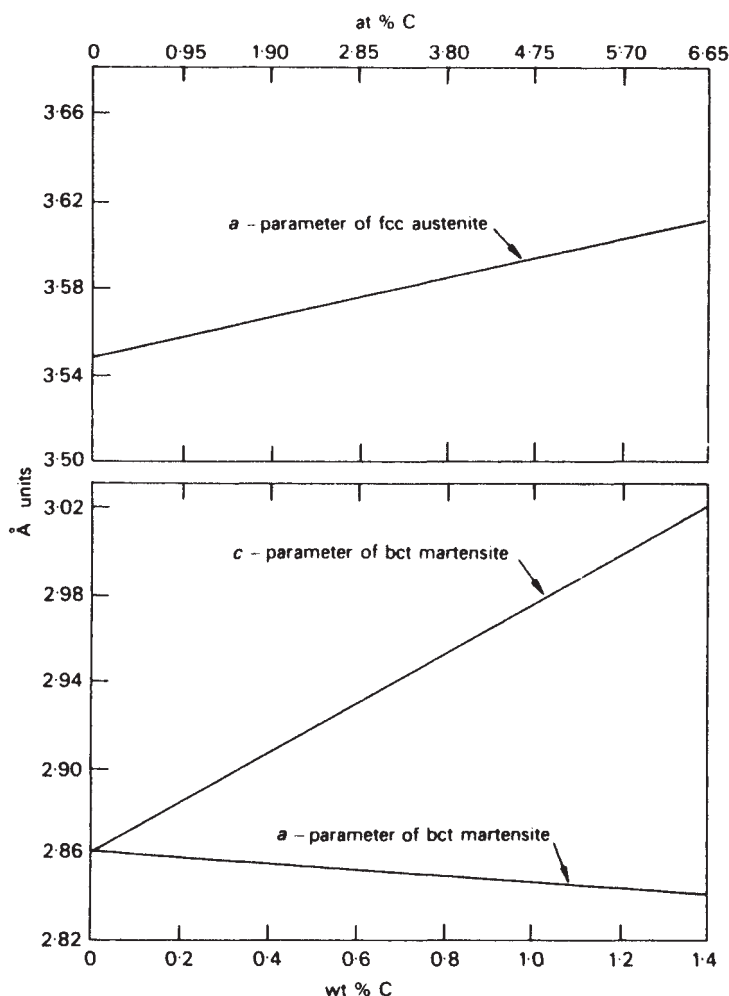


**Fig. 5.5** Effect of carbon on the lattice parameters of austenite and of martensite (after Roberts, in Cohen, *Transactions of the Metallurgical Society of AIME* **224**, 638, 1962).

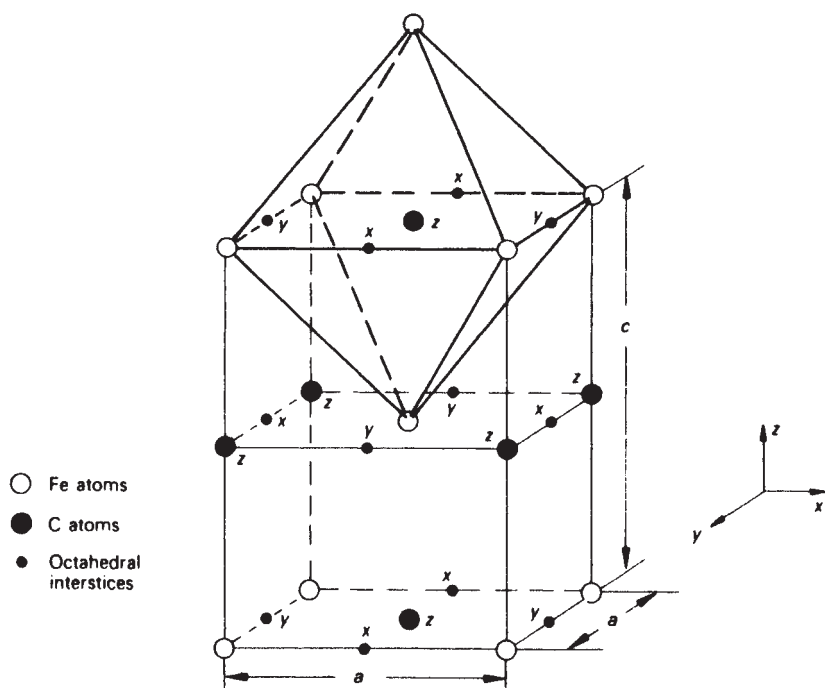


**Fig. 5.6** Martensite bct lattice illustrating the three sets of octahedral interstices. The  $z$ -set is fully occupied by carbon atoms (Cohen, *Transactions of the Metallurgical Society of AIME* **224**, 638, 1962).

It is interesting to note that carbon in interstitial solid solution expands the fcc iron lattice uniformly, but with bcc iron the expansion is non-symmetrical giving rise to tetragonal distortion. To understand this important difference in behaviour, it is necessary to compare the interstitial sites for carbon in the two lattices. In each case, carbon atoms occupy octahedral sites, indicated for martensite in black in Fig. 5.6, and have six near-neighbour iron atoms. In the fcc lattice the six iron atoms around each interstitial carbon atoms form a regular octahedron, whereas in the bcc case the corresponding octahedra are not regular, being shortened along the  $z$ -axis (Figs 1.4e, f). These compressed octahedra only have four-fold symmetry along the shortened axis in each case, in contrast to the fcc structure in which the regular octahedra have three four-fold axes of symmetry.

Analysis of the distortion produced by carbon atoms in the several types of site available in the fcc and bcc lattices, has shown that in the fcc structure the distortion is completely symmetrical, whereas in the bcc one, interstitial atoms in  $z$  positions will give rise to much greater expansion of iron-iron atom distances along  $z$  than in the  $x$  and  $y$  positions.

Assuming that the face-centred cubic (fcc)  $\rightarrow$  bcc transformation occurs in a diffusionless way, there is no opportunity for carbon atoms to move. The ferrite contains three octahedral interstices per iron atom whereas the austenite has only one octahedral interstice per iron atom. Each of the three sets of octahedral interstices (the three sublattices) in the ferrite is associated with one of the cube edges of the ferrite unit cell. Upon diffusionless transformation, all the carbon atoms in the austenite end up on just one of the octahedral sublattices of ferrite, causing a tetragonal distortion of the bcc lattice into a bct lattice. Thus, in Fig. 5.6, since only the  $z$  sites are common to both the fcc and bcc lattices, on transformation the  $z$ -axis becomes the  $c$ -axis of the tetragonal form.

Therefore, the tetragonality of martensite arises as a direct result of interstitial solution of carbon atoms in the bcc lattice, together with the preference for a particular type of octahedral site imposed by the diffusionless character of the reaction.

## 5.4 THE CRYSTALLOGRAPHY OF MARTENSITIC TRANSFORMATIONS

Martensitic transformation is diffusionless so the change in crystal structure is achieved by a homogeneous deformation of austenite. The strain needed to transform the fcc lattice of  $\gamma$  into the bcc or bct lattice of  $\alpha'$  was first proposed by Bain in 1924 and hence is known as the 'Bain strain' (Fig. 5.7). There is a compression of about 17% along the  $[0\ 0\ 1]_\gamma$  corresponding to the  $c$ -axis of the martensite cell, and a uniform expansion of about 12% in the  $(0\ 0\ 1)_\gamma$  plane.

The Bain strain implies the following orientation relationship between the parent and the product lattices:

$$[0\ 0\ 1]_\gamma \parallel [0\ 0\ 1]_{\alpha'} \quad [1\ \bar{1}\ 0]_\gamma \parallel [1\ 0\ 0]_{\alpha'} \quad [1\ 1\ 0]_\gamma \parallel [0\ 1\ 0]_{\alpha'},$$

but this is inconsistent with the observed orientation relationship which is irrational, and has corresponding closest-packed planes and close-packed directions approximately parallel. The reason is that the Bain strain on its own is not the complete deformation because it is necessary to ensure a high degree of coherency in the interface. It is a requirement that the deformation which changes austenite into martensite must leave one line fully coherent, i.e. it must be unrotated and undistorted, an invariant line. Such a deformation is said to be an invariant-line strain (ILS).

In Figs 5.8a, b, the austenite is represented as a sphere which, as a result of the Bain strain **B**, is deformed into an ellipsoid of revolution which represents the martensite. There are no lines which are left undistorted or unrotated by **B**. There are no lines in the  $(0\ 0\ 1)_\gamma$  plane which are undistorted. The lines  $wx$

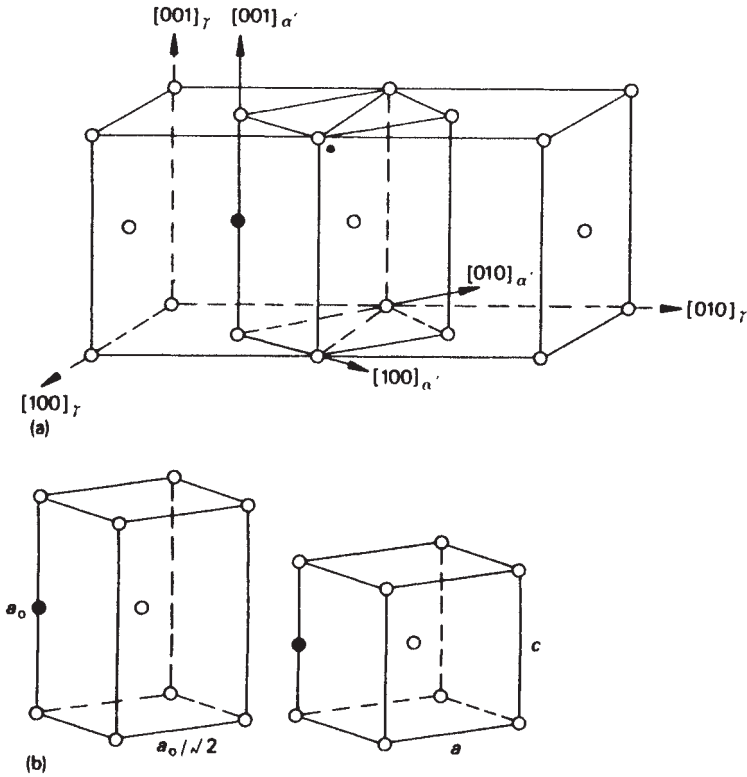


**Fig. 5.7** The lattice correspondence for formation of martensite from austenite: (a) tetragonal unit cell outlined in austenite, (b) lattice deformation (compression along  $c$ -axis) to form martensite of correct  $c/a$  ratio Bain strain (Christian, in *Martensite: Fundamentals and Technology* (ed. Petty, E. R.), Longmans, UK, 1970).

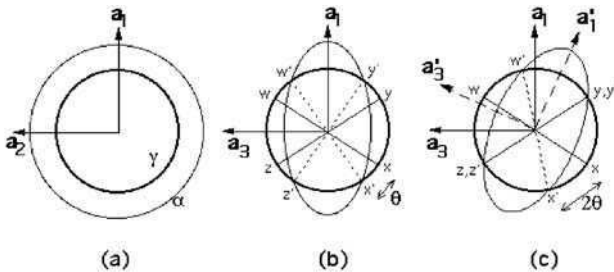


**Fig. 5.8** (a) and (b) show the effect of the Bain strain on austenite, which when undeformed is represented as a sphere of diameter  $wx = yz$  in three-dimensions. The strain transforms it to an ellipsoid of revolution. (c) shows the ILS obtained by combining the Bain strain with a rigid body rotation through an angle  $\theta$ .  $a_1$ ,  $a_2$  and  $a_3$  refer to  $[100]_{\gamma}$ ,  $[010]_{\gamma}$  and  $[001]_{\gamma}$  axes respectively.

and  $yz$  are undistorted but are rotated to the new positions  $w'x'$  and  $y'z'$ . Such rotated lines are not invariant. However, the combined effect of the Bain strain **B** and the rigid body rotation **R** is indeed an ILS because it brings  $yz$  and  $y'z'$  into coincidence (Fig. 5.8c). This is the reason why the observed irrational orientation relationship differs from that implied by the Bain strain. Indeed, the rotation required to convert **B** into an ILS precisely corrects the Bain orientation into that which is observed experimentally.

There remains a further discrepancy. As can be seen from Fig. 5.8c, there is no rotation which can make **B** into an invariant-plane strain since this would require two non-parallel invariant lines. It follows that austenite cannot be transformed into martensite by a homogeneous strain which leaves a plane invariant. And yet, the observed shape deformation leaves the habit plane undistorted and unrotated, i.e. it is an invariant-plane strain.

The phenomenological theory of martensite crystallography elegantly solves this remaining problem (Fig. 5.9). The Bain strain converts the structure of the parent phase into that of the product phase. When combined with an appropriate rigid body rotation, the net homogeneous lattice deformation **RB** is an ILS (step *a* to *c* in Fig. 5.9). However, the observed shape deformation is an

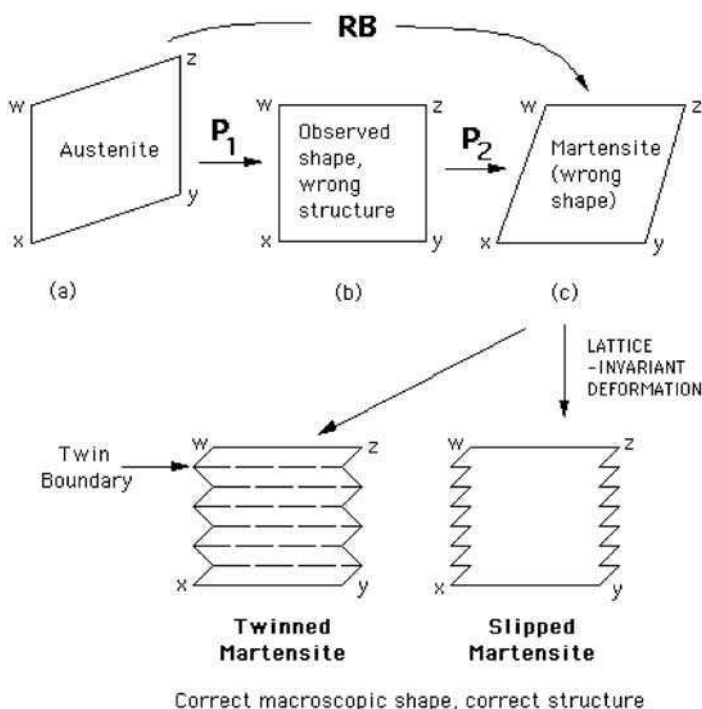


**Fig. 5.9** The phenomenological theory of martensite crystallography.

invariant-plane strain  $\mathbf{P}_1$  (step *a* to *b* in Fig. 5.9), but this gives the wrong crystal structure. If a second homogeneous shear  $\mathbf{P}_2$  is combined with  $\mathbf{P}_1$  (step *b* to *c*), then the correct structure is obtained but the wrong shape since:

$$\mathbf{P}_1\mathbf{P}_2 = \mathbf{RB}.$$

These discrepancies are all resolved if the shape changing effect of  $\mathbf{P}_2$  is cancelled macroscopically by an inhomogeneous lattice-invariant deformation, which may be slip or twinning as illustrated in Fig. 5.9.

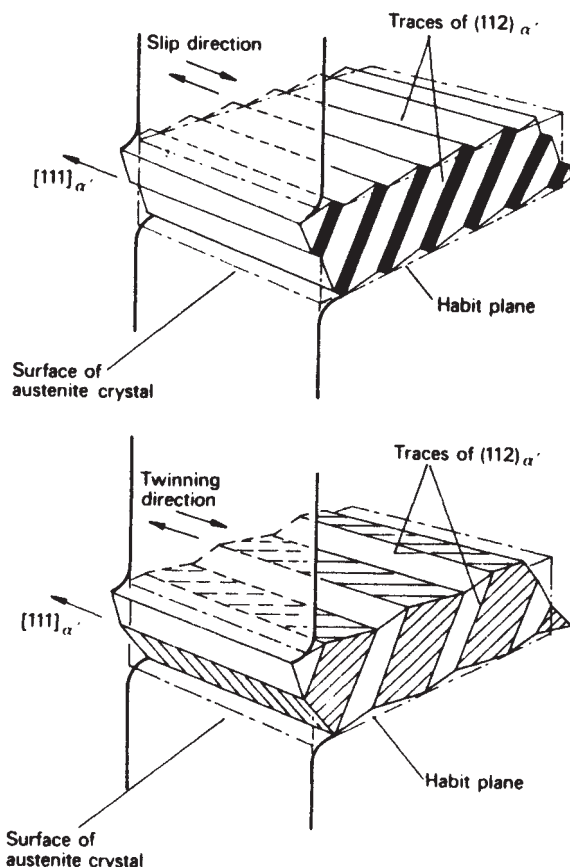
The theory explains all the observed features of the martensite crystallography. The orientation relationship is predicted by deducing the rotation needed to change the Bain strain into an ILS. The habit plane does not have rational indices because the amount of lattice-invariant deformation needed to recover the correct macroscopic shape is not usually rational. The theory predicts a substructure in plates of martensite (either twins or slip steps) as is observed experimentally. The transformation goes to all the trouble of ensuring that the shape deformation is macroscopically an invariant-plane strain because this reduces the strain energy when compared with the case where the shape deformation might be an ILS.

Figure 5.10 shows schematically the two types of lattice invariant deformation occurring within a martensite plate. It should be noted that the block of martensite formed has produced a surface tilt and that the observed habit is preserved by the accommodation provided by either slip (Fig. 5.10a) or twinning (Fig. 5.10b). The result is a macroscopically planar interface which would clearly have irregularities on a very fine scale.

The above theoretical approach had considerable success in predicting the observed habit planes, the orientation relationships between matrix and the martensite, as well as the shape deformation for a number of martensitic transformations including ferrous martensites. It is, however, necessary to have accurate data, so that the habit planes of individual martensite plates can be directly associated with a specific orientation relationship of the plate with the adjacent matrix. For example, Greninger and Troiano used an iron–22 nickel–0.8 wt% carbon alloy in which austenite was retained in association with martensite to predict successfully the correct habit plane, which in this alloy is an irrational plane near  $\{3\ 10\ 15\}_\gamma$  and also the shape change and the orientation relationship between martensite and austenite.

## 5.5 THE MORPHOLOGY OF FERROUS MARTENSITES

The two-shear theory of martensite formation was first confirmed by crystallographic measurements on the two phases, but the existence of the inhomogeneous lattice invariant deformation could only be directly established by microscopic examination. Examination of a number of non-ferrous martensite



**Fig. 5.10** Formation of martensite plate, illustrating two types of lattice deformation: slip and twinning (Christian, in *Martensite: Fundamentals and Technology* (ed. Petty, E. R.), Longmans, UK, 1970).

transformations in the optical microscope revealed that the martensite lamellae contained numerous very fine twins in uniform arrays. For example, the martensite reaction in the indium–thallium system has some similar characteristics to ferrous martensites in so far as the transformation is from fcc to a tetragonal lattice (face-centred). The martensitic lamellae are very uniform, and contain fine twins on a single variant  $(101) [10\bar{1}]$  in one lamella.

Martensitic plates in steel are frequently not parallel sided, instead they are lenticular as a result of constraints in the matrix which oppose the shape change resulting from the transformation. This is one of the reasons why it is difficult to identify precisely habit planes in ferrous martensite. However, it is not responsible for the irrational planes, but rather the scatter obtained in experiments. Another feature of higher carbon martensites is the burst phenomenon,





**Fig. 5.11** Fe-1.8C-3Mn-2Si. Lenticular martensite illustrating the burst phenomenon. Optical micrograph,  $\times 300$ .

in which one martensite plate nucleates a sequence of plates presumably as a result of stress concentrations set up when the first plate reaches an obstruction such as a grain boundary or another martensite plate (Fig. 5.11).

Perhaps the most striking advances in the structure of ferrous martensites occurred when thin-foil electron microscopy was first used on this problem. The two modes of plastic deformation needed for the inhomogeneous deformation part of the transformation, i.e. slip and twinning, were both observed by Kelly and Nutting. All ferrous martensites show very high dislocation densities of the order of  $10^{11}$ – $10^{12}$   $\text{cm}^{-2}$  Fig. 5.12b, which are similar to those of very heavily

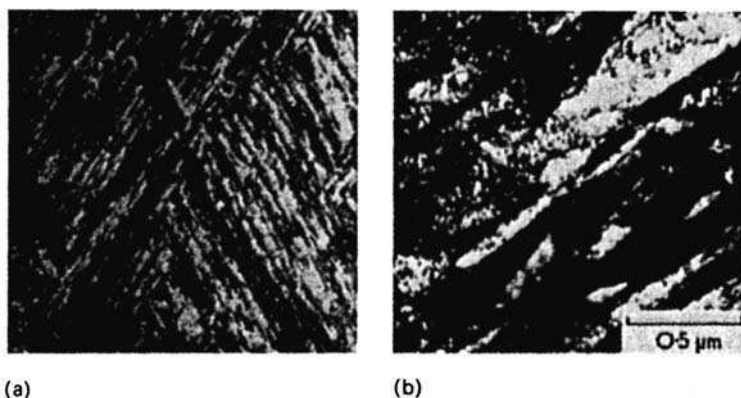


**Fig. 5.12** Fe-0.16C wt% alloy. Martensite formed by quenching from  $1050^{\circ}\text{C}$ : (a) optical micrograph,  $\times 95$ ; (b) thin-foil electron micrograph showing heavily dislocated laths (courtesy of Ohmori).

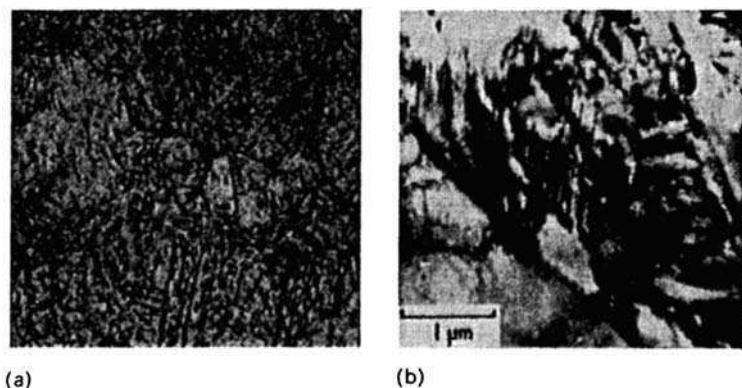


**Fig. 5.13** Fe–0.8C wt% alloy quenched from 1100°C: (a) optical micrograph  $\times 200$ ; (b) thin-foil electron micrograph showing twinning in martensite laths (courtesy of Ohmori).

cold-worked alloys. Thus, it is usually impossible to analyse systematically the planes on which the dislocations occur or determine their Burgers vectors.

The lower carbon ( $<0.5$  wt% C) martensites on the whole exhibit only dislocations. At higher carbon levels very fine twins (5–10 nm wide) commonly occur (Fig. 5.13b). The twinning plane is  $\{112\}_{\alpha'}$  derived from  $\{110\}_{\gamma}$ , and the twinning direction is  $\{111\}_{\alpha'}$  corresponding to the  $\{110\}_{\gamma}$  direction. In favourable circumstances the twins can be observed in the optical microscope, but the electron microscope allows the precise identification of twins by the use of the selected area electron diffraction technique. Thus the twin shears can be analysed precisely and have provided good evidence for the correctness of the crystallographic theories discussed above. However, twinning is not always fully developed and even within one plate some areas are often untwinned. The phenomenon is sensitive to composition.

The evidence suggests that deformation by dislocations and by twinning are alternative methods by which the lattice invariant deformation occurs. From general knowledge of the two deformation processes, the critical resolved shear stress for twinning is always much higher than that for slip on the usual slip plane. This applies to numerous alloys of different crystal structure. Thus it might be expected that those factors which raise the yield stress of the austenite, and martensite, will increase the likelihood of twinning. The important variables are: carbon concentration; alloying element concentration; temperature of transformation; strain rate.

The yield stress of both austenite and martensite increases with carbon content, so it would normally be expected that twinning would, therefore, be encouraged. Likewise, an increase in the substitutional solute concentration raises the strength and should also increase the substitutional solute concentration in the absence of carbon, which would account for the twins observed in martensite in high concentration binary alloys such as Fe–32Ni wt%.

A decrease in transformation temperature, i.e. reduction in  $M_s$ , should also help the formation of twins, and one would particularly expect this in alloys transformed, e.g. well below room temperature. It should also be noted that carbon concentration and alloying element concentration should assist by lowering  $M_s$ . As martensite forms over a range of temperatures, it might be expected in some steels that the first formed plates would be free of twins whereas the plates formed nearer to  $M_f$  would more likely be twinned. The observed inhomogeneities within plates could arise if growth of the plate near  $M_s$  was continued at lower temperatures. However, often plates have a mid-rib along which twinning occurs, the outer regions of the plate being twin-free. This could possibly take place when the  $M_s$  is below room temperature leading to twinned plates which might then grow further on resting at room temperature.

Returning to the three types of martensite referred to in Section 5.2, the morphological and crystallographic characteristics can now be summarized. Note that the stated orientations are approximate.

### 5.5.1 Low carbon martensite

Habit plane close to  $\{111\}_\gamma$

Kurdjumov–Sachs relation  $\{111\}_\gamma \parallel \{110\}_{\alpha'}, <\bar{1}\bar{1}0>_\gamma \parallel <\bar{1}\bar{1}1>_{\alpha'}$

Referred to as lath martensite

This type of martensite is found in plain carbon and low alloy steels up to about 0.5 wt% carbon. The morphology is lath- or plate-like (Fig. 5.10a), where the laths are very long and about  $0.5 \mu\text{m}$  wide. These are grouped together in packets with low angle boundaries between each lath, although a minority of laths is separated by high angle boundaries (Fig. 5.12b). In plain carbon steels practically no twin-related laths have been detected.

However, in iron–nickel alloys adjacent laths are frequently twin related. The boundaries between laths are not strictly planar, nor can they be described as lenticular, but dovetailing within the packets is frequent. Internally, the laths are highly dislocated and it is frequently difficult to resolve individual dislocations which form very tangled arrays. Twins are not observed to occur extensively in this type of martensite.

### 5.5.2 Medium carbon martensite

Habit plane close to  $\{225\}_\gamma$

Kurdjumov–Sachs relation

Referred to as acicular

It is perhaps unfortunate that the term acicular is applied to this type of martensite because its characteristic morphology is that of lenticular plates (Fig. 5.13), a fact easily demonstrated by examination of plates intersecting two surfaces at right angles. These plates first start to form in steels with about 0.5 wt% carbon

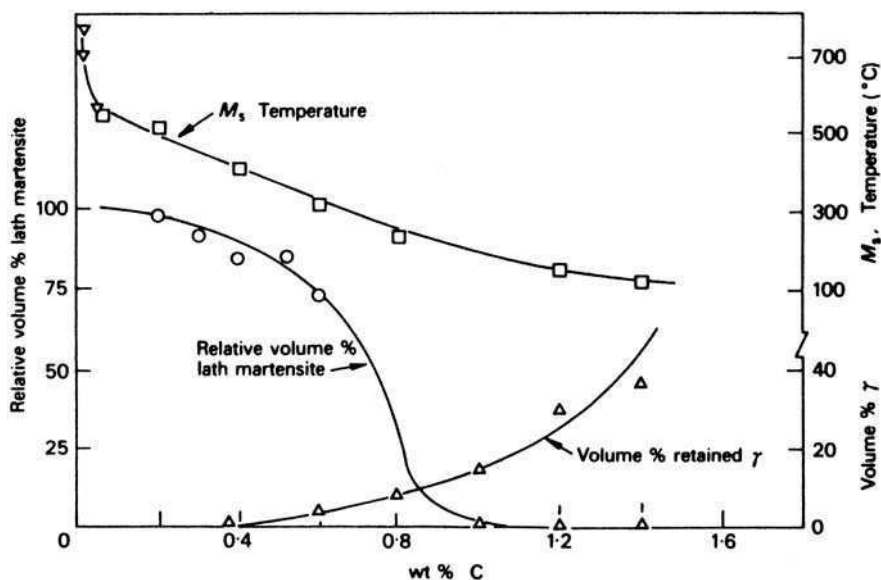


Fig. 5.14 Effect of carbon content on the type of martensite and the amount of retained austenite in Fe-C alloys (Speich, *Metallurgical Transactions* **3**, 1045, 1972).

(Fig. 5.14), and can be concurrent with lath martensite in the range 0.5–1 wt% carbon. Unlike the laths, the lenticular plates form in isolation rather than in packets, on planes approximating to  $\{225\}_{\gamma}$  and on several variants within one small region of a grain, with the result that the structure is very complex (Fig. 5.13). The burst phenomenon probably plays an important part in propagating the transformation, and the austenite is thus not as uniformly or as efficiently eliminated as with lath martensites. This physical difference cannot be unconnected with the fact that higher percentages of retained austenite occur as the carbon level is increased (Fig. 5.14), and the martensite is predominantly lenticular. The micro-twinning referred to earlier is found predominantly in this type of martensite (Fig. 5.13b), which forms at lower  $M_s$  temperatures, as the carbon content increases.

### 5.5.3 High carbon martensite

Habit plane close to  $\{259\}_{\gamma}$

Nishiyama–Wasserman relation  $\{111\}_{\gamma} \parallel \{110\}_{\alpha'}, <11\bar{2}>_{\gamma} \parallel <\bar{1}\bar{1}0>_{\alpha'}$

When the carbon content is  $>1.4$  wt%, the orientation relationship changes from Kurdjumov–Sachs to Nishiyama, and the habit plane changes to around  $\{259\}_{\gamma}$ . The change is not detectable microscopically as the morphology is still lenticular plates which form individually and are heavily twinned. Detailed

crystallographic analysis shows that this type of martensite obeys more closely the theoretical predictions than the {225} martensite. The plates are formed by the burst mechanism and often an audible click is obtained (cf. mechanical twinning). The {259} martensite only forms at very high carbon levels in plain carbon steels, although the addition of metallic alloying elements causes it to occur at much lower carbon contents, and in the extreme case in a carbon-free alloy such as Fe–Ni when the nickel content exceeds about 29 wt%.

## 5.6 KINETICS OF TRANSFORMATION TO MARTENSITE

Martensitic transformations are usually described as athermal, since transformation commences at a well-defined temperature  $M_s$ , but for transformation to continue the temperature must continue to fall until  $M_f$  is reached when the reaction is considered complete. However, there are martensitic reactions which can proceed at constant temperature.

### 5.6.1 Nucleation and growth of martensite

The driving force for the start of transformation can be expressed as  $T_0 - M_s$ , where  $T_0$  is the temperature at which stress-free austenite and martensite possess the same free energy. Figure 5.15 shows this schematically by plotting the two curves for the free energy of austenite and of martensite as a function of temperature. The  $M_s$  temperature is also shown as is the  $A_s$  temperature, the temperature at which martensite starts to revert to austenite on reheating. Both reactions require a degree of supercooling or superheating. Observations on numerous systems indicate that where the transformation results in a large shape change, the driving force ( $T_0 - M_s$ ) is large and the temperature range  $M_s - M_f$  is also large, whereas with small shape changes the reverse is true. With ferrous martensites the shape change is large and the  $M_s - M_f$  range is often several hundred degrees. It seems likely, therefore, that the strain energy arising when a small martensite plate is formed plays a significant role in nucleation.

The classical theory of homogeneous nucleation can be applied to an athermal reaction where either:

- (a) the nuclei form rapidly at  $M_s$ ,
- (b) subcritical nuclei pre-exist which become supercritical at  $M_s$ .

The overall free energy change,  $\Delta G$ , when nucleation takes place, is a result of three components:

- the change in chemical free energy,  $\Delta g (= g^{\alpha'} - g^{\gamma})$ ;
- the strain energy;
- the interfacial energy between matrix and martensite.

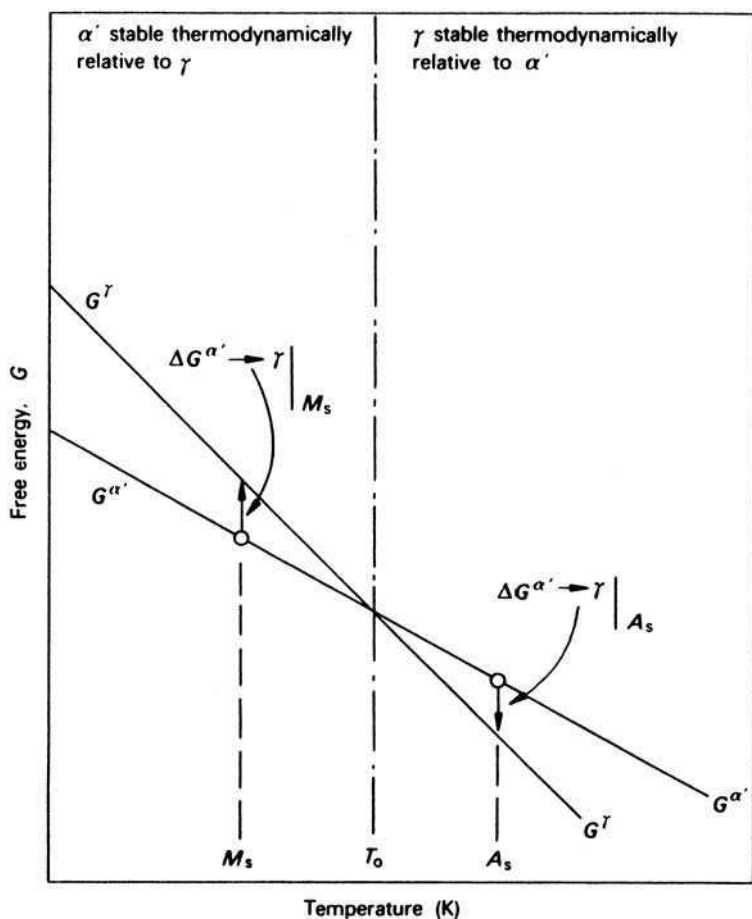


**Fig. 5.15** Free energy of austenite and martensite as a function of temperature (Kaufmann and Cohen, *Progress in Metal Physics* **7**, 165, 1958).

For a semicoherent nucleus of martensite with an oblate spheroid shape, radius  $r$ , semi-thickness  $c$  (Fig. 5.16):

$$\Delta G = \frac{4}{3}\pi r^2 c \Delta g + \frac{4}{3}\pi r c^2 A + 2\pi r^2 \sigma, \quad (5.3)$$

where

$A$  = strain energy factor

$\sigma$  = free energy per unit area of  $\gamma/\alpha'$  interface

$\Delta g$  = chemical free energy change per unit volume.

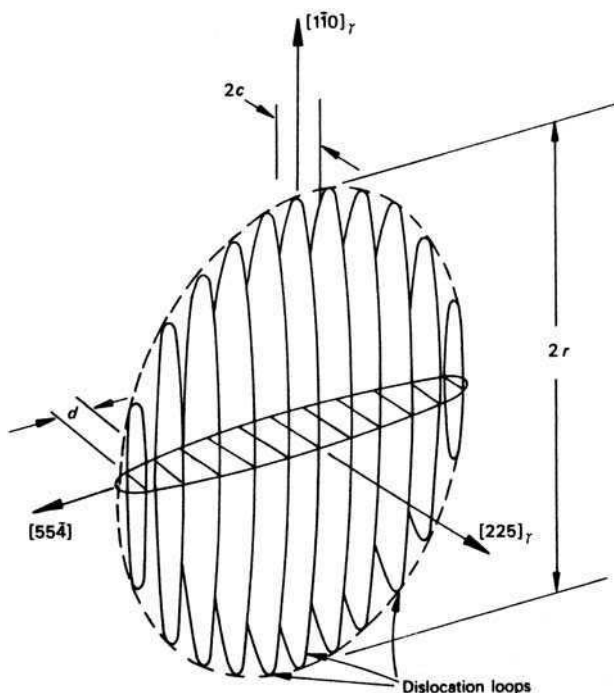


**Fig. 5.16** Model of a martensitic nucleus (Knapp and Dehlinger, in Kaufmann and Cohen, *Progress in Metal Physics* **7**, 165, 1958).

The critical nucleus size is determined by  $c^*$  and  $r^*$ , at which the free energy change is  $\Delta G^*$ , which defines a saddle on the free energy  $c$ - $r$  curve, thus:

$$c^* = -2\sigma/\Delta g, \quad (5.4)$$

$$r^* = 4A\sigma/\Delta g^2, \quad (5.5)$$

and

$$\Delta G^* = 32\pi A^2 \sigma^3 / 3(\Delta g)^4. \quad (5.6)$$

However, if reasonable values of  $\Delta g$ ,  $A$  and  $\sigma$  are used in Equation (5.5), the value of  $\Delta G^*$  is so high ( $\simeq 3 \times 10^5$  kJ) that the barrier to nucleation is orders of magnitude too large. It would, therefore, be quite impossible for martensite nuclei to occur as a result of random fluctuations.

The results of these calculations suggest that nucleation of martensite must take place heterogeneously on pre-existing embryos, which it is assumed are already beyond the saddle point in the free energy curve. However, the search for such nuclei has not been very successful and they still remain a deduction from formal nucleation theory. In some special cases nuclei can be obtained. For

example, in high manganese steels stacking faults readily occur as the austenite has a low stacking fault energy. On transformation to martensite, an  $\varepsilon$ -martensite of hexagonal structure is obtained which has been shown to nucleate at stacking faults.

The embryos are postulated to have a semicoherent dislocation interface with the austenite, envisaged as arrays of parallel dislocation loops which join the embryo to its matrix (Fig. 5.16). Growth then takes place by nucleation of new dislocation loops which join the interface and extend it. Recently, Olson and Cohen have developed a new theory of nucleation in which the first step is faulting on the closest-packed planes derived from existing groups of dislocations. The most likely sites for such nuclei are grain boundaries, incoherent twin boundaries and inclusion particle interfaces.

Normally individual martensite plates grow at extremely rapid rates, forming in times of the order of  $10^{-7}$  s. It has been found that the growth velocity is constant over a wide temperature range which indicates that the growth process is not strongly thermally activated. This is consistent with the crystallographic evidence that the atomic movements are small and orderly, and that atoms do not change places by diffusion. The growth is envisaged as the movement of an array of parallel dislocations lying in the interface, all having the same Burgers vector. As the interface moves forward into the austenitic matrix the dislocations keep up with the interface by gliding on the appropriate slip planes. This type of movement involves motion of the habit plane in a direction normal to itself.

Isothermal growth of martensite plates has often been observed at rates permitting direct observation in the optical microscope, e.g. in iron–nickel–manganese alloys. Other alloys, e.g. iron–nickel and iron–nickel–carbon, exhibit the burst phenomenon, although there is substantial evidence that isothermal transformation often takes place in alloys with low  $M_s$  which exhibited this phenomenon. In these cases it seems that the main factor is slow isothermal nucleation rather than slow growth.

Looking at the kinetics of martensite formation in broad terms, there are three different types of behaviour which can take place (Fig. 5.17). The first

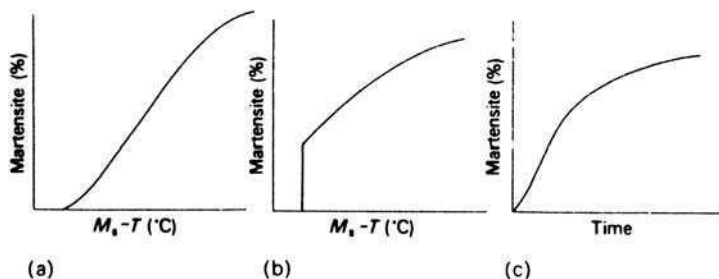


**Fig. 5.17** Transformation curves for martensite: (a) athermal transformation; (b) athermal with bursts; (c) isothermal transformation (Christian, in *Martensite: Fundamentals and Technology* (ed. Petty, E. R.), Longmans, UK, 1970).



type involves normal athermal transformations with a sigmoidal type of curve where the fraction of austenite transformed is a function solely of the temperature (Fig. 5.17a). The second type also involves athermal transformation, but the reaction commences suddenly with a burst phenomenon which effectively causes a proportion of the austenite to transform isothermally (Fig. 5.17b). Further transformation is again athermal in character. Finally, with true isothermal transformation (Fig. 5.17c) the proportion of a austenite transformed is proportional to time at a given temperature. This last type of behaviour has only been found in carbon-free iron base alloys.

### 5.6.2 Effect of alloying elements

Most alloying elements which enter into solid solution in austenite lower the  $M_s$  temperature, with the exception of cobalt and aluminium. However, the interstitial solutes carbon and nitrogen have a much larger effect than the metallic solutes. The effect of carbon on both  $M_s$  and  $M_f$  is shown in Fig. 5.18, from which it can be seen that 1 wt% of carbon lowers the  $M_f$  by over 300°C. Note that above 0.7 wt% C the  $M_f$  temperature is below room temperature and consequently higher carbon steels quenched into water will normally contain substantial amounts of retained austenite.

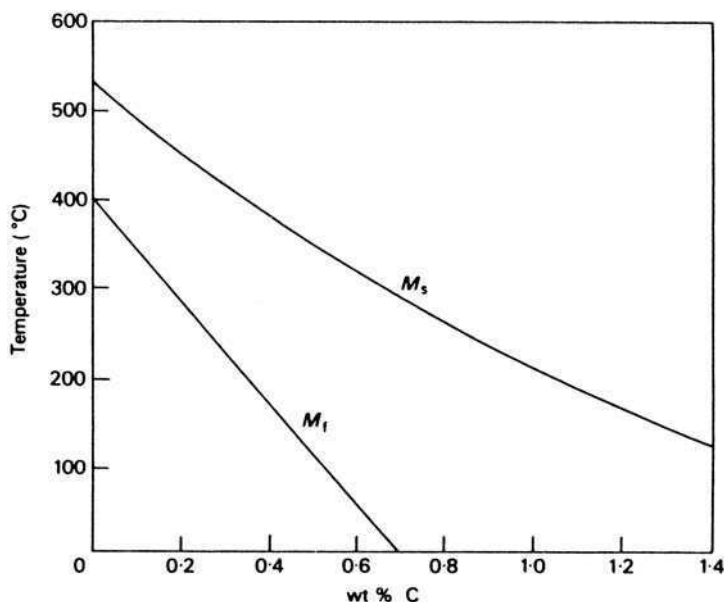


**Fig. 5.18** The effect of carbon on  $M_s$  and  $M_f$  (Petty, E. R. (ed.), *Martensite: Fundamentals and Technology*, Longmans, London, 1970).

The relative effect of other alloying elements is indicated in the following empirical relationship due to Andrews (concentrations in wt%):

$$M_s(^{\circ}\text{C}) = 539 - 423(\% \text{C}) - 30.4(\% \text{Mn}) - 17.7(\% \text{Ni}) \\ - 12.1(\% \text{Cr}) - 7.5(\% \text{Mo}). \quad (5.7)$$

The equation applies to a limited class of steels. Thus, the gradient of the curve in Fig. 5.18 is different from that implied by the Andrews relationship. A better approach is to express  $M_s$  in terms of the driving force for transformation.

The effect of alloying elements on the austenite/martensite transformation was originally explained by a thermodynamic analysis due to Zener. Using a binary Fe-X system equations can be written for the chemical free energy of the austenite  $G^{\gamma}$  and martensite  $G^{\alpha'}$  phases. In austenite:

$$G^{\gamma} = (1 - x)G_{\text{Fe}}^{\gamma} + G_{\text{X}}^{\gamma} + G_{\text{M}}^{\gamma}, \quad (5.8)$$

where  $x$  is the atomic fraction of alloying element;  $G_{\text{Fe}}^{\gamma}$  is the free energy of iron in the  $\gamma$  form;  $G_{\text{X}}^{\gamma}$  is the free energy of element X in the  $\gamma$  form, which must be deduced for elements that do not exist in fcc form; and  $G_{\text{M}}^{\gamma}$  is the free energy of mixing of austenite.

A similar equation can be written for  $G^{\alpha'}$  and subtracting from Equation (5.8) gives:

$$\Delta G^{\alpha' \rightarrow \gamma} = (1 - x)\Delta G_{\text{Fe}}^{\alpha \rightarrow \gamma} + \Delta G_{\text{X}}^{\alpha \rightarrow \gamma} + \Delta G_{\text{M}}^{\alpha' \rightarrow \gamma}. \quad (5.9)$$

Zener approached the alloying problem by assuming that the solid solutions were sufficiently dilute to be ideal, so that the mixing term  $\Delta G_{\text{M}}^{\alpha' \rightarrow \gamma}$  is zero. Now:

$$\Delta G_{\text{X}}^{\alpha \rightarrow \gamma} = \Delta H_{\text{X}}^{\alpha \rightarrow \gamma} - T\Delta S_{\text{X}}^{\alpha \rightarrow \gamma}, \quad (5.10)$$

where  $\Delta S$  is the entropy change between  $\alpha$  and  $\gamma$ ,  $\Delta H$  is the enthalpy change and  $T$  is the temperature. Also:

$$\Delta G_{\text{X}}^{\alpha \rightarrow \gamma} = RT \ln \frac{x_{\alpha}}{x_{\gamma}}, \quad (5.11)$$

where  $x_{\alpha}$  and  $x_{\gamma}$  are the compositions of  $\alpha$  and  $\gamma$  in equilibrium with  $\gamma$  and  $\alpha$  at any temperature.

Zener simplified the argument by assuming that  $RT \ln(x_{\alpha}/x_{\gamma})$  is constant, and that  $\Delta S_{\text{X}}^{\alpha' \rightarrow \gamma}$  is zero, so that with ideal solutions:

$$\Delta H_{\text{X}}^{\alpha \rightarrow \gamma} = RT \ln \frac{x_{\alpha}}{x_{\gamma}} = \Delta H_{\text{X}}^{\alpha' \rightarrow \gamma}, \quad (5.12)$$

which is defined as the difference in enthalpies of alloying element X in the austenitic and martensitic phases. Therefore, Equation (5.9) can now be

**Table 5.3** Values of difference in enthalpy of element X in austenite ( $\gamma$ ) and in martensite ( $\alpha'$ )

X	C	N	Mn	Ni	Cu	Cr	W	Mo	V	Ti
$\Delta H_X^{\alpha' \rightarrow \gamma}$ (kJ mol <sup>-1</sup> )	-33.9	-22.4	-10.7	-8.4	-5.4	-5.0	+5.7	+5.7	+11.8	+37.7

rewritten, expressing the driving force of the reaction  $\Delta G^{\alpha' \rightarrow \gamma}$  as:

$$\Delta G^{\alpha' \rightarrow \gamma} = (1 - x)\Delta G_{\text{Fe}}^{\alpha \rightarrow \gamma} + x\Delta H_X^{\alpha' \rightarrow \gamma}. \quad (5.13)$$

After determining  $\Delta H_X^{\alpha' \rightarrow \gamma}$ , the free energy change for the martensite reaction  $\Delta G^{\alpha' \rightarrow \gamma}$  can be calculated. Values for  $T_0$ , the temperature at which  $\gamma$  and  $\alpha'$  have the same free energies, can be calculated by putting  $\Delta G^{\alpha' \rightarrow \gamma}$  equal to zero.

Alloying elements either expand the  $\gamma$ -loop, i.e. stabilize  $\gamma$ , or contract the loop and encourage  $\alpha$ -formation, and this will have different effects on  $\Delta H_X^{\alpha' \rightarrow \gamma}$  (Section 4.1). Elements which expand the  $\gamma$ -loop will make this term negative and lower  $T_0$ , while elements which favour  $\alpha$ -formation will make the term positive and raise  $T_0$ .

It is interesting to look at the values of  $\Delta H_X^{\alpha' \rightarrow \gamma}$  which are available in the literature for a number of common alloying elements (Table 5.3). There are some anomalies, e.g. chromium, which contracts the  $\gamma$ -loop, has a negative  $\Delta H$  value, suggesting that  $\Delta H$  has been computed from data at too low a temperature.

Cohen and co-workers have provided detailed data for iron–carbon alloys between 0 and 1.1 wt% carbon and in Fig. 5.19 the temperature dependence of  $\Delta G^{\alpha' \rightarrow \gamma}$  is plotted for several carbon levels. The intersection of the curves with the  $\Delta H^{\alpha' \rightarrow \gamma} = 0$  axis provides values of  $T_0$  for the various compositions. It was found that the driving force  $\Delta G^{\alpha' \rightarrow \gamma}$  at the  $M_s$  temperatures of the alloys was practically constant, approximately 1250 J mol<sup>-1</sup>, independent of carbon content. However, work on iron–nickel alloys has shown that the driving force increases with increasing nickel content, i.e. as the  $M_s$  is depressed.

### 5.6.3 The effect of deformation

The effect of uniaxial stress on the martensitic transformation is normally to raise the  $M_s$  temperature. The superimposed stress field from the plastic, or elastic, deformation reinforces that caused by the nucleation of a martensite plate, and in one sense the subsequent shape change is a further plastic deformation process. We can define a temperature  $M_d$ , greater than  $M_s$ , above which deformation of the parent phase does not form any martensite. However, it is likely that deformation of the austenite above  $M_d$  will alter the  $M_s$  on subsequent cooling through the martensitic range. Usually in these circumstances, the  $M_s$  is

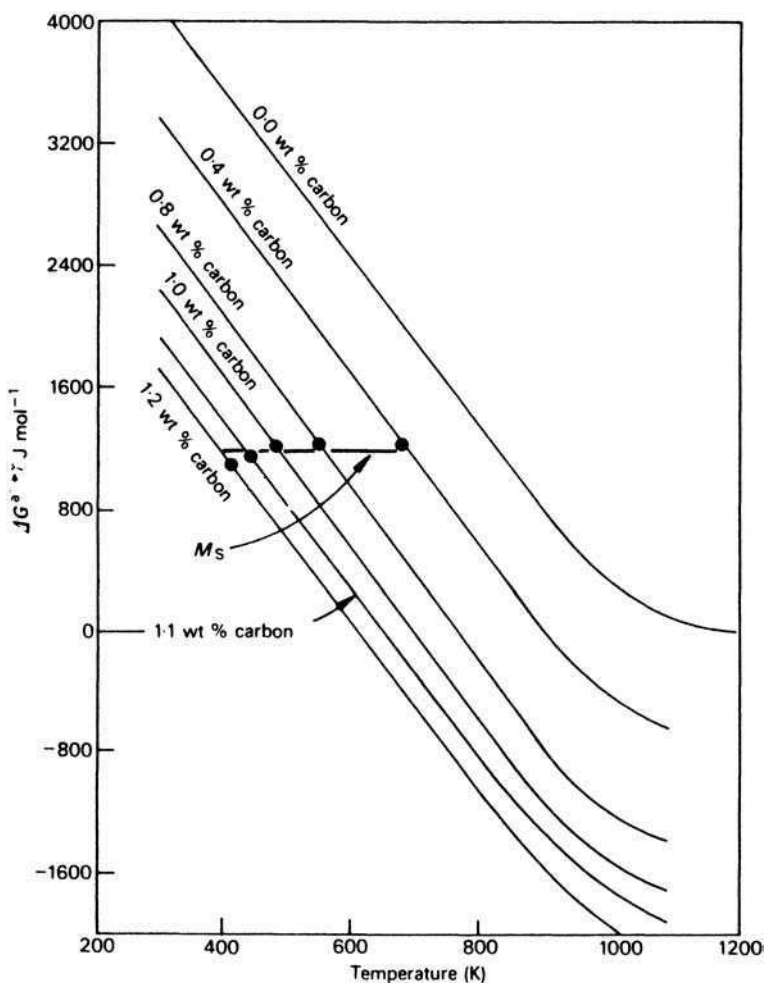


**Fig. 5.19** Free energy change for the austenite–martensite reaction as a function of temperature and carbon content (Kaufmann and Cohen, *Progress in Metal Physics* **7**, 165, 1958).

lowered, and the resultant increased stability of the austenite is referred to as *mechanical stabilization*.

#### 5.6.4 Stabilization

Stabilization means a reduction in the amount of transformation of austenite to martensite, as a result of processes which interfere with the nucleation and growth of the plates. Plastic deformation above the  $M_d$  temperature can achieve this. However, the term stabilization is normally applied when the cooling of a

steel is arrested in the  $M_s - M_f$  range. The transformation, when resumed by lowering the temperature, does not result in as complete a transformation to martensite as would have been the case if no isothermal pause had occurred. At the chosen delay temperature, the degree of stabilization increases to a maximum with time, and as the temperature approaches  $M_f$ , the extent of stabilization increases. It appears that stabilization is at a minimum when only a small amount of martensite is present in the matrix.

The explanation of these complex effects lies in the fact that the formation of martensite plates leads to accommodating plastic deformation in the surrounding matrix, which can result in high concentrations of dislocations in the austenite. Interaction of some of these dislocations with the glissile dislocations in the martensite plate boundary will then cause it to be no longer mobile, so that the plate cannot grow further. Any phenomena which help to encourage this process will achieve stabilization. Resting at an intermediate temperature gives time for plastic relaxation, i.e. movement of dislocations, as well as the locking of interfacial dislocations by carbon atoms.

## 5.7 THE STRENGTH OF MARTENSITE

The high hardness and brittleness of rapidly quenched steels is the result of the formation of martensite, yet many shear transformations in non-ferrous alloy systems do not produce this dramatic hardening. Indeed, if carbon is eliminated from the steel the resulting hardness is very much lower. Figure 5.20 shows the large effect of carbon content on the hardness of martensite compared with the relatively small effect of carbon on the strength of austenite, retained to room temperature by the addition of nickel.

The strength levels reached depend also on the detailed structure of the martensite, e.g. whether it has remained stable during quenching and testing at room temperature. By addition of nickel to iron carbon alloys, Winchell and Cohen depressed the  $M_s$  temperature to  $-35^\circ\text{C}$ , so that martensite formed only at low temperatures and auto-tempering was eliminated (Chapter 8). In addition, the samples were deformed at  $0^\circ\text{C}$ , with the results shown in Figure 5.21, indicating that the flow stress of martensite increases with carbon content up to about 0.5 wt% C. Allowing the martensite to rest for 3 h at  $0^\circ\text{C}$ , resulted in the upper curve (Fig. 5.21), demonstrating that martensite can age harden at ambient temperature or below.

The question of the origin of the high strength of martensite is a difficult one, compounded by the complexity of the structure, a tetragonal lattice with interstitial carbon in solid solution, formed by shear which leads to high densities of dislocations and fine twins. There are, as a result, several possible strengthening mechanisms:

- (a) substitutional and interstitial solid solution;
- (b) dislocation strengthening, i.e. work hardening;

- (c) fine twins;
- (d) grain size;
- (e) segregation of carbon atoms;
- (f) precipitation of iron carbides.

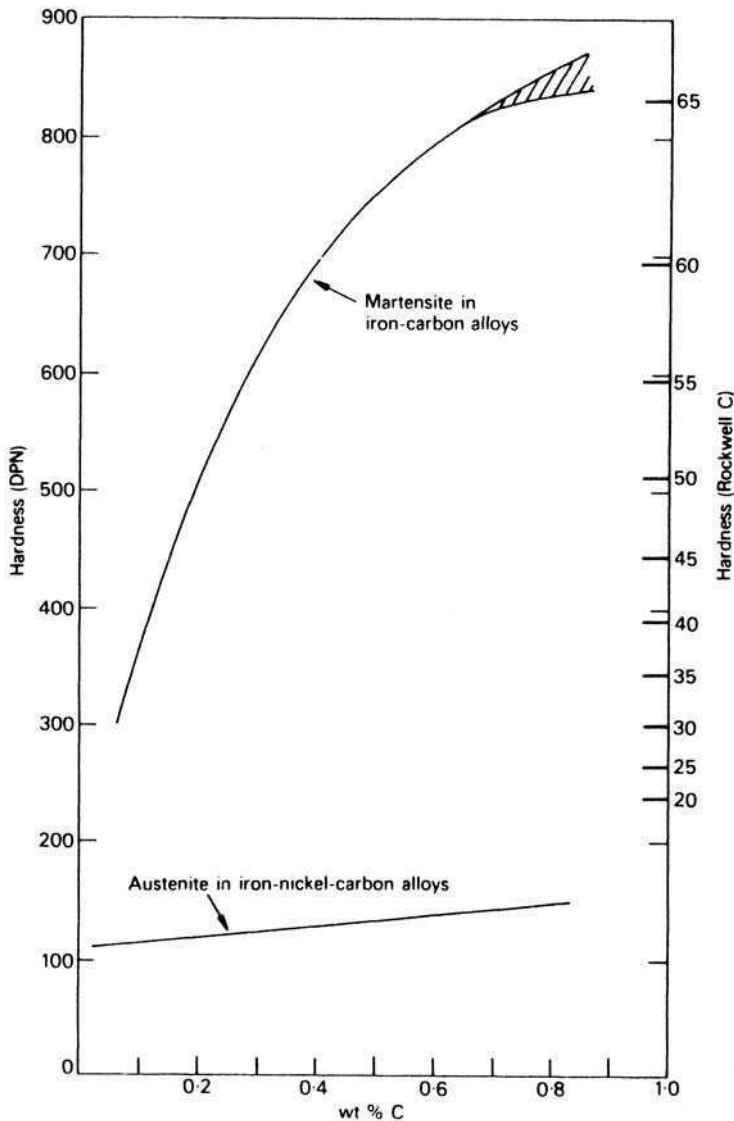


**Fig. 5.20** The effect of carbon on the hardness of martensite and austenite (Winchell and Cohen, *Transactions of the Metallurgical Society of AIME* **224**, 638, 1962).

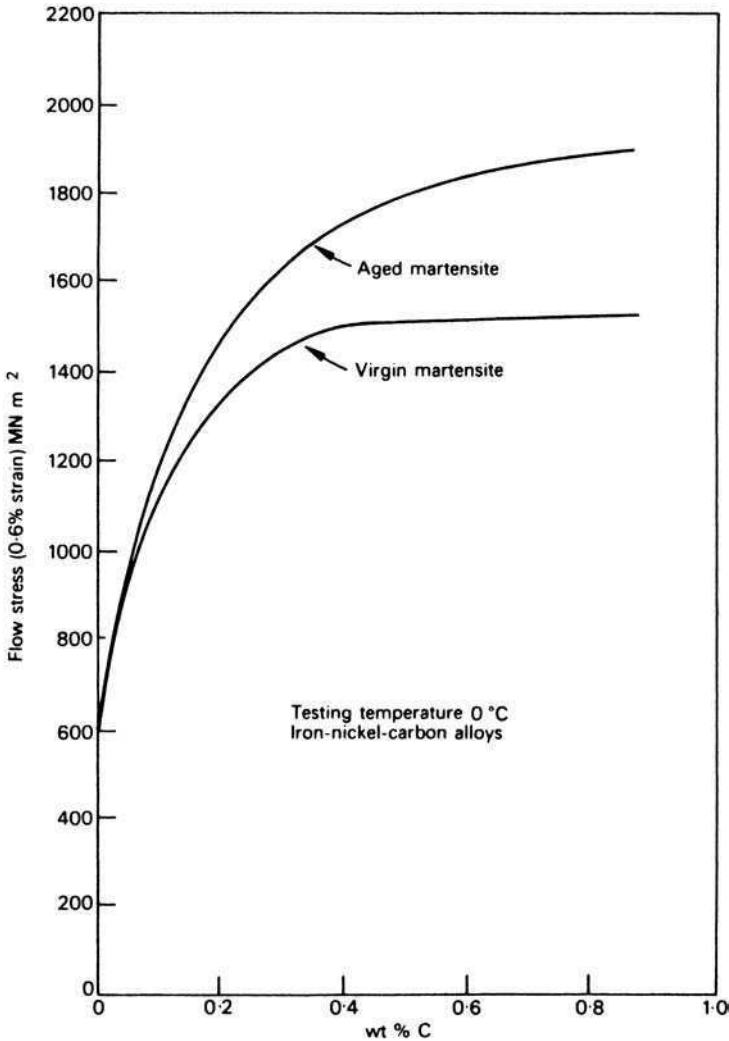


**Fig. 5.21** Ageing of martensite at 0°C in Fe-Ni-C alloys (Winchell and Cohen, *Transactions of the Metallurgical Society of AIME* **224**, 638, 1962).

The interstitial solid solution of carbon which results in the tetragonality of martensite is a prime candidate for the role of major strengthening factor. The work of Winchell and Cohen enabled the determination of the yield stress as a function of carbon content under conditions when the carbon atoms were unable to diffuse to form atmospheres and precipitates. The flow stress was shown to vary as  $c^{1/3}$ , where  $c$  = carbon and concentration, but later it was found that the strength could be shown equally well to vary as  $c^{1/2}$ .

Fleischer examined the situation theoretically with a model of a dislocation bending away from interstitial solute atoms with short range interactions, and using a parameter  $\Delta\epsilon$ , the difference in longitudinal and transverse lattice strain caused by an interstitial carbon atom in martensite ( $\Delta\epsilon \simeq 0.38$ ). He found the following expression for the flow stress  $\tau$ :

$$\tau = \tau_0 + \frac{2G\Delta\epsilon c^{1/2}}{3}, \quad (5.14)$$

predicting that the flow stress is proportional to  $c^{1/2}$ . The curve has a slope of  $G/15$  to  $G/20$ . Other experiments on martensites with low  $M_s$  temperatures support the  $c^{1/2}$  relationship, with slight differences in slope depending on whether the martensite is of lath type or twinned (Fig. 5.22).

The proposal that the fine twins characteristic of higher carbon martensites make a major contribution to strength has not received wide acceptance. Certainly, a large increase in strength is not found when the transition from dislocated martensite to twinned martensite takes place. However, the high dislocation densities of twin-free martensite must make some contribution to strength, estimated to be not greater than  $300 \text{ MN m}^{-2}$ , and there is reason to believe that the fine twinning makes a similar, but not additive, contribution.

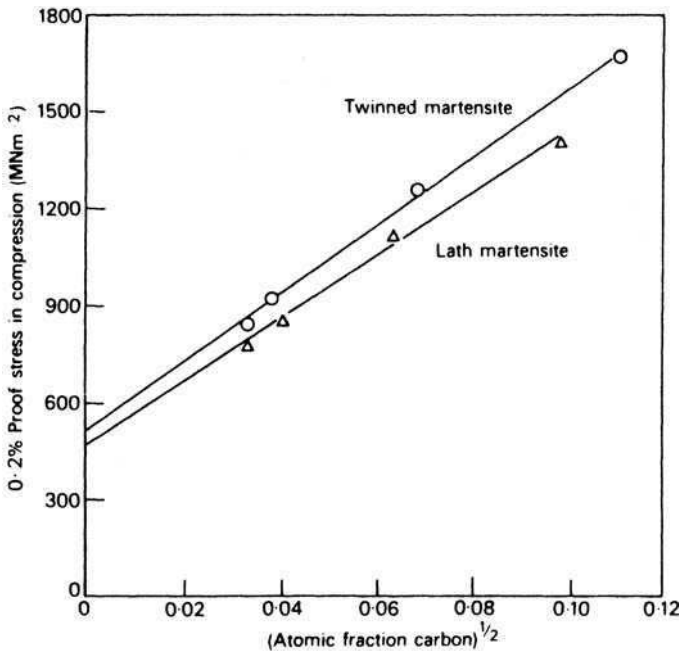


**Fig. 5.22** Effect of carbon on the strength of martensite (Chilton and Kelly, *Acta Metallurgica* 16, 637, 1968).



The austenitic grain size determines the maximum size of a martensitic plate, so some dependence of strength on grain size might be expected. In fact, a Petch-type plot has been found for several alloy steels of different austenitic grain sizes tested in the martensitic condition (Fig. 5.23). However, when the fine structure of martensite is examined other possible grain sizes much finer than the austenitic grain size can be considered as contributors to strength. Firstly, there is the packet size in lath martensite, or the individual plate in lenticular martensite, and beyond these there is the lath substructure which is usually well below  $1\text{ }\mu\text{m}$  in thickness. While many of these boundaries are really low angle sub-boundaries, they do present obstacles to dislocation movement and must, therefore, be considered to make some contribution to the overall strength.

It is also to be expected that carbon atoms segregate to the high dislocation populations typical of martensite, bearing in mind the strong interactions found in the case of ferrite. Internal friction measurements by Kurdjumov and

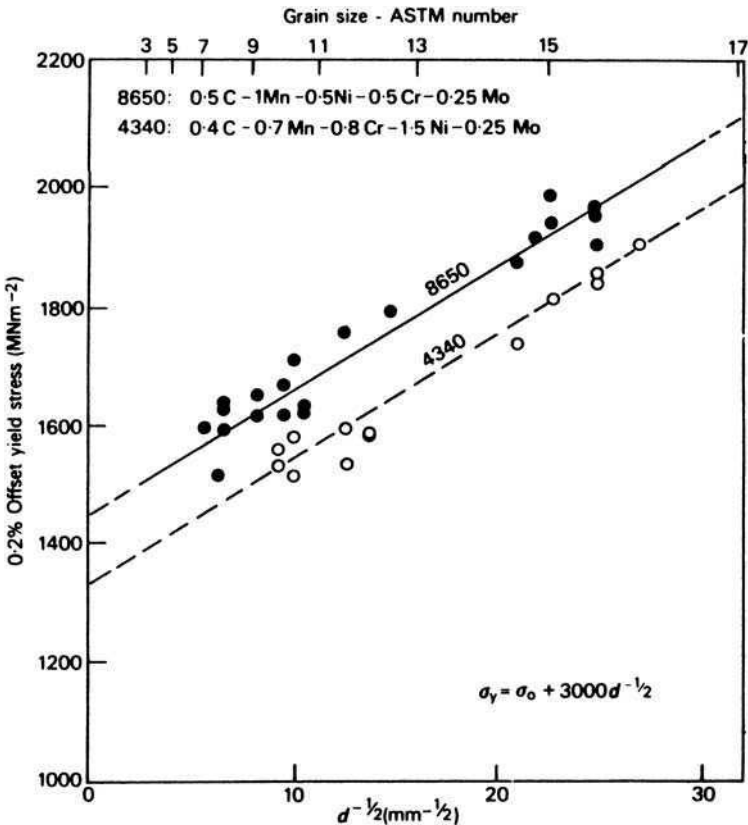


**Fig. 5.23** The effect of prior austenite grain size on the strength of martensite (Grange, *Transactions of the American Society for Materials* **59**, 26, 1966).

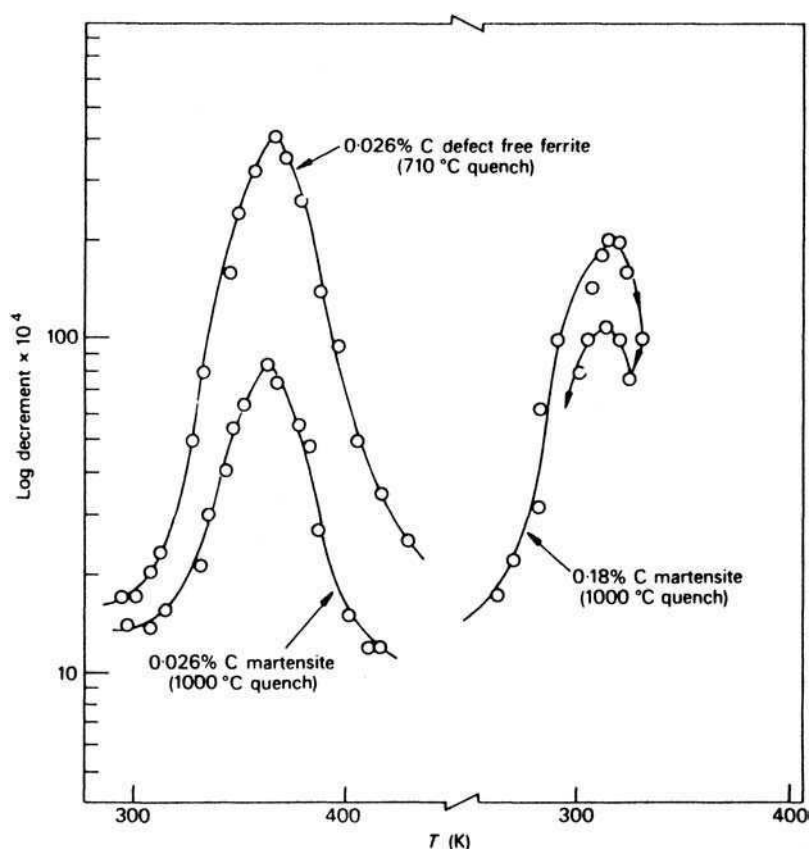


**Fig. 5.24** Comparison of the internal friction behaviour of low carbon martensites with that of ferrite (Speich, *Transactions of the Metallurgical Society of AIME* **245**, 2553, 1969).

co-workers have revealed the well-defined temperature-dependent peak, the Snoek peak (p. 6), which occurs as a result of the stress-induced movement of carbon atoms in ferrite and martensite. Figure 5.24 shows that the Snoek peak is much lower in a 0.026 wt% C martensite than in ferrite of the same composition. This is a direct result of the reduction in free carbon atoms in the martensite structure due to pinning by the high concentration of dislocations. These pinned carbon atoms cannot contribute directly to the Snoek peak, the height of which is proportional to the concentration of free carbon atoms in the lattice. In contrast, ferrite has a very low dislocation density and exhibits a much higher Snoek peak (Fig. 5.24), because a greater concentration of carbon atoms is available to move interstitially between the octahedral sites.

Work on the temperature dependence of the flow stress of martensite in Fe–Ni–C alloys has shown a strong temperature dependence, together with a

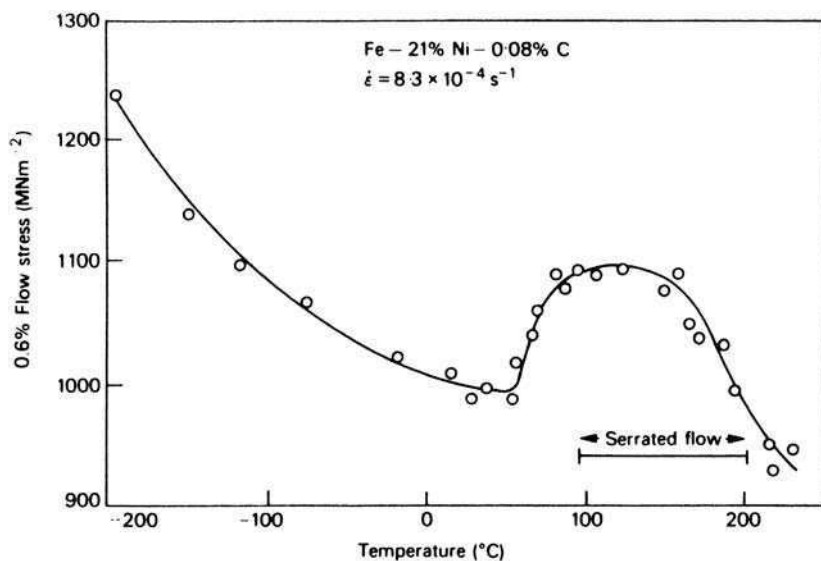


**Fig. 5.25** Temperature dependence of the flow stress of Fe-Ni-C martensite (Owen and Roberts, *International Conference on Strength of Metals and Alloys*, Tokyo, 1968).

peak in the curve associated with serrated flow in the stress-strain curve (Fig. 5.25). Like the development of the yield point in  $\alpha$ -iron, this has been attributed to the Cottrell-Bilby interaction of carbon with dislocations.

However, this phenomenon leads to precipitation of iron carbide on the dislocations which is responsible for the increase in strength shown by martensite aged at room temperature or just above. Also martensites with relatively high  $M_s$  temperatures will form cementite dispersions during the quench (auto-tempering) which will also make some contribution to the observed strength.

The yield strength of martensite, like that of ferrite, is markedly temperature dependent, but this dependence is little affected by the presence or absence of precipitate or by the amount of carbon in solution. It is, therefore, likely that the temperature dependence arises from the basic resistance of the lattice to dislocation movement, i.e. it is a result of the temperature dependence of the Peierls-Nabarro force.

## 5.8 SHAPE MEMORY EFFECT

The shape deformation accompanying martensitic transformation can be reversed by transforming back to the parent phase. Suppose a crystal of austenite

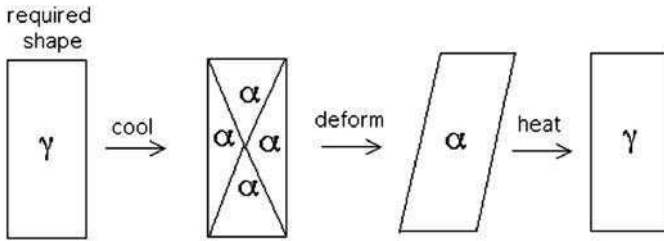


**Fig. 5.26** Shape memory effect.

is cooled to form many variants of martensite, in such a way that they accommodate and hence the overall shape is unaffected by transformation. When a stress is applied, the favoured variant of martensite grows, leading to a shape change (Fig. 5.26). On heating the shape change is reversed, thus regaining the original shape. This is the basis of the shape memory effect. The memory can be lost by introducing defects during transformation, e.g. by repeated cycling. Excessive deformation, beyond that required to produce a single martensite variant, will lead to irreversible strain and a loss of memory.

The most successful shape-memory alloys are based on nickel containing titanium and aluminium. A large variety of iron-based shape-memory alloys exists but their recoverable strains are smaller and less reversible. They do have cost advantages and find engineering applications such as pipe-couplings, where the memory effect need operate only once to make an integral joint. Some of these alloys exploit the  $\gamma \rightarrow \alpha'$  transformation whereas others rely on  $\gamma \rightarrow \epsilon$  martensite. There are even alloys in which the austenite transforms into face-centred tetragonal martensite.

## FURTHER READING

- Bhadeshia, H. K. D. H., *Geometry of Crystals*, 2nd edition, Institute of Materials, London, 2001. [www.msm.cam.ac.uk/phase-trans/2001/crystal.html](http://www.msm.cam.ac.uk/phase-trans/2001/crystal.html)
- Bhattacharya, K., *Microstructure of Martensite*, Oxford University Press, Oxford, UK, 2003.
- Christian, J. W., *Theory of Transformations in Metals and Alloys*, 3rd edition, Pergamon Press, Oxford, 2003.
- Kajiwar, S., Shape memory effect and transformation behaviour in iron-based alloys, *Materials Science and Engineering* **A273–A275**, 67, 1999.
- Krauss, G., *Steels: Heat Treatment and Processing Principles*. ASM International, Ohio, USA, 1990.
- Krauss, G., Martensite in steel: strength and microstructure, *Materials Science and Engineering* **A273–A275**, 40, 1999.
- Maki, T., Recent developments in iron-based shape memory alloys, *1st Japan International SAMPE Symposium*, 225, 1989.
- Martensite (A Tribute to Morris Cohen)* (eds Olson, G. B. and Owen, W. S.), ASM International, Ohio, USA, 1992.

- Nishiyama, Z., *Martensite Transformation*, English edition, Academic Press, New York, 1978.
- Olson, G. B. and Cohen, M., A general mechanism of martensitic nucleation, Parts I–III. *Metallurgical Transactions* **7A**, 1897–1923, 1976.
- Roytburd, A. L., Kurdjumov and his school in martensite, *Materials Science and Engineering* **A273–A275**, 1, 1999.
- Wayman, C. M., The crystallography of martensitic transformations, in alloys of iron. *Advances in Materials Research* **3**, 147, 1968.
- Wayman, C. M. and Bhadeshia, H. K. D. H., *Physical Metallurgy* (eds R. W. Cahn and P. Hassen), 4th edition, Elsevier, Netherlands, 1996.

# 6

---

## THE BAINITE REACTION

### 6.1 INTRODUCTION

Examination of the *time–temperature–transformation (TTT)* diagram for an eutectoid carbon steel (Fig. 3.5), bearing in mind the fact that the pearlite reaction is essentially a high temperature one occurring between 550°C and 720°C and that the formation of the martensite is a low-temperature reaction, reveals that there is a wide range of temperature  $\sim 250\text{--}550^\circ\text{C}$  within which neither of these phases forms. This is the region in which fine aggregates of ferrite plates (or laths) and cementite particles are formed. The generic terms for these intermediate structures is *bainite*, after Edgar Bain who with Davenport first found these structures during their pioneering systematic studies of the isothermal decomposition of austenite. Bainite also occurs during athermal treatments at cooling rates too fast for pearlite to form, yet not rapid enough to produce martensite.

The nature of bainite changes as the transformation temperature is lowered. Two main forms can be identified: *upper* and *lower* bainite.

### 6.2 UPPER BAINITE (TEMPERATURE RANGE 550–400°C)

The microstructure of upper bainite consists of fine plates of ferrite, each of which is about  $0.2\ \mu\text{m}$  thick and about  $10\ \mu\text{m}$  long. The plates grow in clusters called sheaves. Within each sheaf the plates are parallel and of identical crystallographic orientation, each with a well-defined crystallographic habit. The individual plates in a sheaf are often called the ‘sub-units’ of bainite. They are usually separated by low-misorientation boundaries or by cementite particles (see Fig. 6.1).

Upper bainite evolves in distinct stages beginning with the nucleation of ferrite plates at the austenite grain boundaries. The growth of each plate is accompanied by a change in the shape of the transformed region (Fig. 6.2a), a change which can be described precisely as an invariant-plane strain (IPS) with

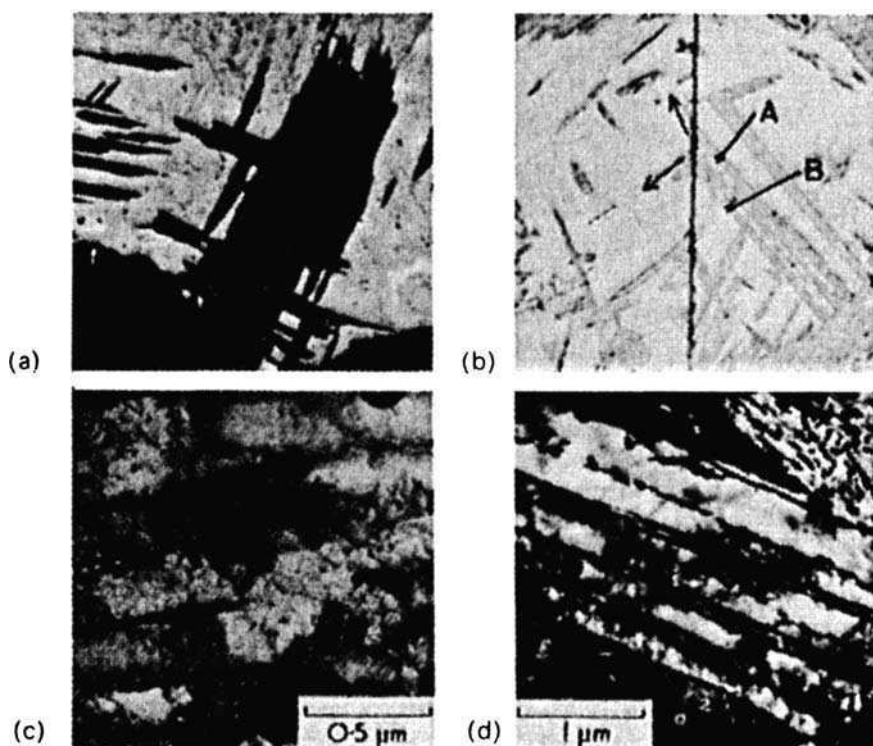


**Fig. 6.1** The microstructure of upper bainite. (a) Optical micrograph of a sheaf of upper bainite in Fe–0.8C wt% steel, transformed 20 s at 400°C. (b) Two-surface composite micrograph showing the plate-like structure of a sheaf. (c) Thin-foil transmission electron micrograph showing the sub-micrometre sub-units which make up a sheaf. Also illustrates the dislocations. (d) Thin-foil electron micrograph showing the sub-units and carbides within a sheaf of upper bainite (courtesy of Ohmori).

a large shear component, virtually identical to that observed during martensitic transformation<sup>1</sup>. However, bainite grows at relatively high temperatures when compared with martensite. The large strains associated with the shape change cannot be sustained by the austenite, the strength of which decreases as the temperature rises. These strains are relaxed by the plastic deformation of the adjacent austenite. The local increase in dislocation density caused by the yielding of the austenite blocks the further movement of the glissile transformation interface (Fig. 6.2b). This localized plastic deformation therefore halts the growth of the ferrite plate so that each sub-unit only achieves a limited size which is much less than the size of an austenite grain.

<sup>1</sup> Swallow, E. and Bhadeshia, H. K. D. H., *Materials Science and Technology* **12**, 121, 1996.

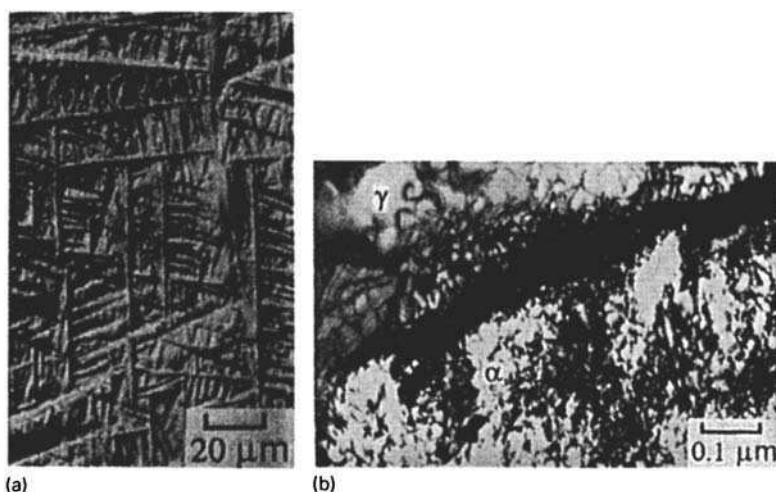


**Fig. 6.2** Fe–0.43C–3.0Mn–2.0Si wt% alloy transformed to bainite. (a) Surface relief caused by the formation of bainite in a sample which was first polished and then transformed. (b) Intense dislocation debris at a bainite/austenite interface.

As with martensite, the shape change implies that the mechanism of growth of bainitic ferrite is displacive. It is the minimization of the strain energy associated with the displacements that ensures that bainite grows in the form of thin plates. Since the crystal structure of bainite is generated by a coordinated movement of atoms, it follows that there must exist an orientation relationship between the austenite and the bainite. This relationship is found experimentally to be of the type where a pair of the most densely packed planes of the two lattices are approximately parallel, as are a corresponding pair of close-packed directions within those planes.

This is loosely described by a Kurdjumov–Sachs type orientation relationship.

Bainite forms on particular crystallographic planes, but the indices of the habit plane show considerable scatter (Fig. 6.3). This is because most of the measurements are made using light microscopy, in which case the habit plane determined is not that of an individual sub-unit. It corresponds instead to some average value depending on the number, size and distribution of sub-units within the sheaf. All of these factors can vary with the transformation temperature, time and chemical composition.

It was emphasized earlier that upper bainite forms in two distinct stages, the first involving the formation of bainitic ferrite which has a very low solubility for carbon (<0.02 wt%). The growth of the ferrite therefore enriches the remaining austenite in carbon. Eventually, cementite precipitates from the residual austenite layers in between the ferrite sub-units. The amount of cementite depends on the carbon concentration of the alloy. High concentrations lead to



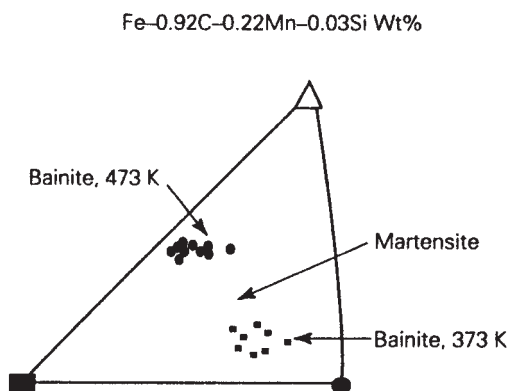


**Fig. 6.3** Stereographic triangle showing the habit plane of bainite compared with that of martensite in the same steel (after Greninger and Troiano, 1940).

microstructures in which the ferrite platelets are separated by continuous layers of cementite. Small, discrete particles of cementite form when the alloy carbon concentration is low.

The cementite particles have a 'Pitsch' orientation relationship with the austenite from which they precipitate:

$$\begin{aligned} [0\ 0\ 1]_{\text{Fe}_3\text{C}} &\parallel [\bar{2}\ 2\ 5]_{\gamma}, \\ [1\ 0\ 0]_{\text{Fe}_3\text{C}} &\parallel [5\ \bar{5}\ 4]_{\gamma}, \\ [0\ 1\ 0]_{\text{Fe}_3\text{C}} &\parallel [\bar{1}\ \bar{1}\ 0]_{\gamma}. \end{aligned}$$

Many variants of carbide may precipitate from the austenite, each particle being indirectly related to the ferrite via the ferrite/austenite orientation relationship.

If sufficient quantities of alloying elements (such as Si or Al) which retard the formation of cementite are added to the steel, then it is possible to suppress the formation of cementite altogether. An upper bainite microstructure consisting of just bainitic ferrite and carbon-enriched retained austenite is obtained instead (Fig. 6.4). The microstructure may also contain martensite if the residual austenite decomposes on cooling to ambient temperature.

### 6.3 LOWER BAINITE (TEMPERATURE RANGE 400–250°C)

Lower bainite has a microstructure and crystallographic features which are very similar to those of upper bainite. The major distinction is that cementite particles also precipitate inside the plates of ferrite (Fig. 6.5). There are, therefore, two kinds of cementite precipitates: those which grow from the carbon-enriched austenite which separates the platelets of bainitic ferrite, and others which appear to precipitate from supersaturated ferrite. These latter particles exhibit

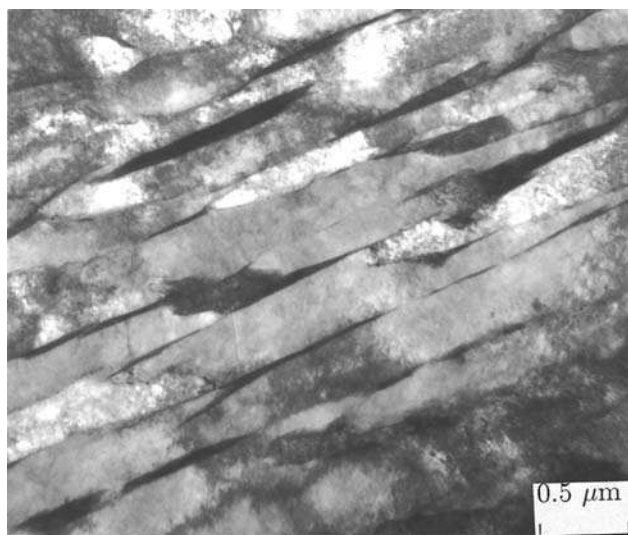


**Fig. 6.4** Upper bainite in Fe–0.095C–1.63Si–2Mn–2Cr wt% steel transformed isothermally at 400°C. The cementite has been suppressed to leave austenite films between the bainite ferrite plates.

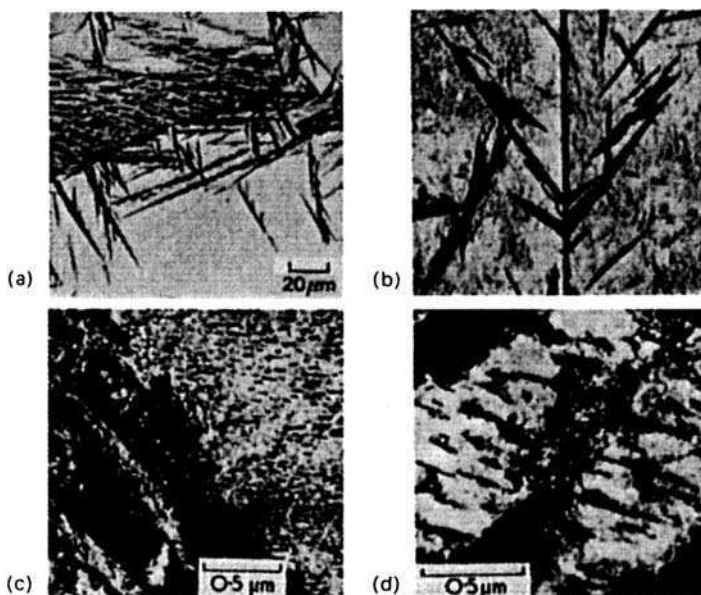


**Fig. 6.5** Microstructure of lower bainite. (a) Optical micrograph, Fe–0.8C wt% steel transformed at 300°C, showing sheaves of lower bainite. (b) Two-surface composite micrograph. (c) and (d) Thin-foil electron micrographs showing the carbide precipitation within the sub-units of lower bainite (courtesy of Ohmori).

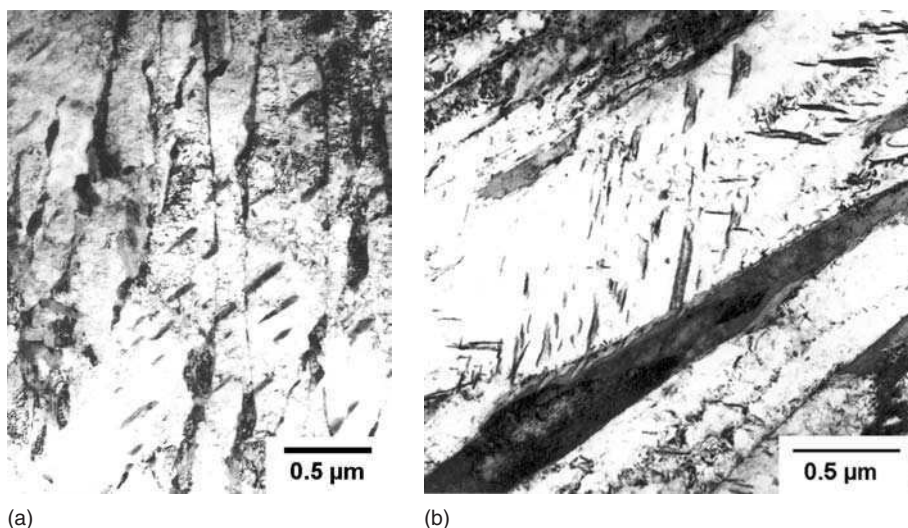


**Fig. 6.6** (a) Single variant of cementite in lower bainite, Fe-0.3C-4Cr wt%, transformed isothermally at 435°C. (b) Multiple variants of cementite in lower bainite, Fe-0.4C-2Si-3Mn wt%, transformed isothermally at 300°C.

the ‘tempering’ orientation relationship which is found when carbides precipitate during the heat treatment of martensite, often described as the Bagaryatski orientation relationship:

$$\begin{aligned} [0\ 0\ 1]_{\text{Fe}_3\text{C}} &\parallel [\bar{1}\ 0\ 1]_{\alpha}, \\ [1\ 0\ 0]_{\text{Fe}_3\text{C}} &\parallel [1\ 1\ 1]_{\alpha}, \\ [0\ 1\ 0]_{\text{Fe}_3\text{C}} &\parallel [\bar{1}\ 2\ \bar{1}]_{\alpha}. \end{aligned}$$

The carbides in the ferrite need not always be cementite. Depending on the chemical composition and the transformation temperature, other transition carbides may precipitate first. For example, in high-carbon steels containing more than about 1 wt% silicon (which retards cementite formation), epsilon carbide is commonly observed to precipitate in the bainitic ferrite.

In contrast to tempered martensite, the cementite particles in lower bainite frequently precipitate in just one variant of the orientation relationship (Fig. 6.6a), such that they form parallel arrays at about 60° to the axis of the bainite plate. In tempered martensite, the carbides tend to precipitate in Widmanstätten arrays.

However, these general observations are not always true. Widmanstätten arrays of cementite are also found in lower bainite when the latter forms in high-carbon steels or when the transformation occurs at low temperatures. Similarly, martensite in low-carbon steels exhibits only a single variant of carbide on tempering. This is because the carbide precipitation is influenced by the stresses

associated with the displacive growth of lower bainite or martensite – those variants of cementite which best comply with the stress are dominant. If the driving force for precipitation is large (i.e. the carbon concentration inherited by the bainite is large) then multiple variants including those which do not comply with the stress are able to precipitate.

The carbides in the lower bainite are extremely fine, just a few nanometres thick and about 500 nm long. Because they precipitate within the ferrite, a smaller amount of carbon is partitioned into the residual austenite. This in turn means that fewer and finer cementite particles precipitate between the ferrite plates, when compared with an upper bainitic microstructure. An important consequence is that lower bainite is usually found to be much tougher than upper bainite, in spite of the fact that it also tends to be stronger. The coarse cementite particles in upper bainite are notorious in their ability to nucleate cleavage cracks and voids.

## 6.4 THE SHAPE CHANGE

The IPS surface relief caused by the growth of bainitic ferrite has a large shear strain component of 0.24 in addition to the volume strain (0.03) on transformation. There is, therefore, a coordinated movement of atoms as the transformation occurs. Consistent with this, the iron and substitutional solutes such as Mn, Si, Ni, Mo and Cr, have been demonstrated using high-resolution techniques to be frozen into position during transformation (Fig. 6.7). The change in crystal structure is therefore achieved by a deformation of the austenite crystal. If the strain is elastically accommodated, then the strain energy of bainitic ferrite amounts to about  $400 \text{ J mol}^{-1}$ . Some of the strain can be relaxed by plastic deformation in the adjacent austenite.

The movement of interstitial atoms during the change in crystal structure does not influence the development of surface relief. Conversely, the observation of relief cannot yield information about whether or not carbon diffuses during transformation.

## 6.5 CARBON IN BAINITE

It is simple to establish that martensitic transformation is diffusionless, by measuring the local compositions before and after transformation. Bainite forms at somewhat higher temperatures where the carbon can escape out of the plate within a fraction of a second. Its original composition cannot therefore be measured directly.

There are three possibilities. The carbon may partition during growth so that the ferrite may never contain any excess carbon. The growth may on the other hand be diffusionless with carbon being trapped by the advancing interface. Finally, there is an intermediate case in which some carbon may diffuse with the remainder being trapped to leave the ferrite partially supersaturated. It is

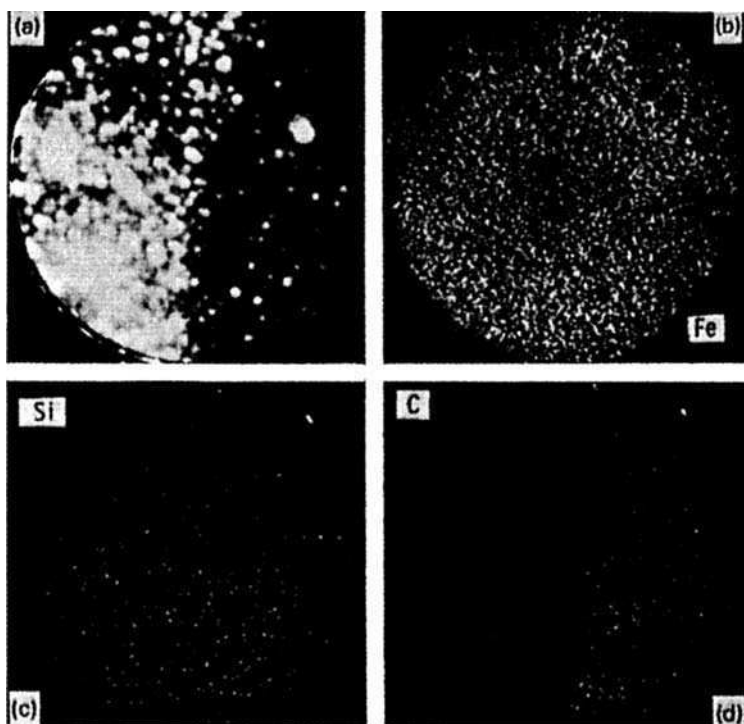


**Fig. 6.7** Imaging atom-probe micrographs, taken across an austenite–bainitic ferrite interface in a Fe–C–Si–Mn alloy. Substitutional atoms clearly do not diffuse during transformation. (a) Field ion image; each dot corresponds to an atom. The interface is vertical in the image, the austenite located on the right-hand side. (b) Fe atom map. (c) Corresponding Si atom map, showing a uniform distribution. (d) C atom map (Bhadeshia and Waugh, 1982).

therefore much more difficult to determine the precise role of carbon during the growth of bainitic ferrite than in martensite.

Diffusionless growth requires that transformation occurs at a temperature below  $T_0$ , when the free energy of bainite becomes less than that of austenite of the same composition. A locus of the  $T_0$  temperature of the function of the carbon concentration is called the  $T_0$  curve, an example of which is plotted on the Fe–C phase diagram in Fig. 6.8. Growth without diffusion can only occur if the carbon concentration of the austenite lies to the left of the  $T_0$  curve.

Suppose that the plate of bainite forms without diffusion, but that any excess carbon is soon afterwards rejected into the residual austenite. The next plate of bainite then has to grow from carbon-enriched austenite (Fig. 6.9a). This process must cease when the austenite carbon concentration reaches the  $T_0$  curve. The reaction is said to be incomplete, since the austenite has not achieved its equilibrium composition (given by the  $Ae_3$  curve) at the point the reaction stops. If on the other hand, the ferrite grows with an equilibrium carbon concentration

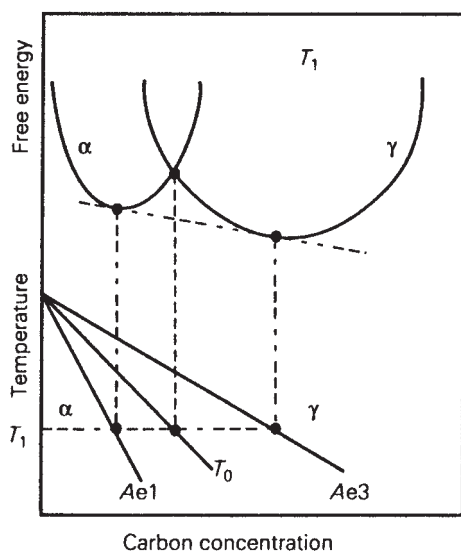


**Fig. 6.8** Schematic illustration of the origin of the  $T_0$  construction on the Fe-C phase diagram. Austenite with a carbon concentration to the left of the  $T_0$  boundary can in principle transform without any diffusion. Diffusionless transformation is thermodynamically impossible if the carbon concentration of the austenite exceeds the  $T_0$  curve.

then the transformation should cease when the austenite carbon concentration reaches the  $Ae_3$  curve.

It is found experimentally that the transformation to bainite does indeed stop at the  $T_0$  boundary (Fig. 6.9b). The balance of the evidence is that the growth of bainite below the  $B_s$  temperature involves the successive nucleation and martensitic growth of sub-units, followed in upper bainite by the diffusion of carbon into the surrounding austenite. The possibility that a small fraction of the carbon is nevertheless partitioned during growth cannot entirely be ruled out, but there is little doubt that the bainite is at first substantially supersaturated with carbon.

These conclusions are not significantly modified when the strain energy of transformation is included in the analysis.

There are two important features of bainite which can be shown by a variety of techniques, e.g. dilatometry, electrical resistivity, magnetic measurements and by metallography. Firstly, there is a well-defined temperature  $B_s$  above which no bainite will form, which has been confirmed for a wide range of alloy steels. The amount of bainite that forms increases as the transformation temperature is reduced below the  $B_s$  temperature. The fraction increases during isothermal transformation as a sigmoidal function of time, reaching an asymptotic limit which does not change on prolonged heat treatment even when substantial quantities of austenite remain untransformed. Transformation in fact ceases

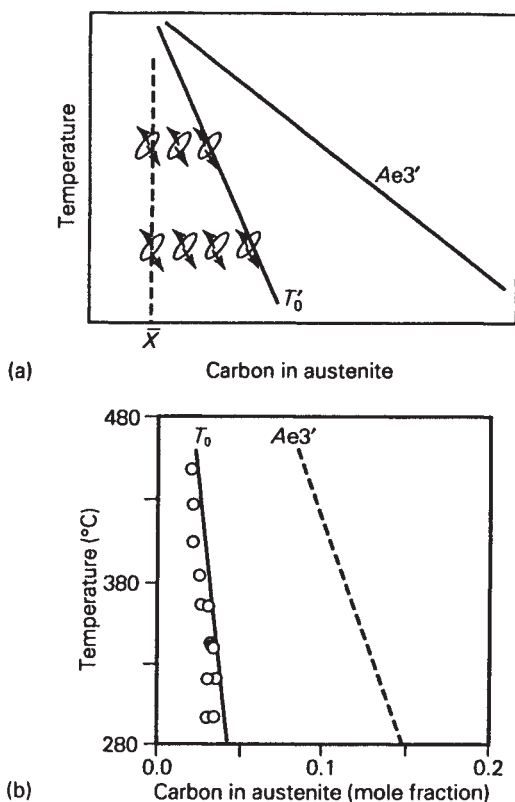


**Fig. 6.9** (a) Illustration of the incomplete-reaction phenomenon. During isothermal transformation, a plate of bainite grows without diffusion, then partitions its excess carbon into the residual austenite. The next plate therefore has to grow from carbon-enriched austenite. This process continues until diffusionless transformation becomes impossible when the austenite composition eventually reaches the  $T_0$  boundary. (b) Experimental data showing that the growth of bainite stops when the austenite carbon concentration reaches the  $T_0$  curve (Fe-0.43C-3Mn-2.12Si wt% alloy).

before the austenite achieves its equilibrium composition, so that the effect is dubbed the 'incomplete-reaction phenomenon'. These observations are understood when it is realized that growth must cease if the carbon concentration in the austenite reaches the  $T_0$  curve of the phase diagram.

Since this condition is met at ever-increasing carbon concentrations when the transformation temperature is reduced, more bainite can form with greater undercoolings below  $B_s$ . But the  $T_0$  restriction means that equilibrium, when the austenite has a composition given by the  $Ae_3$  phase boundary, can never be reached, as observed experimentally. A bainite-finish temperature  $B_F$  is sometimes defined, but this clearly cannot have any fundamental significance.

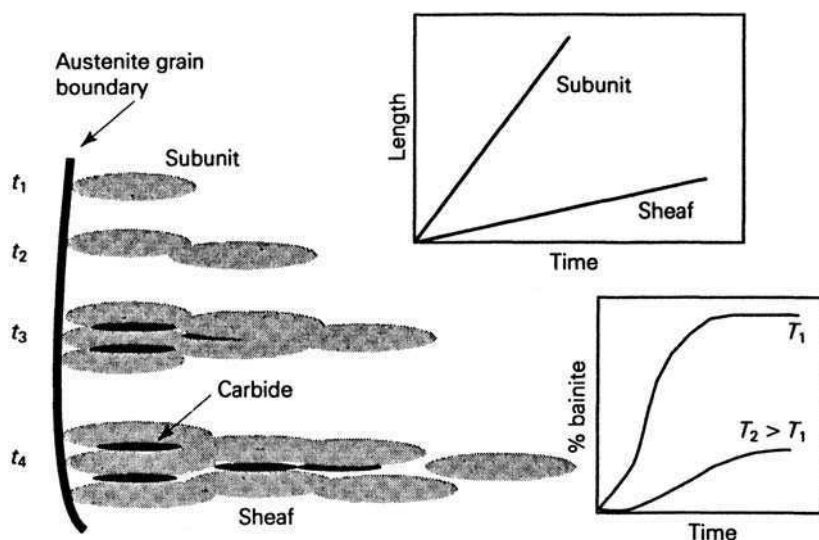


**Fig. 6.10** Schematic illustration of the microstructural features relevant in the kinetic description of a bainitic microstructure.

## 6.6 KINETICS

The rate of the bainite reaction needs to be considered in terms of a number of distinct events (Fig. 6.10). A sub-unit nucleates at an austenite grain boundary and lengthens at a certain rate before its growth is stifled by plastic deformation within the austenite. New sub-units then nucleate at its tip, and the sheaf structure develops as this process continues. The overall lengthening rate of a sheaf is therefore smaller than that of an individual sub-unit because there is an interval between the formation of successive sub-units. The volume fraction of bainite depends on the totality of sheaves growing from different regions in the sample. Carbide precipitation events also influence the kinetics, primarily by removing carbon either from the residual austenite or from the supersaturated ferrite.

Little is known about the nucleation of bainite except that the activation energy for nucleation is directly proportional to the driving force for transformation. This is consistent with the theory for martensite nucleation. However, unlike martensite, carbon must partition into the austenite during bainite nucleation, although the nucleus then develops into a sub-unit which grows without diffusion.

The scale of individual plates of ferrite is too small to be resolved adequately using optical microscopy, which is capable only of revealing clusters of plates. Using higher-resolution techniques such as photoemission electron microscopy (Fig. 6.11) it has been possible to study directly the progress of the bainite reaction. Not surprisingly, the lengthening of individual bainite platelets has



been found to occur at a rate which is much faster than expected from a diffusion-controlled process. The growth rate is nevertheless much smaller than that of martensite, because the driving force for bainite formation is smaller due to the higher transformation temperatures involved. The platelets tend to grow at a constant rate but are usually stifled before they can traverse the austenite grain.

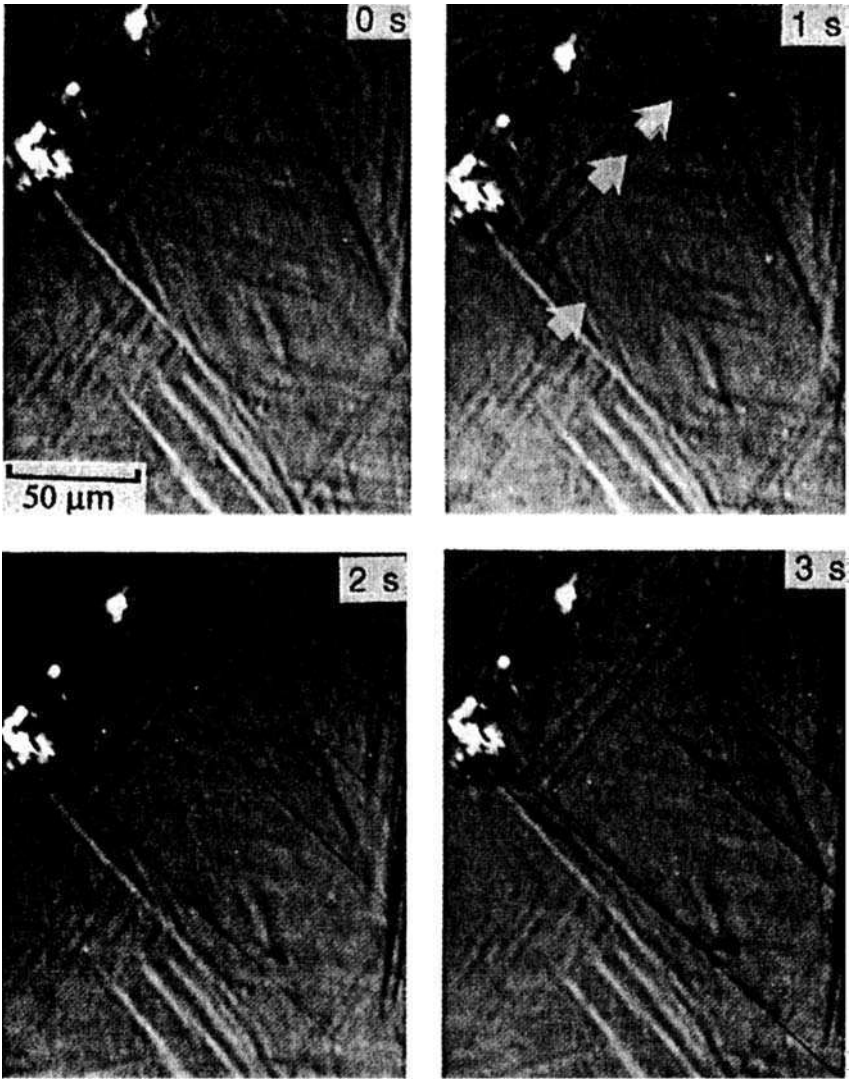


**Fig. 6.11** Photoemission electron microscope observations on the growth of individual sub-units in a bainite sheaf. The pictures are taken at 1 s intervals.

The lengthening rate of a sheaf is slower still, because of the delay caused by the need to repeatedly nucleate new sub-units. Nevertheless, sheaf lengthening rates are generally found to be about an order of magnitude higher than expected from carbon diffusion-controlled growth. Measurements have also been made of the thickening of bainite sheaves, a process which appears to be discontinuous, the thickness increasing in discrete steps of about  $0.5\text{ }\mu\text{m}$ . These step heights correlate with the size of the sub-units observed using thin-foil electron microscopy. The thickening process therefore depends on the rate at which sub-units are nucleated in adjacent locations within a sheaf.

The bainitic reaction has several of the recognized features of a nucleation and growth process. It takes place isothermally, starting with an incubation period during which no transformation is detected, followed by an increasing rate of transformation to a maximum and then a gradual slowing down. These features are illustrated in the dilatometric results of Fig. 6.12, for three

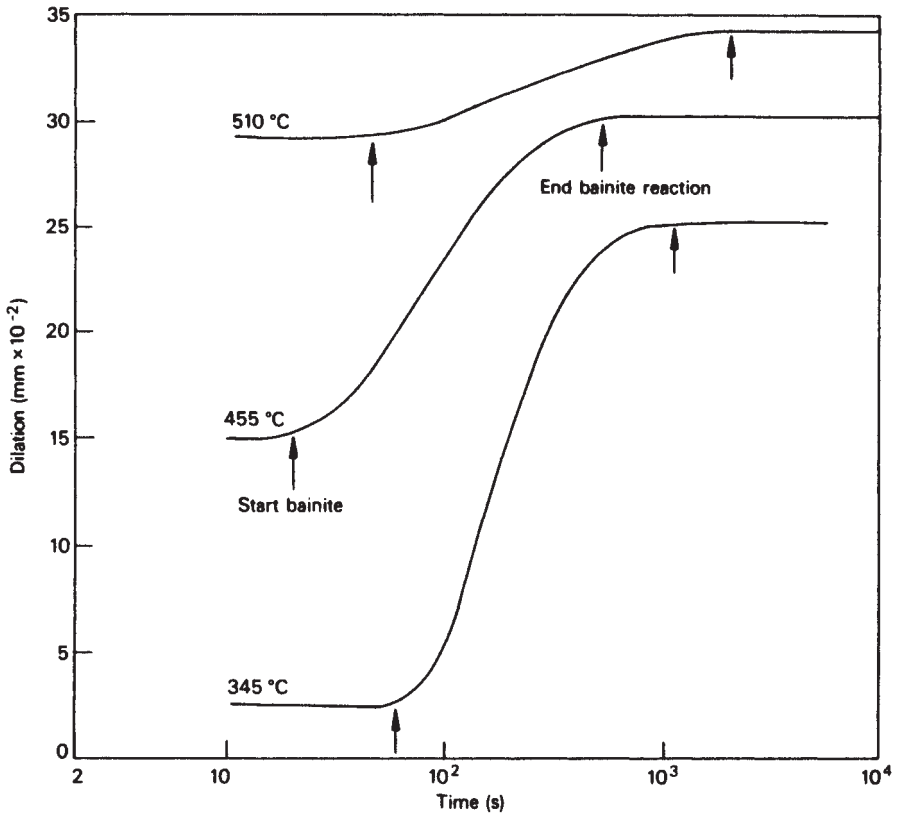


**Fig. 6.12** Isothermal reaction curves for the formation of bainite in Fe-1.0Cr-0.4C wt% steel (Hehemann, in *Phase Transformations*, ASM, Ohio, USA, 1970).

transformation temperatures in the bainitic range for a Fe-1Cr-0.4C wt% steel, the extent of transformation increasing with decreasing temperature. In this steel at 510°C the reaction stops after about 1 h, and the remaining austenite is stable at this temperature for a long time.

These overall transformation characteristics, i.e. the change in the fraction of bainite with time, temperature, austenite grain structure and alloy chemistry are therefore best considered in terms of a *TTT* diagram (Fig. 6.13). A simplified view is that the *TTT* diagram consists of two separable C-shaped curves. The one at higher temperatures describes the evolution of diffusional transformation products such as ferrite and pearlite, whereas the lower C-shaped curve represents displacive reactions such as Widmanstätten ferrite and bainite. In lean steels which transform rapidly, these two curves overlap so much that there is apparently just one curve which is the combination of all reactions. As the alloy concentration is increased to retard the decomposition of austenite, the two overlapping curves begin to become distinct, and a characteristic 'gap' develops at about the  $B_s$  temperature in the *TTT* diagram. This gap is important in the design of some high-strength (ausformed) steels which have to be deformed in the austenitic condition at low temperatures before the onset of transformation.

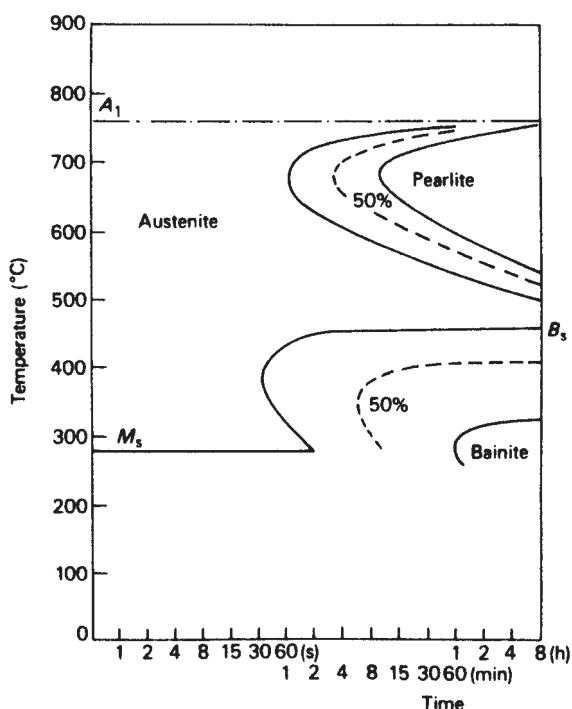


**Fig. 6.13** *TTT* curves for a Fe-3Cr-0.5C wt% steel (Thelning, *Steel and its Heat Treatment*, Bofors Handbook, Butterworth, UK, 1975).

## 6.7 THE TRANSITION FROM UPPER TO LOWER BAINITE

As the isothermal transformation temperature is reduced below  $B_s$ , lower bainite is obtained in which carbides precipitate in the ferrite, with a correspondingly reduced amount of precipitation from the austenite between the ferrite. This transition from upper to lower bainite can be explained in terms of the rapid tempering processes that occur after the growth of a supersaturated plate of bainite (Fig. 6.14). Excess carbon tends to partition into the residual austenite by diffusion, but the supersaturation may also be reduced by precipitation in the ferrite.

The time required for a supersaturated plate of ferrite to decarburize by diffusion into austenite is illustrated in Fig. 6.15 for a typical steel. At elevated temperatures the diffusion is so rapid that there is no opportunity to precipitate carbides in the ferrite, giving rise to an upper bainitic microstructure. Cementite eventually precipitates from the carbon-enriched residual austenite.

As the transformation temperature is reduced and the time for decarburization increases, some of the carbon has an opportunity to precipitate as fine carbides in the ferrite, whereas the remainder partitions into the austenite, eventually to precipitate as inter-plate carbides. This is the lower bainite microstructure. Because only a fraction of the carbon partitions into the austenite the inter-plate carbides are much smaller than those associated with upper bainite. This is why lower bainite with its highly refined microstructure is always

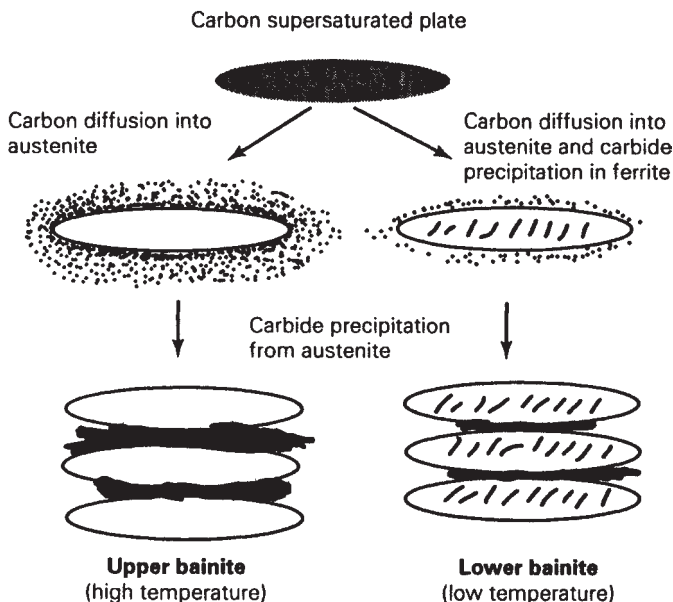


**Fig. 6.14** Schematic representation of the transition from upper to lower bainite.

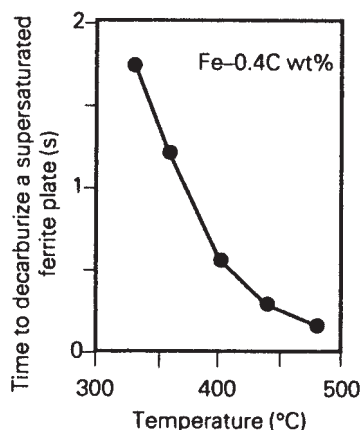


**Fig. 6.15** The approximate time required to decarburize a supersaturated plate of bainite.

found to be much tougher than upper bainite, even though it usually has a much higher strength.

A corollary to the mechanism of the transition from upper to lower bainite is that in steels containing high concentrations of carbon, only lower bainite is ever obtained. The large amount of carbon that is trapped in the ferrite by transformation simply cannot escape fast enough into the austenite so that precipitation from ferrite is unavoidable. Conversely, in very low-carbon steels, the time for decarburization is so small that only upper bainite is obtained by transformation at all temperatures between the pearlite-finish and the martensite-start temperatures.

It is also possible to obtain mixtures of upper and lower bainite by isothermal transformation. As upper bainite forms first, the residual austenite becomes richer in carbon and the tendency to form lower bainite increases as the transformation progresses.

## 6.8 GRANULAR BAINITE

Granular bainite (Fig. 6.16) is a term frequently used to describe the bainite that occurs during continuous cooling transformation. This terminology is used widely in industry, where most steels undergo non-isothermal heat treatments. A good example is the energy generation industry where larger Cr-Mo steel components are allowed to cool naturally from the austenitic state, to generate bainitic microstructures.

Granular bainite cannot readily be distinguished from ordinary bainite when examined using transmission electron microscopy, because its mechanism of formation is not different. However, because the microstructure forms gradually during cooling, the sheaves of bainite can be rather coarse. The optical

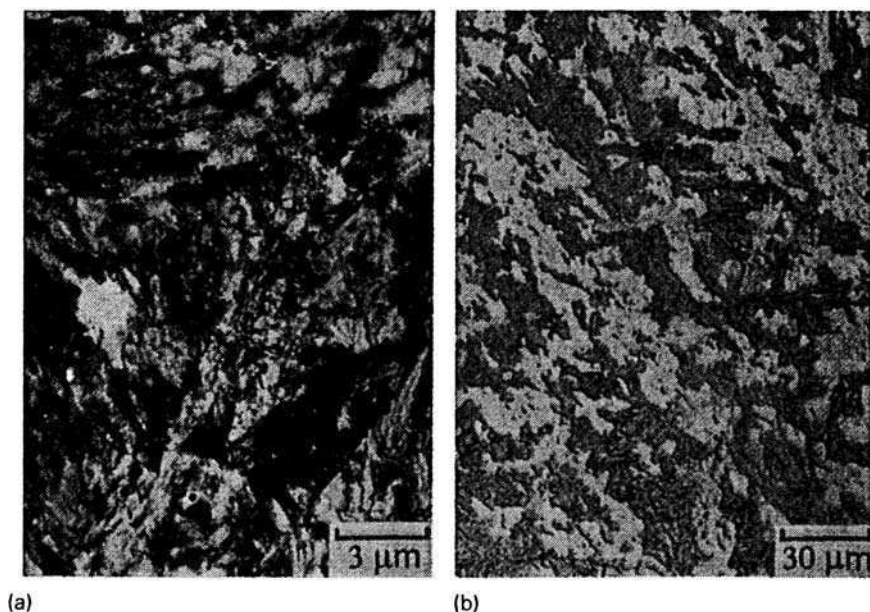


**Fig. 6.16** Granular bainite in a Fe-0.15C-2.25Cr-0.5Mo wt% steel of the kind used extensively in the energy generation industry. (a) Light micrograph. (b) Corresponding transmission electron micrograph (after Joseffson, 1989).

microstructure then gives the appearance of blocks of bainite and austenite, so that it is appropriate to use the adjective ‘granular’.

A characteristic (though not unique) feature of granular bainite is the lack of carbides in the microstructure. Instead, the carbon that is partitioned from the bainitic ferrite stabilizes the residual austenite, so that the final microstructure contains both retained austenite and some high-carbon martensite in addition to the bainitic ferrite.

## 6.9 TEMPERING OF BAINITE

The extent and the rate of change of the microstructure and properties during tempering must depend on how far the initial sample deviates from equilibrium. The behaviour of bainite during tempering is therefore expected to be different from that of martensite.

Unlike martensite, bainitic ferrite usually contains only a slight excess of carbon in solution. Most of the carbon in a transformed sample of bainite is in the form of cementite particles, which in turn tend to be coarser than those associated with tempered martensite. The effects of tempering heat treatments are therefore always milder than is the case when martensite in the same steel is annealed.

Bainite forms at relatively high temperatures where some recovery occurs during transformation. Consequently, when low-carbon bainitic steels are annealed at temperatures as high as 700°C (1 h), there are only minor changes in recovery, morphology or carbide particles. Rapid softening occurs only when the plate-like structure of ferrite changes into equi-axed ferrite. Associated with this change is the spheroidization and coarsening of cementite. Further tempering has minimal effects.

In marked contrast with martensitic steels, small variations in the carbon concentration (0.06–0.14 wt%) have little effect on the tempering of bainite. Carbon has a very potent solid solution strengthening effect. Thus, the strength of martensite drops sharply as the carbon precipitates during tempering. With bainite the carbon is mostly present as coarse carbides which contribute little to strength. It is not therefore surprising that the tempering response is rather insensitive to the bulk carbon concentration.

Many bainitic microstructures contain appreciable quantities of retained austenite. Tempering, usually at temperatures in excess of 400°C, induces the decomposition of this austenite into a mixture of ferrite and carbides.

Bainitic steels containing strong carbide-forming elements such as Cr, V, Mo and Nb, undergo secondary hardening during annealing at high temperatures. Secondary hardening occurs when fine (more stable) alloy carbides form at the expense of cementite (Chapter 9). Because the cementite in bainite is coarse, the secondary hardening reaction tends to be sluggish when compared with martensite.

There is considerable interest in the use of copper-bearing bainitic steels for applications in heavy engineering. Tempering induces the formation of fine particles of copper which contribute to strength without jeopardizing toughness.

To summarize, there are significant differences in the tempering behaviour of bainite and martensite, the most prominent being that there is little carbon in solid solution in bainite. This has the consequence that bainitic microstructures are much less sensitive to tempering, since there is hardly any loss of strength due to the removal of the small quantity of dissolved carbon. Major changes in strength occur only when the bainite plate microstructure coarsens or recrystallizes into one consisting of equi-axed grains of ferrite. Minor changes in strength are due to cementite particle coarsening and a general recovery of the dislocation substructure. Bainitic steels containing strong carbide-forming elements tend to exhibit secondary hardening phenomena rather like those observed in martensitic steels which depends on the precipitation of fine alloy carbides.

## 6.10 ROLE OF ALLOYING ELEMENTS

### Carbon

Carbon has a large effect on the range of temperature over which upper and lower bainite occur. The  $B_s$  temperature is depressed by many alloying

elements but carbon has the greatest influence, as indicated by the following empirical equation:

$$B_s(^{\circ}\text{C}) = 830 - 270\text{C} - 90\text{Mn} - 37\text{Ni} - 70\text{Cr} - 83\text{Mo},$$

where the concentrations are all in wt%. Carbon has a much larger solubility in austenite than in ferrite, and is a very powerful austenite stabilizer which leads to a general retardation of reaction kinetics. The fraction of carbides to be found in the final microstructure increases in proportion to the carbon concentration, so that the concentration must be kept below about 0.4 wt% to ensure reliable mechanical properties. We have already seen that an increase in carbon makes it easier for lower bainite to form because it becomes more difficult for plates of supersaturated bainitic ferrite to decarburize before the onset of cementite precipitation.

### Other alloying elements

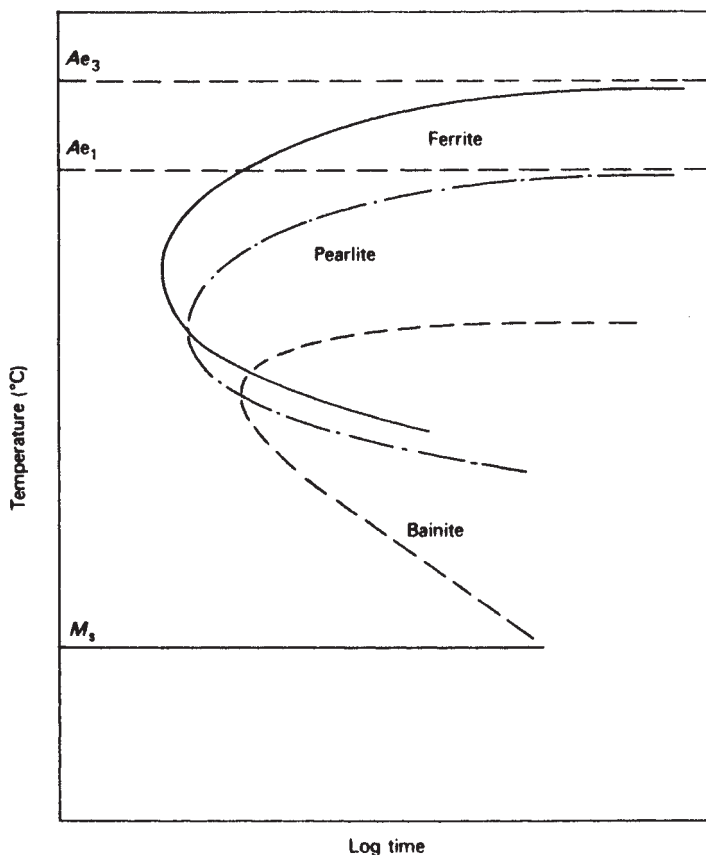
In plain carbon steels, the bainitic reaction is kinetically shielded by the ferrite and pearlite reactions which commence at higher temperatures and shorter times (Fig. 6.17a), so that in continuously cooled samples bainitic structures are difficult to obtain. Even using isothermal transformation, difficulties arise if, e.g., the ferrite reaction is particularly rapid. As explained in Chapter 4, the addition of metallic alloying elements usually results in the retardation of the ferrite and pearlite reactions. In addition, the bainite reaction is depressed to lower temperatures. This often leads to a greater separation of the reactions, and the *TTT* curves for many alloy steels show much more clearly separate C-shaped curves for the pearlite and bainitic reactions (Fig. 6.17b). However, it is still difficult to obtain a fully bainitic microstructure because of its proximity to the martensite reaction.

A very effective means of isolating the bainite reaction in low-carbon steels has been found by adding about 0.002 wt% soluble boron to a ½ wt% Mo steel. While the straight molybdenum steel encourages the bainite reaction (Fig. 6.17c), the boron markedly retards the ferrite reaction, probably by preferential segregation to the prior austenite boundaries. This permits the bainite reaction to occur at shorter times. At the same time, the bainite C-shaped curve is hardly affected by the boron addition, so that martensite formation is not enhanced. Consequently, by the use of a range of cooling rates, fully bainitic steels can be obtained.

## 6.11 USE OF BAINITIC STEELS

There are large markets for steels with strengths less than 1000 MPa, and where the total alloy concentration rarely exceeds 2 wt%. Bainitic steels are well suited for applications within these constraints. However, alloy design must be careful in order to obtain the right microstructures. Steels with inadequate hardenability



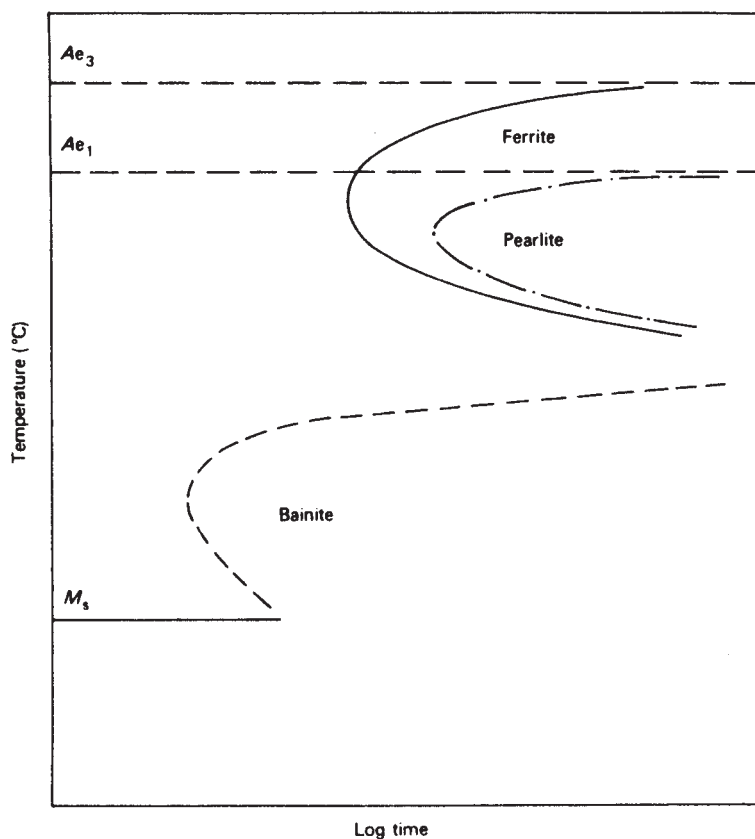


(a)

**Fig. 6.17a** Effect of alloying elements on the bainite reaction TTT curves. (a) Schematic diagram for a low-carbon steel.

tend to transform to mixtures of allotriomorphic ferrite and bainite. Attempts to improve hardenability usually lead to partially martensitic microstructures. The solution therefore lies in low-alloy, low-carbon steels, containing small amounts of boron and molybdenum to suppress allotriomorphic ferrite formation. Boron increases the bainitic hardenability. Other solute additions can, in the presence of boron, be kept at sufficiently low concentrations to avoid the formation of martensite. A typical composition might be Fe-0.1C-0.25Si-0.50Mn-0.55Mo-0.003B wt%. Steels like these are found to transform into virtually fully bainitic microstructures with very little martensite using normalizing heat treatments.

The most modern bainitic steels are designed with much reduced carbon and other alloying element concentrations. They are then processed using accelerated cooling in order to obtain the necessary bainitic microstructure. The



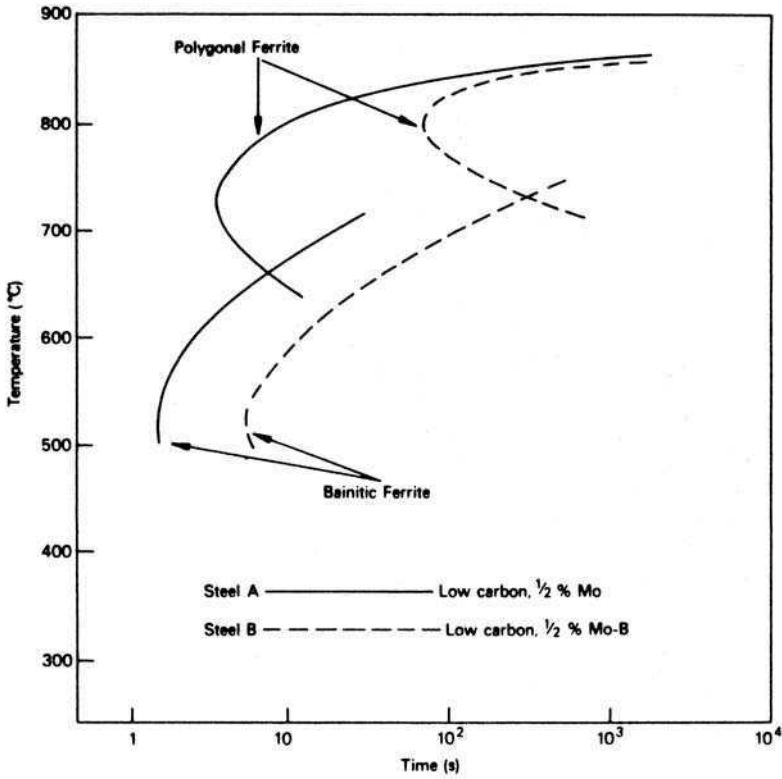
(b)

**Fig. 6.17b** Effect of alloying elements on the bainite reaction TTT curves. (b) Schematic diagram for a low-alloy steel.

reduced alloy concentration not only gives better weldability, but also a larger strength due to the refined bainitic microstructure.

The range of bainitic alloys available commercially is summarized in Fig. 6.18, and some typical alloy compositions are stated in Table 6.1. The ultra-high-strength steels consist of mixtures of bainite ferrite, martensite and retained austenite. They have an enhanced hardenability using manganese, chromium and nickel, and usually also contain a large silicon concentration ( $\sim 2$  wt%) in order to prevent the formation of cementite. High-strength steels are made with very low impurity and inclusion concentrations, so that the steel then becomes susceptible to the formation of cementite particles, which therefore have to be avoided or refined.

Medium-strength steels with the same microstructure but somewhat reduced alloy content have found applications in the automobile industry as crash



(c)

**Fig. 6.17c** Effect of alloying elements on the bainite reaction TTT curves. (c) Low carbon 0.5M. steel with and without soluble born *Journal of the Iron and Steel Institute* (Irvine and Pickering, 187, 292, 1957).

reinforcement bars to protect against sidewise impact. Another major advance in the automobile industry has been in the application of bainitic forging alloys to the manufacture of components such as cam shafts. These were previously made of martensitic steels by forging, hardening, tempering, straightening and finally stress-relieving. All of these operations are now replaced by controlled cooling from the die forging temperature, to generate the bainitic microstructure, with cost savings which on occasions have made the difference between profit and loss for the entire unit.

Creep-resistant bainitic steels have been used successfully in the power generation industry since the early 1940s. Their hardenability has to be such that components as large as 1 m in diameter can be cooled continuously to generate a bainitic microstructure throughout the section. The alloys utilize chromium and molybdenum, which serve to enhance hardenability but also, during subsequent

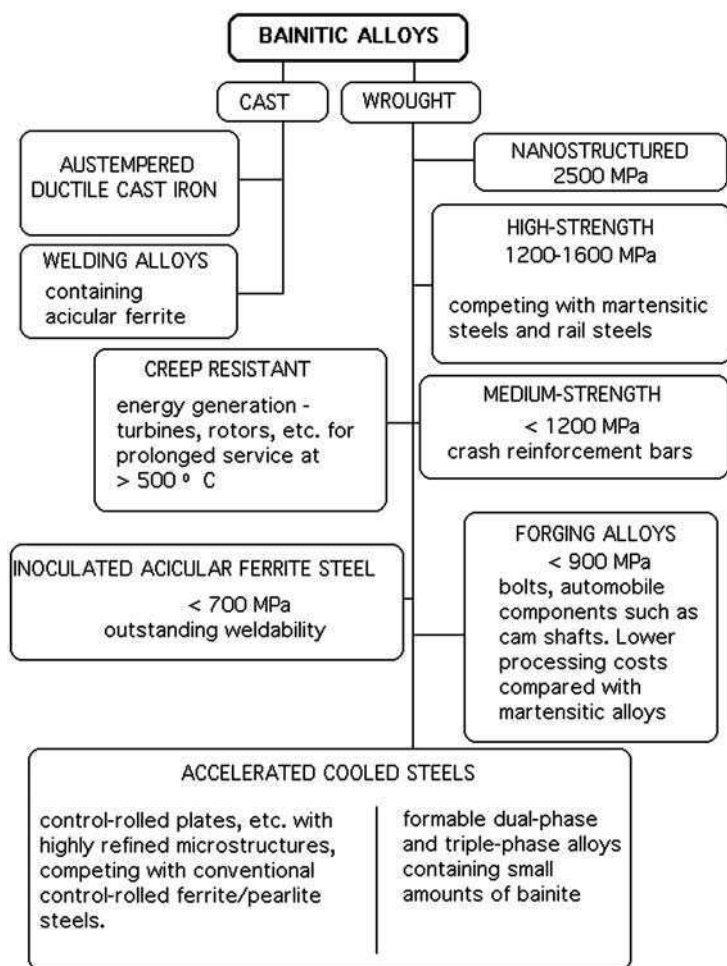


**Fig. 6.18** Bainitic alloys currently available commercially.

heat-treatment, cause the precipitation of alloy carbides which greatly improve the creep resistance.

By inoculating molten steel with controlled additions of non-metallic particles, bainite can be induced to nucleate intragranularly on the inclusions, rather than from the austenite grain surfaces. This intragranularly nucleated bainite is called 'acicular ferrite'. It is a much more disorganized microstructure with a larger ability to deflect cracks. Inoculated steels are now available commercially and are being used in demanding structural applications such as the fabrication of oil rigs for hostile environments.

Advances in rolling technology have led to the ability to cool the steel plate rapidly during the rolling process, without causing undue distortion.

**Table 6.1** Chemical composition, wt%, of typical bainitic steels

Alloy	C	Si	Mn	Ni	Mo	Cr	V	B	Nb	Other
Early bainitic steel	0.10	0.25	0.5	–	–	0.003	–	–	–	
Ultra-low carbon	0.02	0.20	2.0	0.3	0.30	–	–	0.010	0.05	
Ultra-high strength	0.20	2.00	3.0	–	–	–	–	–	–	
Creep resistant	0.15	0.25	0.50	–	1.00	2.30	–	–	–	
Forging alloy	0.10	0.25	1.00	0.50	1.00	–	–	–	0.10	
Inoculated	0.08	0.20	1.40	–	–	–	–	–	0.10	0.012 Ti
Nanostructured	1.0	1.50	1.90	–	0.26	1.26	0.1	–	–	

This has led to the development of ‘accelerated cooled steels’ which have a bainitic microstructure, can be highly formable and compete with conventional control-rolled steels.

## 6.12 NANOSTRUCTURED BAINITE

It would be nice to have a strong material which can be used for making components which are large in all their dimensions, and which does not require mechanical processing or rapid cooling to reach the desired properties. The following conditions are required to achieve this:

- (i) The material must not rely on perfection to achieve its properties. Strength can be generated by incorporating a large number density of defects such as grain boundaries and dislocations, but the defects must not be introduced by deformation if the shape of the material is not to be limited.
- (ii) Defects can be introduced by phase transformation, but to disperse them on a sufficiently fine scale requires the phase change to occur at large undercoolings (large free energy changes). Transformation at low temperatures also has the advantage that the microstructure becomes refined.
- (iii) A strong material must be able to fail in a safe manner. It should be tough.
- (iv) Recalescence limits the undercooling that can be achieved. Therefore, the product phase must be such that it has a small latent heat of formation and grows at a rate which allows the ready dissipation of heat.

Recent discoveries have shown that carbide-free bainite can satisfy these criteria.<sup>2</sup> Bainite and martensite are generated from austenite without diffusion

<sup>2</sup> Caballero, F. G. and Bhadeshia, H. K. D. H., *Current Opinion in Solid State and Materials Science* **8**, 251, 2004.

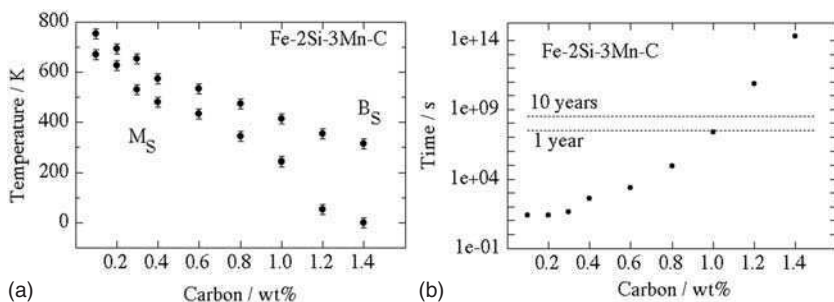


**Fig. 6.19** (a) Calculated transformation start temperatures in Fe-2Si-3Mn wt% steel as a function of the carbon concentration. (b) The calculated time required to initiate bainite at the  $B_S$  temperature.

by a displacive mechanism. Not only does this lead to solute-trapping but also a huge strain energy term, both of which reduce the heat of transformation. The growth of individual plates in both of these transformations is fast, but unlike martensite, the *overall rate* of reaction is much smaller for bainite. This is because the transformation propagates by a sub-unit mechanism in which the rate is controlled by nucleation rather than growth. This mitigates recalescence.

The theory of the bainite transformation allows the estimation of the lowest temperature at which bainite can be induced to grow.<sup>3</sup> Such calculations are illustrated in Fig. 6.19a, which shows how the bainite-start ( $B_S$ ) and martensite-start ( $M_S$ ) temperatures vary as a function of the carbon concentration, in a particular alloy system. There is in principle no lower limit to the temperature at which bainite can be generated. On the other hand, the rate at which bainite forms slow down dramatically as the transformation temperature is reduced (Fig. 6.19b). It may take hundreds or thousands of years to generate bainite at room temperature. For practical purposes, the carbon concentration has to be limited to about 1 wt% for the case illustrated.

An alloy has been designed in this way, with the approximate composition Fe-1C-1.5Si-1.9Mn-0.25Mo-1.3Cr-0.1V wt%, which on transformation at 200°C, leads to bainite plates which are only 20–40 nm thick. The slender plates of bainite are dispersed in stable carbon-enriched austenite which, with its face-centred cubic lattice, buffers the propagation of cracks (Fig. 6.20).

The bainite obtained by transformation at very low temperatures is the hardest ever (700 HV, 2500 MPa), has considerable ductility, is tough (30–40 MPa m<sup>1/2</sup>) and does not require mechanical processing or rapid cooling. The steel after heat treatment therefore does not have long-range residual stresses, it is very cheap to produce and has uniform properties in very large sections. In effect, the hard bainite has achieved all of the essential objectives of

<sup>3</sup> Bhadeshia, H. K. D. H., *Acta Metallurgica* **29**, 1117, 1981.

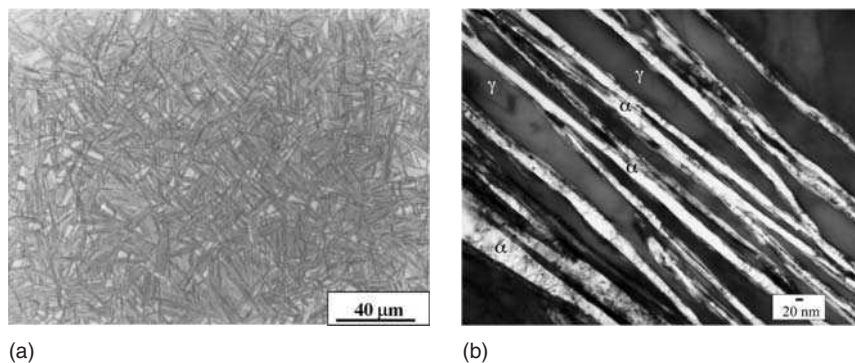


**Fig. 6.20** Bainite obtained by transformation at 200°C. (a) Optical micrograph. (b) Transmission electron micrograph (Caballero, Mateo and Bhadeshia).

structural nanomaterials which are the subject of so much research, but in large dimensions.

## FURTHER READING

- Abe, F., Bainitic and martensitic creep-resistant steels, *Current Opinion in Solid State and Materials Science* **8**, 313, 2004.
- Bhadeshia, H. K. D. H., The lower bainite transformation and the significance of carbide precipitation, *Acta Metallurgica* **28**, 1103, 1980.
- Bhadeshia, H. K. D. H., The bainite transformation: unresolved issues, *Materials Science and Engineering A* **273–275**, 58, 1999.
- Bhadeshia, H. K. D. H., *Bainite in Steels*, 2nd edition, Institute of Materials, London, UK, 2001.
- Bhadeshia, H. K. D. H., 52nd Hatfield Memorial Lecture: Large chunks of strong steel, *Materials Science and Technology* **21**, 1293, 2005.
- Brown, P. M. and Baxter, D. P., Hyper-strength bainitic steels, *Proceedings of Materials Science and Technology 2004*, New Orleans, Louisiana, p. 433, 2004.
- Caballero, F. G. and Bhadeshia, H. K. D. H., Very strong bainite, *Current Opinion in Solid State and Materials Science* **8**, 251, 2004.
- Christian, J. W., *Theory of Transformations in Metals and Alloys*, 3rd edition, Pergamon Press, Oxford, 2003.
- Christian, J. W. and Edmonds, D. V., The bainite transformation, *Phase Transformations in Ferrous Alloys*, TMS-AIME, Pennsylvania, USA, p. 293, 1984.
- García-Mateo, C., Caballero, F. G. and Bhadeshia, H. K. D. H., Development of hard bainite, *ISIJ International* **43**, 1238, 2003.
- Hehemann, R. F., The bainite reaction, *Phase Transformations*, American Society for Metals, Ohio, USA, p. 397, 1970.
- Pickering, F. B., *Physical Metallurgy and the Design of Steels*, Applied Science Publishers, London, UK, 1978.
- Takahashi, M., Kinetics of the bainite transformation, *Current Opinion in Solid State and Materials Science* **8**, 213, 2004.

# 7

---

## ACICULAR FERRITE

### 7.1 INTRODUCTION

Highly organized microstructures can often be found in steels, e.g., ferrite can grow in the form of packets containing parallel plates which are in the same crystallographic orientation (Fig. 7.1a). This can be harmful to mechanical properties because cleavage cracks, or deformation processes, can extend readily across the packets. The effects of the individual plates within these packets then have a minimal effect on the mechanical properties.

Some of the most exciting recent developments in wrought and welded steel technology have involved ‘acicular ferrite’. Far from being organized, this microstructure is better described as chaotic. The plates of acicular ferrite nucleate heterogeneously on small non-metallic inclusions and radiate in many different directions from these ‘point’ nucleation sites (Fig. 7.1b). It is believed that propagating cleavage cracks are frequently deflected as they cross an acicular ferrite microstructure with its many different orientations. This gives rise to superior mechanical properties, especially toughness.

Acicular ferrite is therefore widely recognized to be a desirable microstructure. This chapter deals with the mechanism by which it forms and with the role of inclusions in stimulating its formation.

### 7.2 MICROSTRUCTURE

The term *acicular* means shaped and pointed like a needle, but it is generally recognized that acicular ferrite has in three dimensions the morphology of thin, lenticular plates (Fig. 7.2). In two-dimensional sections, the acicular ferrite always appears like a plate rather than a section of a rod. Serial sectioning experiments which have a depth resolution of about  $0.5\ \mu\text{m}$  have confirmed that the shape is between that of a lath or plate, with the length, width and thickness normally less than about 36, 6 and  $3\ \mu\text{m}$ , respectively.<sup>1</sup>

---

<sup>1</sup> Wu, K. M., *Scripta Materialia* **54**, 569, 2006.



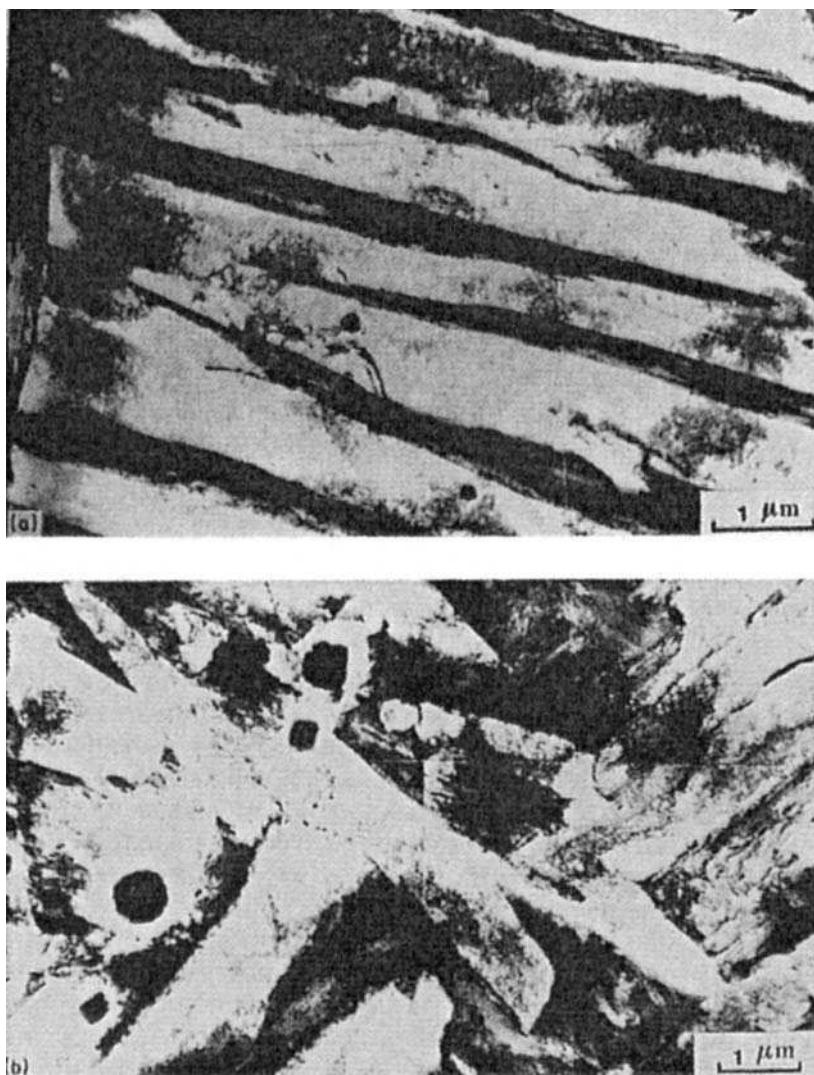


**Fig. 7.1** Transmission electron micrographs taken from samples transformed at the same temperature but with different austenite grain size. (a) Small austenite grain size leading to plates of ferrite growing in parallel formations. (b) Large austenite grain size with plates of ferrite nucleating intragranularly on non-metallic inclusions and growing along many different directions (courtesy of J. R. Yang).

Although the plates are nucleated heterogeneously on non-metallic inclusions, the chance of observing an inclusion in any given plate is rather small. The probability is approximately the ratio of the inclusion volume to that of a ferrite plate. The volume of a typical plate of acicular ferrite is about  $10^{-16} \text{ m}^3$



**Fig. 7.2** Replica transmission electron micrograph of acicular ferrite plates in martensite matrix, in a steel weld deposit which was partially transformed and quenched (courtesy of Barritte).

and an inclusion about  $4 \times 10^{-20} \text{ m}^3$ , so that about 7.4% of the plates might be expected to actually display the nucleating particle. Better estimates which take account of the anisotropy of the plate shape increase this value to about 13%. It is also likely that once a plate forms on a particle, it stimulates the nucleation of others, an effect known as autocatalysis. A fraction of the plates will therefore not directly be associated with nucleation on non-metallic particles.

### 7.3 MECHANISM OF TRANSFORMATION

Acicular ferrite and bainite are in many respects similar in their transformation mechanisms. Their microstructures differ in detail because bainite sheaves grow as a series of parallel platelets emanating from austenite grain *surfaces*, whereas acicular ferrite platelets nucleate intragranularly at *point* sites so that parallel formations of plates cannot develop. The nucleation site in the later case is smaller than the thickness of the plate, so that the inclusion is normally engulfed by the plate of ferrite which it stimulates.

The growth of both bainite and acicular ferrite causes an invariant-plane strain shape deformation with a large shear component (Fig. 7.3). Consequently, plates of acicular ferrite cannot cross austenite grain boundaries, because the coordinated movement of atoms implied by the shape change cannot in general be sustained across grains in different crystallographic orientations. The lattice of the acicular ferrite is therefore generated by a deformation of the austenite, so that the iron and substitutional solutes are unable to diffuse during the course of



**Fig. 7.3** Interference contrast micrograph showing the surface relief caused when a metallographically polished sample of steel is transformed to acicular ferrite (courtesy of Strangwood).

transformation. It is not therefore surprising that the concentrations of substitutional alloying elements are unchanged during the growth of acicular ferrite.

The deformation which changes the austenite into acicular ferrite occurs on particular planes and directions, so that the ferrite structure and orientation are intimately related to that of the austenite. It follows that plates of acicular ferrite, like bainite, must without exception have an orientation relationship with the austenite. This is not necessarily the case when a transformation occurs by a diffusional mechanism, because a grain of ferrite can easily grow into any adjacent grain of austenite with which it happens to come into contact.

During isothermal transformation, the acicular ferrite reaction stops when the carbon concentration of the remaining austenite makes it impossible to decompose without diffusion. This implies that the plates of acicular ferrite grow supersaturated with carbon, but the excess carbon is shortly afterwards rejected into the remaining austenite. This of course is the incomplete reaction phenomenon described in Chapter 6 for bainite, where the austenite never reaches its equilibrium composition since the reaction stops at the  $T'_0$  curve of the phase diagram (Fig. 7.4). The obvious conclusion is that acicular ferrite cannot form at temperatures above the bainite-start temperature, and this is indeed found to be the case in practice.

There are many other correlations which reveal the analogy between acicular ferrite and bainite. For example, the removal of inclusions by vacuum arc melting, without changing any other feature, causes an immediate change in the microstructure from acicular ferrite to bainite. The same effect can be obtained

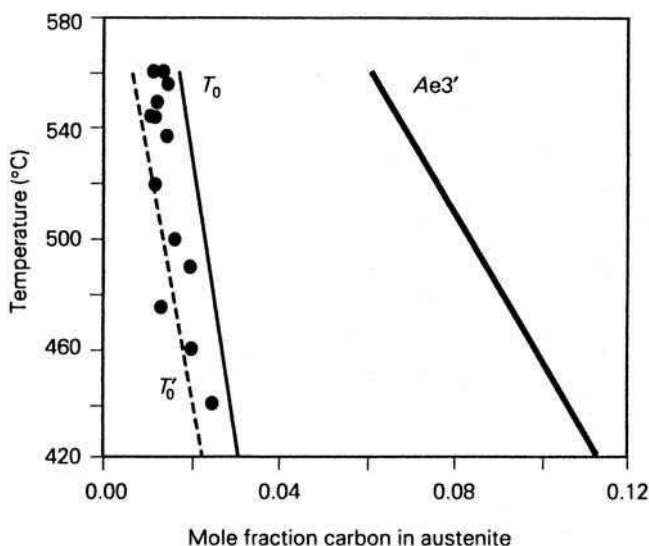


**Fig. 7.4** Data from experiments in which the austenite is transformed isothermally to acicular ferrite, showing that the reaction stops when the carbon concentration of the austenite reaches the  $T_0$  curve (courtesy of Strangwood).

by increasing the number density of austenite grain nucleation sites relative to intragranular sites. This can be done by refining the austenite grains to obtain a transition from an acicular ferrite microstructure to one which is predominantly bainitic (Fig. 7.5).

The opposite phenomenon, in which an inclusion-containing steel with bainite can be induced to transform into an acicular ferrite microstructure is also observed. This can be done by rendering the austenite grain surfaces ineffective as nucleation sites, either by decorating the boundaries with a thin layer of inert

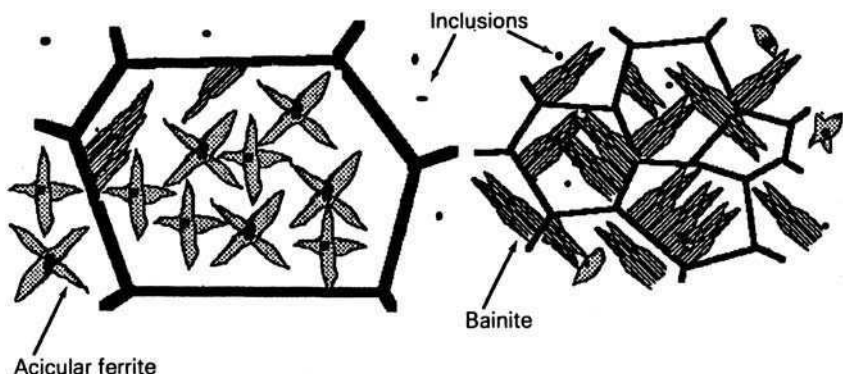
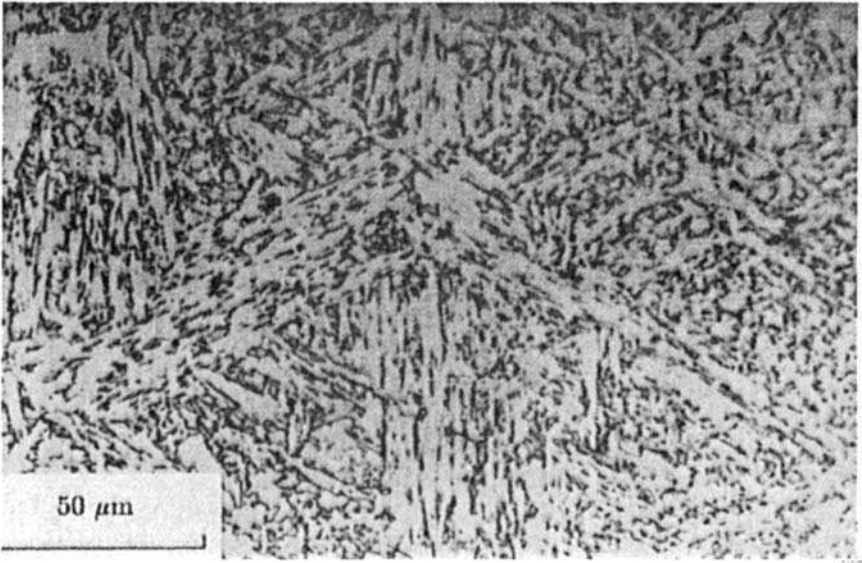
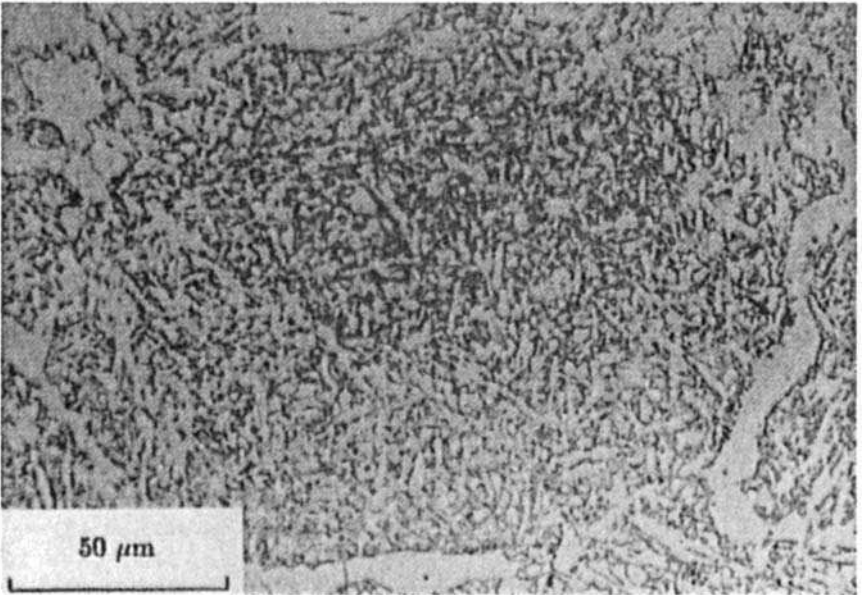


**Fig. 7.5** Illustration of how the microstructure changes from one which is predominantly acicular ferrite, to another which is mostly bainitic as the austenite grain size is refined.



(a)



(b)

**Fig. 7.6** The change from a bainitic (a) to an acicular ferrite (b) microstructure when the austenite grain boundaries are eliminated as nucleation sites by decoration with inert layers of ferrite (courtesy of Babu).

allotriomorphic ferrite (Fig. 7.6) or by adding a small amount of boron (30 ppm). The boron segregates to the boundaries, thereby reducing the boundary energy and making them less favourable sites for heterogeneous nucleation. In general, any method which increases the number density of intragranular nucleation sites relative to austenite grain boundary sites will favour the acicular ferrite microstructure.

## 7.4 THE INCLUSIONS AS HETEROGENEOUS NUCLEATION SITES

Many experiments show that inclusions rich in titanium are most effective in acicular ferrite production (Fig. 7.7). A number of different mechanisms have been proposed. It is rare, however, that the specific titanium compound responsible for the observed effects is identified. This is because many of the compounds have similar crystal structures and lattice parameters. When microanalysis is used, elements such as C, N and O are either undetectable or cannot be estimated with sufficient accuracy to determine the stoichiometric ratio with respect to Ti. In reality, the non-metallic inclusions tend to consist of many crystalline and amorphous phases, so that it becomes difficult to identify the particular component responsible for nucleation of acicular ferrite.

There are now many results which prove that the inclusions responsible for the heterogeneous nucleation of acicular ferrite are themselves inhomogeneous, as illustrated in Fig. 7.8. The microstructure of the *inclusions* is particularly important from the point of view of developing a clear understanding of their role in stimulating the nucleation of ferrite. As an example, it is sometimes found that the non-metallic particles in some submerged arc weld deposits consist of titanium nitride cores, surrounded by a glassy phase containing manganese,

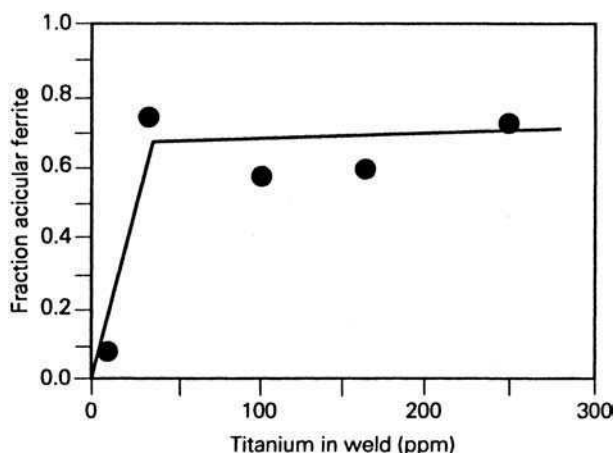


**Fig. 7.7** Large change in the acicular ferrite content as titanium is introduced into a welding alloy (after G. Evans, 1992).

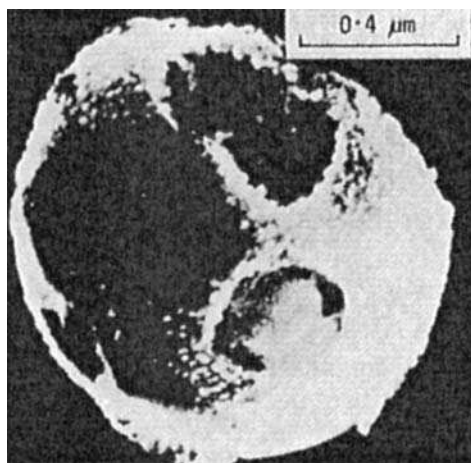


**Fig. 7.8** Scanning transmission electron micrograph of a non-metallic inclusion in a steel weld metal. The inclusion surface is very irregular, and it features many phases (courtesy of Barritte).

silicon and aluminium oxides, with a thin layer of manganese sulphide (and possibly, titanium oxide) partly covering the surface of the inclusions. The inclusions may therefore be a wide variety of oxides or other compounds, but some can influence the development of microstructure during cooling.

## 7.5 NUCLEATION OF ACICULAR FERRITE

It has been demonstrated, assuming classical nucleation theory, that inclusions are less effective in nucleating ferrite when compared with austenite grain surfaces. Experiments confirm this since ferrite formation first begins at the austenite grain boundaries. Furthermore, larger inclusions are expected to be more effective since the curvature of the inclusion/ferrite interface will then be reduced. This is confirmed by experimental observations.

### 7.5.1 Lattice matching theory

Inclusions have long been used to control solidification in aluminium alloys. The aluminium melts are inoculated with particles in order to increase the solid nucleation rate and hence produce a refined grain structure in the fully solidified condition. It is found that inclusions whose lattices match well with solid aluminium are quite effective nucleating agents. This idea has been extrapolated to solid state transformations in steels, where it is argued that those inclusions which show the best 'lattice matching' with ferrite are most effective in nucleating the ferrite.

**Table 7.1** Some misfit values between different substrates and ferrite. The data are from a more detailed set published Mills, A. R., Thewlis, G. and Whiteman, J. A., *Materials Science and Technology* **3**, 1051, 1987) and include all cases where the misfit is found to be less than 5%. The inclusions all have a cubic-F lattice and the ferrite is body-centred cubic (cubic-I)

Inclusion	Orientation	Plane of epitaxy	Misfit (%)
TiO	Bain	{1 0 0}	3.0
TiN	Bain	{1 0 0}	4.6
$\gamma$ -alumina	Bain	{1 0 0}	3.2
Galaxite	Bain	{1 0 0}	1.8
CuS	Cube	{1 1 1}	2.8

The lattice matching is expressed in terms of a mean percentage planar misfit  $\kappa$ . To calculate  $\kappa$ , it is assumed that the inclusion is faceted on a plane  $(h k l)_I$ , and that the ferrite deposits epitaxially with its plane  $(h k l)_\alpha || (h k l)_I$ , with the corresponding rational directions  $[u v w]_I$ , and  $[u v w]_\alpha$  being inclined at an angle  $\phi$  to each other. The interatomic spacings  $d$  along three such directions ( $j = 1, 2, 3$ ) within the plane of epitaxy are examined to obtain:

$$\kappa = \frac{100}{3} \sum_{j=1}^3 |d_j^I \cos \phi - d_j^\alpha| / d_j^\alpha. \quad (7.1)$$

Data calculated in this manner, for a variety of inclusions phases, are presented in Table 7.1.

To enable the lattice matching concept to be compared against experiments, it is necessary not only to obtain the right orientation relationship, but the inclusion must also be faceted on the correct plane of epitaxy. Many compounds, including some of the titanium oxides, show good matching with ferrite, and indeed seem effective in nucleating ferrite. However, there are other compounds, such as  $\gamma$ -alumina, which show good fit but are ineffective nucleants. It is likely that there is more than one mechanism which helps make a nonmetallic phase a potent heterogeneous nucleation site.

### 7.5.2 Other possibilities

Other ways in which inclusions may assist the formation of acicular ferrite include stimulation by thermal strains or by the presence of chemical heterogeneities in the vicinity of the inclusion/matrix interface. Alternatively, the inclusions may simply act as inert sites for heterogeneous nucleation. Chemical reactions are also possible at the inclusion matrix interface (Table 7.2). Those minerals which are natural oxygen sources are found to be very effective in stimulating nucleation, probably by inducing decarburization in the adjacent steel. This effect seems to be independent of the crystallographic nature of the



**Table 7.2** List of ceramics which have been tested for their potency in stimulating the nucleation of ferrite plates Gregg, J. M., Bhadeshia, H. K. D. H., *Acta Materialia* **45**, 739, 1997

Effective: oxygen sources	Effective: other mechanisms	Ineffective
TiO <sub>2</sub> , SnO <sub>2</sub> MnO <sub>2</sub> , PbO <sub>2</sub> KNO <sub>3</sub>	Ti <sub>2</sub> O <sub>3</sub> TiO	TiN, CaTiO <sub>3</sub> SrTiO <sub>3</sub> , $\alpha$ -Al <sub>2</sub> O <sub>3</sub> NbC

mineral, except in the ability of the mineral to tolerate oxygen vacancy defects, or to thermally decompose. Ti<sub>2</sub>O<sub>3</sub> has the ability to cause a dramatic reduction in the manganese concentration of the adjacent steel, and this in turn stimulates nucleation since manganese is an austenite stabilizer. TiO is puzzling in the sense that it is an effective nucleant and yet does not cause any pronounced modification of the adjacent steel. It does have a good lattice match with ferrite, but so does TiN, which is not an effective nucleant.

7.6 SUMMARY

Bainite and acicular ferrite have essentially the same transformation mechanism, but their microstructures differ in detail because the former nucleates at grain surfaces and hence grows in the form of sheaves of parallel platelets. Acicular ferrite, on the other hand, nucleates intragranularly on non-metallic inclusions, which are in effect point nucleation sites. The platelets of acicular ferrite therefore radiate from the individual inclusions, thus generating a microstructure which is much more disorganized with adjacent platelets pointing in different directions. There are many kinds of non-metallic inclusions which are effective in stimulating intragranular nucleation, but some titanium compounds are found to be particularly potent. The exact mechanism of nucleation remains to be resolved.

Acicular ferrite grows without diffusion, but the excess carbon is not retained in the supersaturated ferrite. It is partitioned into the residual austenite shortly after growth. The transformation is accompanied by shear, and rather smaller dilatational displacements which together with the reproducible orientation relationship, the plate shape and lack of chemical composition change fit a displacive mechanism of transformation.

FURTHER READING

Abson, D. J. and Pargeter, R. J., *International Metals Reviews* **31**, 141, 1986.  
Babu, S., The mechanism of acicular ferrite in weld deposits, *Current Opinion in Solid State and materials Science* **8**, 267, 2004.

- Bhadeshia, H. K. D. H., Acicular ferrite, *Bainite in Steels*, 2nd edition Institute of Materials, pp. 237–276, 2001.
- Bhadeshia, H. K. D. H., Models of acicular ferrite, *International Trends in Welding Science and Technology* (eds David S. A. and Vitek, J. M.), ASM International, pp. 213–222, 1993.
- Bhadeshia, H. K. D. H. and Svensson, L.-E., *Mathematical Modelling of Weld Phenomena* (eds Cerjak, H. and Easterling, K. E.), Institute of Materials, London, pp. 109–182, 1993.
- Chandrasekharaiah, M. N., Dubben, G. and Kolster, B. H., Atom probe study of retained austenite in ferritic weld metal, *Welding Journal* **71**, 247s, 1994.
- Gourgues, A. F., Flower, H. M. and Lindley, T. C., EBSD study of acicular ferrite, bainite and martensite, *Materials Science and Technology* **16**, 26, 2000.
- Grong, Ø., *Metallurgical Modelling of Welding*, Institute of Materials, London, 1994.
- Grong, Ø. and Matlock, D. K., *International Metals Reviews*, **31**, 27, 1986.
- Nishioka, K. and Temehiro, H., *Microalloying* '88, Chicago, 1988.
- Sugden, A. A. B. and Bhadeshia, H. K. D. H., Lower acicular ferrite, *Metallurgical Transactions* **20A**, 1811. 1989.
- Svensson, L.-E. *Control of Weld Microstructures and Properties*, CRC Press, London, 1994.

*This page intentionally left blank*

# 8

---

## THE HEAT TREATMENT OF STEELS: HARDENABILITY

### 8.1 INTRODUCTION

The traditional route to high strength in steels is by quenching to form martensite which is subsequently reheated or *tempered* at an intermediate temperature, increasing the toughness of the steel without too great a loss in strength. Therefore, for the optimum development of strength, a steel must first be fully converted to martensite. To achieve this, the steel must be quenched at a rate sufficiently rapid to avoid the decomposition of austenite during cooling to such products as ferrite, pearlite and bainite. The effectiveness of the quench will depend primarily on two factors: the geometry of the specimen, and the composition of the steel.

A large diameter rod quenched in a particular medium will obviously cool more slowly than a small diameter rod given a similar treatment. Therefore, the small rod is more likely to become fully martensitic. With the exception of cobalt and aluminium, the addition of common alloying elements to a steel usually moves the time–temperature–transformation (*TTT*) curve to longer times, thus making it easier to pass the nose of the curve during a quenching operation, i.e. there is a reduction in the critical rate of cooling needed to make a steel specimen fully martensitic. If this critical cooling rate is not achieved a steel rod will be martensitic in the outer regions which cool faster but, in the core, the slower cooling rate will give rise to bainite, ferrite and pearlite depending on the exact circumstances.

The ability of a steel to form martensite on quenching is referred to as the *hardenability*. This can be simply expressed for steel rods of standard size, as the distance below the surface at which there is 50% transformation to martensite after a standard quenching treatment, and is thus a measure of the depth of hardening.

## 8.2 USE OF *TTT* AND CONTINUOUS COOLING DIAGRAMS

*TTT* diagrams provide a good starting point for an examination of hardenability, but as they are statements of the kinetics of transformation of austenite carried out *isothermally*, they can only be a rough guide. To take one example, the effect of increasing molybdenum, Fig. 8.1 shows the *TTT* diagrams for a 0.4 wt% C–0.2 wt% Mo steel and a steel with 0.3 wt% C–2 wt% Mo. The 0.2 wt% Mo steel begins to transform in about 1 s at 550°C, but on increasing the molybdenum to 2 wt% the whole C-shaped curve is raised and the reaction substantially slowed so that the nose is above 700°C, the reaction starting after 4 min. The latter steel will clearly have a greatly enhanced hardenability over that of the 0.2 wt% Mo steel.

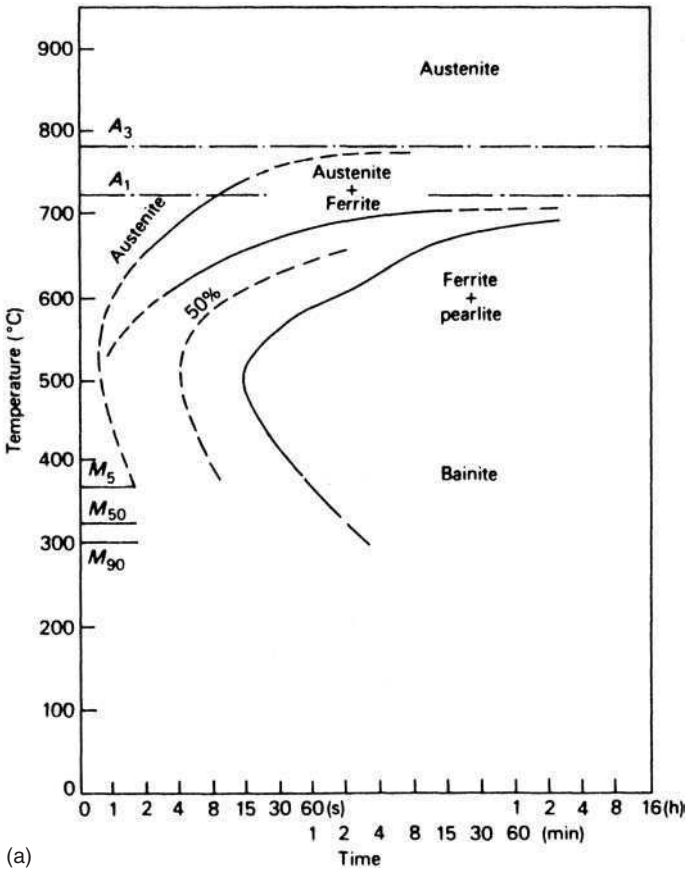


**Fig. 8.1** (a) *TTT* diagram of a molybdenum steel 0.4C, 0.2Mo (Thelning, *Steel and its Heat Treatment*, Bofors Handbook, Butterworth, 1975).

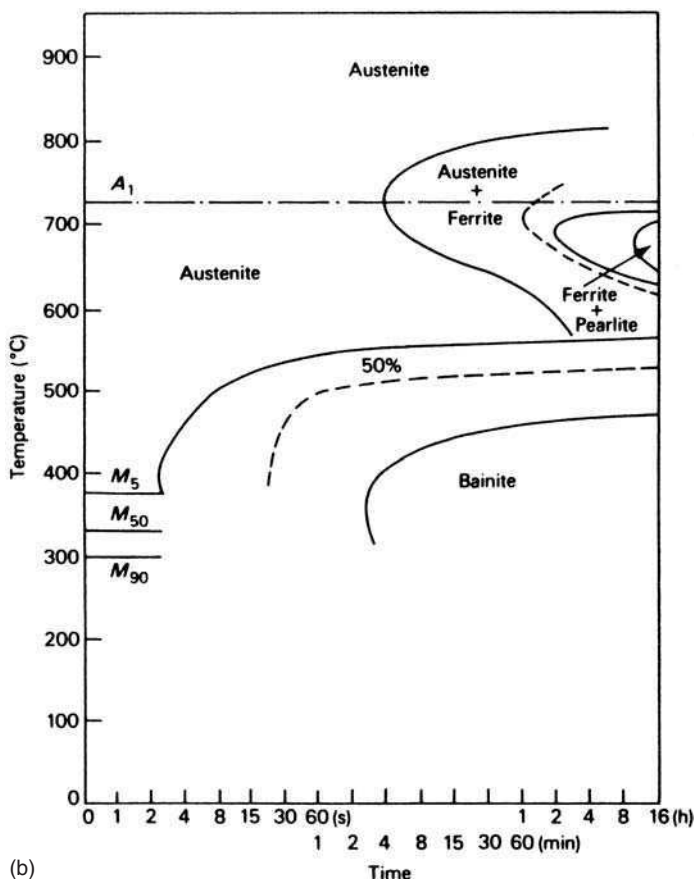


**Fig. 8.1** (b) TTT diagram of a molybdenum steel: 0.3C, 2.0Mo (Thelning, *Steel and its Heat Treatment*, Bofors Handbook, Butterworth, 1975).

The obvious limitations of using isothermal diagrams for situations involving a range of cooling rates through the transformation temperature range have led to efforts to develop more representative diagrams, i.e. continuous cooling transformation (CCT) diagrams. These diagrams record the progress of the transformation with falling temperature for a series of cooling rates. They are determined using cylindrical rods which are subjected to different rates of cooling, and the onset of transformation is detected by dilatometry, magnetic permeability or some other physical technique. The products of the transformation, whether ferrite, pearlite or bainite, are partly determined from isothermal diagrams, and can be confirmed by metallographic examination. The results are then plotted on a temperature/cooling time diagram, which records, e.g. the time to reach the beginning of the pearlite reaction over a range of cooling rates. This series of results will give rise to an austenite-pearlite boundary on the

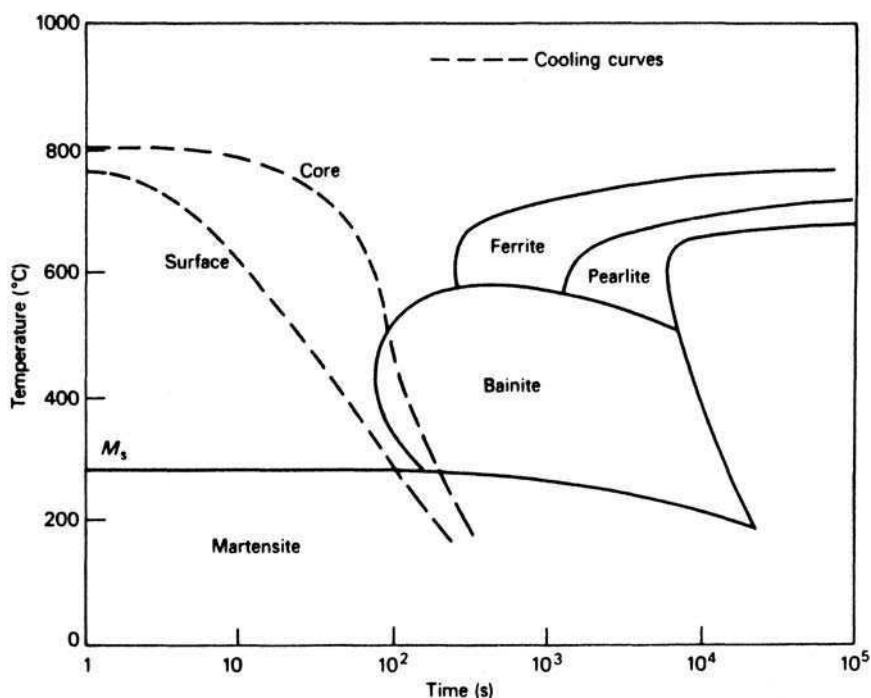


**Fig. 8.2** Relation between cooling curves for the surface and core of an oil-quenched 95-mm diameter bar and the microstructure. The surface is fully martensitic (Thelning, *Steel and its Heat Treatment*, Bofors Handbook, Butterworth, 1975).

diagram and, likewise, lines showing the onset of the bainite transformation can be constructed. A schematic diagram is shown in Fig. 8.2 in which the boundaries for ferrite, pearlite, bainite and martensite are shown for a hypothetical steel. The diagram is best used by superimposing a transparent overlay sheet with the same scales and having lines representing various cooling rates drawn on it. The phases produced at a chosen cooling rate are then those which the superimposed line intersects on the CCT diagram. In Fig. 8.2 two typical cooling curves are superimposed for the surface and the centre of an oil-quenched 95-mm diameter bar. In this example, it should be noted that the centre cooling curve intersects the bainite region and consequently some bainite would be expected at the core of the bar after quenching in oil.

### 8.3 HARDENABILITY TESTING

The rate at which austenite decomposes to form ferrite, pearlite and bainite is dependent on the composition of the steel, as well as on other factors such as the austenite grain size, and the degree of homogeneity in the distribution of the alloying elements. It is now possible to estimate hardenability using phase

transformation theory, but there is also a reliance on one of several practical tests, which allow the hardenability of any steel to be readily determined.

### 8.3.1 The Grossman test

Much of the earlier systematic work on hardenability was done by Grossman and co-workers who developed a test involving the quenching, in a particular cooling medium, of several cylindrical bars of different diameter of the steel under consideration. Transverse sections of the different bars on which hardness measurements have been made will show directly the effect of hardenability. In Fig. 8.3, which plots this hardness data for an SAE 3140 steel (1.1–1.4Ni, 0.55–0.75Cr, 0.40C wt%) oil-quenched from 815°C, it is shown that the full martensitic hardness is only obtained in the smaller sections, while for larger diameter bars the hardness drops off markedly towards the centre of the bar. The softer and harder regions of the section can also be clearly resolved by etching.

In the Grossman test, the transverse sections are metallographically examined to determine the particular bar which has 50% martensite at its centre. The diameter of this bar is then designated the critical diameter  $D_0$ . However, this dimension is of no absolute value in expressing the hardenability as it will obviously vary if the quenching medium is changed, e.g. from water to oil. It is therefore necessary to assess quantitatively the effectiveness of the different quenching media. This is done by determining coefficients for the severity of the

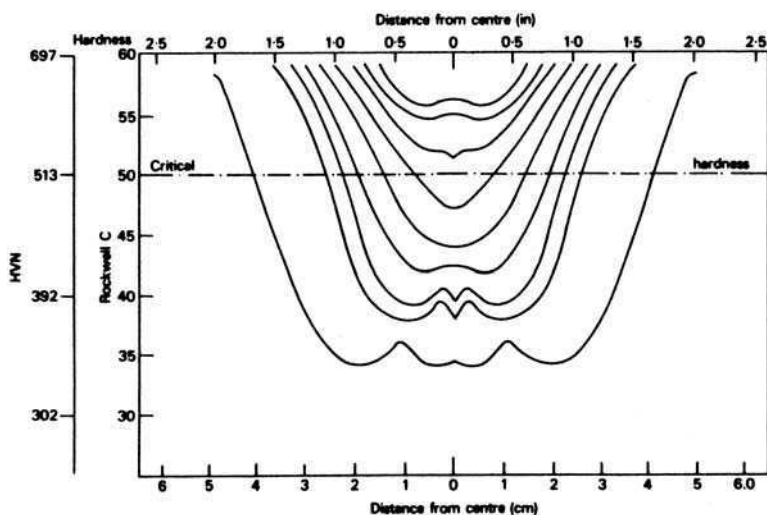


**Fig. 8.3** 1.1 Ni–0.75Cr–0.4C steel. Hardness data from transverse sections through water-quenched bars of increasing diameter (Grossman et al., in *Alloying Elements in Steel* (eds Bain and Paxton), ASM, Ohio, USA, 1961).



**Table 8.1**  $H$ -coefficients of quenching media.

Agitation	Cooling medium		
	Oil	Water	Brine
None	0.25–0.30	1.0	2.0
Moderate	0.35–0.40	1.2–1.3	
Violent	0.8–1.1	4.0	5.0

quench usually referred to as  $H$ -coefficients. Typical values for three common quenching media and several conditions of agitation are shown in Table 8.1. The value for quenching in still water is set at 1, as a standard against which to compare other modes of quenching.

Using the  $H$ -coefficients, it is possible to determine in place of  $D_0$ , an ideal critical diameter  $D_i$  which has 50% martensite at the centre of the bar when the surface is cooled at an infinitely rapid rate, i.e. when  $H = \infty$ . Obviously, in these circumstances  $D_0 = D_i$ , thus providing the upper reference line in a series of graphs for different values of  $H$  (Fig. 8.4). In practice,  $H$  varies between about 0.2 and 5.0 (Table 8.1), so that if a quenching experiment is carried out at an  $H$ -value of, say, 0.4, and  $D_0$  is measured, then the graph of Fig. 8.4 can be used

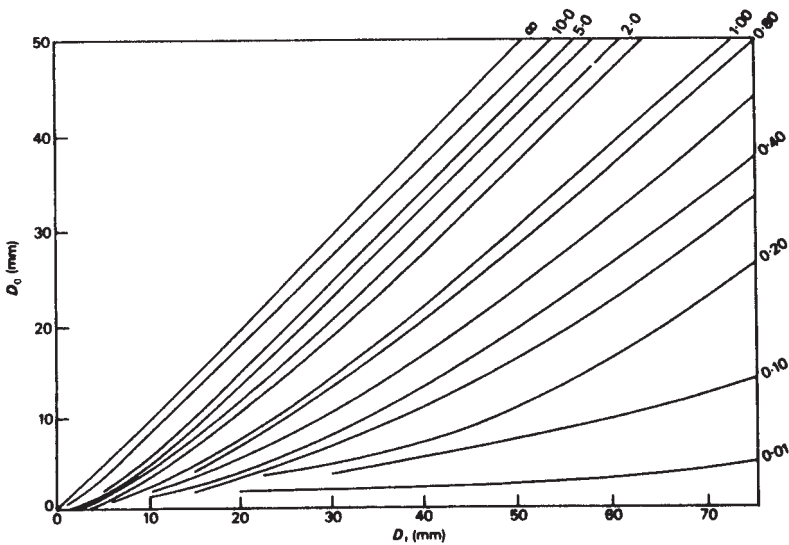


**Fig. 8.4** Chart for determining ideal diameter ( $D_i$ ) from the critical diameter ( $D_0$ ) and the severity of quench ( $H$ ) for carbon and medium alloy steels (Grossman and Bain, *Principles of Heat Treatment*, ASM, Ohio, USA, 1964).

to determine  $D_i$ . This value will be a measure of the hardenability of a given steel, which is independent of the quenching medium used.

### 8.3.2 The Jominy end quench test

While the Grossman approach to hardenability is very reliable, other less elaborate tests have been devised to provide hardenability data. Foremost amongst these is the Jominy test, in which a standardized round bar (25.4 mm diameter, 102 mm long) is heated to the austenitizing temperature, then placed on a rig in which one end of the rod is quenched by a standard jet of water (Figs. 8.5a, b). This results in a progressive decrease in the rate of cooling along the bar from the quenched end, the effects of which are determined by hardness measurements on flats ground 4 mm deep and parallel to the bar axis (Fig. 8.5c). A typical hardness plot for a steel containing 0.4C–1Cr–0.25Mo wt% (En 19B) is shown in Fig. 8.6, where the upper curve represents the hardness obtained with the upper limit of composition for the steel, while the lower curve is that for the composition at the lower limit. The area between the lines is referred to as a hardenability or Jominy band. Additional data, which are useful in conjunction with these results, is the hardness of quenched steels as a function both of carbon content and of the proportion of martensite in the structure. These data are given in Fig. 8.7 for as-quenched steels with 50–90% martensite. Therefore, the hardness for 50% martensite can be easily determined for a particular carbon content and, by inspection of the Jominy test results, the depth at which 50% martensite is achieved can be determined.

The Jominy test is now widely used to determine hardenabilities in the range  $D_i = 1\text{--}6\text{ cm}$ ; beyond this range the test is of limited use. The results can be readily converted to determine the largest diameter round bar which can be fully hardened. Figure 8.8 plots bar diameter against the Jominy positions at which the same cooling rates as those in the centres of the bars are obtained for a series of different quenches. Taking the ideal quench ( $H = \infty$ ), the highest curve, it can be seen that 12.5 mm along the Jominy bar gives a cooling rate equivalent to that at the centre of a 75-mm diameter bar. This diameter reduces to just over 50 mm for a quench in still water ( $H = 1$ ). With, e.g., a steel which gives 50% martensite at 19 mm from the quenched end after still oil quenching ( $H = 0.3$ ), the critical diameter  $D_0$  for a round rod will be 51 mm.

The diagram in Fig. 8.8 can also be used to determine the hardness at the centre of a round bar of a particular steel, provided a Jominy end quench test has been carried out. For example, if the hardness at the centre of a 50-mm diameter bar, quenched in still water, is required, Fig. 8.8 shows that this hardness will be achieved at about 12 mm along the Jominy test specimen from the quenched end. Reference to the Jominy hardness distance plot then gives the required hardness value. If hardness values are required for other points in round bars, e.g. surface or at half-radius, suitable diagrams are available for use.

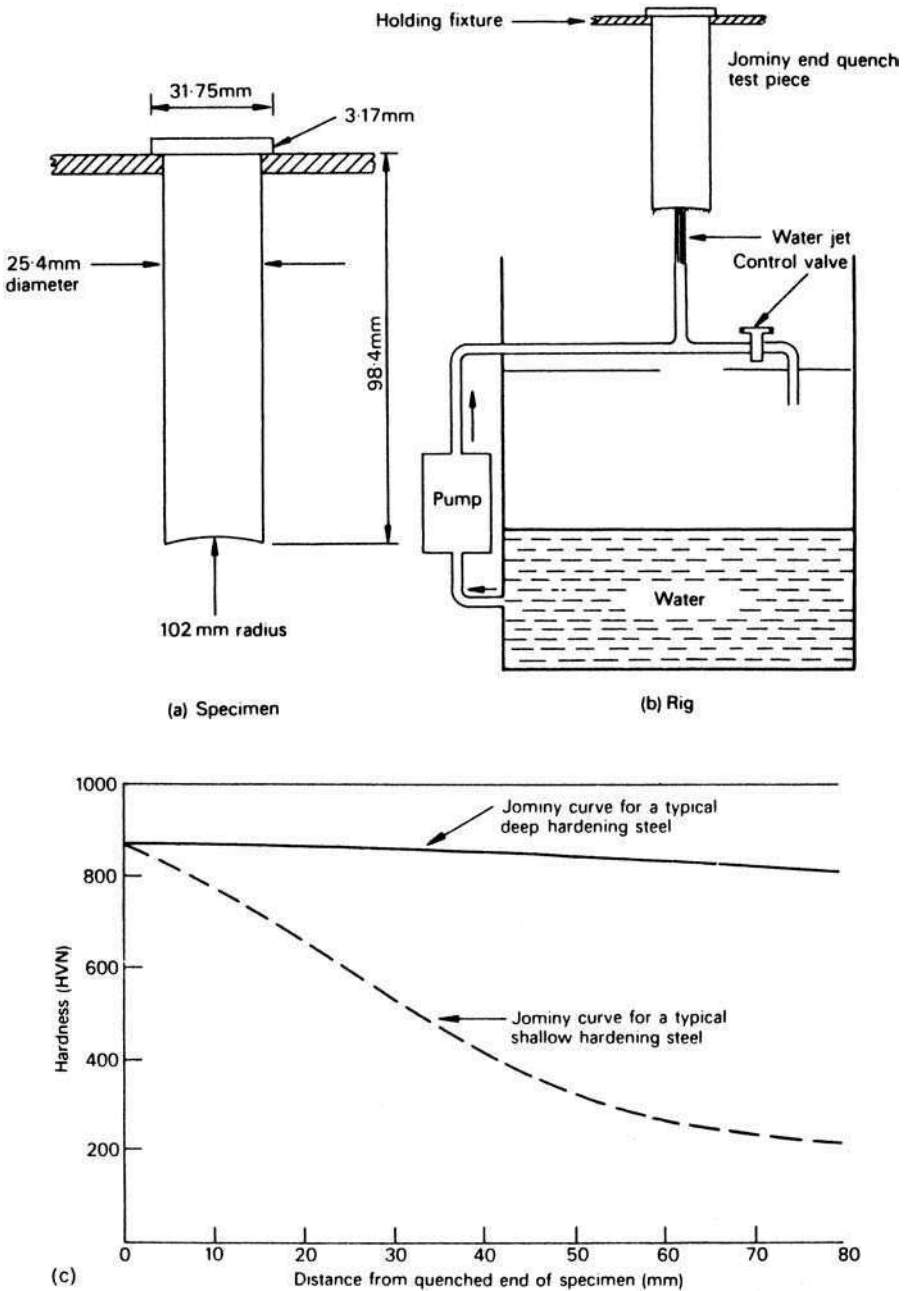


**Fig. 8.5** The Jominy end quench test: (a) specimen size; (b) quenching rig; (c) Jominy hardness-distance curves for a shallow and a deep hardening steel (Wilson, *Metallurgy and Heat Treatment of Tool Steels*, McGraw-Hill, 1975).

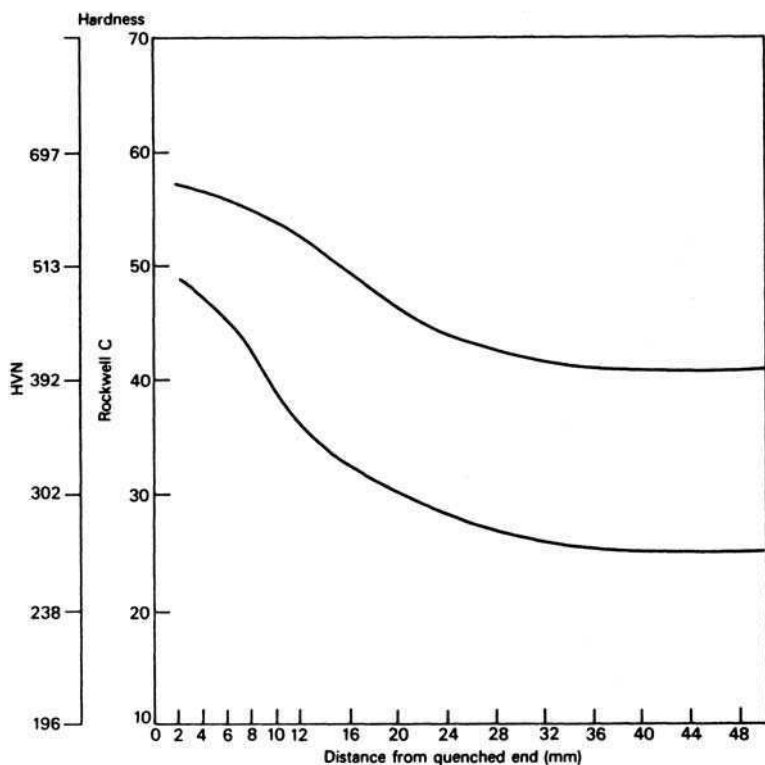


**Fig. 8.6** Jominy curves for upper and lower limits of a steel, En 19B, giving a hardenability band (Thelning, *Steel and its Heat Treatment*, Bofors Handbook, Butterworth, 1975).

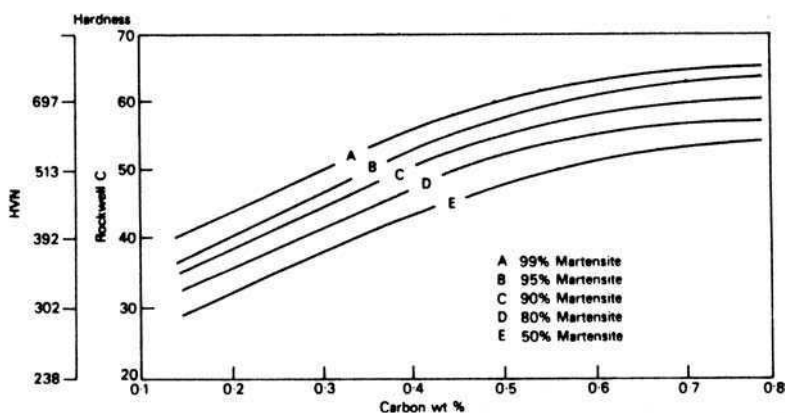


**Fig. 8.7** The effect of percentage of martensite and carbon content on as-quenched hardness (Thelning, *Steel and its Heat Treatment*, Bofors Handbook, Butterworth, 1975).

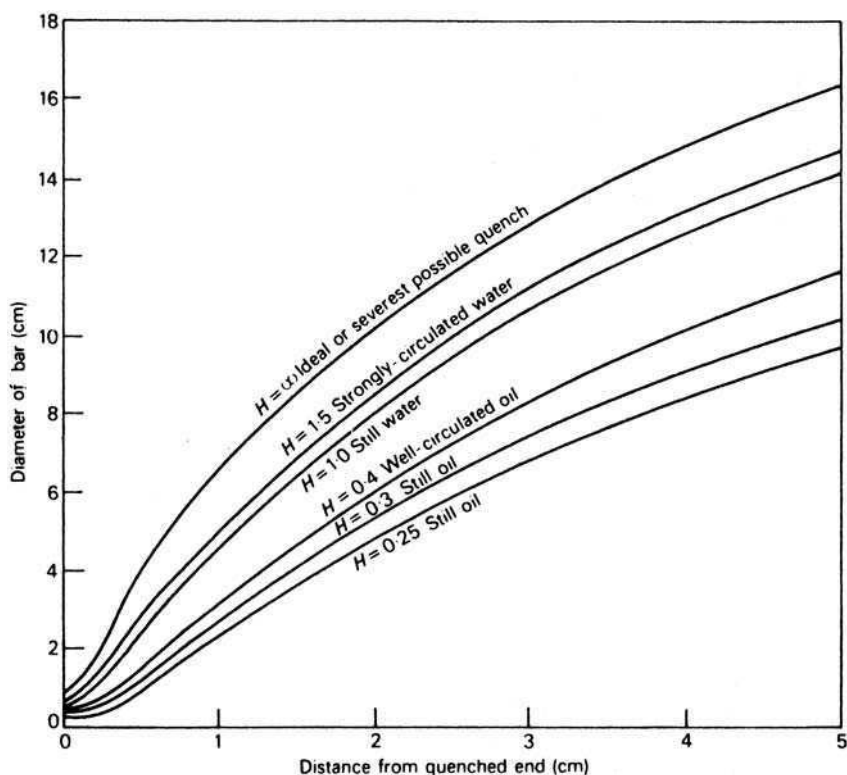


**Fig. 8.8** Equivalent Jominy positions and bar diameter, where the cooling rate for the bar centre is the same as that for the point in the Jominy specimen. Curves are plotted for a range of cooling rates (Grossman and Bain, *Principles of Heat Treatment*, ASM, Ohio, USA, 1964).

#### 8.4 EFFECT OF GRAIN SIZE AND CHEMICAL COMPOSITION ON HARDENABILITY

The two most important variables which influence hardenability are austenite grain size and composition. The hardenability increases with increasing austenite grain size, because the grain boundary area per unit volume decreases. The sites for the nucleation of ferrite and pearlite are reduced in number, with the result that these transformations are slowed down, and the hardenability therefore increases. Alloying elements which slow down the ferrite and pearlite reactions increase hardenability. However, quantitative assessment of these effects is needed.

The first step is to determine the effect of grain size and of carbon content. Data are available, in so far as  $D_i$  has been determined for steels with carbon in the range 0.2–1 wt%, and for a range of grain sizes (ASTM 4–8), as shown in Fig. 8.9. Use of this diagram for any steel provides a base hardenability figure,

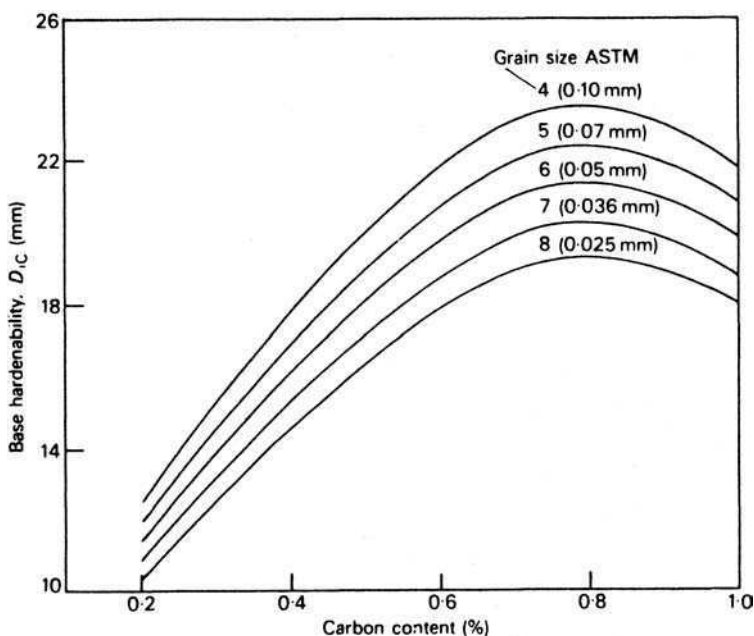


**Fig. 8.9** Effect of carbon content and grain size on base hardenability (Moser and Legat, *Härterei Technische Mitteilungen* **24**, 100, 1969).

$D_{iC}$ , which must be modified by taking into account the effect of additional alloying elements. This is done by use of multiplying factors which have been experimentally determined for the familiar alloying elements (Fig. 8.10). The ideal critical diameter  $D_i$  is then found from the empirical relationship:

$$D_i = D_{iC} \times 2.21 (\% \text{Mn}) \times 1.40 (\% \text{Si}) \times 2.13 (\% \text{Cr}) \\ \times 3.275 (\% \text{Mo}) \times 1.47 (\% \text{Ni}) \text{ (weight percentages)}. \quad (8.1)$$

This relationship, due to Moser and Legat, appears to be more accurate in practice than a much earlier one put forward by Grossman. Further corrections have to be made for different austenitizing temperatures when dealing with high carbon steels, but, on the whole, the relationship is quite effective in predicting actual hardening behaviour.

## 8.5 HARDENABILITY AND HEAT TREATMENT

While alloying elements are used for various reasons, the most important is the achievement of higher strength in required shapes and sizes and often in very large sections which may be up to a metre or more in diameter in the case of large shafts and rotors. Hardenability is, therefore, of the greatest importance, and one must aim for the appropriate concentrations of alloying element needed to

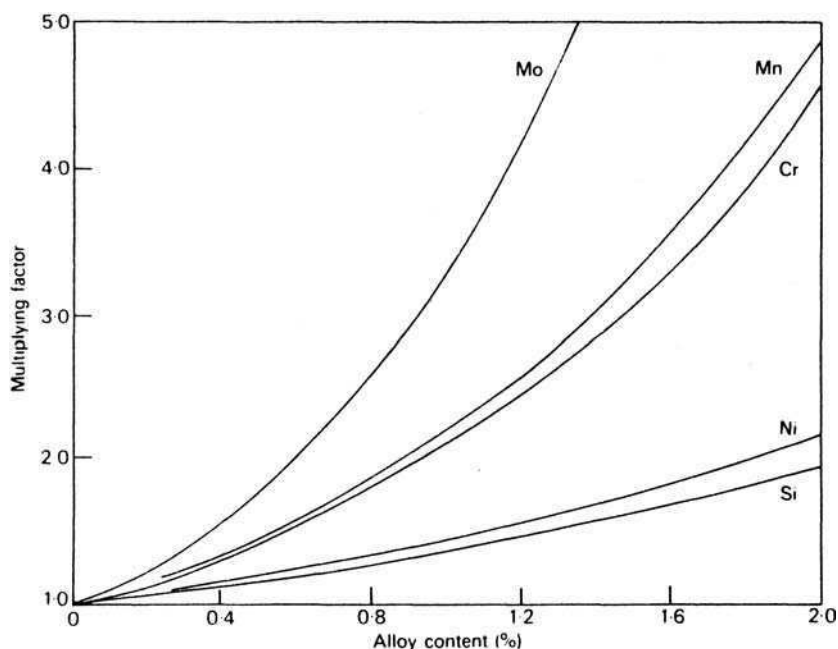


**Fig. 8.10** Hardenability multiplying factors for common alloying elements (Moser and Legat, *Härtereitechnische Mitteilungen* **24**, 100, 1969).

harden fully the section of steel under consideration. Equally, there is little point in using too high a concentration of expensive alloying elements, i.e. more than that necessary for full hardening of the required sections. Carbon has a marked influence of hardenability, but its use at higher levels is limited, because of the lack of toughness which results, as well as the greater difficulties in fabrication and, more important, increased probability of distortion and cracking during heat treatment and welding.

The most economical way of increasing the hardenability of a plain carbon steel is to increase the manganese content, an increase from 0.60 to 1.40 wt%, giving a substantial improvement in hardenability. Chromium and molybdenum are also very effective, and amongst the cheaper alloying additions per unit of increased hardenability. Boron has a particularly large effect when added to a fully deoxidized low carbon steel, even in concentration of the order of 0.001 wt%, and would be more widely used if its distribution in steel could be more easily controlled. The role of grain size should not be overlooked because an increase in grain diameter from 0.02 to 0.125 mm can increase the hardenability by as much as 50%, which is very acceptable provided the mechanical properties, particularly toughness, are not too adversely affected.

High hardenability is not always desirable for many tool and machine parts, where a hard wear-resistant surface is best combined with a tough core. Such

shallow hardening situations are additionally preferred because, on quenching, the core develops a tensile internal stress while the surface becomes stressed in compression. This situation is very desirable because any fatigue cracks nucleated at surface stress concentrations will find propagation more difficult when a compressive stress is present.

## 8.6 QUENCHING STRESSES AND QUENCH CRACKING

The act of quenching often leads to distortion in the part and even serious cracking (*quench cracking*). These defects arise from internal stresses which develop during quenching from two sources:

- 1 *Thermal stresses* arising directly from the different cooling rates experienced by the surface and the interior of the steel.
- 2 *Transformation stresses* due to the volume changes which occur when austenite transforms to other phases.

An example of the effect of thermal stresses is given in Fig. 8.11 for a 100-mm diameter steel bar quenched into water from 850°C. The temperature–time relationship for the surface and the core are given in Fig. 8.11a, from which it is seen that the maximum temperature difference occurs after a time  $t$ , when it is about 500°C, which could give rise to a stress in excess of  $1000 \text{ MN m}^{-2}$ , if no relaxation took place. Under these conditions, the surface stress–time relationship would be that of curve A, Fig. 8.11b. However, the maximum stress level is not sustained because plastic deformation takes place and the stress–time relationship in reality is that indicated by curve B. The tensile stress in the surface is balanced by a compressive stress in the core as shown by curve C. At some lower temperature  $t_2$  the compressive and tensile stresses will both fall to zero but as the temperature drops further to room temperature the stress situation reverses and the core goes into tension and the surface into compression. Figure 8.11c shows the stress distribution through the bar at room temperature.

The more rapid the quench, the higher the temperature difference between core and surface during quenching and, therefore, the higher the resulting stresses at room temperature. In practical terms this means that avoidance of distortion involves the use of less drastic quenching media, e.g. oil instead of water, and consequently adjustments have to be made to the hardenability if full hardening through the section is required.

Transformation stresses arise from the change in volume associated with the formation of a new phase. For example, when austenite transforms to martensite in a 1 wt% carbon steel, there is an increase in volume of 4%, while the transformation to pearlite results in an increase of 2.4%. The effect of these volume changes on the stress pattern developed depends on whether the reaction at surface and core start simultaneously, and whether the hardenability is sufficient to permit full hardening or not. If the martensite reaction starts at the surface, a



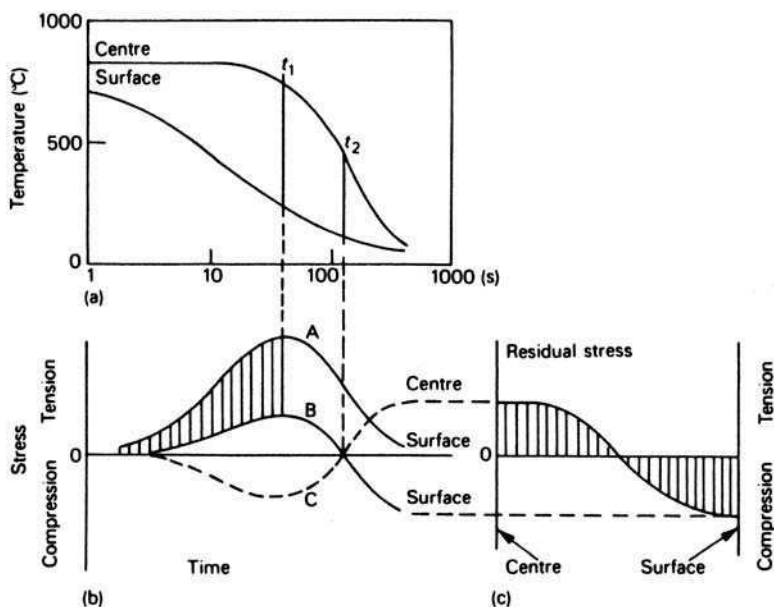


**Fig. 8.11** Development of thermal stresses during cooling of a 100-mm diameter bar quenched into water from 850°C (after Rose, *Härterei Technische Mitteilungen* 21, 1, 1966).

tensile stress is generated there and a compressive stress occurs at the centre, a situation which is accentuated by having the martensite reaction throughout the diameter, i.e. in small sections, or in steels of high hardenability. The presence of a tensile stress in the surface is not advisable for reasons given above, so it is clear that in some cases high hardenability can create problems. These can be avoided by the use of steels which provide only a relative thin hardened layer at the surface which can be maintained in a state of compression. Surface treatment methods such as carburizing and nitriding, where the interstitial element concentration is substantially increased by a diffusive process, not only lead to hard wear resistant surfaces, but also surfaces which resist crack propagation by being subject to compressive stresses.

Martensite becomes more brittle with increasing carbon content. In higher carbon martensites, which tend to exhibit the burst phenomenon in which individual martensite plates are successively nucleated by previous plates, cracks are often observed in plates at points of impact of later plates upon them. These micro-cracks provide obvious nuclei for the propagation of major cracks. In broader terms, quench cracking is likely to occur when quenching stresses have not been sufficiently released by plastic deformation at elevated temperatures, and they therefore reach the fracture stress of the steel. As in the case of fatigue cracking, the safest situation is to have the most sensitive region of the steel under compressive stresses.

There are some fairly obvious precautions which can be taken to avoid such cracking, including the use of the slowest quench compatible with the achievement of adequate hardenability. Also stress concentrations in the form of notches, heavy machining grooves and sudden changes in cross section should be avoided where possible, as these will all encourage quench-crack nucleation.

The composition of the steel is important because the transformation characteristics will influence the incidence of cracking. The effect of carbon has already been referred to but, additionally, the  $M_s$  temperature decreases with increasing carbon content. Thus, in higher carbon steels, the quenching stresses are less likely to be relieved than would be the case if the martensite begins to form at a higher temperature where the steel is more able to relieve stresses by flow than by fracture. Further, the lower the  $M_s$  temperature the larger the change in volume during the transformation and, therefore, the higher the transformation stresses developed. Metallic alloying elements also depress the  $M_s$ , but by substantially increasing the hardenability they allow the use of less drastic quenching which greatly reduces the probability of distortion and cracking.

## FURTHER READING

- Brooks, C. R., *Heat Treatment of Ferrous Alloys*, McGraw-Hill, USA, 1979.
- Doane, D. V. and Kirkaldy, J. S. (eds), *Hardenability Concepts with Applications to Steel*, The Metallurgical Society of AIME, Pennsylvania, USA, 1978.
- Dobrzanski, L. A., and Sitek, W., Modelling of hardenability using neural networks, *Journal of the Materials Processing Technology* **93**, 8, 1999.
- Grossman, M. A. and Bain, E. C., *Principles of Heat Treatment*, 5th edition, American Society for Metals, Ohio, USA, 1964.
- Kasuya, T., Ichikawa, K. and Fuji, M., Derivation of carbon equivalent to assess hardenability of steels, *Science and Technology of Welding and Joining* **3**, 317, 1998.
- Li, M. V., Niebuhr, D. V., Meekisho, L. L. and Atteridge, D. G., Computational model for the prediction of steel hardenability, *Metallurgical & Materials Transactions* **29B**, 661, 1998.
- Llewellyn, D. T., *Steels – Metallurgy and Applications*, Butterworth, UK, 1992.
- Ohtani, H., Processing – conventional treatments, in *Materials Science and Technology* (eds Cahn, R. W., Haasen, P. and Kramer, E. J.), Vol. 7, *Constitution and Properties of Steels* (ed. Pickering, F. B.), 1992.
- Pickering, F. B., *Physical Metallurgy and the Design of Steels*, Applied Science Publishers, London, UK, 1978.
- Sinha, A. K., *Ferrous Physical Metallurgy*, Butterworth, USA, 1993.
- Thelning, K. E., *Steel and its Heat Treatment*, 2nd edition, Bofors Handbook, Butterworth, London, UK, 1985.
- Wilson, R., *Metallurgy and Heat Treatment of Tool Steels*, McGraw-Hill, USA, 1975.
- Yurioka, N., Physical metallurgy of steel weldability, *ISIJ International* **41**, 566, 2001.

*This page intentionally left blank*

# 9

## THE TEMPERING OF MARTENSITE

### 9.1 INTRODUCTION

Martensite in steels can be a very strong and in its virgin condition rather brittle. It is then necessary to modify its mechanical properties by heat treatment in the range 150–700°C. This process is called *tempering*, in which the microstructure approaches equilibrium under the influence of thermal activation.

The tendency of the microstructure to temper depends on how far it deviates from equilibrium. The data in Table 9.1 show the components of the excess free energy of martensite in a typical low-alloy steel of chemical composition Fe–0.2C–1.5Mn wt%. The reference state is the equilibrium mixture of ferrite, graphite and cementite, with a zero stored energy. Graphite precipitates incredibly slowly in steels and is almost never observed during tempering – not surprising given that it only increases the free energy by a small amount (70 J mol<sup>-1</sup>). Preventing the substitutional solute, manganese, from partitioning between the ferrite and the austenite adds a substantial amount of energy, but the greatest stored energy increase comes from the trapping of carbon in supersaturated ferrite. Martensite is in Table 9.1 distinguished from supersaturated ferrite by including the strain and interfacial energies due to its mechanism of transformation.

The general trend during the tempering of martensite therefore begins with the rejection of excess carbon to precipitate carbides but the substitutional

**Table 9.1** Stored free energies of a variety of microstructures

Phase mixture in Fe–0.2C–1.5Mn wt% at 300 K	Stored energy/J mol <sup>-1</sup>
Ferrite, graphite and cementite	0
Ferrite and cementite	70
Para-equilibrium ferrite and para-equilibrium cementite	385
Supersaturated ferrite	1414
Martensite	1714

solutes do not diffuse during this process. The end result of tempering is a dispersion of coarse carbides in a ferritic matrix which bears little resemblance to the original martensite.

It should be borne in mind that in many steels, the martensite reaction does not go to completion on quenching, resulting in varying amounts of retained austenite which does not remain stable during the tempering process.

## 9.2 TEMPERING OF PLAIN CARBON STEELS

The as-quenched martensite possesses a complex structure which has been referred to in Chapter 5. The laths or plates are heavily dislocated to an extent that individual dislocations are very difficult to observe in thin-foil electron micrographs. A typical dislocation density for a 0.2 wt% carbon steel is between  $0.3$  and  $1.0 \times 10^{12} \text{ cm cm}^{-3}$ . As the carbon content rises above about 0.3 wt%, fine twins about 5–10 nm wide are also observed. Often carbide particles, usually rods or small plates, are observed (Fig. 9.1). These occur in the first-formed martensite, i.e. the martensite formed near  $M_s$ , which has the opportunity of tempering during the remainder of the quench. This phenomenon, which is referred to as *auto-tempering*, is clearly more likely to occur in steels with a high  $M_s$ .

On reheating as-quenched martensite, the tempering takes place in four distinct but overlapping stages:

*Stage 1*, up to 250°C: precipitation of  $\epsilon$ -iron carbide; partial loss of tetragonality in martensite.

*Stage 2*, between 200°C and 300°C: decomposition of retained austenite.

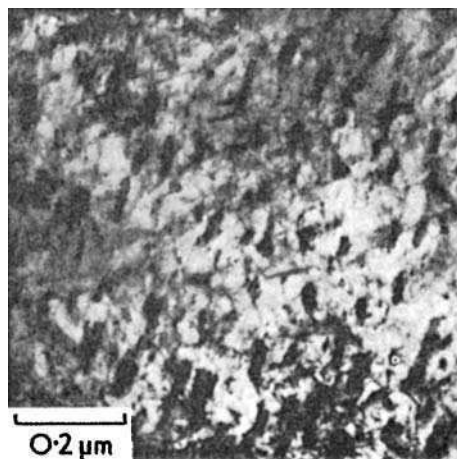


**Fig. 9.1** Fe-0.2C quenched from 1100°C into iced brine. Auto-tempered martensite (courtesy of Ohmori). Thin-foil electron micrograph.

*Stage 3*, between 200°C and 350°C: replacement of  $\epsilon$ -iron carbide by cementite; martensite loses tetragonality.

*Stage 4*, above 350°C: cementite coarsens and spheroidizes; recrystallization of ferrite.

### 9.2.1 Tempering: stage I

Martensite formed in medium and high-carbon steels (0.3–1.5 wt% C) is not stable at room temperature because interstitial carbon atoms can diffuse in the tetragonal martensite lattice at this temperature. This instability increases between room temperature and 250°C, when  $\epsilon$ -iron carbide precipitates in the martensite (Fig. 9.2). This carbide has a close-packed hexagonal structure, and precipitates as narrow laths or rodlets on cube planes of the matrix with a well-defined orientation relationship (Jack):

$$(101)_{\alpha'} // (10\bar{1}1)_{\epsilon},$$

$$(011)_{\alpha'} // (0001)_{\epsilon},$$

$$[11\bar{1}]_{\alpha'} // [\bar{1}210]_{\epsilon}.$$

X-ray measurements indicate that the lattice spacings of  $(101)_{\alpha}$  and  $(10\bar{1}1)_{\epsilon}$  are within about 0.5%, so lattice coherency is likely in the early stages of precipitation. In fact, in the higher-carbon steels, an increase in hardness has been observed on tempering in the range 50–100°C, which is attributed to precipitation hardening of the martensite by  $\epsilon$ -carbide. At the end of stage 1 the martensite still possesses a tetragonality, indicating a carbon content of around

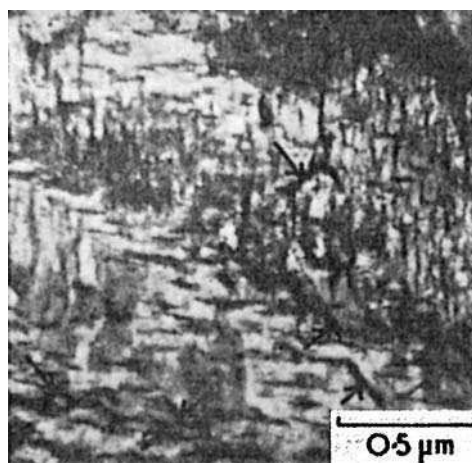


**Fig. 9.2** Fe–0.8C quenched and tempered at 250°C. Precipitates of  $\epsilon$  carbide and cementite (arrowed) (courtesy of Ohmori). Thin-foil electron micrograph.

0.25 wt%. It follows that steels with lower carbon contents are unlikely to precipitate  $\varepsilon$ -carbide. This stage of tempering possess an activation energy of between 60 and 80 kJ mol<sup>-1</sup>, which is in the right range for diffusion of carbon in martensite. The activation energy has been shown to increase linearly with the carbon concentration between 0.2 and 1.5 wt% C. This would be expected as increasing the carbon concentration also increases the occupancy of the preferred interstitial sites, i.e. the octahedral interstices at the mid-points of unit cell edges, and centres of cell faces, thus reducing the mobility of the C atoms.

### 9.2.2 Tempering: stage 2

During stage 2, austenite retained during quenching is decomposed, usually in the temperature range 230–300°C. Cohen and coworkers were able to detect this stage by X-ray diffraction measurements as well as dilatometric and specific volume measurements. However, the direct observation of retained austenite in the microstructure has always been rather difficult, particularly if it is present in low concentrations. In martensitic plain carbon steels below 0.5 wt% carbon, the retained austenite is often below 2%, rising to around 6% at 0.8 wt% C and over 30% at 1.25 wt% C. The little available evidence suggests that in the range 230–300°C, retained austenite decomposes to bainitic ferrite and cementite, but no detailed comparison between this phase and lower bainite has yet been made.

### 9.2.3 Tempering: stage 3

During the third stage of tempering, cementite first appears in the microstructure as a Widemanstätten distribution of plates which have a well-defined orientation relationship with the matrix which has now lost its tetragonality and become ferrite. The relationship is that due to Bagaryatski:

$$(211)_{\alpha} // (001)_{\text{Fe}_3\text{C}},$$

$$[01\bar{1}]_{\alpha} // [100]_{\text{Fe}_3\text{C}},$$

$$[\bar{1}11]_{\alpha} // [010]_{\text{Fe}_3\text{C}}.$$

This reaction commences as low as 100°C and is fully developed at 300°C, with particles up to 200 nm long and ~15 nm in thickness. Similar structures are often observed in lower-carbon steels as-quenched, as a result of the formation of Fe<sub>3</sub>C during the quench. During tempering, the most likely sites for the nucleation of the cementite are the  $\varepsilon$ -iron carbide interfaces with the matrix (Fig. 9.2), and as the Fe<sub>3</sub>C particles grow, the  $\varepsilon$ -iron carbide particles gradually disappear.

The twins occurring in the higher carbon martensites are also sites for the nucleation and growth of cementite which tends to grow along the twin boundaries forming colonies of similarly oriented lath-shaped particles (Fig. 9.3) of

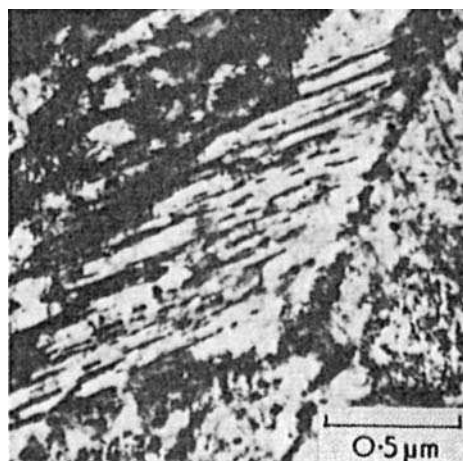


**Fig. 9.3** Fe–0.8C quenched and tempered at 450°C Fe<sub>3</sub>C growing along twin boundaries (courtesy of Ohmori). Thin-foil electron micrograph.

{112}<sub>α</sub> habit, which can be readily distinguished from the normal Widmanstätten habit. The orientation relationship with the ferritic matrix is the same in both these cases.

A third site for the nucleation of cementite is the grain boundary regions (Fig. 9.4), both the interlath boundaries of the martensite and the original austenite grain boundaries. The cementite can form as very thin films which are difficult to detect but which gradually spheroidize to give rise to well-defined particles of Fe<sub>3</sub>C in the grain boundary regions. There is some evidence to show that

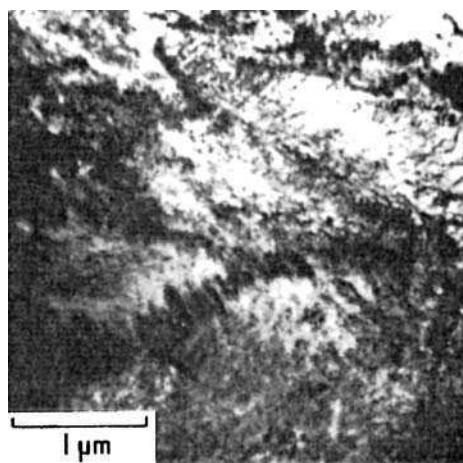


**Fig. 9.4** Fe–0.8C quenched and tempered at 250°C. Grain boundary precipitation of cementite (courtesy of Ohmori). Thin-foil electron micrograph.



these grain boundary cementite films can adversely affect ductility. However, they can be modified by addition of alloying elements.

During the third stage of tempering the tetragonality of the matrix disappears and it is then, essentially, ferrite, not supersaturated with respect to carbon. Subsequent changes in the morphology of the cementite particles occur by an Ostwald ripening type of process, where the smaller particles dissolve in the matrix providing carbon for the selective growth of the larger particles.

#### 9.2.4 Tempering: stage 4

It is useful to define a fourth stage of tempering in which the cementite particles undergo a coarsening process and essentially lose their crystallographic morphology, becoming spheroidized. The coarsening commences between 300°C and 400°C, while spheroidization takes place increasingly up to 700°C. At the higher end of this range of temperature the martensite lath boundaries are replaced by more equi-axed ferrite grain boundaries by a process which is best described as recrystallization. The final result is an equi-axed array of ferrite grains with coarse spheroidized particles of  $\text{Fe}_3\text{C}$  (Fig. 9.5), partly, but not exclusively, at the grain boundaries.

The spheroidization of the  $\text{Fe}_3\text{C}$  is encouraged by the resulting decrease in surface energy. The particles which preferentially grow and spheroidize are located mainly at interlath boundaries and prior austenite boundaries, although some particles remain in the matrix. The boundary sites are preferred because of the greater ease of diffusion in these regions. Also, the growth of cementite

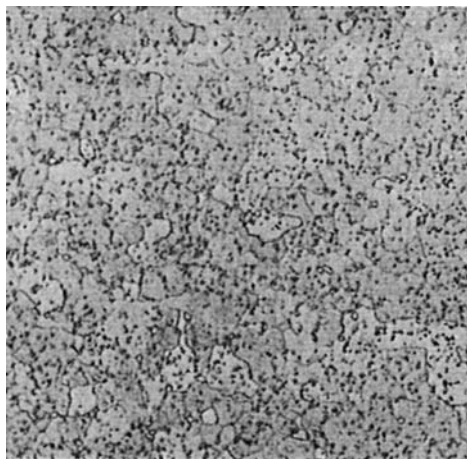


**Fig. 9.5** Fe–0.17C water-quenched from 900°C and tempered 5 h at 650°C. Spheroidized  $\text{Fe}_3\text{C}$  in equi-axed ferrite (courtesy of Lenel). Optical micrograph,  $\times 350$ .

into ferrite is associated with a decrease in density so vacancies are required to accommodate the growing cementite. Vacancies will diffuse away from cementite particles which are redissolving in the ferrite and towards cementite particles which are growing, so that the rate-controlling process is likely to be the diffusion of vacancies. The measured activation energies are much higher ( $210\text{--}315\text{ kJ mol}^{-1}$ ), than that for diffusion of carbon in ferrite ( $\sim 84\text{ kJ mol}^{-1}$ ), and much closer to the activation energy for self diffusion in  $\alpha$ -iron ( $\sim 250\text{ kJ mol}^{-1}$ ).

The original martensite lath boundaries remain stable up to about  $600^\circ\text{C}$ , but in the range  $350\text{--}600^\circ\text{C}$ , there is considerable rearrangement of the dislocations within the laths and at those lath boundaries which are essentially low angle boundaries. This leads to a marked reduction in the dislocation density and to lath-shaped ferritic grains closely related to the packets of similarly oriented laths in the original martensite. This process, which is essentially one of recovery, is replaced between  $600^\circ\text{C}$  and  $700^\circ\text{C}$  by recrystallization which results in the formation of equi-axed ferrite grains with spheroidal  $\text{Fe}_3\text{C}$  particles in the boundaries and within the grains. This process occurs most readily in low-carbon steels. At higher carbon contents the increased density of  $\text{Fe}_3\text{C}$  particles is much more effective in pinning the ferrite boundaries, so recrystallization is much more sluggish. The final process is the continued coarsening of the  $\text{Fe}_3\text{C}$  particles and gradual ferrite grain growth (Fig. 9.6).

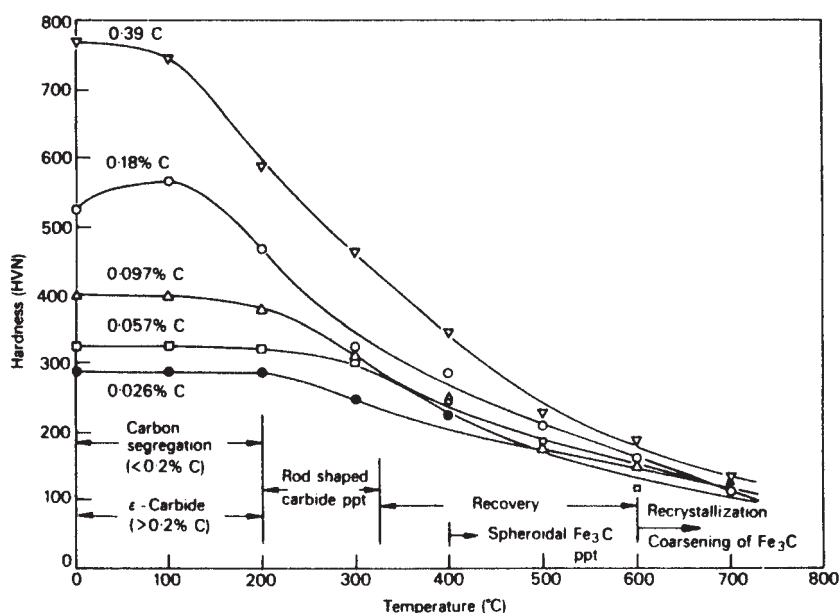


**Fig. 9.6** Hardness of iron-carbon martensites tempered 1 h at  $100\text{--}700^\circ\text{C}$  (Speich, *Transactions of the Metallurgical Society of AIME* **245**, 2553, 1969).

### 9.2.5 Role of carbon content

Carbon has a profound effect on the behaviour of steels during tempering. Firstly, the hardness of the as-quenched martensite is largely influenced by the carbon content (Fig. 9.6), as is the morphology of the martensite laths which have a  $\{111\}_\gamma$  habit plane up to 0.3 wt% C, changing to  $\{225\}_\gamma$  at higher carbon contents. The  $M_s$  temperature is reduced as the carbon content increases, and thus the probability of the occurrence of auto-tempering is less. During fast quenching in alloys with less than 0.2 wt% C, the majority (up to 90%) of the carbon segregates to dislocations and lath boundaries, but with slower quenching some precipitation of cementite occurs. On subsequent tempering of low-carbon steels up to 200°C further segregation of carbon takes place, but no precipitation has been observed. Under normal circumstances it is difficult to detect any tetragonality in the martensite in steels with less than 0.2 wt% C, a fact which can also be explained by the rapid segregation of carbon during quenching or because  $M_s$  exceeds the Zener ordering temperature.

The hardness changes during tempering are also very dependent on carbon content, as shown in Fig. 9.6 for steels up to 0.4 wt% C. Above this concentration, an increase in hardness has been observed in the temperature range 50–150°C, as  $\epsilon$ -carbide precipitation strengthens the martensite. However, the general trend is an overall softening, as the tempering temperature is raised. The diagram indicates the main physical processes contributing to the change in mechanical properties.

## 9.3 MECHANICAL PROPERTIES OF TEMPERED PLAIN CARBON STEELS

The intrinsic mechanical properties of tempered plain carbon martensitic steels are difficult to measure for several reasons. Firstly, the absence of other alloying elements means that the hardenability of the steels is low, so a fully martensitic structure is only possible in thin sections. However, this may not be a disadvantage where shallow hardened surface layers are all that is required. Secondly, at lower carbon levels, the  $M_s$  temperature is rather high, so auto-tempering is likely to take place. Thirdly, at the higher carbon levels the presence of retained austenite will influence the results. Added to these factors, plain carbon steels can exhibit quench cracking which makes it difficult to obtain reliable test results. This is particularly the case at higher carbon levels, i.e. above 0.5 wt% carbon.

Provided care is taken, very good mechanical properties, in particular proof and tensile stresses, can be obtained on tempering in the range 100–300°C. However, the elongation is frequently low and the impact values poor. Table 9.2 shows some typical results for plain carbon steels with between 0.2 and 0.5 wt% C, tempered at low temperatures.

Plain carbon steels with less than 0.25 wt% are not normally quenched and tempered, but in the range 0.25–0.55 wt% C heat treatment is often used to

**Table 9.2** Mechanical properties of plain carbon steels, both as-quenched and tempered (after Irvine *et al.*, *Journal of the Iron and Steel Institute* **196**, 70, 1960)

Steel (% C)	Property	Tempered			
		As-quenched	Tempered 7 h at		
			100°C	200°C	300°C
0.2	0.2% Proof stress ( $\text{MN m}^{-2}$ )	1270	1460	1235	1110
0.3		1360	1370	1270	1140
0.4			1670	1410	
0.2	UTS ( $\text{MN m}^{-2}$ )	1470	1690	1450	1340
0.3		1580	1605	1460	1240
0.5				2040	1600
0.2	Elongation (%)	5.0	6.0	6.0	9.0
0.3		4.5	7.0	7.0	10.0
0.5				4.0	7.0
0.2	Hardness (DPN)	446	444	446	357
0.3		564	517	502	420
0.5		680	666	571	470

upgrade mechanical properties. The usual tempering temperature is between 300°C and 600°C allowing the development of tensile strengths between 1700 and 800  $\text{MN m}^{-2}$ , the toughness increasing as the tensile strength decreases. This group of steels is very versatile as they can be used for crankshafts and general machine parts as well as hand tools, such as screwdrivers and pliers.

The high-carbon steels (0.5–1.0 wt%) are much more difficult to fabricate and are, therefore, particularly used in applications where high hardness and wear resistance are required, e.g. axes, knives, hammers, cutting tools. Typical mechanical properties as a function of tempering temperature are shown in Fig. 9.7 for a steel at the lower level (0.5 wt% C) of this range. Another important application is for springs, where often the required mechanical properties are obtained simply by heavy cold work, i.e. hard drawn spring wire. However, carbon steels in the range 0.5–0.75 wt% C are quenched, then tempered to the required yield stress.

## 9.4 TEMPERING OF ALLOY STEELS

The addition of alloying elements to a steel has a substantial effect on the kinetics of the  $\gamma \rightarrow \alpha$  transformation, and also of the pearlite reaction. Most common alloying elements move the time–temperature–transformation curves to longer times, with the result that it is much easier to ‘miss’ the nose of the curve during quenching. This essentially gives higher hardenability, since martensite structures can be achieved at slower cooling rates and, in practical terms, thicker

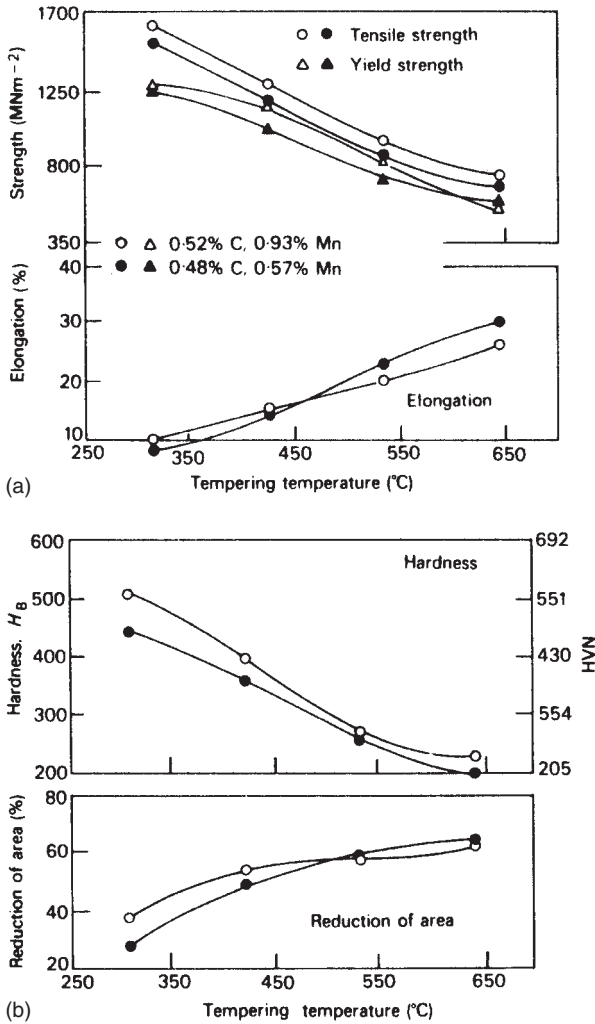


**Fig. 9.7** Properties of water-quenched and tempered 1050 steel (C: 0.48–0.55, Mn: 0.6–1.07) (*Metals Handbook*, 8th edition, Vol. 1, ASM, Ohio, USA).

specimens can be made fully martensitic. Alloying elements have also been shown to have a substantial effect in depressing the  $M_s$  temperature. In this section, we will examine the further important effects of alloying elements during the tempering of martensite, where not only the kinetics of the basic reactions are influenced but also the products of these reactions can be substantially changed, e.g. cementite can be replaced by other carbide phases. Several of the simpler groups of alloy steels will be used to provide examples of the general behaviour.

### 9.4.1 The effect of alloying elements on the formation of iron carbides

The structural changes during the early stage of tempering are difficult to follow. However, it is clear that certain elements, notably silicon, can stabilize the  $\varepsilon$ -iron carbide to such an extent that it is still present in the microstructure after tempering at 400°C in steels with 1–2 wt% Si, and at even higher temperatures if the silicon is further increased. The evidence suggests that both the nucleation and growth of the carbide is slowed down and that silicon enters into the  $\varepsilon$ -carbide structure. It is also clear that the transformation of  $\varepsilon$ -iron carbide to cementite is delayed considerably. While the tetragonality of martensite disappears by 300°C in plain carbon steels, in steels containing some alloying elements, e.g. Cr, Mo, W, V, Ti, Si, the tetragonal lattice is still observed after tempering at 450°C and even as high as 500°C. It is clear that these alloying elements increase the stability of the supersaturated iron carbide solid solution. In contrast manganese and nickel decrease the stability (Fig. 9.8).

Alloying elements also greatly influence the proportion of austenite retained on quenching. Typically, a steel with 4% molybdenum, 0.2% C, in the martensitic

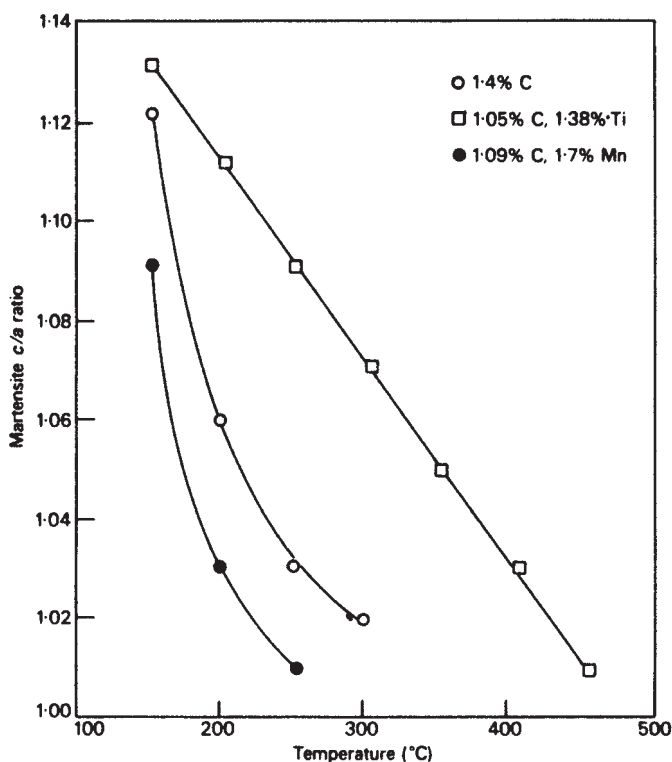


**Fig. 9.8** Effect of Ti and Mn on the tetragonality of martensite during tempering (Kurdjumov, *Journal of the Iron and Steel Institute* **195**, 26, 1960).

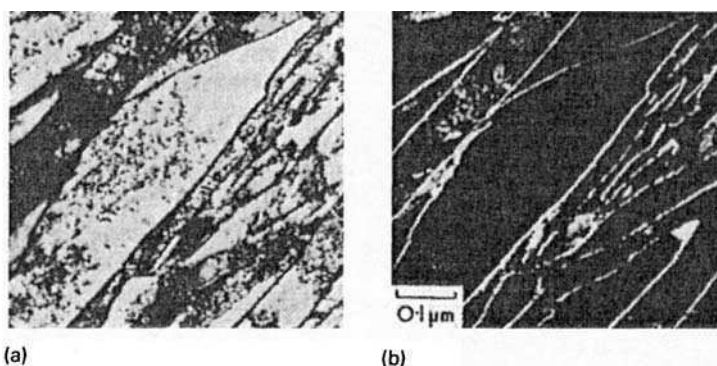


**Fig. 9.9** Fe-10Cr-0.2C quenched in iced brine from 1150°C. Martensite with retained austenite (courtesy of Howell): (a) bright field electron micrograph; (b) dark field electron micrograph using  $\gamma$ -diffraction beam. The  $\gamma$ -areas are light.

state contains less than 2% austenite, and about 5% is detected in a steel with 1% vanadium and 0.2% C. The austenite can be revealed as a fine network around the martensite laths, by using dark field electron microscopy (Fig. 9.9). On tempering each of the above steels at 300°C, the austenite decomposes to give thin grain boundary films of cementite which, in the case of the higher concentrations of retained austenite, can be fairly continuous along the lath boundaries. It is likely that this interlath cementite is responsible for *tempered martensite embrittlement*, frequently encountered as a toughness minimum in the range 300–350°C, by leading to easy nucleation of cracks, which then propagate across the tempered martensite laths.

Alloying elements can also restrain the coarsening of cementite in the range 400–700°C, a basic process during the fourth stage of tempering. Several alloying elements, notably silicon, chromium, molybdenum and tungsten, cause the cementite to retain its fine Widmanstätten structure to higher temperatures, either by entering into the cementite structure or by segregating at the carbide–ferrite interfaces. Whatever the basic cause may be, the effect is to delay significantly the softening process during tempering. This influence on the cementite dispersion has other effects, in so far as the carbide particles, by remaining finer, slow down the reorganization of the dislocations inherited from the martensite, with the result that the dislocation substructures refine more slowly. The cementite particles are also found on ferrite grain boundaries, where they control the rate at which the ferrite grains grow. Gladman has shown, for a precipitate of volume fraction  $f$ , pinning polygonal grains of average radius  $r_0$ , that the critical radius of particle  $r_{\text{crit}}$ , before grain growth can occur is:

$$r_{\text{crit}} = \frac{6r_0f}{\pi} \left( \frac{3}{2} - \frac{2}{Z} \right)^{-1}, \quad (9.1)$$

where  $Z$  is the ratio of radii of matrix and growing grains. This expression has been found to fit well the experimental results on silicon steels.

In plain carbon steels cementite particles begin to coarsen in the temperature range 350–400°C, and addition of chromium, silicon, molybdenum or tungsten delays the coarsening to the range 500–550°C. It should be emphasized that up to 500°C, the only carbides to form are those of iron. However, they will take varying amounts of alloying elements into solid solution and may reject other alloying elements as they grow.

#### 9.4.2 The formation of alloy carbides: secondary hardening

A number of the familiar alloying elements in steels form carbides which are thermodynamically more stable than cementite. It is interesting to note that this is also true of a number of nitrides and borides. Nitrogen and boron are increasingly used in steels in small but significant concentrations. The enthalpies of formation of some of these compounds are shown in Fig. 4.5 (p. 66), in which iron carbide is the least stable compound situated at the right of the diagram. The alloying elements Cr, Mo, V, W and Ti all form carbides with substantially higher enthalpies of formation, while the elements nickel, cobalt and copper do not form carbide phases. Manganese is a weak carbide former, found in solid solution in cementite and not in a separate carbide phase.

It would, therefore, be expected that when strong carbide-forming elements are present in a steel in sufficient concentration, their carbides would be formed in preference to cementite. Nevertheless, during the tempering of all alloy steels, alloy carbides do not form until the temperature range 500–600°C, because below this the metallic alloying elements cannot diffuse sufficiently rapidly to allow alloy carbides to nucleate. The metallic elements diffuse substitutionally, in contrast to carbon and nitrogen which move through the iron lattice interstitially, with the result that the diffusivities of carbon and nitrogen are several orders of magnitude greater in iron than those of the metallic alloying elements (Table 1.4). Consequently, higher temperatures are needed for the necessary diffusion of the alloying elements prior to the nucleation and growth of the alloy carbides and, in practice, for most of the carbide-forming elements this is in the range 500–600°C.

The coarsening of carbides in steels is an important phenomenon which influences markedly the mechanical properties. We can apply in general terms the theory for coarsening of a dispersion due to Lifshitz and Wagner, which gives for spherical particles in a matrix:

$$r_t^3 - r_o^3 = \frac{k}{RT} V_m^2 D \sigma t, \quad (9.2)$$

where

$r_o$  = the mean particle radius at time zero

$r_t$  = the mean particle radius at time  $t$

$D$  = diffusion coefficient of solute in matrix



$\sigma$  = interfacial energy of particle/matrix interface per unit area  
 $V_m$  = molar volume of precipitate  
 $k$  = constant.

The coarsening rate is dependent on the diffusion coefficient of the solute and, under the same conditions, at a given temperature, cementite would coarsen at a greater rate than any of the alloy carbides once formed (see Section 9.2.4 where the role of vacancies is discussed). This occurs in alloy steels in which cementite and an alloy carbide coexist, where the cementite dispersion is always much coarser. It is this ability of certain alloying elements to form fine alloy carbide dispersions in the range 500–600°C, which remain very fine even after prolonged tempering, that allows the development of high strength levels in many alloy steels. Indeed, the formation of alloy carbides between 500°C and 600°C is accompanied by a marked increase in strength, often in excess of that of the as-quenched martensite (Fig. 9.10). This phenomenon, which is referred to as

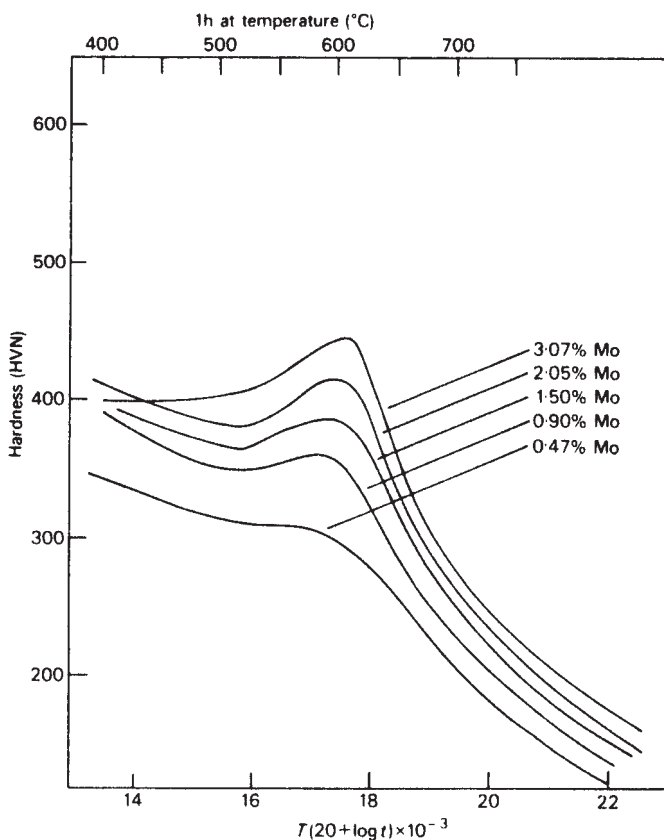


**Fig. 9.10** The effect of molybdenum on the tempering of quenched 0.1 wt% C steels (Irving and Pickering, *Journal of the Iron and Steel Institute* **194**, 137, 1960).

*secondary hardening*, is best shown in steels containing molybdenum, vanadium, tungsten, titanium and also in chromium steels at higher alloy concentrations.

This secondary-hardening process is a type of age-hardening reaction, in which a relatively coarse cementite dispersion is replaced by a new and much finer alloy carbide dispersion. On attaining a critical dispersion parameter, the strength of the steel reaches a maximum, and as the carbide dispersion slowly coarsens, the strength drops. The process is both time and temperature dependent, so both variables are often combined in a parameter:

$$P = T(k + \log t), \quad (9.3)$$

where  $T$  is the absolute temperature and  $t$  is the tempering time in hours, while  $k$  is a constant which is about 20 for alloy steels. Usually referred to as the Holloman–Jaffe parameter, this can be plotted against hardness to give one typical curve for a particular steel. In Fig. 9.10 the effect of increasing molybdenum content is thus effectively demonstrated in a series of steels containing 0.1 wt% carbon. Significantly, non-carbide-forming elements such as nickel, cobalt, silicon, do not give secondary hardening. However, some elements, e.g. silicon, by delaying the coarsening of cementite, lead to a plateau on the tempering curve in the range 300–500°C.

### 9.4.3 Nucleation and growth of alloy carbides

The dispersions of alloy carbides which occur during tempering can be very complex, but some general principles can be discerned which apply to a wide variety of steels. The alloy carbides can form in at least three ways:

1. *In-situ* nucleation at pre-existing cementite particles – it has been shown that the nuclei form on the interfaces between the cementite particles and the ferrite. As they grow, carbon is provided by the adjacent cementite which gradually disappears.
2. By separate nucleation within the ferrite matrix – usually on dislocations inherited from the martensitic structure.
3. At grain boundaries and sub-boundaries – these include the former austenite boundaries, the original martensitic lath boundaries (now ferrite), and the new ferrite boundaries formed by coalescence of sub-boundaries, or by recrystallization.

*In-situ* nucleation at pre-existing cementite particles is a common occurrence but, because these particles are fairly widely spaced at temperatures above 500°C, the contribution of this type of alloy carbide nucleation to strength is very limited. Figure 9.11a shows, in a 4 wt% molybdenum steel tempered 4.5 h at 550°C, the relatively coarse Widmanstätten precipitation of  $\text{Fe}_3\text{C}$ , which at this stage has largely transformed to fine  $\text{Mo}_2\text{C}$  particles. These are readily

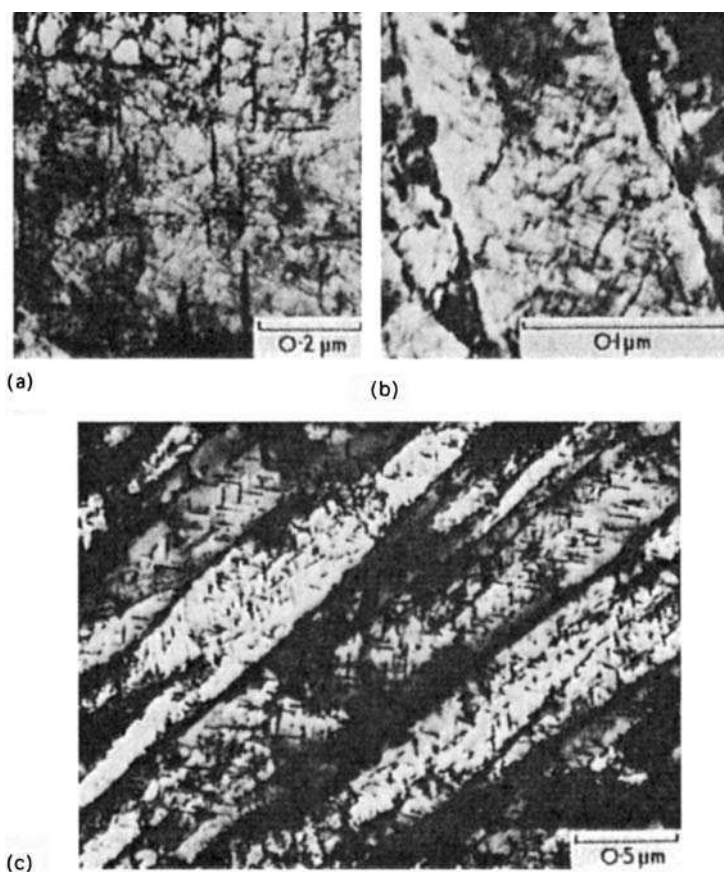


**Fig. 9.11** Tempering of an Fe-4Mo-0.2C steel. Thin-foil electron micrographs: (a) 4.5 h at 550°C. Cementite transforming *in situ* to  $\text{Mo}_2\text{C}$  and start of nucleation on dislocations (Raynor *et al.*, 1966). (b) 5 h at 600°C.  $\text{Mo}_2\text{C}$  precipitation on dislocations within a former martensite lath (courtesy of Irani). (c) 30 min at 700°C.  $\text{Mo}_2\text{C}$  precipitation in ferrite laths inherited from martensite  $\text{M}_6\text{C}$  precipitation at lath boundaries (Irani).

identified by dark field microscopy. On further tempering, the positions of the original cementite particles are indicated by small necklaces of alloy carbides which tend to be coarser than the matrix precipitation.

Figure 9.11a also illustrates the dislocation network characteristic of tempered steels and inherited from the martensite, although there has been considerable rearrangement and reduction in dislocation density. Dark field electron microscopy reveals that these dislocations are the sites for very fine precipitation of the appropriate alloy carbide. On further ageing the particles are more readily resolved, e.g. in Mo steels as a Widmanstätten array,

comprising  $\text{Mo}_2\text{C}$  rodlets lying along  $\langle 001 \rangle_\alpha$  directions. Figure 9.11b illustrates this stage in a single martensitic lath. Heavier precipitation is evident at the lath boundaries.

The nucleation of carbides at the various types of boundary is to be expected because these are energetically favourable sites which also provide paths for relatively rapid diffusion of solute. Consequently the ageing process is usually more advanced in these regions and the precipitate is more massive (Fig. 9.11c). In many alloy steels, the first alloy carbide to form is not the final equilibrium carbide and, in some steels, as many as three alloy carbides can form successively. In these circumstances, the equilibrium alloy carbide frequently nucleates first in the grain boundaries, grows rapidly and eventually completely replaces the Widmanstätten non-equilibrium carbide within the grains. This is illustrated in Fig. 9.11c for a 4 wt% Mo steel tempered 30 min at  $700^\circ\text{C}$ , in which  $\text{M}_6\text{C}$  equi-axed particles are growing at the grain boundaries but Widmanstätten  $\text{Mo}_2\text{C}$  is still visible within the grains. It is interesting to note that the structure still possesses the lath-shaped ferrite grains inherited from the martensite. Recrystallization occurs after longer times at  $700^\circ\text{C}$ .

#### 9.4.4 Tempering of steels containing vanadium

Vanadium is a strong carbide former and, in steel with as little as 0.1 wt% V, the face-centred cubic vanadium carbide (VC) is formed. It is often not of stoichiometric composition, being frequently nearer  $\text{V}_4\text{C}_3$ , but with other elements in solid solution within the carbide. Normally, this is the only vanadium carbide formed in steels, so the structural changes during tempering of vanadium steels are relatively simple.

Vanadium carbide forms as small platelets, initially less than 5 nm across and not more than 1 nm thick. These form within the ferrite grains on dislocations (Fig. 9.12a) in the range  $550$ – $650^\circ\text{C}$ , and produce a marked secondary-hardening peak. There is a well-defined orientation relationship (Baker/Nutting) with the ferrite matrix:  $\{100\}_{\text{VC}}//\{110\}_\alpha$ . In the early stages of precipitation at  $550^\circ\text{C}$ , the particles are coherent with the matrix, there being only a 3% misfit between  $\langle 010 \rangle_\alpha$  and  $\langle 110 \rangle_{\text{VC}}$ . However, at  $700^\circ\text{C}$ , the platelets coarsen rapidly (Fig. 9.12b) and begin to spheroidize. However, the original martensite laths can still be recognized, and are only replaced by equi-axed ferrite grains after long periods at  $700^\circ\text{C}$ .

Many steels containing vanadium, e.g.  $\frac{1}{2}\text{Cr}\frac{1}{2}\text{Mo}\frac{1}{4}\text{V}$ ,  $1\text{Cr}\frac{1}{4}\text{V}$ ,  $3\text{Cr}1\text{Mo}\frac{1}{4}\text{V}$ ,  $1\text{Cr}1\text{Mo}\frac{3}{4}\text{V}$ , will exhibit extensive vanadium carbide precipitation on tempering, because of the stability of this carbide, not only with respect to cementite but also the several chromium carbides and molybdenum carbide (see Fig. 4.5). Because of its ability to maintain a fine carbide dispersion, even at temperatures approaching  $700^\circ\text{C}$ , vanadium is an important constituent of steels for elevated temperature service.

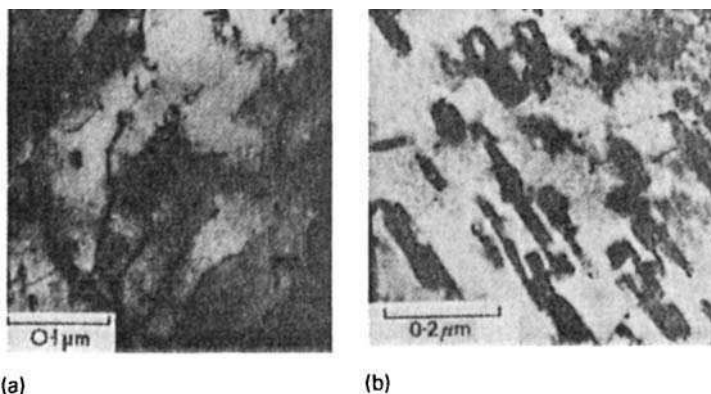
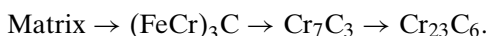


**Fig. 9.12** Fe-1V-0.2C wt% quenched and tempered. Thin-foil electron micrographs: (a) 72 h at 550°C, VC nucleation on dislocations (courtesy of Raynor); (b) 50 h at 700°C. Plates of VC (courtesy of Irani).

#### 9.4.5 Tempering of steels containing chromium

In chromium steels, two chromium carbides are very often encountered:  $\text{Cr}_7\text{C}_3$  (trigonal) and  $\text{Cr}_{23}\text{C}_6$  (complex cubic). The normal carbide sequence during tempering is:



While this sequence occurs in higher-chromium steels, below about 7 wt% Cr,  $\text{Cr}_{23}\text{C}_6$  is absent unless other metals such as molybdenum are present. Chromium is a weaker carbide former than vanadium, which is illustrated by the fact that  $\text{Cr}_7\text{C}_3$  does not normally occur until the chromium content of the steel exceeds 1 wt% at a carbon level of about 0.2 wt%.

In steels up to 4 wt% Cr, the transformation from  $\text{Fe}_3\text{C}$  to  $\text{Cr}_7\text{C}_3$  occurs mainly by nucleation at the  $\text{Fe}_3\text{C}$ /ferrite interfaces. Steels up to 9 wt% Cr do not show secondary-hardening peaks in tempering curves (Fig. 9.13). However, these curves do exhibit plateaus at the higher chromium contents, which are associated with the precipitation of  $\text{Cr}_7\text{C}_3$ . Chromium diffuses more rapidly in ferrite than most metallic alloying elements, with the result that  $\text{Cr}_7\text{C}_3$  is detected during tempering at temperatures as low as 500°C, and in comparison with vanadium carbide, chromium carbide coarsens rapidly. Thus, in a 2 wt% Cr-0.2 wt% C steel, continuous softening will normally occur on tempering between 500°C and 700°C, although addition of other alloying elements, e.g. Mo, can reduce the rate of coarsening of  $\text{Cr}_7\text{C}_3$ .

In contrast, a 12 wt% Cr steel will exhibit secondary hardening in the same temperature range (Fig. 9.13) due to precipitation of  $\text{Cr}_7\text{C}_3$ . Additionally,  $\text{Cr}_{23}\text{C}_6$  nucleates at about the same time but at different sites, particularly former austenite grain boundaries and at ferrite lath boundaries. This precipitate grows at the expense of the  $\text{Cr}_7\text{C}_3$  which eventually disappears from the

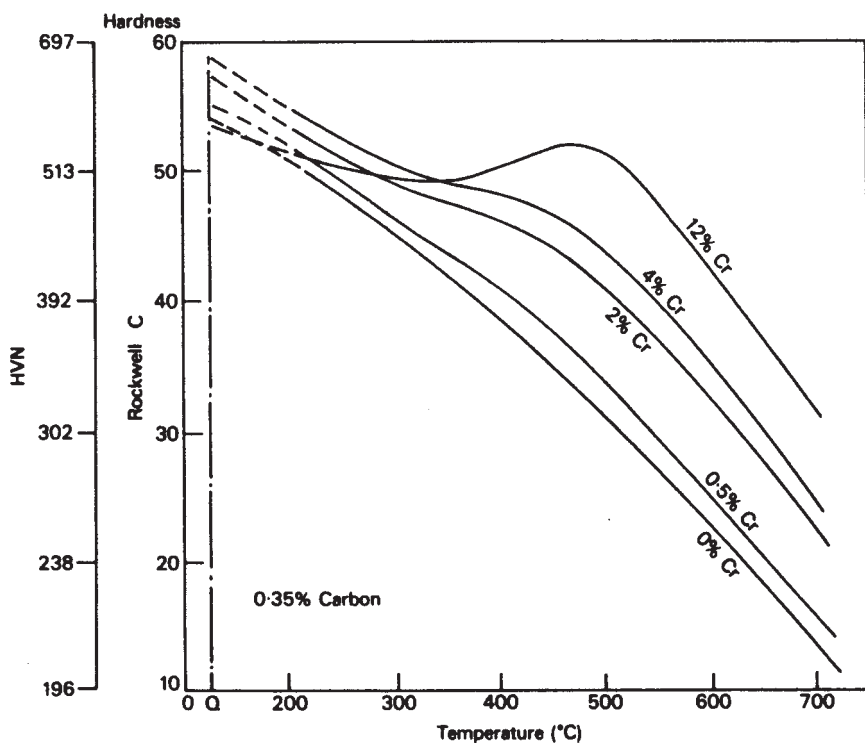
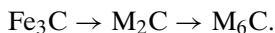


**Fig. 9.13** The effect of chromium on the tempering of a 0.35 wt% C steel (Bain and Paxton, *The Alloying Elements in Steel*, 2nd edition, ASM, Ohio, USA, 1961).

microstructure, at which stage the steel has completely over-aged. This transition from  $\text{Cr}_7\text{C}_3$  to  $\text{Cr}_{23}\text{C}_6$  in high-chromium steels is by separate nucleation and growth. Further alloying additions can promote one or other of these carbide reactions, e.g. addition of tungsten encourages formation of  $\text{Cr}_{23}\text{C}_6$  by allowing it to nucleate faster, while vanadium tends to stabilize  $\text{Cr}_7\text{C}_3$ . In doing so, it decreases the rate of release into solution of chromium and carbon needed for the growth of  $\text{Cr}_{23}\text{C}_6$ . Clearly, vanadium would be a preferred addition to tungsten, if a fine stable chromium carbide dispersion is needed in the temperature range 550–650°C.

#### 9.4.6 Tempering of steels containing molybdenum and tungsten

When molybdenum or tungsten is the predominant alloying element in a steel, a number of different carbide phases are possible, but for composition between 4 and 6 wt% of the element the carbide sequence is likely to be:



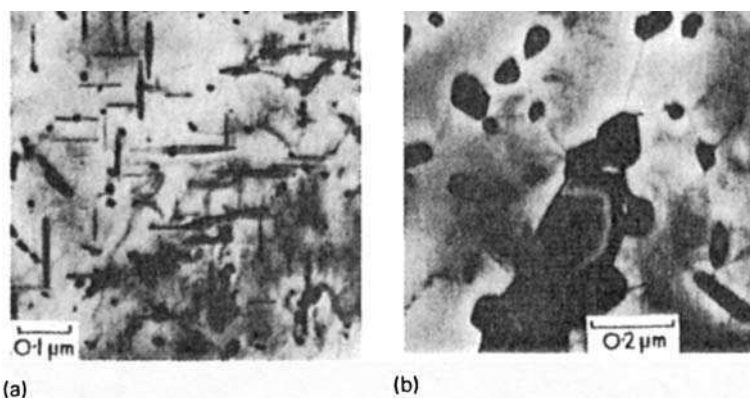


**Fig. 9.14** Fe-6W-0.23C wt% quenched and tempered (courtesy of Davenport). Thin-foil electron micrographs: (a) 100 h at 600°C.  $W_2C$  needles along  $\langle 001 \rangle_\alpha$  some irregular particles of  $M_6C$ . (b) 26 h at 700°C. Massive  $M_6C$ .

The carbides responsible for the secondary hardening in both the case of tungsten and molybdenum are the isomorphous hexagonal carbides  $Mo_2C$  and  $W_2C$ , both of which, in contrast to vanadium carbide, have a well-defined rodlet morphology (Fig. 9.14a). When formed in the matrix,  $M_2C$  adopts a Widmanstätten distribution lying along  $\langle 100 \rangle_\alpha$  directions. In molybdenum steels, peak hardness occurs after about 25 h at 550°C, when the rods are about 10–20 nm long and 1–2 nm in diameter. The orientation relationship is:

$$(0001)_{M_2C} // (011)_\alpha,$$

$$[11\bar{2}0]_{M_2C} // [100]_\alpha \text{ (rod growth direction).}$$

$M_2C$  also nucleates at former austenite and ferrite lath boundaries. As in the case of vanadium steels,  $M_2C$  precipitate nucleates both on dislocations in the ferrite, and at the  $Fe_3C$ /ferrite interfaces, but the secondary hardening arises primarily from the dislocation-nucleated dispersion of  $M_2C$ .

On prolonged tempering at 700°C, the complex cubic  $M_6C$  forms predominantly at grain boundaries as massive particles which grow quickly, while the  $M_2C$  phase goes back into solution. The equilibrium microstructure is equi-axed ferrite with coarse  $M_6C$  in the form of faceted particles at grain boundaries, and plates, illustrated in Fig. 9.14b for a 6 wt% tungsten steel tempered 26 h at 700°C.

For similar atomic concentrations, the secondary hardening response in the case of tungsten steels is less than that of molybdenum steels. The  $M_2C$  dispersion in the former case is coarser, probably because the slower diffusivity of tungsten allows a coarsening of the dislocation network prior to being pinned by the nucleation of  $M_2C$  particles.

At lower concentration of tungsten and molybdenum (0.5–2 wt%), two other alloy carbides are interposed in the precipitation sequences, i.e. the complex

cubic  $M_{23}C_6$  and the orthorhombic  $M_4C_b$ , probably  $Fe_2MoC$ . These carbides are found as intermediate precipitates between  $M_2C$  and  $M_6C$ .

#### 9.4.7 Complex alloy steels

The presence of more than one carbide-forming element can complicate the precipitation processes during tempering. In general terms, the carbide phase which is the most stable thermodynamically will predominate, but this assumes that equilibrium is reached during tempering. This is clearly not so at temperatures below 500–600°C. The use of pseudo-binary diagrams for groups of steels, e.g. Cr–V, Cr–Mo, can be a useful guide to carbide phases likely to form during tempering (see Chapter 4, Section 4.2). The sequence of precipitation for a particular composition can be approximated to by drawing a line from the origin of the diagram, e.g. Fig. 4.6, to the composition of interest. The phase fields passed through would normally be those encountered in tempering, but the exact conditions cannot be forecast from such data.

Certain strong carbide formers, notably niobium, titanium and vanadium, have effects on tempering out of proportion to their concentration. In concentrations of 0.1 wt% or less, provided the tempering temperature is high enough, i.e. 550–650°C, they combine preferentially with part of the carbon and, in addition to the major carbide phase, e.g.  $Cr_7C_3$ ,  $Mo_2C$ , they form a separate, very much finer dispersion, more resistant to over-ageing (Fig. 9.15). This secondary dispersion can greatly augment the secondary-hardening reaction, illustrating the importance of these strong carbide-forming elements in achieving high strength levels, not only at room temperature but also at elevated temperatures, where creep resistance is often an essential requirement.

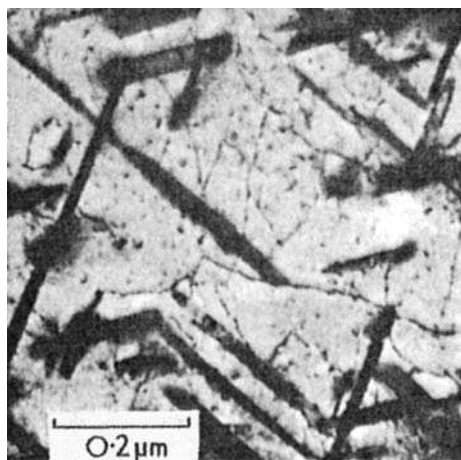


**Fig. 9.15** Fe-4Mo-0.1Nb-0.2C wt% steel tempered 6 h at 700°C. Coarse needles of  $Mo_2C$  in ferrite and fine particles of  $NbC$  on dislocations (courtesy of Irani). Thin-foil electron micrograph.



9.4.8 Mechanical properties of tempered alloy steels

A wide range of mechanical properties is obtainable by tempering alloy steels between 200°C and 700°C. A typical example is shown in Fig. 9.16 for a steel containing 1.5Ni–1Cr–0.25Mo–0.4C wt% (En24), the tensile strength of which can be varied from 1800 down to 900 MN m<sup>-2</sup> by tempering at progressively high temperatures. The ductility of the steel improves as the tensile strength falls. However, there is a ductility minimum around 275–300°C, which is often observed in plain carbon and lower-alloy steels. This has been attributed to the conversion of retained austenite to bainite, but it is more likely to be the result of the formation of thin cementite films, as a result of the transformation of austenite at the interlath boundaries. At higher temperatures, these films spheroidize and the toughness improves.

To obtain really high strength levels in tempered steels (~1500 MN m<sup>-2</sup>), it is usual to temper at low temperatures, i.e. 200–300°C, when the martensite is still heavily dislocated and the main strengthening dispersion is cementite or ε-iron

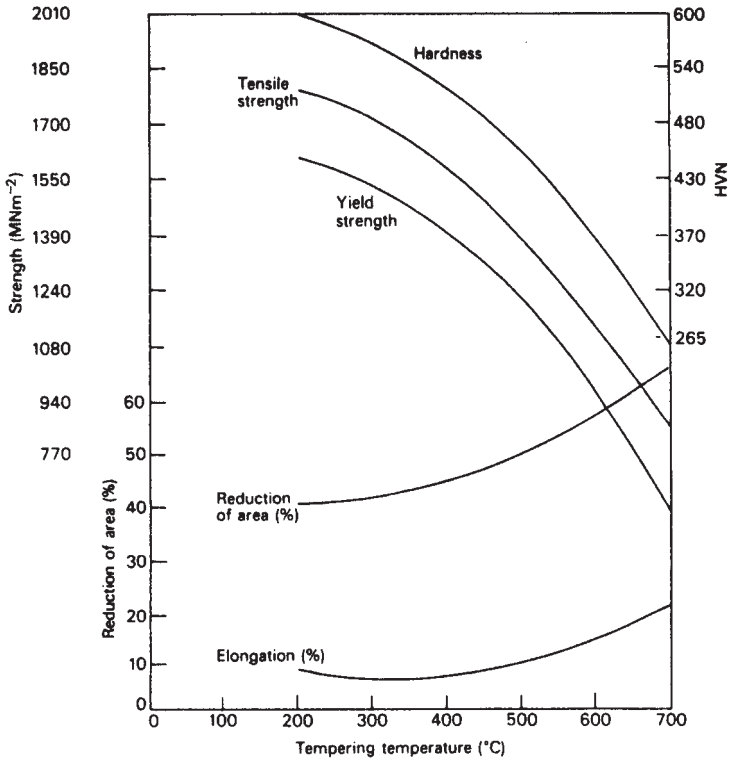
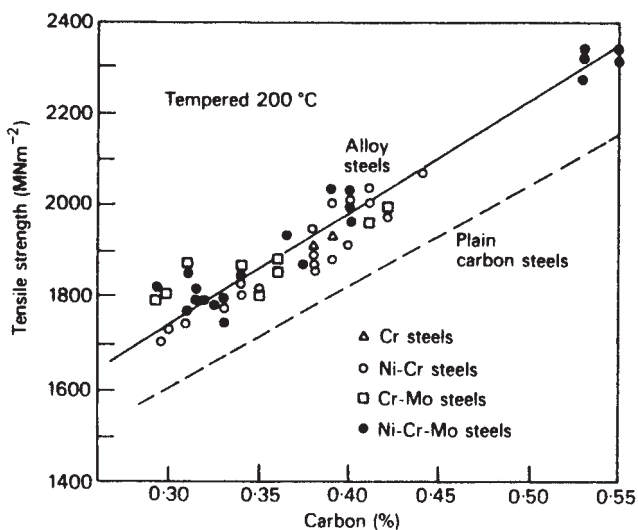
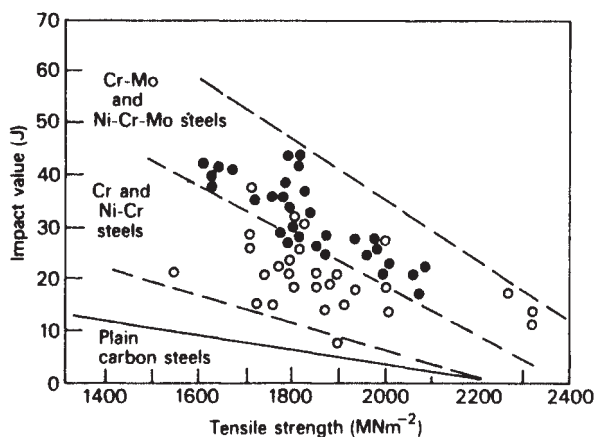


**Fig. 9.16** Mechanical properties of En 24 (1.5Ni–1Cr–0.25Mo–0.4C wt% steel) as a result of tempering for 1 h (Thelning, *Steel and its Heat Treatment*, Bofors Handbook, Butterworth, UK, 1975).



(a)



(b)

**Fig. 9.17** Comparison of mechanical properties of plain carbon and alloy steels tempered at 200°C (Irving and Pickering, *Journal of the Iron and Steel Institute* **194**, 137, 1960): (a) effect of C on tensile strength; (b) relation between tensile strength and impact value. Note the beneficial effect of Mo.

carbide. Alloy steels, when tempered in this range, not only provide very high tensile strengths with some ductility but are also superior to plain carbon steels, as shown in Fig. 9.17. It is clear from Fig. 9.17a that the carbon content has a large influence on the strength. The alloying elements refine the iron carbide dispersion and, as the carbon content is raised, the dispersion becomes more dense and, therefore, more effective. The toughness decreases with increasing strength, as

shown in Fig. 9.17b. However, alloying elements very substantially improve the toughness, when compared with plain carbon steels of similar strength levels. When molybdenum is present in the steel, the toughness is increased further as the scatter bands indicate. This effect of alloying elements is again attributed to the breakdown of carbide films at grain and martensite lath boundaries. These films are particularly less noticeable in steels containing molybdenum.

Alloy steels which exhibit secondary hardening can provide high strength levels on tempering between 500°C and 700°C, with better ductility than that obtained at lower tempering temperatures. However, one of their main advantages is that, once a high strength level is reached by means of an alloy carbide dispersion formed between 550°C and 650°C, this structure will be relatively stable at temperatures up to 500°C. Therefore, the steels are suitable for use under stress at elevated temperatures. A typical example is given in Fig. 9.18 of

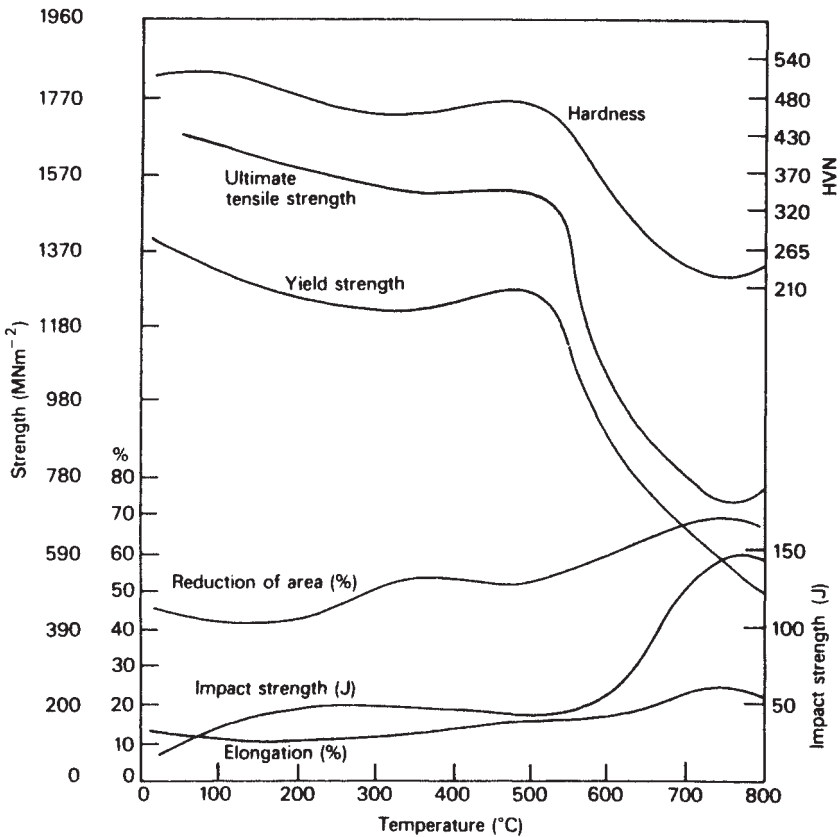


**Fig. 9.18** Effect of tempering for 1 h on the mechanical properties of a 12Cr-1Ni-0.2C wt% stainless steel. Typical results for 50-mm diameter bars, oil-quenched (Thelning, *Steel and its Heat Treatment*, Bofors Handbook, Butterworth, 1975).

a 12Cr–1Ni–0.2C wt% stainless steel, which can be quenched to martensite and then tempered to give a fine dispersion of chromium carbides in a ferritic matrix. The strength is well-maintained up to the secondary-hardening peak at 500°C, and is combined with a reasonable level of ductility. This type of steel is tempered to between 700 and 1000 MN m<sup>-2</sup> yield stress and is frequently used in steam and gas turbines, but can also be used for constructional purposes where lower temperatures are involved. Further improvements in mechanical properties at elevated temperatures can be obtained by addition of small concentrations of stronger carbide formers, e.g. molybdenum (2 wt%) and vanadium (0.25 wt%).

## 9.5 MARAGING STEELS

It has been shown that precipitation of alloy carbides in tempered martensite gives rise to age hardening, usually referred to as secondary hardening. There is no reason why other finely divided phases cannot be used for a similar purpose and, in fact, an important group of high-alloy steels, the maraging steels, reach high strength levels by the precipitation of various intermetallic compounds.

Carbide precipitation is practically eliminated by the use of low carbon compositions, and the steels contain between 18 and 25 wt% nickel so that, on quenching from the austenitic condition, they form a soft but heavily dislocated martensite. The high nickel content lowers the  $M_s$  to around 150°C, but on reheating the martensite there is considerable hysteresis, so that austenite is not reformed until the steel is held between 500°C and 600°C. At somewhat lower temperatures, i.e. 400–500°C, precipitation of intermetallic phases takes place, accelerated by the influence of the high dislocation density on the diffusion of substitutional solute atoms. Elements such as molybdenum and titanium are necessary additions, which result in the precipitation of Ni<sub>3</sub>Mo, Ni<sub>3</sub>Ti and the Laves phase, Fe<sub>2</sub>Mo. Cobalt is also a useful alloying element as it reduces the solubility of molybdenum in the matrix and this increases the volume fraction of molybdenum-rich precipitate.

The precipitate reactions can lead to very high-volume fractions of precipitate, and thus to the achievement of high strength levels (Equations (2.10) and (2.11)). For example, a steel with 18–19 Ni, 8.5–9.5 Co, 4.5–5 Mo and 0.5–0.8 Ti wt% can be heat treated to give a yield stress around 2000 MN m<sup>-2</sup>. However, the important point is that these high strength levels are accompanied by good ductility and toughness.

## FURTHER READING

- Bhadeshia, H. K. D. H., Strang, A. and Gooch, D. J., Remanent life assessment and the approach to equilibrium, *International Materials Reviews* **43**, 45, 1998.
- Brooks, C. R., *Heat Treatment of Ferrous Alloys*, McGraw-Hill, USA, 1979.
- Honeycombe, R. W. K., *Structure and Strength of Alloy Steels*, Climax Molybdenum Co., Michigan, USA, 1973.

- Irvine, K. J. and Pickering, F. B., High strength 12% chromium steels, in *Iron and Steel Institute Special Report No. 86*, London, UK, p. 34, 1964.
- Krauss, G., *Phase Transformation in Ferrous Alloys* (eds Marder, A. R. and Goldstein, J. I.), TMS-AIME, Warrendale, PA, pp. 101–1123, 1984.
- Krauss, G., *Steels: Heat Treatment and Processing Principles*, ASM International, Ohio, USA, 1990.
- Kurdjumov, G., *Journal of the Iron and Steel Institute* **195**, 26, 1960.
- Leslie, W.C., *The Physical Metallurgy of Steels*, McGraw-Hill, Tokyo, Japan, 1981.
- Nutting, J., Physical metallurgy of alloy steels, *Journal of the Iron and Steel Institute* **207**, 872, 1969.
- Pickering, F. B., *Physical Metallurgy and the Design of Steels*, Applied Science Publishers, 1978.
- Roberts, C. S., Averbach, B. L. and Cohen, M., *Transactions of the American Society of Materials* **45**, 576, 1953.
- Speich, G. R., Tempering of plain carbon martensite, *Transactions of the American Institute of Mining, Metallurgical and Petroleum Engineers* **245**, 2553, 1969.
- Speich, G. R., *Symposium Iron and Steel Soc.*, AIME, Warrendale, PA, 1992.
- Speich, G. R. and Clark, J. B. (eds), *Precipitation from Iron-base Alloys*, Gordon and Breach, London, UK, 1965.
- Stewart, J., Thomson R. C. and Bhadeshia, H. K. D. H., Cementite precipitation during tempering of martensite under stress, *Journal of Materials Science* **29**, 6079, 1994.
- Thomas, G., Retained austenite and tempered martensite embrittlement. *Met. Trans.* **9**, 439, 1978.
- Winchell, G., Symposium on 'The Tempering of Steel', *Metallurgical Transactions A*, 991–1145, 1983.
- Winchell, P. G. and Cohen, M., *Trans. ASM* **55**, 347, 1962.
- Woodhead, J. H. and Quarrell, A. G., *The Role of Carbides in Low Alloy Creep-resisting Steels*, Climax Molybdenum Co., Michigan, USA, 1965.

# 10

## THERMOMECHANICAL TREATMENT OF STEELS

### 10.1 INTRODUCTION

Thermomechanical treatment involves the simultaneous application of heat and a deformation process to an alloy, in order to change its shape and refine the microstructure. Thus, hot rolling of metals, a well-established industrial process, is a thermomechanical treatment which plays an important part in the processing of many steels, particularly those produced in very large quantities. Continuously cast segments of steel, ranging from 1 to 50 tonnes in weight, are introduced into the rolling sequence at a temperature typically in the range 1200–1300°C. They are then progressively rolled into a variety of shapes depending on application. The deformation leads to a breaking down of the original coarse microstructure by repeated recrystallization of the steel while in the austenitic condition, and by the gradual reduction in the chemical segregation introduced during casting. Also, the inevitable non-metallic inclusions, i.e. oxides, sulphides and silicates, are broken up, some deformed and distributed throughout the steel in a more refined and uniform manner.

The hot rolling process is now a highly controlled operation in which a billion tonnes of steel is produced annually using computer-controlled arrays of equipment, resulting in impressive levels of productivity and reproducibility. The compositions of the low-alloy steels are carefully chosen to provide optimum mechanical properties when the hot deformation and subsequent cooling is complete. This process, in which the rolling parameters (temperature, strain, number of rolling passes, finishing temperature, *etc.*) are predetermined and precisely defined, is called *controlled rolling*. It is now of the greatest importance in obtaining reliable mechanical properties in steels for pipelines, bridges, buildings and a huge variety of other products.

## 10.2 CONTROLLED ROLLING OF LOW-ALLOY STEELS

### 10.2.1 General

Before the Second World War, strength in hot-rolled low-alloy steels was achieved by the addition of carbon up to 0.4 wt% and manganese up to 1.5 wt%, giving yield stresses of 350–400 MN m<sup>-2</sup>. However, such steels are essentially ferrite–pearlite aggregates, which do not possess adequate toughness for many modern applications. Indeed, the toughness, as measured by the ductile/brittle transition, decreases dramatically with carbon content, i.e. with increasing volume of pearlite in the steel (Fig. 10.1). Furthermore, with the introduction of welding as the main fabrication technique, the high carbon contents led to serious cracking problems, which could only be eliminated by the use of lower-carbon steels. The great advantage of producing in these steels a fine ferrite grain size soon became apparent (see Section 2.5), so controlled rolling in the austenitic condition was gradually introduced to achieve this. Fine ferrite grain sizes in the finished steel were found to be greatly expedited by the addition of small concentrations (<0.1 wt%) of grain refining elements such as niobium, titanium and vanadium, and also aluminium. On adding such elements to steels with 0.03–0.008% C and up to 1.5 wt% Mn, it became possible to produce fine-grained material with yield strengths between 450 and 550 MN m<sup>-2</sup>, and with ductile/brittle transition temperatures as low as –70°C. Such steels are now referred to as high-strength low-alloy (HSLA) steels, or micro-alloyed

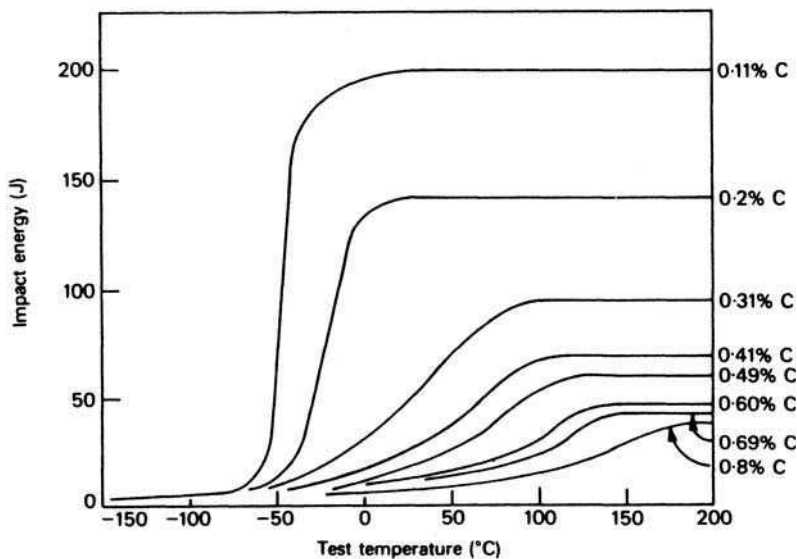


**Fig. 10.1** Effect of carbon content on the impact transition temperature curves of ferrite/pearlite steels (Pickering, in *Micro-alloying 75*, Union Carbide Corporation, New York, USA, 1975).

steels. This progress, from the relatively low strength of ordinary mild steel ( $220\text{--}250\text{ MN m}^{-2}$ ) in a period of 20 years represents a major metallurgical development, the importance of which, in engineering applications, cannot be overstated.

The general features of controlled rolling are summarized in Fig. 10.2.

### 10.2.2 Grain size control during controlled rolling

The primary grain refinement mechanism in controlled rolling is the recrystallization of austenite during hot deformation, known as *dynamic recrystallization*. This process is clearly influenced by the temperature and the degree of deformation which takes place during each pass through the rolls. However, in austenite devoid of second-phase particles, the high temperatures involved in

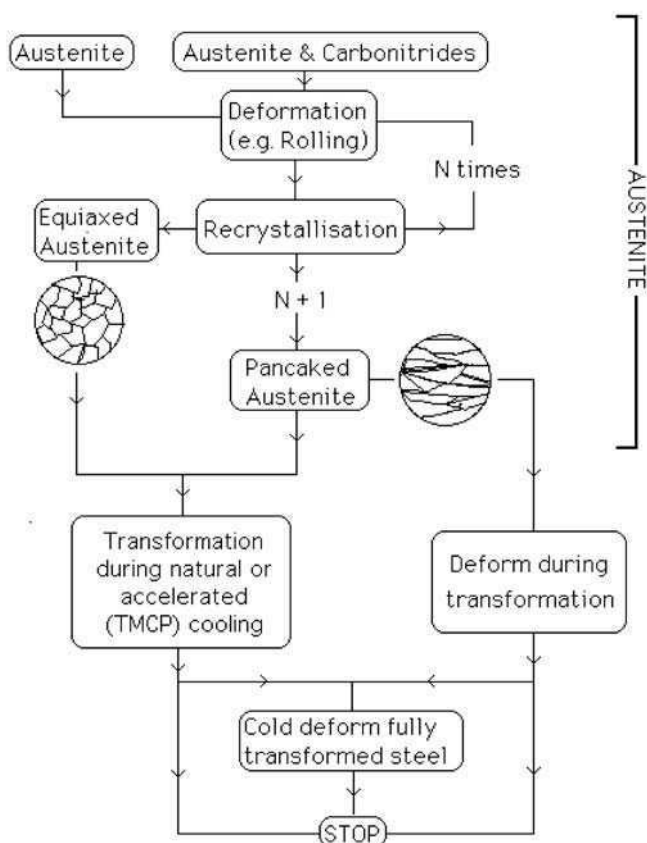


**Fig. 10.2** The variety of thermomechanical processing routes. Controlled rolling, followed by accelerated cooling is often designated *thermomechanical controlled processing* or TMCP.



hot rolling lead to marked grain growth, with the result that grain refinement during subsequent working is limited.

The situation is greatly improved if fine particles are introduced into the austenitic matrix. The particles are usually found on grain boundaries, because an interaction takes place between the particles and the boundary. A short length of grain boundary is replaced by the particle and the interfacial energy ensures a stable configuration. When the grain boundary attempts to migrate away from the particles, the local energy increases and thus a drag is exerted on the boundary by the particles.

The theory of boundary pinning by particles has already been referred to in Chapter 9. Equation (9.1) defines the critical size of particle below which pinning is effective. Clearly, the control of grain size at high austenitizing temperatures requires as fine a grain boundary precipitate as possible, and one which will not dissolve completely in the austenite, even at the highest working temperatures (1200–1300°C). The best grain refining elements are very strong carbide and nitride formers, such as niobium, titanium and vanadium, also aluminium which forms only a nitride. As both carbon and nitrogen are present in control-rolled steels, and as the nitrides are even more stable than the carbides (see Fig. 4.5, Chapter 4), it is likely that the most effective grain refining compounds are the respective carbo-nitrides, except in the case of aluminium nitride.

Equally important is the degree of solubility that such stable compounds have in austenite. It is essential that there is sufficient solid solubility at the highest austenitizing (soaking) temperatures to allow fine precipitation to occur during controlled rolling at temperatures which decrease as rolling proceeds. The solubility products (in atomic per cent) of several relevant carbides and nitrides have been shown in Fig. 4.12 as a function of the reciprocal of the temperature. All of these compounds have a small but increasing solubility in the critical temperature range (900–1300°C) (Fig. 10.3). In contrast, the carbides of chromium and molybdenum have much higher solubilities, which ensure that they will normally go completely into solution in the austenite, if the temperature is high enough, and will not precipitate until the temperature is well below the critical range for grain growth. Data from another source<sup>1</sup> have provided the following equations for solubilities expressed in weight per cent as a function of absolute temperature:

$$\log_{10}[\text{Al}][\text{N}] = -6770/T + 1.03,$$

$$\log_{10}[\text{V}][\text{N}] = -8330/T + 3.46,$$

$$\log_{10}[\text{Nb}][\text{C}] = -6770/T + 2.26,$$

$$\log_{10}[\text{Ti}][\text{C}] = -7000/T + 2.75.$$

---

<sup>1</sup> Irvine, K. J. *et al.*, *Journal of the Iron and Steel Institute* **205**, 161, 1967.

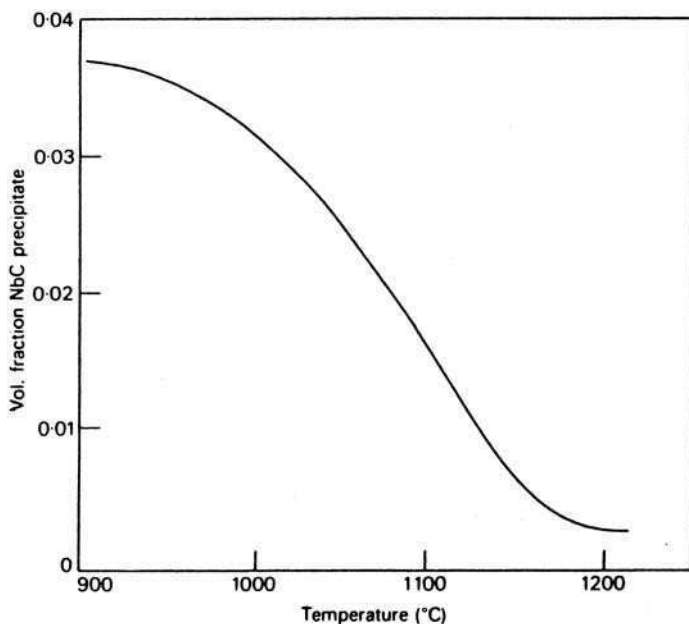


**Fig. 10.3** Solubility curve for NbC in a steel with 0.15C–1.14Mn–0.04Nb wt% (Hoogendoorn and Spanraet, *Micro-alloying* 75, Union Carbide Corporation, New York, USA, 1975).

The compositional changes possible are many, so discussion will be limited to general principles which apply equally, whichever compound is the effective grain refiner in a given steel. While grain growth at the highest austenitizing temperatures may be restricted to some extent by a residual dispersion, the main refinement is achieved during rolling as the temperature progressively falls, and fine carbo-nitrides are precipitated from the austenite. These new precipitates will:

1. Increase the strain, for a given temperature, at which recrystallization will commence (Fig. 10.4).
2. Restrict the movement of recrystallized grain boundaries.

It should be borne in mind that the austenite may recrystallize several times during a controlled-rolling schedule and the total effect of this will be a marked austenite grain refinement by the time the steel reaches the  $\gamma/\alpha$  transformation temperature (Fig. 10.4). In the later stages of austenite deformation, at the lower temperatures, recrystallization may not occur, with the result that deformed austenite grains elongated and flattened by rolling may transform directly to ferrite. In the final stages of controlled rolling, austenite grain growth can be further suppressed by rapid cooling from the finishing temperature, which allows

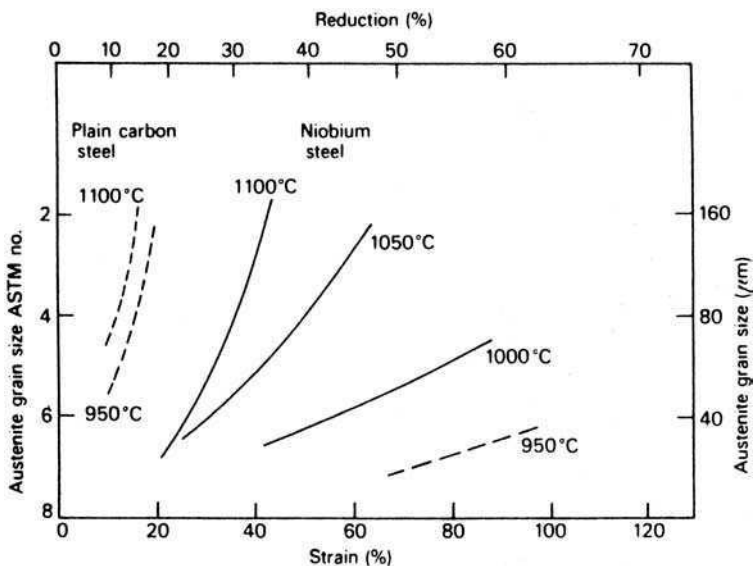


**Fig. 10.4** Critical strain needed to complete recrystallization of austenite as a function of deformation temperature and grain size. Comparison of Nb steel with plain carbon steel (Tanaka *et al.*, *Micro-alloying* 75, Union Carbide Corporation, New York, USA, 1975).

the  $\gamma/\alpha$  transformation to take place sub-critically, i.e. below  $A_{r1}$ , in austenite which is still deformed. It is becoming common practice now to continue rolling through the  $\gamma/\alpha$  transformation and even into the fully ferritic region. Such treatments lead to finer grain sizes, and higher yield stresses in the finished product (Fig. 10.5), but impose much higher load factors on the rolling mills.

As a result of the combined use of controlled rolling and fine dispersions of carbo-nitrides in low-alloy steels, it has been possible to obtain ferrite grain sizes between 5 and 10  $\mu\text{m}$ , in commercial practice. Laboratory tests have achieved grain sizes approaching 1  $\mu\text{m}$ , which would appear to be a practical limit using this approach. The Hall-Petch relationship between grain size and yield strength, which was discussed in Chapter 2, is very relevant to micro-alloyed steels and, in fact, linear plots are obtained for the yield stress against  $d^{-1/2}$  (Fig. 10.6). Addition of 0.05–0.09 wt% Nb to a plain carbon steel refines the ferrite grain size, allowing it to be reduced to below 5  $\mu\text{m}$  ( $d^{-1/2} = 14 \text{ mm}^{-1/2}$ ), with a consequent substantial increase in yield strength. The displacement of  $\sim 100 \text{ MN m}^{-2}$  between the C–Mn and C–Mn–Nb curves arises from dispersion strengthening due to NbC. This is further illustrated in the two lower curves of Fig. 10.7, which were obtained from specimens austenitized at 950°C prior to air cooling. If, however, progressively higher austenitizing temperatures are used, e.g. 1100°C and 1250°C followed by air cooling, the resulting curves, although still linear, have much steeper slopes, indicating a marked increase in yield

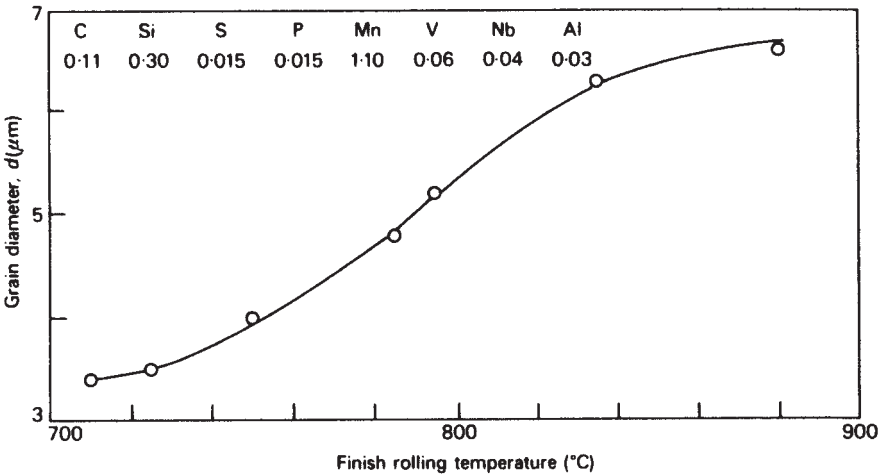


**Fig. 10.5** Effect of finish rolling temperature on final ferrite grain size of a micro-alloyed steel (after McKenzie, *Proceedings of the Rosenhain Centenary Conference*, Royal Society, London, UK, 1976).

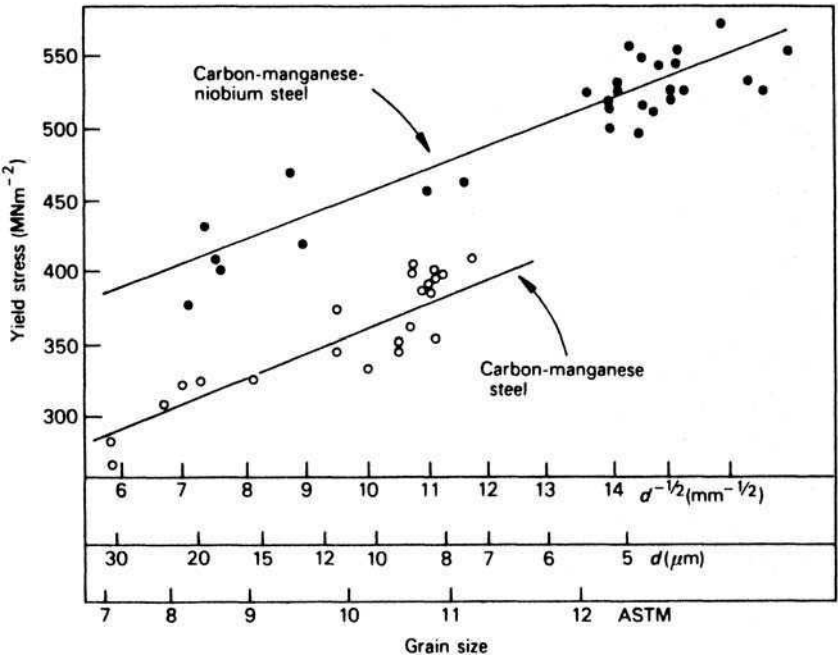


**Fig. 10.6** Effect of grain size on yield stress of a carbon–manganese–niobium steel (Le Bon and Saint Martin, *Micro-alloying 75*, Union Carbide Corporation, New York, USA, 1975).

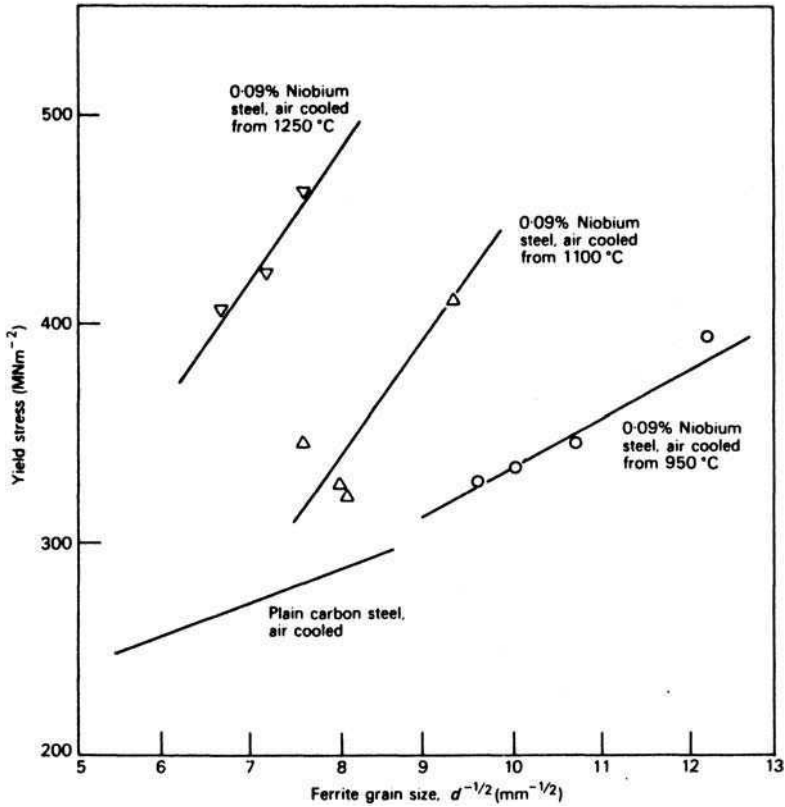


**Fig. 10.7** Effect of austenitizing temperature on the yield strength of a 0.1C–0.6Mn–0.09Nb wt% steel (Gladman *et al.*, *Micro-alloying 75*, Union Carbide Corporation, New York, USA, 1975).

strength for a particular grain size. This large increment in strength is due to the precipitation of NbC during cooling, following its solution at the higher austenitizing temperatures.

### 10.2.3 Minimum achievable grain size

It is interesting to consider what might be the smallest grain size achievable using large-scale thermomechanical processing. A reduction in ferrite grain size (linear intercept  $d$ ) is equivalent to an increase in the amount of grain boundary surface per unit volume ( $S_V$ ) since  $d = 2/S_V$ . Grain boundaries have an energy  $\sigma$  per unit area, so that the interfacial energy stored per unit volume of steel is:

$$\sigma \times S_V \equiv 2\sigma/d.$$

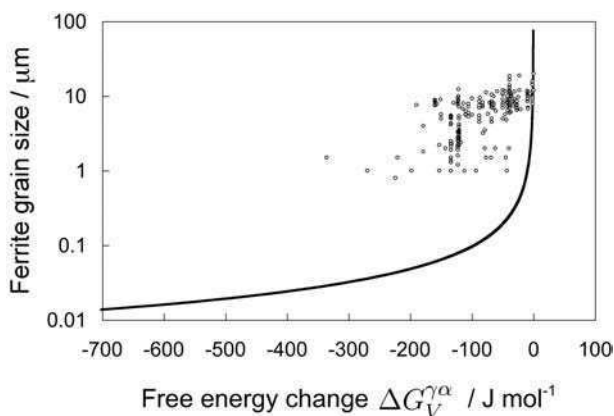


**Fig. 10.8** Plot of the logarithm of ferrite grain size versus the free energy change available to generate grain boundaries. The curve represents the values of  $d_{\alpha}^{\min}$ . The points are experimental data.

This stored energy cannot exceed the magnitude of the free energy change when austenite transforms to ferrite, i.e.  $|\Delta G_V^{\gamma/\alpha}|$ :

$$|\Delta G_V^{\gamma/\alpha}| \geq \frac{2\sigma_{\alpha}}{d_{\alpha}}.$$

It follows that the smallest ferrite grain size that can be achieved is when all of  $\Delta G_V^{\gamma/\alpha}$  is used up in creating  $\alpha/\alpha$  grain boundaries, so that:

$$d_{\alpha}^{\min} = \frac{2\sigma_{\alpha}}{|\Delta G_V^{\gamma/\alpha}|}.$$

Figure 10.8 shows the variation in this limiting ferrite grain size as a function of  $\Delta G_V^{\gamma/\alpha}$ , together with a compilation of experimental data on the smallest grain size achieved commercially, using thermomechanical processing.<sup>2</sup> The curve indicates that at large grain sizes,  $d_{\alpha}^{\min}$  is sensitive to  $\Delta G_V^{\gamma/\alpha}$  and hence to the undercooling below the equilibrium transformation temperature. However, reductions in grain size in the sub-micrometre range require huge values of  $|\Delta G_V^{\gamma/\alpha}|$ , meaning that the transformations would have to be suppressed to large undercoolings to achieve fine grain size.

Comparison of the industrial data against the calculated curve indicates that in spite of tremendous efforts in developing processing routes, the smallest ferrite grain size obtained commercially using thermomechanical processing is

<sup>2</sup> Yokota, T., Garcia-Mateo, C. and Bhadeshia, H. K. D. H., *Scripta Materialia* **51**, 767, 2004.

stuck at about  $1\text{ }\mu\text{m}$ . The reason is *recalcescence*, which is the rise in temperature of the steel caused by release of the latent heat of transformation at a rate which is so high that it cannot easily be dissipated by diffusion. It causes the temperature of the steel to rise, thus reducing  $\Delta G_V^{\gamma\alpha}$  and preventing the achievement of ultrafine grain structures. Large-scale thermomechanical processing is therefore limited by recalcescence and is unlikely to lead to grain sizes which are uniformly less than about  $1\text{ }\mu\text{m}$ .

#### 10.2.4 Dispersion strengthening during controlled rolling

The solubility data imply that, in a micro-alloyed steel, carbides and carbonitrides of Nb, Ti and V will precipitate progressively during controlled rolling as the temperature falls. While the primary effect of these fine dispersions is to control grain size, dispersion strengthening will take place. The strengthening arising from this cause will depend both on the particle size  $r$ , and the interparticle spacing  $\Lambda$  which is determined by the volume fraction of precipitate (Equation (2.10)). These parameters will depend primarily on the type of compound which is precipitating, and that is determined by the micro-alloying content of the steel. However the maximum solution temperature reached and the detailed schedule of the controlling rolling operation are also important variables.

It is now known, not only that precipitation takes place in the austenite, but that further precipitation occurs during the transformation to ferrite. The precipitation of niobium, titanium and vanadium carbides has been shown to take place progressively as the interphase boundaries move through the steel. This is the interphase precipitation discussed in Section 4.4.3. As this precipitation is normally on an extremely fine scale occurring between  $850^\circ\text{C}$  and  $650^\circ\text{C}$ , it is likely to be the major contribution to the dispersion strengthening. In view of the higher solubility of vanadium carbide in austenite, the effect will be most pronounced in the presence of this element, with titanium and niobium in decreasing order of effectiveness. If the rate of cooling through the transformation is high, leading to the formation of supersaturated plates of ferrite, the carbides will tend to precipitate within the grains, usually on the dislocations which are numerous in this type of ferrite.

In arriving at optimum compositions of micro-alloyed steels, it should be borne in mind that the maximum volume fraction of precipitate which can be put into solid solution in austenite at high temperatures is achieved by use of stoichiometric compositions. For example, if titanium (atomic weight 47.9) is used, it will combine with approximately one quarter its weight of carbon (atomic weight 12), so that for a 0.025 wt% C steel, 0.10 wt% of Ti will provide carbide of the stoichiometric composition. In Fig. 10.9 the stoichiometric line for TiC is shown superimposed on the solubility curves for titanium carbide at  $1100^\circ\text{C}$ ,  $1200^\circ\text{C}$  and  $1300^\circ\text{C}$ . If the precipitation in steels with 0.10 wt% titanium cooled from  $1200^\circ\text{C}$  is considered, at low carbon contents, i.e. to the left of the

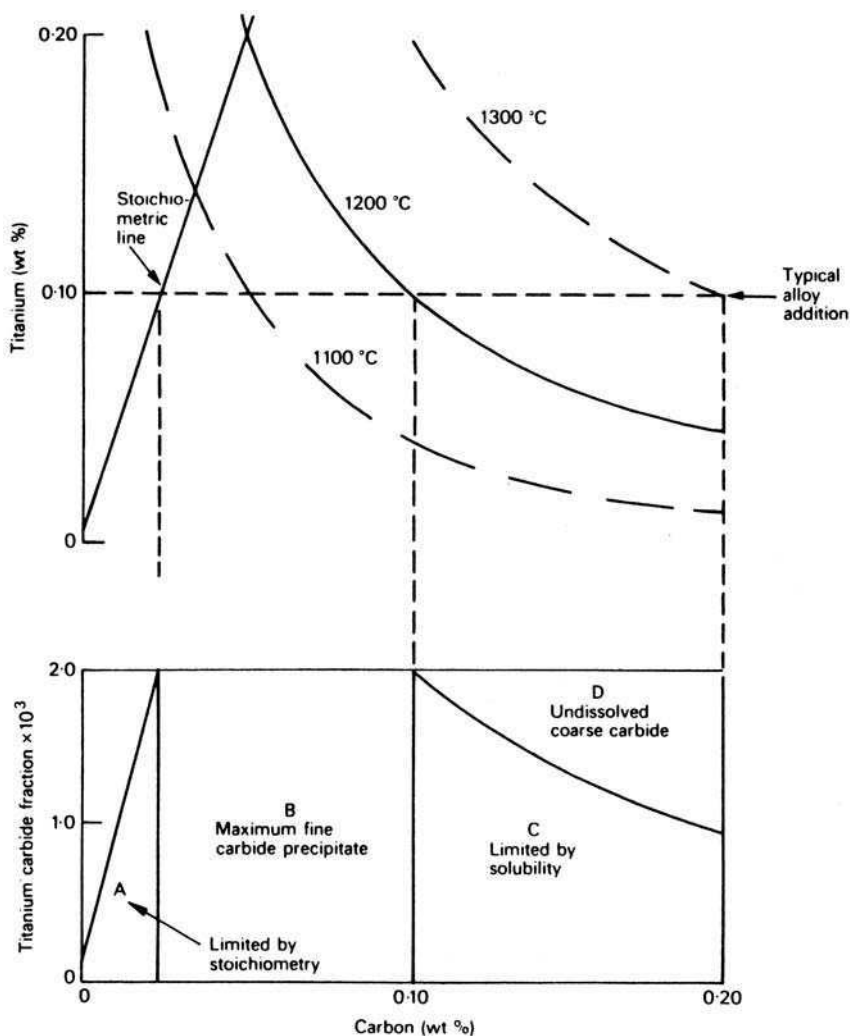


**Fig. 10.9** Effect of stoichiometry on the precipitation of TiC in a micro-alloyed steel (Gladman *et al.*, *Micro-alloying 75*, Union Carbide corporation, New York, USA, 1975).

stoichiometric line, the carbide fraction is limited by the carbon content, i.e. zone A, lower diagram. For carbon contents between the stoichiometric line and the solubility line at 1200°C, the full potential volume fraction of fine TiC will form on cooling (zone B). When the carbon content exceeds the solubility limit ( $>0.10$  wt%), the titanium is progressively precipitated at 1200°C as coarse carbide, thus reducing the amount of titanium available to combine with carbon to form fine TiC during cooling. As coarse carbide particles are ineffective in



controlling grain growth, it is highly desirable to have steel compositions which avoid their formations. It also follows from Fig. 10.9 that high austenitizing temperatures are essential to obtain full benefit from the precipitation of finely divided carbide phases.

### 10.2.5 Strength of micro-alloyed steels: an overall view

In modern control-rolled micro-alloyed steels, there are at least three strengthening mechanisms which contribute to the final strength achieved. The relative contribution from each is determined by the composition of the steel and, equally important, the details of the thermomechanical treatment to which the steel is subjected. The several strengthening contributions for steels with 0.2 wt% carbon, 0.2 wt% silicon, 0.15 wt% vanadium and 0.015 wt% nitrogen as a function of increasing manganese content are shown schematically in Fig. 10.10. Firstly, there are the solid solution strengthening increments from manganese, silicon and uncombined nitrogen. Secondly, the grain size contribution to the yield stress is shown as a very substantial component, the magnitude of which is very sensitive to the detailed thermomechanical history. Finally, a typical increment for dispersion strengthening is shown. The total result is a range of yield strengths between about 350 and 500 MN m<sup>-2</sup>. In this particular example, the steel was normalized (air cooled) from 900°C, but had it been control rolled down to 800°C or even lower, the strength levels would have been substantially raised.

The effect of the finishing temperature for rolling is important in determining the grain size and, therefore, strength level reached for a particular steel. It is now becoming common to roll through the transformation into the completely ferritic condition, and so obtain fine subgrain structures in the ferrite, which provide an additional contribution to strength. Alternatively, the rolling is finished above the  $\gamma/\alpha$  transformation, and the nature of the transformation is altered by increasing the cooling rate. Slow rates of cooling obtained by coiling at a particular temperature will give lower strengths than rapid rates imposed by water spray cooling following rolling. The latter route can change the ferrite from equi-axed to Widmanstätten with a much higher dislocation density. The result is a steel with improved mechanical properties and, in many cases, the sharp yield point can be suppressed. This has practical advantages in fabrication of sheet steel, e.g. pipe manufacture, where a continuous stress-strain curve is preferred.

## 10.3 DUAL-PHASE STEELS

The HSLA steels described in Section 10.2 give improved strength to weight ratios over ordinary standard steels. However, they are not readily formed, e.g. by cold pressing and related techniques. The worldwide demand for safety

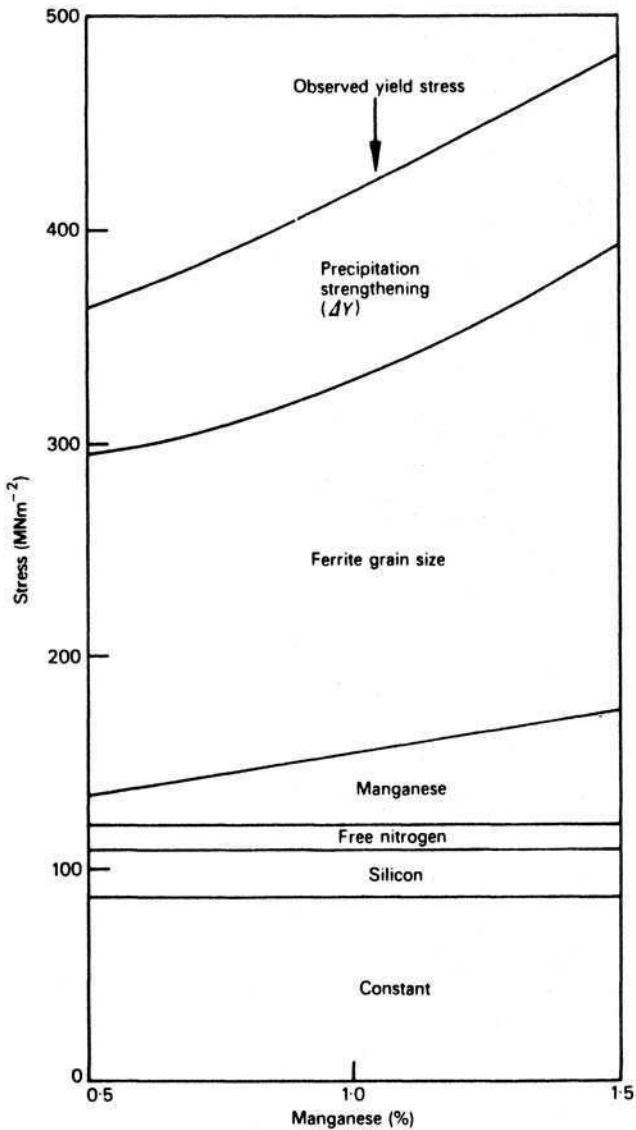


**Fig. 10.10** The contributions to strength in a 0.2C-0.15V wt% steel as a function of Mn content (Gladman *et al.*, *Micro-alloying 75*, Union Carbide Corporation, 1975).

and fuel economy in automobiles has led to the development of a number of steel types which are not only strong, but at the same time have the formability required for mass production of car bodies and components. A measure of formability is the product of strength and uniform elongation.

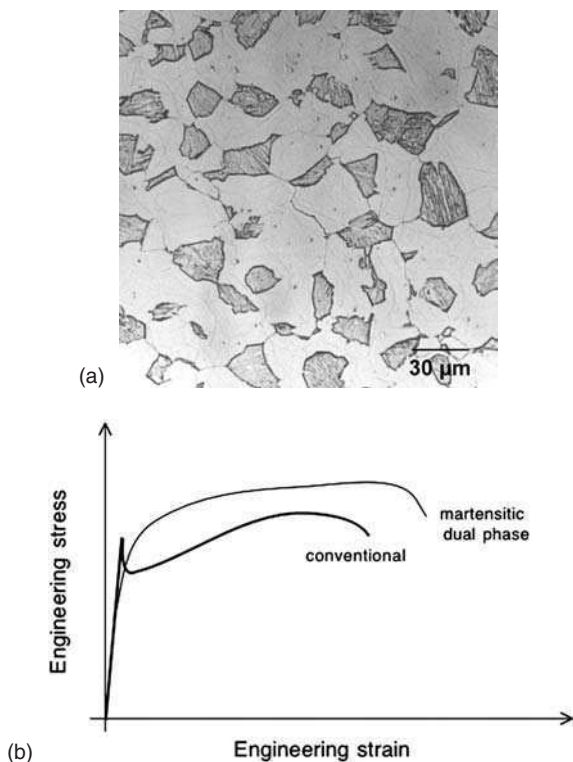


**Fig. 10.11** (a) Typical microstructure of dual-phase steel, consisting of a mixture of martensite (dark) and ferrite. (b) Schematic stress–strain curves comparing the behaviour of a conventional automobile steel with that of a dual-phase steel.

The *dual-phase* steels are low-alloy steels which satisfy these requirements by exploiting microstructures in which there are two major phases (Fig. 10.11), one of which is soft and the other significantly harder. The ferrite–martensite dual-phase steels typically contain manganese and silicon, and are strong and yet are formable. They exhibit continuous yielding, i.e. no sharp yield point, and a relatively low proof strength ( $300\text{--}350\text{ MN m}^{-2}$ ). The simplest steels in this category contain 0.08–0.2C, 0.5–1.5Mn wt%, but steels micro-alloyed with vanadium are also suitable, while small additions of Cr (0.5 wt%) and Mo (0.2–0.4 wt%) are frequently used to control the development of microstructure.

The simplest way of achieving a duplex structure is to use intercritical annealing in which the steel is heated into the ( $\alpha + \gamma$ ) region between the  $Ae_1$  and  $Ae_3$  and held, typically at  $790^\circ\text{C}$  for several minutes to allow small regions of austenite to form in the ferrite. As it is essential to transform these regions of austenite into martensite, cooling to ambient temperature must be sufficiently rapid to

avoid other intervening transformations. Alternatively, the hardenability of the austenite must be enhanced by adding between 0.2 and 0.4 wt% Mo to a steel already containing 1.5 wt% manganese. The required microstructure can then be obtained by air cooling after intercritical annealing.

To eliminate an extra heat treatment step, dual-phase steels have now been developed which can be given the required structure during cooling after controlled rolling. Typically, these steels have additions of 0.5Cr and 0.4Mo wt%. After completion of hot rolling around 870°C, the steel forms approximately 80% ferrite on the water cooled run-out table from the mill. The material is then coiled in the metastable region (510–620°C) below the pearlite/ferrite transformation and, on subsequent cooling, the austenite regions transform to martensite.

## 10.4 TRIP-ASSISTED STEELS

The steels developed to exploit the properties obtained when the martensite reaction occurs during plastic deformation are known as *transformation-induced plasticity* (TRIP) steels. They are strong and exhibit considerable uniform elongation before failure. There are several varieties of such steels. Those which are made fully austenitic by using large quantities of austenite-stabilizing solutes, but transform to martensite when stressed, are simply called the TRIP steels (discussed in Chapter 12). When the austenite is a minor phase in the overall microstructure, but undergoes martensitic transformation during straining, the steels are said to be TRIP assisted and are usually low alloy steels.

Martensitic transformation induced by local stress has the effect of relieving stress concentrations, increasing the work-hardening rate, and promoting homogeneous deformation, with consequent improvements in the strength, ductility and toughness of steels. TRIP-assisted steels are mass produced, made using a complex heat treatment which is often completed within a short time during the processing of steel strip. Their microstructure consists of allotriomorphic ferrite as the major phase together with a total of 30–40% of harder regions. The latter consist of mixtures of bainite, martensite and carbon-enriched retained austenite. The chemical composition is typically Fe–0.12C–1.5Si–1.5Mn wt%. Some austenite is retained in spite of the low overall solute content because when the bainite forms, the silicon prevents cementite precipitation, thereby enriching the residual austenite with carbon (Chapter 6). The major application of TRIP-assisted steels is in the automobile industries, both for painted surfaces and for enhancing the safety of the passenger compartment in the event of a crash.

There are two kinds of TRIP-assisted steels. In the first case a cold-rolled strip is heated rapidly from ambient temperature for intercritical treatment in the  $\alpha + \gamma$  phase field between the  $A_{c1}$  and  $A_{c3}$  temperatures (Fig. 10.12). The intercritical annealing induces partial transformation to austenite and at the

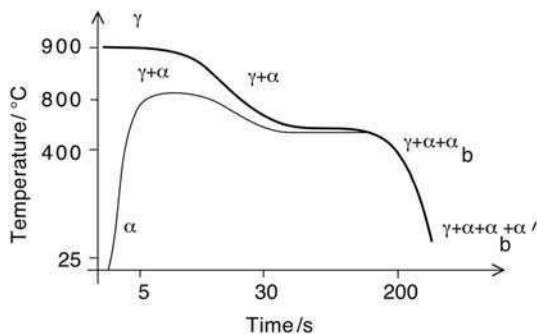


**Fig. 10.12** The two kinds of heat treatment used to generate the microstructures of TRIP-assisted steels. The terms  $\gamma$ ,  $\alpha$ ,  $\alpha_b$  and  $\alpha'$  represent austenite, allotriomorphic ferrite, bainite and martensite, respectively.

same time recrystallizes the residual ferrite. The strip is then cooled at a controlled rate during which some of the austenite transforms into allotriomorphic ferrite and at lower temperatures into bainitic ferrite. This latter reaction causes the austenite to become enriched in carbon, allowing it to be retained to ambient temperature (Fig. 10.13).

The details of the microstructure and mechanical properties can be altered by manipulating the cooling condition. For example, it is common practice to allow more time in the bainite transformation range than at the higher temperatures where allotriomorphic ferrite grows. Figure 10.14 shows the effect of holding in the bainite transformation temperature range on the final microstructure. An inadequate amount of bainite leaves the austenite susceptible to martensitic transformation. Similarly, because the carbon concentration in the austenite is limited by the  $T_0$  curve (Chapter 6), transformation to bainite at too high a temperature also renders the austenite unstable.

The second kind of heat treatment starts from a hot-rolled strip which is fully austenitic (Fig. 10.12) and forms both allotriomorphic ferrite and bainite during the cooling part of the thermal cycle. This has the advantage that the microstructure can be produced directly from the hot strip which has been rolled to its final dimensions. The process is cheap since the strip does not have to be heated to the intercritical annealing temperature. However, hot-rolling mills are restricted by rolling loads to strips thicker than about 3 mm, although there are modern mills which can cope with 1.4 mm thickness. Cold-rolled strips can, on the other hand, be made routinely into thinner gauges. Hot-rolled strips are preferred for automobile applications where cost is a prime factor in the choice of materials.

The transformation strain due to the formation of martensite does not account for the observed uniform tensile elongation of some 15–30%. The shape deformation due to martensite (Chapter 5) is at most equivalent to a 2% tensile strain because the amount of austenite available for transformation

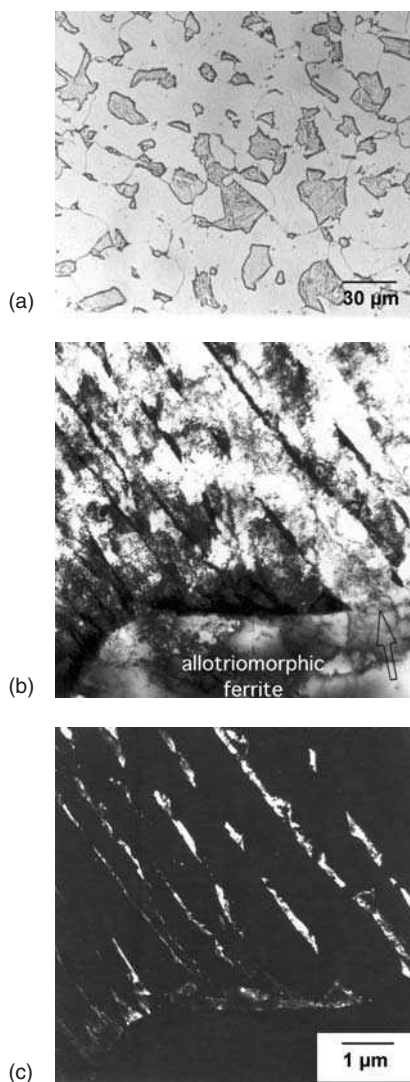


**Fig. 10.13** TRIP-assisted steel showing a mixed microstructure of allotriomorphic ferrite, bainitic ferrite and retained austenite films. (a) Optical micrograph. (b) Bright field transmission electron micrograph. (c) Dark field image of retained austenite.

is quite small in TRIP-assisted steels. The major contributions to uniform elongation arise partly from the enhanced work-hardening coefficient of the material due to the progressive formation of hard martensite during deformation. There is a further significant contribution from dislocations induced into the ferrite

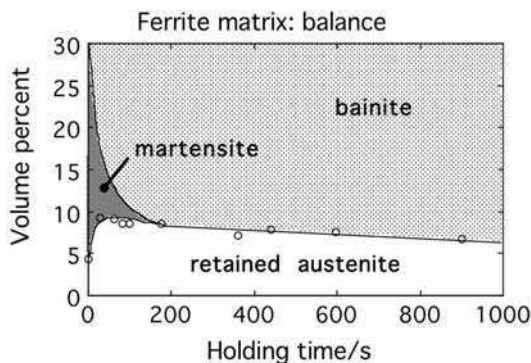


**Fig. 10.14** Evolution of room temperature microstructure as a function of the time during isothermal transformation to bainite (Girault, E., Mertens, A., Jacques, P., Houbaert, Y., Verlinden, B. and van Humbeek, J., *Scripta Materialia* **44**, 885, 2001).

by the strains associated with martensitic transformation.<sup>3</sup> These dislocations strengthen the ferrite and are visible in Fig. 10.13.

The austenite also delays the necking process during a tensile test by transforming to martensite at stress concentrations. It is therefore important to delay the transformation of retained austenite to the late stages of deformation when significant damage accumulates in the steel. It is at this point that the TRIP effect can be most beneficial. It is useful therefore to examine further the transformation of austenite as a function of plastic strain.

It is reasonable to assume that the change in the fraction of martensite ( $dV^{\alpha'}$ ) obtained for a given increment of plastic strain ( $d\epsilon$ ) should be proportional to the fraction of remaining austenite:

$$\frac{dV^{\alpha'}}{d\epsilon} = k_{\gamma} V^{\gamma}, \quad (10.1)$$

where  $k_{\gamma}$  is a function of the steel composition and test temperature and  $V^{\gamma}$  is the fraction of austenite remaining untransformed. If the fraction of austenite at zero strain is  $V_0^{\gamma}$ , then  $V^{\alpha'} = V_0^{\gamma} - V^{\gamma}$ , and integration of Equation (10.1) gives:

$$\ln\{V_0^{\gamma}\} - \ln\{V^{\gamma}\} = k_{\gamma}\epsilon.$$

The form of this equation is illustrated in Fig. 10.15.

#### 10.4.1 Low- or zero-silicon TRIP-assisted steels

The substantial silicon addition to TRIP-assisted steels leads to the formation of hard, adherent oxide ( $\text{Fe}_2\text{SiO}_4$ ) which is difficult to remove prior to hot

<sup>3</sup> Jacques, P., Furnemont, Q., Mertens, A. and Delannay, F. *Philosophical Magazine A* **81**, 1789, 2001.

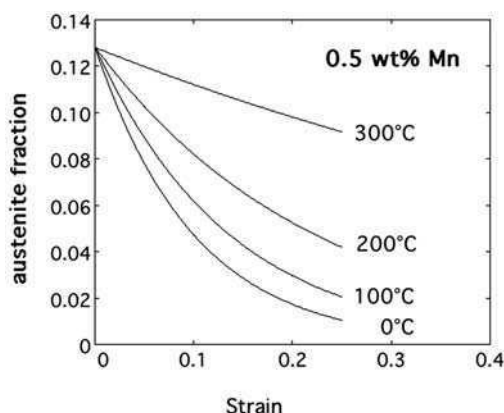


**Fig. 10.15** Martensitic transformation of retained austenite in a TRIP-assisted steel as a function of deformation temperature and plastic strain (Sherif, M., Garcia-Mateo, C., Sourmail, T. and Bhadeshia, H. K. D. H. *Materials Science and Technology* **20**, 319, 2004).

rolling, resulting in a poor surface finish. This restricts automobile applications to components which are hidden from view. Low-silicon TRIP steels do exist, as illustrated in Fig. 10.16. The austenite in such alloys is more difficult to retain because of the tendency to precipitate cementite, but this can be minimized with careful heat treatment. When this is done, strengths in excess of 600 MPa with a uniform ductility of 15% have been achieved.

#### 10.4.2 Galvanizing of TRIP-assisted steels

There are two basic methods of galvanizing, by dipping the steel in liquid zinc or by electrolytically depositing the zinc. The typical concentrations of silicon and manganese in TRIP-assisted steels lead to a stable  $\text{Mn}_2\text{SiO}_4$  oxide film on the surface during the heat treatment that leads to the desired microstructure. This makes it difficult for the zinc to wet the steel surface, making it necessary to electrolytically galvanize such alloys.

The problem can be alleviated by increasing the humidity in the annealing furnace. The oxide coverage of the surface is then reduced, giving better wetting by zinc. The higher humidity causes the internal oxidation of Mn and Si below the steel surface, thus reducing their availability to form  $\text{Mn}_2\text{SiO}_4$  at the surface.

An alternative approach is to eliminate the silicon and add aluminium to retain the cementite-free microstructure. Aluminium oxidizes easily to form alumina by internal oxidation near the surface, again limiting the amount of  $\text{FeAl}_2\text{O}_4$  that can form at the free surface when the humidity in the annealing furnace is low. Such a steel can easily be hot-dip galvanized. At high humidity,



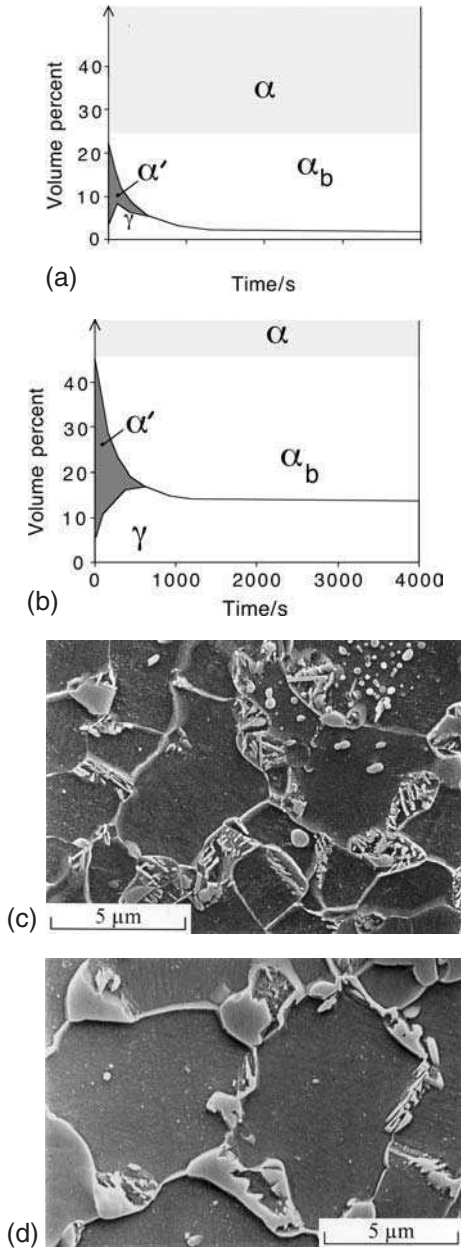


**Fig. 10.16** Evolution of room-temperature microstructure as a function of time during isothermal transformation to bainite. (a) Low-silicon steel Fe-0.16C-0.38Si-1.3Mn wt%. (b) High-silicon steel Fe-0.29C-1.41Si-1.42Mn wt%. (c) Scanning electron micrograph of low-silicon alloy isothermally transformed to bainite for 1800 s. Much of the austenite has decomposed to bainitic ferrite and cementite. (d) Corresponding micrograph for high-silicon steel transformed to bainite for 900 s with plenty of austenite evident (courtesy of Pascal Jacques).

MnO begins to cover the surface leading to a deterioration in the ability of the liquid zinc to wet the surface. The aluminium-containing steels are therefore better suited to continuous galvanizing lines.

It is clear that silicon and manganese must diffuse to the surface to form oxides. Some of the diffusion flux is via grain boundaries. When phosphorus is present, its segregation to the grain boundaries reduces the boundary diffusion-flux, thereby reducing the extent to which oxides form. Such steels are more amenable to wetting by molten zinc (in contrast, the same effect makes it more difficult to form iron–zinc compounds during the galvannealing process).

## 10.5 TWIP STEELS

There are three essential modes by which steels can be permanently deformed at ambient temperature, without recourse to diffusion. Individual dislocations whose Burgers vectors correspond to lattice vectors can glide, leading to a change in shape without altering the crystal structure or volume. In contrast, a displacive transformation (e.g. martensite or bainite) results not only in a plastic strain, but also a change of crystal structure and density; this is the phenomenon exploited in the TRIP steels.

The third mode of deformation is mechanical twinning, in which the crystal structure of the steel is preserved but the twinned region is reoriented in the process. Mechanical twinning results in a much larger shear strain  $s = 1/\sqrt{2}$ , compared with displacive transformations where  $s$  is typically 0.25. There is a particular class of extraordinarily ductile alloys of iron, known as the TWIP steels, which exploit mechanical twinning to achieve their properties.

TWIP stands for twinning-induced plasticity. The alloys are austenitic and remain so during mechanical deformation, but the material is able to accommodate strain via both the glide of individual dislocations and through mechanical twinning on the  $\{1\ 1\ \bar{1}\}_{\gamma} < 1\ 1\ \bar{2} >_{\gamma}$  system. The alloys typically contain a large amount of manganese, some aluminium and silicon (e.g. Fe–25Mn–3Si–3Al wt%) with carbon and nitrogen present essentially as impurities. Larger concentrations of carbon may be added to enhance strength. At high manganese concentrations, there is a tendency for the austenite to transform into  $\epsilon$ -martensite (hexagonal close packed) during deformation.  $\epsilon$ -martensite can form by the dissociation of a perfect  $a/2 < 0\ 1\ 1 >_{\gamma}$  dislocation into Shockley partials on a close packed  $\{1\ 1\ \bar{1}\}_{\gamma}$  plane, with a fault between the partials. This faulted region represents a three layer thick plate of  $\epsilon$ -martensite. A reduction in the fault energy therefore favours the formation of this kind of martensite. The addition of aluminium counters this because it raises the stacking fault energy of the austenite. Silicon has the opposite effect of reducing the stacking fault energy, but like aluminium, it leads to a reduction in the density of the steel; the combination of Al and Si at the concentrations used typically reduces the overall density from some  $7.8\text{ g cm}^{-3}$  to about  $7.3\text{ g cm}^{-3}$ .

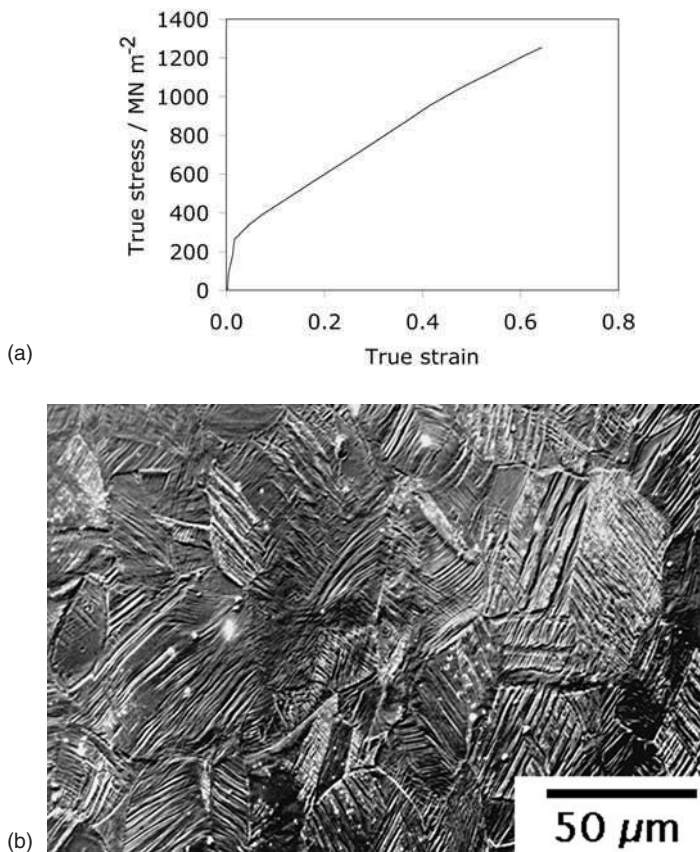


**Fig. 10.17** (a) Typical stress–strain curve for a TWIP steel. (b) Optical microstructure of a TWIP steel following deformation, showing profuse twinning (image and data courtesy of Frommeyer, G., Brück, U. and Neumann, P).

The alloys have a rather low yield strength at 200–300 MN m<sup>-2</sup> but the ultimate tensile strength can be much higher, in excess of 1100 MN m<sup>-2</sup>. This is because the strain-hardening coefficient is large, resulting in a great deal of uniform elongation, and a total elongation of some 60–95%. The effect of mechanical twinning is two-fold. The twins add to plasticity, but they also have a powerful effect in increasing the work-hardening rate by subdividing the untwinned austenite into finer regions (Fig. 10.17).

One major advantage of TWIP steels is that they are austenitic and they maintain attractive properties at cryogenic temperatures (–150°C) and high strain rates, e.g., 10<sup>3</sup> s<sup>-1</sup>. They therefore have great potential in enhancing the safety of automobiles by absorbing energy during crashes.

## 10.6 INDUSTRIAL STEELS SUBJECTED TO THERMOMECHANICAL TREATMENTS

Micro-alloyed steels produced by controlled rolling are a most attractive proposition in many engineering applications because of their relatively low cost, moderate strength, and very good toughness and fatigue strength, together with their ability to be readily welded. They have, to a considerable degree, eliminated quenched and tempered steels in many applications.

These steels are most frequently available in control-rolled sheet, which is then coiled over a range of temperatures between 750°C and 550°C. The coiling temperature has an important influence as it represents the final transformation temperature, and this influences the microstructure. The lower this temperature, under the same conditions, the higher the strength achieved. The normal range of yield strength obtained in these steels varies from about 350 to 550 MN m<sup>-2</sup> (50–80 ksi). The strength is controlled both by the detailed thermomechanical treatment, by varying the manganese content from 0.5 to 1.5 wt%, and by using the micro-alloying additions in the range 0.03 to above 0.1 wt%. Niobium is used alone, or with vanadium, while titanium can be used in combination with the other two carbide-forming elements. The interactions between these elements are complex, but in general terms niobium precipitates more readily in austenite than does vanadium as carbide or carbo-nitride, so it is relatively more effective as a grain refiner. The greater solubility of vanadium carbide in austenite underlines the superior dispersion strengthening potential of this element shared to a lesser degree with titanium. Titanium also interacts with sulphur and can have a beneficial effect on the shape of sulphide inclusions. Bearing in mind that the total effect of these elements used in conjunction is not a simple sum of their individual influence, the detailed metallurgy of these steels becomes extremely complex.

One of the most extensive applications is in pipelines for the conveyance of natural gas and oil, where the improved weldability due to the overall lower alloying content (lower hardenability) and, particularly, the lower carbon levels is a great advantage. Furthermore, as the need for larger diameter pipes has grown, steels of higher yield stress have to be used to avoid excessive wall thicknesses. In practice, wall thicknesses of 10–12.5 mm have been found to be the most convenient. Typical compositions (wt%) to achieve a yield stress of around 410 MN m<sup>-2</sup> (60 ksi):

C 0.12   S 0.012   Mn 1.35   Nb 0.03

C 0.12   S 0.006   Mn 1.33   Nb 0.02   V 0.04

for higher yield strengths (450 MN m<sup>-2</sup>):

C 0.06   S 0.006   Mn 1.55   Nb 0.05   V 0.10

However, it should be emphasized that often higher yield stresses are achieved by control of the fabrication variables such as the temperature at which

**Table 10.1** Typical compositions of micro-alloyed vanadium steels

Element	Typical composition (%)	
	Yield strength 345 (MN m <sup>-2</sup> ) (50 ksi)	550 (MN m <sup>-2</sup> ) (80 ksi)
Carbon	0.08–0.12	0.12–0.17
Manganese	0.75–1.10	1.20–1.55
Phosphorus	0.008–0.013	0.008–0.013
Sulphur	0.007–0.020	0.007–0.020
Silicon	0.05–0.15	0.30–0.55
Aluminium	0.03–0.06	0.03–0.06
Vanadium	0.03–0.07	0.10–0.14
Nitrogen	0.006–0.012	0.015–0.022
Cerium	0.02–0.06	0.02–0.06

rolling is finished and the temperature used for coiling the sheet. Nitrogen is often deliberately used as an alloying element. One successful range of steels relies on vanadium to form carbo-nitride precipitates for grain size control and dispersion strengthening. In some steels, rare earth additions are made to control the inclusion shape. Typical compositions at lower and higher strength levels are given in Table 10.1.

At the higher strength levels, micro-alloyed steels are used for heavy duty truck frames, tractor components, crane booms and lighting standards, etc. The control of sulphide inclusions gives the steels a high degree of formability in cold fabrication processes. This recent development has allowed the use of HSLA steels for many applications involving substantial cold forming which previously led to cracking in the absence of rare earth additions.

A steel is said to have been ausformed when martensite is produced from plastically deformed austenite. Ausforming has provided some of the strongest, toughest steels so far produced, with the added advantage of very good fatigue resistance. However, they usually have high concentrations of expensive alloying elements and must be subjected to large deformations which impose heavy work loads on rolling mills. Nevertheless, these steels are particularly useful where a high strength to weight ratio is required and where cost is a secondary factor. Typical applications have included parts for undercarriages of aircraft, special springs and bolts.

The 12 wt% Cr transformable steels respond readily to ausforming to the extent that tensile strengths of over 3000 MN m<sup>-2</sup> (>200 tsi) can be obtained in appropriate compositions. A 0.4C–6Mn–3Cr–1.5Si steel has been ausformed to a tensile strength of 3400 MN m<sup>-2</sup>, with an improvement in ductility over the conventional heat treatment. Similar high strength levels with good ductility have been reported for 0.4C–5Cr–1.3Mo–1.0Si–0.5V wt% steel (H11) (Fig. 10.18). All

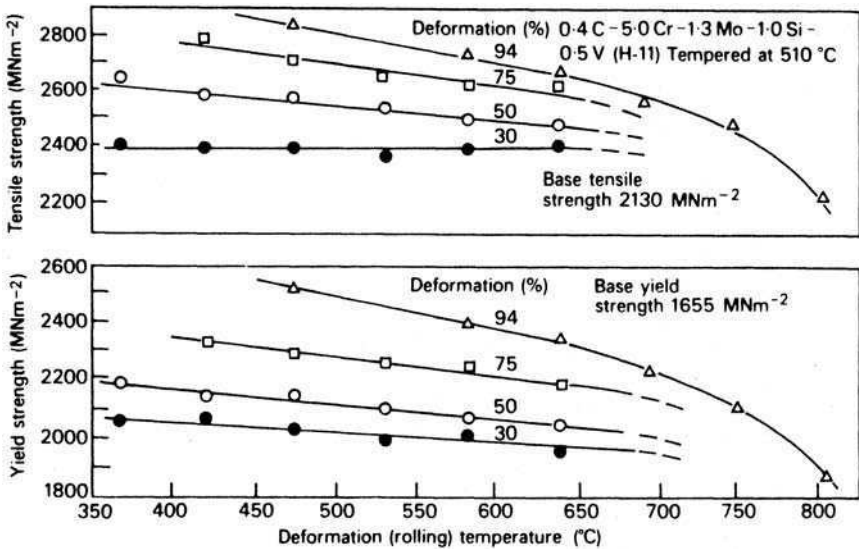


**Fig. 10.18** Effect of amount and temperature of deformation on the yield and tensile strength of 0.4C–5.0Cr–1.3Mo–1.0Si–0.5V wt% steel (H11) (Zackay, in *National Physical Laboratory Symposium*, No. 15, HMSO, London, UK, 1963).

of these steels are sufficiently highly alloyed to allow adequate time for substantial deformation in the austenitic bay of the time–temperature–transformation curve prior to transformation.

## FURTHER READING

- Bhadeshia, H. K. D. H., TRIP-Assisted Steels? *ISIJ International*, **42**, 1059, 2002.
- Cooman, B. C. de, Structure–properties relationship in TRIP steels containing carbide-free bainite, *Current Opinion in Solid State and Materials Science* **8**, 285, 2004.
- Davenport, A. T. (ed.), *Formable HSLA and Dual-phase Steels*, The Metallurgical Society of AIME, USA, 1979.
- Davies, G., *Materials for Automobile Bodies*, Elsevier, London, 2003.
- Frommeyer, G., Brück, U. and Neumann, P., Supra-ductile and high-strength manganese-TRIP/TWIP steels for high energy absorption purposes, *ISIJ International* **43**, 438, 2003.
- Gladman, T., *Physical Metallurgy of Microalloyed Steels*, Institute of Materials, London, 1997.
- HSLA Steels – Metallurgy and Applications. Proceedings of an International Conference*, Beijing, 1985, Chinese Society of Metals, ASM International.
- International Conference on Processing, Microstructure and Properties of Microalloyed and Other Modern Low Alloy Steels*, Pittsburgh, 1991.
- Jacques, P. J., Transformation-induced plasticity for high strength formable steels, *Current Opinion in Solid State and Materials Science* **8**, 259, 2004.

- Kozasu, I., Processing – thermomechanical controlled processing in *Materials Science and Technology* (eds Cahn, R. W., Haasen, P. and Kramer, E. J.), Vol. 7, *Constitution and Properties of Steels* (ed. Pickering, F. B.), VCH, Weinheim, Germany, 1992.
- Krauss, G. (ed.), *Deformation, Processing and Structure*, American Society for Metals, Ohio, USA, 1984.
- Maki, J., Mahieu, J., de Cooman, B. C. and Claessens, S., Galvanisability of silicon free CMnAl TRIP steels, *Materials Science and Technology* **19**, 125, 2003.
- Physical Metallurgy of Thermo-mechanical Processing of Steels and other Metals* (Thermec 88), Iron and Steel Institute of Japan, 1988.
- Yokota, T., Garcia-Mateo, C., and Bhadeshia, H. K. D. H., Transformation-induced plasticity for high strength formable steels, *Scripta Materialia* **51**, 767, 2004.



---

# THE EMBRITTLEMENT AND FRACTURE OF STEELS

## 11.1 INTRODUCTION

Most groups of alloys can exhibit failure by cracking in circumstances where the apparent applied stress is well below that at which failure would normally be expected. Steels are no exception to this, and probably exhibit a wider variety of failure mechanisms than any other category of material. While ultimate failure under excessive stress must occur and can be reasonably predicted by appropriate mechanical tests, premature failure is always dangerous, involving a considerable element of unpredictability. However, a detailed knowledge of structure and of the distribution of impurities in steels is gradually leading to a much better understanding of the origins and mechanisms of the various types of cracks encountered. Furthermore, the now well-established science of fracture mechanics allows the quantitative assessment of growth of cracks in various stress situations, to an extent that it is now frequently possible to predict the stress level to which steel structures can be confidently subjected without the risk of sudden failure.

## 11.2 CLEAVAGE FRACTURE IN IRON AND STEEL

Cleavage fracture is familiar in many minerals and inorganic crystalline solids as a crack propagation frequently associated with very little plastic deformation and occurring in a crystallographic fashion along planes of low indices, i.e. high atomic density. A low temperatures zinc cleaves along the basal plane, while body-centred cubic (bcc) iron cleaves along  $\{100\}$  planes (Fig. 11.1), as do all bcc metals. This behaviour would appear to be an intrinsic characteristic of iron, but it has been shown that iron, highly purified by zone refining and containing minimal concentrations of carbon, oxygen and nitrogen, is very ductile even at



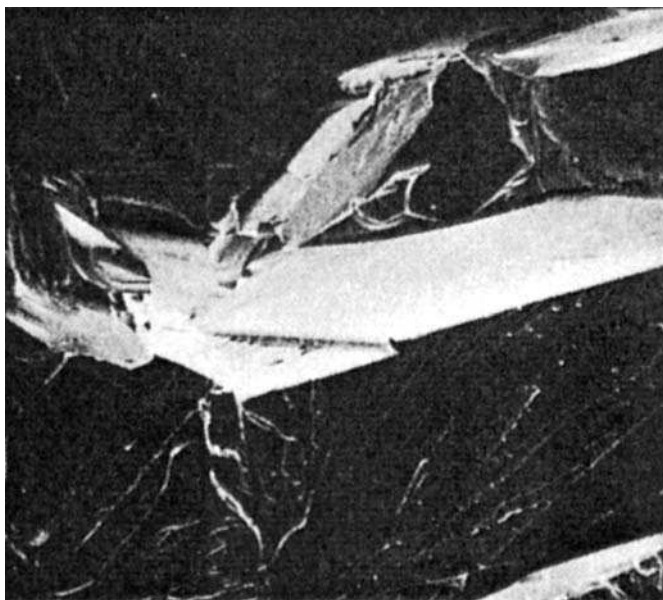


**Fig. 11.1** Cleavage fracture in pure iron–0.04 P at 55°C (courtesy of Shell)  $\times 60$ .

extremely low temperatures. For example, at 4.2 K reductions in area in tensile tests of up to 90% have been observed with iron specimens of the highest available purity. As the carbon and nitrogen content of the iron is increased, the transition from ductile to brittle cleavage behaviour takes place at increasing temperatures, until in some steels this can occur at ambient and above-ambient temperatures. Clearly, the significant variables in such a transition are of great basic and practical importance.

The propagation of a cleavage crack in iron and steel requires much less energy than that associated with the growth of a ductile crack. This is easily shown by carrying out impact tests in a pendulum apparatus (Charpy, Izod and Housfield type tests) over a range of temperature. The energy absorbed by the specimen from the pendulum when plotted as a function of temperature usually exhibits a sharp change in slope (Fig. 11.2) as the mode of fracture changes from ductile to brittle. These impact transition curves are a simple way of defining the effect of metallurgical variables, e.g. heat treatment (Fig. 11.2) on the fracture behaviour of a steel from which a fairly precise transition temperature,  $T_c$ , can be readily obtained for a particular heat treatment. However, it should be emphasized that  $T_c$  is not an absolute value and it is likely to change appreciably as the mode of testing is altered. It nevertheless provides a simple way of comparing the effects of metallurgical variables on the fracture behaviour.

More sophisticated tests have been developed in which it is recognized that the propagation of the fracture is the important stage. These fracture toughness

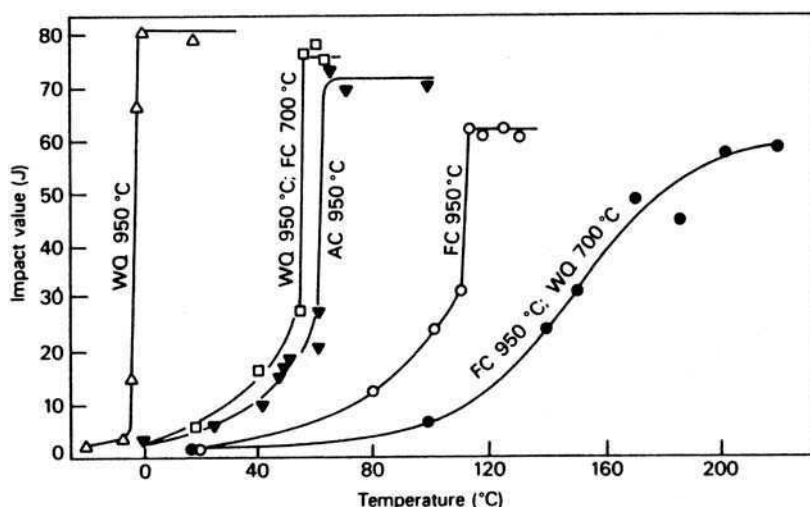


**Fig. 11.2** Effect of heat treatments on the impact transition temperature of a pure iron-0.12C wt% alloy (after Allen et al., *Journal of Iron and Steel Institute* **174**, 108, 1953). AC, FC and WQ represent air-cooling, furnace-cooling and water-quenching, respectively.

tests used notched and pre-cracked specimens, the cracks being initiated by fatigue. The stress intensity factor,  $K$ , at the root of the crack is defined in terms of the applied stress  $\sigma$  and the crack size  $c$ :

$$K = \sigma(\pi c)^{1/2}.$$

When a critical stress intensity  $K_c$  is reached, the transition to rapid fracture takes place.

### 11.3 FACTORS INFLUENCING THE ONSET OF CLEAVAGE FRACTURE

There are several factors, some interrelated, which play an important part in the initiation of cleavage fracture:

1. The temperature dependence of the yield stress.
2. The development of a sharp yield point.
3. Nucleation of cracks at twins.
4. Nucleation of cracks at carbide particles.
5. Grain size.

All bcc metals including iron shown a marked temperature dependence of the yield stress, even when the interstitial impurity content is very low, i.e. the stress necessary to move dislocations, the Peierls-Nabarro stress, is strongly

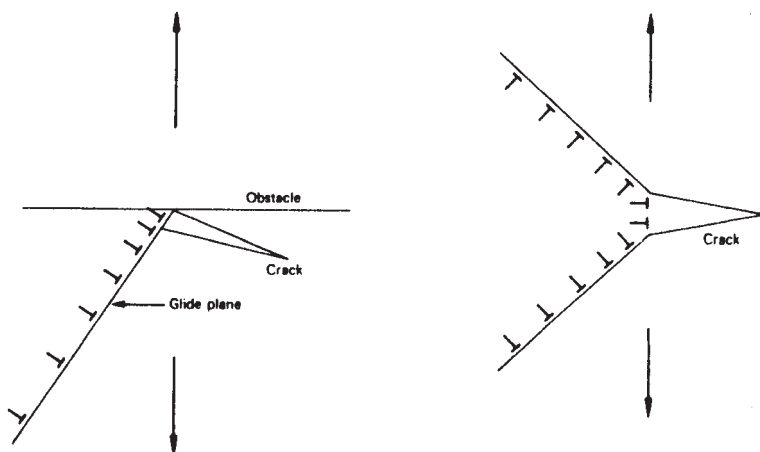


**Fig. 11.3** Schematic diagram of dislocation mechanisms for crack nucleation.

temperature dependent. This means that as the temperature is lowered the first dislocations to move will do so more rapidly as the velocity is proportional to the stress, and so the chances of forming a crack nucleus, e.g. by dislocation coalescence (Fig. 11.3), will increase. Figure 11.3 shows schematically two ways in which dislocation pile-ups could nucleate cracks.

The interstitial atoms, carbon and nitrogen, will cause the steel to exhibit a sharp yield point (Chapter 2) either by the catastrophic break-away of dislocations from their interstitial atom atmospheres (Cottrell–Bilby theory), or by the rapid movement of freshly generated dislocations (Gilman–Johnson theory). In either case, the conditions are suitable for the localized rapid movement of dislocations as a result of high stresses which provides a favourable situation for the nucleation of cracks by dislocation coalescence.

The flow stress of iron increases rapidly with decreasing temperature (Fig. 2.2) to a point where the critical stress for deformation twinning is reached, so that this becomes a significant deformation mechanism. It has been shown that cracks are preferentially nucleated at various twin configurations, e.g. at twin intersections and at points where twins contact grain boundaries, so that, under the same conditions, crack propagation is more likely in twinned iron. It should also be noted that the temperature dependence of the flow stress makes plastic deformation more difficult at the tip of a moving crack, so less plastic blunting of the crack tip will take place at low temperatures, thus aiding propagation.

So far, we have discussed crack nucleation mechanisms which can take place in a single phase material, e.g. relatively pure iron, but in the presence of a second phase such as cementite it is still easier to nucleate cracks. Plastic deformation can crack grain boundary cementite particles or cementite lamellae in pearlite so as to produce micro-cracks (Fig. 11.4) which, in certain circumstances, propagate

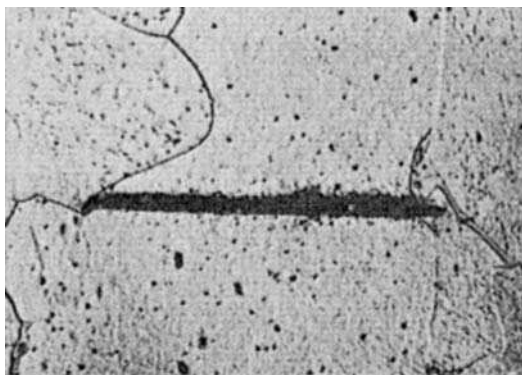


**Fig. 11.4** Nucleation of a cleavage crack at a carbide particle in a low-carbon steel (courtesy of Knott). Optical micrograph,  $\times 400$ .

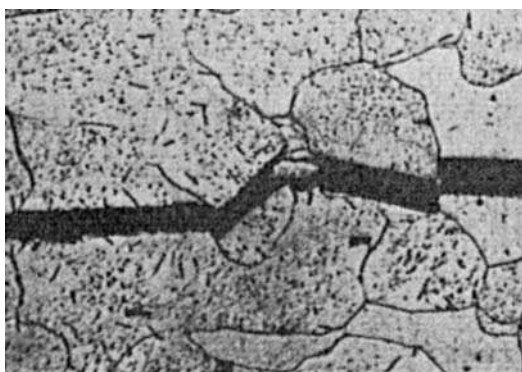


**Fig. 11.5** Transgranular propagation of a crack in a low-carbon steel (courtesy of Knott). Optical micrograph,  $\times 275$ .

to cause catastrophic cleavage failure (Fig. 11.5). Recent work supports the view that this microstructural parameter is extremely important in determining the fracture characteristics of a steel. Brittle inclusions such as alumina particles or various silicates found in steels can also be a source of crack nuclei.

Grain size is a particularly important variable for, as the ferrite grain size is reduced, the transition temperature  $T_c$  is lowered, despite the fact that the yield strength increases. This is, therefore, an important strengthening mechanism which actually improves the ductility of the steel. It has been shown by Petch that  $T_c$  is linearly related to  $\ln d^{-1/2}$ , and an appropriate relationship of this type can be derived from a dislocation model involving the formation of crack nuclei at dislocation pile-ups at grain boundaries. The smaller the grain size, the smaller the number of dislocations piling-up where a slip band arrives at a boundary. Bearing in mind that the shear stress at the head of such a pile-up

is  $n\tau$ , where  $n$  is the number of dislocations and  $\tau$  is the shear stress in the slip direction, it follows that as the grain size is reduced,  $n$  will be smaller and the local stress concentrations at grain boundaries will be correspondingly less. This situation will lead to less crack nuclei regardless of whether they are formed by dislocation coalescence or by dislocation pile-ups causing carbides to crack or by twinning interactions.

#### 11.4 CRITERION FOR THE DUCTILE/BRITTLE TRANSITION

The starting point of all theories on brittle fracture is the work of Griffith, who considered the condition needed for propagation of a pre-existing crack, of length  $2c$ , in a brittle solid. When the applied stress  $\sigma$  is high enough, the crack will propagate and release elastic energy. This energy  $U_e$  in the case of thin plates (plane stress) is:

$$U_e = \frac{\pi c^2 \sigma^2}{E} \text{ per unit plate thickness,} \quad (11.1)$$

where  $E$  is Young's modulus. The term is negative because this energy is released. However, as the crack creates two new surfaces, each with energy  $= 2c\gamma$ , there is a positive surface energy term  $U_s$ :

$$U_s = 4c\gamma, \quad \text{where } \gamma = \text{surface energy per unit area.}$$

Griffith showed that the crack would propagate if the increase in surface energy,  $U_s$ , was less than the decrease in elastic energy  $U_e$ . The equilibrium position is defined as that in which the change in energy with crack length is zero:

$$\frac{dU}{dc} = \frac{d(U_e + U_s)}{dc} = 0. \quad (11.2)$$

This is the elastic energy release rate, usually referred to as  $G$ :

$$\therefore \left( -\frac{2\pi c \sigma^2}{E} + 4\gamma \right) = 0,$$

and

$$\sigma_f = \left( \frac{2\gamma E}{\pi c} \right)^{1/2}, \quad (11.3)$$

where  $\sigma_f$  is the fracture stress, which is defined as that just above which energy is released and the crack propagates. This equation shows that the stress  $\sigma$  is inversely related to crack length, so that as the crack propagates the stress needed drops and the crack thus accelerates. Orowan pointed out that in crystalline solids plastic deformation will occur both during nucleation of the crack, and then at the root of the crack during propagation. This root deformation

blunts the crack and, in practice, means that more energy is needed to continue the crack propagation. Thus, the Griffith equation is modified to include a plastic work term  $\gamma_p$ :

$$\sigma_f = \left( \frac{E(2\gamma + \gamma_p)}{\pi c} \right)^{1/2}. \quad (11.4)$$

It has been found that  $\gamma_p \gg \gamma$ , hence the condition for crack spreading in a crystalline solid such as iron is:

$$\sigma_f = \left( \frac{E\gamma_p}{\pi c} \right)^{1/2}. \quad (11.5)$$

The local stress field at the crack tip is usually characterized by a parameter  $K$ , the stress intensity factor, which reaches a critical value  $K_c$  when propagation takes place. This critical value is given by:

$$K_c = \sigma_f \sqrt{\pi c}. \quad (11.6)$$

In plane stress conditions:

$$K_c = \sqrt{EG_c},$$

where  $G_c$  is the critical release rate of strain energy.

In plane strain conditions, the critical value of strain energy release rate is  $G_{1C} = \gamma_p$ , where:

$$\sigma_f = \left( \frac{EG_{1C}}{\pi(1 - \nu^2)c} \right)^{1/2}, \quad (11.7)$$

and where  $\nu$  is the Poisson's ratio.

The critical value of stress intensity,  $K_{1C}$ , is then related to  $G_{1C}$ :

$$K_{1C} = \left( \frac{EG_{1C}}{\pi(1 - \nu^2)} \right)^{1/2}. \quad (11.8)$$

The fracture toughness of a steel is often expressed as a  $K_{1C}$  value obtained from tests on notched specimens which are pre-cracked by fatigue, and are stressed to fracture in bending or tension.

The nucleation and the propagation of a cleavage crack must be distinguished clearly. Nucleation occurs when a critical value of the *effective shear stress* is reached, corresponding to a critical grouping, ideally a pile-up, of dislocations which can create a crack nucleus, e.g. by fracturing a carbide particle. In contrast, propagation of a crack depends on the magnitude of the local *tensile stress* which must reach a critical level  $\sigma_f$ . Simple models of slip-nucleated fracture assume either interaction of dislocations or cracks formed in grain boundary carbides. However, recently it has been realized that both these structural features must be taken into account in deriving an expression for the critical fracture stress

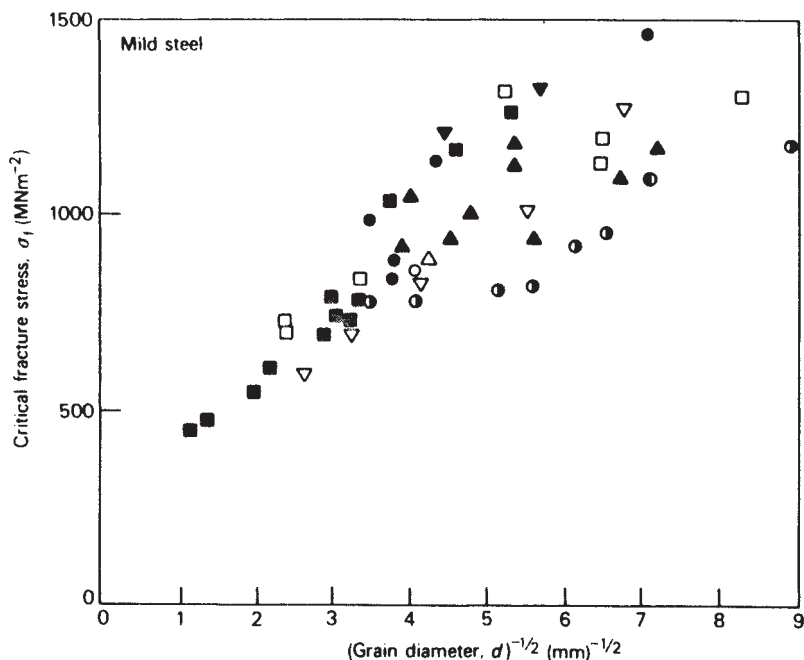


**Fig. 11.6** Dependence of local fracture stress  $\sigma_f$  on the grain size of mild steel. Data from many sources (courtesy of Knott).

$\sigma_f$ . The critical stress does not appear to be temperature dependent. At low temperatures the yield stress is higher, so the crack propagates when the plastic zone ahead of the crack is small, whereas at higher temperatures, the yield stress being smaller, a larger plastic zone is required to achieve the critical local tensile stress  $\sigma_f$ .

This tensile stress  $\sigma_f$  has been determined for a wide variety of mild steels, and has been shown to vary roughly linearly with  $d^{-1/2}$  (Fig. 11.6). The scatter probably arises from differences in test temperature and carbide dimensions. This is conclusive evidence for the role of finer grain sizes in increasing the resistance to crack propagation. Regarding grain boundary carbide size, effective crack nuclei will occur in particles above a certain critical size so that, if the size distribution of carbide particles in a particular steel is known, it should be possible to predict its critical fracture stress. Therefore, in mild steels in which the structure is essentially ferrite grains containing carbide particles, the particle size distribution of carbides is the most important factor. In contrast, in bainitic and martensitic steels the austenite grains transform to lath structures where the lath width is usually between 0.2 and 2  $\mu\text{m}$ . the laths occur in bundles or packets (see Chapter 5) with low angle boundaries between the laths. Larger misorientations occur across packet boundaries. In such structures, the packet width is the main microstructural feature controlling cleavage crack propagation.

The critical local fracture stress  $\sigma_f$  has been related to the two types of structure, as follows:

1. For ferritic steels with spheroidal carbide particles:

$$\sigma_f = \left( \frac{\pi E \gamma_p}{2c_0} \right)^{1/2}, \quad (11.9)$$

where  $c_0$  is carbide diameter.

2. For bainitic and martensitic steels with packets of laths:

$$\sigma_f = \left( \frac{4E\gamma_p}{(1-\nu^2)d_p} \right)^{1/2} \quad (11.10)$$

where  $d_p$  is packet width and  $\nu$  is Poisson's ratio.

## 11.5 PRACTICAL ASPECTS OF BRITTLE FRACTURE

At the onset of fracture, elastic energy stored in the stressed steel is only partly used for creation of the new surfaces and the associated plastic deformation and the remainder provides kinetic energy to the crack. Using a Griffith-type model, the crack velocity  $v$  can be shown to be:

$$v = \sqrt{\frac{2\pi}{k}} \sqrt{\frac{E}{\rho}} \left( 1 - \frac{c_0}{c} \right)^{1/2},$$

where  $c_0$  is the critical size,  $c$  is the half crack size at a given instant,  $\rho$  is density and  $k$  is the constant. This relation shows that the velocity increases with increasing crack size and reaches a limiting value  $v_{\text{lim}}$  at large values of  $c$ . In practice,  $v_{\text{lim}}$  is between 0.4 and 0.5 of the speed of sound, so brittle fracture occurs with catastrophic rapidity, as many disasters testify.

The phenomenon of brittle fracture became particularly prevalent with the introduction of welding as the major steel fabrication technique. Previously, brittle cracks often stopped at the joints of riveted plates but the steel structures resulting from welding provided continuous paths for crack propagation. Added to this, incorrect welding procedures can give rise to high stress concentrations and also to the formation of weld-zone cracks which may initiate brittle fracture. While brittle failures of steels have been experienced since the latter half of the nineteenth century when steel began to be used widely for structural work, the most serious failures have occurred in more recent years as the demand for integral large steel structures has greatly increased, e.g. in ships, pipelines, bridges and pressure vessels. Spectacular failures took place in many of the all-welded Liberty ships produced during the Second World War, when nearly 1500 incidents involving serious brittle failure were recognized and 19 ships broke



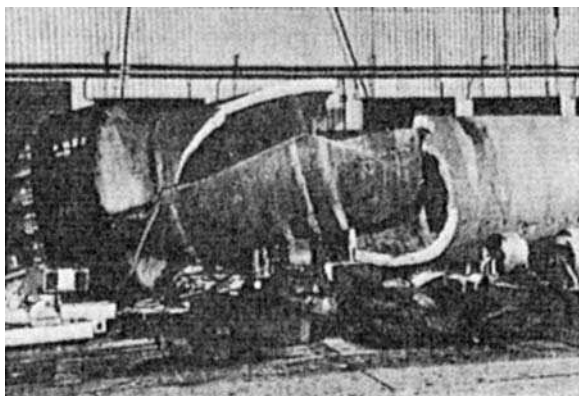


**Fig. 11.7** Brittle fracture of a thick-walled steel pressure vessel (The Welding Institute).

completely in two without warning. Despite our increasing understanding of the phenomenon and the great improvements in steel making and in welding since then, serious brittle failures still occur (Fig. 11.7), a constant reminder that human error and lack of scientific control can be disastrous.

Bearing in mind the temperature dependence of the failure behaviour, and the widening use of steels at low temperatures, e.g. in Arctic pipelines, for storage of liquid gases, etc., it is increasingly necessary to have steels with very low transition temperatures and high fracture toughness. While there are many variables to consider in achieving this end, including the detailed steel-making practice, the composition including trace elements and the fabrication processes involved, the most important is probably grain size refinement. The development of high strength low alloy steels (HSLA) or micro-alloyed steels (Chapter 9), in the manufacture of which controlled rolling plays a vital part, has led to the production of structural steels with grain sizes often less than  $10\text{ }\mu\text{m}$  combined with good strength levels (yield strength between  $400$  and  $600\text{ MN m}^{-2}$ ) and low transition temperatures. In these steels, to which small concentrations ( $<0.1\text{ wt}\%$ ) of niobium, vanadium or titanium are added, the carbon level is usually less than  $0.15\text{ wt}\%$  and often below  $0.10\text{ wt}\%$ , so that the carbide phase occupies a small volume fraction. In any case, cementite, which forms relatively coarse particles or lamellae in pearlite, is partly replaced by much finer dispersions of alloy carbides,  $\text{NbC}$ , etc. Addition of certain other alloying elements to steel, notably manganese and nickel, results in a lowering of the transition temperature. For example, alloy steels with  $9\text{ wt}\%$  nickel and less than  $0.1\text{ wt}\%$  carbon have a sufficiently low transition temperature to be able to be used for large containers of liquid gases, where the temperature can be as low as  $77\text{ K}$ . Below this temperature, austenitic steels have to be used. Of the elements unavoidably present in steels, phosphorus, which is substantially soluble in  $\alpha$ -iron, raises the transition temperature and thus must be kept to as low a concentration as possible. On the other hand, sulphur has a very low solubility, and

is usually present as manganese sulphide with little effect on the transition temperature but with an important role in ductile fracture. Oxygen is an embrittling element even when present in very small concentrations. However, it is easily removed by deoxidation practice involving elements such as manganese, silicon and aluminium.

Finally, the fabrication process is often of crucial importance. In welding it is essential to have a steel with a low carbon equivalent, i.e. a factor incorporating the effects on hardenability of the common alloying elements. A simple empirical relationship, as a rough guide, is:

$$\% \text{ carbon equivalent} = C + \frac{\text{Mn}}{6} + \left( \frac{\text{Cr} + \text{Mo} + \text{V}}{5} \right) + \left( \frac{\text{Ni} + \text{Cu}}{15} \right) \text{ (in wt\%)},$$

where a steel with an equivalent of less than 0.45 should be weldable with modern techniques. The main hazard in welding is the formation of martensite in the heat-affected zone (HAZ), near the weld, which can readily lead to microcracks. This can be avoided, not only by control of hardenability but also by preheating the weld area to lead to slower cooling after welding or by post-heat treatment of the weld region. However, in some high-strength steels, slower cooling may result in the formation of upper bainite in the HAZ which encourages cleavage fracture.

Attention must also be paid to the possibility of hydrogen absorption leading to embrittlement. The presence of hydrogen in steels often leads to disastrous brittle fracture, e.g. there have been many failures of high-strength steels into which hydrogen was introduced during electroplating of protective surface layers. Concentration of a few parts per million are often sufficient to cause failure. While much hydrogen escapes from steel in the molecular form during treatment, some can remain and precipitate at internal surfaces such as inclusion/matrix and carbide/matrix interfaces, where it forms voids or cracks. Cleavage crack growth then occurs slowly under internal hydrogen pressure, until the critical length for instability is reached, and failure occurs rapidly. Hydrogen embrittlement is not sensitive to composition, but to strength level of the steel, the problem being most pronounced in high strength alloy steels. It is frequently encountered after welding (Fig. 11.8), where it can be introduced by use of damp welding electrodes, leading to cracking which is variously referred to as *underbead cracking*, *cold cracking* and *delayed cracking*. This phenomenon can be minimized by the use of welding electrodes with very low hydrogen contents, which are oven-dried prior to use.

## 11.6 DUCTILE OR FIBROUS FRACTURE

### 11.6.1 General

The higher temperature side of the ductile/brittle transition is associated with a much tougher mode of failure, which absorbs much more energy in the impact

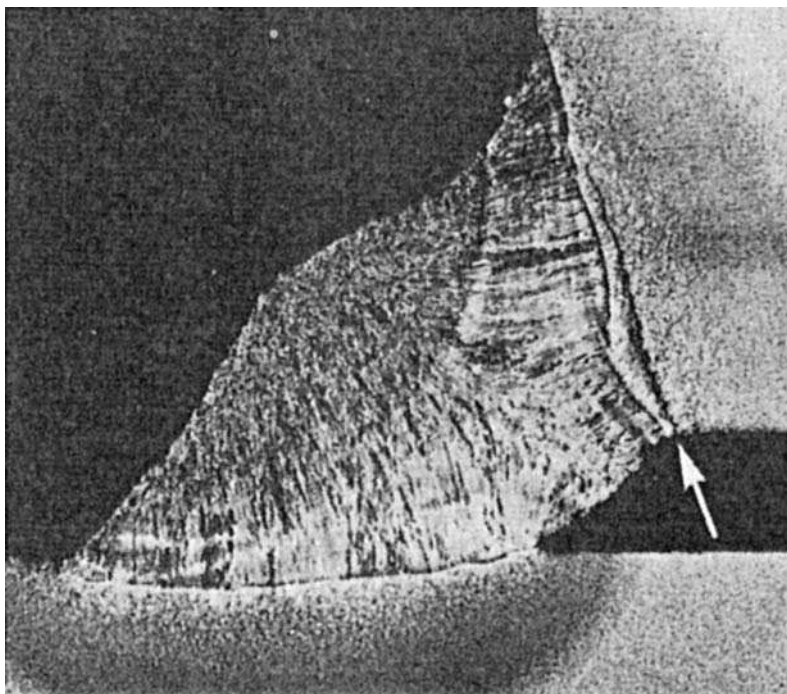


**Fig. 11.8** Cleavage crack due to hydrogen embrittlement in the HAZ of a weld in BS 968 steel (The Welding Institute).

test. While the failure mode is often referred to as ductile fracture, it could be described as rupture, a slow separation process which, although transgranular, is not markedly crystallographic in nature. Scanning electron micrographs of the ductile fracture surface (Fig. 11.9), in striking contrast to those from the smooth faceted cleavage surface, reveal a heavily dimpled surface, each depression being associated with a hard particle, either a carbide or non-metallic inclusion.

It is now well established that ductile failure is initiated by the nucleation of voids at second-phase particles. In steels these particles are either carbides, sulphide or silicate inclusions. The voids form either by cracking of the particles, or by decohesion at the particle/matrix interfaces, so it is clear that the volume fractions, distribution and morphology of both carbides and of inclusions are important in determining the ductile behaviour, not only in the simple tensile test, but in complex working operations. Therefore, significant variables, which determine ductility of steels, are to be found in the steel-making process, where the nature and distribution of inclusions is partly determined, and in subsequent solidification and working processes. Likewise, the carbide distribution will depend on composition and on steel-making practice, and particularly

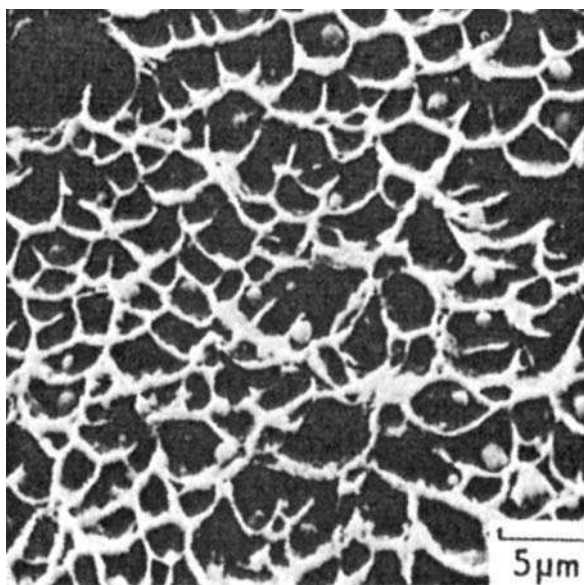


**Fig. 11.9** Ductile fracture of a low alloy steel (courtesy of R. F. Smith). Scanning electron micrographs.

on the final heat treatment involving the transformation from austenite, which largely determines the carbide size, shape and distribution.

The formation of voids begins very early in a tensile test, as a result of high stresses imposed by dislocation arrays on individual hard particles. Depending on the strength of the particle/matrix bond, the voids occur at varying strains, but for inclusions in steels the bonding is usually weak so voids are observed at low plastic strains. These elongate under the influence of the tensile stress but, additionally, a lateral stress is needed for them to grow sideways and link up with adjacent voids forming *micronecks*. These necks progressively part (Fig. 11.10) leading to the ductile fracture surfaces with a highly dimpled appearance. The second-phase particles (MnS) can be clearly seen in Fig. 11.10.

Many higher-strength steels exhibit lower work-hardening capacity as shown by relatively flat stress-strain curves in tension. As a result, at high strains the flow localizes in shear bands, where intense deformation leads to decohesion, a type of shear fracture. While the detailed mechanism of this process is not yet clear, it involves the localized interaction of high dislocation densities with carbide particles.

### 11.6.2 Role of inclusions in ductility

It is now generally recognized that the deformability of inclusions is a crucial factor which plays a major role, not only in service where risk of fracture exists, but also during hot and cold working operations such as rolling, forging, machining.

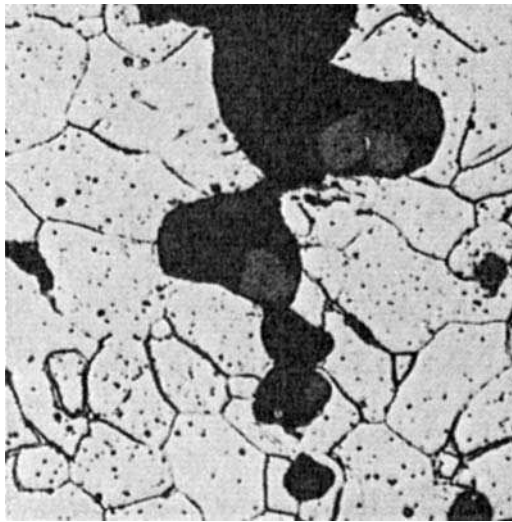


**Fig. 11.10** Growth of a ductile crack in a free-cutting mild steel containing sulphides (courtesy of R. F. Smith). Optical micrograph.  $\times 600$ .

Kiessling has divided the inclusions found in steels into five categories relating to their deformation behaviour:

1.  *$Al_2O_3$  and calcium aluminates*: these arise during deoxidation of molten steels. They are brittle solids, which are in practical terms undeformable at all temperatures.
2. *Spinel-type oxides  $AO-B_2O_3$* : these are undeformable in the range room temperature to  $1200^\circ C$ , but may be deformed above this temperature.
3. *Silicates of calcium, manganese, iron and aluminium in various proportions*: these inclusions are brittle at room temperature, but increasingly deformable at higher temperatures. The formability increases with decreasing melting point of the silicate, e.g. from aluminium silicate to iron and manganese silicates.
4.  *$FeO$ ,  $MnO$  and  $(FeMn)O$* : these are plastic at room temperature, but appear gradually to become less plastic above  $400^\circ C$ .
5. *Manganese sulphide  $MnS$* : this common inclusion type is deformable, becoming increasingly so as the temperature falls. There are three main types of  $MnS$  inclusion dependent on their mode of formation, which markedly influences their morphology:
  - Type I: Globular, formed only when oxygen is present in the melt, e.g. in rimming steels (Fig. 11.11a).
  - Type II: Interdendritic eutectic form, familiar in killed steels (Fig. 11.11b).
  - Type III: Random angular particles, found in fully deoxidized steels (Fig. 11.11c).

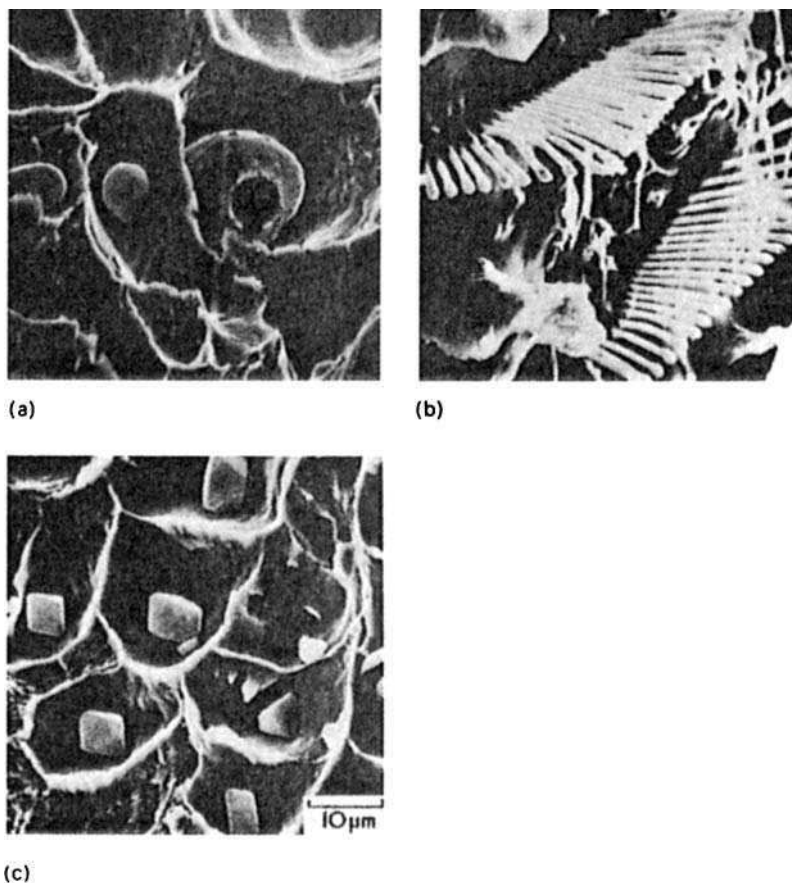


**Fig. 11.11** Manganese sulphide inclusions in steels: (a) type I; (b) type II; (c) type III (courtesy of T. J. Baker). Scanning electron micrographs.  $\times 1000$ .

It is now known that ductile failure can be associated with any of the types of inclusion listed above, from the brittle alumina type to the much more ductile sulphide inclusions. However, the inclusions are more effective in initiating ductile cracks above a critical size range. The coarser particles lead to higher local stress concentrations, which cause localized rupture and microcrack formation. Some quantitative work has now been done on model systems, e.g. iron–alumina where the progressive effect on ductility of increasing volume fraction of alumina is readily shown. The reduction in yield stress, also observed, arises from stress concentrations around the inclusions and is already evident at relatively low volume fractions.

The presence of particles in the size range  $1\text{--}35\text{ }\mu\text{m}$  broadens substantially the temperature range of the ductile/brittle transition in impact tests and also lowers the energy absorbed during ductile failure, the *shelf energy*. A fine

dispersion of non-brittle type inclusions can delay cleavage fracture by localized relaxation of stresses with a concomitant increase in yield stress.

Regarding cyclic stressing, it appears that inclusions must reach a critical size before they can nucleate a fatigue crack but the size effect depends also very much on the particular shape, e.g. whether spherical or angular. It has been found in some steels, e.g. ball bearing steels, that fatigue cracks originate only at brittle oxide inclusions, and not at manganese sulphide particles or oxides coated with manganese sulphide. In such circumstances the stresses which develop at particle interfaces with the steel matrix, as a result of differences in thermal expansion, appear to play an important part. It has been found that the highest stresses arise in calcium aluminates, alumina and spinel inclusions, which have substantially smaller thermal expansion coefficients than steel. These inclusions have the most deleterious effects on fatigue life.

The behaviour of ductile inclusions such as MnS during fabrication processes involving deformation has a marked effect on the ductility of the final product. Types I and III manganese sulphide will be deformed to ellipsoidal shapes, while type II colonies will rotate during rolling into the rolling plane, giving rise to very much reduced toughness and ductility in the transverse direction. This type of sulphide precipitate is the most harmful so efforts are now made to eliminate it by addition of strong sulphide forming elements such as Ti, Zr and Ca. The lack of ductility is undoubtedly encouraged by the formation at the inclusion interfaces of voids because the MnS contracts more than the iron matrix on cooling, and the interfacial bond is probably insufficiently strong to suppress void formation. The variation in ductility with direction in rolled steels can be extreme because of the directionality of the strings of sulphide inclusions, and this in turn can adversely affect ductility during many working operations.

Cracking can also occur during welding of steel sheet with low transverse ductility. This takes place particularly in the parent plate under butt welds, the cracks following the line of the sulphide inclusion stringers. The phenomenon is referred to as *lamellar tearing* (Fig. 11.12).

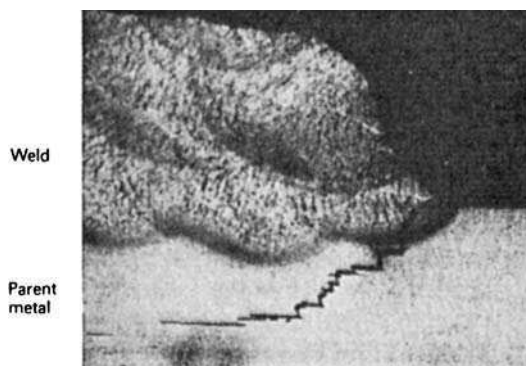


**Fig. 11.12** Lamellar tearing near a weld (The Welding Institute).

### 11.6.3 Role of carbides in ductility

The ductility of steel is also influenced by the carbide distribution which can vary from spheroidal particles to lamellar pearlitic cementite. Comparing spheroidal cementite with sulphides of similar morphology, the carbide particles are stronger and do not crack or exhibit decohesion at small strains, with the result that a spheroidized steel can withstand substantial deformation before voids are nucleated and so exhibits good ductility. The strain needed for void nucleation decreases with increasing volume fraction of carbide and so can be linked to the carbon content of the steel.

Pearlitic cementite also does not crack at small strains, but the critical strain for void nucleation is lower than for spheroidized carbides. Another factor which reduces the overall ductility of pearlitic steels is the fact that once a single lamella cracks, the crack is transmitted over much of a pearlite colony leading to well-defined cracks in the pearlite regions. The result is that the normal ductile dimpled fractures are obtained with fractured pearlite at the base of the dimples.

The effects of second phases on the ductility of steel are summarized in Fig. 11.13, where the sulphides are shown to have a more pronounced effect than either carbide distribution. This arises because, in the case of the sulphide inclusions, voids nucleate at a very early stage of the deformation process. The secondary effect of the particle shape both for carbides and sulphides is also indicated.

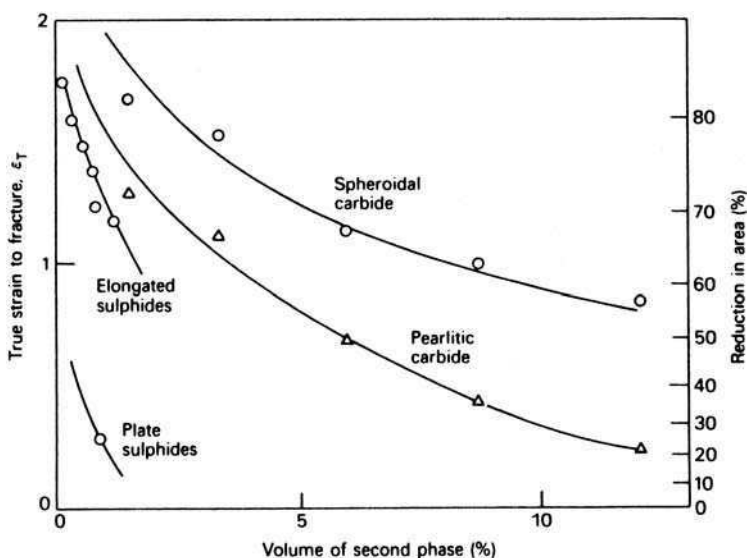


**Fig. 11.13** Effect of second-phase particles on the ductility of steel (Gladman *et al.*, in *Effect of Second-phase Particles on the Mechanical Properties of Steel*, Iron and Steel Institute, London, UK, 1971).



### 11.7 INTERGRANULAR EMBRITTLEMENT

While cleavage fracture in steels is a common form of embrittlement, in many cases the embrittlement is intergranular (IG), i.e. it takes place along the grain boundaries, usually the former austenitic boundaries (Fig. 11.14). This behaviour is encountered in as-quenched steels, on tempering (*temper embrittlement*), after heating at very high austenitizing temperatures (*overheating* and *burning*), and in *rock candy fracture* in cast steels. These forms of embrittlement are exhibited at or around room temperature. There are, however, other phenomena involving failure along grain boundaries which are essentially high temperature events, e.g. hot shortness during the hot working of steels and high temperature creep failure. It is clear that no one mechanism will explain the various types of embrittlement, but the processes leading to IG fracture all lead to reduced cohesion along the grain boundaries. This can arise in different ways but the most relevant appear to be:

1. Segregation of solute atoms preferentially to grain boundaries.
2. Distribution of second-phase particles at grain boundaries.

These phenomena reduce the work of fracture, i.e. the  $(2\gamma + \gamma_p)$  term in Equation (11.4) either by lowering the grain boundary energy by segregation, or by reducing the plastic work term  $\gamma_p$  by having particles which more easily provide crack nuclei.

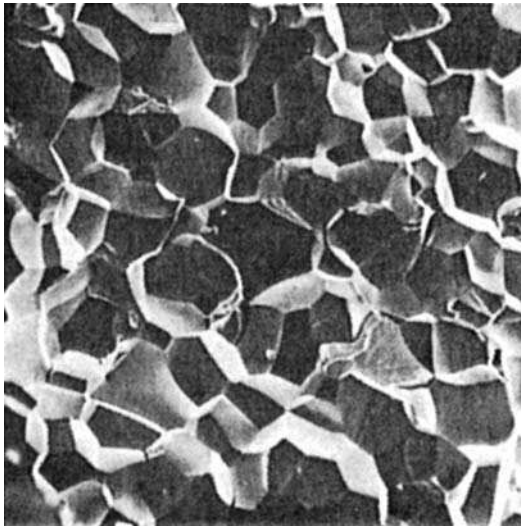


**Fig. 11.14** IG embrittlement of an Fe-0.26Pwt% alloy after holding at 500°C (courtesy of Shell).  $\times 80$ .

### 11.7.1 Temper embrittlement

Many alloy steels when tempered in the range 500–650°C following quenching to form martensite become progressively embrittled in an IG way. A similar phenomenon can also occur when the steels are continuously cooled through the critical range. It is revealed by the effect on the notched bar impact test, where the transition temperature is raised and the shelf energy lowered, the transgranular fracture mode being replaced by an IG mode below the transition temperature (Fig. 11.15).

This phenomenon is now known to be associated with the segregation of certain elements to the grain boundaries, which reduce the IG cohesion of iron. Elements which segregate fall into three groups of the Periodic Classification (Table 11.1). It has been shown that many of these elements reduce the surface energy of iron substantially and would, therefore, be expected to lower the grain boundary energy and to reduce cohesion. Moreover, the actual segregation of atoms to the boundaries has been conclusively demonstrated by Auger electron

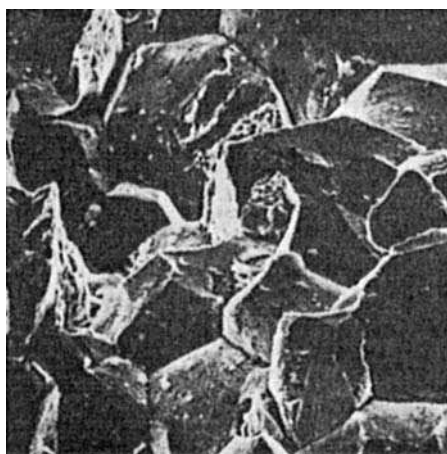


**Fig. 11.15** Temper embrittlement of a 4.5Ni–1.5Cr–0.3C wt% steel fractured at 77 K (courtesy of Knott).  $\times 800$ .

**Table 11.1** Elements which segregate to iron grain boundaries

Group	IVB	VB	VIB
	C	N	O
	Si	P	S
	Ge	As	Se
	Sn	Sb	Te
		Bi	

spectroscopy on specimens fractured intergranularly within the vacuum system of the apparatus.

This technique has allowed the precise determination of the concentrations of segregating species at the boundaries, usually expressed in terms of fractions of a monolayer of atoms. These fractions vary between about 0.3 and 2.0 for steels containing the above elements, usually in bulk concentrations well below 0.1 wt%.

With the individual elements, the tendency to embrittle appears to increase both with Group and Period number, i.e. S, Se and Te in increasing order are the most surface active elements in iron. However, it is doubtful whether they contribute greatly to temper embrittlement because they combine strongly with elements such as Mn and Cr which effectively reduce their solubility in iron to very low levels. While the elements in Groups IVB and VB are less surface active, they play a greater role in embrittlement because they interact with certain metallic elements, e.g. Ni and Mn, which are common alloying elements in steels. These interactions lead to co-segregation of alloy element and impurity

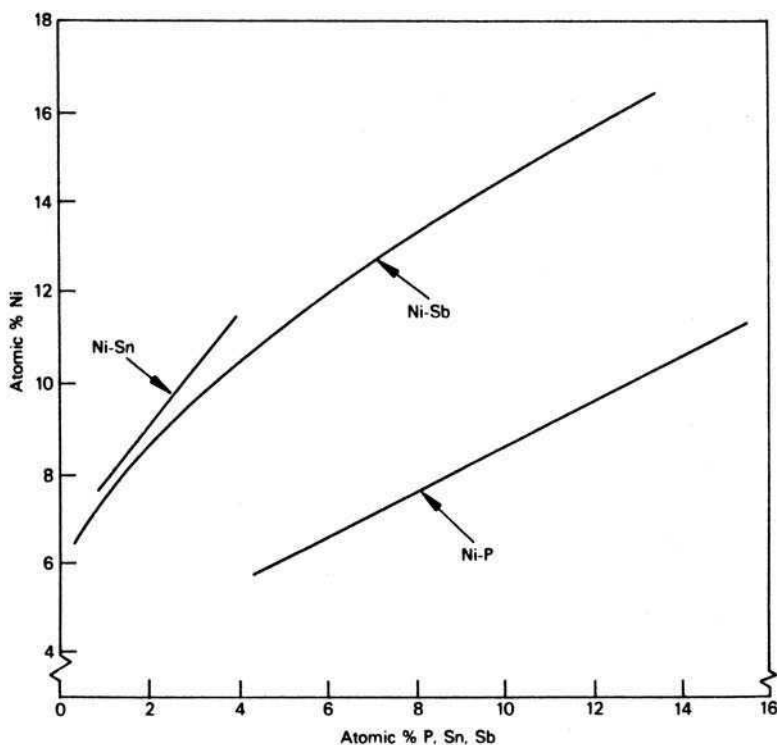


**Fig. 11.16** Interrelation between concentrations of Sn, Sb and P and of Ni at grain boundaries in Ni-Cr steels of constant hardness and grain size (McMahon, *Materials Science and Engineering* 25, 233, 1976).

elements at the grain boundaries, and to resultant lowering of cohesion by the impurity element. Analysis of the composition of grain boundaries by Auger spectroscopy has confirmed strong interactions between Ni-Sb, Ni-P, Ni-Sn and Mn-Sb. Figure 11.16 shows the grain boundary concentrations for three of these interactions in Ni-Cr steels, while the relative effects of Sb, Sn and P on the transition temperature of Ni-Cr steels are shown in Fig. 11.17.

Therefore, the driving force for co-segregation to boundaries is a stronger interaction between the alloying element and the impurity element than between either of these and iron. If the interaction is too strong, segregation does not take place. Instead a scavenging effect is obtained, as exemplified by Ti-P and Mo-P interactions in Ni-Cr steels. In this connection it is well known that molybdenum additions to Ni-Cr steels can eliminate temper embrittlement. A third inter-alloy effect is also possible which is that one alloying element, e.g. Cr, promotes the segregation of Ni and P, also Ni and Sb.

In addition to solute atom segregation to boundaries, there are also microstructural factors which influence the intensity of temper embrittlement. In most alloy steels in which this phenomenon is encountered the grain boundaries are also the sites for carbide precipitation, either cementite or alloy carbides. It is likely that these provide the sites for IG crack nuclei. As in the nucleation of cleavage fracture, dislocations impinge on a grain boundary carbide particle and as it is not deformable the carbide will either crack or the

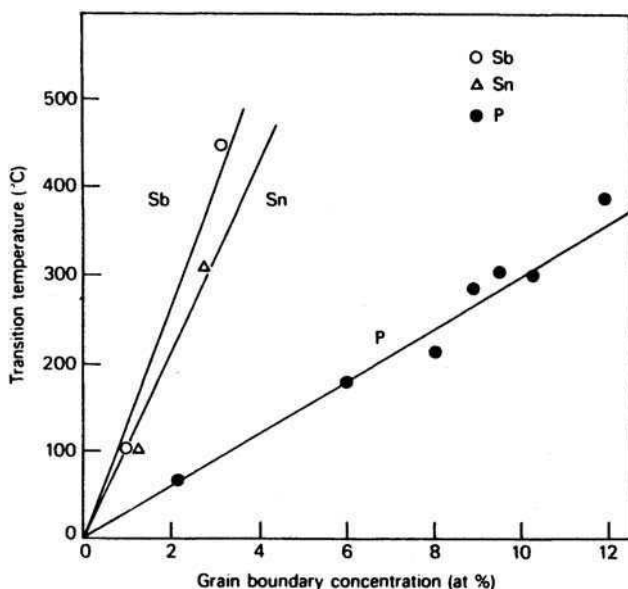


**Fig. 11.17** Effect of grain boundary concentrations of P, Sb and Sn on the ductility of Ni-Cr steels of constant hardness and grain size (McMahon, *Materials Science and Engineering* **25**, 233, 1976).

ferrite/carbide interface will part. The latter separation is more likely if the interfacial energy has been reduced by segregation of impurity atoms to it. This can occur by rejection of these impurity atoms during the growth of the carbide or by equilibrium segregation. Interfacial separation has been observed in iron containing coarse grain boundary iron carbide, the interfaces of which contained Sb, As, Sn or P. The effectiveness of this nucleating stage of IG crack formation will be influenced by the extent of grain boundary carbide and the concentration of surface active impurities in the steel, in particular at carbide/matrix interfaces.

The propagation of the grain boundary crack will depend not only on the cohesion of the boundary but also on the relative toughness of the grain interior. For example, if the grain interior has a microstructure which gives high toughness, the IG crack nucleus is more likely to propagate along the boundary. Further, as the yield stress of a steel rises sharply with decreasing temperature IG failure will, like cleavage fracture, be encouraged by reducing the testing temperature. Increasing the austenite grain size, by use of high austenitizing temperatures, under the same conditions, should increase the embrittlement because the size of the dislocation arrays impinging on the grain boundary carbides will be larger and thus more effective in forming crack nuclei.

The optimum temperature range for temper embrittlement is between 500°C and 575°C. However, in some steels embrittlement occurs in the range 250–400°C. This phenomenon is called 350°C (500°F) embrittlement, and occurs at too low a temperature to attribute it to the diffusion of metalloids such as Sb to the austenite grain boundaries. It seems more likely that it could arise from smaller and more mobile atoms, e.g. P, which would be rejected during grain boundary growth of iron carbide which takes place in this temperature range. However, the morphology of the grain boundary  $\text{Fe}_3\text{C}$ , if predominantly sheet-like, could be a prime cause of low ductility in this temperature range.

Stress corrosion cracking involves failure by cracking in the presence of both a stress and of a corrosive medium. It can occur in either a transgranular or an IG mode. The latter mode appears to be encouraged in some alloy steels by heat treatments which produce temper embrittlement. For example, a temper embrittled Cr–Mo steel cracks along the grain boundaries when stressed in a boiling NaOH solution. Use of a heat treatment to remove the temper embrittlement also removes the sensitivity to stress corrosion.

### 11.7.2 Overheating and burning

Many alloy steels when held in the range 1200–1400°C and subsequently heat treated by quenching and tempering, fail intergranularly along the original austenitic boundaries. There is strong evidence to suggest that this phenomenon is associated with the segregation of sulphur to the austenite grain boundaries at the high temperature, and indeed the phenomenon is not obtained when the sulphur content of a steel is less than 0.002 wt%. Sulphur has been shown to be

one of the most surface active elements in iron. Work by Goux and colleagues on pure iron–sulphur alloys has shown that an increase in sulphur content from 5 to 25 ppm raises the ductile/brittle transition temperature by over 200°C. Further, Auger spectroscopy on the IG fracture surfaces has given direct evidence of sulphur segregation. However, this embrittling effect of sulphur as a result of equilibrium segregation is only seen in pure iron and not in steels where there are other impurity elements, and also where interaction of sulphur occurs with alloying elements, notably manganese and chromium.

The presence of manganese substantially lowers the solubility of sulphur in both  $\gamma$ - and  $\alpha$ -iron, with the result that when sulphur segregates to high-temperature austenite boundaries, manganese sulphide is either formed there or during subsequent cooling. In either case, the manganese sulphide particles lying on the austenite boundaries are revealed by electron microscopy of the IG fracture surfaces where they are associated with small dimples. Typically the MnS particles are about 0.5  $\mu\text{m}$  while the dimples are approximately 2–5  $\mu\text{m}$  in diameter. Thus, the grain boundary fracture process is nucleated by the sulphide particles, and the mode of fracture will clearly be determined by the size distribution, which will in turn be controlled by the rate of cooling from the austenite temperature, assuming that MnS forms during cooling. With very slow cooling rates, the IG fracture is replaced by cleavage or transgranular fibrous fracture as the grain boundary sulphide distribution is too coarse. Oil quenching from the austenitizing temperature does not eliminate the phenomenon which is accentuated on tempering in the range 600–650°C. This arises from the redistribution of carbides which will strengthen the grain interiors, and by precipitation at the grain boundaries which may further reduce grain boundary ductility.

When very high austenitizing temperatures are used (1400–1450°C) extensive MnS precipitate is formed, often in impressive dendritic forms (Fig. 11.18). In extreme cases, partial formation of liquid phase occurs (liquidation) which, on subsequent heat treatment, greatly accentuates the IG embrittlement. In the absence of manganese, e.g. in wrought iron, liquid films of the iron–iron sulphide eutectic cause embrittlement during hot working processes down to 1000°C (*hot shortness*). The fact that in normal steels burning occurs only at very high temperatures should not be allowed to detract from its significance. The phenomenon may well intrude in high temperature working processes such as forging if temperature control is not exact, but in any case it can certainly be significant in steels which are cast, and by definition pass through the burning and overheating temperature range. In many cases IG fracture is encountered in cast alloy steels where the as-cast grain structure is clearly involved. Examination of the fractures reveals extensive grain boundary sheets of manganese sulphide, often only 0.2–0.5  $\mu\text{m}$  thick but covering large areas. Marked embrittlement can occur in the as-cast state or after subsequent heat treatment in the range 500–600°C, and is often referred to as-cast brittleness or rock candy fracture. Precipitation of aluminium nitride may also play an important role in this type of fracture.

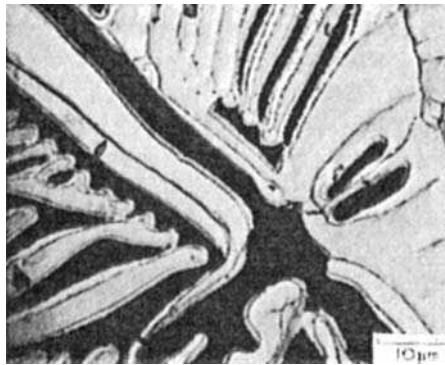


**Fig. 11.18** Fe-1Mn-0.4C-0.02S air cooled from 1445°C then fractured (courtesy of Brammar). Extraction replica,  $\times 1000$ .

## FURTHER READING

- Baker, T. N. (ed.), *Yield, Flow and Fracture of Polycrystals* (N. J. Petch Symposium), Applied Science Publishers, London, UK, 1983.
- Bilby, B. A., Miller, K. J. and Willis, J. R. (eds), *Fundamentals of Deformation and Fracture*, Cambridge University Press, Cambridge, UK, 1985.
- Briant, C. L. and Banerji, S. K., Intergranular failure in steels: the role of grain-boundary composition. *International Metallurgical Reviews* **23**, 4, 164, 1978.
- Charles, J. A. and Smith, G. C. (eds), *Advances in Physical Metallurgy*. (Sir Alan Cottrell 70th Birthday Meeting), The Institute of Materials, London, 1990.
- Firrao, D. (ed.), *Fracture Behaviour and Design of Structures, Proceedings of the 8th European Conference on Fracture*, EMAS, Budapest, Hungary, 1990.
- Hondros, E. D. and Seah, M. P., Segregation to interfaces. *International Metallurgical Reviews*, Review 222, 261, 1977.
- Hull, D., *Fractography: Observing, Measuring and Interpreting Fracture Surface Topography*, Cambridge University Press, Cambridge, UK, 1999.
- Knott, J. F., Mechanics and mechanisms of large scale brittle fracture in steels. *Materials Science and Engineering* **7**, 1, 1971.
- Knott, J. F., *Fundamentals of Fracture Mechanics*, Butterworth, London, 1973.
- Lawn, B., *Fracture of Brittle Solids*, 2nd edition, Cambridge University Press, Cambridge, UK, 1993.
- Leslie, W. C., *The Physical Metallurgy of Steels*, McGraw-Hill, Tokyo, Japan, 1981.
- Olefjord, I., Temper embrittlement. *International Metallurgical Reviews*, **23**, 4, 149, 1978.
- Pratt, P. L. (ed.), *Fracture 1969*, Chapman and Hall, London, UK, 1969.
- Production and Application of Clean Steels*, Iron and Steel Institute, 1972.
- Residuals, Additives and Materials Properties, *Proceedings of a Joint Conference by the National Physical Laboratory*, The Metals Society and the Royal Society, London, The Royal Society, 1980.
- Taplin, D. M. R. (ed.), *Fracture 1977*, University of Waterloo Press, Ontario, Canada, 1977.
- Tetelman, A. S. and McEvily, A. J., *Fracture of Structural Materials*, John Wiley, UK, 1967.
- The Effect of Second Phase Particles on the Mechanical Properties of Steels*, Iron and Steel Institute, 1971.

# 12

---

## STAINLESS STEEL

### 12.1 INTRODUCTION

Some elements extend the  $\gamma$ -loop in the iron–carbon equilibrium diagram (see Chapter 4), e.g. nickel and manganese. When sufficient alloying element is added, it is possible to preserve the face-centred cubic (fcc) austenite at room temperature, either in a stable or metastable condition. Chromium added alone to a plain carbon steel tends to close the  $\gamma$ -loop and favour the formation of ferrite. However, when chromium is added to a steel-containing nickel it retards the kinetics of the  $\gamma \rightarrow \alpha$  transformation, thus making it easier to retain austenite at room temperature. The presence of chromium greatly improves the corrosion resistance of the steel by forming a very thin stable oxide film on the surface, so that chromium–nickel stainless steels are now the most widely-used materials in a wide range of corrosive environments both at room and elevated temperatures. Added to this, austenitic steels are readily fabricated and do not undergo a ductile/brittle transition which causes so many problems in ferritic steels. This has ensured that they have become a most important group of construction steels, often in very demanding environments. Nevertheless, there are also some important ferritic stainless steels which will be discussed in this chapter.

### 12.2 THE IRON–CHROMIUM–NICKEL SYSTEM

The binary iron–chromium equilibrium diagram (Fig. 12.1) shows that chromium restricts the occurrence of the  $\gamma$ -loop to the extent that above 13 wt% Cr the binary alloys are ferrite over the whole temperature range, while there is a narrow ( $\alpha + \gamma$ ) range between 12 and 13 wt% Cr. The ferrite is normally referred to as delta ferrite, because in these steels the phase can have a continuous existence from the melting point to room temperature. The addition of carbon to the binary alloy extends the  $\gamma$ -loop to higher chromium contents (Fig. 12.2), and also widens the ( $\alpha + \gamma$ ) phase field up to 0.3 wt% C. When carbon is progressively



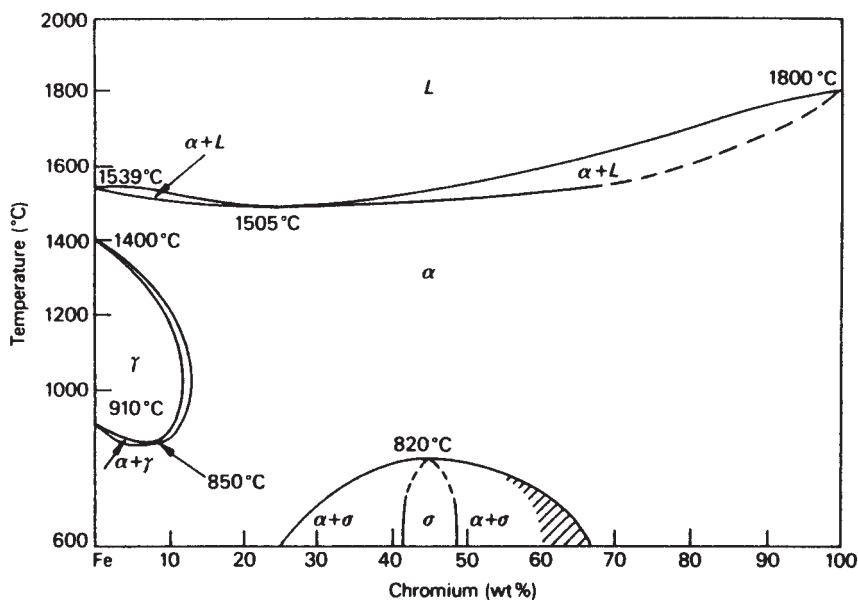


Fig. 12.1 The Fe-Cr equilibrium diagram.

added to an 18 wt% Cr steel, in the range up to about 0.04 wt% C, the steel is fully ferritic (Fig. 12.2a) and cannot be transformed. Between 0.08% and 0.22% C, partial transformation is possible leading to  $(\alpha + \gamma)$  structures, while above 0.40 wt% C the steel can be made fully austenitic (Fig. 12.2b) if cooled rapidly from the  $\gamma$ -loop region. The second effect of carbon is to introduce carbides to the structure as indicated in Fig. 12.2:

$$K_0 = M_3C, \quad K_1 = M_{23}C_6, \quad K_2 = M_7C_3.$$

where 'M' represents a mixture of metal atoms. In austenitic steels,  $M_{23}C_6$  is the most significant carbide formed and it can have a substantial influence on corrosion resistance.

If nickel is added to a low carbon iron-18 wt% Cr alloy, the  $\gamma$ -phase field is expanded until at about 8 wt% Ni the  $\gamma$ -phase persists to room temperature (Fig. 12.3) leading to the familiar group of austenitic steels based on 18Cr-8Ni wt%. This particular composition arises because a minimum nickel content is required to retain  $\gamma$  at room temperature. With both lower and higher Cr contents more nickel is needed. For example, with more corrosion resistant, higher-Cr steels, e.g. 25 wt% Cr, about 15 wt% nickel is needed to retain the austenite at room temperature. Lack of complete retention is indicated by the formation of martensite. A stable austenite can be defined as one in which the  $M_s$  is lower than room temperature. The 18Cr-8Ni steel, in fact, has an  $M_s$

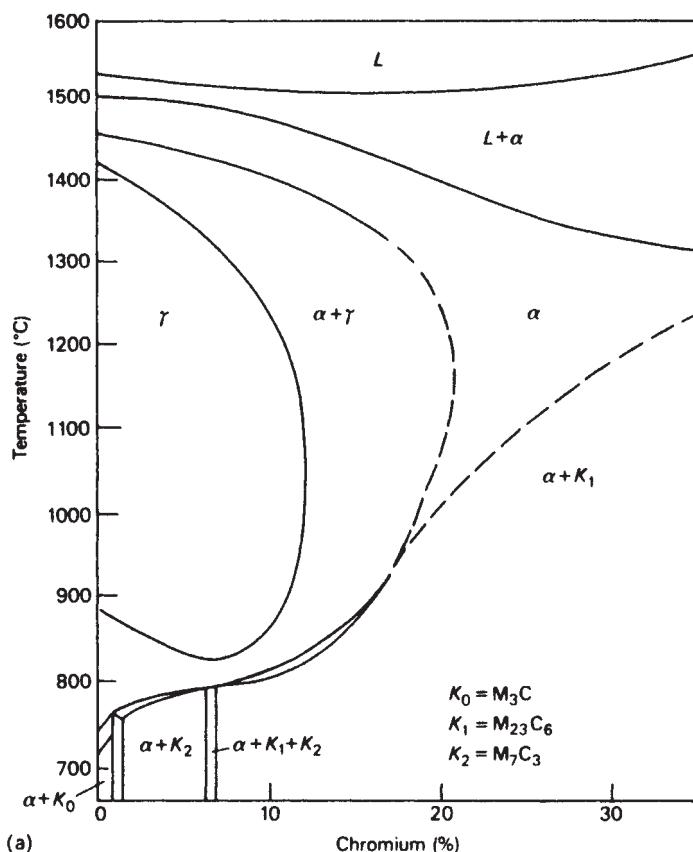


**Fig. 12.2** Effect of carbon on the Fe–Cr diagram: (a) 0.05C wt% (Colombier and Hoffman, *Stainless and Heat Resisting Steels*, Edward Arnold, London, UK, 1967).

just below room temperature and, on cooling, e.g. in liquid air, it will transform very substantially to martensite.

Figure 12.3 also shows that the carbide phase  $M_{23}C_6$  exists below about 900°C. However, it goes into solution when the steel is heated to 1100–1150°C and on quenching a precipitate-free austenite is obtained. However, on reheating in the range 550–750°C,  $M_{23}C_6$  is reprecipitated preferentially at the grain boundaries.

Manganese expands the  $\gamma$ -loop and can, therefore, be used instead of nickel. However, it is not as strong a  $\gamma$ -former but about half as effective, so higher concentrations are required. In the absence of chromium, around 12 wt% Mn is required to stabilize even higher carbon (1–1.2 wt%) austenite, achieved in Hadfields steel which approximates to this composition. Typically Cr–Mn steels require 12–15 wt% Cr and 12–15 wt% Mn to remain austenitic at room temperature if the carbon content is low.

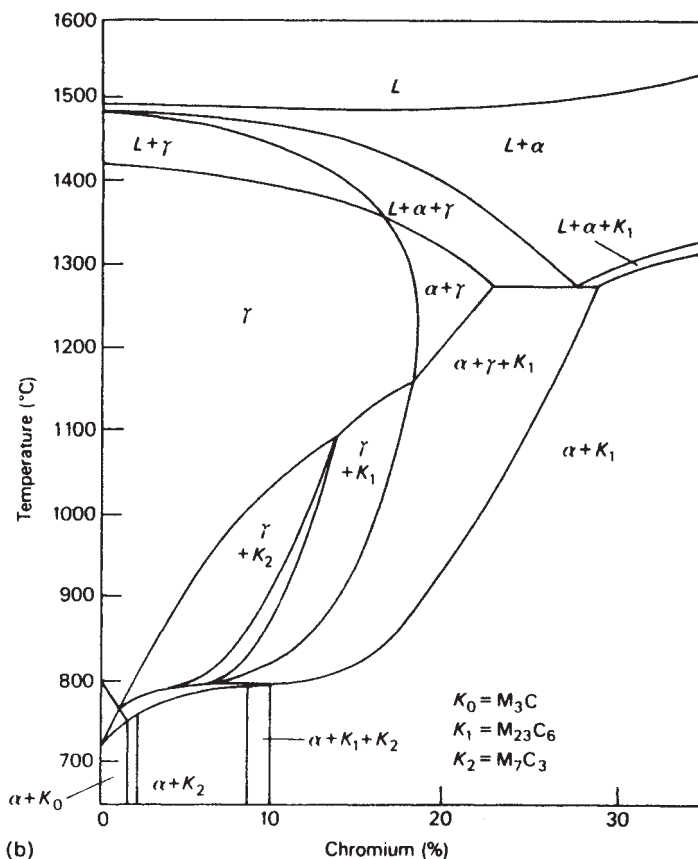


**Fig. 12.2** Effect of carbon on the Fe–Cr diagram: (b), 0.4C wt% (Colombier and Hoffman, *Stainless and Heat Resisting Steels*, Edward Arnold, London, UK, 1967).

Like carbon, nitrogen is a very strong austenite former. Both elements, being interstitial solutes in austenite, are the most effective solid solution strengtheners available. Nitrogen is more useful in this respect as it has less tendency to cause intergranular corrosion. Concentrations of nitrogen up to 0.25 wt% are used, which can nearly double the proof stress of a Cr–Ni austenitic steel.

One of the most convenient ways of representing the effect of various elements on the basic structure of chromium–nickel stainless steels is the Schaeffler diagram, often used in welding. It plots the compositional limits at room temperature of austenite, ferrite and martensite, in terms of nickel and chromium equivalents (Fig. 12.4). At its simplest level, the diagram shows the regions of existence of the three phases for iron–chromium–nickel alloys. However, the diagram becomes of much wider application when the equivalents of chromium

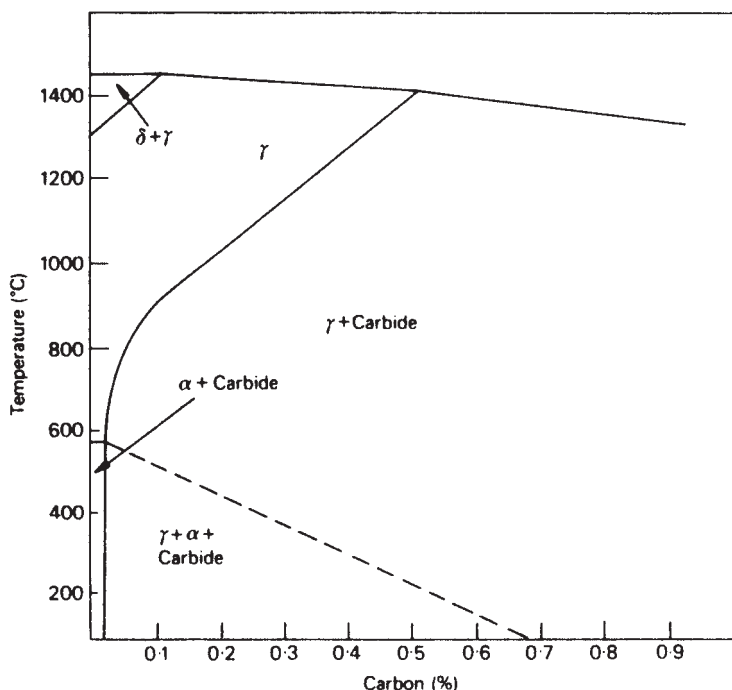


**Fig. 12.3** Effect of carbon on the phase diagram for an 18Cr-8Ni steel (Colombier and Hoffman, *Stainless and Heat Resisting Steels*, Edward Arnold, London, UK, 1967).

and of nickel are used for the other alloying elements. The chromium equivalent has been empirically determined using the most common ferrite-forming elements:

$$\text{Cr equivalent} = (\text{Cr}) + 2(\text{Si}) + 1.5(\text{Mo}) + 5(\text{V}) + 5.5(\text{Al}) + 1.75(\text{Nb}) + 1.5(\text{Ti}) + 0.75(\text{W})$$

while the nickel equivalent has likewise been determined with the familiar austenite-forming elements:

$$\text{Ni equivalent} = (\text{Ni}) + (\text{Co}) + 0.5(\text{Mn}) + 0.3(\text{Cu}) + 25(\text{N}) + 30(\text{C})$$

all concentrations being expressed in weight percentages.

The large influence of C and N relative to that of the metallic elements should be particularly noted. The diagram is very useful in determining whether a particular steel is likely to be fully austenitic at room temperature. This is relevant to bulk steels, particularly to weld metal where it is frequently important to predict the structure in order to avoid weld defects and excessive localized corrosive attack.

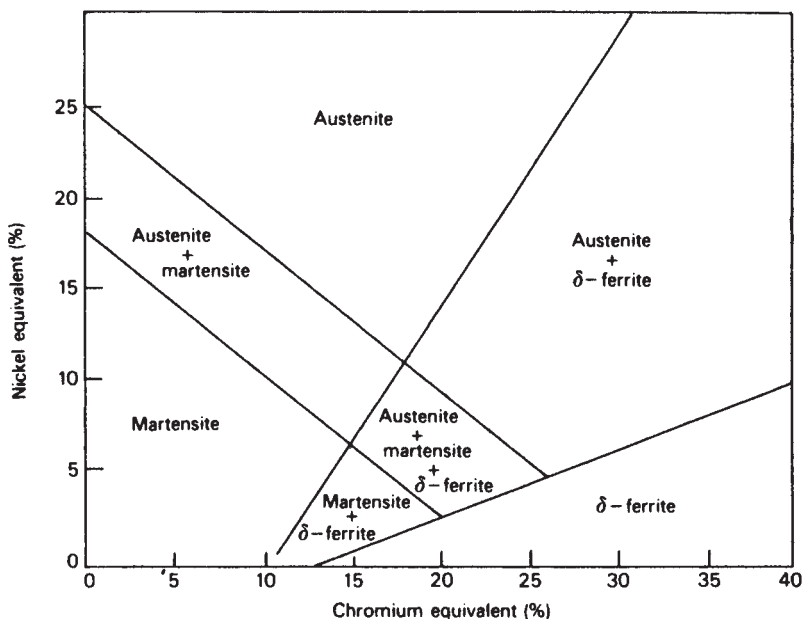


**Fig. 12.4** Schaeffler diagram. Effect of alloying elements on the basic structure of Cr-Ni stainless steels (Schneider and Climax Molybdenum Co., *Foundry Trade Journal* **108**, 562, 1960).

### 12.3 CHROMIUM CARBIDE IN CR-NI AUSTENITIC STEELS

Simple austenitic steels usually contain between 18 and 30 wt% chromium, 8 to 20 wt% nickel and between 0.03 and 0.1 wt% carbon. The solubility limit of carbon is about 0.05 wt% at 800°C, rising to 0.5 wt% at 1100°C. Therefore, solution treatment between 1050°C and 1150°C will take all of the carbon into solution and rapid cooling from this temperature range will give a supersaturated austenite solid solution at room temperature. However, slow cooling or reheating within the range 550–800°C will lead to the rejection of carbon from solution, usually as the chromium-rich carbide,  $\text{Cr}_{23}\text{C}_6$ , even when the carbon content of the steel is very low (<0.05 wt%).

This carbide nucleates preferentially at the austenitic grain boundaries as faceted particles (Fig. 12.5) or often as complex dendritic arrays. While such precipitation can have an adverse effect on mechanical properties, in particular low-temperature ductility, the most significant result is the depletion of the regions adjacent to the grain boundaries with respect to chromium. This has been revealed directly by microprobe analysis. The surface film in these regions is thus depleted in chromium and as a result the steel is more prone to corrosive attack. Consequently, a classic form of intergranular corrosion is experienced which, in severe cases, can lead to disintegration of the steel. This type of corrosion is also

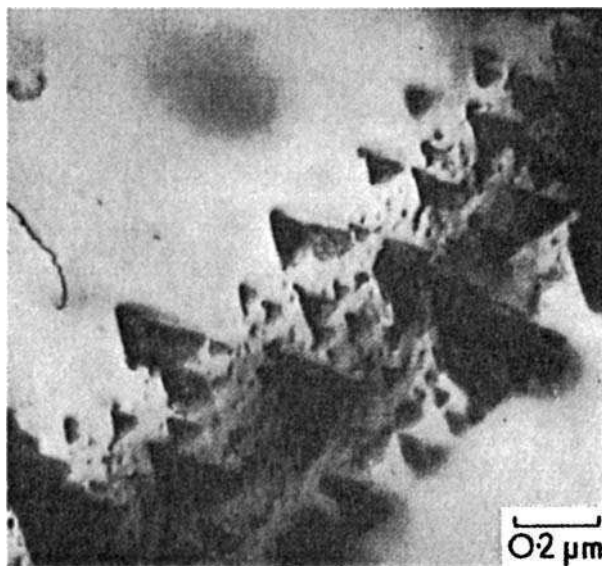


**Fig. 12.5** Grain boundary precipitation of  $\text{Cr}_{23}\text{C}_6$  in a 25Cr–24Ni–0.27Ti–0.034C wt% steel aged 5 h at 750°C (courtesy of Singhal and Martin). Thin-foil electron micrograph.

experienced in martensitic chromium steels, e.g. 12 wt% Cr steel, in which grain boundary precipitation of  $\text{Cr}_{23}\text{C}_6$  occurs as well.

$\text{Cr}_{23}\text{C}_6$  also precipitates within the austenite grains, particularly at higher supersaturations, on dislocations and on solute atom/vacancy clusters. Both the matrix and the carbide have cubic symmetry, and electron diffraction evidence from thin-foil specimens invariably gives the orientation relationship:

$$\{100\}_{\text{M}_{23}\text{C}_6} // \{100\}_{\gamma} : \langle 100 \rangle_{\text{M}_{23}\text{C}_6} // \langle 100 \rangle_{\gamma}.$$

The lattice parameter of  $\text{M}_{23}\text{C}_6$  is approximately three times that of austenite, so the electron diffraction patterns are readily identified. The particles usually develop a polyhedral habit, but occasionally in steels deformed at elevated temperatures a more regular cubic morphology is displayed (Fig. 12.6). As the critical temperature range for chromium carbide nucleation and growth is between 500°C and 850°C, any process which allows the steel to pass slowly through this temperature range will render it sensitive to intergranular corrosion in service. Welding, in particular, provides these conditions in the heat affected zone (HAZ) leading to localized attack in certain chemical media. It is, therefore, important to have information about the reaction kinetics for the formation of  $\text{Cr}_{23}\text{C}_6$ . Being a typical nucleation and growth process, the time–temperature–transformation (TTT) curve is typically C-shaped with the nose at about 750°C

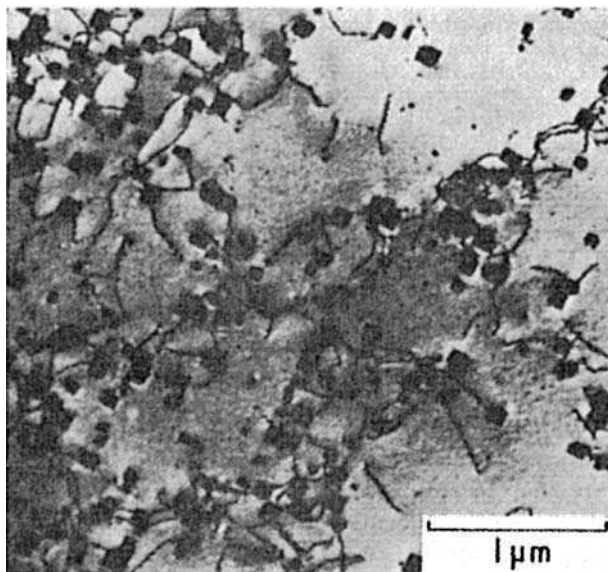


**Fig. 12.6** Precipitation of  $M_{23}C_6$  on dislocations in a 18Cr–12Ni steel after 80 h at 700°C under stress (courtesy of Sully). Thin-foil electron micrograph.

(Fig. 12.7). For some steel compositions the minimum time for the formation of  $Cr_{23}C_6$  sufficient to give subsequent intergranular corrosion, i.e. time to achieve *sensitization*, is as short as 100 s. Several ways of reducing or eliminating the formation of  $Cr_{23}C_6$  are available. The term *stabilization* is used to describe these processes:

1. Resolution treatment: after welding, the steel can be reheated to 950–1100°C to allow  $Cr_{23}C_6$  to redissolve, and further precipitation is then prevented by rapid cooling to avoid the C-shaped curve.
2. Reduction of the carbon content: this can be reduced below 0.03 wt% by modern steel-making methods involving oxygen lancing. For complete immunity from intergranular corrosion in 18/8 steels, a carbon level of 0.02 wt% should not be exceeded.
3. Control of  $M_{23}C_6$  reaction kinetics: addition of molybdenum to Cr/Ni stainless steels markedly lengthens the sensitization time. An increase in nickel content has an adverse effect, while increasing chromium has a beneficial effect.
4. Use of strong carbide-forming elements, Nb, Ti—niobium and titanium form carbides which are much more stable than  $Cr_{23}C_6$ , so they preferentially combine with the available carbon and thus lessen the opportunity for  $Cr_{23}C_6$  to nucleate.

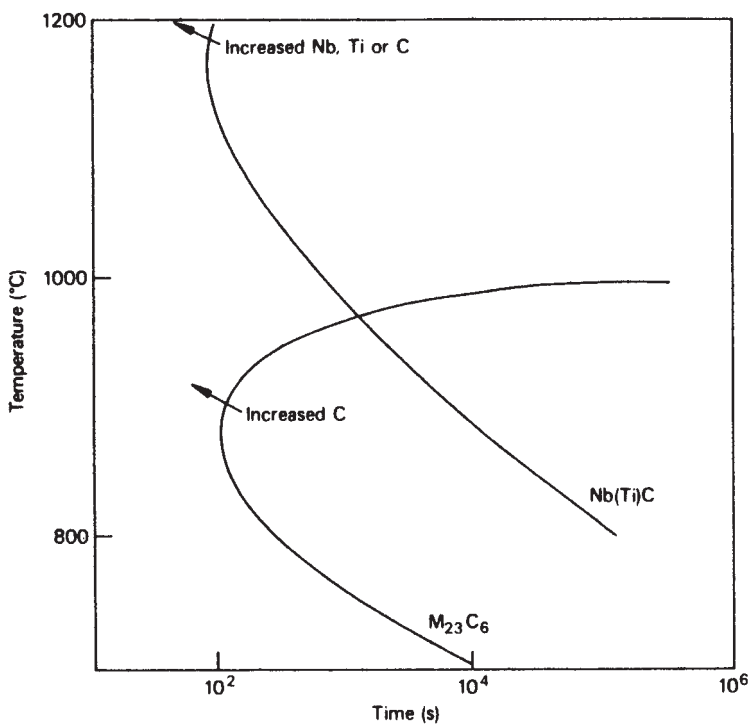


Fig. 12.7 Temperature-time growth curves for  $M_{23}C_6$  and  $Nb(Ti)C$  in Cr-Ni austenitic steels.

## 12.4 PRECIPITATION OF NIOBIUM AND TITANIUM CARBIDES

In normal practice, sufficient niobium or titanium is added to the steel to combine with all the carbon, the stoichiometric ratios being:

	Ti:C	Nb:C
Atomic weights	48:12	93:12
Ratios	4:1	8:1

However, the additions are in excess of these proportions to allow for some solid solution of Ti or Nb, and for combination with any nitrogen which may be present. Titanium and niobium carbides are much less soluble in austenite than is chromium carbide, so they will form at much higher temperatures as relatively stable particles. These should remain relatively inert during commercial heat treatments involving solution temperatures no higher than  $1050^{\circ}\text{C}$ , and thus minimize the possible nucleation of  $Cr_{23}C_6$ . However, TiC and NbC have some solubility in austenite at  $1050^{\circ}\text{C}$  and can subsequently precipitate at lower temperatures. During high-temperature processes such as welding, these carbides dissolve to a greater extent in austenite and can then reprecipitate at lower temperatures. Therefore, NbC and TiC will not always form inert dispersions, and



are often likely to be redistributed by heat treatment. They do, however, have the great advantage of not depleting the matrix of chromium, particularly at sensitive areas such as grain boundaries. The ability to form dispersions of NbC and TiC has a further advantage in that these dispersions can remain very fine at temperatures in the range 500–750°C, and so provide a means of dispersion strengthening austenitic steels to achieve greater strength in this temperature range. The development of creep-resistant austenitic steels owes much to the properties of these carbide dispersions.

The formation of NbC and TiC in austenite is most conveniently studied by subjecting the steel to high-temperature solution treatment (1100–1300°C), followed by rapid cooling to room temperature. On subsequent ageing in the range 650–850°C precipitation takes place. The carbides are both fcc of the NaCl crystal type with lattice parameters within 2–3% of each other, but differing from that of austenite by 20–25%. They both exist over a range of stoichiometry  $MC_{0.6}$ – $MC_{1.0}$ . Precipitation in each case occurs in several different ways.

**Grain boundary:** Grain boundaries are preferred sites, but because chromium diffuses more rapidly in austenite than does Nb or Ti,  $Cr_{23}C_6$  usually forms first (Fig. 12.8a). This emphasizes that NbC or TiC should not be taken into solution if full stabilization is to be achieved. In Fig. 12.7, *TTT* curves for  $Cr_{23}C_6$  and (NbTi)C illustrate that, at lower temperatures and shorter times, the chromium carbide forms first, but at longer times it can redissolve and be replaced by (NbTi)C.

**Dislocations:** NbC and TiC nucleate extensively on dislocations (Fig. 12.8b), an important mechanism relevant to the precipitation of equilibrium phases which have not been preceded by GP zone formation. It should also be noted that a significant part of the creep resistance of this group of alloys arises from nucleation of alloy carbides on dislocations generated by deformation at elevated temperatures (e.g. Fig. 12.6). The carbides always have a cube–cube Widmanstätten orientation relationship with the matrix, as do other MC carbides such as VC, TaC. Since the lattice parameter of austenite is 20–25% less than that of the carbides, a flux of vacancies into the precipitates is needed to reduce internal stresses resulting from growth of the particles. Only a few of these vacancies can be quenched in, so carbide particles will grow most readily in situations where further vacancies are generated, e.g. at dislocations or boundaries.

**Precipitation in association with stacking faults:** Often NbC, TaC and TiC precipitate on  $\{111\}_\gamma$  plates as thin discs which exhibit stacking fault contrast in thin foils in the electron microscope (Fig. 12.8c). These discs grow very substantially on ageing, e.g. at 700°C. Analysis has shown that the discs are formed by the climb of partial dislocations (Frank type), which by climbing generate a continuous source of vacancies. The (NbTi)C precipitate particles nucleate on

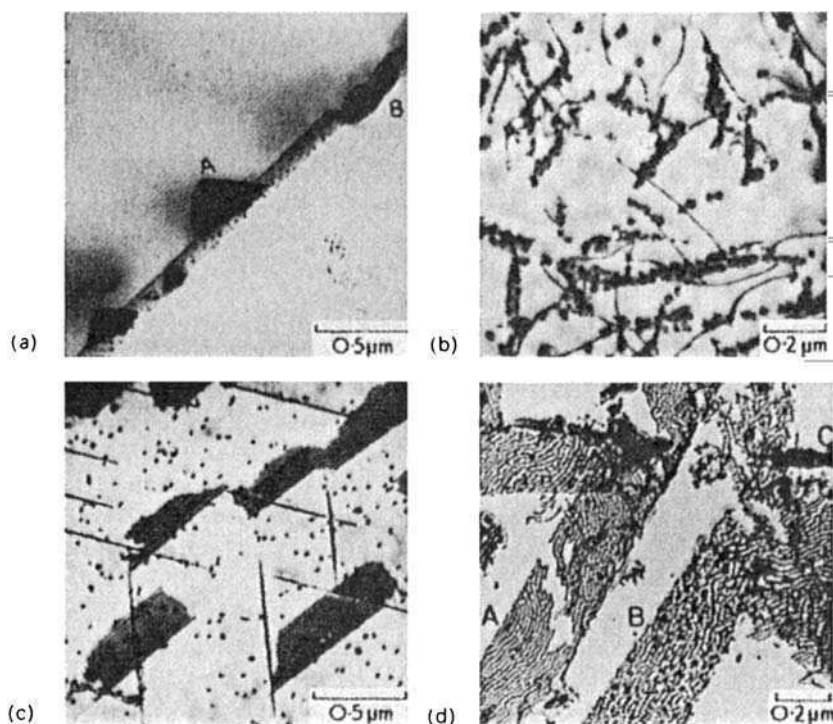


**Fig. 12.8** Different modes of precipitation in austenitic steels solution heated between 1150°C and 1300°C: (a) 25Cr–24Ni–0.27Ti–0.03C, aged 3 h at 700°C. Grain boundary precipitation of  $M_{23}C_6$  (coarse) and TiC (fine) (Singhal and Martin). Thin-foil electron micrograph; (b) 18Cr–10Ni–1Ti–0.1C, aged 48 h at 700°C. TiC on dislocations (Van Aswegen). Thin-foil electron micrograph; (c) 18Cr–12Ni–2Ta–0.1C, aged 25 h at 700°C. Matrix and stacking fault precipitation of TaC (Froes). Thin-foil electron micrograph; (d) 18Cr–12Ni–1.25Nb–0.04N, aged 500 h at 700°C. NbN in association with stacking faults A and B,  $M_6N$  at C (courtesy of Borland). Extraction replica.

the partial dislocations and make use of the vacancies in growing, a process which is repeated many times as the partial dislocation escapes from the rows of particles it has nucleated. The final result is a pseudo-Widmanstätten array of discs on  $\{111\}_\gamma$  planes, which contain very fine dispersions of (NbTi)C. This complex precipitate morphology can occur side by side with normal nucleation on undissociated dislocations.

**Matrix precipitation:** Random precipitation of (NbTi)C in the matrix, not on dislocations, is occasionally observed, but it is the rarest morphology encountered. The particles still exhibit the cube–cube orientation relationship with the matrix, and are apparently nucleated on solute atom/vacancy clusters. Consequently, they are only obtained after heat treatments which result in high

supersaturations of vacancies in the austenite matrix, i.e. very high solution temperatures and rapid quenching (Fig. 12.8c). However, there is some evidence that certain elements, e.g. phosphorus, encourage this type of precipitation by trapping vacancies, the phosphorus atoms being 20% smaller than the other atoms in the austenite solid solution, and so cause localized strain fields.

The carbide morphologies have been presented in decreasing order of occurrence. The evidence suggests that this order is dictated by increasing degree of supersaturation, which is a function of the solution temperature. In practice, high solution temperatures can usually be avoided, except in welding, so grain boundary precipitation and dislocation precipitation are the dominant mechanisms observed.

## 12.5 NITRIDES IN AUSTENITIC STEELS

In simple austenitic steels the role of nitrogen is largely that of a solid solution strengthening element, although it can replace carbon in  $\text{Cr}_{23}\text{C}_6$ . While higher nitrogen concentrations can be maintained without deleterious precipitation than is the case with carbon, in steels with 0.2–0.3 wt% N,  $\text{Cr}_2\text{N}$  can precipitate at grain boundaries, and also within the grains. Exposure of austenitic steels to air at temperatures greater than 600°C can lead to very high (>1 wt%) nitrogen concentrations under the oxide layer, with coarse  $\text{Cr}_2\text{N}$  matrix precipitation, as well as discontinuous lamellar precipitation at grain boundaries. Such regions often lead to cracks under creep conditions.

In the presence of Nb or Ti, more stable nitrides of these elements are formed, which are much less soluble in austenite than  $\text{Cr}_2\text{N}$ .  $\text{TiN}$  and  $\text{NbN}$ , isomorphous with the corresponding carbides, have been identified, and also  $\text{M}_6\text{N}$  which can eventually replace  $\text{NbN}$  during ageing (Fig. 12.8d). These phases can precipitate in the range 650–850°C after rapid cooling from high solution temperatures. They may, therefore, occur as a result of welding or in alloys subject to creep conditions at high temperatures. The modes of nucleation of these nitride phases are similar to those of the corresponding carbides, although there are morphological differences.

## 12.6 INTERMETALLIC PRECIPITATION IN AUSTENITE

Austenitic steels, as a class, possess relatively modest mechanical properties, which are largely outweighed by their excellent corrosion resistance in many media. However, it is often desirable to develop higher-strength alloys, particularly for use at elevated temperatures where deformation by creep needs to be minimized. Carbide dispersions offer one solution, but the volume fraction of precipitate is limited by solubility considerations and there are also problems associated with high-temperature ductility and the stability of the dispersions.

The highly alloyed matrices of many austenitic alloys have allowed the development of intermetallic phases as suitable dispersions to achieve high

temperature strength. The most important of these phases is the  $\gamma'$  fcc phase  $\text{Ni}_3(\text{AlTi})$  first found in nickel-base alloys, with an fcc matrix analogous to austenite, containing titanium and aluminium which can replace each other in the precipitate. The  $\gamma'$  precipitate is obtained in stable austenitic steels, e.g. 20Cr25Ni with an (Al + Ti) content of 1–5 wt% by quenching from a solution temperature of 1100–1250°C, and ageing in the range 700–800°C. The dispersion developed in this way has two important advantages. Firstly, the precipitate particles have the cubic crystal structure similar to that of the matrix with which they have a cube–cube orientation relationship. Moreover, the lattice parameters are similar, so that the interfaces between precipitate and matrix are coherent, and therefore, of low energy. The familiar Lifshitz–Wagner equation (Equation (9.2)) shows that the coarsening rate is directly related to the interfacial energy. Secondly, this type of reaction allows a large volume fraction (0.3–0.5) of precipitate particles to be achieved, the particles being strong, but not catastrophically brittle, cf. sigma phase.

The  $\gamma'$  precipitate normally observed in austenite is spherical when the precipitate is very fine (Fig. 12.9a), and indeed there is evidence for the formation of pre-precipitation spherical zones. However, on prolonged ageing at 750°C, the  $\gamma'$  particles gradually adopt a more complex morphology as they lose coherency with the austenitic matrix (Fig. 12.9b). By varying the ratio of Ti to Al in  $\gamma'$  the coarsening characteristics can be substantially modified. Addition of Al to  $\gamma'/\text{Ni}_3\text{Ti}$  decreases the lattice parameter from about 3.590 Å for 25Ni–15Cr wt%, resulting in greater stability of the precipitate. However, complete replacement of titanium lowers the  $\gamma'$  parameter to 3.559 Å, which results in an increase in mismatch parameter. This helps to explain why an (Al + Ti) content of 1–1.5 wt% Al and 3–3.5 wt% Ti was found to be optimum for high-strength austenitic steels, resistant to coarsening.

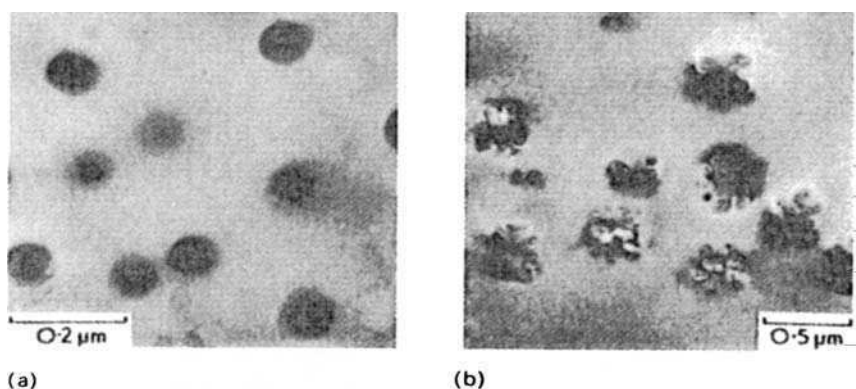


**Fig. 12.9** Precipitation of  $\gamma'$   $\text{Ni}_3\text{Ti}$  in a 21Cr–24Ni–1.3Ti–0.04C wt% steel solution treated at 1150°C: (a) 80 h at 750°C; (b) 800 h at 750°C (courtesy of Singhal and Martin). Thin-foil electron micrographs.

The  $\gamma'$  phase is not the equilibrium phase in austenitic steels with Al and Ti. It is replaced eventually by a coarsely dispersed hexagonal phase  $\eta(\text{Ni}_3\text{Ti})$  in titanium-containing steels. In steels with a high Al/Ti ratio, the equilibrium intermetallic phase is body-centred cubic (bcc)  $\beta$  NiAl. Both these phases coarsen excessively, and are undesirable constituents of the microstructure in austenitic creep-resistant alloys.

While a number of other intermetallic phases have been observed in austenitic steels, mention will be made only of sigma phase ( $\sigma$ ), as it usually has a catastrophic influence on mechanical properties at room temperature. The phase, which is tetragonal in structure, is already present in the binary Fe–Cr system and occurs over a wide composition range between 25 and 60 wt% Cr. In CrNi austenitic steel,  $\sigma$  formation is encouraged when the Cr content exceeds 17 wt%, but is discouraged by increasing the nickel content. The phase forms at austenite grain boundaries and requires, for full development, long-term ageing (up to 1500 h) at 750°C. However, in some circumstances,  $\sigma$  has been detected in 25Cr–20Ni steels after 70 h at this temperature. The presence of ferrite in the austenite greatly accelerates the formation of sigma, which has been shown to nucleate at the  $\gamma/\alpha$  boundaries (Fig. 12.10). The ferrite, being richer in chromium, tends to be preferentially absorbed during the growth of sigma phase. Elements such as Mo and Ti achieve a further acceleration of sigma formation, e.g. in an 18Cr–8Ni–3Mo–1Ti wt% steel,  $\sigma$  can be formed after only 30 min at 870°C.

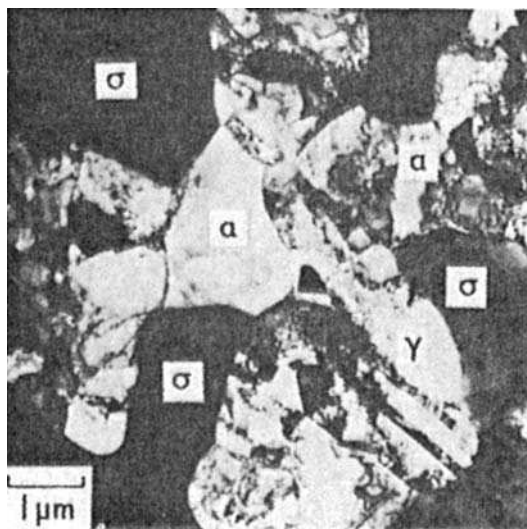


**Fig. 12.10** Nucleation of sigma phase at  $\alpha/\gamma$  boundaries (courtesy of Southwick). Thin-foil electron micrograph.

## 12.7 AUSTENITIC STEELS IN PRACTICAL APPLICATIONS

The commonest austenitic steel is the so-called 18/8 containing around 18 wt% Cr and 8 wt% Ni. It has the lowest nickel content concomitant with a fully austenitic structure. However, in some circumstances, e.g. after deformation, or if the carbon content is very low, it may partially transform to martensite at room temperature. Several of the most familiar austenitic steel specifications are given in Table 12.1.

Greater stability towards the formation of martensite is achieved by increasing the nickel content, as illustrated in the 301 to 310 types of steel in the Table 12.1. The 18/8 stainless steel owes its wide application to its excellent general resistance to corrosive environments. However, this is substantially improved by increasing the nickel content, and increasing the chromium gives greater resistance to intergranular corrosion. Austenitic steels are prone to *stress corrosion cracking*, particularly in the presence of chloride ions where a few ppm can sometimes prove disastrous. This is a type of failure which occurs in some corrosive environments under small stresses, either deliberately applied or as a result of residual stresses in fabricated material. In austenitic steels it occurs as transgranular cracks which are most easily developed in hot chloride solutions. Stress corrosion cracking is very substantially reduced in high nickel austenitic alloys.

Type 316 steel contains 2–4 wt% molybdenum, which gives a substantial improvement in general corrosion resistance, particularly in resistance to *pitting corrosion*, which can be defined as local penetrations of the corrosion-resistant films and which occurs typically in chloride solutions. Recently, some resistant grades with as much as 6.5 wt% Mo have been developed, but the chromium must be changed to 20 wt% and the nickel to 24 wt% to maintain an austenitic structure. Alloys like these are sometimes known as the superaustenitic stainless steels.

**Table 12.1** Some typical austenitic steel specifications

Element	Composition (wt%)						
	AISI type						
	301	302	304	310	316	321	347
C	0.15 max	0.08 max	0.08 max	0.25 max	0.08 max	0.08 max	0.08 max
N	0.03	0.03	0.03	0.03	0.03	0.03	0.03
Cr	16–18	17–19	18–20	24–26	16–18	17–19	17–19
Ni	6–8	8–10	8–12	19–22	10–14	9–12	9–13
Mo					2–4		
Ti						5 × %C	
Nb							10 × %C
Mn	1.5	1.5	1.5	1.5	1.5	1.5	1.5

Corrosion along the grain boundaries can be a serious problem, particularly when a high-temperature treatment such as welding allows precipitation of  $\text{Cr}_{23}\text{C}_6$  in these regions. This type of intergranular corrosion is sometimes referred to as *weld-decay*. To combat this effect some grades of austenitic steel, e.g. 304 and 316, are made with carbon contents of less than 0.03 wt% and designated 304 L and 316 L. Alternatively, niobium or titanium is added in excess of the stoichiometric amount to combine with carbon, as in types 321 and 347.

The austenitic steels so far referred to are not very strong materials. Typically their 0.3% proof stress is about  $250 \text{ MN m}^{-2}$  and the tensile strength between 500 and  $600 \text{ MN m}^{-2}$ , showing that these steels have substantial capacity for work hardening, which makes working more difficult than in the case of mild steel. However, austenitic steels possess very good ductility with elongations of about 50% in tensile tests.

The Cr/Ni austenitic steels are also very resistant to high-temperature oxidation because of the protective surface film, but the usual grades have low strengths at elevated temperatures. Those steels stabilized with Ti and Nb, types 321 and 347, can be heat treated to produce a fine dispersion of TiC or NbC which interacts with dislocations generated during creep. One of the most commonly used alloys is 25Cr–20Ni with additions of titanium or niobium which possesses good creep strength at temperatures as high as  $700^\circ\text{C}$ .

To achieve the best high-temperature creep properties, it is necessary first to raise the room-temperature strength to higher levels. This can be done by precipitation hardening heat treatments on steels of suitable composition to allow the precipitation of intermetallic phases, in particular  $\text{Ni}_3(\text{Al Ti})$ . In Table 12.2 the room-temperature strength of two alloys in this category (A286 and Unitemp 212) after ageing at  $700\text{--}750^\circ\text{C}$  is compared with that of the simpler standard austenitic alloys, e.g. 304. It can be seen that the strength is more than doubled by the precipitation reaction.

## 12.8 DUPLEX AND FERRITIC STAINLESS STEELS

In Section 12.2, the importance of controlling the  $\gamma$ -loop in achieving stable austenitic steels was emphasized. Between the austenite and  $\delta$ -ferrite phase fields there is a restricted ( $\alpha + \gamma$ ) region which can be used to obtain two-phase or duplex structures in stainless steels (Fig. 12.11). The structures are produced by having the correct balance between the  $\alpha$ -forming elements (Mo, Ti, Nb, Si, Al) and the  $\gamma$ -forming elements (Ni, Mn, C and N). To achieve a duplex structure, it is normally necessary to increase the chromium content to above 20 wt%. However, the exact proportions of  $\alpha$  and  $\gamma$  are determined by the heat treatment. It is clear from consideration of the  $\gamma$ -loop section of the equilibrium diagram, that holding in the range  $1000\text{--}1300^\circ\text{C}$  will cause the ferrite content to vary over wide limits. The usual treatment is carried out between  $1050^\circ\text{C}$  and  $1150^\circ\text{C}$ , when the ferrite content is not very sensitive to the subsequent cooling rate.

**Table 12.2** Strengthening of austenitic steels at room temperature

(a) Composition

Element	Composition (wt%)						
	Specification					Unitemp	
	304	304(N)	347	347(N)	A286	212	IN744
C	0.08	0.06	0.06	0.08	0.05	0.08	0.05
N	0.03	0.20	0.03	0.20			
Cr	19.0	18.0	18.0	18.0	15.0	13.5	26.0
Ni	10.0	10.0	12.0	11.0	26.0	26.0	6.5
Mo					1.2	1.75	
Ti					2.0	3.0	0.3
Nb			$10 \times \%C$				
Al					0.15	0.15	
V					0.30		

(N): high nitrogen.

(b) Mechanical properties

	Specification					Unitemp	
	304	304(N)	347	347(N)	A286	212	IN744
0.2% Proof stress ( $\text{MN m}^{-2}$ )	247	340	247	415	700	920	570
Tensile strength ( $\text{MN m}^{-2}$ )	541	695	556	710	1000	1300	740
Elongation (%)	55	46	50	39	25.0 <sup>a</sup>	23.0 <sup>b</sup>	24

(N): high nitrogen.

<sup>a</sup>Aged at 750°C.<sup>b</sup>Aged at 700°C.

The duplex steels are stronger than the simple austenitic steels, partly as a result of the two-phase structure and also because this leads normally to a refinement of the grain size. Indeed, by suitable thermomechanical treatment between 900°C and 1000°C, it is possible to obtain very fine microduplex structures which can exhibit super-plasticity, i.e. very high ductilities at high temperatures, for strain rates less than a critical value. A typical composition, IN744, is shown in Table 12.2 with the mechanical properties at room temperature.

A further advantage is that duplex stainless steels are resistant to *solidification cracking*, particularly that associated with welding. While the presence of  $\delta$ -ferrite may have an adverse effect on corrosion resistance in some



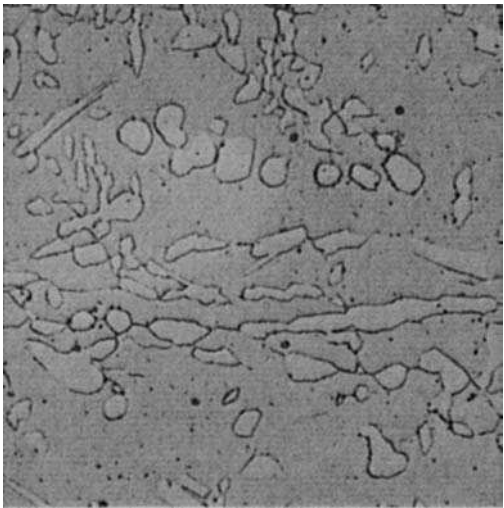


**Fig. 12.11** Duplex stainless steel, 26Cr–5Ni–1.5Mo–0.025C wt%, ( $\alpha + \gamma$ ) microstructure (courtesy of J. Honeycombe). Optical micrograph,  $\times 630$ .

**Table 12.3** Compositions of some ferritic stainless steels

Element	Composition (wt%)		
	AISI 430	AISI 446	18/2
C	0.06	0.08	0.02
Cr	17.0	25.0	18.0
Mo			2.0

circumstances, it does improve the resistance of the steel to transgranular stress corrosion cracking as the ferrite phase is immune to this type of failure.

A new class of steels, the super-duplex stainless steels, has been developed recently with better corrosion resistance than the duplex stainless steels. They are particularly superior in their resistance to localized pitting corrosion, because of their larger concentrations of chromium, molybdenum and nitrogen. To maintain the balanced ferrite/austenite microstructure, it is necessary to also boost the concentration of austenite stabilizing elements such as nickel. Super-duplex stainless steels, therefore, typically contain 27Cr–7Ni–4Mo–0.3N wt%.

There is another important group of stainless steels which are essentially ferritic in structure. They contain between 17 and 30 wt% chromium and, by dispensing with the austenite stabilizing element nickel, possess considerable economic advantage. These steels, particularly at the higher chromium levels, have excellent corrosion resistance in many environments and are completely free from stress corrosion. Typical compositions are shown in Table 12.3.

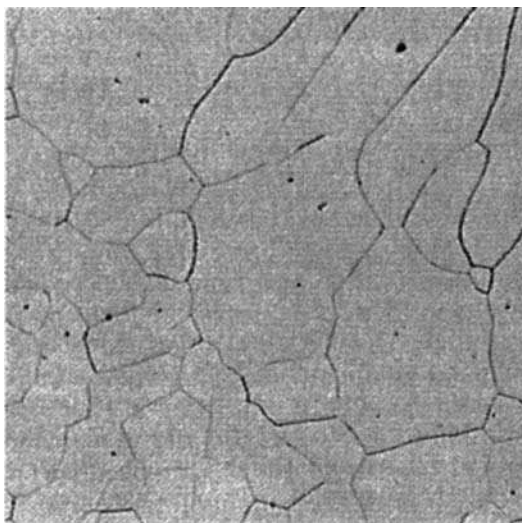


**Fig. 12.12** Grain growth in the HAZ of a weld in a ferritic stainless steel (courtesy of J. Honeycombe). Optical micrograph,  $\times 80$ .

These steels do have some limitations, particularly those with higher chromium contents, where there can be a marked tendency to embrittlement. This arises partly from the interstitial elements carbon and nitrogen, e.g. a 25 wt% Cr steel will normally be brittle at room temperature if the carbon content exceeds 0.03 wt%. An additional factor is that the absence of a phase change makes it more difficult to refine the ferrite grain size, which can become very coarse after high-temperature treatment such as welding (Fig. 12.12). This raises still further the ductile/brittle transition temperature, already high as a result of the presence of interstitial elements. Fortunately, modern steel-making methods such as argon–oxygen refining can bring the interstitial contents below 0.03 wt%, while electron beam vacuum melting can do better still.

The ferritic stainless steels are somewhat stronger than austenitic stainless steels, the yield stresses being in the range  $300\text{--}400\text{ MN m}^{-2}$ , but they work harden less so the tensile strengths are similar, being between 500 and  $600\text{ MN m}^{-2}$ . However, ferritic stainless steels, in general, are not as readily deep drawn as austenitic alloys because of the overall lower ductility. However, they are suitable for other deformation processes such as spinning and cold forging.

Welding causes problems due to excessive grain growth in the HAZ but, recently, new low-interstitial alloys containing titanium or niobium have been shown to be readily weldable. The higher chromium ferritic alloys have excellent corrosion resistance, particularly if 1–2 wt% molybdenum is present.

There are two phenomena which may adversely affect the behaviour of ferritic stainless steels. Firstly, chromium-rich ferrites when heated between  $400^{\circ}\text{C}$  and  $500^{\circ}\text{C}$  develop a type of embrittlement ( $475^{\circ}\text{C}$  embrittlement). The most

likely cause is the precipitation of a very fine coherent chromium-rich phase (bcc  $\alpha'$ ) arising from the miscibility gap in the Fe–Cr system, probably by a spinodal type of decomposition. This phenomenon becomes more pronounced with increasing chromium content, as does a second phenomenon, the formation of sigma phase. The latter phase occurs more readily in chromium-rich ferrite than in austenite, and can be detected below 600°C. As in austenite, the presence of sigma phase can lead to marked embrittlement.

12.9 MECHANICALLY ALLOYED STAINLESS STEELS

Mechanical alloying is a process in which mixtures of fine powders consisting of elemental metals or master alloys are changed into solid solutions, apparently without any melting (Fig. 12.13). The powders are forced to collide with each other and with much larger, hardened steel balls whilst contained in a ball mill.

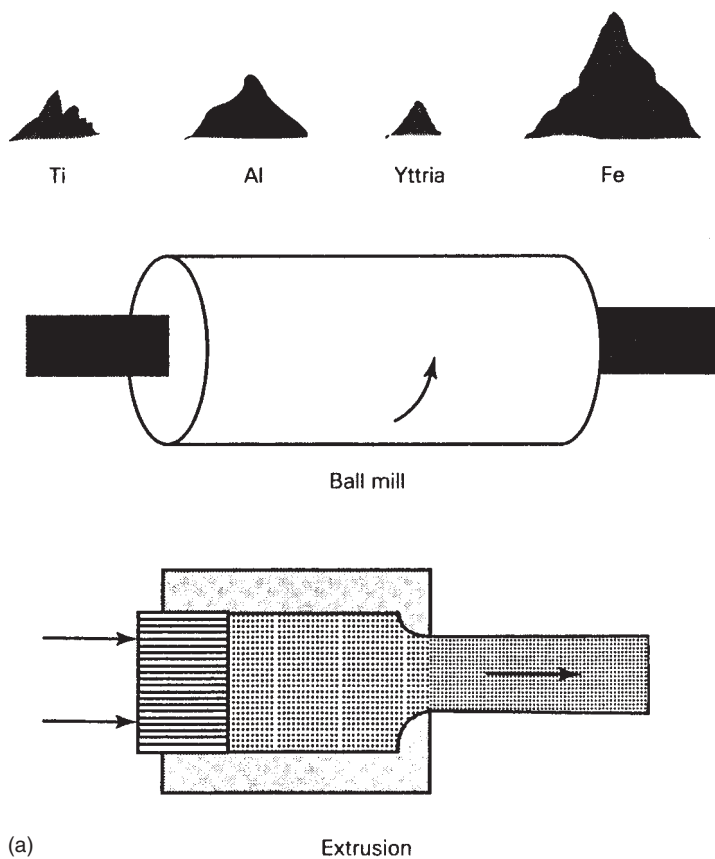
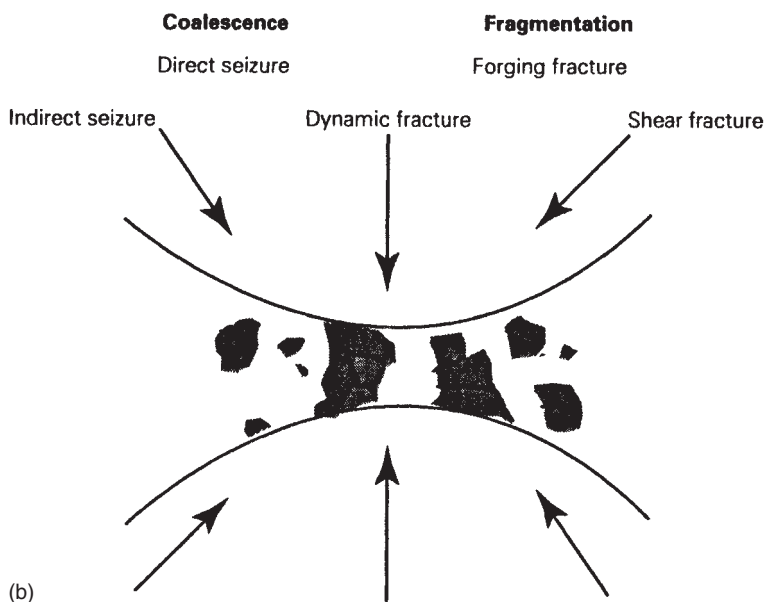


Fig. 12.13 (a) Schematic illustration of the mechanical alloying process.



**Fig. 12.13 (b)** The repeated fragmentation and coalescence of particles trapped between impacting balls leads eventually to solution during mechanical alloying. Dynamic fracture occurs during normal impact whereas the other processes are a feature of impact occurring in an inclined fashion (Maurice and Courtney, *Metallurgical Transactions* **21A**, 289–303, 1990).

The collisions are very energetic, involve large contact pressures (Fig. 12.13b), and lead eventually to the formation of an intimate solid solution. Refractory oxides (commonly yttrium oxide) can also be finely dispersed into the mechanically alloyed powder in order to obtain dispersion strengthening. The mechanically alloyed powder is finally extruded to form full density bulk samples in rod, sheet or other useful shapes.

After consolidation by extrusion, the alloys are usually very hard and possess an extremely small grain size, typically a small fraction of a micrometre (Fig. 12.14a). Such a small grain size is impossible to achieve by any other process for bulk samples. The material is usually extremely hard in the as-consolidated state, and has to be softened before further fabrication. The grain boundary area locked into the material gives it a large stored energy, which under suitable heat-treatment conditions triggers recrystallization into a much coarser grain structure. If annealing is carried out by passing the sample through a hot zone (zone annealing), then the recrystallization front is localized within the high-temperature region. The front then advances at the same rate as the sample, thereby leading to *directional recrystallization* in which the microstructure consists of a series of very coarse columnar grains parallel to the zone annealing direction (Fig. 12.14b). It resembles in fact the microstructure obtained during

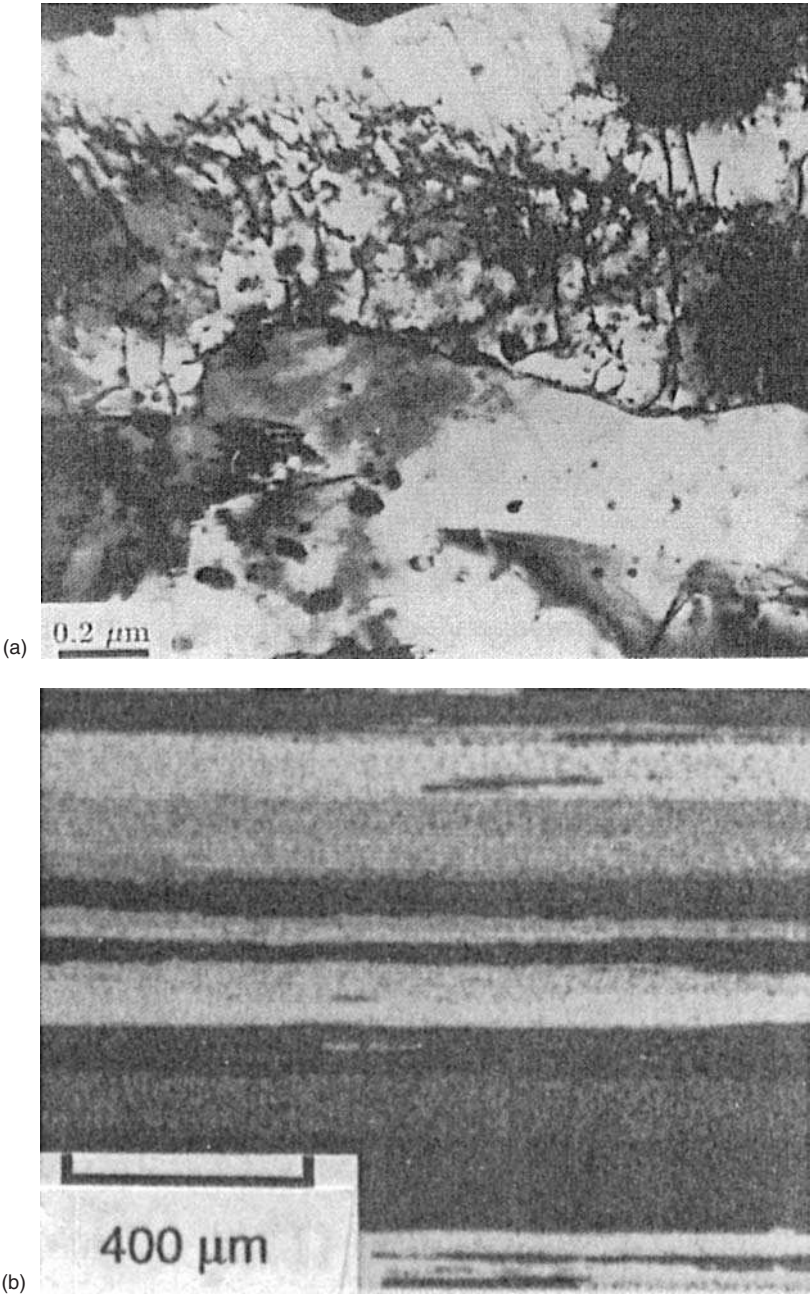


**Fig. 12.14** (a) Transmission electron micrograph of a mechanically alloyed steel prior to recrystallization, showing the ultrafine grained microstructure. (b) Light micrograph illustrating the columnar recrystallized grain structure.

**Table 12.4** Chemical compositions of mechanically alloyed oxide dispersion strengthened stainless steels (wt%)

C	Cr	Al	Ti	Mo	Y <sub>2</sub> O <sub>3</sub>
0.01	20	4.5	0.5	—	0.5
0.01	14	—	1.0	0.3	0.27

directional solidification. The columnar grains are highly anisotropic, usually only restricted by the size of the sample, and can reach lengths in excess of a metre. In some instances, even isothermal annealing can lead to the development of columnar recrystallized grains. The yttria particles introduced during mechanical alloying are not isotropically dispersed, but are aligned parallel to the extrusion direction. Consequently, anisotropic grain boundary pinning leads to the columnar grain growth during recrystallization.

There are two kinds of mechanically alloyed ferritic stainless steels available commercially, with many other varieties under development (Table 12.4). The alloy with the largest aluminium and chromium concentrations naturally has a better oxidation resistance. Its oxide content permits its use as a creep-resistant material to temperatures in excess of 1000°C, whereas normal ferritic steels are not used when the service temperature exceeds about 600°C.

The ferritic state also makes the steels less susceptible to radiation induced swelling. The lower chromium alloys (also without aluminium) are therefore designed for nuclear reactor applications. The significant titanium concentration, in the absence of carbon, leads to the precipitation of a bcc. FeCrTiMo intermetallic compound ( $\chi$ -phase) during ageing at around 800°C. This can further boost the creep strength.

## 12.10 THE TRANSFORMATION OF METASTABLE AUSTENITE

Some austenitic steels are often close to transformation, in that the  $M_s$  temperature may be just below room temperature. This is certainly true for low-carbon 18Cr8Ni austenitic steel, which can undergo a martensitic transformation by cooling in liquid nitrogen or by less severe refrigeration. The application of plastic deformation at room temperature can also lead to formation of martensite in metastable austenitic steels, a transformation of particular significance when working operations are contemplated. The increase in  $M_s$  by cold work is specified by an  $M_d$  temperature below which transformation to martensite occurs when the steel is plastically deformed. In general, the higher the alloying element content the lower the  $M_s$  and  $M_d$  temperatures, and it is possible to obtain an approximate  $M_s$  temperature using empirical equations. Useful data concerning the  $M_d$  temperature are also available in which an arbitrary amount of deformation has to be specified. Normally this is a true strain of 0.30.

The martensite formed in Cr–Ni austenitic steels either by refrigeration or by plastic deformation is similar to that obtained in related steels possessing an  $M_s$  above room temperature.

Manganese can be substituted for nickel in austenitic steels, but the Cr–Mn solid solution then has a much lower stacking fault energy. This means that the fcc solid solution is energetically closer to an alternative close-packed hexagonal structure, and that the dislocations will tend to dissociate to form broader stacking faults than is the case with Cr–Ni austenites. In these circumstances, the martensite which forms first is hexagonal in structure ( $\epsilon$ -martensite), with a habit plane  $\{0001\}_\epsilon$  parallel to the stacking fault plane  $\{111\}_\gamma$ . This phase has been shown to nucleate on stacking faults, with the following orientation relationship with austenite:

$$\begin{aligned} \{0001\}_\epsilon // \{111\}_\gamma, \\ (11\bar{2}0)_\epsilon // (110)_\gamma. \end{aligned}$$

This type of martensite forms as parallel-sided plates which can be easily confused with annealing twins, common in fcc matrices with low stacking fault energies. Frequently  $\alpha'$  martensite eventually forms, nucleating at the interface between  $\epsilon$  and the austenitic matrix.

Manganese on its own can stabilize austenite at room temperature provided sufficient carbon is in solid solution. The best example of this type of alloy is the Hadfields manganese steel with 12 Mn–1.2C wt% which exists in the austenitic condition at room temperature and even after extensive deformation does not form martensite. However, if the carbon content is lowered to 0.8 wt%, then  $M_d$  is above room temperature and transformation is possible in the absence of deformation at 77 K. Both  $\epsilon$  and  $\alpha'$  martensites have been detected in manganese steels. Alloys of the Hadfields type have long been used in wear resistance applications, e.g. grinding balls, railway points, excavating shovels, and it has often been assumed that partial transformation to martensite was responsible for the excellent wear resistance and toughness required. However, it is likely that the very substantial work-hardening characteristics of the austenitic matrix are more significant in this case.

In general, fcc metals exhibit higher work-hardening rates than bcc metals because of the more stable dislocation interactions possible in the fcc structure. This results in the broad distinction between the higher work hardening of austenitic steels and the lower rate of ferritic steels, particularly well exemplified by a comparison of ferritic stainless steels with austenitic stainless steels. Within the austenitic category, however, there are two factors which influence the extent of work hardening:

- (a) the stacking fault energy of the matrix, determined by the composition;
- (b) the stability of the matrix.

The chromium nickel austenitic steels have stacking faults energies in the range  $5\text{--}60\text{ mJ m}^{-2}$ , and it would be expected that the highest nickel alloys

would show the lowest work hardening as nickel is one of the elements that raises the stacking fault energy of austenite. The elements Cr, Mn, Co, Si, C and N tend to lower the stacking fault energy of austenite. This can be deduced from the greater tendency for annealing twins to occur in austenites rich in these elements. Plastic deformation of such solid solutions not only produces stable dislocation interactions but also, after heavy deformations, many very fine deformation twins, both factors contributing to the high flow stresses observed in the deformed alloys. By severe cold working, e.g. up to 80% reduction in wire drawing, the relatively modest yield strengths of ordinary austenitic steels can be raised to over  $1200 \text{ MN m}^{-2}$ .

However, the largest effect on work-hardening rates is undoubtedly the transformation to martensite, as illustrated by the true stress-strain curves of several austenitic steels of decreasing nickel content, i.e. decreasing stability of austenite (Fig. 12.15). By this means yield stresses of well over  $1500 \text{ MN m}^{-2}$  can be achieved, e.g. a metastable austenite containing 17Cr-4Ni-3Mn-0.1C wt% after almost complete transformation following 40% deformation at room temperature has a 0.2% proof stress of  $1700 \text{ MN m}^{-2}$ . It should be noted that the increase in strength is accompanied by a substantial decrease in ductility, so such steels should not be used for deep drawing, an application where stability of the austenite is essential. In contrast, in stretch forming applications unstable austenitic steels can be used because the transformation, by raising the

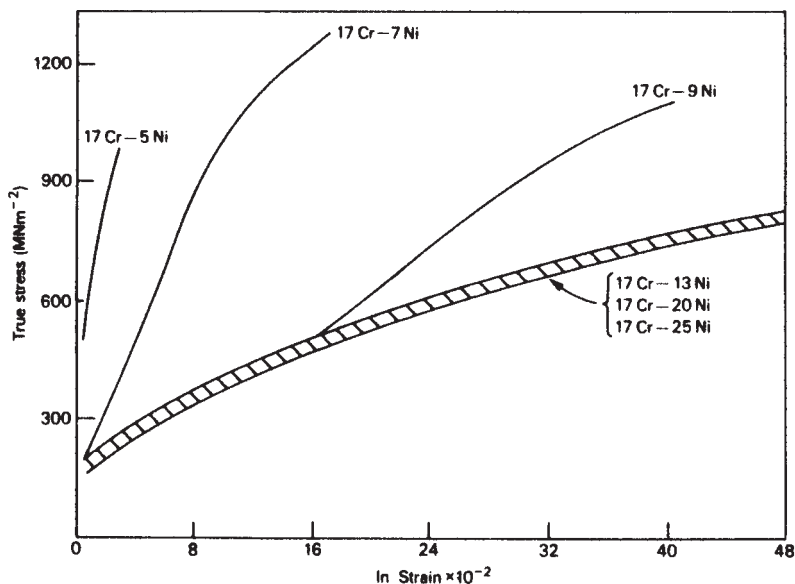


**Fig. 12.15** Effect of decreasing nickel content on the stress-strain curves of stainless steels (Pickering, *Metallurgical Achievements*, Pergamon Press, Oxford, UK, 1965).



work-hardening rate, also increases the extent of uniform straining, as distinct from localized straining, which the steel will undergo prior to failure.

The advantages obtainable from the easily fabricated austenitic steels led naturally to the development of *controlled transformation* stainless steels, where the required high strength level was obtained after fabrication, either by use of refrigeration to take the steel below its  $M_s$  temperature or by low-temperature heat treatment to destabilize the austenite. Clearly the  $M_s$ – $M_f$  range has to be adjusted by alloying so that the  $M_s$  is just below room temperature. The  $M_f$  is normally about 120°C lower, so that refrigeration in the range –75°C to –120°C should result in almost complete transformation to martensite. Alternatively, heat treatment of the austenite can be carried out at 700°C to allow precipitation of  $M_{23}C_6$  mainly at the grain boundaries. This reduces the carbon content of the matrix and raises the  $M_s$  so that, on subsequent cooling to room temperature, the austenite will transform to martensite. This precipitation reaction can be accelerated by designing the steel to include a small volume fraction of  $\delta$ -ferrite. The  $\delta/\gamma$  interfaces then provide very effective nucleating sites for  $M_{23}C_6$ .

Further heat treatment is then necessary to give improved ductility and a high proof stress; this is achieved by tempering in the range 400–450°C. Typical compositions of these steels and the properties which can be obtained by alternative heat treatments are given in Table 12.5. This category of steels places large demands on metallurgical control, the treatments are complex and the cost high. Consequently, they tend only to be used in critical applications such as highly stressed skins of supersonic aircraft and rocket casings.

Another group of steels has been developed to exploit the properties obtained when the martensite reaction occurs during low-temperature plastic deformation. These steels, which are called *transformation-induced plasticity* (TRIP) steels (Chapter 10), exhibit the expected increases in work-hardening rate and a marked increase in uniform ductility prior to necking. Essentially the principle is the same as that employed in controlled transformation steels, but plastic deformation is used to form martensite and the approach is broader as far as the thermomechanical treatment is concerned.

In one process, the composition of the steel is balanced to produce an  $M_d$  temperature above room temperature. The steel is then heavily deformed (~80%) above the  $M_d$  temperature, usually in the range 250–550°C, which results in austenite which remains stable at room temperature. Subsequent tensile testing at room temperature gives high strength levels combined with extensive ductility as a direct result of the martensitic transformation which takes place during the test. For example, a steel containing 0.3C–2Mn–2Si–9Cr–8.5Ni–4Mo wt% after 80% reduction at 475°C gives the following properties at room temperature:

0.2% Proof stress	1430 MN m <sup>-2</sup>
Tensile strength	1500 MN m <sup>-2</sup>
Elongation	50%

**Table 12.5** Compositions and properties of controlled transformation steels (after Pickering, 1976)

Composition	Heat treatment	0.2% proof stress ( $\text{MN m}^{-2}$ )	Tensile strength ( $\text{MN m}^{-2}$ )	Elongation (%)
0.1C, 17 Cr, 4Ni, 3Mn	1. Solution treated 925°C, cold worked 40% reduced, tempered 3 h at 450°C	1670	1700	3.5
	2. Solution treated 950°C, refrigerated at $-78^\circ\text{C}$ , tempered 1 h at 400°C	1200	1440	19
0.06C, 16.5Cr, 5Ni, 2Mn, 1.5Mo, 2Co, 1Al	1. Solution treated 1050°C, aged 2 h at 700°C, cooled to RT, then aged 4 h at 450°C	1270	1430	3
	2. Solution treated 950°C, refrigerated at $-78^\circ\text{C}$ , tempered 4 h at 450°C	1240	1520	21
0.07C, 17.5Cr, 3Ni, 2Mn 2Mo, 2Co, 1Cu	1. Solution treated 1050°C, aged 2 h at 700°C, cooled to RT, then tempered 4 h at 450°C	1110	1250	10
	2. Solution treated 950°C, refrigerated at $-78^\circ\text{C}$ , tempered 4 h at 450°C	1240	1360	20

RT: room temperature.

Higher strength levels (proof stress  $\sim 2000 \text{ MN m}^{-2}$ ) with ductilities between 20% and 25% can be obtained by adding strong carbide-forming elements such as vanadium and titanium, and by causing the  $M_d$  temperature to be below room temperature. As in the earlier treatment, severe thermomechanical treatments in the range 250–550°C are then used to deform the austenite and dispersion strengthen it with fine alloy carbides. The  $M_d$  temperature is, as a result, raised to above room temperature so that, on mechanical testing, transformation to martensite takes place, giving excellent combinations of strength and ductility as well as substantial improvements in fracture toughness.

Like the controlled transformation steels, the TRIP steels require extremely good metallurgical control and are very expensive to make. They are only used in applications where extremely high demands are made on mechanical, as distinct from environmental properties. They do, however, illustrate how a combination of basic principles can be carefully balanced and controlled to achieve outstanding mechanical properties in alloy steels.

**FURTHER READING**

- Barr, Robert Q. (ed.), *Stainless Steel '77*, Climax Molybdenum Co. Conference, London, 1977.
- Bhadeshia, H. K. D. H., Recrystallisation of practical mechanically alloyed iron base alloys, *Materials Science and Engineering* **A223**, 64, 1997.
- Colombier, L. and Hochmann, J., *Stainless and Heat Resisting Steels*, Edward Arnold, London, UK, 1967.
- Gavriljuk, V. G. and Berns, H., *High Nitrogen Steels*, Springer, Berlin, Germany, 1999.
- Gooch, T. G., Welding Stainless Steels, in *Future Developments in Metals and Ceramics*, Professor Sir Robert Honeycombe 70th birthday Symposium, The Institute of Materials, London, UK, 1992.
- Iron and Steel Institute, *Metallurgical Developments in High Alloy Steels*, Special Report No. 86, 1964.
- Iron and Steel Institute, *Stainless Steels*, Special Report No. 117, 1969.
- Lula, R. A. (ed.), *Duplex Stainless Steels*, American Society for Metals, Ohio, USA, 1988.
- Marshall, P., *Austenitic Stainless Steels – Microstructure and Properties*, Elsevier, Barking, UK, 1984.
- Monypenny, J. K. G., *Stainless Iron and Steels*, Vols 1 and 2, Chapman and Hall, UK, 1951.
- Peckner, D. and Bernstein, I. M., *Handbook of Stainless Steels*, McGraw-Hill, UK, 1977.
- Pickering, F. B., Physical metallurgy of stainless steel developments, *International Metallurgical Reviews*, Review 211, 1976.
- Pickering, F. B. (ed.), *The Metallurgical Evolution of Stainless Steels*, American Society for Metals/Metals Society, Ohio, USA, 1979.
- Schmidt, W. and Jarleborg, O., *Ferritic Stainless Steels*, Climax Molybdenum Co., Michigan, USA, 1974.
- Sourmail, T., Too, C. H. and Bhadeshia, H. K. D. H., Sensitisation and evolution of Cr-depleted zones in Fe-Cr-Ni-C systems, *ISIJ International* **43**, 1814, 2003.
- Stainless Steels '87*, The Institute of Metals, 1988.
- Stainless Steels '91* (2 Vols) Iron and Steel Institute of Japan. *International Conference on Stainless Steels*, Chiba, 1991.
- Truman, J. E., Stainless Steels, in *Materials Science and Technology* (eds Cahn, R. W., Haasen, P. and Kramer, E. J.), Vol. 7, *Constitution and Properties of Steels* (ed. Pickering, H. B.), Germany, 1992.

# 13

---

## WELD MICROSTRUCTURES

### 13.1 INTRODUCTION

Fusion welding is of greatest importance in the fabrication of engineering structures. There are many ways in which fusion welding can be carried out, but all of them involve the deposition of a small amount of molten steel within a gap between the components to be joined. When the steel solidifies, it welds the components together. The metallurgy of the welded joint can be categorized into two major regions, the fusion zone and the heat-affected zone (HAZ). The fusion zone represents both the deposited metal and the parts of the steel component melted during the process, and is a solidification microstructure. The HAZ, on the other hand, represents those regions in the close proximity of the weld, where the heat input during welding changes the microstructure without melting the steel. This chapter describes the development of microstructure in both zones, beginning with the fused regions. Virtually every aspect of phase transformation in steels is relevant to the subject of welding. There is an opportunity for a whole series of transformations to occur successively as the weld cools from the liquid state.

### 13.2 THE FUSION ZONE

#### 13.2.1 Weld solidification

Iron is ferritic at temperatures just below the melting point. As it cools, the ferrite then transforms to austenite, only to revert back to ferrite on continued cooling. Most steels contain modest concentrations of alloying elements, and hence show similar crystal structure changes as pure iron. Weld deposits, therefore begin solidification with the epitaxial growth of columnar delta-ferrite ( $\delta$ -ferrite) from the hot-grain-structure of the parent plate at the fusion surface (Fig. 13.1a). The grains are anisotropic because they grow along the direction of heat flow. Those grains with their (100) directions parallel to the heat-flow direction grow fastest

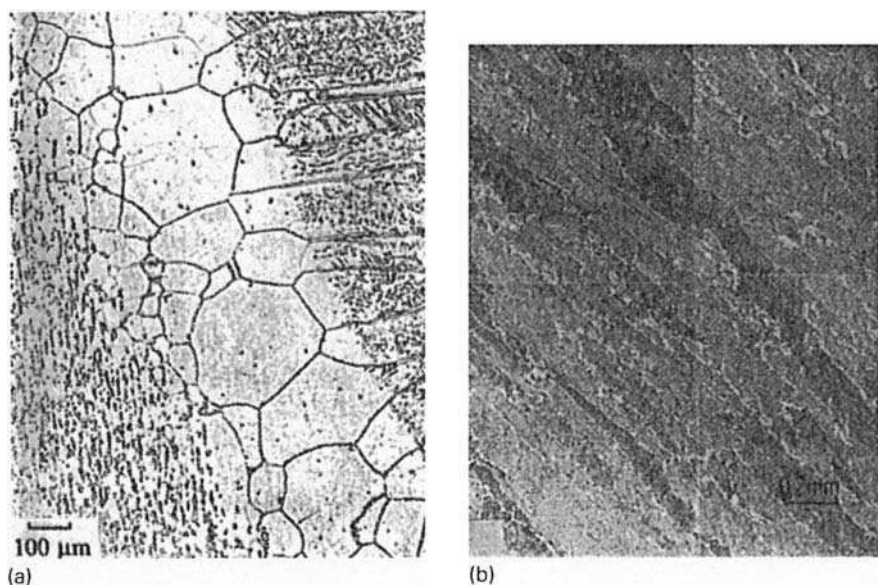


**Fig. 13.1** (a) Illustration of the epitaxial growth of columnar grains from the fusion boundary of a stainless steel weld (courtesy of Honeycombe and Gooch). (b) Optical micrograph showing the columnar prior-austenite grain structure typical in steel weld deposits.

and hence stifle the growth of unsuitably oriented grains. The width of the columnar grains therefore increases with distance away from the fusion boundary.

As already pointed out, the  $\delta$ -ferrite undergoes a solid-state transformation to austenite as the temperature decreases. The austenite nucleates at the  $\delta$ - $\delta$  grain boundaries and develops into a columnar austenite grain structure which strongly resembles that of the original  $\delta$ -grains (Fig. 13.1b).

The detailed shape and size of the austenite grains is of importance in the evolution of the final microstructure. The effect of the austenite grain size is two-fold. Firstly, the number density of austenite grain boundary nucleation sites changes inversely with the grain size. Coarse-grained weld deposits therefore have a higher hardenability. The second, and more subtle effect, arises from the columnar shape of the austenite grains, a shape which is like that of a hexagonal prism. The grains are typically about  $100\ \mu\text{m}$  wide and about  $5000\ \mu\text{m}$  in length. This is quite unlike an equi-axed grain structure, and because of the fewer grain junctions involved, allows the hardenability of a weld to be larger than that of a wrought alloy.

Solidification does not occur under equilibrium conditions during welding. Solidification-induced chemical segregation, and composition variations due to uncontrolled changes in the welding conditions, make the solidification microstructure inhomogeneous. The amplitude of these variations becomes larger as the alloy concentration increases.

**Table 13.1** A comparison of the chemical composition (wt%) of a submerged arc weld with that of the plate being welded, and the wire used as the consumable electrode. The welding conditions used were 34V, 900Amp (D.C. positive), at a welding speed of  $0.005 \text{ m s}^{-1}$ , with a calcium silicate flux.

	C	Mn	Si	Cu	Al	N	O
Plate	0.21	1.0	0.2	0.05	0.04	0.01	0.004
Wire	0.14	1.5	0.2	0.31	0.01	0.01	0.001
Weld	0.16	1.1	0.3	0.16	0.01	0.01	0.053

Mineral fluxes or inert gas shrouds are employed in order to protect the hot metal against environmental attack during welding. Such protection is not entirely effective, with the result that the oxide content of welds tends to be much larger than that of wrought steel (Table 13.1). The oxide particles are entrapped in the fusion zone during solidification. As discussed later, these non-metallic particles serve as heterogeneous nucleation sites and hence are of considerable importance in the evolution of the microstructure. Table 13.1 reveals some other interesting differences between the plate and weld compositions. The copper concentration of the weld is large because in this case, the welding wire has a copper coating to enable better electrical contact. The silicon concentration in the weld is larger than both the wire and the plate, because the excess silicon is acquired by decomposition of the protective flux. These observations emphasize the complexity of the welding process, in which the chemical composition of the final weld deposit depends on many variables, including the plate, wire and flux compositions.

### 13.2.2 The as-deposit microstructure

The microstructure obtained as the weld cools from the liquid phase to ambient temperature is called the *as-deposited* or *primary* microstructure. Its major components include allotriomorphic ferrite, Widmanstätten ferrite, and acicular ferrite (Fig. 13.2). There may also be some martensite, retained austenite or degenerate pearlite. These latter phases occur in very small fractions, and are known by the collective term *microphases*. Bainite, consisting of sheaves of parallel platelets, is not generally found in well-designed welding alloys. Instead, acicular ferrite is induced to nucleate heterogeneously on non-metallic inclusions.

In practice, the gap between the components to be joined has to be filled by a sequence of several weld deposits. These multirun welds have a complicated microstructure (Fig. 13.3). The deposition of each successive layer heat treats the underlying microstructure. Some of the regions of original primary microstructure are reheated to temperatures high enough to cause the reformation of austenite, which during the cooling part of the thermal cycle transforms into a different microstructure. Other regions may simply be tempered by the

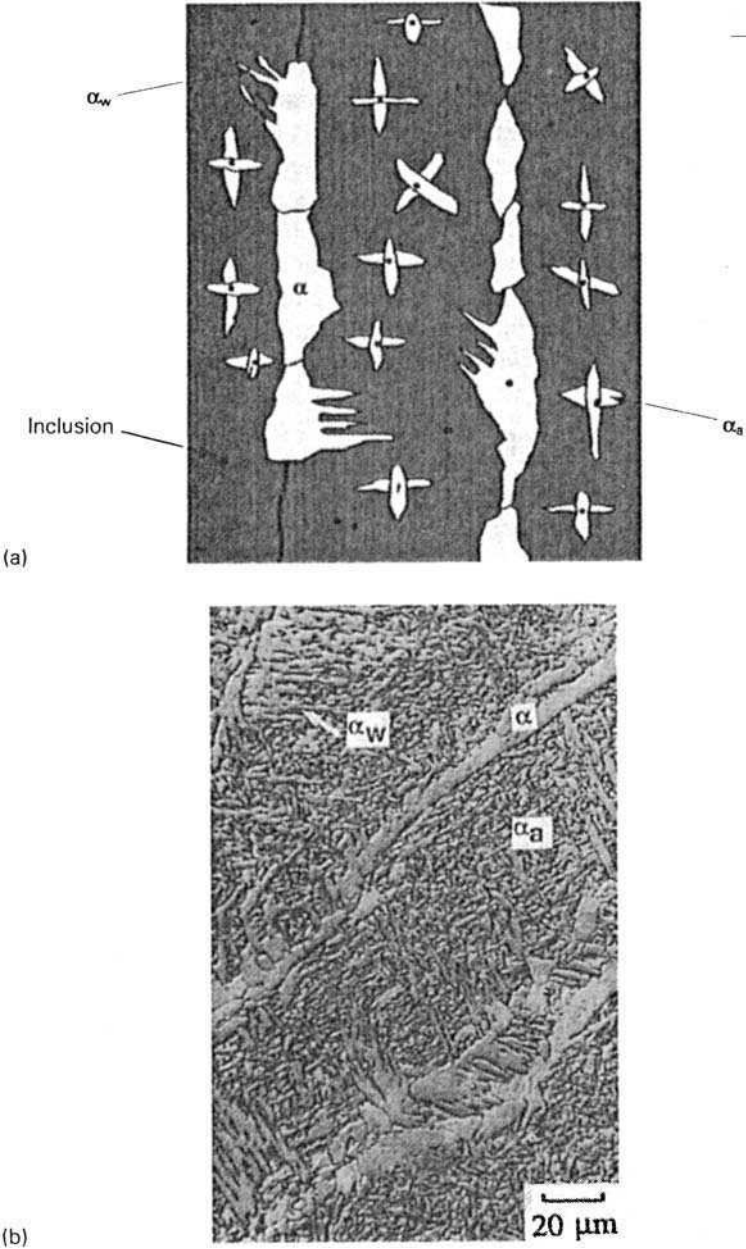


**Fig. 13.2** (a) Schematic illustration of the essential constituents of the primary microstructure in the columnar austenite grains of a steel weld deposit. (b) Scanning electron micrograph of the primary microstructure of a steel weld (courtesy of Rees). The terms  $\alpha$ ,  $\alpha_w$  and  $\alpha_a$  refer to allotriomorphic ferrite, Widmanstätten ferrite and acicular ferrite, respectively.

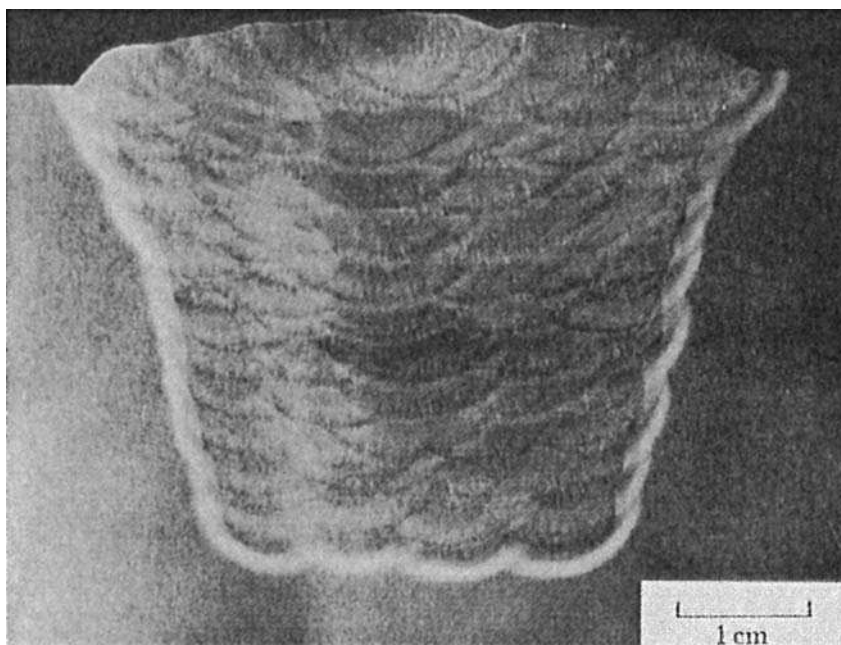


**Fig. 13.3** The macrostructure of a multirun weld, made by sequentially depositing a number of beads in each of the 12 layers (courtesy of Reed).

deposition of subsequent runs. The microstructure of the reheated regions is called the *reheated* or *secondary* microstructure.

### 13.2.3 Allotriomorphic ferrite

Allotriomorphic ferrite ( $\alpha$ ) is the first phase to form on cooling the austenite grains below the  $A_{e3}$  temperature. It nucleates at the columnar austenite grain boundaries. Because these boundaries are easy diffusion paths, they become decorated with thin, continuous layers of ferrite. The layers then thicken at a rate which is controlled by the diffusion of carbon in the austenite ahead of the transformation interface. Under isothermal conditions, the ferrite thickness  $S$  changes parabolically with time  $t$  (Chapter 3):

$$S = \alpha_1 t^{1/2}, \quad (13.1)$$

where  $\alpha_1$  is called the parabolic rate constant. This is illustrated in Fig. 13.4 for alloys with different carbon concentrations; note that the growth kinetics become sensitive to the carbon concentration as the latter approaches the solubility of carbon in the ferrite.

The magnitude of the parabolic rate constant depends on the equilibrium compositions of the austenite and ferrite, and on the diffusivity of carbon in



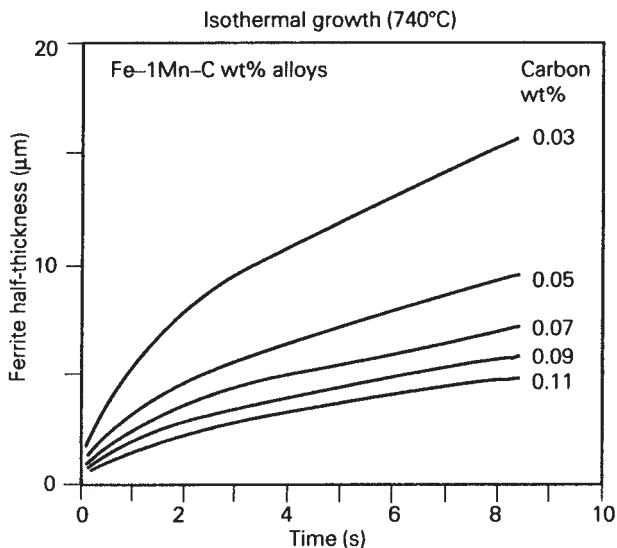


**Fig. 13.4** An illustration of the parabolic thickening of ferrite during isothermal transformation. Each curve represents a Fe-1Mn-C wt% steel with the carbon concentration as indicated on the diagram.

austenite (Chapter 3). Alloying elements such as manganese, which stabilize austenite, are associated with a smaller value of  $\alpha_1$ . In welding, transformations are not isothermal, but nevertheless, because nucleation is not rate limiting, the fraction of allotriomorphic ferrite obtained correlates directly with the parabolic rate constant (Fig. 13.5a).

The fact that the thickness of the ferrite varies with the square root of time, means that the rate of growth decreases as the ferrite layer gets thicker. This is because the distance over which carbon has to diffuse increases with time (Fig. 13.5b). The growth rate for a given alloy goes through a maximum as a function of temperature, because the driving force for transformation increases with undercooling whereas the diffusivity decreases. Consequently, as the weld cools to temperatures less than about 600°C, the diffusional growth of ferrite slows down so much that the layers of allotriomorphic ferrite reach a limiting thickness. Widmanstätten ferrite formation does not involve the diffusion of substitutional solutes, and therefore its growth is not sluggish at low temperatures. The remaining austenite, therefore, begins to transform to Widmanstätten ferrite (Fig. 13.6).

#### 13.2.4 Widmanstätten ferrite and acicular ferrite

Although substitutional solutes and iron atoms do not diffuse during the growth of Widmanstätten ferrite, carbon does partition during transformation. Because

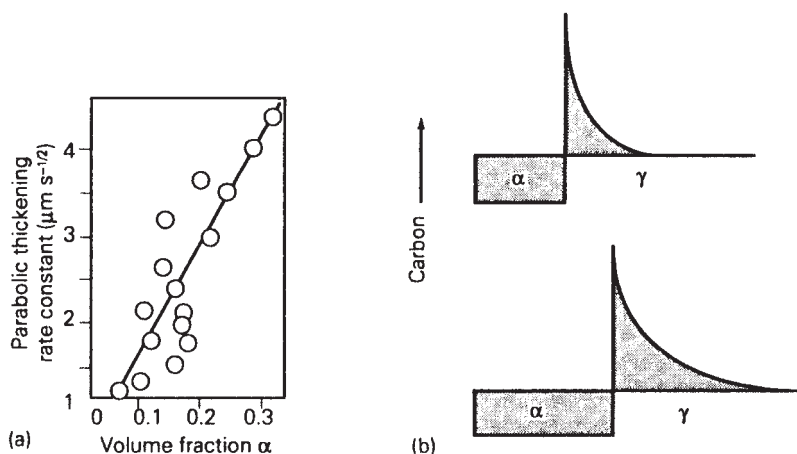


**Fig. 13.5** (a) The correlation between the calculated parabolic thickening rate constant (a variable related to the growth rate) and the volume fraction of allotriomorphic ferrite obtained in a series of manual metal arc weld deposits, fabricated using similar welding parameters but with different chemical compositions. The rate constant is calculated for transformation at 700°C. (b) The diffusion distance increases as the ferrite layer thickens, slowing down the rate of growth.

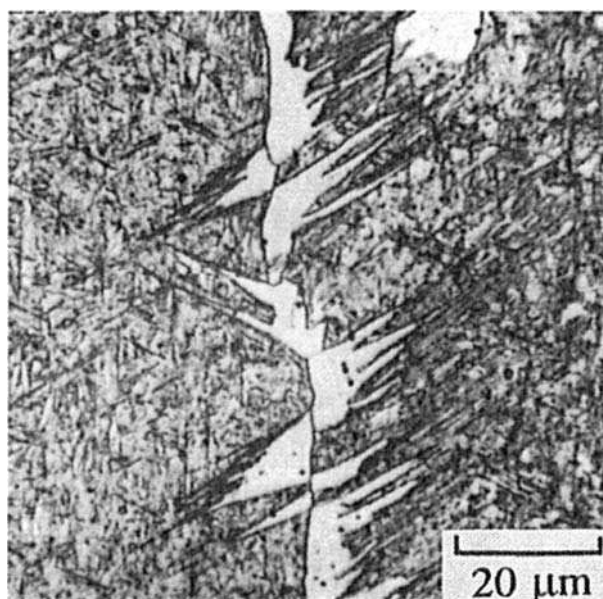


**Fig. 13.6** Widmanstätten ferrite plates growing from allotriomorphic ferrite in a partially transformed steel weld which was quenched from the transformation temperature. The matrix is martensitic (courtesy of Barritte).

of its plate shape, much of the carbon can be accommodated at the sides of the growing plate, so that the plate tip always encounters fresh austenite. This is unlike the case for allotriomorphic ferrite, where the partitioned carbon builds up ahead of the interface and progressively slows down the rate of growth. Widmanstätten ferrite plates therefore lengthen at a constant rate.

The growth rates are found to be so large for typical weld compositions, that the formation of Widmanstätten ferrite is usually completed within a fraction of a second. Hence, for all practical purposes, the transformation can be regarded as being isothermal (Fig. 13.7a).

Unfortunately, the fraction of Widmanstätten ferrite that forms in weld deposits correlates badly with the plate lengthening rate, as illustrated in Fig. 13.7b. This is because there is an interference between the plates of Widmanstätten ferrite that grow from the austenite grain boundaries, and acicular ferrite plates which nucleate at non-metallic particles dispersed throughout the weld (Fig. 13.8). The formation of Widmanstätten ferrite and acicular ferrite is therefore competitive. Anything that increases the number density of inclusion nucleation sites relative to austenite grain nucleation sites, favours the formation of acicular ferrite at the expense of Widmanstätten ferrite. Hence, the refinement of austenite grain size, or a reduction in the oxide content of the weld below a limiting value, both lead to a decrease in the acicular ferrite content.

By the time the weld deposit cools to about 500°C, most of the austenite has been consumed. The small quantity of remaining austenite (about 5%) is enriched in carbon and either transforms to martensite, or into pearlite, which is degenerate because it does not have the opportunity to establish a lamellar structure. Slower cooling rates favour the formation of pearlite relative to martensite. Some austenite may also be retained to ambient temperature. Because of their small volume fractions in the overall microstructure, these phases are, in welding terminology, called 'microphases'. The microphases are relatively hard and behave in many respects like brittle inclusions. They are, therefore, of importance in determining the toughness of weld deposits.

### 13.2.5 Sensitivity to carbon

It is striking that small variations in carbon concentration can have a major influence on the microstructure of welds, especially since the average carbon concentration of a weld is usually kept very small. It is apparent from the previous discussions of the growth rates of allotriomorphic and Widmanstätten ferrite, that the sensitivity of growth kinetics to carbon becomes larger as the concentration of carbon decreases.

These are important observations given that the general trend in the steel industry is to reduce the carbon concentration, sometimes to levels approaching the maximum solubility of carbon in ferrite. The rate at which ferrite grows increases sharply as the carbon concentration of the steel approaches

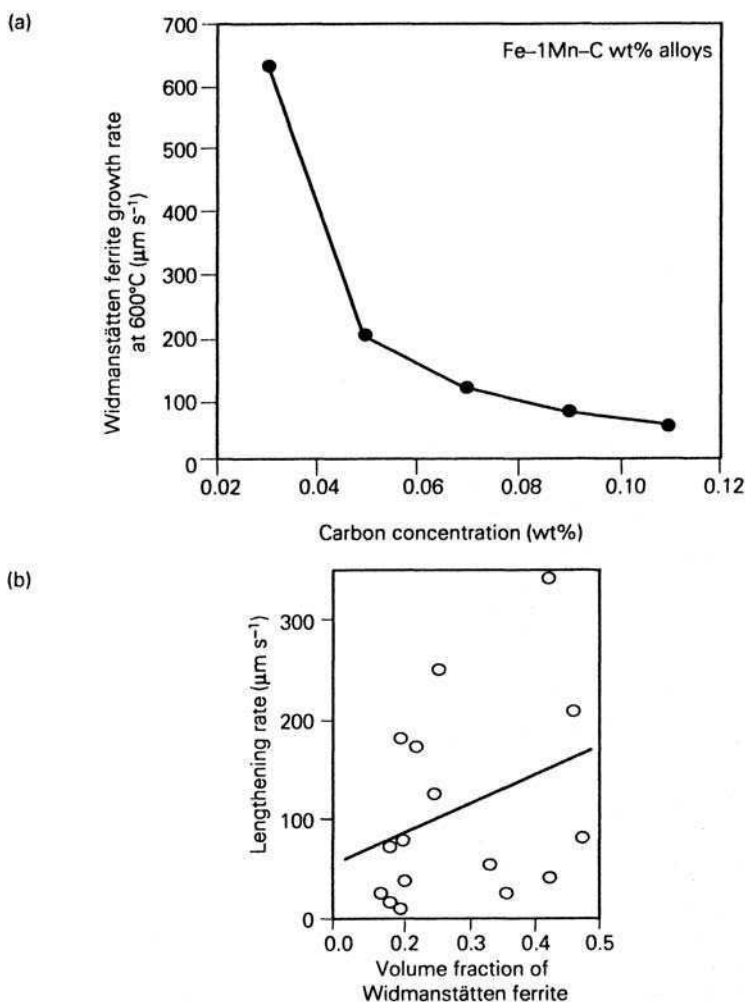


**Fig. 13.7** (a) The isothermal growth rate of Widmanstätten ferrite in a series of Fe-1Mn-C wt% alloys as a function of carbon concentration. Notice that the growth rates are so large, that the plates could grow right across typical austenite grains within a fraction of a second. (b) Poor correlation of the volume fraction of Widmanstätten ferrite against the calculated growth rate.

its solubility in ferrite. This is because there is no need for the carbon to diffuse ahead of the  $\gamma/\alpha$  interface, since it can all be accommodated in the ferrite.

Hence, the effect of carbon is seen to be larger (Figs 13.4 and 13.6a) when its concentration changes from 0.03  $\rightarrow$  0.05 wt%, when compared with the change from 0.09  $\rightarrow$  0.11 wt%. Changes in mechanical properties are found to reflect this behaviour, the strength of low-carbon steels being particularly sensitive to

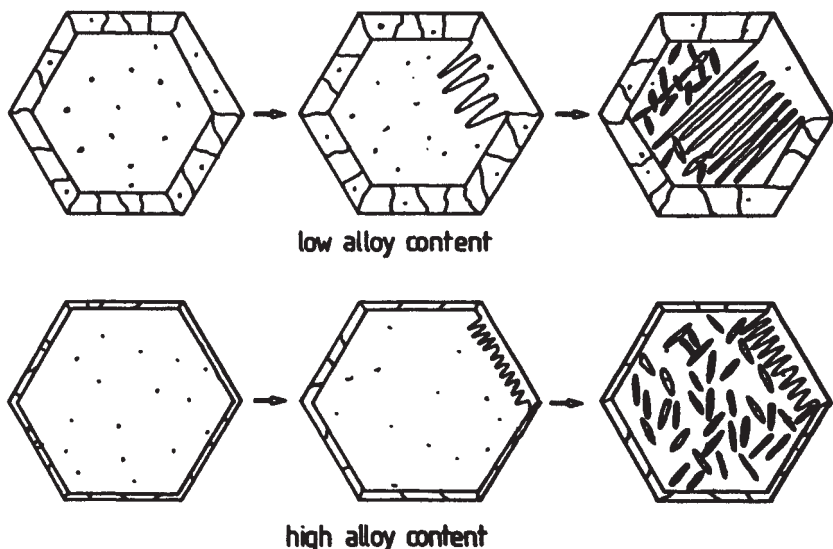


**Fig. 13.8** Diagrams illustrating the development of microstructure in two weld deposits with different chemical compositions. The hexagons represent cross-sections of columnar austenite grains whose boundaries first become decorated with uniform, polycrystalline layers of allotriomorphic ferrite, followed by the formation of Widmanstätten ferrite. Depending on the relative transformation rates of Widmanstätten ferrite and acicular ferrite, the former can grow entirely across the austenite grains or become stifled by the intragranularly nucleated plates of acicular ferrite.

the carbon concentration. This increased sensitivity of the  $\gamma/\alpha$  transformation to carbon at low concentrations, leads to a corresponding decreased sensitivity to substitutional alloying elements. Carbon in effect controls the kinetics of transformation.

In welding, the hardenability of the steel is often expressed as a carbon equivalent (CE). The concentration of each solute is scaled by a coefficient which expresses its ability, relative to carbon, to retard the  $\gamma/\alpha$  transformation. Steels with a CE in excess of about 0.4 wt% cannot easily be welded because of their increased tendency to form martensite. There are in fact two popular expressions for the CE, one due to the International Institute for Welding (IIW), and the other due to Ito and Besseyo, covering the high and low ranges of carbon, respectively:

$$\text{IIW} > 0.18 \text{ wt\% C,}$$

$$\text{CE} = \text{C} + \frac{\text{Mn} + \text{Si}}{6} + \frac{\text{Ni} + \text{Cu}}{15} + \frac{\text{Cr} + \text{Mo} + \text{V}}{5} \text{ wt\%,} \quad (13.2)$$

$$\text{Ito-Besseyo} < 0.18 \text{ wt\% C,}$$

$$CE = C + \frac{Si}{30} + \frac{Mn + Cu + Cr}{20} + \frac{Ni}{60} + \frac{Mo}{15} + \frac{V}{10} + 5B \text{ wt\%}. \quad (13.3)$$

The Ito–Besseyo CE formula has smaller coefficients for the substitutional solutes when compared with the IIW formula. It is believed to be more reliable for low-carbon steels. The IIW formula shows much smaller tolerance to substitutional alloying elements than the Ito–Besseyo equation. As already discussed, with low carbon concentrations the kinetics of transformation are more sensitive to carbon than to substitutional solutes. Hence, it is logical that there should be two different empirical expressions for the CE for the low- and high-carbon weldable steels. Figure 13.9 illustrates that, as expected, both the

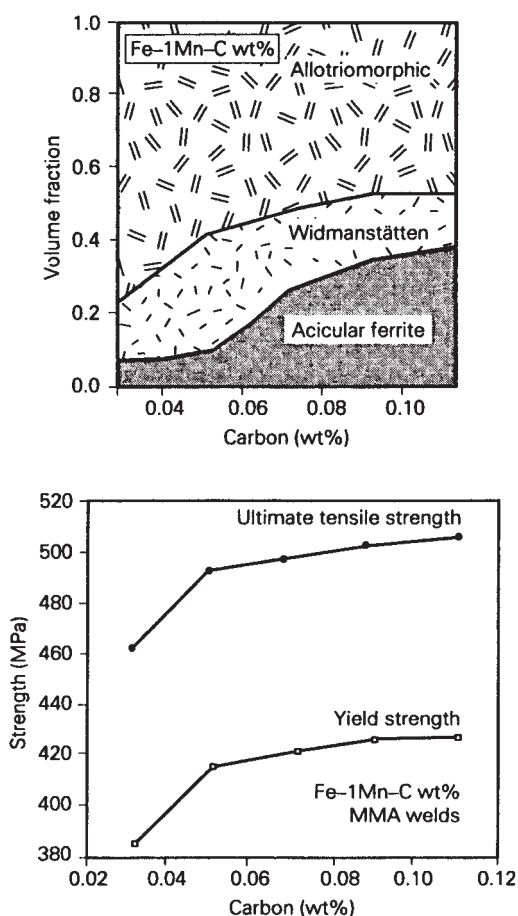


**Fig. 13.9** Variations in microstructure and mechanical properties as a function of carbon concentration in Fe–1Mn–C wt% steel weld deposit using manual metal arc welding (1 kJ/mm).

microstructure and mechanical properties change more rapidly at low carbon concentrations.

13.3 THE HAZ

The HAZ is the portion of the material which has not been melted, but whose microstructure and mechanical properties are altered by the heat of welding.

13.3.1 Heat flow

All welding processes involve a source of heat, the prime purpose of which is to cause melting. Subsequent solidification should lead to the formation of an integral joint. Much of the heat manages to diffuse from the fusion zone into the adjacent solid regions. As a consequence, those regions experience a heating and cooling cycle, the severity of which depends on the distance from the fusion boundary (Fig. 13.10). The peak temperature and the heating rate decrease with distance away from the fusion boundary. The cooling rate, on the other hand, is less sensitive to this distance, and can be stated as the time  $\Delta t_{8-5}$  taken to cool over the range 800–500°C. For many weldable steels, this defines the temperature range within which austenite decomposes by solid-state transformation.

The nature of the thermal cycle at any position within the HAZ can be characterized by two parameters, the peak temperature  $T_P$  and the time period  $\Delta t_{8-5}$ . Both of these parameters increase with the heat input  $q$ :

$$T_P \propto \frac{q}{r},$$

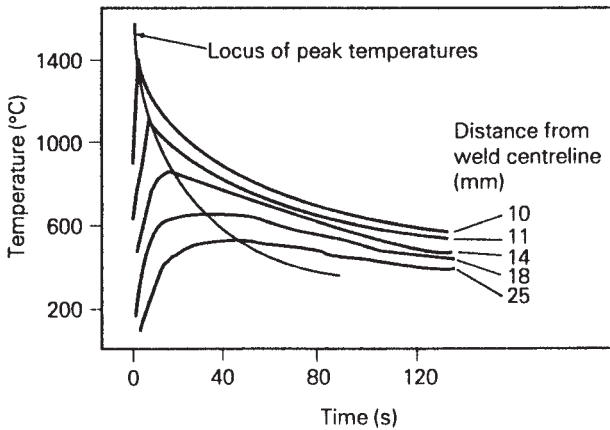


**Fig. 13.10** Temperature–time curves representing typical thermal cycles experienced in the HAZ of a weld (adapted from data published in the *Welding Handbook*, editor C. Weisman, Vol. I, American Society for Welding, Florida, USA, 1981).

$$\Delta t_{8-5} \propto q^n,$$

where  $r$  is the distance from the fusion boundary and  $n$  has a value (1 or 2) which depends on whether the component being welded is thick compared with the size of the weld bead. The relative thickness determines whether the flow of heat is two- or three-dimensional (Fig. 13.11). The heat input  $q$  is per unit length of weld, and typically is in the range about 1–5 kJ mm<sup>-1</sup>.

### 13.3.2 Microstructural zones

There is a well-defined gradient of microstructure in the HAZ, as a function of the distance from the fusion boundary (Fig. 13.12):

1. Those regions immediately adjacent to the fusion boundary are heated to very high temperatures and hence transform completely to austenite. During continuous heating, austenite begins to form at a temperature  $Ac_1 \simeq 800^\circ\text{C}$ , and the samples become fully austenitic at  $Ac_3 \simeq 950^\circ\text{C}$ . These temperatures are different from the corresponding equilibrium temperatures  $Ae_1$  and  $Ae_3$  because they increase with the heating rate. The peak temperatures in the HAZ close to the fusion boundary are well in excess of the  $Ac_3$  temperature of weldable steels. Consequently, the austenite that forms is annealed during heating beyond  $Ac_3$ , giving rise to a very coarse grain structure. This forms the *coarse-grained austenite zone*.
2. The austenite grain size decreases sharply with distance from the fusion boundary. It is necessary to distinguish this as the *fine-grained zone* because its mechanical properties tend to be superior to those of the coarse zone.
3. As the peak temperature decreases, regions of the HAZ further away from the fusion boundary become only partially austenitic during the heating part of the thermal cycle. The austenite that forms has a rather high carbon concentration, due to the increase in the solubility of carbon in  $\gamma$  with decreasing temperature. The part that does not transform into austenite becomes tempered.

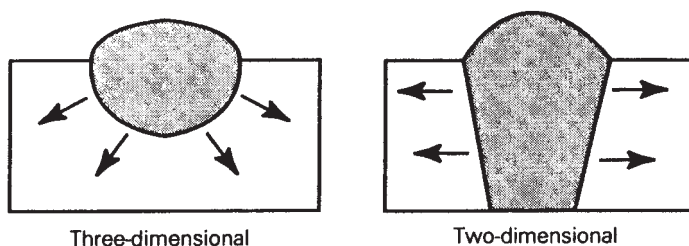
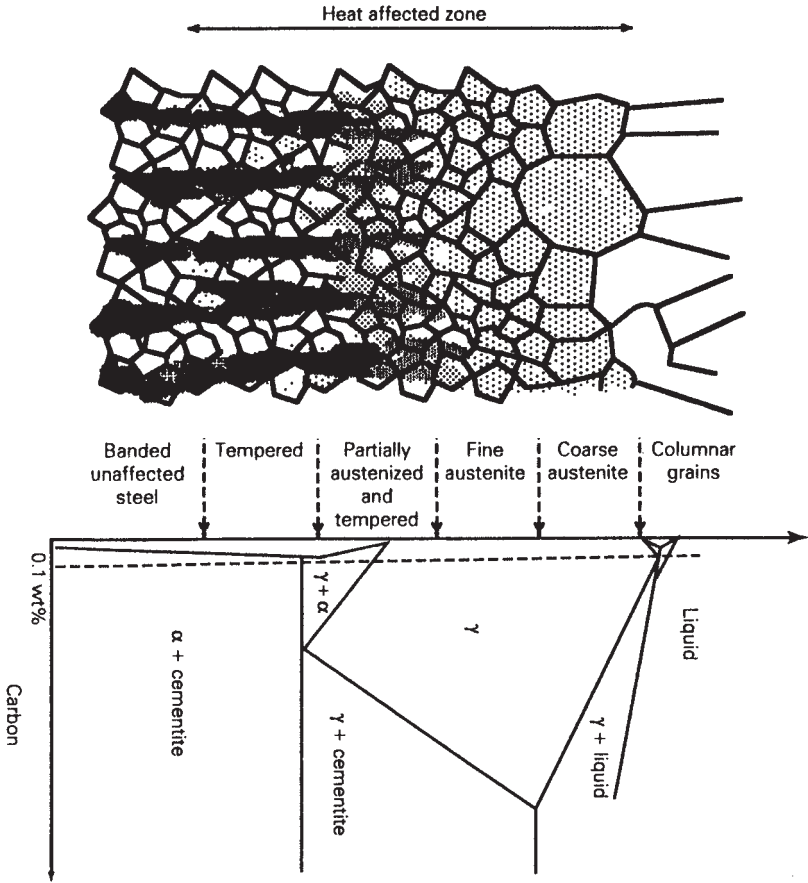


Fig. 13.11 Schematic illustration of two- and three-dimensional heat-flow conditions.





**Fig. 13.12** Schematic illustration of the microstructural variation to be expected in the HAZ of steel welds.

4. When the peak temperature becomes less than the  $A_{c1}$  temperature, the only effect of the heat input is to temper the microstructure, the extent of tempering decreasing with distance from the fusion boundary.

The individual microstructures are illustrated in Fig. 13.13, and discussed in detail in the sections that follow (Table 13.2).

### 13.3.3 The coarse-grained austenite

The formation of austenite during heating is in many ways different from transformations which occur during cooling below the equilibrium temperature. As discussed in Chapter 6, the formation of ferrite follows a C-shaped curve kinetic

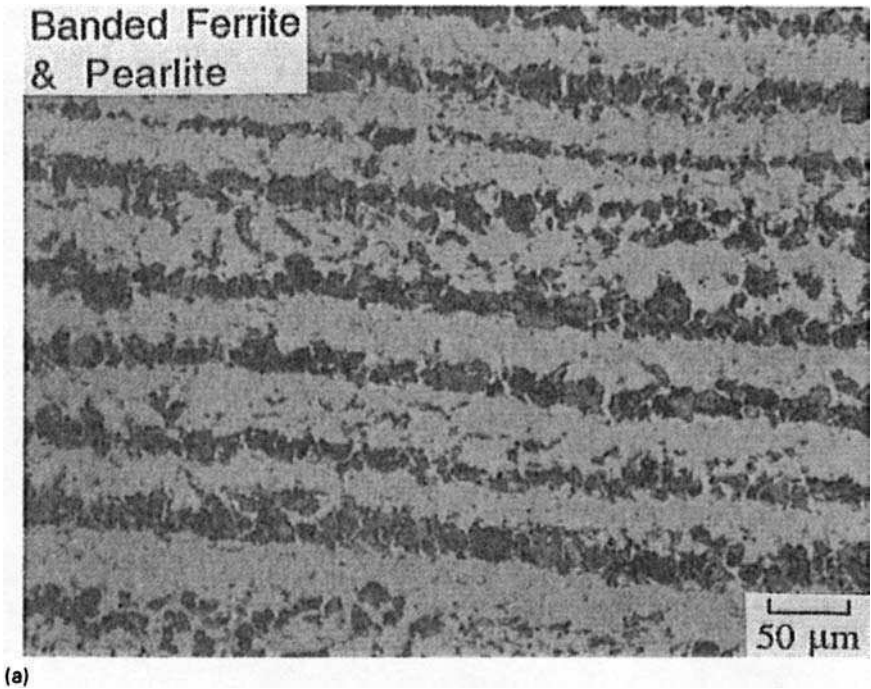


**Fig. 13.13** The gradient of microstructure in the HAZ of a mild steel plate (courtesy of C. Davis). (a) The plate microstructure far away from the weld, completely unaffected by welding. The bands of ferrite/pearlite are typical of many structural steels which are chemically inhomogeneous.

behaviour on a time–temperature–transformation (*TTT*) diagram; the overall transformation rate, therefore, goes through a maximum as a function of the supercooling below the equilibrium temperature. This is because of two opposing effects; the diffusion coefficient decreases as the temperature falls, but the driving force for transformation increases.

During heating, however, both the diffusion coefficient and the driving force increase with temperature. The overall rate of transformation, therefore, increases continuously as the transformation temperature is raised, Fig. 13.14.

For practical purposes, the formation of austenite during heating can be represented by a continuous heating transformation (CHT) diagram, analogous in concept to the continuous cooling transformation (CCT) diagrams so useful in illustrating the formation of ferrite (Fig. 13.15a). The CHT diagram is displaced to longer times when compared with the isothermal transformation diagram for austenite formation. For typical heating rates encountered in the region adjacent to the fusion boundary, the formation of austenite should be completed when the temperature has exceeded the  $A_{c3}$  temperature by about  $100^{\circ}\text{C}$ . Since the peak temperature in this zone is much higher than  $A_{c3}$ , the

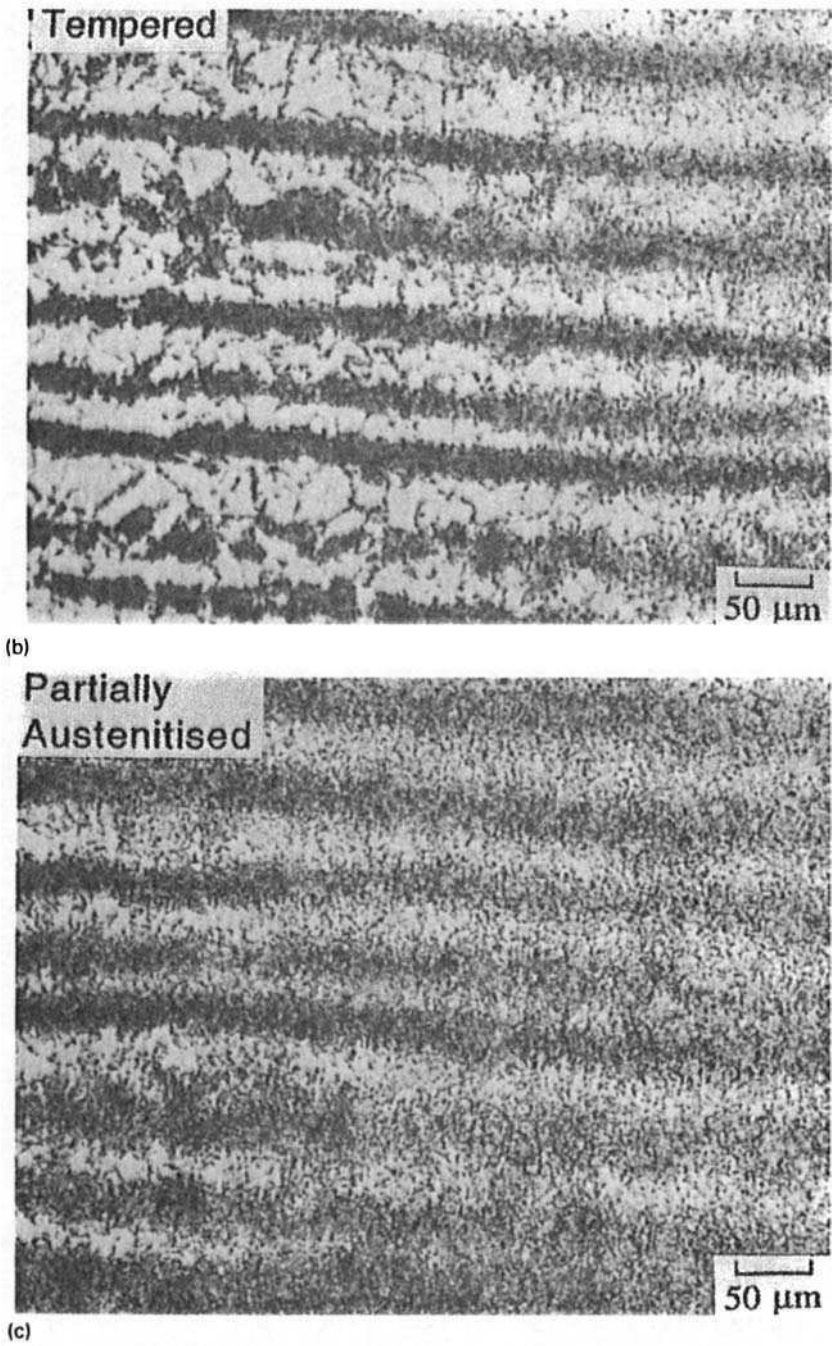
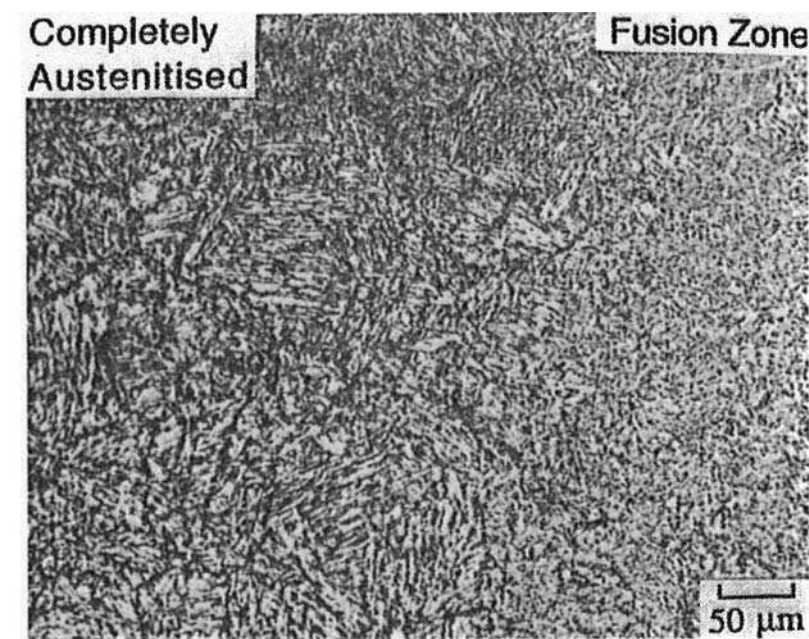
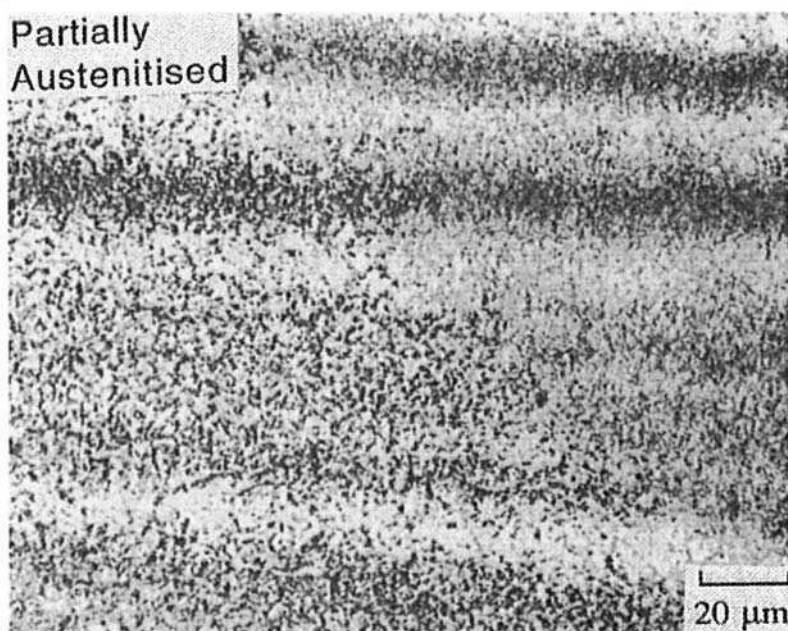


**Fig. 13.13** (Continued). (b) The tempered region. (c) The partially reaustenitized region.



(d)



(e)

**Fig. 13.13** (Continued). (d) The fully austenitized region. (e) High magnification image of the partially austenitized region.

**Table 13.2** Characteristic temperature ranges for the variety of microstructural regions within the HAZ of steel welds

HAZ microstructure	Temperature range
Coarse-grained austenite	$1500^{\circ}\text{C} > T_P > 1200^{\circ}\text{C}$
Fine-grained austenite	$1200^{\circ}\text{C} > T_P > A_{c3}$
Partially austenitized zone	$A_{c3} > T_P > A_{c1}$
Tempered regions	$A_{c1} > T_P$

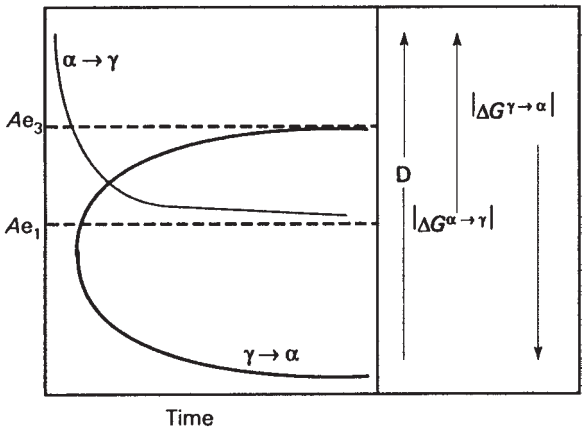


**Fig. 13.14** A comparison of the TTT curves for the  $\gamma \rightarrow \alpha$  transformation, and for the reverse  $\alpha \rightarrow \gamma$  transformation.  $\Delta G$  represents the driving force for transformation and  $D$  is the diffusion coefficient.

austenite grains coarsen rapidly as  $T_P$  is approached. In steels which are microalloyed, it may necessary for the grain boundary pinning particles (e.g. niobium carbonitrides) to dissolve before substantial grain coarsening occurs. In any case, once the coarsening begins, it proceeds very rapidly because the effect of temperature increases exponentially during heating. The austenite grain growth can be expressed conveniently in the form of grain growth diagrams (Fig. 13.15b) which contain contours of equal grain size as a function of the peak temperature and  $\Delta t_{8-5}$ .

The importance of the coarse-grained austenite zone is in the mechanical properties which develop as the austenite transforms during the cooling part of the thermal cycle. The coarse grain structure leads to an increase in hardenability, because it becomes easier to avoid intermediate transformation products, so that untempered martensite or other hard phases can form during cooling. The welding process introduces atomic hydrogen into the weld metal, which is able to diffuse rapidly into the HAZ. Hard microstructures are particularly susceptible to embrittlement by hydrogen, the fracture occurring shortly after the weld

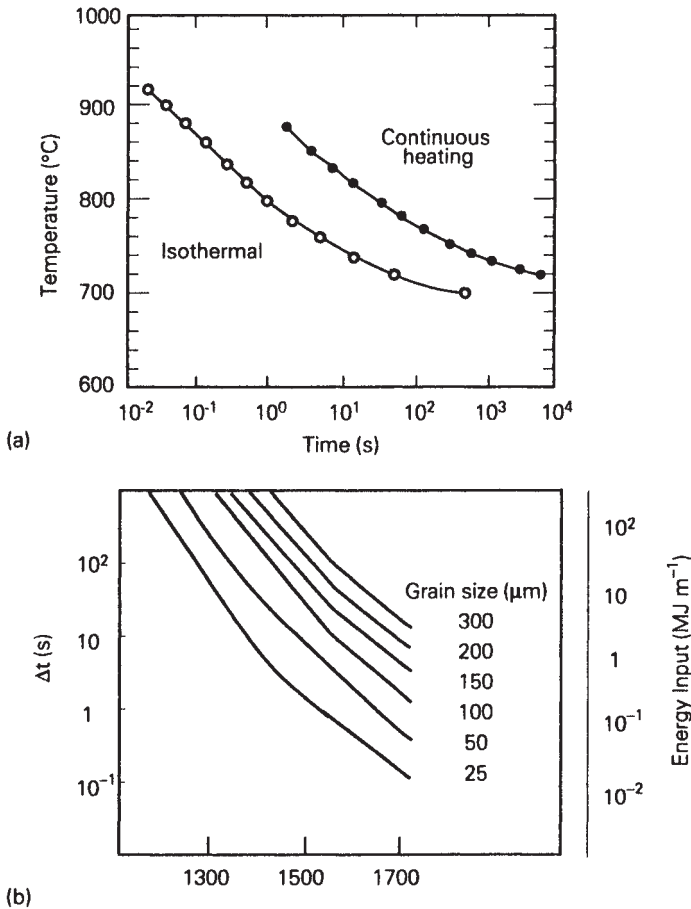


**Fig. 13.15** (a) The TTT and CHT diagrams for the beginning of austenite growth in a Fe–0.15C–0.5Si–1.5Mn wt% alloy (courtesy of Suzuki). (b) Schematic austenite grain growth diagram for a microalloyed steel welded using a preheat of 200°C (after Ashby and Easterling, 1982).

has cooled to room temperature. This hydrogen-induced phenomenon is called ‘cold-cracking’. This is why the CE of the steel has to be kept low enough to prevent the hardness in the coarse-grained region from becoming unacceptably large.

### 13.3.4 Fine-grained austenite zone

This region is typified by austenite grains some 20–40  $\mu\text{m}$  in size. The grain structure and hardenability are, therefore, not very different from those associated with control-rolling operations during the manufacture of the steel. The fine

austenite grains thus transform into more desirable ferritic phases, with lower hardness values and higher toughness.

### 13.3.5 Partially austenitic regions and local brittle zones

At a sufficiently large distance from the fusion boundary, the peak temperature is such that the steel cannot transform completely to austenite. The small amount of austenite that does form has a larger carbon concentration. This is because the solubility of carbon in austenite, which is in equilibrium with ferrite, increases as the temperature decreases. The subsequent transformation behaviour of this enriched austenite is then quite different, since it has a higher hardenability.

If the cooling rate is sufficiently large, then the carbon-enriched austenite transforms partially into hard martensite, the remaining austenite being retained to ambient temperature. These minute regions of hard martensite are known as 'local brittle zones'. They are located in much softer surroundings consisting of tempered ferrite. Consequently, they do not cause a general reduction in toughness, but lead to an increase in the scatter associated with toughness tests. This is because the test specimen only sometimes samples the local brittle zone, in which case the recorded toughness will be poor. On other occasions, the measured toughness can be very high, presumably because the test region does not include a local brittle zone. Such scatter in mechanical property data is not only disconcerting, but also makes design difficult because of the existence of a few very low values.

When the cooling rate in this region is not high enough to induce martensitic transformation, the carbon-enriched austenite can decompose into a mixture of coarse cementite and ferrite. The cementite particles again constitute local brittle zones and increase the variability in mechanical properties.

### FURTHER READING

- Cerjak, H. and Easterling, K. E. (eds), *Mathematical Modelling of Weld Phenomena*, Institute of Materials, London, 1993.
- Easterling, K. E., *Introduction to the Physical Metallurgy of Welding*, 2nd edition, Butterworth-Heinemann, London, 1992.
- Grong, Ø., *Metallurgical Modelling of Welding*, 2nd edition, Institute of Materials, London, 1997.
- Kou, S., *Welding Metallurgy*, 2nd edition, John Wiley & Sons, New Jersey, USA, 2002.
- Lancaster, J. F., *Metallurgy of Welding*, 6th edition, Abington Publishing, London, 1999.
- Svensson, L.-E., *Control of Microstructure and Properties in Steel Arc Welds*, CRC Press, London, 1994.

# 14

## MODELLING OF MICROSTRUCTURE AND PROPERTIES

### 14.1 INTRODUCTION

Steels are useful materials because of their sophistication and low cost. The many phase transformations and processing variables associated with them can be exploited to achieve a very large range of desirable properties. For example, there are reliable commercial alloys available for the whole range of strength from 250 up to 5500 MN m<sup>-2</sup>. The very complexity which makes steels so useful also makes their design difficult. This chapter illustrates how the design process can be enhanced using models, which can be of many different kinds. Blind procedures, such as regression analysis, are one type which deal with the recognition of patterns in experimental data. Models based on firm physical principles have predictive capabilities. A practically useful model is always one which is a compromise between these two extremes.

The general method for constructing a model is summarized in the flow chart presented in Fig. 14.1. The first stage consists of an identification of the problem and a consideration of the likely physical mechanisms involved. A model should be constructed using the most advanced theory available and after making a thorough assessment of the published literature. This usually identifies areas where adequate knowledge does not exist, in which case approximations must be made in order to progress. The lack of theory or data can be investigated further as resources become available, but need not unduly hinder the formulation of a model. In practice, this means that the target precision has to be chosen to suit the state of the subject.

It is important to understand that modelling is not simply an application of a computer program, but rather the combination of a deep understanding of physical principles and quantitative scientific method.

These issues are illustrated by two examples concerning steels, one an elementary microstructure model, and the other dealing with the mechanical properties of mixed microstructures.



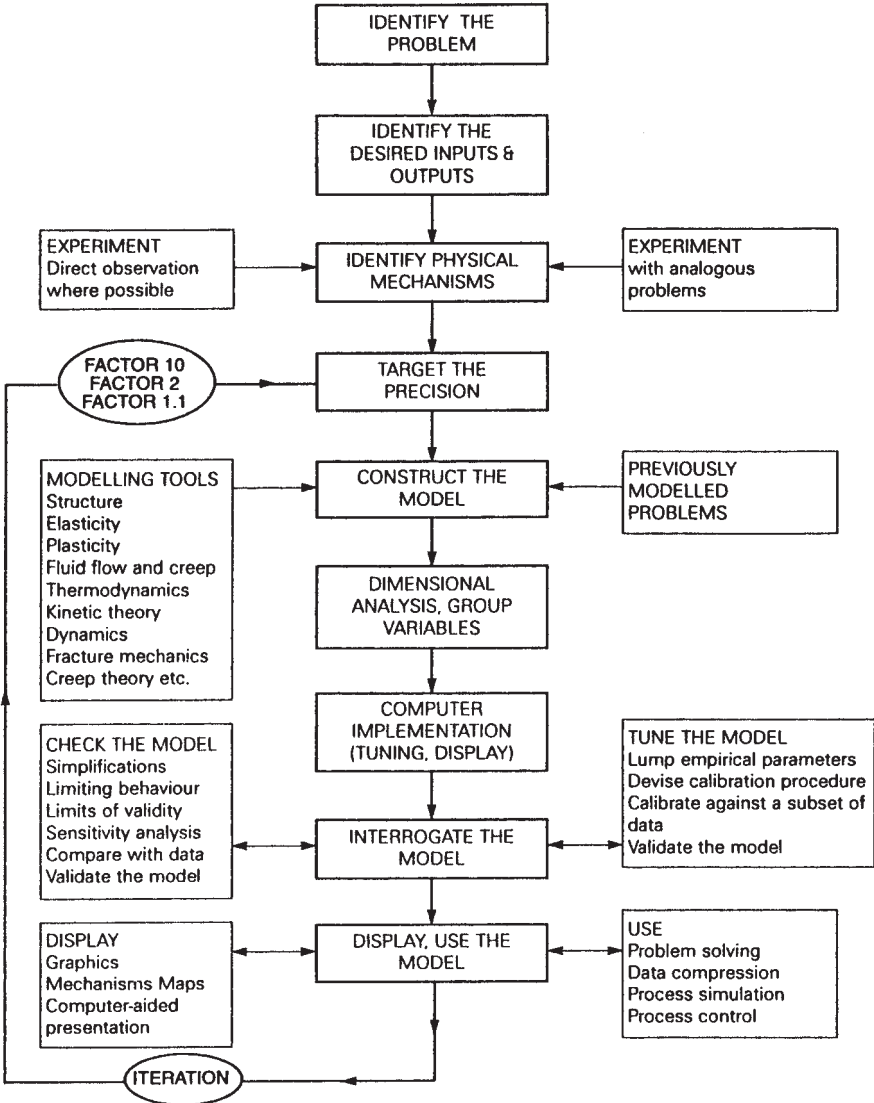


**Fig. 14.1** Flow chart illustrating the stages in the construction of a physical model. At each stage, an iteration back to the earlier stages may be required (after Ashby, *Materials Science and Technology* **8**, 102–112, 1992).

The first example illustrates how phase transformation theory can be used in the optimization of a microstructure consisting of a mixture of bainite and austenite. The problem is first identified to be associated with the occurrence of large regions of carbon-enriched austenite which are detrimental to toughness.

The mechanism of transformation is then utilized to reduce the fraction of this detrimental phase. The major component of this model is the physical metallurgy of the transformation. The model is quantitative, in the sense that it requires the calculation of a phase boundary for a multi-component steel.

The second example helps to understand what is at first sight a strange result, that the strength of a mixed microstructure of martensite and bainite peaks as a function of the volume fraction of martensite. It also illustrates how a variety of approximations can be made in order to formulate a model, both by searching the published literature for relationships and data, and by adopting a pragmatic approach.

## 14.2 EXAMPLE 1: ALLOY DESIGN – HIGH-STRENGTH BAINITIC STEEL

High-strength bainitic steels have not in practice been as successful as quenched and tempered martensitic steels, because the coarse cementite particles in bainite are detrimental for toughness (Chapter 6). However, it is now known that the precipitation of cementite during bainitic transformation can be suppressed. This is done by alloying the steel with about 1.5 wt% of silicon, which has a very low solubility in cementite and greatly retards its growth.

An interesting microstructure results when this silicon-alloyed steel is transformed into upper bainite. The carbon that is rejected into the residual austenite, instead of precipitating as cementite, remains in the austenite and stabilizes it down to ambient temperature. The resulting microstructure consists of fine plates of bainitic ferrite separated by carbon-enriched regions of austenite (Fig. 14.2).

The potential advantages of the mixed microstructure of bainitic ferrite and austenite can be listed as follows:

1. Cementite is responsible for initiating fracture in high-strength steels. Its absence is expected to make the microstructure more resistant to cleavage failure and void formation.
2. The bainitic ferrite is almost free of carbon, which is known to embrittle ferritic microstructures.
3. The microstructure derives its strength from the ultrafine grain size of the ferrite plates, which are less than  $1\ \mu\text{m}$  in thickness. It is the thickness of these plates which determines the mean free slip distance, so that the effective grain size is less than a micrometer. This cannot be achieved by any other commercially viable process. It should be borne in mind that grain refinement is the only method available for simultaneously improving the strength and toughness of steels.
4. The ductile films of austenite which are intimately dispersed between the plates of ferrite have a crack blunting effect. They further add to toughness by increasing the work of fracture as the austenite is induced to transform

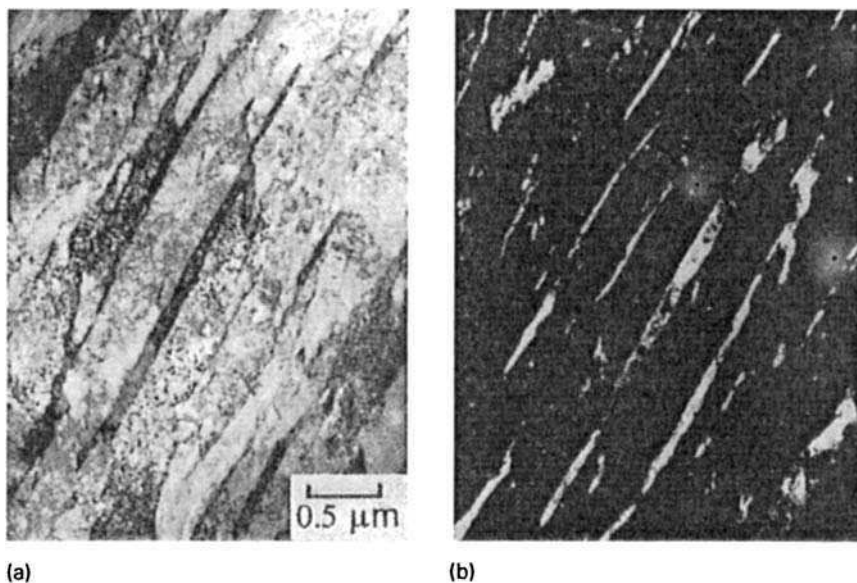


**Fig. 14.2** Transmission electron micrograph of a mixture of bainitic ferrite and stable austenite. (a) Bright field image. (b) Retained austenite dark field image.

to martensite under the influence of the stress field of a propagating crack. This is the TRIP, or transformation-induced plasticity effect (Chapter 12).

5. The diffusion of hydrogen in austenite is slower than in ferrite. The presence of austenite can, therefore, improve the stress corrosion resistance of the microstructure.
6. Steels with the bainitic ferrite and austenite microstructure can be obtained without the use of any expensive alloying additions. All that is required is that the silicon concentration should be large enough to suppress cementite.

In spite of these appealing features, the bainitic ferrite/austenite microstructure does not always give the expected good combination of strength and toughness. This is because the relatively large 'blocky' regions of austenite between the sheaves of bainite (Fig. 14.3) readily transform into high-carbon martensite under the influence of stress. This untempered, hard martensite embrittles the steel.

The blocks of austenite are clearly detrimental to toughness, and anything that can be done to reduce their fraction, or increase their stability to martensitic transformation, would be beneficial. Both of these effects are controlled by the  $T'_0$  curve of the phase diagram (Chapters 5 and 6). This curve determines the composition of the austenite at the point where the reaction to bainite stops. By displacing the curve to larger carbon concentrations, both the fraction of bainite that can form, and the carbon concentration of the residual austenite can be

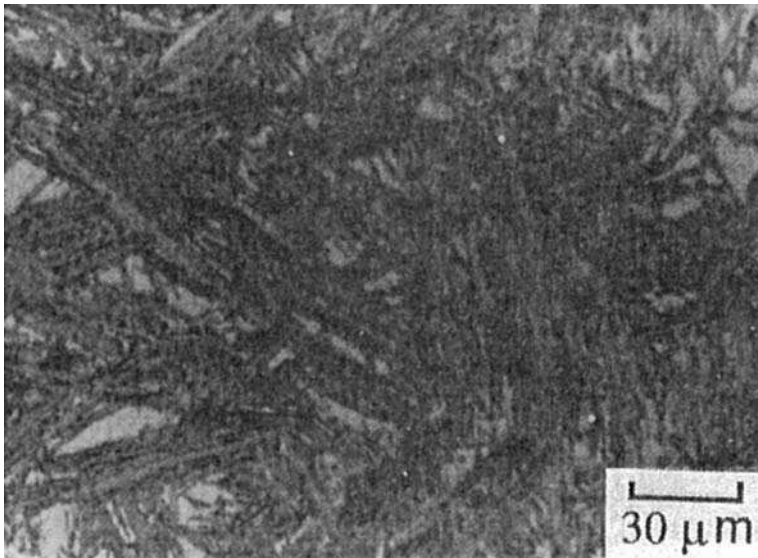


**Fig. 14.3** Optical micrograph of upper bainite in an Fe-0.43C-3Mn-2.02Si wt% showing the blocks of retained austenite between sheaves of bainite.

increased. Modifications to the  $T'_0$  curve can be achieved by altering the alloy composition. It is therefore necessary to calculate the effect of substitutional solutes on the  $T'_0$  curve.

#### 14.2.1 Calculation of the $T'_0$ curve

At the  $T'_0$  temperature, the free energies of austenite and ferrite of the same chemical composition are identical (Chapter 6). A calculation of the  $T'_0$  temperature for binary alloys was discussed in Chapter 5. A simplified method is presented here for multi-component steels. At the  $T'_0$  temperature point, the change in free energy as austenite transforms to ferrite is zero:

$$\Delta G^{\gamma\alpha} = 0. \quad (14.1)$$

Zener argued that the free energy difference can be factorized into two components, the magnetic ( $\Delta G_M^{\gamma\alpha}$ ) and non-magnetic ( $\Delta G_{NM}^{\gamma\alpha}$ ) terms:

$$\Delta G^{\gamma\alpha} = \Delta G_M^{\gamma\alpha} + \Delta G_{NM}^{\gamma\alpha}. \quad (14.2)$$

The non-magnetic component varies approximately linearly with temperature (Fig. 14.4) but the magnetic component varies non-linearly, becoming nearly zero at low temperatures. However, over a restricted temperature range (in which bainite usually forms), both functions can be represented approximately as in Table 14.1.

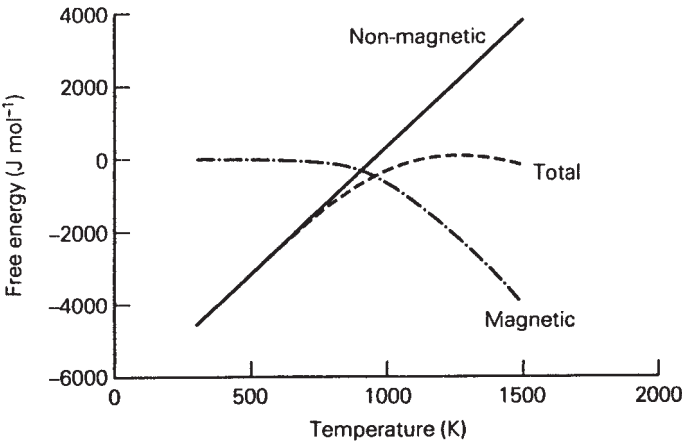


**Fig. 14.4** Zener’s factorization of the free energy difference between the austenite and ferrite phases into magnetic and non-magnetic components.

**Table 14.1** Approximate representations of the free energy components for the  $\gamma \rightarrow \alpha$  transformation in pure iron

Function	<i>a</i>	<i>b</i>	Temperature range
$\Delta G_{NM}^{\gamma\alpha} = a + bT \text{ J mol}^{-1}$	−6660	7	$900 > T > 300 \text{ K}$
$\Delta G_{NM}^{\gamma\alpha} = a + bT \text{ J mol}^{-1}$	650	−1	$900 > T > 620 \text{ K}$
$\Delta G_M^{\gamma\alpha} = a + bT \text{ J mol}^{-1}$	0	0	$T < 620 \text{ K}$

The Zener factorization of the free energy into magnetic and non-magnetic components helps to account for the effects of alloying elements, via a modification of the temperature at which the free energy is evaluated:

$$\Delta G^{\gamma\alpha}\{T\} = \Delta G_M^{\gamma\alpha}\{T - x\Delta T_M\} + \Delta G_{NM}^{\gamma\alpha}\{T - x\Delta T_{NM}\}. \tag{14.3}$$

$\Delta T_M$  and  $\Delta T_{NM}$  are temperature changes due to a unit concentration ( $x$ ) of substitutional solute (Table 14.2). The  $T_0$  temperature is therefore calculated by setting  $\Delta G^{\gamma\alpha}$  to zero:

$$\Delta G_M^{\gamma\alpha}\{T_0 - x\Delta T_M\} + \Delta G_{NM}^{\gamma\alpha}\{T_0 - x\Delta T_{NM}\} = 0. \tag{14.4}$$

On substituting the expressions listed in Table 14.1, this becomes:

$$a_{NM} + b_{NM}T_0^{Fe} + a_M + b_M T_0^{Fe} = 0 \text{ for pure iron,}$$

and

$$a_{NM} + b_{NM}(T_0^{FeX} - x\Delta T_{NM}) + a_M + b_M(T_0^{FeX} - x\Delta T_M) = 0 \text{ for an iron alloy.}$$

It follows that the change in the  $T_0$  temperature caused by the addition of a substitutional element is given by the difference between these two equations:

$$\Delta T_0 = \frac{x(b_{NM}\Delta T_{NM} + b_M\Delta T_M)}{b_{NM} + b_M}. \quad (14.5)$$

The effect of several alloying elements can be approximated by assuming additivity:

$$\Delta T_0 = \frac{\sum_i x_i(b_{NM}\Delta T_{NM_i} + b_M\Delta T_{M_i})}{b_{NM} + b_M}. \quad (14.6)$$

To calculate the shift in the  $T'_0$  temperature, we simply set  $\Delta G^\gamma$  to the value of the stored energy (say  $400 \text{ J mol}^{-1}$  for bainite) instead of to zero. The actual  $T'_0$  curve for an alloy, rather than just the shift  $\Delta T'_0$  relative to pure iron, can be estimated by noting for an Fe–C alloy, allowing for  $400 \text{ J mol}^{-1}$  of stored energy:

$$T'_0(K) \simeq 970 - 80x_c, \quad (14.7)$$

where  $x_c$  is the at % of carbon.

We can now proceed to apply this methodology to the design of a tough bainitic ferrite/austenite microstructure.

### 14.2.2 The improvement in toughness

An apparently ideal microstructure consisting of bainitic ferrite and ductile austenite in a Fe–3Mn–2.02Si–0.43C wt% exhibits poor toughness because of the presence of blocky unstable austenite (Fig. 14.5a). It is necessary to increase the amount of bainitic ferrite in the microstructure and to increase the stability of the austenite. Both of these aims can be achieved by changing the substitutional solute concentration such that the  $T'_0$  curve is shifted to higher carbon concentrations (i.e.  $T'_0$  is raised at any given carbon concentration).

Using Equation (14.6), we see that for the Fe–3Mn–2.02Si–0.43C wt% (2.97 Mn, 3.87Si at%) alloy:

$$\Delta T_0 = \frac{\overbrace{2.97[7 \times (-39.5) + (-1) \times (-37.5)]}^{\text{Mn}}}{7 - 1} + \frac{\overbrace{3.87[7 \times (0) + (-1) \times (-3)]}^{\text{Si}}}{7 - 1} = 116,$$

the first term on the right-hand side being the effect of manganese and the second the effect of silicon. Hence, for this alloy Equation (14.7) can be modified to give:

$$T'_0(K) \simeq 970 - 80x_c - 116. \quad (14.8)$$

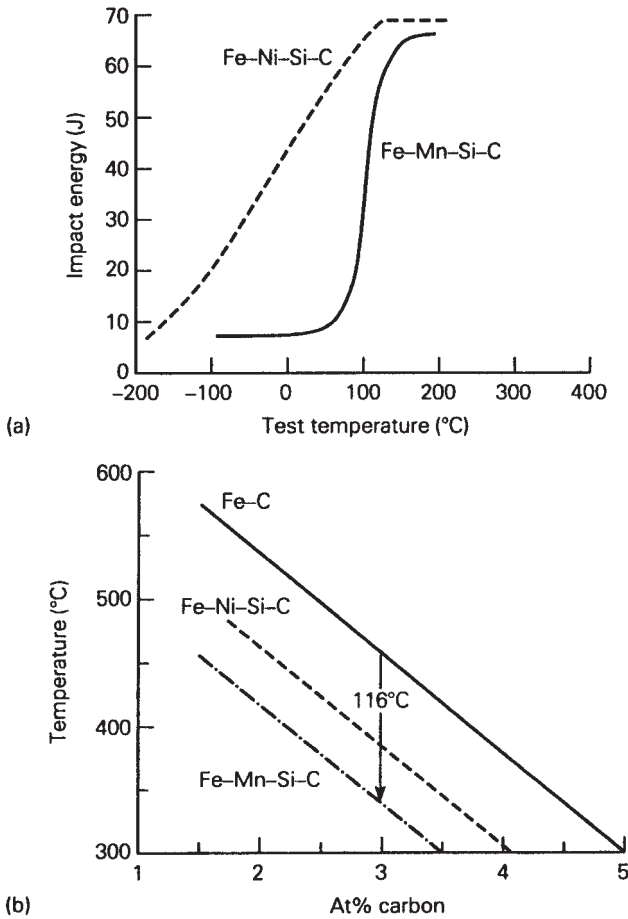


**Fig. 14.5** (a) Experimentally determined impact transition curves showing how the toughness improves as the amount of blocky austenite is reduced. (b) Calculated  $T'_0$  curves for the Fe-C, Fe-Mn-Si-C and Fe-Ni-Si-C steels.

Manganese is seen to have a large effect in depressing the  $T'_0$  temperature. An examination of Table 14.2 shows that one possibility is to replace all of the manganese with nickel. Thus, for a Fe-4Ni-2Si-0.4C wt % (3.69Ni, 3.85Si at %) alloy, a similar calculation shows that  $\Delta T_0 \simeq 72$  so that:

$$T'_0(\text{K}) \simeq 970 - 80x_c - 72. \quad (14.9)$$

The remarkable improvement in toughness achieved by doing this, without any sacrifice of strength, is illustrated in Fig. 14.5, along with the  $T'_0$  curves as calculated above.

**Table 14.2** Values of  $\Delta T_M$  and  $\Delta T_{NM}$  for a variety of substitutional solutes (Aaronson *et al.*, *Transitions of the Metallurgical Society of AIME* **236**, 753–780, 1966)

Alloying element	$\Delta T_M/\text{K}$ per at %	$\Delta T_{NM}/\text{K}$ per at %
Si	−3	0
Mn	−37.5	−39.5
Ni	−6	−18
Mo	−26	−17
Cr	−19	−18
V	−44	−32
Co	19.5	16
Al	8	15
Cu	4.5	−11.5

14.2.3 The precision of the model

The model discussed above has helped in achieving the desired goal of improved toughness, even though the method used is in fact crude. The  $T'_0$  curves are not really linear functions of carbon, and the interactions of carbon with the substitutional solutes are not accounted for. Rigorous methods are available and could be used when considering a higher degree of optimization of steel chemistry. The model also does not incorporate kinetics. This could be a major disadvantage because in commercial practice, microstructures are usually generated using complex non-isothermal heat treatments.

Referring to Fig. 14.1, it is obvious that the exploitation of these concepts would require several iterations to improve precision, and to adapt the model for complex industrial processing. These examples illustrate the essentials of the modelling technique. Models can be constructed in stages, with significant advances being made at each stage, even though the ultimate problem may not be solved completely. These successes at each stage of the model can be used to justify further development until a point of diminishing returns is reached.

14.3 EXAMPLE 2: MECHANICAL PROPERTIES OF MIXED MICROSTRUCTURES

A peculiar feature of mixed microstructures of bainite and tempered martensite, is that the strength is found to go through a peak as the volume fraction of martensite decreases (Fig. 14.6). This is against intuition in that martensite is usually considered to be the strongest microstructure in steels, in which case the strength should decrease continuously as the fraction of martensite is reduced. However, quantitative modelling, by helping to reveal the mechanisms involved, can explain this anomalous behaviour.



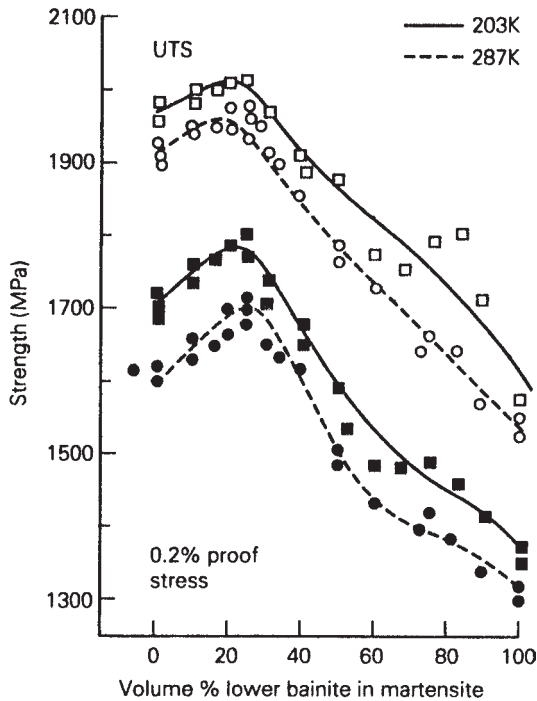


**Fig. 14.6** Strength of bainite and tempered martensite as a function of the volume fraction of bainite (Tomita and Okabayashi, *Metallurgical Transactions A* **14A**, 485, 1983).

#### 14.3.1 Calculation of the strength of individual phases

It is reasonable to assume that the strength of martensite and bainite can be factorized into a number of intrinsic components:

$$\sigma = \sigma_{Fe} + \sum_i x_i \sigma_{SSi} + \sigma_C + K_L (\bar{L})^{-1} + K_D \rho_D^{0.5}, \quad (14.10)$$

where  $x_i$  is the concentration of a substitutional solute which is represented here by a subscript  $i$ . The other terms in this equation can be listed as follows:

$K_L$  = coefficient for strengthening due to lath size,  $115 \text{ MN m}^{-1}$

$K_D$  = coefficient for strengthening due to dislocations,  $7.34 \times 10^{-6} \text{ MN m}^{-1}$

$\sigma_{Fe}$  = strength of pure, annealed iron,  $219 \text{ MN m}^{-2}$  at 300 K

$\sigma_{SSi}$  = substitutional solute ( $i$ ) strengthening

$\sigma_c$  = solid solution strengthening due to carbon

$\rho_D$  = dislocation density, typically  $10^{16} \text{ m}^{-2}$

$\bar{L}$  = measure of the ferrite plate size, typically  $0.2 \mu\text{m}$ .

The individual strengthening contributions are discussed below.

**Table 14.3** Strength ( $\text{MN m}^{-2}$ ) of pure iron as a function of temperature and solid solution strengthening terms for ferrite, for one wt% of solute. The data are for a strain rate of  $0.0025 \text{ s}^{-1}$

	200°C	100°C	Room temperature (23°C)	-40°C	-60°C
Fe	215	215	219	355	534
Si	78	95	105	70	-44
Mn	37	41	45	8	-57
Ni	19	23	37	-2	-41
Mo	-	-	18	-	-
Cr	7.8	5.9	5.8	7.4	15.5
V	-	-	4.5	-	-
Co	1.0	1.8	4.9	9.1	5.8

### 14.3.2 Iron and substitutional solutes

Pure body-centred cubic iron in a fully annealed condition makes an intrinsic contribution  $\sigma_{\text{Fe}}$  to the overall strength. Substitutional solutes do not partition during the displacive growth of either martensite or bainite, so that their concentrations are fixed by the composition of steel as a whole. Solid solution strengthening contributions,  $\sigma_{\text{SSi}}$  can be estimated as a function of temperature and strain rate from published data. Table 14.3 shows that whereas the strength of pure iron increases as the temperature is reduced, strengthening due to substitutional solutes often goes through a maximum as a function of temperature. Indeed, there is some solution softening at low temperatures because the presence of a foreign atom locally assists a dislocation to overcome the Peierls barrier at low temperatures.

### 14.3.3 Carbon

Bainitic ferrite has only a small amount of carbon dissolved in interstitial solution, assumed to be less than 0.02 wt%. Martensite, on the other hand, can have concentrations well in excess of  $\bar{x}$  (the average concentration of the alloy), since the prior formation of bainite enriches the residual austenite according to the following relationship derived from a balance of mass. The total carbon concentration in the alloy ( $\bar{x}$ ) is the sum of the concentrations in the austenite ( $x_\gamma$ ) and bainitic ferrite ( $x_b$ ):

$$\bar{x} = x_\gamma V_\gamma + x_b V_b, \tag{14.11}$$

where  $V_\gamma$  and  $V_b$  are the volume fractions of austenite and bainitic ferrite, respectively. It follows that:

$$x_\gamma = \frac{\bar{x} - V_b x_b}{1 - V_b}, \tag{14.12}$$

$x_\gamma$  is the concentration in the residual austenite before it transforms into martensite, so that its value is important in determining the hardness of the martensite. Solid-solution theory indicates that the strength increment due to dissolved carbon should vary with the square root of the carbon concentration:

$$\sigma_{SSC} = 1722.5 \times x^{1/2}, \quad (14.13)$$

where strength is in  $\text{MN m}^{-2}$  and the concentration  $x$  is expressed in wt%.

#### 14.3.4 Dislocations

When martensite or bainite form at high temperatures, the shape change due to shear transformation causes plastic deformation, and hence the accumulation of dislocations in both the parent and product phases (Chapter 6). The extent of the plasticity depends on the yield strength, and hence on the temperature. Takahashi and Bhadeshia have therefore suggested that the dislocation density ( $\rho_D$ ) of both martensite and bainite can be represented empirically as a function of temperature alone, for the temperature range 570–920 K:

$$\log_{10}\{\rho_D\} = 9.2840 + \frac{6880.73}{T} - \frac{1780360}{T^2}, \quad (14.14)$$

where  $T$  is the transformation temperature in Kelvin, and  $\rho_D$  is stated in units of  $\text{m}^{-2}$ . The strengthening  $\sigma_\rho$  ( $\text{MN m}^{-2}$ ) due to dislocations is given by:

$$\sigma_\rho = 0.38 \mu b (\rho_D)^{0.5} \simeq 7.34 \times 10^{-6} (\rho_D)^{0.5}, \quad (14.15)$$

where  $\mu$  is the shear modulus and  $b$  is the magnitude of the Burgers vector.

#### 14.3.5 Lath size

Martensite and bainite grow in the form of very fine plates or laths. The resulting grain size strengthening  $\sigma_G$  is defined as:

$$\sigma_G \simeq 115(\bar{L})^{-1} \text{ MN m}^{-2}, \quad (14.16)$$

where  $\bar{L}$  ( $\mu\text{m}$ ) is the mean linear intercept measured on random sections. This is not the classical Hall–Petch relation (Chapter 2) but another relation due to Langford and Cohen, because at the typically sub-micrometre grain sizes, the mechanism of yield is different, involving the initiation of dislocation sources in the grain boundaries.

#### 14.3.6 Martensite composition and transformation temperature

The excess carbon in the bainitic ferrite partitions into the residual austenite, which then transforms to martensite. The carbon concentration of the martensite

can therefore be calculated from a simple mass balance (Equation (14.11)). The martensite-start temperature (Chapter 4,  $M_S$ ) of the residual austenite can be written:

$$M_S = M_S^0 - 564(x_\gamma - \bar{x}), \quad (14.17)$$

where the concentrations are in wt%, the temperatures in centigrade and  $M_S^0$  is the martensite-start temperature of austenite with the average composition of the alloy.

The different contributions to the strength of martensite are illustrated in Fig. 14.7. Carbon is a major contributor since it causes a severe, asymmetrical distortion of the martensite crystal structure and hence interacts strongly with the movement of dislocations. The dislocation density itself makes a significant contribution to the overall strength.

#### 14.3.7 Strength of mixed microstructures

The normal way to calculate the strength of a multiphase alloy is to use a rule of mixtures, i.e. to calculate a mean strength from the strength of each component phase weighted by its volume fraction. However, this is not adequate for the present purposes because of constraint effects. It is well established in fracture mechanics that the yield strength is increased by plastic constraint. This is why a weak brazing alloy can be used to effectively bond much stronger samples, as long as the thickness of the braze material is small enough to be constrained throughout by the surrounding stronger matrix. Indeed, the strength of the joint increases as the thickness of the braze layer decreases.

Dispersions of bainite plates form in austenite which subsequently transforms to much stronger martensite. Young, therefore, assumed that deformation

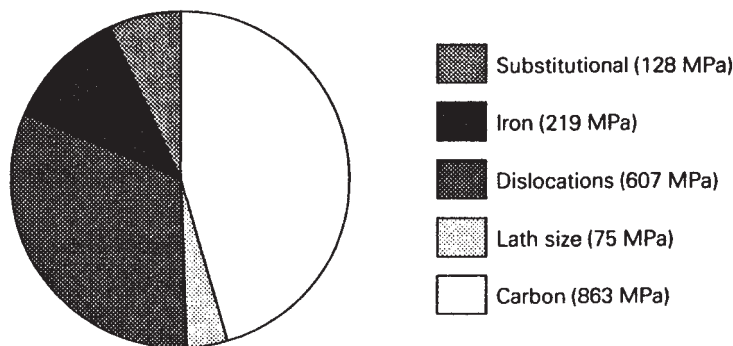


**Fig. 14.7** Calculated components of the room-temperature strength of virgin martensite in Fe-0.4C-0.2Si-0.71Mn-1.9Ni-0.25Mo-0.88Cr wt% alloy. This is a typical ultra-high-strength steel of the type used in the manufacture of gears, gun barrels, etc.

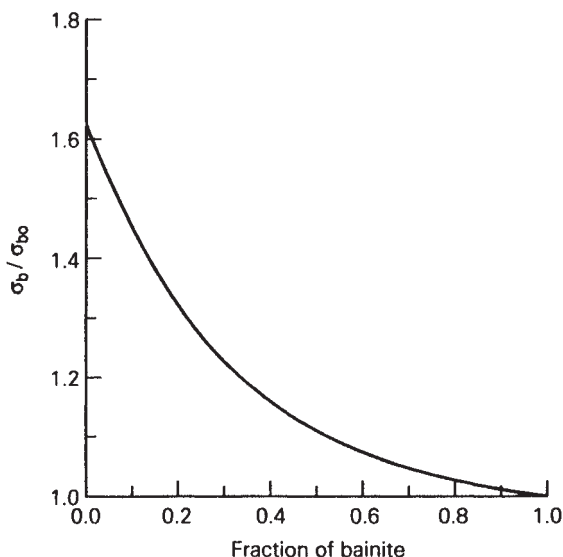


**Fig. 14.8** Plot of the normalized strength of a brazed joint versus the normalized thickness of the brazing material, the latter being identified with the fraction of bainite in a martensitic matrix (Young and Bhadeshia, *Materials Science and Technology* **10**, 209, 1994).

of the bainitic ferrite is constrained by the harder martensite in the same way as the braze material is constrained by the surrounding matrix. The constraint can, therefore, be modelled using experimental data available from brazed joints in high-strength steels. The brazing alloys used in making the joints were non-ferrous materials which are ordinarily rather weak. The data, in a normalized form, are summarized in Fig. 14.8. The vertical axis is the joint strength normalized with respect to that of the unconstrained braze material; the horizontal axis is the braze thickness normalized relative to a thickness value where the restraint effect vanishes.

To analyse the properties of a mixed microstructure, it can be assumed that the normalized braze thickness is equivalent to the volume fraction of bainite. Using this assumption, and the form of the normalized strength versus normalized thickness plot (Fig. 14.8), the strength of constrained bainite may be represented by the equation:

$$\sigma \simeq \sigma_0[0.65 \exp\{-3.3V_b\} + 0.98] \leq \sigma_M, \quad (14.18)$$

where  $\sigma$  and  $\sigma_0$  represent the strengths of constrained and unconstrained bainite, respectively,  $\sigma_M$  is the strength of the martensite and  $V_b$  is the volume fraction of the bainite. The strength of bainite is always less than or equal to that of martensite.

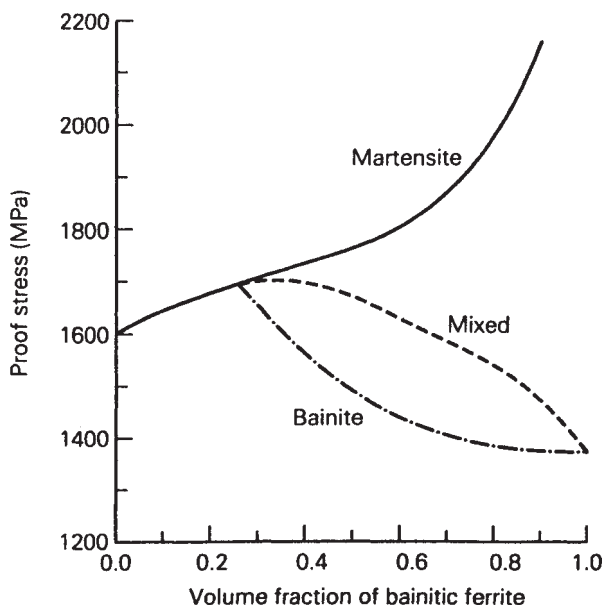


**Fig. 14.9** The strength contributions of bainite and martensite in the mixed microstructure.

When the volume fraction  $V_b$  of bainite is small, its strength nearly matches that of martensite (Fig. 14.9), always remaining above that of bainite on its own. The strength of martensite continues to increase with the fraction of bainite, as the carbon concentration of the residual austenite from which it grows, increases.

Figure 14.10 shows how the strength of the mixed microstructure is predicted. Line (a) on Fig. 14.10 shows that a rule of mixtures cannot account properly for the variations observed. The agreement between calculation and experiment improves (curve b) as allowance is made for the change in the strength of martensite as carbon partitions into the austenite, due to the formation of bainite. The consistency between experiment and theory becomes excellent as constraint effects are also included in the calculations (curve c).

## 14.4 METHODS

The two examples described in the preceding sections are necessarily simplified presentations of quite complex models. It is useful to illustrate some of methods that are now common in the mathematical modelling of steels. It is worth emphasizing that in general it is a combination of methods that leads to useful solutions, with the optimum approach to a problem being one that is interdisciplinary.

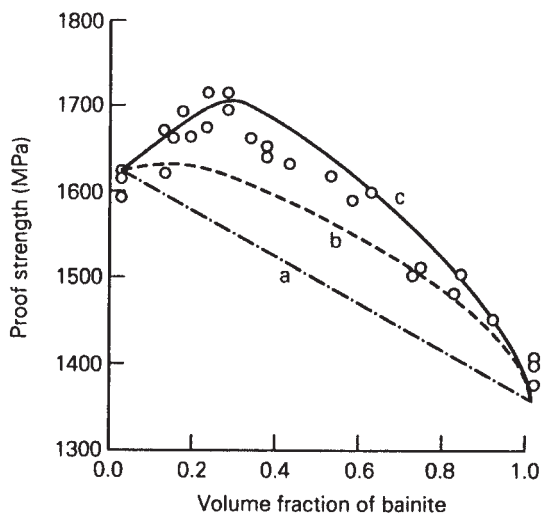


**Fig. 14.10** Comparison of calculations against experimental data due to Tomita and Okabayashi.

#### 14.4.1 Electron theory

A metal is created when atoms are brought so close together, that the electrostatic repulsion in transferring a valency electron between the adjacent atoms is offset by the gain due to the delocalization of electrons. This enables the valency electrons to move within the metal. The delocalized electrons feel a weak electrostatic field from the positively charged cores of atoms because of repulsion by the core electrons. The valence electrons are also screened from each other by positive holes which surround them. All this makes it possible to introduce approximations which allow a single-electron wave function to be exploited in calculating the energy of an electron gas in a metal.

These electrons are able to move, without being scattered by the partly screened potential of the positive ion cores because the latter provide a *periodic* potential whose effect is simply to modulate the free-electron wave function. Difficulties only arise when the electrons satisfy the Bragg condition within the metal. This introduces *band gaps* in the distribution of electron energies. The metallic state can only exist if the valency bands are partly filled.

Using these concepts, the energy of the electron gas can be expressed in terms of the potential due to the ion cores, Coulomb interactions, kinetic energy and exchange and correlation effects. It is then possible to calculate with an input of the electronic charge and the atomic number of the element, properties such as the cohesive energy of crystals, the elastic moduli, magnetic and acoustic properties. The calculations are limited to small numbers of atoms because they are extremely computer intensive. Figure 14.11 shows some calculations of the

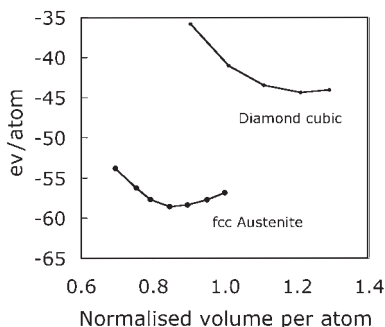


**Fig. 14.11** The cohesive energy at 0 K versus the volume per atom divided by the volume of an iron atom, for two crystal structures of iron. Data from Paxton, A. T., Methfessel, M. and Polatoglou, H. M., *Physical Review B* **41**, 8127, 1990.

cohesive energy of two allotropic forms of iron, austenite (face-centred cubic (fcc)) and diamond cubic. In each case the cohesive energy goes through a minimum, which gives the expected density of the allotrope. The calculation of the diamond form of iron shows how it is possible, using electron theory, to estimate the properties of phases which do not exist in reality. Such a form would have a density of only  $5 \text{ g cm}^{-3}$ , but unfortunately, the energy difference relative to the stable forms of iron is simply too large, meaning that it would be improbable for the fcc  $\rightarrow$  diamond transition to be induced, e.g. by alloying.

#### 14.4.2 Phase diagram calculations and thermodynamics

Given experimentally determined thermodynamic data, it is possible to estimate in multi-component, multiphase alloys, the stable phases, their equilibrium fractions and equilibrium chemical compositions as a function of temperature, pressure, magnetic fields and the detailed composition of the alloy. In other words, all the information plotted on phase diagrams.

The free energy of a phase  $\alpha$  is simply the weighted mean of the free energies of its component atoms ( $\mu_i$ ) which for a binary solution containing components  $A$  and  $B$  is:

$$G^\alpha = (1 - x)\mu_A^\alpha + x\mu_B^\alpha,$$

where  $x$  is the mole fraction of  $B$ .  $\mu_i^\alpha$  is also known as the *chemical potential* of component  $i$  in phase  $\alpha$ . Although this equation is expressed for a binary solution, it is generally true that equilibrium between any number of phases in contact, containing any number of components, is defined by:

$$\mu_i^\alpha = \mu_i^\beta = \dots \quad \text{for } i = 1, 2, 3, \dots \quad \text{and phase } = \alpha, \beta, \dots$$

The chemical potential must be uniform everywhere at equilibrium.



There are many thermodynamic methods which express the chemical potential as a function of the mixing of solutes in a phase. Most of these methods are either too simple or so complex that they cannot easily be generalized. Therefore, in the computer calculations, the deviation of the free energy of mixing from that of an ideal solution,<sup>1</sup> i.e. the excess Gibbs free energy, is written as an empirical polynomial equation:

$$\Delta_e G_{AB} = x_A x_B \sum_i L_{AB,i} (x_A - x_B)^i,$$

where  $L_i$  are measured interaction coefficients, in this case for a binary solution. For a ternary solution:

$$\begin{aligned} \Delta_e G_{ABC} = & x_A x_B \sum_i L_{AB,i} (x_A - x_B)^i, \\ & + x_B x_C \sum_i L_{BC,i} (x_B - x_C)^i, \\ & + x_C x_A \sum_i L_{CA,i} (x_C - x_A)^i. \end{aligned}$$

The advantage of this kind of a polynomial becomes clear, since the relation reduces to the binary problem when one of the components is set to be identical to another, e.g.  $B \equiv C$ . The method can be extended to deal with any number of components, with the great advantage that few coefficients have to be changed when the data due to one component are improved. It is therefore adopted in many of the phase diagram calculation programs available commercially.

Although thermodynamics is usually associated with the state of equilibrium, the calculation method can also be used to estimate constrained equilibria, e.g. para-equilibrium (Chapter 3) and diffusionless transformation (Chapter 5). Figure 14.12 illustrates calculated isothermal Fe–Cr–C phase diagrams for both the equilibrium and para-equilibrium states – notice the dramatic change when substitutional solutes are not allowed to partition between the phases.

There is another subtle application of thermodynamics in the design of steels, dealing with steady-state processes in which the system is not at equilibrium but an appropriate observer may not perceive change. An example is diffusion across a constant gradient; neither the flux nor the concentration at any point changes with time, and yet the free energy of the system is decreasing since diffusion occurs to minimize free energy. The rate at which energy is dissipated is the product of the temperature and the rate of entropy production (i.e.  $T\sigma$ ):

$$T\sigma = JX,$$

<sup>1</sup> An ideal solution is one in which the atoms mix at random at all temperatures.

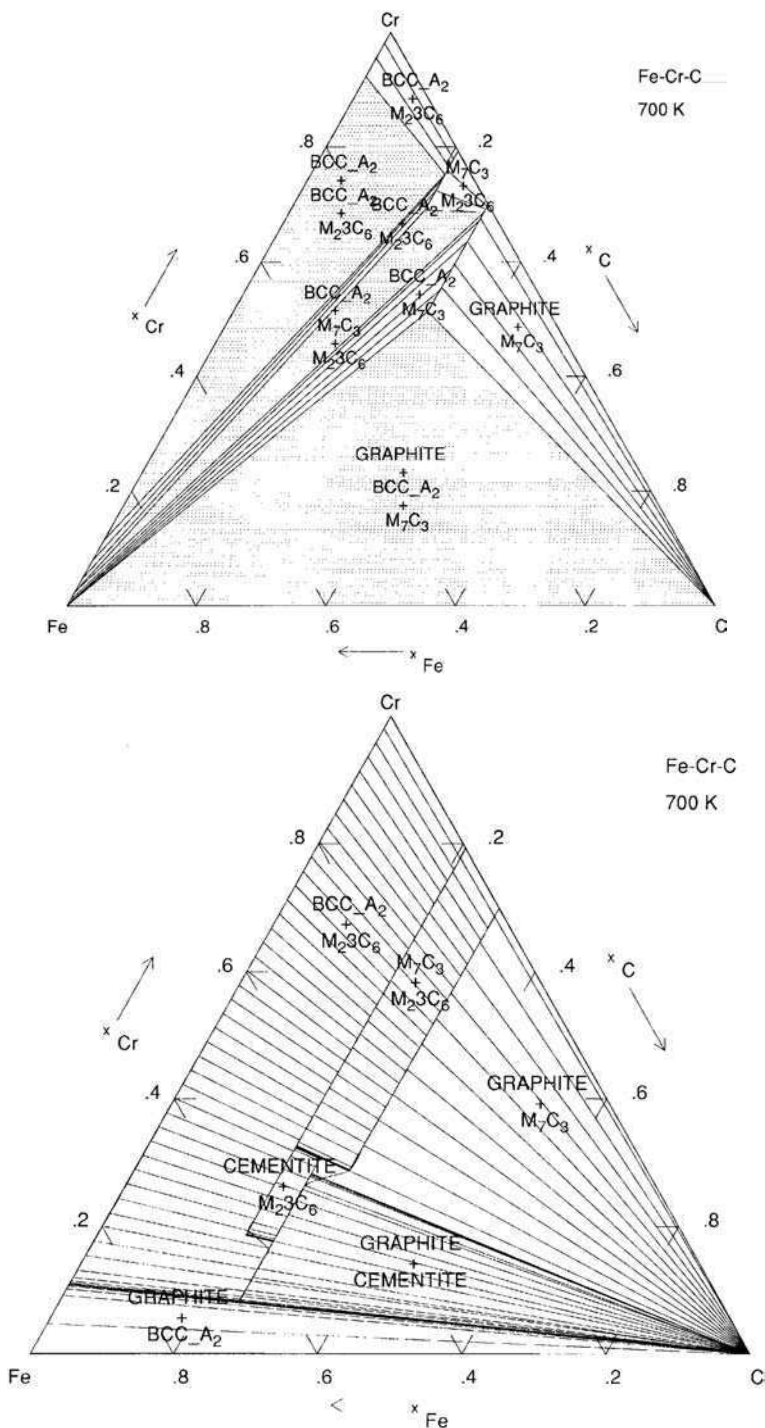


**Fig. 14.12** Isothermal section of the Fe–Cr–C system. The body-centred cubic phase is ferrite and M stands for a mixture of iron and chromium atoms in a variety of carbide phases (courtesy of J. Robson).

where  $J$  is a generalized flux of some kind, and  $X$  a generalized force. In the case of an electrical current, the heat dissipation is the product of the current ( $J$ ) and the electromotive force ( $X$ ). Provided that flux-force sets can be expressed as in this way, it is found that  $J \propto X$  for small deviations from equilibrium. In the case of the electrical current, this leads to Ohm's law where the current is proportional to the electromotive force.

This concept can be applied to the case where a number of irreversible processes occur simultaneously. In a ternary Fe–Mn–C alloy, the diffusion flux of carbon depends not only on the gradient of carbon, but also on that of manganese. Thus, a uniform distribution of carbon will tend to become inhomogeneous in the presence of a manganese concentration gradient. When there is more than one dissipative process, the total energy dissipation rate is the sum of all the dissipations:

$$T\sigma = \sum_i J_i X_i,$$

with

$$J_i = M_{ij} X_j \quad \text{with} \quad i, j = 1, 2, 3 \dots$$

and it is the cross coefficients  $M_{ij} \ i \neq j$  that drive the diffusion of carbon in a gradient of manganese. The theory is widely applied in computer calculations of the kinetics of phase transformations in steels.

## 14.5 KINETICS

Almost all the solid-state transformations in steels involve nucleation and growth. The theories for these two processes are well established and have been described in previous chapters. The evolution of the volume fraction requires the additional treatment of *impingement* between particles which nucleate at different locations. This can be done using the powerful extended volume concept of Kolmogorov, Johnson, Mehl and Avrami.

Consider the two particles illustrated in Fig. 14.13 for time  $t$ ; a small interval  $\delta t$  later, new regions marked  $a, b, c$  and  $d$  are formed assuming that they are able to grow unhindered whether or not the region into which they grow is already transformed. However, only those components of  $a, b, c$  and  $d$  which lie in previously untransformed matrix can contribute to a change in the real volume of the product phase ( $\alpha$ ):

$$dV^\alpha = \left(1 - \frac{V^\alpha}{V}\right) dV_e^\alpha,$$

where it is assumed that the microstructure develops at random. The subscript  $e$  refers to extended volume,  $V^\alpha$  is the volume of  $\alpha$  and  $V$  is the total volume. Multiplying the change in extended volume by the probability of finding

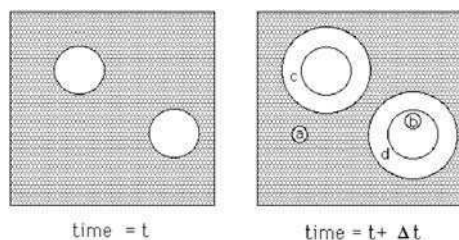


**Fig. 14.13** The concept of extended volume. Two precipitate particles have nucleated together and grown to a finite size in the time  $t$ . New regions  $c$  and  $d$  are formed as the original particles grow, but  $a$  and  $b$  are new particles, of which  $b$  has formed in a region which is already transformed.

untransformed regions has the effect of excluding regions such as  $b$ , which clearly cannot contribute to the real change in volume of the product. For a random distribution of precipitated particles, integration gives the real volume fraction:

$$\frac{V^\alpha}{V} = 1 - \exp \left\{ -\frac{V_e^\alpha}{V} \right\}.$$

The extended volume  $V_e^\alpha$  is straightforward to calculate using nucleation and growth models and neglecting any impingement effects. Solutions typically take the form:

$$\xi = 1 - \exp\{-k_A t^n\},$$

which can be compared with, e.g. Equation (3.9) for the progress of the pearlite reaction.

The idea can be extended to the case where more than one reaction occurs at the same time, as is frequently the case with precipitation reactions during the tempering of martensite. Suppose  $\alpha$  and  $\beta$  precipitate simultaneously, then the relation between extended and real space becomes a coupled set of two equations:

$$dV^\alpha = \left(1 - \frac{V^\alpha + V^\beta}{V}\right) dV_e^\alpha \quad \text{and} \quad dV^\beta = \left(1 - \frac{V^\alpha + V^\beta}{V}\right) dV_e^\beta, \quad (14.1)$$

which in general must be solved numerically.

There has in recent years been much prominence given to the phase field method as an alternative technique for calculating the evolution of microstructure. This begins with the description of the entire microstructure in terms of an *order parameter*. The precipitate and matrix each have a particular value of the order parameter and the interface between these is located by the position where the order parameter changes from its precipitate-value to its matrix-value. The range over which it changes is the *width* of the interface. The set of values of the order parameter over the whole microstructure is the *phase field*.

The free energy per atom is then written for the whole of the (heterogeneous) phase field as a single functional and the evolution of microstructure with time is assumed to be proportional to the variation of this functional with respect to the order parameter.

The method has been extremely successful in dealing with spinodal reactions and in the modelling of solidification, but its utility with respect to solid-state reactions of the kind important in steels has yet to be demonstrated. The definition of the width of the interface and associated coefficients, and handling nucleation are two difficulties which require fitting to experimental data. On the other hand, effects such as the overlap of diffusion fields are natural outcomes.

### 14.5.1 Finite difference method

The finite difference is a discrete analogue of a derivative. Consider one-dimensional diffusion in a concentration gradient along a coordinate  $z$  (Fig. 14.14). The concentration profile is divided into slices, each of thickness  $h$ . The matter entering a unit area of the face at  $a$  in a time increment  $\tau$  is given approximately by  $J_a = -D\tau(C_1 - C_0)/h$ . That leaving the face at  $b$  is  $J_b = -D\tau(C_2 - C_1)/h$ . If  $C'_1$  is the new concentration in slice 1, then the net gain in solute is  $(C'_1 - C_1)h$  so that:

$$C'_1 - C_1 = \frac{D\tau}{h^2}(C_0 - 2C_1 + C_2). \quad (14.2)$$

This allows the concentration at a point to be calculated as a function of that at the two neighbouring points. By successively applying this relation at each slice, and advancing the time  $\tau$ , the entire concentration profile can be estimated as a function of time.

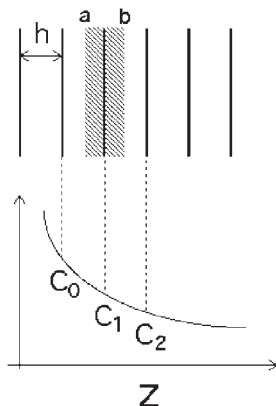


**Fig. 14.14** Finite difference representation of diffusion.

The approximation is that the concentration gradient within each slice has been assumed to be constant. This approximation will be better for smaller values of  $h$ , but at the expense of computation time. The accuracy can be assessed by changing  $h$  and seeing whether it makes a significant difference to the calculated profile.

## 14.6 FINITE ELEMENT METHOD

In this, continuous functions are replaced by piecewise approximations. The consequence of applying force to a body represented as a set of springs is illustrated here, assuming that the force  $F$  in each spring varies linearly with the displacement  $\delta$ , with the constant of proportionality labelled the stiffness  $k$ . The body is at rest at equilibrium, so for the case illustrated in Fig. 14.15a,  $F_1 = -F_2$  so that:

$$\begin{bmatrix} F_1 \\ F_2 \end{bmatrix} = \begin{pmatrix} k & -k \\ -k & k \end{pmatrix} \begin{bmatrix} \delta_1 \\ \delta_2 \end{bmatrix},$$

The forces at the nodes of the springs illustrated in Fig. 14.15b are therefore

$$\begin{bmatrix} F_1 \\ F_2 \\ 0 \end{bmatrix} = \begin{pmatrix} k_1 & -k_1 & 0 \\ -k_1 & k_1 & 0 \\ 0 & 0 & 0 \end{pmatrix} \begin{bmatrix} \delta_1 \\ \delta_2 \\ \delta_3 \end{bmatrix} \quad \begin{bmatrix} 0 \\ F_2 \\ F_3 \end{bmatrix} = \begin{pmatrix} 0 & 0 & 0 \\ 0 & k_2 & -k_2 \\ 0 & -k_2 & k_2 \end{pmatrix} \begin{bmatrix} \delta_1 \\ \delta_2 \\ \delta_3 \end{bmatrix},$$

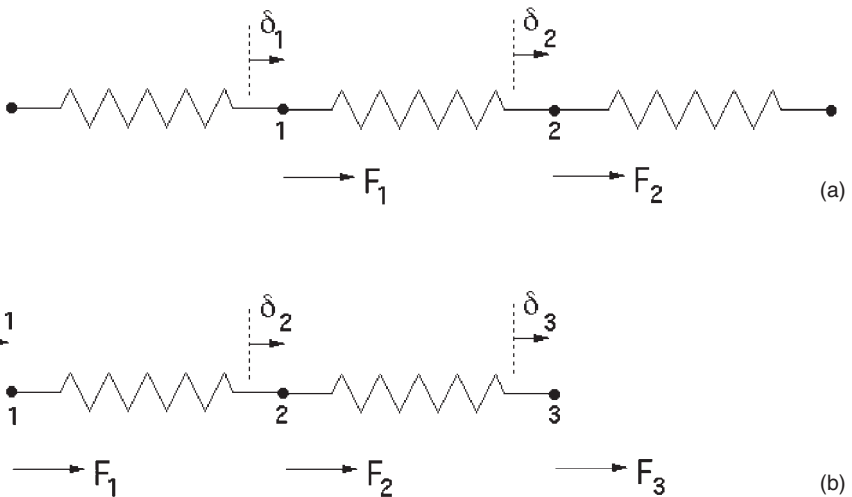


**Fig. 14.15** Forces on springs.

$$\begin{aligned}
 \begin{bmatrix} F_1 \\ F_2 \\ F_3 \end{bmatrix} &= \underbrace{\begin{pmatrix} k_1 & -k_1 & 0 \\ -k_1 & k_1 & 0 \\ 0 & 0 & 0 \end{pmatrix} + \begin{pmatrix} 0 & 0 & 0 \\ 0 & k_2 & -k_2 \\ 0 & -k_2 & k_2 \end{pmatrix}}_{\text{Component stiffnesses}} \begin{bmatrix} \delta_1 \\ \delta_2 \\ \delta_3 \end{bmatrix} \\
 &\equiv \underbrace{\begin{pmatrix} k_1 & -k_1 & 0 \\ -k_1 & k_1 + k_2 & -k_1 \\ 0 & -k_2 & k_2 \end{pmatrix}}_{\text{Overall stiffness}} \begin{bmatrix} \delta_1 \\ \delta_2 \\ \delta_3 \end{bmatrix}.
 \end{aligned}$$

This illustrates how the properties of the simple elements can be combined to yield an overall response function for a more complex body, which is extremely useful when dealing with intricate industrial problems.

## 14.7 NEURAL NETWORKS

The usual approach when dealing with difficult problems is to correlate the results against chosen variables using linear regression analysis; a more powerful method of empirical analysis involves the use of neural networks, which have had tremendous success in the quantitative treatment of structure–property relationships.

In linear regression, fitting data to a specified relationship yields an equation which relates the inputs  $x_j$  via weights  $w_j$  and a constant  $\theta$  to obtain an estimate of the output  $y = \sum_j w_j x_j + \theta$ . Equations like these are used widely in industry, e.g. in the formulation of the *carbon equivalents* which assign the effect of individual solutes in steel on its overall behaviour:

$$\text{CE} = \text{C} + \frac{\text{Mn} + \text{Si}}{6} + \frac{\text{Ni} + \text{Cu}}{15} + \frac{\text{Cr} + \text{Mo} + \text{V}}{5} \quad \text{wt\%}.$$

It is well understood that there is risk in using the relationships beyond the range of fitted data, but the risk is not quantified.

With neural networks, the input data  $x_j$  are again multiplied by weights, but the sum of all these products forms the argument of a flexible mathematical function, often a hyperbolic tangent. The output  $y$  is therefore a non-linear function of  $x_j$ . The exact shape of the hyperbolic tangent can be varied by altering the weights (Fig. 14.16a). The weights are changed systematically until a best-fit description of the output is obtained as a function of the inputs; this operation is known as *training* the network.

Further degrees of non-linearity can be introduced by combining several of these hyperbolic tangents (Fig. 14.16b), so that the neural network method is able to capture almost arbitrarily non-linear relationships.

Figure 14.17 illustrates the complexity of the surface that can be produced when representing the output (vertical axis) as a function of two inputs using just four hyperbolic tangents.

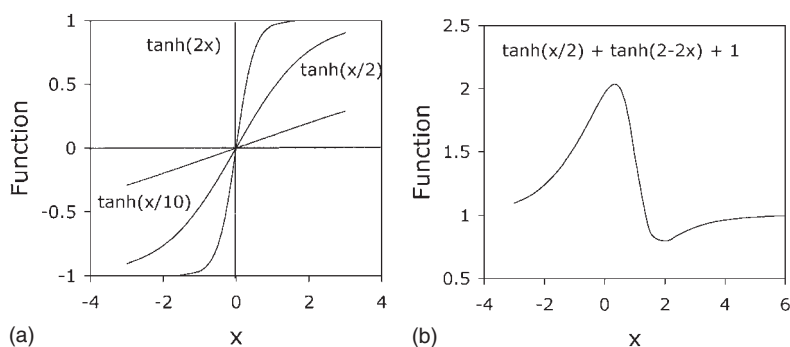


**Fig. 14.16** (a) Three different hyperbolic tangent functions; the 'strength' of each depends on the weights. The diagram shows how flexible a hyperbolic tangent is. (b) A combination of two hyperbolic tangents to produce a more complex model. Such combinations can be continued indefinitely to produce functions of ever greater complexity.

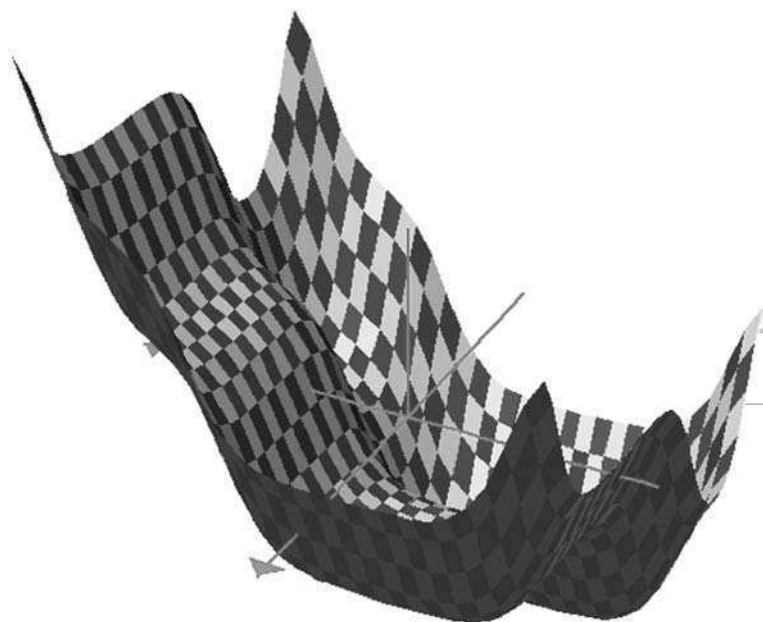


**Fig. 14.17** Variation in the output (vertical axis) as a function of two input variables (horizontal axes), the whole surface being generated using just four hyperbolic tangent functions.

A potential difficulty with the ability to produce complex, non-linear functions is the possibility of overfitting of data. To avoid this difficulty, the experimental data can be divided into two sets, a *training* dataset and a *test* dataset. The model is produced using only the training data. The test data are



then used to check that the model behaves itself when presented with previously unseen data. This is illustrated in Fig. 14.18 which shows three attempts at modelling noisy data for a case where  $y$  should vary with  $x^3$ . A linear model (Fig. 14.18a) is too simple and does not capture the real complexity in the data. An overcomplex function such as that illustrated in Fig. 14.18c accurately models the training data but generalizes badly. The optimum model is illustrated in Fig. 14.18b. The training and test errors are shown schematically in Fig. 14.18d; not surprisingly, the training error tends to decrease continuously as the model complexity increases. It is the minimum in the test error which enables that model to be chosen which generalizes best to unseen data.

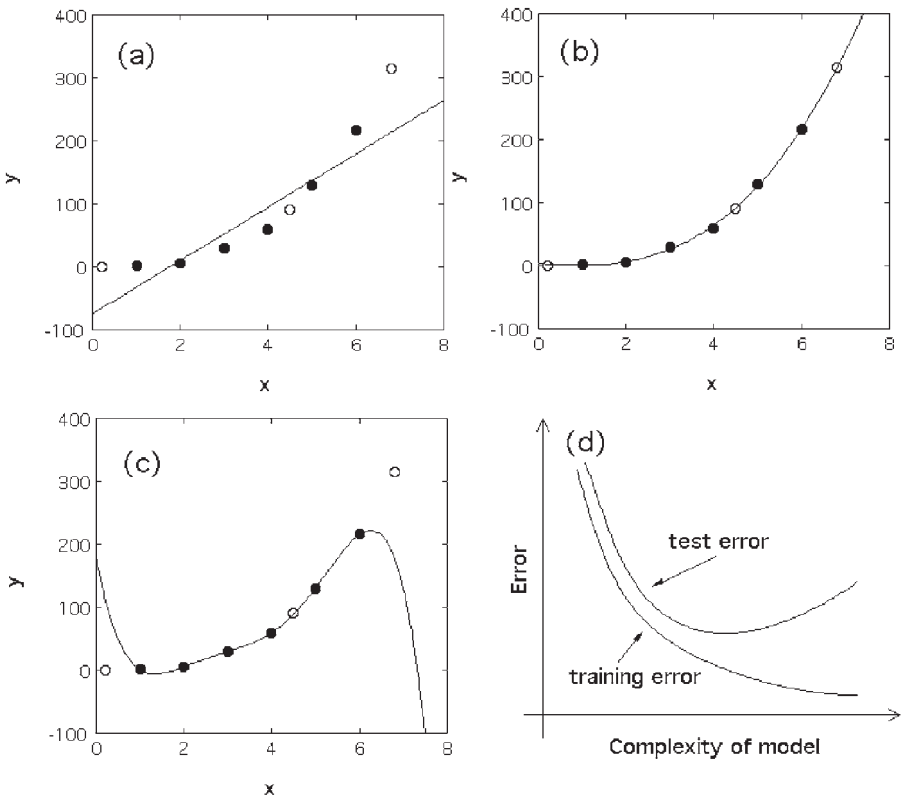


**Fig. 14.18** Variations in the test and training errors as a function of model complexity, for noisy data in a case where  $y$  should vary with  $x^3$ . The filled points were used to create the models (i.e. they represent training data), and the circles constitute the test data. (a) A linear function which is too simple. (b) A cubic polynomial with optimum representation of both the training and test data. (c) A fifth-order polynomial which generalizes poorly. (d) Schematic illustration of the variation in the test and training errors as a function of the model complexity.

A neural network like this can capture interactions between the inputs because the hidden units are non-linear. Appropriate measures must be taken to avoid overfitting. With complex networks it is also important to consider the *modelling uncertainty*, i.e. what is the range of models which can adequately represent the known data? A large modelling uncertainty corresponds to the case where these models behave differently when extrapolated.

## 14.8 DEFINING CHARACTERISTICS OF MODELS

Modelling is a quantitative approach to the design of steels and other materials and processes. It is relevant to ask how it differs from ordinary science which also strives to be quantitative.

The difference lies in the method when faced with a complex problem (Fig. 14.19). The technique of conventional science is to reduce the problem until it can be expressed using rigorous mathematical theory and then to do simplified experiments to validate the theory. This procedure often loses the technology relevant in the original problem, although the method adds to the pool of knowledge.

Modelling by contrast, faces the problem at the level of complexity posed. It begins with wide consultation to identify all the relevant issues. Methods are then assembled and developed, and if necessary combined with empirical techniques to create an overall procedure, taking considerable care to estimate uncertainties. Validation of the model is by testing against unseen data, by creating components and by exposing the software to other applications. In this

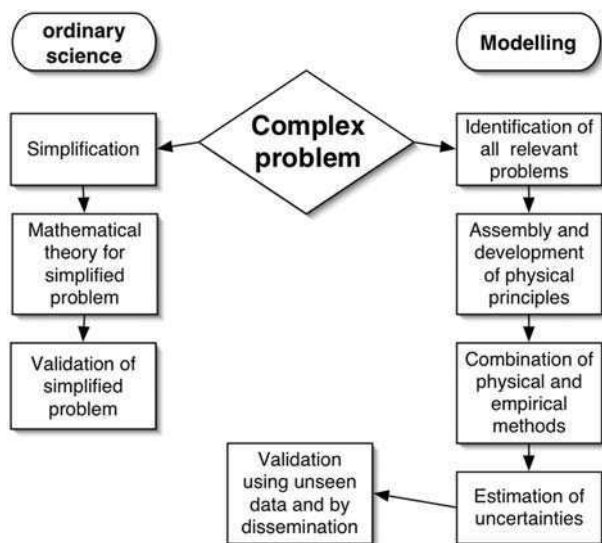


**Fig. 14.19** The defining qualities of a model compared with the conventional scientific method.

way, the technological goal is hopefully achieved, and problems are identified which in the longer term need to be resolved using the scientific approach.

## FURTHER READING

- Ashby, M. F., *Materials Science and Technology* **8**, 102–112, 1992.
- Barber, Z. (ed.), *Introduction to Materials Modelling*, Maney, London, 2005.
- Bhadeshia, H. K. D. H., Neural networks in materials science, *ISIJ International* **39**, 966, 1999.
- Bhadeshia, H. K. D. H. and Svensson, L. -E., *Mathematical Modelling of Weld Phenomena* (eds Cerjak, H. and Easterling, K. E.), Institute of Materials, London, UK, pp. 109–182, 1993.
- Crank, J., *The Mathematics of Diffusion*, 2nd edition, Clarendon Press, Oxford, 1975.
- Cottrell, A. H., *Introduction to the Modern Electron Theory of Alloys*, Institute of Materials, London, 1989.
- Entwistle, K. M., *Basic Principles of the Finite Element Method*, Institute of Materials, London, 1999.
- Lehner, T. and Szekely, J., *Scandinavian Journal of Metallurgy* **19**, 174–181, 1990.
- MacKay, D. J. C., *Information Theory, Inference and Learning Algorithms*, Cambridge University Press, Cambridge, UK, 2003.
- Raabe, D., *Computational Materials Science*, Wiley-VCH, Weinheim, Germany, 1998.
- Takahashi, M. and Bhadeshia, H. K. D. H., *Materials Science and Technology* **6**, 592–603, 1990.
- Young, C. H. and Bhadeshia, H. K. D. H., *Materials Science and Technology* **10**, 209–214, 1994.

# INDEX

---

- $A_1, A_2, A_3, A_4$ , temperatures, 40–1
- acicular ferrite, 155–64
  - austenite grain size effect, 157–61
  - inclusions, 161–2
  - lattice matching, 162–3
  - mechanism, 157–61
  - microstructure, 155–7
  - nucleation, 162–4
  - oxides, 161–2
- allotropes, of pure iron,
  - thin films and isolated particles, 3–4
- alloy carbides, 76–7
  - enthalpies of formation, 76
  - fibrous growth, 87, 90
  - in tempered martensite, 195–203
  - interphase precipitation, 87, 89–91
  - nucleation in ferrite, 87, 91
  - stability, 76
- alloying elements,
  - $\alpha$ -stabilizing, 71–4
  - distribution in steels, 74–7
  - effect on equilibrium diagram, 71–4
  - effect on kinetics of  $\gamma/\alpha$  transformation, 77–83
  - $\gamma$ -stabilizing, 71–4
  - solubility in cementite, 81–2
- annealing,
  - intercritical, 223–4
  - isothermal, 68
  - spheroidize, 68
  - subcritical, 69
- atmospheres, 23–7
  - condensed, 23
- Auger spectroscopy of grain boundaries, 253–6
- ausforming, 232
- austenite, 741–65
  - effect of carbon on lattice parameter, 100–3
  - $\gamma$ -cementite transformation, 44–5
  - $\gamma$ -pearlite transformation, 53–67
  - hardness, 120–2
  - twin boundaries, 45
- austenite–ferrite interfaces,
  - curved, 42–4
  - planar, 42–4, 51
- austenite–ferrite transformation, 42–4
  - effect of alloying elements, 77–83
  - para-equilibrium, 79
  - partition of alloying elements, 78–82
- austenite–pearlite interface, 54–5
- austenitic steels, 259–74
  - chromium carbide in, 264–7
  - corrosion resistance, 273–4
  - Fe–Cr–Ni system, 259–64
  - intermetallic precipitation in, 270–2
  - mechanical properties, 274
  - niobium and titanium carbides in, 267–70
  - nitrides in, 270
  - practical applications, 273–4
  - specifications, 273
  - stacking fault energies, 282
  - titanium carbide in, 267–70
  - work hardening rate, 284
- auto-tempering, 120, 126, 184
- Bain strain, 103–6
- bainite, 129–54
  - alloy design, 141–52
  - atom probe, 135, 136

bainite (*Continued*)

- effect of carbon on bainite transition, 135–9
  - granular, 144–5
  - incomplete reaction, 136–7
  - lower bainite, 132–5
  - nanostructured bainite, 152–4
  - reaction kinetics, 139–42
  - retained austenite, 132
  - role of alloying elements, 146–7
  - shape change, 135
  - tempering, 145–6
  - transition from upper to lower bainite, 143–4
  - $T_0$  curve, 136–8
  - upper bainite, 129–32
- bainitic steels, 141–52
- role of boron, 148
  - role of molybdenum, 148
- blue brittleness, 24–6
- borides, enthalpies of formation, 76
- body-centred cubic ferrite, 4
- brittle fracture, 235–45, 252–7
- cleavage, 235–45
  - intergranular, 252–7
  - practical aspects, 243–5
- burning, 256–7

## CCT (continuous cooling transformation) diagrams, 167–70

C-curve, *see* *TTT* curve

## carbon,

- atmospheres, 23–7
- effect on bainite formation, 146–7
- on hardenability, 176–9
- on impact transition temperature, 210
- on martensite crystallography, 107–12
- on martensite strength, 120–3
- on phase diagram for 18Cr–18 Ni steel, 263
- on tempering, 190, 204–7
- solubility in  $\alpha$ - and  $\gamma$ - iron, 8–11
- strengthening of iron, 20–7

## carbon equivalent, 245

## carbon steels, 67–9

- applications, 69

- mechanical properties, 68
  - tempering behaviour, 184–91
- carbide forming elements, 74–7
- carbide pinning of boundaries, 193–5
- in controlled rolling, 211–14
- carburizing, 15
- cast brittleness, 257
- cementite, 13–14, 39–42
- austenite–cementite transformation, 44–5
  - cementite–austenite orientation relation, 44–5
  - in lower bainite, 134–5
  - in upper bainite, 131–2
  - orientation relation with ferrite, 185
  - precipitation in ferrite, 13–15
  - precipitation in martensite, 186–8, 193–5
- Charpy test, 236
- chromium carbides,
- during tempering, 200–1
  - formed during isothermal transformation, 89–91
  - grain boundary precipitation, 264–5
  - in Cr–Ni austenitic steels, 264–7
  - pseudo-equilibrium diagram, 76–7
  - sequence in tempering, 200
- chromium equivalent, 263
- chromium nitride, in austenite, 270
- chromium steels,
- ausformed, 232–3
  - isothermal transformation, 90
  - properties of 12% Cr steels, 206–7
  - tempering behaviour, 200–1
- cleavage fracture, 235–40
- criterion, 240–3
  - dislocation mechanisms, 237–8
  - effect of fabrication, 235–6
  - grain size, 239–40
  - hydrogen, 245
- factors influencing onset, 237–40
- influence of lath packet width, 242
- nucleation by carbides, 238, 241
- by inclusions, 238
  - by twins, 238
- practical aspects, 243–5
- compressive stresses in surfaces, 178–80

- computer determination of ternary equilibria, 75
- controlled rolling, 210–18
  - boundary pinning, 212
  - carbide precipitation, 23–4
  - dispersion strengthening, 218–20
  - grain size control, 211–16
  - minimum grain size, 216–18
  - properties of steels, 231–2
- controlled transformation stainless steels, 284
- coring of dendrites, 16
- corrosion,
  - intergranular in Cr–Ni steels, 264–7
  - pitting, 273
  - stress, 256, 273–4
- crack nuclei, 237–9
- cracks, 235–58
  - cleavage, 235–6
  - ductile, 245–7
  - hot short, 257
  - hydrogen embrittlement, 245–6
  - intergranular, 252–8
  - lamellar tearing, 250–1
  - overheating and burning, 256–8
  - quenching, 179–81
  - rock candy fracture, 252
  - solidification, 275–6
  - stress corrosion, 256
  - temper embrittlement, 253–6
- critical diameter ( $D_0$ ), 171–2
  - ideal critical diameter ( $D_i$ ), 172, 173
- crystal structure, of martensite, 100–3
- crystallography, of martensitic transformation, 103–6
  - phenomenological theory, 105–6
- Deep drawing steels, 34
- delayed cracking, 245
- delta ferrite, 4, 259
  - effect on stress corrosion of stainless steels, 275–6
  - on nucleation of  $M_{23}C_6$ , 284
- diffusion,
  - activation energies of, 13
  - during  $\gamma/\alpha$  transformation, 45–53
  - during pearlite reaction, 62–5
  - of C in  $\alpha$ - and  $\gamma$ -iron, 11–13
  - of N in  $\alpha$ - and  $\gamma$ -iron, 11–13
  - of substitutional elements in  $\alpha$ - and  $\gamma$ -iron, 11–13
- dislocation locking, 20–7
- dislocation pile-up, 29–30
  - in crack nucleation, 237–40
- dislocation precipitation,
  - in austenitic steels, 264–5, 268
  - ferrite, 13–14, 91
  - tempering, 197–9
- dislocations,
  - in ausforming,
    - ferrite, 19, 23–5, 44, 45
    - martensite, 106–9
    - stainless steels, 268
    - tempered steels, 197–9
  - screw dislocations in iron, 18
- dispersion strengthening, 32–3
  - Ashby equation, 32
  - of austenitic steels, 264–70
  - of HSLA steels, 218–20
  - Orowan equation, 32
- displacive mechanisms, 7
- dual phase steels, 220–3
- Dubé classification, 42
- ductile fracture (fibrous), 245–7
  - dimples and voids, 246–7
  - micro-necks, 247
  - role of carbides, 251
  - role of inclusions, 247–51
- ductility, 247–50
  - role of carbides, 251
  - role of inclusions, 247–50
- dynamic recrystallization, 211
- Electron theory, 322–3
- embrittlement,
  - 475°, 277–8
  - hot short, 257
  - hydrogen, 245
  - intergranular, 252–7
  - overheating and burning, 256–8
  - temper, 253–6
- epsilon martensite ( $\epsilon$ ), in austenitic steels, 282
- equilibrium diagrams
  - Fe–C, 39–41
  - Fe–Cr, 259–60

equilibrium diagrams (*Continued*)

Fe–Cr–C, 260–4

Fe–Cr–Ni, 262–4

Fe–X, 71–4

equivalents, Cr and Ni in austenitic steels, 262–4

eutectoid reaction, 39–42, 54

crystallography of pearlite, 59–60

kinetics, 60–2

morphology of pearlite, 54–9

rate controlling process, 62–5

Face-centred tetragonal iron, 3

fatigue,

effect of ausforming, 232

effect of strain ageing, 34

role of inclusions, 247–50

fatigue limit in steels, 34

ferrite,

austenite–ferrite transformation, 42–4

growth by step migration, 44, 45, 52

growth kinetics, 45–53

orientation relationship with

austenite, 44

planar interfaces, 44, 45

precipitation of carbon and nitrogen, 13–15

quench ageing, 14–15

Widmanstätten, 42–4

ferritic stainless steels, 274–8

fibrous carbides, 85–7, 89

Fick's second diffusion law, 15

finite difference method, 328–9

finite element method, 329–30

fracture, 235–58, 37–8

cleavage, 235–45

ductile, 245–51

intergranular, 252–8

fracture toughness, 241, 243–4

friction stress, 29

Gamma loop, 73, 259–61

gamma prime phase, 270–2

stability of  $\text{Ni}_3\text{Ti}$ , 271

gigatubes, 36–7

grain boundary

allotriomorphs, 42–4, 47–52

cracking, 252–8

precipitation, 188–9, 200, 264–5

segregation, 253–6

grain growth

during controlled rolling, 211

in heat affected zone, 277

grain size,

effect on fracture stress, 242–3

hardenability, 176–7

Hall–Petch effect, 27–30

nanostuctured steels, 30–2

refinement, 68–9

strength of martensite, 123–4

yield stress, 214–16

granular bainite, 144–5

Griffith criterion for fracture, 240

Grossman test, 171–3

*H*-coefficient, 172–3

habit plane, 96–7

Hadfields steel, 261, 282

Hall–Petch relationship, 27–8,  
124, 214

hardenability, 168, 170–9

effect of composition, 176–7

effect of grain size, 176–7

Grossman test, 171–3

Jominy test, 173–6

testing, 171–6

hardenability band (Jominy), 173–6

hardness

of martensite, 120

of tempered C steels, 188–9, 191

of tempered alloy steels, 195–7, 204–7

Holloman–Jaffe parameter, 197

homogenizing, 13–14, 16

hot-rolling process, 209

Hultgren extrapolation, 63–4

hydrogen embrittlement, 245

Idiomorphs, 42

impact transition curves, 66–8, 210,  
235–6

impurity drag, 79

inclusions, 247–50

categories, 248

role in ductile fracture, 245–8

types of MnS, 248

- in situ* nucleation
  - of alloy carbides, 197–9
  - of cementite, 187
- intergranular corrosion in austenitic steels, 264–5, 274
- intergranular fracture, 252–8
  - effect of P, Sb, Sn, 255–6
  - hot shortness, 257
  - overheating and burning, 256–8
  - temper embrittlement, 253–6
- intermetallic precipitation
  - in austenite, 270–2
  - $\gamma'/\text{Ni}_3(\text{AlTi})$ , 271–2
  - sigma phase, 272, 277–8
- internal friction, 11, 124–5
  - for determination of soluble carbon and nitrogen, 11
  - determining diffusivities, 11
  - of martensite, 125
- interphase precipitation, 87, 89–91
  - in micro-alloyed steels, 218–20
  - precipitate sheet spacing, 88–91
- interstices
  - in  $\alpha$ -iron, 4–8
  - in  $\gamma$ -iron, 4–8
- interstitial
  - atmospheres, 23–6
  - atoms, 8–10
  - solid solutions, 8–10
    - strengthening, 20–27
  - yield point phenomena, 21–6
- iron,
  - bcc structure, 4
  - deformation, 18–19
  - fcc structure, 4
  - flow stress temperature dependence, 18–19
  - orientation relationship with ferrite (Jack), 185
  - slip systems in  $\alpha$ -iron, 18
  - strengthening, 17 *et seq.*
  - work hardening, 18–20
    - $\epsilon$ -iron carbide, 13–14, 184–6
- iron–carbon alloys, 1–16, 39–66
  - austenite–cementite reaction, 44
  - austenite–ferrite reaction, 42–4
  - equilibrium diagram, 39–42
  - eutectoid reaction, 41–2, 53–9
  - kinetics of transformation, 45–53
- iron–chromium system, 259–61
- iron–chromium–nickel system, 259–64
- isothermal transformation of alloy steels, 91–2
  - of plain carbon steels, 46
- Izod test, 236
- Johnson Mehl equation, 60–1
- Jominy test, 173–6
  - Jominy hardness–distance curves, 173
- Kinetics, 326–9
  - finite difference method, 328–9
- Lattice invariant deformation, 106
- Liberty ships, brittle fracture, 243–4
- Lifshitz–Wagner theory of coarsening, 195–6, 271
- limits to strength,
  - fracture, 37–8
  - gigatubes, 36–7
  - theoretical strength, 35–6
- local fracture stress ( $\sigma_f$ ), 243
- lower bainite, 132–5
  - cementite in, 135
  - change of habit plane with temperature, 143–4
  - growth of plates, 135
  - lath size, 132–3
  - morphology and crystallography, 132
- Luders bands, 21–4
  - extension, 21–2
  - propagation, 21–2
- $M_d$  temperature, 118, 281–5
- manganese sulphide
  - formed in overheating and burning, 256–8
  - inclusions, Types I, II and III, 247–50
- maraging, 207
- martensite, 26, 95 *et seq.*
  - age-hardening, 120
  - burst phenomenon, 106, 111, 115
  - characteristics, 95–100
  - crystal structure, 100–3
  - dislocation density, 108–9, 123
  - habit plane, 96–7, 110–12, 120



- martensite (*Continued*)
  - hardness, 120
  - high carbon, 111–12
  - interface structure, 98
  - isothermal, 115
  - loss of tetragonality, 184–6
  - low carbon, 110
  - medium carbon, 110–111
  - orientation relationships, 97–8
  - pinning of dislocations in, 125–6
  - shape deformation, 98–100
  - temperature dependence of flow stress, 125–6
  - tetragonality, 100–3, 185–8, 193–4
  - twins in, 108–9
  - yield strength, 120–4
- martensite nuclei, 112–16
  - classical theory, 112–16
  - Olson and Cohen theory, 115
- martensite start temperature ( $M_s$ ), 95, 112, 116, 284–5
- martensite strength, 120–6
  - effect of austenite grain size, 124
  - effect of carbide precipitation, 120–2
  - effect of carbon content, 120–3
  - effect of plate size, 124–5
  - Fleischer theory, 123
- martensitic transformation
  - Bain strain, 103–5
  - crystallography, 103–6
  - effect of alloying elements, 116–18
  - effect of deformation, 118–19
  - kinetics, 112–20
  - mechanical stabilization, 119–20
  - morphology, 106–12
  - role of slip and twinning, 106–10
  - shape memory effect, 126–7
  - stabilization, 119–20
  - surface displacements, 89
  - two-shear theory, 106
- mechanical alloying, 278
- mechanical properties of steels,
  - alloy, 190–1, 192
  - ausformed, 232–3
  - austenitic, 273–4, 283–4
  - carbon, 190–1, 192
  - controlled transformation, 284–5
  - ferrite–pearlite, 67–9
  - high strength low alloy, 214, 216, 231–3
  - iron–alloy crystals, 27
  - martensite, 120–4
  - mild steel, 30
  - quench-aged iron, 14–15
  - TRIP, 285
- mechanical twinning, 229
- Metastable austenite, 283–5
  - transformation of, 284
- micro-alloyed steels (high strength low alloy steels), 210–20, 244
  - applications, 231–2
  - contributions to strength, 220
  - effect of austenitizing temperature, 213–16
  - final grain size, 213–16
  - Hall-Petch relation, 214
  - mechanical properties, 220, 231–2
  - role of stoichiometry, 218
  - suppression of yield point, 220
- modelling, 307–334
  - alloy design, 309–15
  - characteristics, 333–4
  - electron theory, 322–3
  - finite difference method, 328–9
  - finite element method, 329–30
  - flow chart, 307–8
  - kinetics, 326–9
  - mechanical properties, 315–21
  - methods, 321–6
  - neural networks, 330–3
  - phase diagram, calculations and thermodynamics, 323–6
  - physical models, 307
  - regression analysis, 307
  - target precision, 307
- molybdenum carbide
  - formed in isothermal transformation, 85–6
  - formed in tempering, 199, 202
  - orientation relationship with ferrite, 201
  - transformation to other carbides, 199, 202
- Nanostructured bainite, 152–4
- nanostructured steels, 30–2

- neural networks, 330–3
- nickel equivalent, 263
- niobium carbide,
  - in austenitic steels, 267–70, 273–4
  - in micro-alloyed steels, 68–9, 213–20, 231
  - in tempered steels, 203–4
- nitride formers, 34, 76
- nitrides,
  - enthalpies of formation, 77
  - in  $\alpha$ -iron, 14–15
  - in austenitic steels, 270
  - in micro-alloyed steels, 211–12
  - solubilities in austenite, 85
- nitriding, 15–16
- nitrogen,
  - alloying elements, 71, 76, 262, 263
  - solubility in  $\alpha$ - and  $\gamma$ -iron, 8–11
- normalizing, 67
- nucleation,
  - in situ*, 186, 197–9
  - of alloy carbides, 89–91, 197–9
  - of iron carbides, 185–6
  - of pearlite, 55–6
  - on dislocations, 13–14, 24–5, 197–9, 264–8
- Ostwald ripening of cementite, 188
- overheating, 256–8
- oxidation resistance,
  - Cr–Ni austenitic steels, 273
- Para-equilibrium, 79–80
- partition of alloying elements, 78–82
- pearlite,
  - alloy carbides in, 82–3
  - Bagaryatski relation, 59–60
  - crystallography, 59–60
  - directional growth, 58
  - effect of alloying elements on kinetics, 80–2
  - effect on ductility, 63
  - effect on toughness, 63
  - kinetics, 60–2
  - lamellar spacing, 56–9
  - morphology, 54–9
  - Pitsch–Petch relation, 59–60
  - rate controlling process, 62–5
  - rate of growth, 60–5
  - rate of nucleation, 60–2
  - strength, 34, 65–7
- pearlitic steels, 67–9
- Peierls–Nabarro stress, 18, 126, 237–8
- phase diagram calculations and thermodynamics, 323–6
- phase transformation  $\gamma/\alpha$ , 4–8
  - transformation mechanism, 7–8
- phenomenological theory, of martensite crystallography, 105–6
- pitting corrosion, 273
- precipitation,
  - alloy carbides during  $\gamma/\alpha$  transformation, 88–91
  - alloy nitrides in austenite, 270
  - cementite in martensite, 184–6
  - during tempering, 195–203
  - in austenite, 264–70
  - in ferrite, 91
  - intermetallics in austenite, 270–2
    - in ferrite, 207
  - $\varepsilon$ -iron carbide in martensite, 184–6
  - iron carbide in  $\alpha$ -iron, 13–15
  - iron nitrides in  $\alpha$ -iron, 14–15
- precipitation on dislocations
  - in austenite, 265, 267–70
  - in ferrite, 13–14, 86–7, 91, 218
- pseudo-binary diagrams, 76–7
- pure iron, 1
  - allotropes, 2–4
- Quench ageing, 14–15
- quench cracking, 179–81
- quenching media, 171–3, 179
- quenching stresses, 179–81
- Recalescence, 218
- recovery, in ferrite, 189
- recrystallization,
  - of austenite, 211–14, 215
  - of ferrite, 188–9
- retained austenite, 96, 110–11, 130–2, 184, 186, 193–4
- rock candy fracture, 252, 257

- Schaeffler diagram, 262–4  
secondary hardening, 195–7  
  Cr steels, 200–1  
  Mo and W steels, 201–3  
  V steels, 199–200  
segregation,  
  in cast steel, 16  
  to grain boundaries, 254–6, 257  
sensitization, 266–7  
severity of quench ( $H$ -coefficient), 171–2  
shallow hardening, 178–9  
shape deformation, 98–100, 126–7  
shape memory effect, 126–7  
shelf energy, 249–50  
sigma phase ( $\sigma$ ), 272, 277–8  
Snoek peak, 11, 124–5  
soaking pits, 16  
solid solution,  
  elastic behaviour of solute and solvent, 27  
  Hume-Rothery size effect, 27  
  interstitial, 9–10  
  substitutional, 9–10, 27  
solid solution strengthening, 20–32  
  interstitial, 20–7  
  substitutional, 27  
solidification cracking, 275–6  
solubility products of carbides and nitrides, 85–6, 212  
solute trapping, 7  
stabilization,  
  austenitic steels, 266  
  during martensite transformation, 120  
  mechanical, 119–20  
stacking fault energy of austenite, 282  
stacking faults in austenitic steels, 268–9  
stainless steels, 259–86  
  austenitic, 259–74  
  carbides in, 264–70  
  controlled transformation, 284–5  
  corrosion behaviour, 264–5, 274–6  
  duplex, 274–6  
  ferritic, 274–8  
  intermetallic precipitation in, 270–2  
  nitrides in, 270  
  superduplex, 276  
  steels (industrial),  
    ausformed, 232–3  
    austenitic, 273–4  
    bainitic, 147–52  
    carbon, 67–9  
    controlled transformation, 284–5  
    hardenability, 167–81  
    high strength low alloy (HSLA), 210–11  
    mechanical properties of  
      alloy steels, 203–7  
      carbon steels, 190–1  
    thermomechanical treatments, 213–14, 231–3  
    TRIP, 284–5  
steels for low temperatures, 244–5  
stoichiometric ratio for TiC and NbC, 267–8  
stoichiometry, effect on precipitation of TiC, 219  
strain ageing, 23–4  
  dynamic, 24, 26  
strengthening of iron,  
  dispersion, 14–15, 32–3  
  grain size, 27–32  
  solid solution (interstitial), 20–7  
  solid solution (substitutional), 26–7  
  work hardening, 18–20  
stress,  
  critical local fracture stress, 241–3  
  effective shear stress (Fe crystals), 19  
  effective shear stress (crack nucleation), 241  
  flow stress of iron, 18–20  
  friction, 29  
  yield, 21–6  
stresses in heat treatment, 179–81  
stress corrosion, 256, 273, 276  
stress intensity factor ( $K$ ), 236–7, 241  
  critical ( $K_{IC}$ ), 241  
superplasticity in duplex stainless steels, 275–6  
  
*TTT* (time temperature transformation)  
  diagrams,  
    alloy steels, 91–2, 168–7  
    plain carbon steel, 45–7

- temper embrittlement, 253–6
  - inter-element effects, 254–5
  - optimum temperature, range, 256
  - role of carbide particles, 255–6
  - segregation of alloying elements, 254–6
  - use of Auger spectroscopy, 253–5
- tempered martensite embrittlement, 194, 204–5
- tempering, 183–207
  - alloy steels, 191–207
  - chromium steels, 201
  - molybdenum and tungsten steels, 201–3
  - plain carbon steels, 184–90
  - vanadium steels, 199–200
- tempering of alloy steels, 191–207
  - carbide transformation, 200–3
  - coarsening of cementite, 194–5
  - complex steels, 203
  - mechanical properties, 204–7
  - nucleation of alloy carbides, 197–9
  - retained austenite, 193–4
  - role of dislocations, 197–9
  - secondary dispersions, 204–6
  - temper embrittlement, 253–6
  - tempered martensite embrittlement, 193–4
- tempering of carbon steels,
  - activation energies, 189
  - coarsening of cementite 188–9
  - effect of carbon, 190
  - grain boundary cementite, 186–8
  - mechanical properties, 190–1
  - nucleation and growth of  $\text{Fe}_3\text{C}$ , 186–8
  - precipitation of  $\epsilon$ -iron carbide, 184–5
  - recrystallization of ferrite, 189
- temper rolling, 34
- tetragonality of martensite, 100–3
  - changes during tempering, 184–6, 193–4
- thermal stresses, 179
- thermionic emission microscopy, 45–53
- thermodynamics, 324
- thermomechanical treatment, 209–34
  - controlled rolling, 210–20
- thin films and isolated particles, 3–4
- titanium carbide,
  - in austenitic steels, 267–70, 274
  - micro-alloyed steels, 68–9, 218–20, 231
- TTT* curves for precipitation, 268
- transformation mechanism, 7–8
- transformation stresses, 4, 179
- transition temperature (ductile brittle ( $T_c$ )), 67–8, 210, 236–7
  - effect of grain size, 239–40
- TRIP-assisted steels, 223–9
  - Cold-rolled strip, 223–4
  - galvanization, 227–9
  - hot-rolled strip, 224
  - low or zero-silicon, 226–7
- TRIP steels, 284–5
- tungsten carbide,
  - formed during tempering, 201–3
  - orientation relationship with ferrite, 201–2
  - transformation to other carbides, 201–2
- twinning,
  - in austenite, 282
  - in martensite, 109–10
- TWIP steels, 229–30
- Upper bainite, 129–32
  - cementite in, 132
  - growth of plates, 139–40
  - morphology and crystallography, 129–32
- underbead cracking, 245
- Vacancies,
  - in austenitic steels, 267–70
  - in coarsening of  $\text{Fe}_3\text{C}$ , 188–9
  - trapping of by phosphorus, 268–70
- vanadium carbide,
  - formed during isothermal transformation, 89–91
  - formed during tempering, 199–200
  - in micro-alloyed steels, 218–20
  - orientation relationship with ferrite, 199
- Welding,
  - as-deposited microstructure, 289–90
  - acicular ferrite, 289
  - allotriomorphic ferrite, 291–2
  - carbon equivalent, 296–7

**Welding (*Continued*)**

effect of carbon, 294

epitaxial solidification, 287–8

heat-affected zone,

coarse austenite grains, 299, 300–5

fine austenite grains, 299, 305–6

heat flow, 298–9

local brittle zones, 306

partially austenitised zone, 306

tempered regions, 299–300

HSLA steels, 210–11

hydrogen embrittlement, 245

lamellar tearing, 250

microphases, 289–98

multirun, 289

retained austenite, 289

Schaeffler diagram, 262–4,

sensitivity to carbon, 294–8

solidification, 288

solidification cracking 275–6

stainless steels

austenitic, 273–4

duplex, 274–8

ferritic, 274–8

weld zone cracks, 245–6

Widmanstätten ferrite, 292–4

weld-decay, 274

Wever classification, 71

Widmanstätten precipitation,

alloy carbides, 89, 199–201,

267–70

cementite, 44–5, 81–2

ferrite, 42–4, 91

Yield drop, 26

yield point, 21–6

Cottrell–Bilby theory, 23–4,

238

Gilman–Johnson theory, 24–6, 238

in mild steel, 24–5

lower, 21

Luders band, 21

strain ageing, 21, 22

stretcher strains, 21

upper, 21

Zener–Hillert equation, 51–2